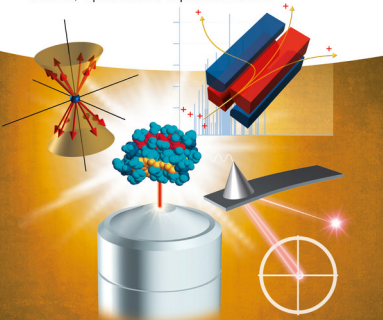


Peter Jomo Walla

# Modern Biophysical Chemistry

Detection and Analysis of Biomolecules

Second, Updated and Expanded Edition





*Peter Jomo Walla*

**Modern Biophysical  
Chemistry**

## ***Related Titles***

Kubitscheck, U. (ed.)

### **Fluorescence Microscopy From Principles to Biological Applications**

2013

ISBN: 978-3-527-32922-9 (Also available  
in a variety of electronic versions)

Murphy, D.B., Davidson, M.W.

### **Fundamentals of Light Microscopy and Electronic Imaging**

Second Edition

2013

ISBN: 978-0-471-69214-0 (Also available  
in a variety of electronic versions)

Gault, V.V.

### **Understanding Bioanalytical Chemistry Principles and Applications**

2008

ISBN: 978-0-470-02907-7 (Also available  
in a variety of electronic versions)

Sheehan, D.

### **Physical Biochemistry Principles and Applications**

Second Edition

2009

ISBN: 978-0-470-85603-1 (Also available  
in a variety of electronic versions)

*Peter Jomo Walla*

# **Modern Biophysical Chemistry**

Detection and Analysis of Biomolecules

Second, Updated and Expanded Edition

**WILEY-VCH**  
Verlag GmbH & Co. KGaA

### **The Author**

**Prof. Dr. Peter Jomo Walla**

University of Braunschweig  
Institute of Physical and Theoretical  
Chemistry  
Hans-Sommerstr. 10  
38106 Braunschweig  
Germany

and

Max-Planck-Institute for  
Biophysical Chemistry  
Am Faßberg 11  
37077 Göttingen  
Germany

The reproduction of the figures in this book  
was kindly supported by Silke Lubahn.

All books published by **Wiley-VCH** are carefully produced. Nevertheless, authors, editors, and publisher do not warrant the information contained in these books, including this book, to be free of errors. Readers are advised to keep in mind that statements, data, illustrations, procedural details or other items may inadvertently be inaccurate.

**Library of Congress Card No.:** applied for

**British Library Cataloguing-in-Publication Data**

A catalogue record for this book is available from the British Library.

**Bibliographic information published by the  
Deutsche Nationalbibliothek**

The Deutsche Nationalbibliothek lists this publication in the Deutsche Nationalbibliografie; detailed bibliographic data are available on the Internet at <http://dnb.d-nb.de>.

© 2014 Wiley-VCH Verlag GmbH & Co. KGaA,  
Boschstr. 12, 69469 Weinheim, Germany

All rights reserved (including those of translation into other languages). No part of this book may be reproduced in any form – by photostriping, microfilm, or any other means – nor transmitted or translated into a machine language without written permission from the publishers. Registered names, trademarks, etc. used in this book, even when not specifically marked as such, are not to be considered unprotected by law.

**Print ISBN:** 978-3-527-33773-6

**ePDF ISBN:** 978-3-527-68354-3

**ePub ISBN:** 978-3-527-68355-0

**Mobi ISBN:** 978-3-527-68356-7

**oBook ISBN:** 978-3-527-68350-5

**Cover Design** Grafik-Design Schulz,  
Fußgönheim, Germany

**Typesetting** Thomson Digital, Noida, India

**Printing and Binding** Markono Print Media Pte Ltd.,  
Singapore

Printed on acid-free paper

*To my wonderful wife Uli and my great kids Christian,  
Maike, Paul and Johanna*



## Contents

### Foreword to the Second Edition *XIII*

#### **Introduction 1**

What is Biophysical Chemistry? – An Example from Drug Screening 1

### **Part One Basic Methods in Biophysical Chemistry 11**

#### **1 Basic Optical Principles 13**

1.1 Introduction 13

1.2 What Does the Electronic Structure of Molecules Look Like?

Orbitals, Wave Functions and Bonding Interactions 15

1.3 How Does Light Interact with Molecules? Transition Densities and the Transition Dipole Moment 20

1.4 Absorption Spectra of Molecules in Liquid Environments.

Vibrational Excitation and the Franck–Condon Principle 24

1.5 What Happens After Molecules have Absorbed Light? Fluorescence, Nonradiative Transitions and the Triplet State 27

1.6 Quantitative Description of all Processes: Quantum Efficiencies, Kinetics of Excited State Populations and the Jablonski Diagram 33  
Problems 38

Bibliography 39

#### **2 Optical Properties of Biomolecules 41**

2.1 Introduction 41

2.2 Experimental Determination of Absorption and Fluorescence Spectra 41

2.3 Optical Properties of Proteins and DNA 45

2.3.1 Intrinsic Absorption and Fluorescence of Amino Acids, Peptides and Proteins 45

2.3.2 Intrinsic Absorption of Nucleotides, DNA and RNA 47

2.4 Optical Properties of Important Cofactors 49

2.4.1	Haem	49
2.4.2	Nicotinamide Adenine Dinucleotides	52
2.4.3	Flavins	53
2.4.4	Chlorophylls	54
2.4.5	Carotenoids	56
	Problems	58
	Bibliography	58
<b>3</b>	<b>Basic Fluorescence Techniques</b>	<b>61</b>
3.1	Introduction	61
3.2	Fluorescent Labelling and Linking Techniques	61
3.2.1	Primary Amino Group Reactive Labels	63
3.2.2	Thiol Group Reactive Labels	64
3.2.3	Avidin–Biotin Techniques	65
3.2.4	His-Tag	66
3.2.5	Thiolinkers and Gold Surfaces	67
3.2.6	Fluorescent Proteins	67
3.3	Fluorescence Detection Techniques	68
3.4	Fluorescence Polarization Anisotropy	70
3.4.1	Principles and Theoretical Background	70
3.4.2	Application Example: Receptor–Ligand Interactions	78
3.4.3	Application Example: Estimation of Molecular Mass	79
3.4.4	Application Example: Enzyme Function and Kinetics	80
3.4.5	Application Example: Enzyme Inhibition, Activation and Regulation	83
3.5	Förster Resonance Energy Transfer	84
3.5.1	Principles and Theoretical Background	84
3.5.2	Application Examples	90
3.6	Fluorescence Kinetics	93
3.7	Fluorescence Recovery after Photobleaching	98
3.8	Biochemiluminescence	99
	Problems	100
	Bibliography	103
<b>4</b>	<b>Chiroptical and Scattering Methods</b>	<b>105</b>
4.1	Chiroptical Methods	105
4.1.1	Circular Dichroism (CD)	105
4.1.2	Optical Rotatory Dispersion	107
4.2	Light Scattering	109
4.2.1	Scattering of Light at Molecules Smaller than the Optical Wavelength	110
4.2.2	Scattering of Light at Particles Equal to or Larger than the Optical Wavelength	112
4.2.3	Dynamic Light Scattering	115
4.3	Vibrational Spectra of Biomolecules	115

Problems	118
Bibliography	119
<b>5</b>	<b>Magnetic Resonance Techniques</b> 121
5.1	Nuclear Magnetic Resonance of Biomolecules 121
5.1.1	Principles 121
5.1.2	Theoretical Framework 123
5.1.3	Primary Information Deduced from NMR Spectra 125
5.1.4	Pulsed NMR Spectroscopy 126
5.1.5	Two-Dimensional NMR Spectroscopy 130
5.1.6	Correlated Spectroscopy (COSY) 130
5.1.7	Nuclear Overhauser Effect and NOESY Spectra 135
5.1.8	NMR-Based Structural Analysis of Biomolecules 138
5.2	Electron Paramagnetic Resonance 141
	Problems 145
	Bibliography 147
<b>6</b>	<b>Mass Spectrometry</b> 149
6.1	Introduction 149
6.2	MALDI-TOF 149
6.2.1	Ionization 149
6.2.2	Analyser 152
6.2.3	Detector 153
6.2.4	Signals and Signal Improvements 154
6.3	ESI-MS 156
6.3.1	Ionization 156
6.3.2	Analyser and Detection 158
6.3.3	Signals and Signal Improvements 161
6.4	Structural and Sequence Analysis Using Mass Spectrometry 163
	Problems 164
	Bibliography 165
<b>Part Two Advanced Methods in Biophysical Chemistry 167</b>	
<b>7</b>	<b>Fluorescence Microscopy</b> 169
7.1	Introduction 169
7.2	Conventional Fluorescence Microscopy 169
7.2.1	Confocal Fluorescence Microscopy 169
7.2.2	Laser Scanning Microscopy 174
7.2.3	Wide-Field Fluorescence Microscopy 174
7.3	Total Internal Reflection Fluorescence Microscopy 176
7.4	Light-Sheet Microscopy 178
	Problems 180
	Bibliography 181

<b>8</b>	<b>Super-Resolution Fluorescence Microscopy</b>	<i>183</i>
8.1	Stimulated Emission Depletion (STED) Microscopy	<i>184</i>
8.2	Photoactivated Localization Microscopy (PALM) and Stochastic Optical Reconstruction Microscopy (STORM)	<i>187</i>
8.3	3D Super-Resolution Fluorescence Microscopy	<i>190</i>
8.3.1	3D-STED	<i>190</i>
8.3.2	3D-PALM/STORM	<i>191</i>
8.4	Imaging of Live Cells	<i>191</i>
8.4.1	Observation Duration	<i>192</i>
8.4.2	Irradiation Intensity	<i>193</i>
8.4.3	Imaging Depths	<i>194</i>
8.4.4	Labelling Conditions	<i>194</i>
8.5	Multicolour Super-Resolution Fluorescence Microscopy	<i>195</i>
8.6	Structured Illumination Microscopy	<i>195</i>
8.7	SOFI	<i>197</i>
8.8	Final Comparison	<i>199</i>
	Problems	<i>201</i>
	Bibliography	<i>202</i>
<b>9</b>	<b>Single-Biomolecule Techniques</b>	<i>203</i>
9.1	Introduction	<i>203</i>
9.2	Optical Single-Molecule Detection	<i>203</i>
9.2.1	Application Example 1: Observation of the Rotation of Single ATPase Complexes	<i>206</i>
9.2.2	Application Example 2: Single-Molecule Observation of the Elementary Steps of Biomolecular Motors	<i>209</i>
9.3	Fluorescence Correlation Spectroscopy	<i>213</i>
9.3.1	Autocorrelation Analysis and Observable Key Parameters	<i>214</i>
9.3.2	Autocorrelation Analysis, Mathematical Background	<i>220</i>
9.3.3	Quantitative Determination of Important Parameters from Autocorrelation Curves	<i>221</i>
9.3.3.1	Relationship Between Volume and Molecular Mass of a Protein and its Diffusion Time	<i>222</i>
9.3.3.2	Two-Dimensional Diffusion and Active Transport	<i>222</i>
9.3.3.3	Mixtures of Fluorescing Particles	<i>223</i>
9.3.4	Further Correlation Effects	<i>224</i>
9.3.5	Cross-Correlation Analysis	<i>226</i>
9.4	Optical Tweezers	<i>230</i>
9.4.1	Theoretical Background	<i>230</i>
9.4.2	Application Examples	<i>236</i>
9.4.2.1	Unfolding of RNA and DNA Hairpins	<i>236</i>
9.4.2.2	RNA Polymerase	<i>238</i>
9.4.2.3	DNA-Polymerase	<i>239</i>
9.5	Atomic Force Microscopy of Biomolecules	<i>240</i>
9.5.1	Principle of an AFM	<i>241</i>

9.5.2	Application Examples	242
9.5.2.1	Unfolding of DNA Hairpins	242
9.5.2.2	Receptor–Ligand Binding Forces	244
9.5.2.3	Protein Unfolding	244
9.6	Patch Clamping	245
9.6.1	Ion Channels	245
9.6.2	Patch Clamp Configurations	246
	Problems	250
	Bibliography	254
<b>10</b>	<b>Ultrafast- and Nonlinear Spectroscopy</b>	257
10.1	Introduction	257
10.2	Nonlinear Microscopy and Spectroscopy	258
10.2.1	Multiphoton Excitation	258
10.2.2	Advantages and Disadvantages of Two-Photon Excitation in Fluorescence Microscopy	259
10.2.3	How are Nonlinear Optical Signals Observed From Biological Samples?	262
10.2.4	Further Distinct Properties and Advantages of Two-Photon Excitation	263
10.2.5	Wavemixing and Other Nonlinear Optical Techniques	266
10.3	Ultrafast Spectroscopy	270
10.3.1	Pump–Probe Spectroscopy	270
10.3.2	Application Example: Ultrafast Light-Harvesting and Energy Conversion in Photosynthesis	274
10.3.2.1	Chlorophyll <i>b</i> → Chlorophyll <i>a</i> → Reaction Centre Energy Flow	276
10.3.2.2	Carotenoid → Chlorophyll Energy Flow	278
	Problems	280
	Bibliography	282
<b>11</b>	<b>DNA Sequencing and Next-Generation Sequencing Methods</b>	285
11.1	Sanger Method	285
11.2	Next-Generation Sequencing Methods	287
11.2.1	Dye Sequencing (Approach I)	289
11.2.2	Sequencing by Ligation, Pyrosequencing and Ion Semiconductor Sequencing (Approaches II to IV)	292
11.2.2.1	Emulsion PCR	292
11.2.2.2	Sequencing by Ligation (Approach II)	294
11.2.2.3	Pyrosequencing (Approach III)	296
11.2.2.4	Ion Semiconductor Sequencing (Approach IV)	297
11.2.3	Single-Molecule Real-Time Sequencing (Approach V)	299
	Problems	300
	Bibliography	301
<b>12</b>	<b>Special Techniques</b>	303
12.1	Introduction	303

12.2	Fluorescing Nanoparticles	303
12.3	Surface Plasmon Resonance Detection	308
12.4	DNA Origami	310
12.5	DNA Microarrays	314
12.6	Flow Cytometry	317
12.7	Fluorescence <i>In Situ</i> Hybridization	319
12.8	Microspheres and Nanospheres	320
	Problems	321
	Bibliography	321
<b>13</b>	<b>Assay Development, Readers and High-Throughput Screening</b>	<b>323</b>
13.1	Introduction	323
13.2	Assay Development and Assay Quality	323
13.3	Microtitre Plates and Fluorescence Readers	326
13.4	Application Example: Drug Discovery and High-Throughput Screening	332
	Problems	336
	Bibliography	337
	<b>Index</b>	<b>339</b>

## Foreword to the Second Edition

It has now been five years since the first edition of this book entitled “Modern Biophysical Chemistry” appeared and of course it was high time that this book was updated with the latest exciting developments that are now established enough to be included in a text book. As already mentioned in the first edition, the field of biophysical chemistry is huge, covering aspects of chemistry, biology, physics and even medicine and so it is not easy to assess which aspects are really the most important ones that must be included. As for the first edition, I have tried to make a selection of methods and application examples that contain general concepts that also cover the basis for most of the techniques and applications that are not considered explicitly in the book. Since this selection can be done in many different ways I ask those who are disappointed that their method or application is not explicitly included here to excuse me. The goal was a book that allows a comparatively quick insight to be gained into the very large range of possibilities provided by modern biophysical chemistry, while still being detailed enough to use this knowledge for the first steps in actually applying it for research.

Amongst the important developments of recent years are certainly significant improvements achieved in DNA sequencing by next-generation methods as well as super-resolution microscopy that goes beyond the resolution of conventional, diffraction-limited microscopy. Therefore, these two developments are now represented by two, entirely new chapters in the book. Also, other new developments have been included, such as light-sheet microscopy, introduced now in Chapter 7, and DNA origami techniques in Chapter 12. In addition, new problems have been added. To further improve the clarity many figures have been coloured and, in general, we have made major efforts to optimize the clarity and conciseness throughout the entire book. To help readers focus on the important equations in all mathematical subjects they are now marked by black boxes throughout the entire book.

I would like to thank again all persons who helped me to improve the first edition and of course also those who helped me with the second edition with their very useful and often essential comments.

Special thanks go to Dr Stefan Bode, Dr Anna Cypionka, Professor Dr Christian Eggeling, Professor Dr Jörg Enderlein, Dr Jan Frähmcke, Professor Dr Karl-Heinz

Gericke, Matthias Grunwald, Dr Ulrich Haupts, Dr Hendrik Hippchen, Professor Dr Henrike Heise, Christoph-Peter Holleboom, Chao-Chen Lin, Dr Martin Michels, Professor Dr Philipp Oesterhelt, Dr Wiebke Pohl, Professor Dr Christoph Schmidt, Sabrina Schröder, Professor Dr Jakob Sørensen, Professor Dr Dirk Schwarzer, Dr Michael Teufel, Dr Andreas Volkmer and finally Laura van den Heuvel. In addition, I especially thank Silke Lubahn for generating most of the figures in this book and Julia Lüttich for her extremely valuable support throughout the entire time this second edition was being prepared. Gratitude is also expressed to Dr Pen-Nan Liao for his assistance with the solutions to the questions asked in the book. Last, but not least, I would like to thank all persons at Wiley-VCH who helped with the production of this book and especially Lesley Fenske, Dr Peter Capper, Mamta Pujari and Dr Frank Weinreich for their patience regarding my special requests and wishes.

Braunschweig and Göttingen, May 2014

## Introduction

### What is Biophysical Chemistry? – An Example from Drug Screening

Biophysical chemistry is a fascinating field of research because it combines aspects of chemistry, biology, physics and sometimes even medicine in one discipline. Owing to this diversity it is difficult to give an exact definition of biophysical chemistry. In principle, everything in biology or medicine is based on a chemical or physical foundation. For a physical chemist, one reasonable definition is 'Biophysical chemistry is the application of principles known from physical chemistry to elucidate biomolecular and biochemical questions'. For a biologist a reasonable definition might be 'Biophysical chemistry is the description of the physicochemical properties of biomolecules'.

Actually, it makes a lot more sense to answer the question 'Why do we need biophysical chemistry?'. In recent years more and more questions relevant to biology have been answered using methods originating from the field of physics or physical chemistry. These problems require at least some basic understanding in all three disciplines. However, often a physicist or chemist feels uncomfortable talking about topics that seem to be quite simple for a biologist and vice versa. In many cases it turns out that something that sounded very complicated to one scientist is not difficult at all after he or she realizes that the other scientist is simply using unfamiliar wording. An example is the definition of a 'vector'. Chemists and physicists usually regard a vector as a mathematical object. However, if molecular biologists are talking about vectors they often mean a plasmid vector for transferring genetic material into a cell. The field of biophysical chemistry is a bridge between these disciplines. The following example illustrates a typical problem that can only be solved with a basic knowledge of all these disciplines.

For the development of a drug, in pharmaceutical research in many cases one very important parameter is the affinity of potential drug candidates for a specific receptor or enzyme. The mechanism by which many drugs act is simply based on their ability to selectively block the active site of specific biomolecules.

For example, the biomolecular targets of many antibiotics are enzymes responsible for the cell-wall synthesis of bacteria. Since it is very hard to find such compounds that also have as few side effects as possible it is useful to look at as many compound structures as possible. Pharmaceutical companies often have a very large pool – up to millions – of already synthesized compound structures. Often, in a first step in the process of industrial drug development, many of these compound structures are tested for their affinity to a specific target using high-throughput screening (HTS). If a compound structure with a high affinity can be found (a ‘Hit’) it can be used as starting point for further drug development. But how can the affinity of a million compounds be measured with sufficient speed and accuracy? A day lasts 86 400 s. If the accurate measurement of the binding affinity takes only one second per compound, then more than 11 days of constant measurements are required for one million compounds.

One possibility for a fast and robust solution to this problem is to use fluorescence polarization anisotropy (FPA) assays. The mathematical and technical aspects of such assays are described in detail in Chapter 3 but here it serves as a first insight into what the field of biophysical chemistry can mean.

The problem is *biological* or medical – for example, you want to find a molecule that blocks specifically the binding site of a certain receptor that is closely associated with the development or progression of a certain disease. In a fluorescence polarization assay you could first label a small natural ligand of the receptor *chemically* with a fluorescent molecule (Figure I.1). When you subsequently mix the labelled ligand with the receptor they form a stable receptor–ligand complex. Often, this complex has a large molecular mass and is therefore tumbling and rotating very slowly in solution. If this complex is excited with

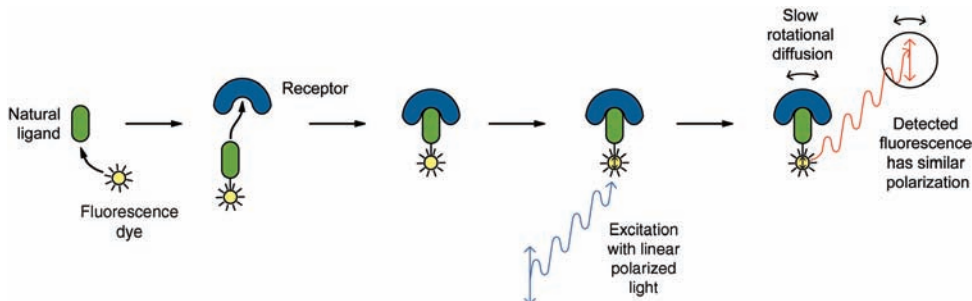


**Figure I.1** Schematic representation of a typical fluorescence polarization assay. In a first step a small ligand is labelled with a fluorescent marker and forms a stable receptor–ligand complex with a receptor. Owing to the large mass of the receptor–

ligand complex its rotational diffusion in solution is very slow. Consequently, the orientation of the polarization of the emitted photons is very similar to the orientation of the polarization of the laser excitation.

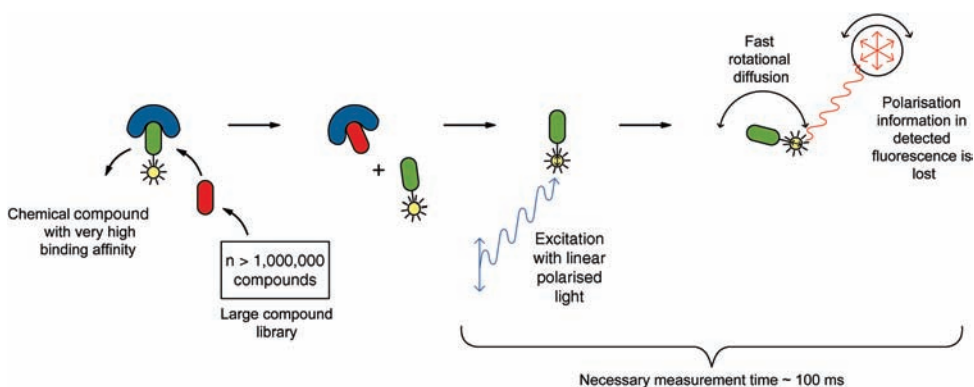


**Figure I.2** If a chemical compound out of a large pool of synthetic compounds has a significantly higher affinity for the receptor it replaces the labelled ligand. The free ligand exhibits very fast rotational diffusion. This can be measured very quickly because now the

polarization orientation of emitted photons is very different from that of the laser excitation. A hit is found that can be used for further tests or modification to evaluate it as a potential drug structure.

polarized laser light, most of the fluorescing molecules emit light with a very similar polarization. This polarization can be measured for instance with polarization filters (here comes the *physics!*).

In a next step, a chemical compound to be tested is added to the solution. If the compound is capable of binding more strongly to the receptor than the natural labelled ligand then the labelled ligand will be forced out of the binding site and the chemical compound itself blocks the site (Figure I.2). Now, however, the fluorescently labelled natural ligand is diffusing and rotating freely in the solution. Since the fluorescently labelled ligand is small its rotational diffusion is faster than the time it typically takes for the label to emit fluorescence. Therefore, most photons are now emitted with an arbitrary, very different polarization from that of the exciting laser light. By measuring this different polarization the binding constant of each chemical compound can be determined very accurately even within a few hundred milliseconds.

This assay principle is an example of a competitive binding assay measured by fluorescence polarization anisotropy. Since this experiment requires knowledge from all three disciplines – chemistry, biology and physics – it is a good example of what biophysical chemistry can mean. Of course, biophysical chemistry methods are not restricted to industrial applications and are probably even more important in basic research.

The intention of this book is to give an insight into the most important basic, as well as modern, biophysical chemistry methods and their application in both basic and industrial science. The book is divided into two parts. In Part 1 (Basic Methods in Biophysical Chemistry) essential traditional, but still

modern, methods are described for the investigation of biomolecular processes and the characterization of biomolecules. Important examples are fluorescence methods such as fluorescence polarization and Förster energy transfer (FRET) techniques as well as more modern methods for the characterization of biomolecules by mass spectroscopy or pulsed NMR. In addition, an insight into important labelling techniques and techniques for linking biomolecules with each other or to immobile supports is given. In Part 2 (Advanced Methods in Biophysical Chemistry) more specialist methods are described that can be employed, for example, when none of the basic methods in Part 1 can be used to answer a particular biomolecular question. Important examples are fluorescence correlation spectroscopy, high-resolution STED microscopy, optical tweezers, atomic force microscopy of biomolecules, patch clamping techniques and the use of fluorescing nanoparticles. In this part, rather technical applications are also discussed, such as DNA sequencing, fluorescence-assisted cell sorters, and DNA chips. This part also contains a section on principles in assay development and applications in industrial high-throughput screening.

Throughout the book you will find application examples that illustrate the use of the described methods for typical biomolecular questions. Table I.1 summarizes the methods along with application fields, important equations and gives the section in which application examples and the equations can be found. As already mentioned, the most important equations are also marked by a box throughout the entire book.

This book was originally based on my lectures on biophysical chemistry. The field of biophysical chemistry is huge and so it is difficult to encapsulate the most relevant methods in a single book. I ask all of those who feel that their methods or application examples should have been included or who think that their method was not described in sufficient detail to excuse me. For the same reasons also the given literature references constitute only selected examples for further reading. It was not our intention to present the entire literature relevant for the topics presented in this book since this would be beyond the scope and also not very didactic. Of course, I am always very happy to receive any comments or criticism that will help improve any future editions of this book.

Table I.1 Methods described in this book.

Method	Section	Examples of Typical Applications Fields	Selected Examples of Specific Applications Presented in this Book	Section	Important Equation	Section
Absorption spectroscopy	Section 2.2	Determination of concentration of certain biomolecules	Determining DNA purity  Measuring oxygen saturation in blood  Measuring cooperativity of haemoglobin	Section 2.3.2  Section 2.4.1	Optical density: $OD(\lambda) = \log \frac{I_0(\lambda)}{I(\lambda)} = \varepsilon(\lambda) \cdot C \cdot l$	Section 2.2
Intrinsic fluorescence spectroscopy	Section 2.2	Identification of the presence of fluorescing or fluorescently labelled biomolecules	Determination of metabolic activity from NADPH-fluorescence  Determination of plant fitness by chlorophyll fluorescence	Section 2.4.2  Section 2.4.4		
Fluorescence labelling	Section 3.2	Identification of labelled biomolecules in complex biological environments				
Fluorescence polarization anisotropy (FPA)	Section 3.4	Determining binding processes or other processes that can affect the rotational diffusion of labelled species	Receptor-ligand binding; molecular mass estimate; enzyme kinetics; enzyme inhibition	Sections 3.4.2–3.4.5	Fluorescence anisotropy: $r = \frac{I_{\text{II}} - I_{\text{I}}}{I_{\text{II}} + 2I_{\text{I}}}$	Section 3.4.1

(continued)

Table I.1 (Continued)

Method	Section	Examples of Typical Applications Fields	Selected Examples of Specific Applications Presented in this Book	Section	Important Equation	Section
Förster resonance energy transfer (FRET)	Section 3.5	Determining binding processes, conformational transitions and biomolecular distances	Receptor–ligand binding. Conformational changes in DNA. Determining distances during protein unfolding, Membrane fusion	Section 3.5.2	FRET efficiency: $\Phi_{ET} = \frac{R_0^6}{R_0^6 + r^6}$ $I_{FI}^D / I_{FI}^{D,0} = 1 - \Phi_{ET}$	Section 3.5.1
Fluorescence kinetics	Section 3.6	Sensing changes in the environmental polarity of biomolecules or other processes that can affect the excited state lifetime of fluorescence markers	Detecting FRET or FPA via fluorescence kinetics	Section 3.6	Time-dependent fluorescence intensity: $I_{FI}(t) \propto P_{S_1}(t)$ $I_{FI}(t) = I_{FI}^0 \cdot e^{-t/\tau_{S_1}}$	Section 1.6
Fluorescence recovery after photobleaching	Section 3.7	Membrane diffusion				
Biochemiluminescence	Section 3.8	Monitoring ATP concentrations. Monitoring protein expression				
Circular dichroism (CD), optical rotation dispersion	Section 4.1.1	Determination of amount of secondary structure elements in proteins			Molar ellipticity: $[\Theta](\lambda) = \frac{100 \cdot \Theta(\lambda)}{C \cdot l} = 3298 \cdot \Delta e(\lambda)$ . Molar circular birefringence/optical rotation: $[\Phi](\lambda) = \frac{100 \Phi(\lambda)}{C \cdot l}$	Sections 4.1.1 and 4.1.2

Light scattering	Section 4.2	Determination of molecular mass of biomolecules. Aggregation and shape of biological objects	Rayleigh ratio: $R_0 = \frac{I_{\text{Scat}}}{I_0} \frac{r^2}{V(1 + \cos^2 \Theta)} = K \cdot c \cdot M$	Section 4.2.1
Vibrational spectroscopy (infrared/Raman spectroscopy)	Section 4.3	Determination of secondary structure elements. Label-free identification of chemical composition		
Nuclear magnetic resonance (NMR)	Section 5.1	Structure determination under physiological conditions. Determination of structural flexibility of biomolecules. Label-free observation of biomolecular processes	Comparison of NMR structure of insulin and severin with X-ray structure. Flexibility of severin structure under physiological conditions	Section 5.1.3
Electron paramagnetic resonance (EPR)	Section 5.2	Observation of redox reactions in photosynthesis or haemoglobin. Determination of rotational diffusion using spin labels	Determination of membrane structure and dynamics	Section 5.2
Mass spectrometry	Chapter 6	Identifying biomolecules from mixtures. Determining biomolecular structures from fragments	Peptide sequencing	Section 6.4
Fluorescence microscopy	Chapter 7	Imaging of labelled proteins in a whole cell context. Real-time imaging of biological processes	Diffraction-limited resolution: $r_0 \approx \frac{\lambda}{n \cdot \sin \varphi}$	Section 7.2.1

(continued)

Table I.1 (Continued)

Method	Section	Examples of Typical Applications Fields	Selected Examples of Specific Applications Presented in this Book	Section	Important Equation	Section
Super-Resolution Fluorescence Microscopy	Chapter 8	High resolution imaging of fluorescently labelled biological objects and/or under more physiological conditions	High resolution images of neuronal actin filaments	Section 8.2		
Optical single-molecule detection	Section 9.2	Real-time observation of biomolecular mechanisms	Mechanism of ATPase. Mechanism of motor proteins	Sections 9.2.1 and 9.2.2		
Fluorescence correlation spectroscopy	Section 9.3	Observation of binding and aggregation processes. Determination of microscopic concentrations. Determination of diffusional properties	Receptor-ligand binding. Determination of microscopic concentration. Determination of aggregation. Estimate of molecular mass	Sections 9.3.1, and 9.3.3.2	Correlation function: $G(\tau) = \frac{\langle I_{\text{fl}}(t) \cdot I_{\text{fl}}(t + \tau) \rangle}{\langle I_{\text{fl}}(t) \rangle^2} - 1$ $G_{\text{Dif}}(\tau) = \frac{1}{(C)\pi^2 r_0^2 \tau_0} \cdot \frac{1}{1 + \frac{\tau}{\tau_0}} \cdot 1 \sqrt{1 + \left(\frac{\tau}{\tau_0}\right)^2 \frac{4}{\pi^2}}$ $G_{\text{Dif}}(0) = \frac{1}{(C)V_{\text{eff}}} = \frac{1}{\langle N \rangle}$	Sections 9.3.1–9.3.3
Fluorescence cross-correlation spectroscopy	Section 9.3.5	Binding processes	Determination of binding degree	Section 9.3.5	Cross-correlation function: $G_X(\tau) = \frac{\langle I_{\text{fl}}^G(t) \cdot I_{\text{fl}}^G(t + \tau) \rangle}{\langle I_{\text{fl}}^G(t) \rangle^2} - 1$ $C_{\text{RG}} = \frac{G_X(0)}{G_R(0)G_G(0) \cdot V_{\text{eff}}}$	Section 9.3.5
Optical tweezers	Section 9.4	Force-distance measurements with single biomolecules	Unfolding RNA-hairpins. Forces exerted by RNA-polymerase. Forces exerted by DNA-polymerase	Sections 9.4.2.1–9.4.2.3	Trap stiffness: $k_{\text{Trap}} = \frac{\Delta \vec{x}_{\text{Trap}}}{\vec{F}_{\text{Trap}}}$	Section 9.4.1

Atomic force microscopy	Section 9.5	Determination of surface topology of membranes containing transmembrane proteins. Force-distance measurements with single biomolecules	Unfolding DNA-hairpins. Receptor-ligand forces. Unfolding titin	Sections 9.5.2.1–9.5.2.3	Forces exerted at cantilever: $\vec{F}_{\text{AFM}} = -k \cdot \Delta z$	Section 9.5.1
Patch clamping	Section 9.6	Measuring ion currents through single ion channels	Measuring open and closed times at a ligand gated ion channel as a function of ligand concentration	Section 9.6.1		
Multiphoton excitation	Section 10.2.1	3D laser scanning microscopy. Fluorescence cross-correlation spectroscopy	Two-photon microscopy. Selective carotenoid excitation in photosynthetic proteins	Sections 10.2.2 and 10.2.4	Probability of two-photon excitation: $P_{\text{Two-Photon Absorption}} \propto I_{\text{Excitation}}^2$	Section 10.2.1
Second-harmonic generation; third-harmonic generation	Section 10.2.5	Label-free microscopy of structures like collagen, muscle fibres, cell membranes or lipid bodies			Generated frequency: $\nu_{\text{wavenmixing}} = \pm \nu_1 \pm \nu_2 \pm \nu_3 \dots$	Section 10.2.5
CARS microscopy	Section 10.2.5	Label-free microscopy of biological objects based on vibrational frequencies of chemical bonds			Generated frequency: $\nu_{\text{Anti-Stokes}} = 2 \cdot \nu_{\text{Pump}} - \nu_{\text{Stokes}}$ Direction of detected anti-Stokes beam: $\vec{k}_{\text{Anti-Stokes}} = -(2 \cdot \vec{k}_{\text{Pump}} - \vec{k}_{\text{Stokes}})$	Section 10.2.5
Ultrafast spectroscopy	Section 10.3	Observation of fastest processes in biology	Investigation of ultrafast light-harvesting and energy conversion in photosynthesis	Section 10.3.2		
DNA sequencing	Chapter 11	Determining and identifying genetic code				
Fluorescing nanoparticles	Section 12.2	Fluorescence labelling with superior signal-to-noise ratio	Encoded microspheres	Section 12.8		

(continued)

Table I.1 (Continued)

Method	Section	Examples of Typical Applications Fields	Selected Examples of Specific Applications Presented in this Book	Section	Important Equation	Section
Surface plasmon resonance detection	Section 12.3	Determination of receptor-ligand binding and dissociation kinetics				
DNA chips	Section 12.5	Determining gene expression as a function of regulators or drugs				
Flow cytometry	Section 12.6	Sorting cells as a function of distinct cell properties monitored by fluorescence or light scattering				
Fluorescence <i>in situ</i> hybridization	Section 12.7	Identifying certain genes in genomes				
Micro- and nanospheres	Section 12.8	Many different application possibilities				
Microtitre plates, fluorescence readers	Section 13.3	Measurements in dilution series and high-throughput screening, assay development	High-throughput screening for finding lead-structures in drug design	Section 14.4	Quality of assay: $Z' = 1 - 3 \frac{\delta^+ + \delta^-}{ \bar{x}^+ - \bar{x}^- }$	Section 13.2

## Part One

### Basic Methods in Biophysical Chemistry

In Part 1 of this book the more established modern techniques are presented that are nowadays very broadly applied in many labs throughout the world. It starts with a chapter that introduces the basic principles governing the interactions of electromagnetic radiation (“light”) with molecules and biomolecules. These interactions are the basis for many of the methods presented not only in Part 1 but also in some chapters of Part 2. Important examples are general methods such as absorption spectroscopy and a plethora of advanced fluorescence techniques (Chapters 2 and 3) as well as very important techniques such as NMR studies of biomolecules (Chapter 5), but also methods such as super-resolution microscopy (Chapter 8), single-biomolecule detection (Chapter 9), nonlinear spectroscopy (Chapter 10) and next-generation DNA-sequencing methods (Chapter 11).

The introductory chapter (Chapter 1) aims at providing a brief and concise but still thorough review of the interaction of electromagnetic radiation with molecules for readers with a more chemical or physical background and serves as an introduction into these interactions for readers with a more biological background. Readers who require a rather quick overview and who have at least some basic knowledge about orbitals of molecules might focus on Sections 1.1, 1.3, 1.5 and the beginning of Section 1.6 only. These parts should suffice to have enough background information to understand the subsequent chapters. For example, they will already give an in-depth idea about transition dipole moments and the polarization of light, which are central for quite a number of the methods presented in this book.

In Chapters 2 and 3, absorption and fluorescence properties in the visible spectral range of important biomolecules and fluorescence markers are presented as well as the application of the corresponding techniques to investigate biomolecules and biomolecular processes. Important examples are the determination of biomolecule concentrations or purities as well as investigations of receptor–ligand equilibria, enzymatic conversions and activators and inhibitors. In Chapter 3 some very central concepts in modern biophysical chemistry are also discussed in more detail, such as labelling and linking techniques, Förster

resonance energy transfer (FRET) and fluorescence polarization assays. Also, the mathematical framework for the latter two is discussed in more detail, but readers who require a quick overview can also focus only on the description of the equations that are marked by boxes, which represent, in general, the central equations throughout this book.

Chapter 4 summarizes some very important optical methods that do not primarily rely on the absorption and emission of unpolarized or linearly polarized light in the visible spectral range but rather on scattering of light, the use of left- and right-handed circular light or light in the infrared spectral region. These techniques are, in general, of great use to derive information about the size, shape and secondary structural elements of biomolecules without any labelling of the samples.

Chapter 5 gives an overview of the application of nuclear magnetic resonance (NMR) techniques, which work with electromagnetic radiation in the radiowave range. NMR allows for the analysis of biomolecular structures under more physiological conditions than is possible with classical electron or X-ray microscopies. Chapter 5 also aims at providing an insight into the physical basics behind multidimensional NMR that are essential for such studies and how the information derived from such techniques can be used to derive a final 3D structure of proteins. Also, the use of electron paramagnetic resonance (EPR) for investigating biomolecules is described in this chapter.

Chapter 6, finally, presents techniques that allow very accurate determination of one of the most central parameters for characterizing biomolecules, namely their molecular weight. In this chapter it is discussed how mass spectrometry can be applied to biomolecules without harming their structural integrity and what further very useful information can be derived using advanced mass spectrometric methods.

# 1

## Basic Optical Principles

### 1.1

#### Introduction

To understand important optical methods used to investigate biomolecules, such as fluorescence polarization anisotropy, Förster resonance energy transfer, fluorescence lifetime techniques (Chapter 3), optical single-molecule detection techniques (Chapter 9), fluorescing nanoparticles (Chapter 12) or high-resolution fluorescence microscopy such as STED and PALM (Chapter 8), a basic understanding of the interaction of light with molecules and biomolecules is required. Such basic knowledge is also necessary in understanding the use of magnetic resonance techniques (Chapter 5). In the following sections we discuss a few fundamental principles of the physical processes that govern the interaction of light with biomolecules, optical markers or other relevant matter such as nanoparticles. This chapter provides a brief but wide-ranging insight into important physical and quantum mechanical basics of these processes also for, but not limited to, readers without a physical or chemical background, while being mathematically and physically as exact and concise as possible. Readers that look for a rather quick overview and that have at least some basic knowledge about orbitals of molecules might focus on sections 1.1, 1.3, 1.5 and 1.6 only. Please be aware that a complete, indepth treatment of quantum mechanics and molecular spectroscopy is beyond the scope of this chapter. Only the fundamentals that are needed for the biophysical chemistry methods presented in the following chapters are discussed. For further information about quantum mechanics and molecular spectroscopy, the reader might refer to the more specialized books given in the bibliography at the end of this chapter.

Light is a wave of oscillating electric and magnetic fields propagating through space (Figure 1.1). The electric- and magnetic-field components of this electromagnetic radiation are oscillating in phase perpendicular to the propagation direction and with respect to each other. The smallest possible units of light are elementary particles called photons. These possess a specific amount of energy,  $E$ ,

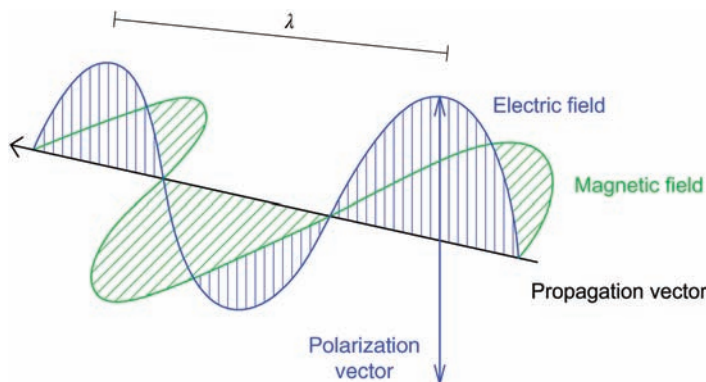


**Figure 1.1** Light is a wave of oscillating electric and magnetic fields propagating through space.

which depends on the frequency or wavelength of the light radiation:

$$E = h\nu = \frac{hc}{\lambda} = hc\bar{\nu} \quad (1.1)$$

Here,  $h$  is Planck's constant,  $\nu$  is the frequency of the electric- and magnetic-field oscillation,  $c$  is the speed of light,  $\lambda$  is the wavelength of the oscillation and  $\bar{\nu}$  is the corresponding wave number. The energy  $E$  of a photon is linear proportional to the frequency  $\nu$  and wave number  $\bar{\nu} = \frac{1}{\lambda}$ . The wavelength, in turn, is inversely proportional to the energy.

Figure 1.2 shows the spectrum of electromagnetic radiation. Optical methods make use of electromagnetic radiation having wavelengths from  $\sim 200$  nm to a few  $\mu\text{m}$ . This interval can be subdivided into the ultraviolet (UV) region ( $\sim 200$ – $400$  nm), the visible region ( $\sim 400$ – $700$  nm) and the near infrared (NIR) region ( $\sim 700$  nm to a few  $\mu\text{m}$ ). The UV range, for example, is important for the characterization of proteins and DNA, which is described in Chapter 2. The visible region is important for most fluorescence techniques, which are described in

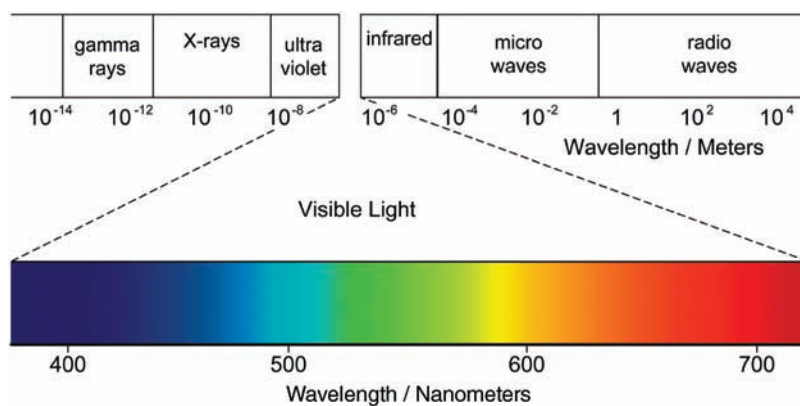


**Figure 1.2** Spectrum of electromagnetic radiation.

detail in Chapters 2 and 3 and partly in Chapters 7–13. The infrared region enables the identification and investigation of biomolecules based on their characteristic molecular vibrations (Chapter 4). Radiowaves and microwaves are used for nuclear and magnetic resonance techniques. Chapter 5 describes the application of these techniques for the investigation of biomolecules.

The size of typical molecules or biomolecules is usually on the order of a few nanometres, which is far smaller than the dimensions of the oscillating electric-field waves of visible light, which are on the order of a few hundred nanometres. When molecules are within the waves of the light, the charged components of the molecules, especially the electrons, are affected by the oscillating electric-field component of the light. If a molecule possesses a suitable electronic structure it can absorb a photon of a specific wavelength, resulting in an electronic structure rearrangement. In the next section, we discuss what the electronic structure of molecules looks like.

## 1.2

### What Does the Electronic Structure of Molecules Look Like? Orbitals, Wave Functions and Bonding Interactions

As with photons, electrons possess also both wave- and particle-like properties. Because of the wave-like character of electrons, only probabilities can be given of finding electrons at a certain place around the nuclei of a molecule. This electronic structure is usually visualized by electron clouds or probability densities, which are mathematically described by three-dimensional probability density functions. Depending on the molecular structure, only distinct eigenstates of the electron probability densities are possible. Such a state simply describes a possible three-dimensional standing wave of the negatively charged electron waves in the presence of the positively charged nuclei – similar to a string of an instrument, which can also vibrate only with certain frequencies and overtones. Each of these states corresponds to distinct energies.

During the absorption of a photon the electronic structure of the molecules is usually transferred from an electronic ground state into an energetically higher electronic excited state. In an excited state the three-dimensional, electronic probability densities are different from the ground-state probability densities. Only photons having energies corresponding to the energy difference between these electronic states can be absorbed by the molecules. This is the origin of the colour of a compound: only light of certain wavelengths is absorbed by the compound – light of other wavelengths is either transmitted or scattered. The photon energy corresponding to the absorbed wavelength is equal to the necessary excitation energy for the respective transition.

What does the probability density function,  $P(x, y, z)$ , corresponding to a certain electronic state look like? In quantum theory, the probability density for finding electrons at a certain place  $P(x, y, z)$  is calculated from the electronic wave function,  $\psi(x, y, z)$ , corresponding to this state:

$$P(x, y, z) = \psi^*(x, y, z)\psi(x, y, z) \quad (1.2)$$

The probability of finding an electron in a certain volume element  $x \dots x + dx$ ;  $y \dots y + dy$ ,  $z \dots z + dz$  can be calculated by integrating the probability density  $P(x, y, z)$  in the corresponding range. The electronic wave function is also a three-dimensional mathematical function that contains all information about the electrons in a molecule. Some of the most relevant parameters for optical techniques in the biosciences, such as the transition dipole moment, can only be properly derived from electronic wave functions. Therefore, we will briefly introduce some important aspects about wave functions here.

Usually, the wave function is simply written as  $\psi$  rather than  $\psi(x, y, z)$  but the meaning is the same. In addition, we will use for the coordinates of the electrons and nuclei in the following  $\vec{r} = (x, y, z)$ :

$$\psi(x, y, z) = \psi(\vec{r}) = \psi \quad (1.3)$$

Electronic wave functions describing single electrons of a molecule in a certain electronic state are called orbitals,  $\varphi(x, y, z) = \varphi(\vec{r}) = \varphi$ .<sup>1)</sup> For example, the simplest possible single electron wave function is an atomic s orbital,  $\varphi_s$  (on the left in Figure 1.3). It corresponds to a spherically symmetrical probability density of a single electron around a single nucleus. An examination of the time dependence of wave functions shows that they are actually oscillating. The sign of positive

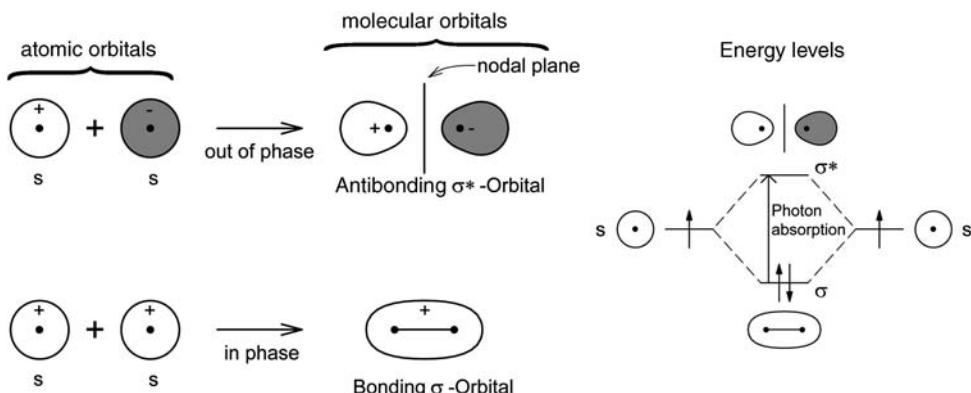


**Figure 1.3** Schematic construction of bonding and antibonding molecular orbitals from atomic orbitals along with the resulting electron energy levels. Probability functions for finding an electron at a certain place can be calculated from the orbitals using (1.2) and look qualitatively similar, with the most

important difference that probabilities exhibit no negative regions. The height of the horizontal lines on the right represents the energies of electrons in the corresponding orbitals. Electrons occupying certain orbitals are depicted by arrows. The direction of the arrows assigns the spin of the electrons.

1) The description that an electron occupies orbitals independently from all other electrons is only a very useful approximation, which is close to reality in many cases. Since all charged particles in a molecule influence each other, an exact description would be only possible by wave functions that describe a state of an entire molecule,  $\psi_{\text{molecule}}$ , in a certain environment including all electrons and nuclei simultaneously.

and negative parts of the three-dimensional wave function changes with a certain frequency. The negative and positive signs of the orbitals are not to be confused with negative or positive charges. They are rather a consequence of the wave character of the electrons. For example, the waves of light (Figure 1.1) are also mathematically described by oscillating functions having negative and positive values but of course this has nothing to do with positive or negative charges. However, often, it is sufficient to work with time-independent versions of the wave functions, which represent stationary states or standing waves and in which the oscillating, time-dependent factor is omitted. In Figure 1.3, for example, time-independent wave functions or orbitals are visualized for which negative parts are depicted in grey, whereas the positive parts are unfilled. The oscillation also has no effect on the probability density of finding an electron at certain places,  $P(\vec{r})$ , negative signs are cancelled out by the multiplication described by (1.2). The shape of the three-dimensional probability densities,  $P(\vec{r})$ , as calculated by (1.2) are visually often quite similar to the shape of the wave functions, with the most important difference that there are no “negative” regions for the probability density of electrons.

Orbitals, and thus probability densities, never change abruptly. For an electron in an s orbital, for example, the corresponding probability density increases smoothly when approaching the nucleus. Presentations of orbitals, such as shown in Figure 1.3, or probability densities usually symbolize a certain volume of the corresponding probability density in which the electron can be found, for example, with 90% probability. The shown surfaces are called isosurfaces because they correspond to equal values for the probability of finding the electron or to equal absolute values of the wave function.

To contain all information on the electrons, for example the actual phase of the oscillation, wave functions can also contain mathematically complex terms. The symbol “\*” in (1.2) simply denotes a transformation in which all imaginary parts of complex numbers in the wave function are multiplied by  $-1$ . However, for a qualitative understanding of the following sections, an indepth knowledge about the imaginary parts of the wave functions is not mandatory.

If an atom approaches another atom this affects the possible eigenstates of the electrons because they are then in the vicinity of two positively charged nuclei. The possible wave functions for single electrons in the presence of several nuclei are called molecular orbitals. Molecular orbitals can be approximated by linear combinations of atomic orbitals (LCAO). If the wave functions of two atomic s orbitals with the same sign (corresponding to the situation that they oscillate in phase) are combined they form a new a bonding molecular orbital called a  $\sigma$ -orbital, ( $\varphi_{\sigma} \propto \varphi_s^1 + \varphi_s^2$ , in the lower middle of Figure 1.3). The energy of an electron occupying a bonding molecular  $\sigma$  orbital is lower than that of an electron in an atomic s orbital. This is the driving force for molecular bonds. So, if, for example, two hydrogen atoms with a single electron in an s orbital approach, both electrons can then be found in the newly formed bonding  $\sigma$ -orbital. The probability density of finding the electrons at a certain place of the molecular  $\sigma$ -orbital can again be calculated from the corresponding molecular orbital  $\varphi_{\sigma}$ .

using (1.2). Notably, an orbital can only be occupied by a maximum of two electrons with opposite spins (We will discuss the meaning of electron spins further below.) If two atomic s-orbitals with opposite signs (corresponding to the situation that they oscillate out of phase) are combined they form an antibonding molecular  $\sigma^*$ -orbital,  $\varphi_{\sigma^*} \propto \varphi_s^1 - \varphi_s^2$  (in the upper middle of Figure 1.3). Electrons in antibonding  $\sigma^*$ -orbitals have higher energies than electrons in bonding  $\sigma$ -orbitals (orbital energies are visualized as horizontal lines on the right in Figure 1.3, the corresponding electrons with opposite spins as arrows on these lines). By absorbing a photon with an energy corresponding to the energy difference between these orbitals one of the electrons in the bonding  $\sigma$ -orbital can be excited into the antibonding  $\sigma^*$  orbital. The large energy gap of the  $\sigma \rightarrow \sigma^*$  transition usually requires excitation with photons corresponding to UV light. The antibonding  $\sigma^*$ -orbital has one nodal plane, which constitutes a region of zero electron density. Therefore, a  $\sigma \rightarrow \sigma^*$  excitation can lead to bond breakage. Notably, it is a convention to assign antibonding orbitals also by a star, which is not to be confused with the meaning of the star in equations such as (1.2) where it assigns the earlier mentioned transformation of imaginary parts of the wave functions.

The second simplest atomic orbitals are p-orbitals (left-hand side in Figure 1.4). They have a nodal plane at the nucleus and the sign of the real part of the wave function is always opposite across this nodal plane. Two atomic p-orbitals of appropriate relative orientation at neighbouring nuclei can form molecular  $\pi$ -orbitals.<sup>2)</sup> In organic molecules and biomolecules most  $\pi$ -orbitals are found at

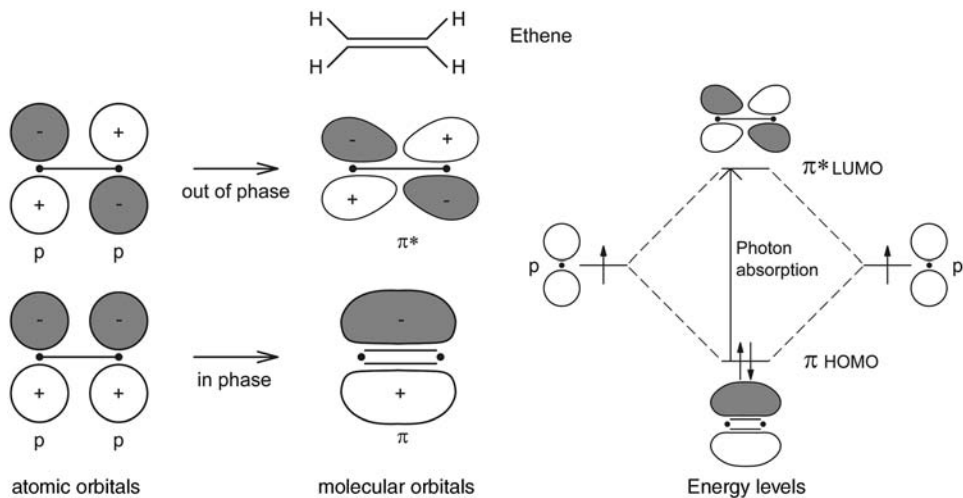


**Figure 1.4** Schematic construction of bonding and antibonding molecular  $\pi$ -orbitals from atomic p-orbitals in the case of ethene.

2) Also, a molecular  $\sigma$ -orbital can be constructed from two atomic p-orbitals if the latter are orientated parallel to the bond axis (perpendicular to the ones shown in Figure 1.3). In general, molecular orbitals are defined as a  $\sigma$ -orbital when they are symmetrical with respect to a rotation about the bond axis.

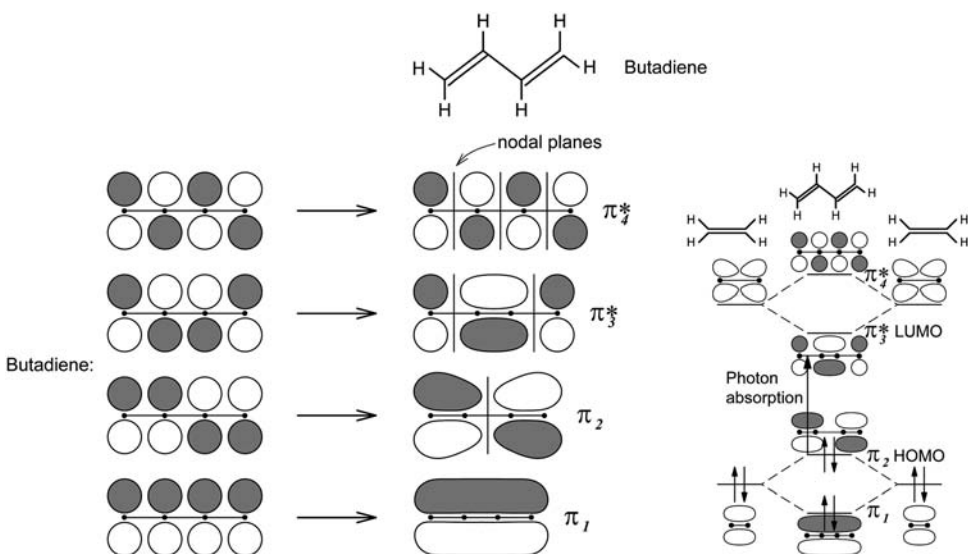


**Figure 1.5** Schematic construction of an extended molecular  $\pi$ -orbital system from conjugated atomic p-orbitals. The example corresponds to butadiene. The HOMO and LUMO of butadiene correspond to the  $\pi_2$  and  $\pi_3^*$  orbitals, respectively. The four molecular orbitals  $\pi_1, \pi_2, \pi_3^*, \pi_4^*$  of butadiene can also be

thought of as being constructed from the two molecular orbitals,  $\pi, \pi^*$ , of two ethene molecules. Direct comparison of the energy levels of the HOMO and LUMO of ethene with the HOMO and LUMO of butadiene shows that the energy gap of the latter is smaller.

carbon, oxygen and nitrogen atoms and often constitute double bonds together with simultaneously existing  $\sigma$ -bonds. A simple example is ethene.

Similarly, several p-orbitals can form  $\pi$ -orbitals that are delocalized over multiple nuclei (Figure 1.5). Such molecular orbitals are called conjugated  $\pi$ -systems. In Figure 1.5, four atomic p-orbitals form four molecular orbitals. In a similar manner,  $n$  molecular  $\pi$ -orbitals can be constructed from  $n$  atomic p-orbitals. The energy of the newly formed molecular orbitals increases with the number nodal planes (see energies of the molecular  $\pi$ -orbitals  $\pi_1, \pi_2, \pi_3^*, \pi_4^*$  in Figure 1.5). The electrons from the original atomic p-orbitals (four in Figure 1.5) are then filled into molecular orbitals, starting with the lowest-energy orbitals and obeying the rule that only a maximum of two electrons are allowed per molecular orbital. If orbitals have equal energies, they are first occupied by single electrons before any of them is filled with a second electron.

The highest occupied molecular orbital and the lowest unoccupied molecular orbital are usually assigned by their acronyms HOMO and LUMO, respectively. For most organic molecules, the electronic ground state corresponds to the situation that all orbitals up to the HOMO electrons are occupied by two electrons (see, for example, Figures 1.4 and 1.5). Similarly, for organic molecules the first excited state corresponds often to the situation that one electron has been promoted from the HOMO to the LUMO. The electronic ground state and the first possible

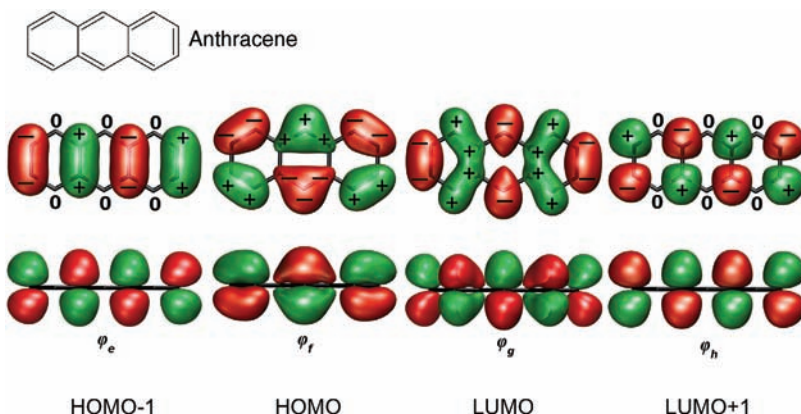


**Figure 1.6** Schematic top and side views of examples of the  $\pi$ -orbitals of anthracene. HOMO-1 and LUMO+1 assign those orbitals that are the energetically next orbitals below or above the HOMO and LUMO orbitals, respectively. Figure created using VMD (see Bibliography for details).

electronically excited state of molecules are often referred to as  $S_0$  and  $S_1$  states, respectively. The reasons for this nomenclature are explained below (Section 1.5).

For butadiene (Figure 1.5), for example,  $S_0$  corresponds to the situation in which the lowest two molecular orbitals  $\pi_1$  and  $\pi_2$  are each occupied by two electrons. As can be seen by a comparison of the orbital energies of ethene in Figure 1.4 and the corresponding orbital energies of butadiene in Figure 1.5 the energy difference between the electrons in the HOMO and the LUMO decreases as the system of conjugated p-orbitals becomes larger. In general, larger conjugated  $\pi$ -systems typically absorb photons of lower energy and thus longer wavelengths than smaller conjugated  $\pi$ -systems [compare with (1.1)].

The molecular  $\pi$ -orbitals of more complicated molecules, like biomolecules or optical markers, naturally look more complicated. Figure 1.6 shows wave functions of the  $\pi$ -system of the organic molecule anthracene as an example. The general rule that electrons in orbitals having more nodal planes have higher energies still applies in most cases.

Electronic transitions involving conjugated  $\pi$ -systems are especially important in the spectroscopy of biomolecules, or optical markers, because absorption and emission of photons of these systems are often strong and correspond to light in the spectroscopically convenient visible region. Since  $\sigma$ -bonds remain,  $\pi \rightarrow \pi^*$  transitions usually do not cause bond breakage.

### 1.3

#### How Does Light Interact with Molecules? Transition Densities and the Transition Dipole Moment

In the previous section we discussed the electronic structure of molecules before and after they have absorbed a photon and what photon energy is necessary for

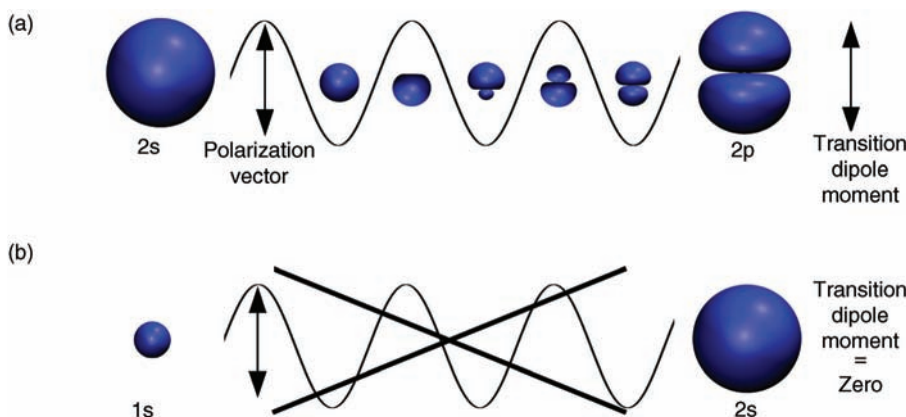


**Figure 1.7** (a) The oscillating electric field component of light can induce a transition from an s to a p orbital when it has the correct polarization (direction of oscillating electric field component of light). Please note that here probability densities and not wave functions are visualized. The response of the

electron probability densities to the oscillating electric field during the transition is also schematically illustrated. (b) In contrast, the oscillating electric-field component of light cannot induce a transition from one s-orbital to another s orbital. Figure created using VMD (see Bibliography for details).

such a transition. Here we take a closer look at the mechanism by which a photon or optical radiation can actually interact physically with molecular orbitals to promote the molecule from one electronic state to another.

The probability by which a photon of correct energy is absorbed by a molecule depends on the ability of the light's oscillating electric field to change the initial electronic state into the final electronic state. For example, light can excite the single electron of an isolated hydrogen atom from an s-orbital into a p-orbital, when the orientation of its oscillation electric field vector is perpendicular to the nodal plane of the p-orbital (Figure 1.7a). In turn, it is not possible to excite the electron from one s-orbital into another s-orbital of higher energy because such a transition cannot be promoted by an oscillating electric field (Figure 1.7b).

As can be seen from this simple example, it is important that the direction of the oscillation of the electric field of the light fits somehow with the orientation and shape of the electron clouds and the wave functions describing the initial and the final electronic state of the atom or molecule. The direction of the oscillating electric field of the light is defined by its polarization vector (Figure 1.1). The direction and magnitude of the change in the charge distribution during the transition is closely related to the so-called transition dipole moment, which can be calculated from the wave functions of the initial and final electronic state (1.4):

$$\vec{M}_{I \rightarrow F} = \int \psi_F^*(\vec{r}) e \vec{r} \psi_I(\vec{r}) dV \quad (1.4)$$

Here,  $\psi_F$  is the electronic wave function of the molecule in the final state and  $\psi_I$  of the molecule in the initial state;  $e$  is the elementary charge of an electron

and  $\vec{r} = (x, y, z)$  constitutes coordinates, which have their origin ( $x=0, y=0, z=0$ ) in the centre of the molecules charge distribution. The integration  $\int \dots dV = \iiint \dots dx dy dz$  runs over the entire space. The transition dipole moment is one of the most important optical parameters of optical markers in general and in understanding techniques such as fluorescence polarization or Förster resonance energy transfer. Therefore, we will discuss the transition dipole moment in some more detail.

It can be shown that  $\psi_F^* e \vec{r} \psi_I = \psi_F^* \psi_I \cdot e \vec{r}$ . It is easy to see that the first part of this product, the so-called transition density  $\psi_F^* \psi_I$ , has some similarities with  $\psi^* \psi$  (1.2). However, whereas  $\psi^* \psi$  describes the probability density of finding an electron at a certain position in a distinct state  $\psi_F^* \psi_I$ , describes changes in the electronic structure and charge distributions during the transition from the initial state to the final state. Figure 1.8 visualizes the meaning of the transition density exemplarily with a transition of an electron in anthracene (Figure 1.6) from the orbital  $\varphi_f$  to the orbital  $\varphi_h$ . In this case the transition density can be graphically estimated by simply multiplying the signs of the electrons initial and final orbitals,  $\varphi_f$  and  $\varphi_h$ , close to each atom (indicated in Figure 1.8 by + and -, with the number 0 for zero values at nodal planes). At the atom of anthracene, for example, placed in the upper left-hand corner of Figure 1.8 (arrow 1),  $\varphi_f$  has a negative sign, whereas  $\varphi_h$  has a positive sign. As a result of the multiplication the transition density,  $\varphi_f \varphi_h$  must have also a negative sign at this position. At the atom depicted with arrow 5 both  $\varphi_f$  and  $\varphi_h$  have a positive sign and thus the resulting transition density has a positive sign. Repeating this procedure for all atoms helps to generate a graphical estimate of the transition density  $\varphi_f^* \varphi_h$  shown on the right-hand side in Figure 1.8. Obviously, the transition density is dominated by positive signs on the right-hand side of the molecule and by

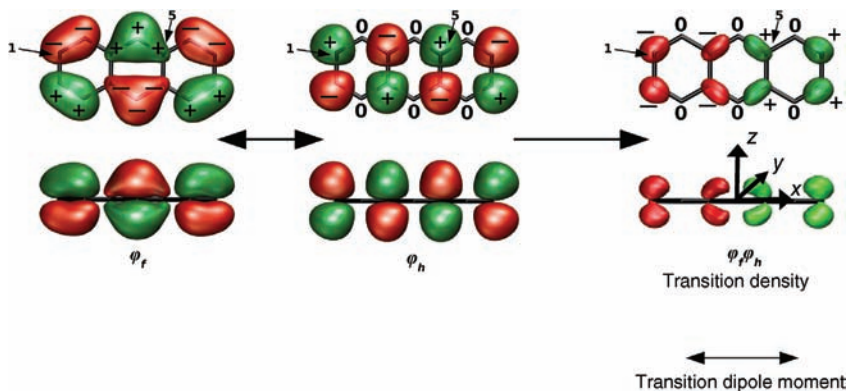


**Figure 1.8** Schematic representation of the construction of the transition density and the direction of the transition dipole moment for the transition between the  $\varphi_f$  and  $\varphi_h$  orbitals of anthracene. In this illustration the size of

the transition density is reduced in comparison to the orbitals for better visibility (higher isosurface values for the transition density). Figure created using VMB (see Bibliography for details).

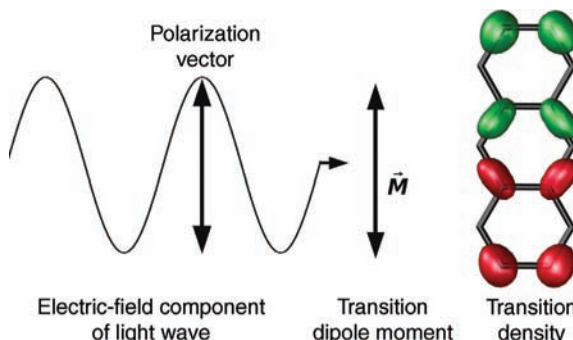


**Figure 1.9** Schematic representation of the optimum direction of the oscillating electric-field component of light (polarization vector) in relation to the direction of the transition dipole moment and the corresponding transition density for a  $\varphi_f \leftrightarrow \varphi_h$  transition in

anthracene. The probability that photons of correct energy can induce this transition is the highest when the polarization vector is parallel to the transition dipole moment. Figure created using VMB (see Bibliography for details).

negative signs on the left-hand side. The consequence is that light with an oscillating electric-field component orientated in the same or a similar direction in which the most dominant difference in the transition density is present has the highest chance of promoting an electron from the molecular orbital  $\varphi_f$  to the molecular orbital  $\varphi_h$  (Figure 1.9).

The direction of the largest difference in the transition density for a certain transition is calculated by integration over the entire transition density using (1.4) and results in a vector  $\vec{M}$ , which is the transition dipole moment. The highest probability that light excites electrons in a molecule is observed when its oscillating electric-field component, that is its polarization vector, is exactly parallel with the transition dipole moment for the corresponding transition (Figure 1.9). Since the wave functions oscillate, the signs of the orbitals in Figure 1.8 are arbitrary. As a result, it is also arbitrary whether the transition dipole moment vector points in one or the other direction (indicated by the double arrow in Figures 1.8 and 1.9).

The probability that a photon is absorbed is higher the larger the corresponding transition dipole moment vector becomes. It depends quadratically on the absolute value of the transition dipole moment vector:

$$P_{I \rightarrow F} \propto |\vec{M}_{I \rightarrow F}|^2 \quad (1.5)$$

Also, the probability of the reverse process, the transition of an electron from an energetically higher state to an energetically lower state with a simultaneous emission of a photon is directly proportional to the square of the transition dipole moment.

Inspecting the time dependence of the transition density reveals that it has one oscillating component that corresponds to the difference frequency between the final and initial wave-function oscillations. This difference frequency corresponds exactly to the frequency and thus the energy of photons that can induce the

transition. A transition thus corresponds to the case where the oscillating electric-field component of light is in resonance with the corresponding transition density oscillation between initial and final states.

A calculation of the transition density and the transition dipole moment between the two s-orbitals (Figure 1.7b) explains why this transition cannot be induced by light. The corresponding transition density is spherically symmetrical around the spherically symmetrical origin at the nucleus (position of the nucleus is at  $x=0$ ,  $y=0$ ,  $z=0$ ). Since the term  $e\vec{r}$  in (1.4) switches signs at the origin ( $x=0$ ,  $y=0$ ,  $z=0$ ), in the overall integration different parts around the origin cancel each other out exactly. For example, at the arbitrary position ( $x=l$ ,  $y=0$ ,  $z=0$ ) the value of the transition density,  $\psi_F^*\psi_I$ , is exactly the same as at the position ( $x=-l$ ,  $y=0$ ,  $z=0$ ). The term  $e\vec{r}$  also has the same absolute value at these two positions but opposite signs [remember that  $\vec{r} = (x, y, z)$ ]. Consequently,  $\psi_F^*\psi_I \cdot e\vec{r}$  at these two positions also have the same absolute values but opposite signs and therefore cancel each other out exactly in the integration described by (1.4). The same applies for any other two positions ( $x, y, z$ ) and ( $-x, -y, -z$ ). As an overall result the transition dipole moment is zero. In general, transitions are called optically forbidden or dipole forbidden when they have a zero transition dipole moment.

Some important selection rules for optical transitions can be deduced directly from the above argument. For instance, the parity selection rule, also called Laporte's rule, that applies for molecules having an inversion symmetry centre. Molecules having an inversion symmetry centre always have identical atoms at the positions ( $x, y, z$ ) and ( $-x, -y, -z$ ). The centre itself is located in the middle of the molecules and has the coordinates  $x=0$ ,  $y=0$ ,  $z=0$ . This is the case for ethene (Figure 1.4), butadiene (Figure 1.5) and also for anthracene (Figure 1.6). The corresponding molecular orbitals of these molecules can either have a g (gerade) or a u (ungerade) symmetry. For orbitals with g symmetry the wave functions have identical values for any pair of positions ( $x, y, z$ ) and ( $-x, -y, -z$ ). Examples are the orbitals  $\pi_2$  and  $\pi_4$  of butadiene (Figure 1.5). All other orbitals of such molecules have u symmetry. Laporte's rule states that transitions of electrons between two orbitals that both have either g (gerade) or u (ungerade) symmetry have vanishing transition dipole moments. Therefore, g  $\rightarrow$  g and u  $\rightarrow$  u transitions are forbidden, while u  $\rightarrow$  g and g  $\rightarrow$  u transitions are allowed. As an example the  $\pi_2(g) \rightarrow \pi_3^*(u)$  transition of butadiene (Figure 1.5) is allowed whereas the  $\pi_2(g) \rightarrow \pi_4^*(g)$  transition is dipole forbidden. In the next chapter we will see that these rules also apply for important biological pigments such as carotenoids.

## 1.4

### Absorption Spectra of Molecules in Liquid Environments. Vibrational Excitation and the Franck–Condon Principle

Having learnt what determines the magnitude of absorption and emission of photons by molecules we now turn to the question of what factors affect the overall shape of an absorption or emission spectrum. An absorption spectrum

describes the frequency or wavelength dependence of the probability that a molecule absorbs photons of the corresponding photon energy. Figures 1.10a and b show schematic absorption spectra of two different molecules in liquid solution. The absorption spectra are composed of various peaks or absorption bands. The absorption band observed for the longest wavelength (lowest photon energy), eq. 1.1 corresponds to the absorption of photons having energies corresponding to transitions from the electronic ground state to the first possible electronically excited state,  $S_0 \rightarrow S_1$ . The absorption band is not a narrow line, corresponding to an exact defined transition energy, because molecules in liquids are exposed to many different solvent environments. The different momentary solvent charge distributions and other environmental effects affect the electrons of the molecule and result in slight shifts in the  $S_0$  and  $S_1$  state energies. Other effects can also result in an additional line broadening of the observed absorption bands.

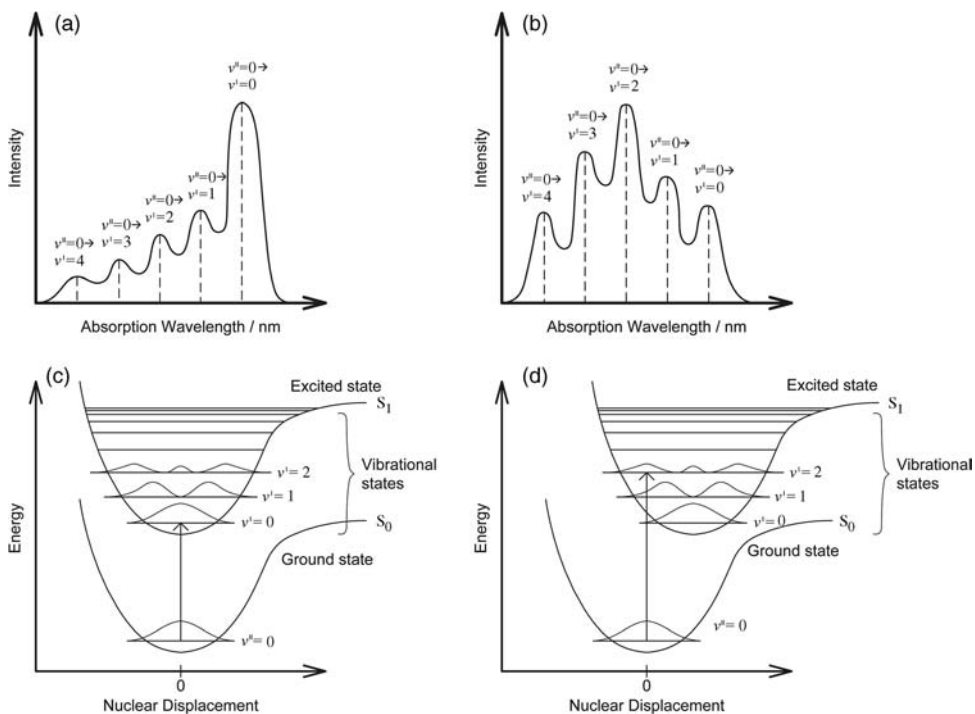


**Figure 1.10** (a) and (b) Schematic absorption spectra of two different molecules. Parts (c) and (d) show, schematically, the respective potential curves for the molecules in the ground and in the excited states,  $S_0$  and  $S_1$ . For the vibrational eigenstates the probabilities of finding the nuclei at certain positions relative to the equilibrium positions are visualized. Because nuclei are heavier than electrons the nuclei remain mainly stationary during electronic transitions and therefore “vertical”

transitions are most likely. For the molecule depicted in (b) and (d), for example, it is most probable that a simultaneous excitation into the third vibrational state ( $v = 2$ ) occurs during an electronic excitation,  $S_0 \rightarrow S_1$ . Please note that here probability densities for finding the nuclei at a certain place,  $P_v(\vec{r})$  (1.6), are visualized and not the vibrational wave functions,  $\chi_v(\vec{r})$ , from which the Franck–Condon integrals are actually calculated according to (1.7).

The bands observed at shorter wavelengths or higher photon energies correspond to transitions in which, simultaneously, vibrations of the nuclei in the molecules are excited in addition to the pure electronic excitation (Figures 1.10c and d). Such transitions are called vibronic transitions. What determines the probability that a certain vibrational state is excited simultaneously? As with electrons, for the nuclei of a molecule only probabilities can be given of finding them at a certain position. For a certain vibrational state,  $\nu$ , of molecules this probability can be calculated from vibrational wave functions,  $\chi_\nu(\vec{r})$ :

$$P_\nu(\vec{r}) = \chi_\nu^*(\vec{r}) \chi_\nu(\vec{r}) \quad (1.6)^3$$

Again, only certain vibrational eigenstates are possible. At room temperature, molecules are usually in the lowest vibrational state of the electronic ground state,  $S_0$ . Vibrational eigenstates are defined by the vibrational quantum number, being zero for the vibrational ground state,  $\nu=0$ . Figure 1.10c and d shows that for a diatomic molecule the probability distribution of finding the two nuclei at a certain position displaced from their equilibrium distance is given by a Gaussian function for  $\nu=0$ . In Figure 1.10 the equilibrium position in the  $S_0$  state is defined by the nuclear displacement 0 on the  $x$ -axis. A displacement of the nuclei to longer distances acts against the electronic bonding forces. A displacement of the nuclei to shorter distances acts against the repulsion forces between the positively charged nuclei. Consequently, any displacement leads to an increase in the energy contained in the molecule. This energy increase for the  $S_0$  and in the  $S_1$  states is visualized by the parabolic-like curves in Figure 1.10c and d. Such curves are called potential-energy curves. For very large separations of the nuclei, of course, bond breakage or dissociation occurs. This is indicated by the asymmetry of the curves for high vibrational energies.

Why is the probability for a pure electronic excitation ( $\nu''=0 \rightarrow \nu'=0$ )<sup>4)</sup> for some molecules (Figures 1.10a and c) the highest, whereas for other molecules (Figure 1.10b and d) an excitation into the third vibrational state of  $S_1$  ( $\nu''=0 \rightarrow \nu'=2$ ) apparently has the highest probability? This can be rationalized by the so-called Franck–Condon principle. Since the timescale of excitation of the light electrons into a higher electronic state is far shorter than the vibrational motions of the heavier nuclei, the molecular geometry remains constant during the excitation process (vertical transitions in Figure 1.10). In the first molecule (Figures 1.10a and c) the equilibrium positions of the atoms in the excited state,  $S_1$ , are very similar to those in the  $S_0$  state. As a consequence, no vibrations are

- 3) The separate description of vibrational wave functions,  $\chi_\nu$ , that are independent from wave functions describing the only the electrons,  $\psi$  (1.2), is again only an approximation that is usually close to the real situation. This approximation is called the Born–Oppenheimer approximation. Again, an exact description is only possible by a wave function,  $\psi_{\text{molecule}}$ , that describes the states of an entire molecule in a certain environment including all electrons and nuclei simultaneously:  

$$\psi_{\text{molecule}} \approx \psi \cdot \chi_\nu$$
- 4) The convention is to define the number of the vibrational quantum states of molecules in the electronic ground state,  $S_0$ , by  $\nu''$ , whereas the corresponding number for vibrational quantum states of the excited state,  $S_1$ , is defined by  $\nu'$ .

induced by the electronic transition,  $S_0 \rightarrow S_1$ , and the molecule is preferentially excited into the vibrational ground state of the  $S_1$  state. In the absorption spectrum the band corresponding to this transition dominates. In the other molecule, however, the equilibrium positions of the nuclei in the  $S_1$  state are shifted towards longer internuclear distances (Figure 1.10d). This situation often applies simply because excited states usually have more antibonding character (Figures 1.3–1.5) and, therefore, the equilibrium distances of the nuclei are longer. Because the nuclei are heavier than the electrons, they can change their position very little during the excitation of an electron. As a consequence, the vibrational state observed after this transition is the most probable, in which the nuclear geometry can remain the same or similar to the nuclear geometry in the ground state,  $S_0$ ,  $v'' = 0$ . For the molecule in Figure 1.10b and d the third vibrational state ( $v' = 2$ ) of the  $S_1$  state has a very large overlap of its vibrational probability distribution with the vibrational probability distribution in the ground state, or to be more quantitative the nuclear overlap integral

$$\int \chi_{v''}(r)\chi_{v'}(r)dV \quad (1.7)$$

is the largest for this transition. Here  $\chi_{v''}(r)$  describes the vibrational wave function of the vibrational ground state ( $v'' = 0$ ) in the  $S_0$  state and  $\chi_{v'}(r)$  the vibrational wave functions in the  $S_1$  state. Integrals described by (1.7) are called Franck–Condon integrals. In the absorption spectrum the relative magnitudes of the vibrational bands are proportional to the square of the corresponding Franck–Condon integrals:

$$P_{v'' \rightarrow v'} \propto \left| \int \chi_{v''}(r)\chi_{v'}(r)dV \right|^2 \quad (1.8)$$

Figures 1.10c and d show only the potential curves, vibrational energy levels and probabilities of finding the nuclei separated by certain displacements for a diatomic molecule. In more complex molecules of course various different vibrational modes are possible that cannot be visualized in a single two-dimensional plot. Nevertheless, the most important conclusions derived here are also valid for more complicated molecules.

## 1.5

### What Happens After Molecules have Absorbed Light? Fluorescence, Nonradiative Transitions and the Triplet State

Let us now turn to the question of what happens to the excitation energy after a molecule has absorbed a photon. The energy absorbed by a molecule can be released via several pathways. For biomolecules or optical markers, which are usually in an aqueous or liquid environment, in most cases first vibrational relaxation is dominant. This process is the quick release of the entire vibrational

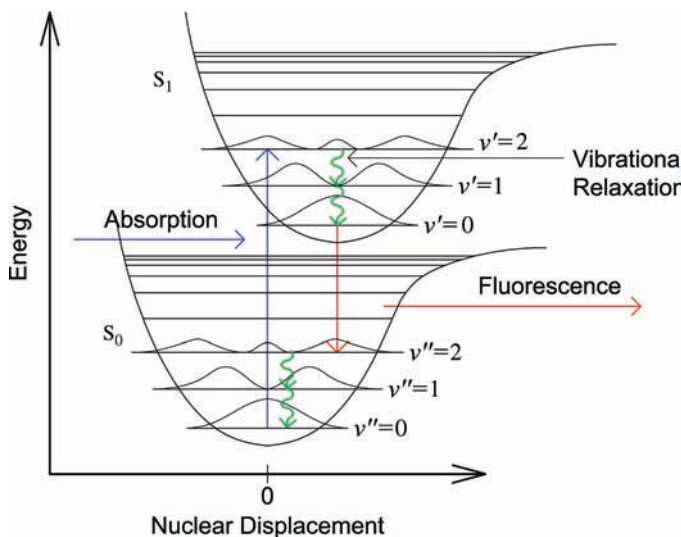


**Figure 1.11** After excitation of a molecule (blue) usually very rapid vibrational relaxation (green) occurs in the excited state. As a consequence, fluorescence (red) normally occurs from the lowest vibrational level of the excited state,  $S_1(v' = 0)$ .

excess energy in the  $S_1$  state, often vibrational quantum by vibrational quantum, to the surrounding solvent molecules. The process is very fast, occurring on the femto- to picosecond ( $10^{-15}$ – $10^{-12}$  s) timescale. In Figure 1.11 this rapid vibrational relaxation is indicated by green wavy arrows. It is a general convention that such nonradiative processes are indicated by wavy arrows, whereas radiative processes, which consist of the absorption or emission of a photon, are indicated by straight arrows. The final result of fast vibrational relaxation is that the molecule is now in the lowest vibrational state of the electronic excited state ( $S_1, v' = 0$ ).

The next obvious pathway is the opposite process to absorption. This radiative de-excitation into the ground state,  $S_1 \rightarrow S_0$ , is called spontaneous emission or simply fluorescence (red arrow in Figure 1.11). Mechanistically, it is governed by very similar processes as absorption. The probability of fluorescence is again proportional to the square of the transition dipole moment. The emitted photon has preferentially a polarization parallel to the transition dipole moment. For the emission, again the Franck–Condon principle applies (Figure 1.10). Because the potential curves and vibrational wave functions for vibrational eigenstates are often very similar and symmetric for both the  $S_0$  and  $S_1$  states, it can be understood from the Franck–Condon principle that the fluorescence spectrum often has a mirror image like shape in comparison to the absorption spectrum (Figure 1.12). Again the Franck–Condon integral (1.7) is the largest for the transition of the lowest vibrational state of the electronically  $S_1$  state to the third vibrational state of  $S_0$  for the example shown in Figures 1.11 and 1.12 [ $S_1(v' = 0) \rightarrow S_0(v'' = 2)$ ]. Consequently, also in the fluorescence spectrum the third vibrational band dominates. The absorption and fluorescence bands with the largest and smallest

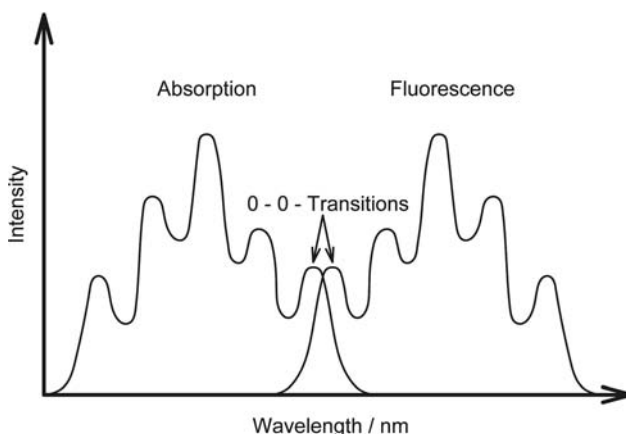


**Figure 1.12** Because the potential curves and vibrational wave functions for the electronic ground and excited states of a molecule, are often very similar and symmetric for small  $v$  in many cases a mirror symmetry of absorption and fluorescence spectra can be observed.

wavelengths, respectively, define the so-called 0–0 transitions. These correspond to transitions between the lowest vibrational eigenstates in the ground and excited states,  $S_0(v' = 0) \rightarrow S_1(v' = 0)$  and  $S_1(v' = 0) \rightarrow S_0(v' = 0)$ . Usually, these bands are not exactly overlapping, because typically the molecule itself and solvent molecules around the solute molecule rearrange themselves as a response to the new electronic structure in excited states. This results in a slight lowering of the  $S_1$  state energy and leads to a shift of the 0–0 transition in the fluorescence spectrum to longer wavelengths in comparison to the 0–0 transition in the absorption spectrum.

The general observation that emitted photons have longer wavelengths than the absorbed photons is called the Stokes shift.

If the energy gap between the  $S_1$  state and the  $S_0$  state is large and the molecular structure is rather rigid, for example because of many double bonds, then often fluorescence dominates the de-excitation of the molecules. However, if the energy gap becomes smaller or if the molecule is very flexible then nonradiative de-excitation of the  $S_1$  state often becomes dominant (energy-gap law). This is shown schematically in Figure 1.13. The smaller the energy gap between  $S_1$  and  $S_0$ , the higher becomes the chance that there is a good overlap between the vibrational ground-state wave function of the  $S_1$  state with wave functions of highly excited vibrations in the electronic ground state. If that is the case, the molecule can switch from the electronic excited state into the electronic ground state,  $S_1 \rightsquigarrow S_0$ , without the emission of a photon (blue horizontal arrow in Figure 1.13) and without a major rearrangement of the nuclear positions during this transition. This process is called internal conversion. Again, the probability for this process can be calculated using overlap integrals similar to (1.7). Once such a high vibrational state of the electronic ground state is populated, fast vibrational relaxation of the vibrational energy into the solvent environment again occurs on the femto- to picosecond timescale.

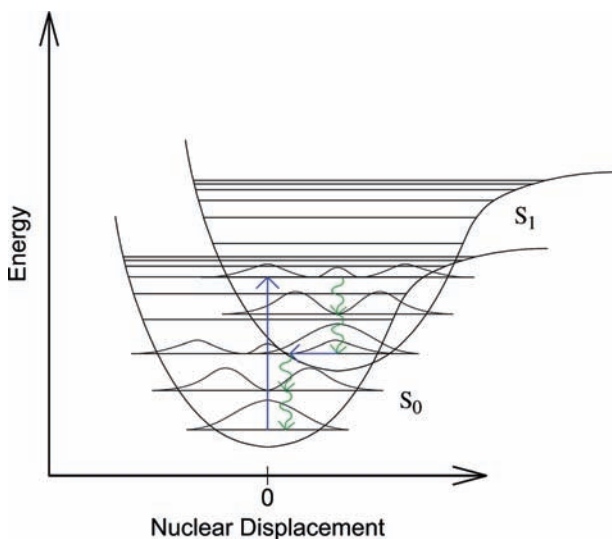


**Figure 1.13** Visualization of nonradiative relaxation (internal conversion) of excited states, which often dominates for small ground state–excited state energy gaps.

If originally a higher electronically excited state,  $S_2, S_3 \dots$ , has been populated then usually very fast internal conversion into the lowest excited state,  $S_1$ , also takes place, because the energy gap between excited states is normally smaller than the energy gap between  $S_1$  and  $S_0$ . Thus, in general, fluorescence occurs from the lowest electronically excited state in its lowest vibrational state, regardless of which excited state was originally populated. This general rule is called Kasha's rule.

For the third possible de-excitation path way we have to introduce a further important class of electronically excited states that are named triplet states. Figure 1.14 shows examples of electrons occupying different orbitals in the ground state,  $S_0$ , and in various possible excited states of a molecule. For most biomolecules and fluorescence markers in their electronic ground state a situation similar to the  $S_0$  state in Figure 1.14 applies, in which all orbitals up to the HOMO

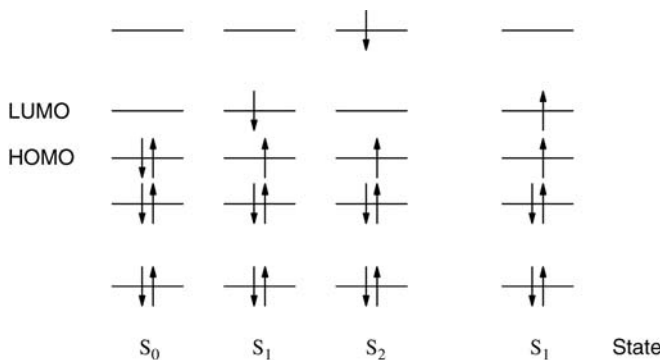


**Figure 1.14** Possible excited-state configurations.

are filled with two electrons of opposite spins. The spin of an electron is a purely quantum mechanical property and can be regarded as a kind of angular momentum of the electron. The electron can only occur in two spins,  $\alpha$  and  $\beta$ , which are depicted by opposite arrows in Figure 1.14. The quantum mechanical Pauli rule states that no electron in a molecule can have the exact same properties as another electron in the molecule. Therefore, an orbital can be occupied by two electrons only if they have different spins.

However, as can be seen from the right most diagram in Figure 1.14, Pauli's rule is not violated if a single electron excited into a higher molecular orbital has the same spin as the remaining electron in the original HOMO, because they occupy different orbitals. Such electronic states with two unpaired electrons of the same spin are referred to as triplet states. The energetically lowest triplet state is usually depicted by  $T_1$ . States in which for each electron another electron with opposite spin is present are called singlet states.

The vector diagrams depicted in Figure 1.15 give us an idea of the origin of this nomenclature. The spin of an electron is a purely quantum mechanical property and has no classical analogue. However, due to the spin, the electron has a small magnetic moment, with the result that an isolated electron acts similarly to a small magnet. In an external magnetic field, the magnetic moment of an electron can be symbolized by a vector representing the orientation of the magnetic moment with respect to the external field (thin arrows in Figure 1.15). Depending on the spin of the electron, the magnetic moment can be either orientated with or against the external magnetic field. These two orientations are assigned  $\alpha$ - or  $\beta$ -spin, respectively. Due to quantum mechanical reasons, it is not orientated exactly parallel to the external field but slightly tilted. In addition, it rotates around the axis of this external field. Further details of the properties of spin states will be discussed in Chapter 4. Here, it shall only be noted that the magnetic moments of electrons paired in an orbital sum to a zero total magnetic moment symbolized by the opposite arrows on the left in Figure 1.15. Therefore, only a single state is possible in an external magnetic field, which is defined as singlet state,  $S$ . In the triplet state, however, the magnetic moments of the

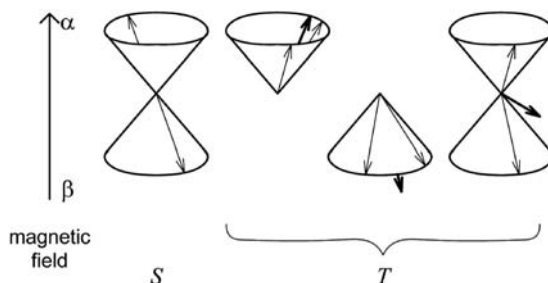


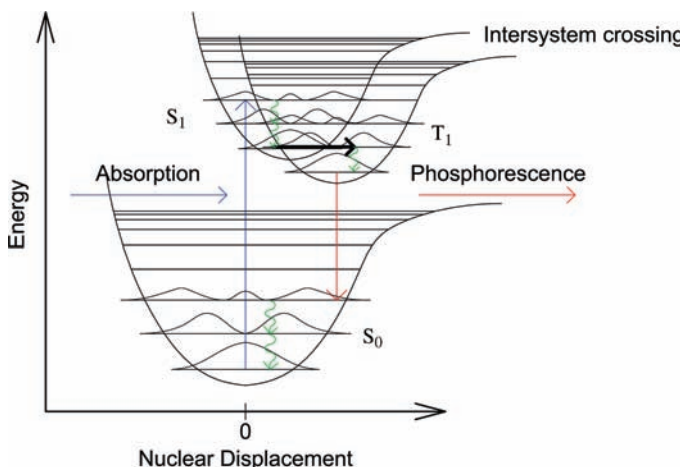
**Figure 1.15** Possible orientations of the magnetic moments of the electron spin of two electrons and the corresponding total magnetic moment (thick arrow) in the vector representation. In the singlet state the magnetic moments of the individual electrons (thin

arrows) cancel each other out resulting in a zero total magnetic moment. In the triplet state the magnetic moments of the individual electrons always span the same angle and their summation can point in three different directions.

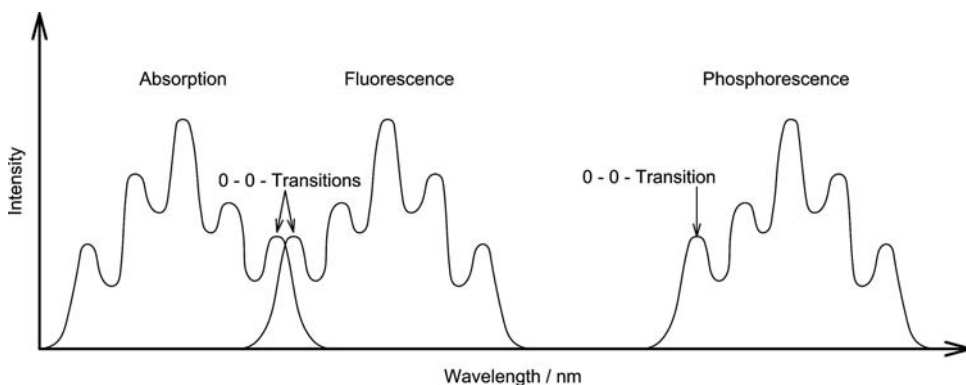
unpaired electrons do not cancel each other out (thick arrows in Figure 1.15). The individual magnetic moments of the two unpaired electrons can be combined in three ways ( $\alpha\alpha$ ,  $\beta\beta$ ,  $\alpha\beta$ ) in an external magnetic field. This is the origin for the name triplet state (T). S and T are also called the multiplicity of an electronic state. Because electrons with the same spin cannot be simultaneously at the same place (Pauli's rule) the repulsive interactions between these electrons are generally smaller. As a consequence, triplet states are usually lower in energy than the respective singlet states.

Figure 1.16 shows how the formation of a triplet state typically takes place. The triplet state is usually also populated from the vibrational ground state of an excited singlet state,  $S_1(v'=0)$ . The corresponding transition,  $S_1 \rightsquigarrow T_1$ , is called intersystem crossing. As in the case of internal conversion, intersystem crossing is favoured when a good overlap exists between vibrational wave functions of the excited singlet state,  $S_1$ , with vibrational wave functions of the triplet state,  $T_1$  [Figure 1.16, (1.7)]. In comparison to fluorescence or internal conversion, the process of intersystem crossing is usually a lot less probable. Intersystem crossing requires a change of the total spin of the electron that corresponds to a change of the angular momentum. However, it is a fundamental law that the overall angular momentum of an isolated system must remain constant. Because there are only very limited possibilities to compensate for the change in angular momentum such spontaneous flips in the spin of electrons are rather unlikely and are therefore called spin forbidden. Only when the change in the spin angular momentum can be compensated by certain mechanisms can such spin flips happen. An important example for such a mechanism is spin-orbit coupling in which, in a classical picture, a change in the angular momentum describing the electron movement around the nuclei compensates the spin flip.

After intersystem crossing, vibrational excitation is also usually generated, which is again dissipated within femto- to picoseconds until the molecule



**Figure 1.16** Visualization of triplet-state formation (intersystem crossing) and phosphorescence.



**Figure 1.17** Schematic representation of typical absorption, fluorescence and phosphorescence spectra. It should be noted that in real spectra with a wavelength scale the phosphorescence spectrum typically appears somewhat broader than the corresponding

fluorescence spectrum. The reason is that wavelengths are not linearly proportional to the state energies (compare with (1.1)). Only on a wavenumber or frequency scale really identical spacings of the vibrational bands can be expected.

remains in the vibrational ground state of  $T_1$ . From here, two path ways are possible. Radiative relaxation from the triplet state,  $T_1 \rightarrow S_0$ , is called phosphorescence. Generally, phosphorescence is the luminescence arising from radiative transitions involving a change in multiplicity. Nonradiative de-excitation or intersystem crossing,  $T_1 \rightsquigarrow S_0$ , is also possible. Similar to the internal conversion,  $S_1 \rightsquigarrow S_0$ , the probability for this process depends on overlap integrals such as (1.7) of the vibrational ground state of  $T_1$  with highly excited vibrational states of  $S_1$ . Both processes also require a spin flip and are thus rather improbable. As an overall result, many biomolecules and fluorescence markers rarely undergo intersystem crossing to the triplet states, but once a triplet state has been formed it is usually quite long lived in comparison to singlet states.

The generally lower energy of the triplet states cause the phosphorescence to appear at longer wavelengths than fluorescence (Figure 1.17). Similarly to fluorescence, the phosphorescence spectrum often appears to be a mirror image of the ground-state absorption, because the vibrational modes are often very similar in all electronic states.

## 1.6

### Quantitative Description of all Processes: Quantum Efficiencies, Kinetics of Excited State Populations and the Jablonski Diagram

All the effects described so far can be summarized in a diagram named after the Polish physicist Aleksander Jabłoński (1898–1980) (Figure 1.18). In the Jablonski diagram only energy levels of the electronic states, and sometimes also vibrational energy levels, are depicted as horizontal lines. As mentioned earlier, all radiative processes (absorption or emission of a photon) are depicted using straight arrows,

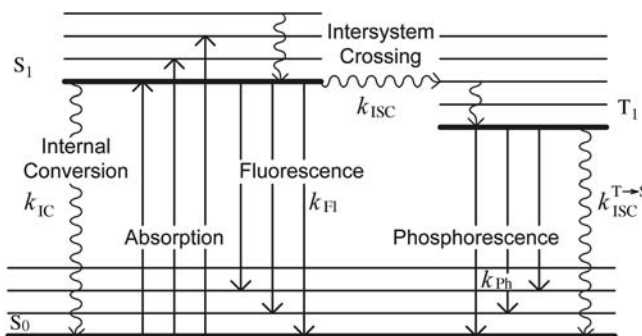


Figure 1.18 A Jablonski diagram.

whereas nonradiative processes are portrayed using wavy arrows. For each process a rate constant  $k$  can be given, which is proportional to the probability per time unit that the corresponding process occurs. For example, if the rate constant for internal conversion,  $S_1 \rightsquigarrow S_0$ , of a molecule is  $k_{IC} = 1 \text{ ns}^{-1}$  and if the rate constant for fluorescence,  $S_1 \rightarrow S_0$ , is only  $k_{FL} = 0.1 \text{ ns}^{-1}$ , the probability that the excitation energy is released via fluorescence is ten times less than via nonradiative internal conversion.

With the Jablonski diagram important parameters like, for example, quantum efficiencies or quantum yields of different processes can be derived. The fluorescence quantum efficiency is the number of photons emitted by a molecule as fluorescence divided by the number of photons that were previously absorbed by the molecule in a larger number of excitation and de-excitation cycles.

$$\Phi_{FL} = \frac{\text{Number of photons emitted as fluorescence}}{\text{Number of absorbed photons}} \quad (1.9)$$

A high fluorescence quantum efficiency is an important property of fluorescence markers. In general, the quantum efficiency of any process is defined as the number of quanta undergoing the process divided by the number of absorbed photons or quanta originally present in the initial state from which this process occurs. Therefore, the quantum efficiency is a direct measure of the probability of certain processes in a molecule. The quantum efficiency of a process can be calculated by dividing the rate constant of the process of interest by the sum of the rate constants of all processes simultaneously depopulating the initial state. The fluorescence quantum yield, for example, can be calculated by:

$$\Phi_{FL} = \frac{k_{FL}}{k_{FL} + k_{IC} + k_{ISC}} \quad (1.10)$$

The quantum yield for  $S_1 \rightsquigarrow T_1$  intersystem crossing can be calculated analogously:

$$\Phi_{ISC} = \frac{k_{ISC}}{k_{FL} + k_{IC} + k_{ISC}} \quad (1.11)$$

To calculate the phosphorescence quantum yield one has to multiply the quantum yield for  $S_1 \rightsquigarrow T_1$  intersystem crossing by the probability for radiative emission from the triplet state,  $T_1 \rightsquigarrow S_0$ :

$$\Phi_{\text{Ph}} = \Phi_{\text{ISC}} \frac{k_{\text{Ph}}}{k_{\text{Ph}} + k_{\text{ISC}}^{\text{T} \rightarrow \text{S}}} \quad (1.12)$$

The sum of all radiative and nonradiative processes must be one:

$$\Phi_{\text{Fl}} + \Phi_{\text{Ph}} + \sum \Phi_{\text{NR}} = 1 \quad (1.13)$$

Here, nonradiative processes can be internal conversion from the singlet or intersystem crossing from the triplet state,  $S_1 \rightarrow S_0$  and  $T_1 \rightarrow S_0$ , or other processes like photochemical reactions or energy-transfer processes (not depicted in Figure 1.18). Energy-transfer processes are described in detail in Chapter 3 (Section 3.5).

A time constant of a process is defined as the inverse of its corresponding rate constant  $\tau_X = k_X^{-1}$ . A rate constant for fluorescence,  $S_1 \rightarrow S_0$ , of  $k_{\text{Fl}} = 0.1 \text{ ns}^{-1}$ , for example, corresponds to a time constant for fluorescence of  $\tau_{\text{Fl}}^{\text{rad}} = 10 \text{ ns}$ . The overall lifetime of an electronic state is also a time constant and can be calculated from the inverse of the sum of the rate constants,  $k_X$ , of all processes depopulating this state:

$$\tau_{\text{State}} = \left( \sum k_X \right)^{-1} \quad (1.14)$$

According to the Jablonski diagram in Figure 1.18 the lifetime of the first excited singlet state of a molecule is for example:

$$\tau_{S_1} = (k_{\text{IC}} + k_{\text{Fl}} + k_{\text{ISC}})^{-1} \quad (1.15)$$

as long as no additional processes depopulate  $S_1$ . Often, the rate constant for intersystem crossing,  $k_{\text{ISC}}$ , is small compared to  $k_{\text{Fl}}$  and  $k_{\text{IC}}$ . Then, the  $S_1$  state lifetime depends on the relative magnitudes of  $k_{\text{Fl}}$  and  $k_{\text{IC}}$ . The magnitude of  $k_{\text{Fl}}$  is directly related to the magnitude of the transition dipole moment for the transition  $S_1 \rightarrow S_0$ :

$$k_{\text{Fl}} \propto |\vec{M}_{S_1 \rightarrow S_0}|^2 \quad (1.16)$$

[see also (1.4)]. Typically, the corresponding time constants,  $\tau_{\text{Fl}}$ , are on the order of a few up to tens of nanoseconds. Consequently, if the corresponding time constant for internal conversion is as short as, for example, 100 ps, for instance due to a small  $S_1 - S_0$  energy gap, then the  $S_1$  state lifetime will also be on the order of only a few 100 ps and almost no fluorescence will be emitted by the molecule. In contrast, if the corresponding time constant for internal conversion is  $> 10 \text{ ns}$  then the  $S_1$  state lifetime will be on the order of the time constant for fluorescence and fluorescence emission will be dominant.

The kinetic behaviour of the different states also depends on the specific rate constants. Basically, the kinetics of the population of excited states of an ensemble of molecules can be treated by the same mathematical frame work as the kinetics of chemical or biochemical reactions. If the  $S_1$  state of the molecules is populated by a short pulse of excitation light its decay can be calculated using the following approach:

$$\frac{dP_{S_1}(t)}{dt} = -(k_{\text{FI}} + k_{\text{IC}} + k_{\text{ISC}}) \cdot P_{S_1}(t) \quad (1.17)$$

Here,  $P_{S_1}(t)$  is the population of the first excited singlet state.  $dP_{S_1}(t)/dt$  is the actual velocity by which the population of molecules in the  $S_1$  state changes; it depends on the rate constants of all depopulating processes and of the actual remaining  $S_1$  population. Integration of Eq. (1.17) shows that the  $S_1$  state population decays monoexponentially after a pulsed population (Figure 1.19):

$$P_{S_1}(t) = P_{S_1}^0 \cdot e^{-(k_{\text{FI}} + k_{\text{IC}} + k_{\text{ISC}})t} = P_{S_1}^0 \cdot e^{-t/\tau_{S_1}} \quad (1.18)$$

Here,  $P_{S_1}^0$  is the initial absolute population generated in the  $S_1$  state due to the pulsed excitation.

The lifetime of the  $S_1$  state,  $\tau_{S_1}$ , determines how fast its population decreases. Since the fluorescence intensity,  $I_{\text{FI}}(t)$ , is always proportional to the actual  $S_1$  state population,  $P_{S_1}(t)$ , it also decays in the same way as the  $S_1$  state population:

$$I_{\text{FI}}(t) \propto P_{S_1}(t)$$

$$I_{\text{FI}}(t) = I_{\text{FI}}^0 \cdot e^{-t/\tau_{S_1}} \quad (1.19)$$

Thus, the lifetime of the first excited state  $S_1$  can be determined experimentally from the fluorescence's decay observed in time-resolved fluorescence

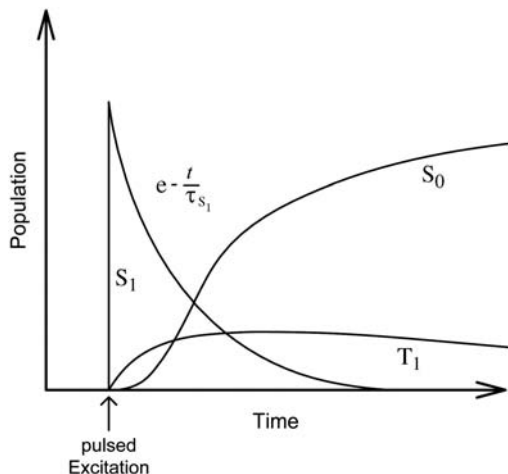


Figure 1.19 Schematic presentation of typical kinetics of excited-state populations.

measurements. The measured fluorescence decay is therefore often also referred to as the fluorescence lifetime of a molecule. Notably, however, this is not to be confused with the time constant for the radiative emission or fluorescence,  $\tau_{\text{Fl}}^{\text{rad}}$ . The time constant for radiative emission or fluorescence,  $\tau_{\text{Fl}}^{\text{rad}} = k_{\text{Fl}}^{-1}$ , is defined for the pure process of depopulation of the first excited singlet state by emission of fluorescence photons (Figure 1.18). This time constant is in general larger than or at most equal to the lifetime of the first excited state,  $\tau_{S_1}$ :  $(\tau_{S_1})^{-1} = (\tau_{\text{IC}})^{-1} + (\tau)^{-1} + (\tau_{\text{ISC}})^{-1}$  [compare with (1.14) and (1.15)]. In this book the time constant for radiative emission or fluorescence is always depicted by  $\tau_{\text{Fl}}^{\text{rad}}$  to clearly differentiate it from  $\tau_{S_1}$ . However, be aware that in the literature the symbol,  $\tau_{\text{Fl}}$ , is very often used to describe measured fluorescence decays that reflect nothing other than the lifetime of the first excited singlet state,  $\tau_{S_1}$  (1.19).

Figure 1.19 depicts schematically typical time-dependent changes of the populations of  $T_1$  and  $S_0$ . Similarly to the kinetic description of the single state population, changes in the triplet-state population can also be described by differential equations. Because the triplet state is populated from the singlet state via intersystem crossing we have to consider a pair of coupled differential equations:

$$\begin{aligned} \frac{dP_{S_1}(t)}{dt} &= -(k_{\text{Fl}} + k_{\text{IC}} + k_{\text{ISC}}) \cdot P_{S_1}(t) \\ \frac{dP_T(t)}{dt} &= +k_{\text{ISC}} \cdot P_{S_1}(t) - (k_{\text{Ph}} + k_{\text{ISC}}^{T \rightarrow S}) \cdot P_T(t) \end{aligned} \quad (1.20)$$

Here,  $P_T(t)$  is the population of the first excited triplet state and  $dP_T(t)/dt$  is the actual velocity by which the population of molecules in the  $T_1$  state changes as a function of  $S_1$  and  $T_1$  state populations and all rate constants populating or depopulating these states.

Integration of these coupled equations gives:

$$\begin{aligned} P_T(t) &= P_{S_1}^0 \cdot k_{\text{ISC}} \left( \frac{-e^{-(k_{\text{Fl}}+k_{\text{IC}}+k_{\text{ISC}})t} + e^{-(k_{\text{Ph}}+k_{\text{ISC}}^{T \rightarrow S})t}}{(k_{\text{Fl}} + k_{\text{IC}} + k_{\text{ISC}}) - (k_{\text{Ph}} + k_{\text{ISC}}^{T \rightarrow S})} \right) \\ &= P_{S_1}^0 \cdot A(-e^{-t/\tau_{S_1}} + e^{-(k_{\text{Ph}}+k_{\text{ISC}}^{T \rightarrow S})t}) \text{ for } \frac{1}{\tau_{S_1}} > (k_{\text{Ph}} + k_{\text{ISC}}^{T \rightarrow S}) \\ \Rightarrow \\ I_{\text{Ph}}(t) &= I_{\text{Ph}}^0 \cdot A(-e^{-t/\tau_{S_1}} + e^{-(k_{\text{Ph}}+k_{\text{ISC}}^{T \rightarrow S})t}) \end{aligned} \quad (1.21)$$

In a manner similar to the way fluorescence kinetics describe population changes in the excited singlet state,  $S_1$ , (1.19) the observable phosphorescence kinetics describe the kinetics of the triplet-state population. The population curve for  $T_1$  in Figure 1.19 is an exemplary illustration of typical triplet-state kinetics. The triplet-state kinetics are an example of a consecutive reaction scheme,  $S_1 \rightarrow T_1 \rightarrow S_0$ , with the  $T_1$  state being an intermediate. According to Eq. (1.21) the intermediate  $T_1$  population kinetics are described by a biexponential function with an exponential rise term, depending on the  $S_1$  state lifetime,  $\tau_{S_1}$ , and an exponential decay term, depending on the rates for intersystem

crossing from the triplet state and phosphorescence,  $k_{\text{Ph}} + k_{\text{ISC}}^{\text{T} \rightarrow \text{S}}$ . The maximum intermediate triplet-state population depends on the relative magnitude of the rate for intersystem crossing,  $k_{\text{ISC}}$ , in comparison to  $k_{\text{FI}} + k_{\text{IC}}$  and  $k_{\text{Ph}} + k_{\text{ISC}}^{\text{T} \rightarrow \text{S}}$ . If  $k_{\text{ISC}}$  is large compared to  $k_{\text{FI}} + k_{\text{IC}}$  and  $k_{\text{Ph}} + k_{\text{ISC}}^{\text{T} \rightarrow \text{S}}$  a large and long-lived intermediate triplet-state population will be observed. In contrast, if  $k_{\text{ISC}}$  is small compared to  $k_{\text{Ph}} + k_{\text{ISC}}^{\text{T} \rightarrow \text{S}}$  or  $k_{\text{FI}} + k_{\text{IC}}$  the intermediate triplet-state population will always remain very small.

### Problems

- 1.1 Orbitals have regions in which they have negative and positive signs. Explain the physical background of the signs and how this relates to the probability of finding electrons at a certain place.
- 1.2 Spectroscopists often describe energies that are necessary to excite certain electronic states by the wave number of the corresponding photons in units of  $\text{cm}^{-1}$ . Why is this more advantageous than describing the corresponding energies in units of the photons wavelength?
- 1.3 Try to estimate the shape of the possible molecular  $\pi$ -orbitals of the molecule hexatriene ( $\text{CH}_2=\text{CH}-\text{CH}=\text{CH}-\text{CH}=\text{CH}_2$ ). How many nodal planes does each orbital have? What is the energetic order of these orbitals? Which orbitals are the HOMO and LUMO orbitals?
- 1.4 What are important prerequisites before a photon can be absorbed by a molecule?
- 1.5 Figure 1.6 shows schematically four  $\pi$ -wave functions of the molecule anthracene. Sketch the transition density for a transition between the states f and g. In what direction relative to the molecular axis is the transition dipole moment orientated?
- 1.6 Figure 1.5 shows schematically the  $\pi$ -wave functions of the molecule butadiene. Which of the following transitions of butadiene are dipole allowed:
  - a) The  $\pi_1 \rightarrow \pi_4^*$  transition?
  - b) The  $\pi_1 \rightarrow \pi_3^*$  transition?
  - c) The  $\pi_2 \rightarrow \pi_3^*$  transition?
- 1.7 Describe in general the important factors that govern the shape of absorption and fluorescence spectra of molecules in a liquid environment.
- 1.8 The probabilities of finding nuclei at certain positions can be calculated from vibrational wave functions (1.6) in the same way as the probabilities of finding electrons at certain positions can be calculated from electronic wave functions. Figure 1.10 shows schematically the probabilities of finding nuclei at certain positions relative to their equilibrium position for

$v' = 0, 1, 2$ . Try to guess what the corresponding vibrational wave functions look like.

- 1.9** Describe in general the factors that determine the probabilities for fluorescence, internal conversion and intersystem crossing of molecules in a liquid environment.
- 1.10** Below are given corresponding wave numbers and time constants for several transitions between various states of a fluorescent molecule:

$$S_0 \rightarrow S_1: \quad 18\,000 \text{ cm}^{-1}$$

$$S_0 \rightarrow S_2: \quad 22\,000 \text{ cm}^{-1}$$

$$T_1 \rightarrow S_0: \quad 15\,000 \text{ cm}^{-1}$$

Radiative  $S_1 \rightarrow S_0$  transition (fluorescence):

$$\tau_{\text{FL}}^{\text{rad}} = 5 \text{ ns}$$

Nonradiative  $S_1 \rightsquigarrow S_0$  transition (internal conversion):

$$\tau_{\text{IC}}^S = 25 \text{ ns}$$

$S_1 \rightsquigarrow T_1$  intersystem crossing:

$$\tau_{\text{ISC}} = 100 \text{ ns}$$

Radiative  $T_1 \rightarrow S_0$  transition (phosphorescence):

$$\tau_{\text{Ph}} = 2 \text{ s}$$

Nonradiative  $T_1 \rightsquigarrow S_0$  transition (intersystem crossing):

$$\tau_{\text{ISC}}^{T \rightarrow S} = 20 \text{ } \mu\text{s}$$

Sketch the Jablonski diagram using the given data. Mark the radiative and nonradiative transitions on the diagram. Which wavelengths are needed to excite the molecule into  $S_1$  and  $S_2$ ? Calculate for this fluorescent molecule (a) the lifetime of the first excited singlet state,  $\tau_{S_1}$ . (b) The fluorescence quantum yield  $\Phi_{\text{FL}}$ . (c) The triplet quantum yield  $\Phi_{\text{Triplet}}$ . (d) The triplet-state lifetime  $\tau_{\text{Triplet}}$ . (e) The phosphorescence quantum yield after excitation into  $S_1$ .

- 1.11** Fluorescent molecules with larger conjugated  $\pi$ -systems often absorb and emit at longer wavelengths and have larger transition dipole moments than molecules with smaller conjugated  $\pi$ -systems. Try to explain why.

## Bibliography

- Atkins, P.W. and Friedman, R.S. (2004) *Molecular Quantum Mechanics*, Oxford University Press, Oxford.
- Haken, H. and Wolf, H.C. (2005) *The Physics of Atoms and Quanta*, Springer, Berlin.
- Haken, H. and Wolf, H.C. (2008) *Molecular Physics and Elements of Quantum Chemistry*, Springer, Berlin.
- Harris, D.C. and Bertolucci, M.D. (1989) *Symmetry and Spectroscopy: An Introduction to Vibrational and Electronic Spectroscopy*, Dover Publications Inc.
- Humphrey, W., Dalke, A. and Schulten K. (1996) *VMD - Visual Molecular Dynamics*, *Journal of Molecular Graphics* **14**, 33–38.
- Kutzelnigg, W. (2002) *Einführung in die Theoretische Chemie*, Wiley-VCH Verlag GmbH, Weinheim.
- Lakowicz, J.R. (2006) *Principles of Fluorescence Spectroscopy*, Springer, Berlin.
- Levine, I.N. (1999) *Quantum Chemistry*, Prentice Hall.
- Turro, N.J. (1991) *Modern Molecular Photochemistry*, University Science Books.



## 2

# Optical Properties of Biomolecules

### 2.1

#### Introduction

In this chapter we will briefly discuss the optical properties of biomolecules such as proteins, DNA and RNA. The optical properties of important cofactors that often contribute to the absorption and fluorescence of biological samples in the visible spectral range are also presented. The use of these optical properties to determine certain biological parameters will be illustrated in selected application examples. However, before we examine the absorption and fluorescence spectra of these biomolecules we first discuss how such spectra are measured experimentally.

### 2.2

#### Experimental Determination of Absorption and Fluorescence Spectra

Figure 2.1 shows the principle of an absorption spectrometer. A light source provides electromagnetic radiation typically ranging from the UV up to the IR range ( $\sim 200$ – $1200$  nm; see also Figure 1.2). The light from this source is typically divided into two parts. This can be performed, for example, by a beam splitter. One part of this light is sent through a sample cell containing the solution of the compound to be measured. The other part is sent through a reference cell containing only the solvent without the compound. After travelling through the cells both light beams are first spectrally separated and then analysed with detectors. The absorption of the compound for a certain wavelength,  $\lambda$ , can be evaluated by a comparison between the light intensity measured after the sample cell,  $I(\lambda)$ , and the light intensity measured after the reference cell,  $I_0(\lambda)$ . From these two parameters the wavelength-dependent transmission,  $T(\lambda)$ , can be calculated directly:

$$T(\lambda) = \frac{I(\lambda)}{I_0(\lambda)} \quad (2.1)$$

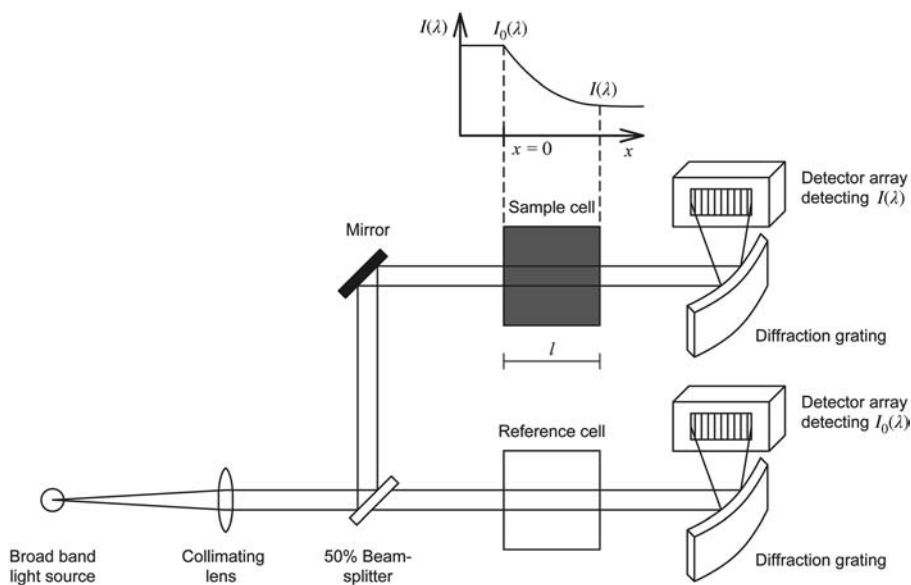


**Figure 2.1** Schematic representation of an absorption spectrometer. In this illustration the intensities  $I(\lambda)$  and  $I_0(\lambda)$  are detected for a larger range of wavelengths simultaneously by combining diffraction gratings with detector

arrays. The diffraction gratings focus light of different wavelengths at different spots on the detector arrays. An arrangement in which several wavelengths are analysed simultaneously is also referred to as a spectrograph.

Of course,  $T$  and all magnitudes described in the following can also be given in units of the frequency,  $\nu$ , or the wave number,  $\bar{\nu}$ , after correct transformation [compare with (1.1)].

At a certain place  $x$  in the sample cell the reduction of the light intensity,  $dI(\lambda, x)/dx$ , is proportional to the concentration,  $C$ , of the absorbing compound:

$$\frac{dI(\lambda, x)}{dx} = -I(\lambda, x) \cdot C \cdot \varepsilon(\lambda) \cdot 2.303 \quad (2.2)$$

Here,  $\varepsilon(\lambda)$  is the decadic molar absorption or extinction coefficient of the compound for the corresponding wavelength,  $\lambda$ ;  $\varepsilon$  is typically given in units of  $M^{-1} \text{cm}^{-1}$ . The contribution of a certain vibronic transition  $S_0^{\nu''} \rightarrow S_1^{\nu'}$  (compare with Figure 1.10) to the extinction coefficient at a distinct wavelength,  $\varepsilon(\lambda)$ , is proportional to the corresponding electronic transition dipole moment (1.5) and Franck–Condon integral, (1.8):

$$\varepsilon(\lambda)_{S_0^{\nu''} \rightarrow S_1^{\nu'}} \propto P_{S_0 \rightarrow S_1} \cdot P_{\nu'' \rightarrow \nu'}. \quad (2.3)$$

Here,  $\varepsilon(\lambda)_{S_0^{\nu''} \rightarrow S_1^{\nu'}}$  is the absorption band that is due only to the distinct vibronic transition  $S_0^{\nu''} \rightarrow S_1^{\nu'}$ . The entire absorption spectrum,  $\varepsilon(\lambda)$ , can be

regarded as a summation over all possible vibronic absorption bands,  $\epsilon(\lambda)_{S_0^{\nu''} \rightarrow S_1^{\nu'}}$ .

Integration of (2.2) shows that the absorption results as an exponential decrease of the light intensity during its path through the sample cell (Figure 2.1):

$$\frac{I(\lambda)}{I_0(\lambda)} = e^{-\epsilon(\lambda) \cdot 2.303 \cdot C \cdot l} = 10^{-\epsilon(\lambda) \cdot C \cdot l} \quad (2.4)$$

Here,  $l$  corresponds to the total optical path length of the light through the sample cell (compare with Figure 2.1). Decadic logarithmation results in the important and very practical Beer–Lambert law:

$$\text{OD}(\lambda) = \log \frac{I_0(\lambda)}{I(\lambda)} = \epsilon(\lambda) \cdot C \cdot l \quad (2.5)$$

Here,  $\text{OD}(\lambda)$  is the optical density, sometimes also called absorbance. If the molar extinction coefficient for a certain wavelength  $\lambda$  of a compound and the optical path length of the sample cell are known, the concentration of the compound can be directly calculated from the measured  $\text{OD}(\lambda)$  using (2.5). Thus, most absorption spectrometers report the measured absorption spectra in units of OD. If several different compounds contribute to the light absorption, it is often a good approximation to assume that the observed optical density is the linear sum of optical densities caused by the individual compounds.

Figure 2.2 shows the principle of a fluorescence spectrometer. Again, a light source provides broad band electromagnetic radiation, typically ranging from the UV up to the visible range ( $\sim 200$ – $800$  nm). A distinct excitation wavelength of this light is selected using, for example, optical gratings or optical filters. Usually, an excitation wavelength is chosen that excites transitions corresponding to strong absorption bands. The excitation is often focused onto a central spot in the sample cell using an optical lens. A second optical lens is adjusted to collect the fluorescence light emitted from this focal region. This light is again spectrally separated and then analysed with detectors. The apparatus returns a spectrum of relative fluorescence intensities,  $I_{\text{Fl}}(\lambda)$ . Similarly to (2.3), the contribution of a certain vibronic transition  $S_1^{\nu'} \rightarrow S_0^{\nu''}$  to the fluorescence spectrum depends on the corresponding electronic transition dipole-moment (1.5) and Franck–Condon integral, (1.8):

$$I_{\text{Fl}}^{S_1^{\nu'} \rightarrow S_0^{\nu''}}(\lambda) \propto P_{S_1 \rightarrow S_0} \cdot P_{\nu' \rightarrow \nu''} \quad (2.6)$$

Here,  $I_{\text{Fl}}^{S_1^{\nu'} \rightarrow S_0^{\nu''}}(\lambda)$  corresponds to the fluorescence band that is due only to the distinct vibronic transition  $S_1^{\nu'} \rightarrow S_0^{\nu''}$ . The entire fluorescence spectrum,  $I_{\text{Fl}}(\lambda)$ , can be regarded as a summation over all possible vibronic fluorescence bands,  $I_{\text{Fl}}^{S_1^{\nu'} \rightarrow S_0^{\nu''}}(\lambda)$ .

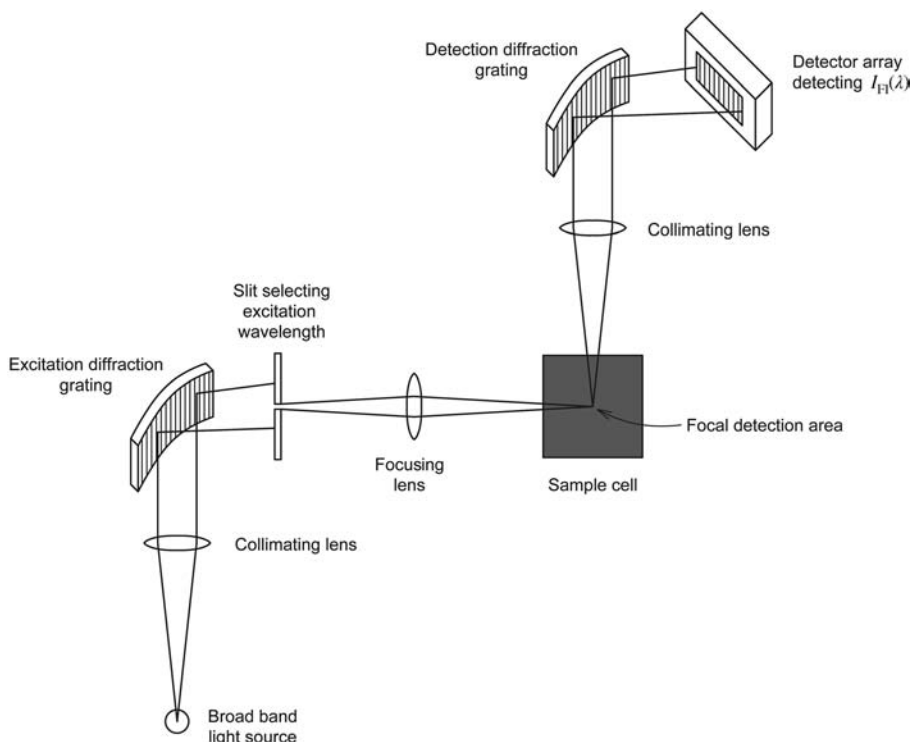


**Figure 2.2** Schematic representation of a standard fluorescence spectrometer. Typically, only one distinct excitation wavelength is focused by an excitation diffraction grating onto a slit. As a consequence, the sample is excited only by this distinct excitation

wavelength. The excitation wavelength can be changed by tilting the excitation diffraction grating, for example. The fluorescence spectrum can then be detected, for example, by the shown combination of a diffraction grating with a detector array.

Also, the fluorescence intensity is in most cases proportional to the concentration of the compound, as long as the concentration is not too high. At too high concentrations reabsorption of the emitted fluorescence by the compound itself can occur or other effects can influence the measured fluorescence. Therefore, the fluorescence spectrum of a compound is often only used to identify it by the characteristic shape of its fluorescence spectrum. Quantitative determination of the compound concentration using fluorescence spectrometry is usually more difficult than with absorption spectrometry because appropriate references are needed and because of the above-mentioned possible artefacts such as reabsorption. Nevertheless, very sensitive methods are based on fluorescence light analysis because the detection of fluorescence in a distinct wavelength range is often an unambiguous indicator for the presence of the fluorescing or fluorescently labelled molecule or biomolecule. These methods are described in Chapter 3 as well as partly in Chapters 7–13.

## 2.3

### Optical Properties of Proteins and DNA

#### 2.3.1

#### Intrinsic Absorption and Fluorescence of Amino Acids, Peptides and Proteins

In the absence of the aromatic amino acids tryptophan, tyrosine and phenylalanine, proteins and peptides show in most cases unspecific absorptions at wavelengths below 240 nm (dotted line in Figure 2.3). Sometimes specific differences caused by secondary protein-structure elements can be observed in that spectral region (solid and dashed lines in Figure 2.3). Because predominantly electronic transitions between  $\sigma$ -orbitals (compare with Figure 1.3) contribute to these absorption bands, excitation using the corresponding wavelengths often leads to degradation of the proteins due to bond breakage.

If aromatic amino acids are present then additional, significant absorptions at wavelengths around 280 nm are present. This absorption is due to the delocalized  $\pi$ -systems of the aromatic amino acids (Figure 2.4). It can be used, for example, for the determination of protein concentration by application of the Beer–Lambert law (2.5) and Table 2.1). In contrast to non-aromatic amino acids the three aromatic amino acids tryptophan, tyrosine and phenylalanine also exhibit a small but significant fluorescence (Figure 2.5). In many cases this is the sole origin of the intrinsic fluorescence of proteins. The optical properties of the three aromatic amino acids differ in absorption and emission wavelengths as well as quantum yields and first excited-state lifetimes. The optical properties of the aromatic residues are summarized in Table 2.1. As one would expect, tryptophan, which possesses

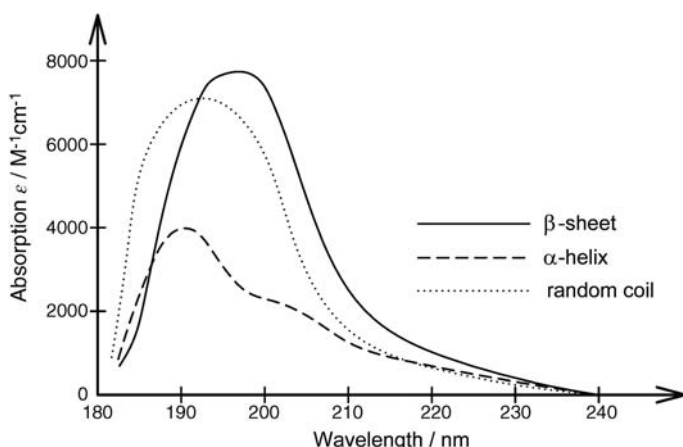


**Figure 2.3** Influence of secondary structural elements on the absorption of nonaromatic amino acids.

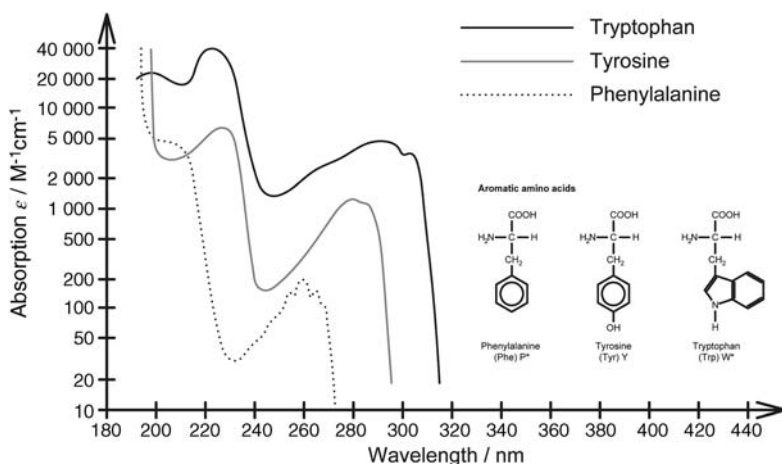


**Figure 2.4** Absorption spectra of the three aromatic amino acids tryptophan (Trp), tyrosine (Tyr) and phenylalanine (Phe). Please note the logarithmical scale of the absorption axis, which demonstrates the large differences in the extinction coefficients of the three amino acids.

the largest system of conjugated  $\pi$ -electrons, has absorption and fluorescence maxima at the longest wavelengths (see also chapter 1, section 1.2 and problem 1.11). The increasing extinction coefficients and fluorescence quantum efficiencies with increasing size of the conjugated  $\pi$ -system of the three amino acids also correlate well with an increasing transition dipole moment. All three aromatic amino acids often show a decrease in fluorescence when incorporated into proteins or peptides. In addition, the fluorescence of aromatic residues in folded and unfolded peptide chains can vary strongly. Such changes in fluorescence intensity can be utilized to monitor protein folding or denaturation. The optical properties of tryptophan, for example, are strongly dependent on its molecular environment. The intensity and energy of the emitted fluorescence are inversely proportional to the solvent polarity. In addition, protonated acidic residues such as aspartic acid or glutamic acid next to tryptophan can effectively reduce its fluorescence quantum yield by

**Table 2.1** Optical properties of aromatic amino acids in aqueous solution.

	Lifetime $\tau_{S1}$ (ns)	Absorption maxima		Fluorescence maxima	
		Wavelength (nm)	Extinction coefficient ( $M^{-1} \text{cm}^{-1}$ )	Wavelength (nm)	Fluorescence quantum efficiency
Phenylalanine	6.4	257	200	282	0.04
Tyrosine	3.6	274	1400	303	0.14
Tryptophan	2.6	280	5600	348	0.20

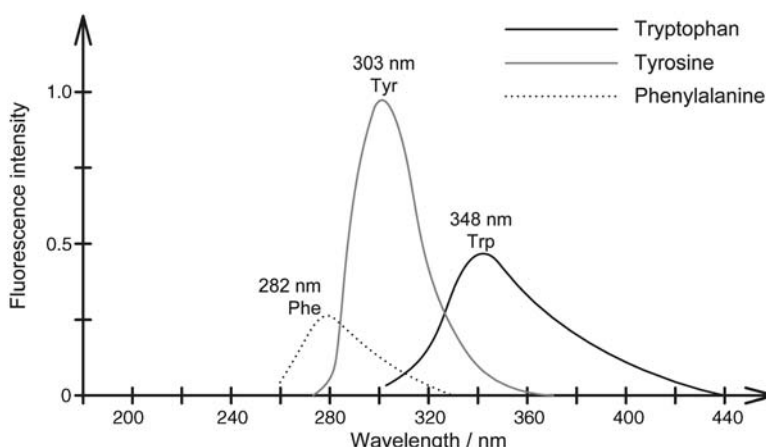


**Figure 2.5** Fluorescence spectra of the three aromatic amino acids Trp, Tyr and Phe. Please note that the fluorescence quantum yield is proportional to the area of the fluorescence spectra, not to the peak heights.

nonradiative deactivation. There can be a shift of up to 40 nm in the fluorescence maximum of tryptophan surface residues as compared to those shielded in the hydrophobic protein centre. Such shifts of absorption or fluorescence bands towards longer wavelengths are often called redshifts. Similarly, a shift of bands towards shorter wavelengths is often called a blueshift.

Even though tyrosine is a much weaker emitter it usually contributes significantly to the overall fluorescence of proteins due to its frequent occurrence. The nearby presence of a tryptophan residue can quench the fluorescence of tyrosines by energy-transfer mechanisms, which will be described in detail in Chapter 3. Because of its very small fluorescence quantum yield phenylalanine fluorescence can only be observed in the absence of the other aromatic residues.

### 2.3.2

#### Intrinsic Absorption of Nucleotides, DNA and RNA

Figure 2.6 gives the absorption spectra of several nucleotides.

DNA and RNA exhibit very similar optical properties. Both have conjugated  $\pi$ -electron systems that show significant absorption around 260 nm. This specific absorption is routinely used to determine the DNA concentration by means of the Beer–Lambert law (2.5). Table 2.2 shows factors for simple estimates of DNA and RNA concentrations based on the measured OD at 260 nm in a sample cell of 1 cm path length.

A comparison of the absorption measured at the absorption band maximum of proteins at 280 nm with the absorption band maximum of DNA at 260 nm is often used to evaluate the purity of a DNA sample. The value of the quotient  $Q = \text{OD}(260 \text{ nm})/\text{OD}(280 \text{ nm})$  of pure double-stranded DNA is around  $Q = 1.8$ .

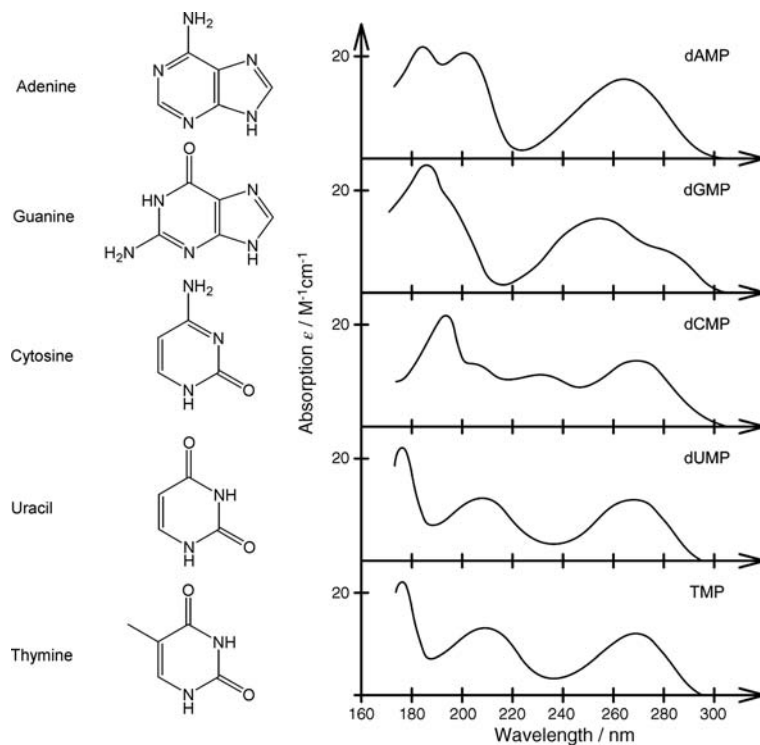


**Figure 2.6** Structural formulas of adenine, guanine, cytosine, uracil and thymine and absorption spectra of their corresponding nucleotides.

A smaller  $Q$  usually indicates protein impurities, whereas larger values indicate RNA impurities.

As can be seen from the values shown in Table 2.2 and Figure 2.7, DNA changes its absorption significantly upon hybridization. This phenomenon is called DNA hypochromism and is caused by changes in the molecular environment of the nucleotides. The effect is very useful for the determination of hybridization and melting of DNA, as shown in Figure 2.8.

**Table 2.2** Calculation of DNA and RNA concentrations from optical densities.

Concentration per OD unit at $\lambda = 260\text{ nm}$ in a sample cell with $l = 1\text{ cm}$ ( $\text{mg L}^{-1}$ )	
Double-stranded DNA	~50
Single-stranded DNA	~40
RNA	~33

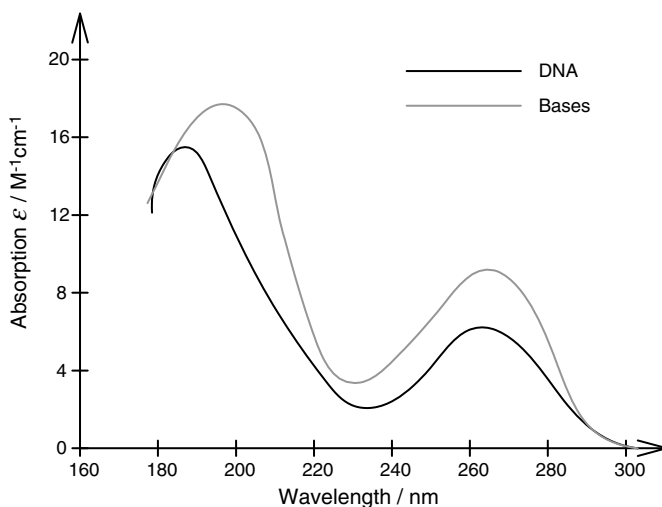


Figure 2.7 Comparison of the absorption of DNA and isolated nucleotides.

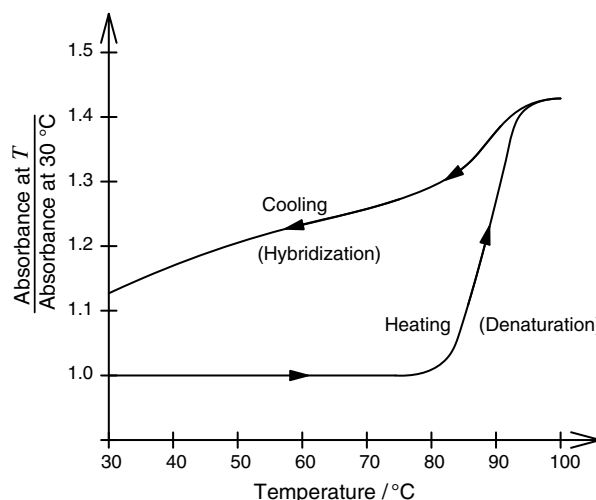


Figure 2.8 Determination of the hybridization of DNA using DNA hypochromism.

## 2.4 Optical Properties of Important Cofactors

### 2.4.1

#### Haem

Haem acts as a cofactor of the protein haemoglobin, which is responsible for the transportation of oxygen in red blood cells. It is structurally based on a porphyrin (a tetrapyrrole) backbone (Figure 2.9). Typical haemoglobin concentration in

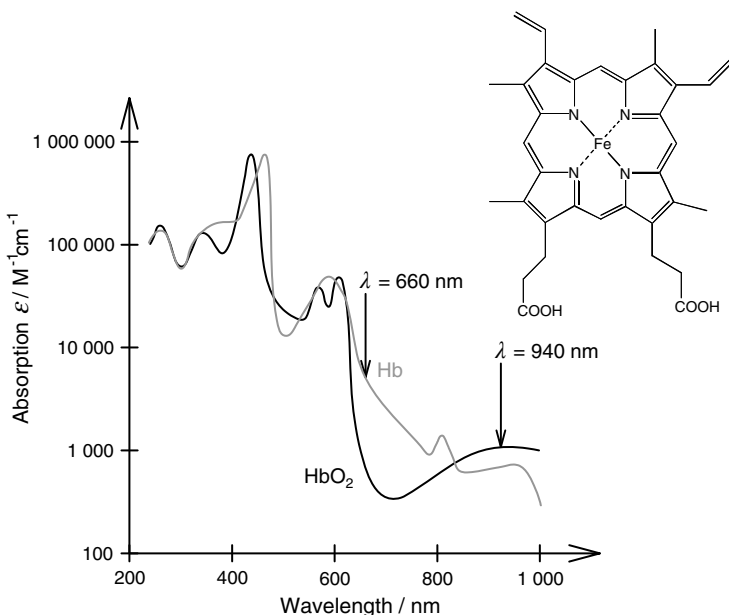


**Figure 2.9** Schematic presentation of the absorption spectra of haemoglobin (Hb) and oxyhaemoglobin ( $\text{HbO}_2$ ). Note the difference in the absorption spectrum upon binding of oxygen. Inset: structural formula of haem.

blood is about  $150 \text{ g L}^{-1}$ . Depending on the oxygen pressure, haemoglobin can carry  $\sim 70$  times more oxygen than blood plasma alone. The central  $\text{Fe}^{2+}$  ion of haem is coordinated to the four nitrogen atoms of the porphyrin ring. The fifth coordination site of  $\text{Fe}^{2+}$  is occupied by the imidazole ring of a histidine residue of the protein and the sixth coordination site can reversibly bind oxygen. Its characteristic absorption is the reason for the red colour of blood.

The absorption spectrum of haemoglobin changes considerably during oxygen exchange. Oxyhaemoglobin has significantly less absorption around  $\sim 650$ – $700$  nm. The absorption change between haemoglobin and oxyhaemoglobin is routinely used to determine continuously and noninvasively the oxygen saturation in a patient's blood (e.g. during surgery). Such oximeters analyse changes in the relative absorption of light at  $\sim 660$  and  $\sim 940$  nm of the patient's tissue. As can be seen from Figure 2.9 comparing the absorption at these two wavelengths allows a robust determination of the amount of oxyhaemoglobin in comparison to haemoglobin.

Haemoglobin is an important example of cooperativity in receptor–ligand binding processes of protein multimers. The saturation of only a single receptor with ligands is usually a smoothly increasing function of the ligand concentration,  $C_L$ , until saturation occurs (dashed line in Figure 2.10). However, in biology most metabolites must be kept within certain tolerable concentration limits. This is often achieved in nature by cooperative interactions between several

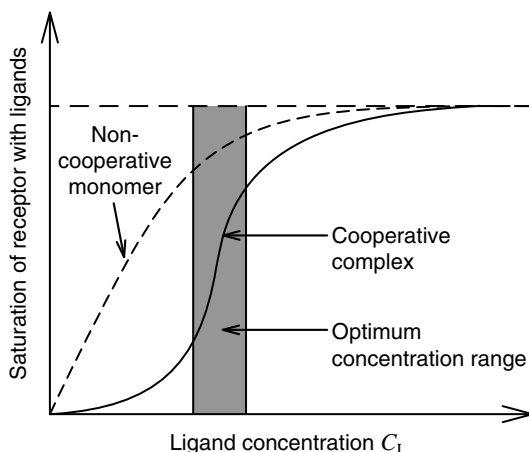


**Figure 2.10** Saturation of a receptor with a ligand for a single receptor (dashed line) and cooperative receptor multimers (solid line). Cooperativity helps to keep the concentration of metabolites within tolerable limits.

receptors in receptor multimers. Haemoglobin, for instance, is a multimer consisting of four subunits (see schematic representation in Figure 2.11). If the first oxygen (L in Figure 2.11) has bound to a free haemoglobin subunit, the binding affinity of oxygen for the other subunits increase by a conformational change in the tetramer subunits (symbolized by the change from circles to squares in Figure 2.11). This is called positive cooperativity and is described by a smaller dissociation constant after a first binding,  $K_2 < K_1$  [for the definition of dissociation constants compare also with (3.19)]. Negative cooperativity corresponds to the situation when the affinity is decreased after binding of ligands,  $K_2 > K_1$ . The result of positive cooperativity is a steep increase in the saturation of the binding sites at a certain ligand concentration. This allows the ligand concentration to be kept within a limited optimum concentration range (solid line in Figure 2.10).

The cooperative effect in the oxygen binding of haemoglobin can be seen from a comparison with myoglobin. Myoglobin is also an oxygen-binding protein but contains only one noncooperative haem-binding site. The saturation of the binding sites of both proteins can be measured by the oxygen-dependent haem absorption (Figure 2.12). In contrast to myoglobin the oxygen saturation of

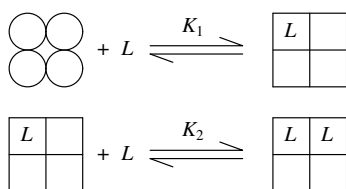


**Figure 2.11** Cooperativity occurs when the binding affinity of other binding sites in a multimer changes when ligands, L, bind to a subunit.

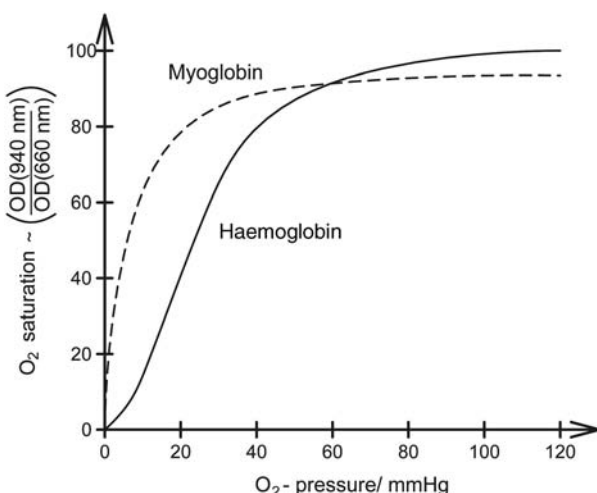


**Figure 2.12** Oxygen binding of haemoglobin and of myoglobin which can be derived from oxygen-pressure-dependent absorption measurements.

haemoglobin increases at oxygen pressures around 26 mmHg, which helps in transporting oxygen and in maintaining the oxygen at physiological concentrations. The noncooperative binding of myoglobin helps rather in storing oxygen, for example, in muscle cells.

#### 2.4.2

##### Nicotinamide Adenine Dinucleotides

A very important molecule for metabolic redox reactions is the electron carrier nicotinamide adenine dinucleotide (NADH). For investigations on the actual redox status of NADH it is very advantageous that the absorption spectra of NADH and its oxidized form NAD<sup>+</sup> differ significantly. The absorption spectrum of NAD<sup>+</sup> has basically only one absorption maximum, at 260 nm (grey line in Figure 2.13). If NAD<sup>+</sup> is reduced to NADH, the intensity of this band decreases slightly and in addition a new absorption band appears at 340 nm (black line in Figure 2.13). The optical properties of the phosphorylated forms, NADPH and NADP<sup>+</sup>, are very similar to the optical properties of NADH and NAD<sup>+</sup>.

The differences in the absorption spectra can be used to follow *in vitro* the oxidation status of NADH/NAD<sup>+</sup>, for instance in the presence of dehydrogenases or oxidoreductases. In addition, NADH exhibits a significant fluorescence around 460 nm, which is basically completely absent in the oxidized form NAD<sup>+</sup>. This difference in the fluorescence quantum yield can be used to follow, even *in vivo*, the consumption or production of NADH in biological samples. In fluorescence microscopy, for example, (see Chapter 7) the significant change in

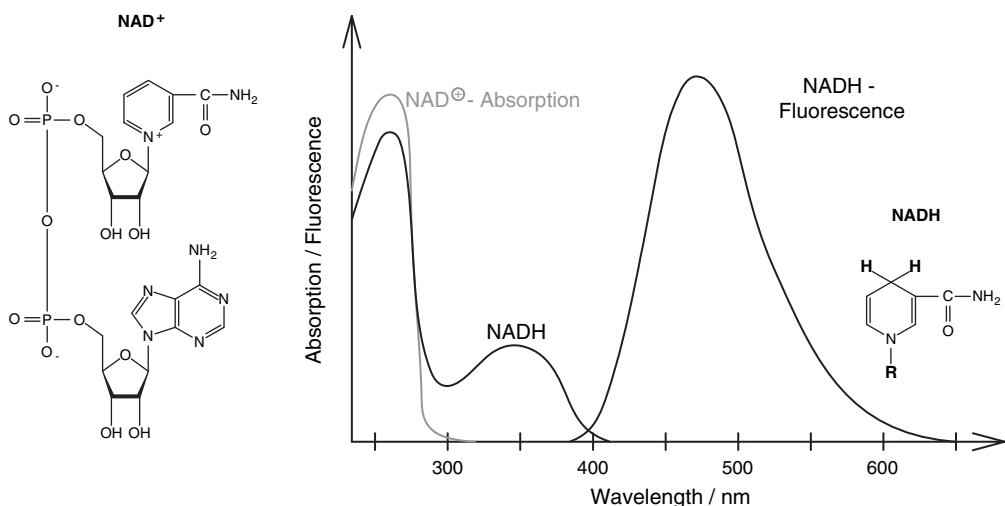


**Figure 2.13** Absorption spectra of  $\text{NAD}^+$  and NADH along with the fluorescence spectrum of NADH.

the fluorescence of  $\text{NAD}^+$  and NADH can be used to identify regions or organelles of a cell that exhibit increased or reduced metabolic activity.

#### 2.4.3

##### Flavins

An important class of cofactors that often dominate the optical properties, especially the fluorescence, of cells and biological samples is flavins, such as flavin mononucleotides (FMNs, Figure 2.14). Flavins are present in many enzymes.

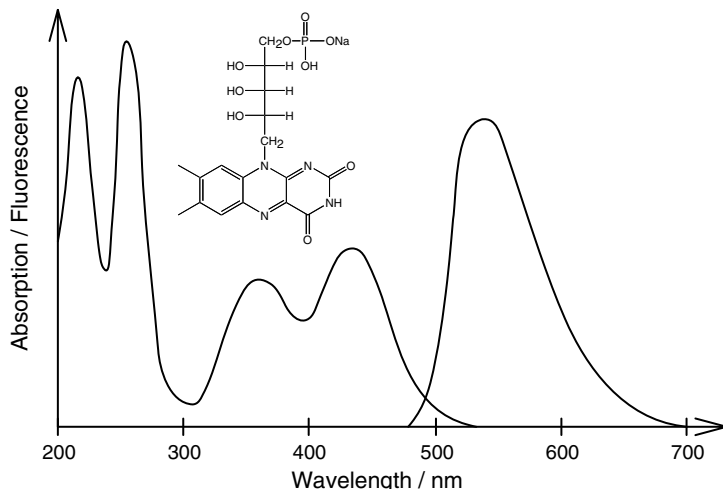


**Figure 2.14** Absorption and fluorescence spectrum of flavin mononucleotide.

The absorption spectra of FMNs, for example, show maxima around 220, 270, 370 and 450 nm. In addition, they exhibit a significant fluorescence with an emission maximum at about 510 nm. Because the absorption and fluorescence span the entire range of visible light and because of their abundance the presence of flavins often must be considered when developing optical detection techniques. For example, flavins are often a main source of the autofluorescence of biological samples. This fluorescence can then give rise to disturbing interferences with the fluorescence of fluorescence markers or other optical signals.

#### 2.4.4

##### Chlorophylls

Like haem, chlorophylls are also structurally based on a porphyrin backbone. Chlorophylls are the most important pigments for photosynthesis in plants, algae and photosynthetic bacteria. Chlorophylls exhibit two dominant absorption bands in the blue (~400–500 nm) and red (~600–700 nm) spectral regions of visible light. These bands are called the Soret band and  $Q_y$  band, respectively. A somewhat weaker  $Q_x$  band is usually present at wavelengths slightly shorter than the  $Q_y$  bands. The names of the  $Q_x$  band and  $Q_y$  band have their origin in the orientation of the corresponding transition dipole moments in the plane of the porphyrin core structure (see inset Figure 2.15). In plants and green algae, chlorophyll *a* and chlorophyll *b* are the two most important chlorophylls.

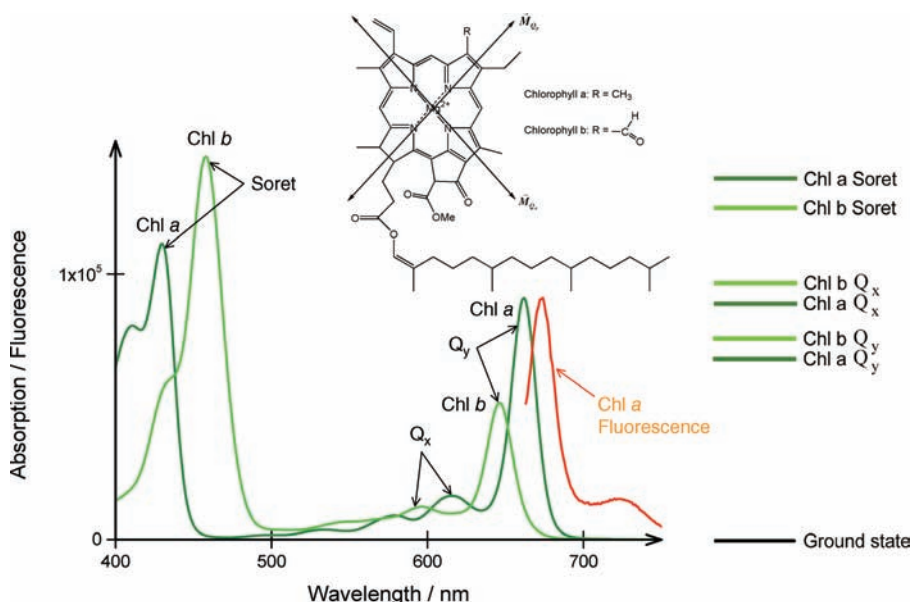


**Figure 2.15** Absorption spectra of chlorophyll *a* and *b* (dark and light green, respectively); fluorescence spectrum of chlorophyll *a* (red) and the corresponding state energy diagram.

Structurally, they differ only slightly, having different C7 groups (R in inset in Figure 2.15).

In photosynthesis, hundreds of chlorophylls collect energy and feed that energy towards a single reaction centre in an energy-funnel-like manner. This funnelling happens via very fast energy-transfer mechanisms that are described in detail in Chapter 3 and Section 10.3. In the reaction centre, which also consists of a so-called special pair of chlorophylls, the electronic excitation energy is used for a primary charge separation. The energy contained in such primary charge separations is then used to drive all subsequent biochemical reactions. It is fascinating how large the quantum efficiency of the energy funnel can be: Under conditions of low light almost all quanta absorbed by any chlorophyll in the photosynthetic apparatus are used for primary charge separations. Further details on the photophysical processes of photosynthesis and its investigation are discussed in Chapter 10.

Chlorophylls also exhibit considerable fluorescence. The fluorescence maximum of chlorophyll *a*, for example, is around  $\sim$ 700 nm. The residual chlorophyll *a* fluorescence of plants can be used to measure *in planta* important parameters like their fitness and photosynthetic regulation behaviour. During a typical day plants are exposed to light intensities suddenly varying over several orders of magnitude. This can be, for example, due to changing weather conditions or simply because of the fast flickering shadow of another leaf in the wind. When plants are exposed to such sudden light intensity changes they must regulate the amount of excitation energy that arrives at the reaction centre to within tolerable limits. When exposed to high light intensities the reaction centre in the plants must be protected from the excessive excitation energy provided by the effective chlorophyll energy funnel. To achieve this, plants open additional energy pathways to dissipate the excessive excitation energy away from the reaction centre. These regulation mechanisms are essential for the survival and fitness of natural or gene-modified plants in the field. The plants regulation ability, which is an important indicator of fitness, is often visualized by measuring the residual chlorophyll fluorescence intensity of the plant leaves using commercial plant chlorophyll fluorimeters. The residual chlorophyll fluorescence is a direct measure of the amount of available excitation energy in the photosynthetic apparatus that has not been dissipated by the regulation mechanisms. Figure 2.16 shows an example of a typical measurement of the regulation of the photosynthetic activity of a plant during an artificial period of high light irradiation and low light irradiation. During high light irradiation the regulation mechanisms decrease the amount of available excitation energy to protect the reaction centre. Consequently, the residual chlorophyll fluorescence also decreases during that period. This residual fluorescence is usually measured during short but intense probe pulses to avoid a regulation response to the probe light (peaks under the dashed line in Figure 2.16). During the subsequent low light period, the dissipative regulation mechanisms recede and the chlorophyll fluorescence measured during the probe pulses increases

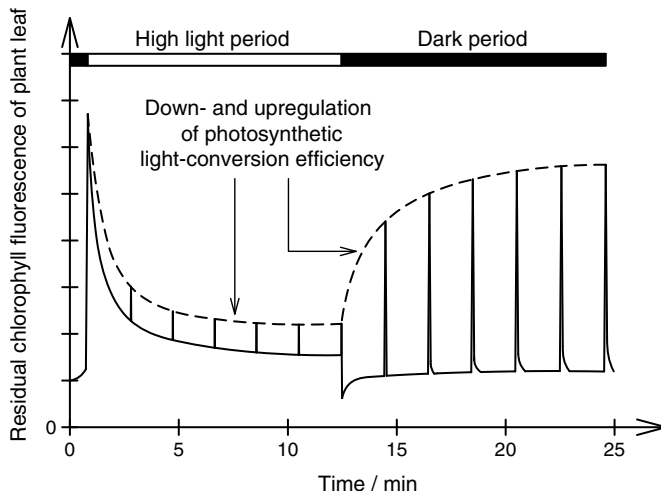


**Figure 2.16** The residual chlorophyll fluorescence of plants can be used to measure their fitness that depends on their ability to regulate the photosynthetic activity as a function of changing light conditions.

accordingly. A large dynamic range of down- und up-regulation during changing conditions of light irradiation indicates high plant fitness.

#### 2.4.5

##### Carotenoids

Carotenoids represent another very important class of pigments involved in many biological processes. Carotenoids are essential in many organisms as anti-oxidative reagents because they can quench dangerous and aggressive singlet oxygen,  $O_2^*$ . In addition, they are also important light-harvesting pigments in photosynthesis and are, to a major extent, responsible for the orange and red colours of leaves in the autumn. Molecules that are structurally very closely related to carotenoids are retinals. These molecules are responsible for the light sensing in the eyes of humans and animals. After absorption of a photon, retinal undergoes a photochemical cis-trans transition in the excited state, which triggers the signal cascade responsible for vision.

The colour of  $\beta$ -carotene and many other carotenoids is due to a very strong absorption of blue light around 500 nm (Figure 2.17). Interestingly this band is due to transitions into the second excited state of the carotenoids,  $S_2$ , only. The first excited state is optically forbidden because the transition dipole moment for the transition  $S_0 \rightarrow S_1$  is almost zero. This can be understood by a comparison with ideally symmetric polyenes having a conjugated  $\pi$ -system of similar size as typical carotenoids. Here, the corresponding ground state and first excited state wave function of  $S_0$  and  $S_1$  both have  $g$  (gerade) symmetry. According to Laporte's rule (Chapter 1) such transitions are optically dipole forbidden.

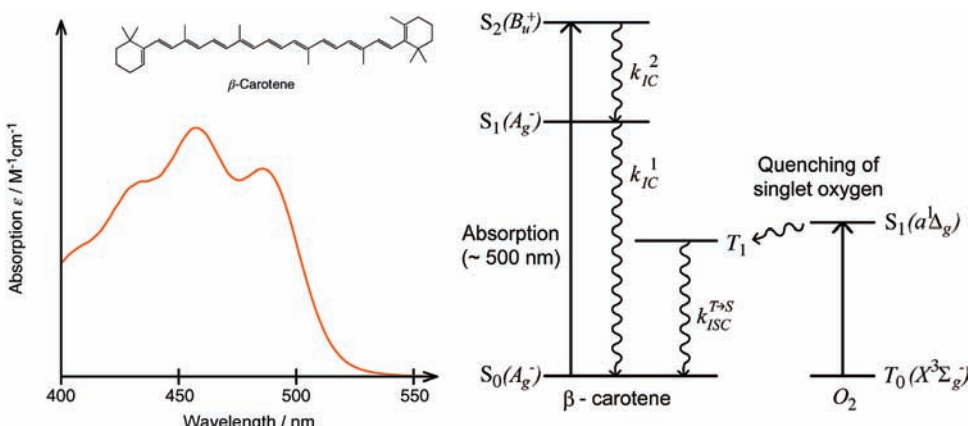
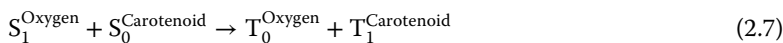


**Figure 2.17** Schematic representation of the absorption of  $\beta$ -carotene along with its energy diagram and the energy diagram of oxygen. The absorption corresponds to a transition into the second excited state of carotenoids,

$S_2$ , since excitations into the first excited state are optically forbidden. The triplet state of carotenoids can quench dangerous singlet oxygen.

Intriguingly, this rule still applies even for more asymmetric carotenoids in a protein environment: Almost no absorption can be detected in the spectral region that would correspond to a  $S_0 \rightarrow S_1$  transition.

In contrast, the transition dipole moment for the transition  $S_0 \rightarrow S_2$  is very strong because the second excited state wave function has a  $u$  (ungerade) symmetry. However, according to Kasha's rule (Chapter 1), usually a fast internal conversion  $S_2 \rightarrow S_1$  occurs directly after an absorption  $S_0 \rightarrow S_2$  with a time constant of about 200 fs. As a consequence, almost no fluorescence can be observed from carotenoids because the transition  $S_1 \rightarrow S_0$  is also optically forbidden. The role of carotenoids as antioxidative reagents can be explained by the fact that the triplet-state energy of carotenoids is below the singlet energy of excited oxygen (see right-hand side of Figure 2.17). This enables an energy transfer:



The product of this reaction is a carotenoid molecule in the excited triplet state and oxygen in its nonaggressive electronic ground state, which in contrast to most organic molecules is a triplet state. Even though this process involves two spin flips it is not spin forbidden since the changes in spin angular momentum in both molecules can compensate each other. Therefore, this quenching process is fast and efficient. The triplet-state energy of carotenoids is then safely dissipated into heat via intersystem crossing,  $T_1^{\text{Carotenoid}} \rightsquigarrow S_0^{\text{Carotenoid}}$ . Further details about similar energy-transfer processes are described in Chapter 3.

### Problems

- 2.1** In a sample cell of path length  $l = 1$  cm a compound of unknown concentration is measured. For light of  $\lambda = 550$  nm the intensity after the sample is reduced to 80% of the original light intensity before the sample cell,  $I_0$ . Assume that this reduction in light intensity is due solely to absorption by the compound of unknown concentration. What is the optical density measured in this experiment for a wavelength of 550 nm? What is the concentration of the compound when it has an extinction coefficient of  $\epsilon = 20\,000\,M^{-1}\,cm^{-1}$  at 550 nm?
- 2.2** The compound of question 2.1 also exhibits considerable fluorescence. A second sample of this compound exhibits about half as much fluorescence intensity as the sample of question 1. What is the approximate concentration of this sample? What possible artefacts do we have to consider in the determination of concentrations from fluorescence intensities and how do they affect the estimated concentration?
- 2.3** Explain why tryptophan has a larger extinction coefficient, fluorescence quantum yield and longer absorption wavelengths than the two other aromatic amino acids phenylalanine and tyrosine? What aromatic amino acid usually dominates the fluorescence properties of proteins?
- 2.4** An unknown sample contains either proteins, DNA or RNA. The ratio of the optical densities measured at 260 and 280 nm,  $Q = OD(260\,nm)/OD(280\,nm)$ , is 1.8 and the optical density at 280 nm is 0.1 in a standard cell of 1 cm path length. What does the sample contain and what is its concentration?
- 2.5** One reaction of the human body in the cold is to reduce the blood circulation in the body's extremities. Explain why Caucasian (white) people often have bluish lips when they are cold.
- 2.6** Explain qualitatively what cooperativity means and why the principle of cooperativity is very important for the regulation of many metabolic processes in biology.
- 2.7** Why are plant leaves green in the summer and orange in the autumn?
- 2.8** In eq. 2.5 the important Beer-Lambert law is introduced. Derive it by integration of eq. 2.2.

### Bibliography

#### General

Cantor C.R. and Schimmel, P.R. (1980)

*Biophysical Chemistry: Part II: Techniques*

*for the Study of Biological Structure and Function*, W.H. Freeman & Co.

Cantor, C.R. and Schimmel, P.R. (1980)

*Biophysical Chemistry: Part III: The*

- Behavior of Biological Macromolecules*,  
W.H. Freeman & Co.
- van Holde, K.E., Johnson, C. *et al.* (2005)  
*Principles of Physical Biochemistry*,  
Prentice-Hall.
- Winter, R. and Noll, F. (1998) *Methoden der Biophysikalischen Chemie*, Teubner Verlag.

### Specific

#### Oximeters for Measuring Oxygen Saturation in the Blood

- Severinghaus, J.W. (2007) Takuo Aoyagi: discovery of pulse oximetry. *Anesth. Analg.*, **105**, 1–4.

#### In Vivo Measurements of Oxidation-Reduction States

- Chance, B., Cohen, P. *et al.* (1962) Intracellular oxidation-reduction states in vivo. *Science*, **137**, 499–508.

### Chlorophyll Fluorescence

- Papageorgiou, G.C. and Govindjee (2005) *Chlorophyll a Fluorescence: A Signature of Photosynthesis (Advances in Photosynthesis and Respiration)*, Kluwer Academic Publishers.

### Optical Properties of Carotenoids

- Frank, H.A., Young, A. *et al.* (1999) *The Photochemistry of Carotenoids (Advances in Photosynthesis)*, Springer.
- Polívka, T. and V. Sundström (2004) Ultrafast dynamics of carotenoid excited states—From solution to natural and artificial systems. *Chem. Rev.* **104**, 2021–2071.



### 3

## Basic Fluorescence Techniques

### 3.1

#### Introduction

This chapter discusses several essential fluorescence detection techniques for the investigation of biomolecules or biomolecular processes. Important examples are the measurement of fluorescence polarization anisotropies, Förster energy transfer and fluorescence lifetimes. An important example for monitoring important biochemical processes by enzymatic biochemiluminescence reactions is also presented. Before these techniques are explained in detail, however, the labelling techniques that actually allow us to conduct all these fluorescence and luminescence methods with biomolecules are presented. In this context, the most important techniques for linking biomolecules to each other, and for immobilizing them to solid supports, are also covered.

### 3.2

#### Fluorescent Labelling and Linking Techniques

Usually, proteins or other relevant biomolecules do not exhibit an intrinsic fluorescence that can be used for a specific identification, characterization or investigation of biomolecular processes. Therefore, often, fluorescence markers are covalently linked to the biomolecules of interest. The resulting fluorescent biomolecule conjugates emit extrinsic fluorescence, originating from the tags that can be used to unambiguously identify the biomolecules in a mixture with other biomolecules or in biological objects like cells. In addition, many sensitive fluorescence techniques can then be applied to elucidate certain biochemical processes. These techniques are described in this chapter as well as in several chapters in Part 2 of this book.

Fluorescing molecules must have several important properties to be suitable as fluorescence markers for biomolecules. First, the absorption spectrum should be rather narrow and the extinction coefficient should be high to enable a selective and exclusive excitation of the fluorescence dye. Usually, absorption bands in the visible range of light corresponding to typical wavelengths of available light

sources, such as lasers, are preferred. A high fluorescence quantum yield, preferably close to unity, is mandatory for a sensitive detection of the labelled protein in the presence of background effects such as autofluorescence from the sample. Also, a narrow fluorescence spectrum is advantageous because then several different fluorescence dyes can be detected simultaneously using spectral filters. A prerequisite for a high fluorescence quantum yield is a small rate of intersystem crossing,  $k_{ISC}$ , and internal conversion,  $k_{IC}$  [compare with (1.10)]. Since the formation of triplet states can never be excluded entirely a low triplet-state lifetime is essential for a rapid de-excitation into the singlet ground state. Besides these optical properties it is important that the fluorescing molecules, which tend to be rather nonpolar organic molecules, are sufficiently soluble in physiological aqueous environments. A very important requirement is that fluorescence markers must have chemical active side chains that allow a nonaggressive but still effective labelling of the biomolecules of interest. Last but not least they must possess very high photostability, which means the ability to be re-excited as many times as possible before photochemical degradation of the dye occurs.

Labelling dyes that fulfil many of the previous requirements are, for example, fluorescein, rhodamine green or tetramethylrhodamine (TMR). Figure 3.1 shows the structure of fluorescein-5-isothiocyanate, and Figure 3.2 gives its corresponding absorption and fluorescence spectra. Fluorescein has a large system of conjugated  $\pi$ -electrons that results in a large transition dipole moment. In general, such a structural part of a molecule that causes the colour of a molecule is called a chromophore. The absorption and fluorescence of fluorescein is in the visible spectral region of light, which is spectrally well separated from the absorption and fluorescence of proteins or DNA. Because of its extended  $\pi$ -system fluorescein has a quite rigid molecular structure. This, together with a sufficiently large  $S_0 - S_1$  energy gap, results in only low probabilities for nonradiative de-excitation pathways such as internal conversion  $S_1 \rightsquigarrow S_0$ . The polar hydroxyl and carboxylic acid residues make the molecule polar enough to be soluble in an aqueous environment. The solubility can be further enhanced by the presence of detergents in the solution, which prevent aggregation, precipitation or adsorption of the fluorescence dye at the walls of the test tubes. Finally,

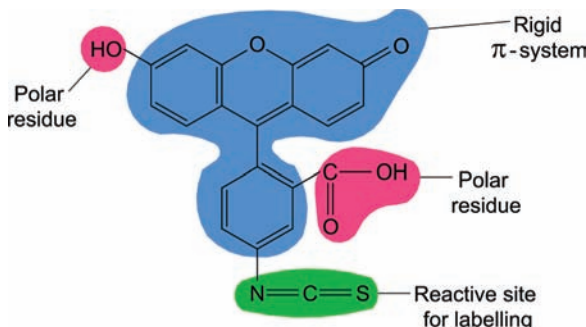
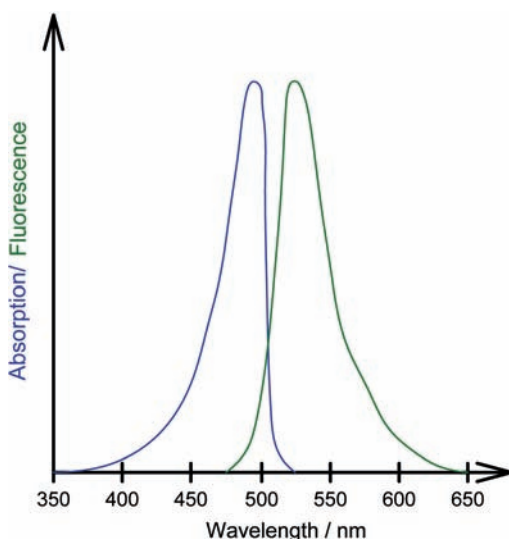


Figure 3.1 Chemical structure of fluorescein-5-isothiocyanate, a typical fluorescence marker.



**Figure 3.2** Absorption (blue line) and fluorescence spectrum (green line) of fluorescein-5-isothiocyanate.

the isothiocyanate group allows us to attach the label to primary amino groups of proteins under gentle conditions, avoiding protein denaturation. In the next section we will discuss a few important chemical labelling reactions in more detail.

The commonly used reagents for labelling proteins can be classified according to the functional groups on the protein surface that they attach to. The prime targets for such labelling reactions are primary amino groups and thiol groups (see below).

### 3.2.1

#### Primary Amino Group Reactive Labels

Primary amino group labels are often used when the specific site of labelling is not particularly important. Most proteins exhibit several primary amino acid residues, from residues such as lysine or the N-terminus of the protein or peptide. Often, a statistical labelling is sufficient, which means that only an average number of fluorescence tags are present per protein. Individual proteins may carry differing numbers of labels at different sites. Important examples of amino group reactive fluorescence marker residues are isocyanates and isothiocyanates, N-succinimides and anhydrides, and sulfonyl halogenides. Figure 3.3 shows the corresponding reactions schemes. Labels attaching themselves to primary amino groups are usually agents forming urea (or thiourea), carboxamide, and sulfonamide groups in the reaction process. Obviously, all other compounds containing free amine groups have to be avoided. Often, DNA can be labelled by similar reactions when primary amino groups have been previously attached to the DNA. The kinetics of the reaction are affected by the reactivity and

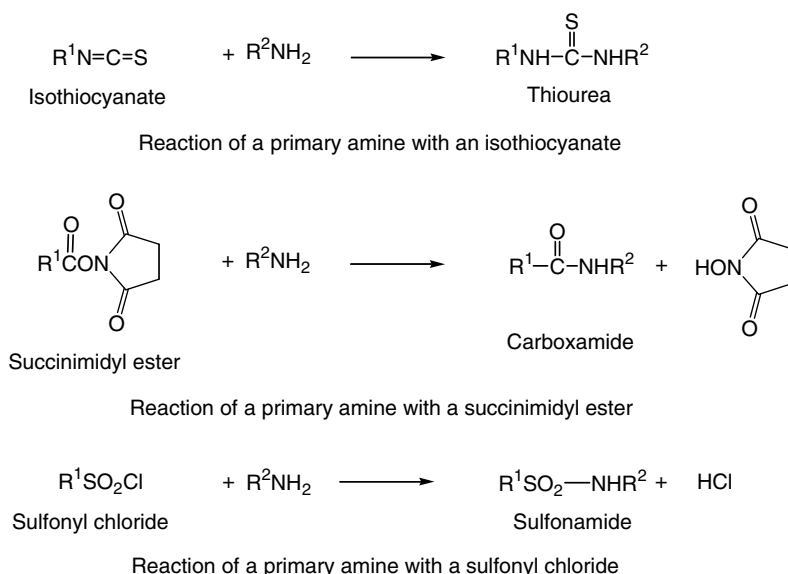


**Figure 3.3** Typical primary amino group labelling reactions.

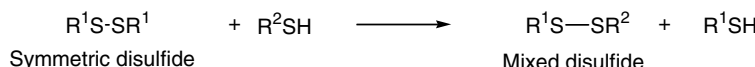
concentration of both the reagent and target group. The target amine's reactivity is determined by its type and basicity. The  $\epsilon$ -amino group of lysine is moderately basic and reactive with most acylating reagents. However, its free base form predominates only at pH values higher than  $\sim 8$ , which leads to an optimal pH range of  $\sim 8$  to  $\sim 10$  for modifying lysine residues. The  $\alpha$ -amino group at a protein's N-terminus on the other hand usually has a  $pK_a$  of  $\sim 7$ . This sometimes allows for a selective modification of the N-terminus by performing the reaction at pH  $\sim 7$ .

Amine-reactive labels are applied to a broad spectrum of biomolecules like proteins, peptides or ligands. A typical application example is the preparation of bioconjugates for immunolabelling, in which an antibody for a specific antigen carries a fluorescence marker and is added to a biological sample. The presence of the antigen, at a certain place or time, of cells, for example, can then be followed directly by the corresponding antibody fluorescence.

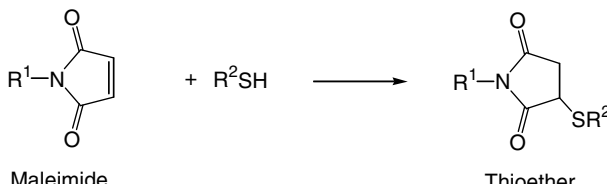
### 3.2.2

## Thiol Group Reactive Labels

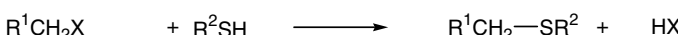
Thiol-reactive dyes are mainly applied on peptides, proteins and oligonucleotides (Figure 3.4). Since the thiol functional group is rare and can be labelled with high selectivity, these reagents allow tagging of a specific site of a biomolecule. In many cases undesired cysteine sites in a protein can be removed and desired cysteine sites can be artificially added by point mutation at the corresponding positions in the DNA. Expression organisms will then generate proteins from



### Reaction of a thiol with a symmetric disulfide



### Reaction of a thiol with a maleimide



Alkyl halide or  
Haloacetamide (X = I, Br, Cl) Thioether

### Reaction of a thiol with an alkyl halide

**Figure 3.4** Typical thiol group labelling reactions.

such DNA, which can then be labelled at almost any desired site. Site-selective labelling is, for example, important for intra- and interprotein distance determinations using the technique of Förster resonance energy transfer (FRET) (Section 3.5). Site-selective labelling is also advantageous for techniques that require that at most one fluorescence dye is present per biomolecule or that even require stoichiometric labelling of the biomolecules. This can be the case, for example, for the measurement of fluorescence polarization anisotropy (Section 3.4). Intramolecular energy-transfer reactions between more than two dyes attached to a single protein can significantly decrease the polarization information in such fluorescence anisotropy measurements.

It is important that the fluorescent labelling interferes as little as possible with biochemical functions. For example, binding affinities or enzyme kinetic constants of native biomolecules are often affected by the labelling procedure. Thus, it is always important to check the native functions of labelled biomolecules and to choose labelling positions remote from the active site of a biomolecule. In many cases minor influences from the fluorescence label cannot be entirely avoided.

### 3.2.3

## Avidin–Biotin Techniques

The streptavidin–biotin method is an important alternative technique for connecting biomolecules, fluorescence dyes or solid carriers with each other. You will find several examples throughout this book where this technique has been applied. The protein streptavidin and the small ligand biotin exhibit an extremely high binding affinity and specificity. Therefore, an almost irreversible

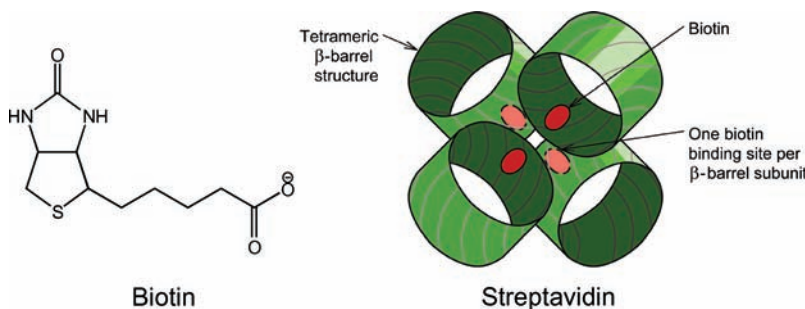


**Figure 3.5** Molecular structure of biotin and schematic presentation of the tetrameric streptavidin protein structure along with the biotin binding sites.

binding interaction occurs between both binding partners in liquid environments as soon as they are present. Amongst other effects this high binding affinity is caused by a conformational change in streptavidin during binding in which a protein loop folds over the biotin. Streptavidin is a tetrameric protein ( $4 \times \sim 14 \text{ kDa}$ ) with each subunit being able to bind to one biotin with a binding affinity of  $K_a \sim 10^{13} \text{ M}^{-1}$  (Figure 3.5). Attaching biomolecules, fluorescence dyes or solid carriers to biotin and streptavidin thus even allows the connection of several different ligands to one streptavidin. Biotinylation of poorly detectable biomolecules can also be used to identify them by a fluorescently labelled streptavidin or to capture them by streptavidin supported on a solid matrix.

### 3.2.4

#### His-Tag

A binding method that is based on an affinity that is as similarly high as in the biotin–streptavidin technique is the His-Tag technique. It takes advantage of the high affinity of  $\text{Ni}^{2+}$  ions for histidine residues of proteins. Often, another binding partner (R in Figure 3.6) is attached via a nitrilotriacetic acid group that

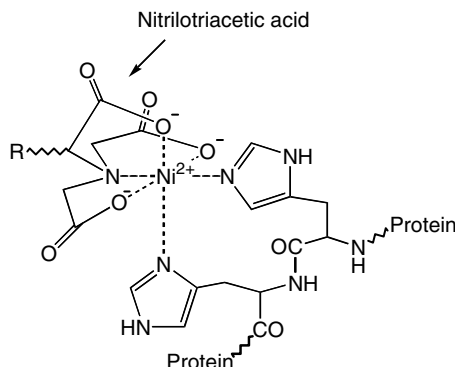


**Figure 3.6** Principle of linking a residue R to a histidine-tagged protein via an  $\text{Ni}^{2+}$ –nitrilotriacetic acid complex.

coordinates four coordination sites of the  $\text{Ni}^{2+}$  ion. Nickel ions are often immobilized on a solid matrix via R. If sequences of histidines are then artificially inserted into a protein it binds with a very high affinity to the remaining two coordination sites of the Ni ions. This can be used, for example, to purify proteins expressed by an expression organism. In biophysical chemistry it is also very often used to bridge or immobilize biomolecules of interest. This book presents several application examples of the immobilization of proteins via the His-Tag technique.

### 3.2.5

#### Thiolinkers and Gold Surfaces

Another common way to immobilize biomolecules on a solid surface is to link molecules carrying thiol residues to gold surfaces. Thiol residues have a high affinity for noble-metal surfaces and form stable connections with them. The exact mechanism of this linking is not completely understood but it is assumed that the thiol is added by oxidation to the surface with subsequent elimination of hydrogen. An important application example is binding receptors to gold surfaces for surface plasmon resonance detection methods (Chapter 12).

### 3.2.6

#### Fluorescent Proteins

Fluorescent proteins contain intrinsically a fluorescing structure. The most prominent example is green fluorescent protein (GFP, Figure 3.7). It occurs in jellyfishes and has an absorption maximum at  $\sim 400\text{ nm}$  and a fluorescence maximum at  $\sim 510\text{ nm}$ . The chromophore forms chemically from the residues of the three amino acids serine, tyrosine and glycine, which are directly neighbouring in the primary sequence of the protein. Formation seems to occur autocatalytically. The chromophore is shielded by the  $\beta$ -barrel structure of the protein. The beauty of fluorescent proteins is that often organisms can be modified genetically in a way that they express native proteins of interest as fusion-proteins with GFP. Then, the spatial and temporal distribution of this protein can be followed within the living organism by fluorescence microscopy (see Chapter 7). GFP has also been applied as a fluorescence marker for many other applications. Meanwhile many fluorescent protein mutations exist. Fluorescent proteins are available with absorption and fluorescence maxima that virtually span the entire range of visible light. So it is even possible to observe several different biomolecules labelled by different fluorescent proteins in one sample. In addition, mutations with enhanced fluorescence quantum yield and photostabilities have been generated. The application of so-called photoactivatable fluorescent proteins for high-resolution microscopy will be discussed in detail in Chapter 8.



**Figure 3.7** Structure of green fluorescent protein (GFP). The chromophore is chemically formed from the residues of the three amino acids serine, tyrosine and glycine within the  $\beta$ -barrel structure of the protein.

### 3.3

#### Fluorescence Detection Techniques

The fluorescence of selectively labelled biomolecules in complex biological environments yields a manifold of parameters, with the fluorescence intensity being the most easily accessible. The fluorescence intensity can be measured either for an entire sample or at selective areas/structures using fluorescence microscopy (Figure 3.8, for fluorescence microscopy see also Chapter 7 and 8). To a first order approximation, the fluorescence intensity is proportional to the concentration,  $C$ , of the utilized fluorescent conjugate at a certain time,  $t$  and/or location,  $r$ :

$$C \propto I_{\text{Fl}}(t, r) \quad (3.1)$$

However, an absolute determination of fluorescence intensities depends sensitively on sample and instrument characteristics. For example, the fluorescence quantum yield of a particular species can be affected by its environment such that even with a homogeneous concentration the intensities in the hydrophobic cell membrane, the aqueous cytoplasm and other parts of the cell can differ significantly. Variations due to pipetting errors also have a direct influence

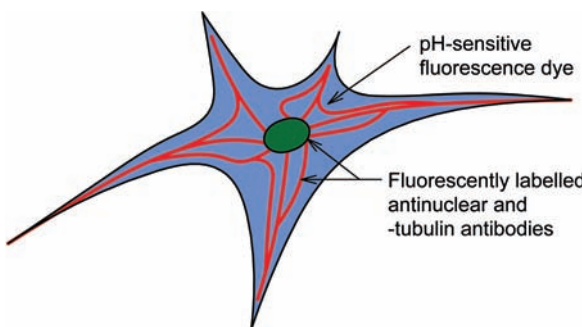


**Figure 3.8** Schematic representation and exemplarily of a fluorescently labelled cell. The nucleus is visualized by *antinuclear antibodies* labelled with a green fluorescence dye. The tubulins of the cytoskeleton are visualized by anti-tubulin antibodies labelled with a red fluorescence dye. In addition, fluorescence dyes

can be injected into the cytoplasm. Some fluorescence dyes change their fluorescence quantum yield or spectrum as a function of important parameters like the pH or  $\text{Ca}^{2+}$  concentration. The principles of fluorescence microscopy are described in detail in Chapter 7.

on the measured fluorescence intensity. Other factors impairing the observable fluorescence are photobleaching, the presence of other light-absorbing molecules and turbidity of the sample. Therefore, the measurement of the fluorescence intensity and spectrum is often used simply for a qualitative identification of labelled biomolecules rather than for quantitative analysis of, for example, concentrations.

For investigations that require robust quantitative information, more sophisticated detection schemes like ratiometric measurement methods are often necessary. Ratiometric methods are based on the measurement of at least two parameters, which are influenced by possible artefacts in the same or at least very similar way. Comparison of these two parameters then allows us to determine the pure information of interest independent from the artefacts. An important example is ratiometric fluorescence dyes, which have two fluorescence bands that differ in intensity as a function of parameters like pH or the  $\text{Ca}^{2+}$  concentration. These dyes are so designed that the parameter of interest can be deduced directly from the measured intensity ratio of these two bands. Even though the overall fluorescence intensity might vary due to pipetting errors or instrumental artefacts the intensity ratio can still be determined robustly.

In the introduction to this book we presented an example of a fluorescence polarization assay, which allows a very quick and robust measurement of binding affinities. Polarization assays are based on the simultaneous measurement and comparison of two photophysical parameters of fluorescence, the horizontal and vertical component of the fluorescence polarization. Again, even though the overall fluorescence intensity might vary due to pipetting errors or instrumental artefacts the measured ratio of these two parameters is often unaffected by these artefacts. Also, Förster resonance energy transfer and fluorescence lifetime measurements are based on the simultaneous determination of at least two

fluorescence parameters from the sample. Like fluorescence polarization, they usually provide very robust quantitative information about the labelled biomolecules. The kind of information differs of course from method to method. In the following sections we discuss in detail the principles of these important measurement techniques and present typical application examples.

### 3.4

#### Fluorescence Polarization Anisotropy

##### 3.4.1

##### Principles and Theoretical Background

The technique of measuring fluorescence polarization anisotropy (FPA) is one of the most important techniques for the development of fluorometric assays. Therefore, we will discuss this technique in more detail. Fluorescence polarization measurements allow the determination of the time constant of the rotational diffusion of fluorescently labelled biomolecules or complexes. Since the rotational diffusion depends very much on the size of the these object, it can be used for quantitative determination of receptor–ligand binding, proteolysis, protein–DNA interactions and membrane fluidity when the corresponding components are fluorescently labelled.

In Figures I.1 and I.2 in the Introduction the principle of a fluorescence polarization measurement has already been sketched schematically. In Figure 3.9 the corresponding experimental set-up is illustrated in more detail. The investigated sample is excited using linearly polarized light. In the sample, the biomolecules with attached fluorescence dyes are randomly orientated. The only fluorescence

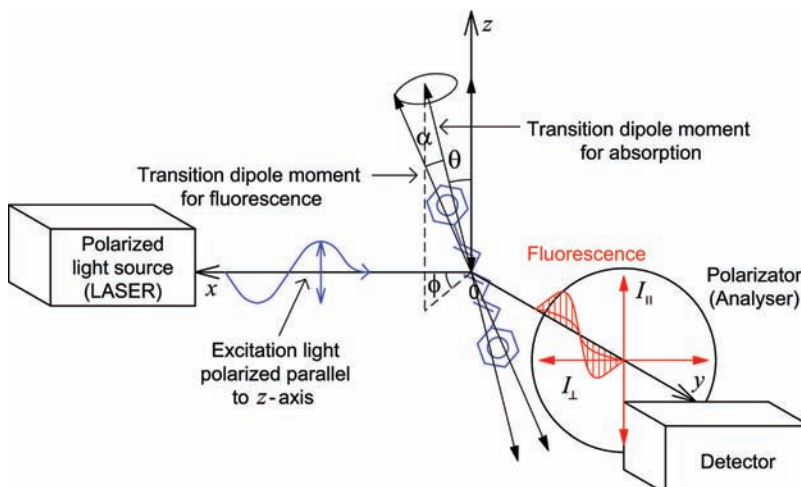


Figure 3.9 Principle of a fluorescence polarization measurement.

dyes that are excited are those that are aligned at the moment of excitation in such a way that their transition dipole moment for absorption is the same as or similar to the polarization vector of the exciting light. The excitation of only this subpopulation of fluorescence dyes is called photoselection. If the dyes are attached to very large biomolecules almost no rotational diffusion occurs before the dyes re-emit their excitation energy as fluorescence. Often, the transition dipole moment vector for fluorescence has a similar orientation to the transition dipole moment vector for absorption. As a consequence, the emitted photons have preferentially a polarization vector that is similarly orientated as the original excitation polarization. However, if the labelled species is rather small, usually fast rotational diffusion occurs before the photons are emitted and thus the overall fluorescence is rather nonpolarized. The polarization of the fluorescence light can be detected using a polarization analyser. It detects the fluorescence polarization by using polarization filters that transmit only fluorescence light that has a polarization either parallel or perpendicular to the original laser excitation polarization. The intensities measured for these polarizations are defined by  $I_{\parallel}$  and  $I_{\perp}$ , respectively. For large labelled particles  $I_{\parallel}$  is significantly larger than  $I_{\perp}$ , whereas small labelled particles have approximately equal values of  $I_{\parallel}$  and  $I_{\perp}$ .

$I_{\parallel}$  and  $I_{\perp}$  can be used to calculate the parameters fluorescence polarization ( $P$ ) and fluorescence anisotropy ( $r$ ):

$$P = \frac{I_{\parallel} - I_{\perp}}{I_{\parallel} + I_{\perp}}, \quad r = \frac{I_{\parallel} - I_{\perp}}{I_{\parallel} + 2I_{\perp}} \quad (3.2)$$

Both parameters represent normalized differences in the detected parallel and perpendicular fluorescence light intensity,  $I_{\parallel}$  and  $I_{\perp}$ . Both increase with increasing rotational diffusion time and thus with the molecular size of the labelled species. However, in the following we will only use  $r$  because this parameter has the advantage that mixtures of different fluorescently labelled species exhibit anisotropies that can be linearly calculated from the fractions of the individual fluorescently labelled components:

$$\bar{r} = \sum_i f_i r_i \quad (3.3)$$

Here,  $\bar{r}$  is the average anisotropy measured for the mixture,  $f_i$  is the fraction of the individually fluorescently labelled component  $i$  in relation to all components labelled with the same fluorescence dye, and  $r_i$  is the corresponding fluorescence anisotropy that would be measured if only the individual component  $i$  were present. Typical values for  $r$  in biological assays are of the order of 0.01 to 0.3. Usually, the anisotropies can be determined with an accuracy of  $\sim r \pm 0.002$  with modern instrumentation. A value of  $\sim 0.05$  corresponds to a free fluorescent dye, whereas a value of 0.3 corresponds to a very large protein labelled with a fluorescence dye having very similar absorption and fluorescence dipole moment vectors.

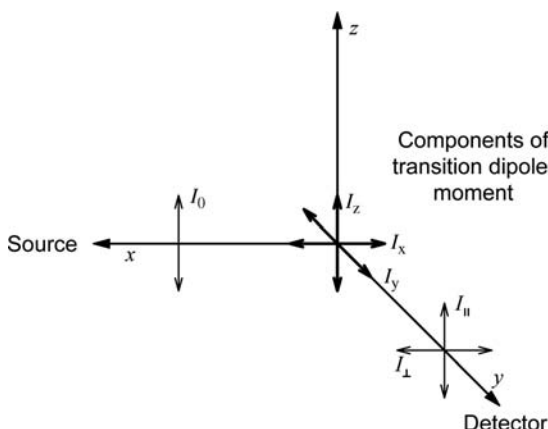


**Figure 3.10** Schematic presentation of the different possible components of the fluorescence transition dipole moment and components that are actually detected.

It is worth briefly discussing why  $P$ , in contrast to  $r$ , is not linearly proportional to the fraction of individual components even though the way it is defined (3.2) might look more intuitive at first glance.

Figure 3.10 illustrates the different possible components of the fluorescence transition dipole moment and the components that are actually detected. The excitation light,  $I_0$ , propagates along the  $x$ -axis with a polarization parallel to the  $z$ -axis. The parallel detector detects the fluorescence light component,  $I_{\parallel}$ , travelling along the  $y$ -axis with a polarization parallel with the  $z$ -axis, corresponding to the case that the dipole moment of the molecule is orientated along the  $z$ -axis in the moment of emission:  $I_{\parallel} = I_z$ . The vertical detector detects the light component,  $I_{\perp}$ , travelling along the  $y$ -axis with a polarization parallel with the  $x$ -axis, corresponding to the case that the dipole moment of the molecule is orientated along the  $x$ -axis in the moment of emission  $I_{\perp} = I_x$ . However, no detector detects light corresponding to the case that the dipole moment of the molecule is orientated along the  $y$ -axis in the moment of emission,  $I_y$ . This intensity, however, is the same as  $I_x$  since the probability that the dipole moment axis of the molecule rotates around the  $y$ -axis before emission is exactly the same as if the dipole moment axis of the molecule rotates around the  $x$ -axis before emission:  $I_x = I_y$ . (Remember that the polarization of the excitation light was originally orientated parallel to the  $z$ -axis orientation.) Therefore, the anisotropy can be rewritten as:

$$r = \frac{I_{\parallel} - I_{\perp}}{I_{\parallel} + 2I_{\perp}} = \frac{I_z - I_x}{I_z + 2I_x} = \frac{I_z - I_x}{I_z + I_y + I_x} \quad (3.4)$$

Hence, the anisotropy can be regarded as the difference in the detected intensities divided by the total intensity of the light emitted by the fluorophores. Only if the detected difference for each component is normalized by the total fluorescence emitted by the markers is a linear relationship such as (3.3) possible.

In contrast, the definition of the polarization that looked more intuitive at first glance contains no normalization by the total intensity and therefore, for mixtures of different components  $i$ , only a complicated relationship can be given:

$$\left(\frac{1}{P} - \frac{1}{3}\right)^{-1} = \sum_i \frac{f_i}{\frac{1}{P_i} - \frac{1}{3}} \quad (3.5)$$

The intrinsic intensity normalization of the anisotropy has another advantage. For the time-dependent change of the anisotropy after pulsed excitation the decay of fluorescence anisotropy can be written by the simple formula:

$$r(t) = r_0 e^{-t/\phi} \quad (3.6)$$

Here,  $\phi$  is the rotational correlation time of the labelled particle, and  $r_0$  the initial anisotropy that would be observed if no diffusional rotation were present, or, in other words, if the molecules were fixed in their original positions. The rotational correlation time,  $\phi$ , describes the time scale by which rotational diffusion occurs for a certain fluorescently labelled biomolecule or isolated fluorescence dye. Here, it is not to be confused with the angle  $\phi$  in Figure 3.9 and 3.13.

In the following we will discuss a mathematical framework for the anisotropy that will allow us to estimate, for example, molecular masses of labelled proteins from the measured fluorescence anisotropies. We will conduct this discussion in the four steps described below. Readers that look only for a quick overview can also go right away to step 4, in which the most important equation is explained.

- 1) We first calculate how many molecules with an absorption transition dipole moment spanning a certain angle  $\theta$  with the  $z$ -axis are excited by light that is linear polarized parallel to the  $z$ -axis (photoselection).
- 2) We then calculate the average anisotropy, which would be observed from many molecules that all have the same angle,  $\theta$ , but different angles  $\phi$  (see Figure 3.9).
- 3) We then use the results of the first and second steps to calculate the maximum fluorescence anisotropy,  $r_0$ , averaged over all angles,  $\theta$  and  $\phi$ , that would be observed when these molecules do not move.
- 4) Finally, we calculate the anisotropy,  $r$ , that is actually observed when labelled particles exhibit rotational diffusion.

1. Let us begin to calculate the random distribution of molecules excited by light of a polarization aligned with the  $z$ -axis. The transition dipole moment of a single fluorescence marker does not have to be exactly collinear with the  $z$ -axis to be excited. The excitation probability is rather a function that depends on the angle  $\theta$  between the  $z$ -axis and the transition dipole moment:

$$P_{\text{exc}}(\theta) \propto \cos^2 \theta \quad (3.7)$$

This cosine square dependence of the excitation probability on the transition dipole moment orientation is visualized in the polar plot in Figure 3.11. A

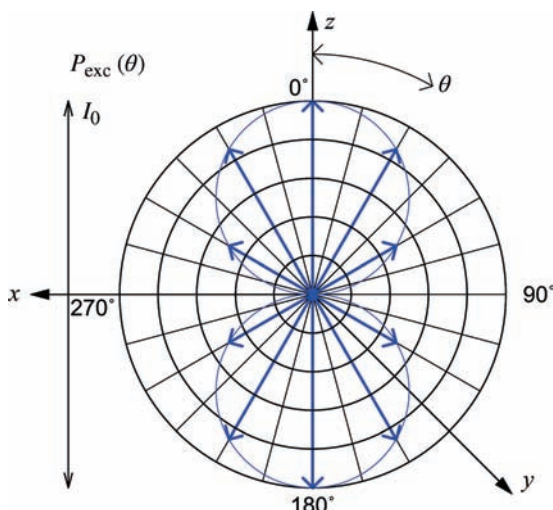


**Figure 3.11** Dependence of excitation probability on the angle between the transition dipole moment vector and the polarization vector of the exciting light.

maximum excitation probability is observed when the transition dipole moment is exactly parallel to the polarization vector of the light. This is indicated by the length of the arrow pointing to  $\theta = 0^\circ$  or  $180^\circ$ . An increasing deviation from collinearity does not immediately lead to a vanishing excitation probability. Only if the transition dipole moment is aligned exactly perpendicular to the polarization vector of the light ( $\theta = 90^\circ$  or  $270^\circ$ ) is the excitation probability zero.

Therefore, linear-polarized light will initially excite a distinct population of molecules with transition dipole moments symmetrically distributed around the  $z$ -axis.

From a simple geometrical consideration one can conclude that in a randomly disordered solution the number of molecules that have a transition dipole moment angle between  $\theta$  and  $\theta + d\theta$  is proportional to the corresponding surface area on a sphere,  $\sin \theta d\theta$  (grey area in Figure 3.12). The population-distribution of molecules having a transition dipole moment tilted by  $\theta$ , which are excited by polarized light,  $f(\theta)$ , is therefore the product of the excitation probability to excite a molecule with that angle (3.7) and the corresponding number of molecules having that angle:

$$f(\theta)d\theta = \cos^2 \theta \sin \theta d\theta \quad (3.8)$$

2. In a next step let us calculate the anisotropy of the emission of a single molecule fixed in Cartesian coordinates. Initially, we assume that the transition dipole moment for absorption is collinear with the transition dipole moment for fluorescence. The intensity of light radiated from a dipole is proportional to the square of its transition dipole moment vector projected onto the axis of observation (Figure 3.13).

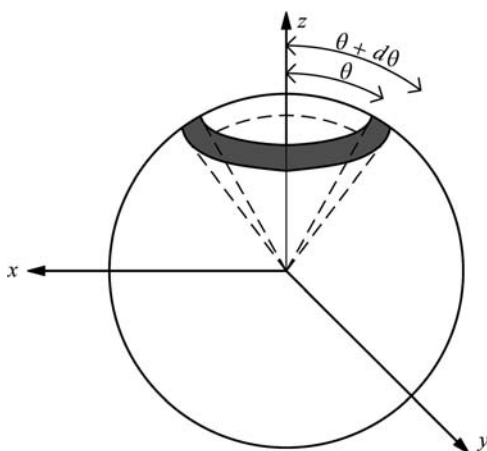


**Figure 3.12** The area on a sphere defined by angles between  $\theta$  and  $\theta + d\theta$  is proportional to the number of molecules in a random distribution that have a transition dipole moment vector pointing in the direction between  $\theta$  and  $\theta + d\theta$ .

If  $\theta$  is the angle by which the transition dipole moment is tilted away from the  $z$ -axis then its projection onto the  $z$ -axis is proportional to  $\cos \theta$  and hence the corresponding intensity observed in the detector parallel to the  $z$ -axis,  $I_{\parallel}$ , is proportional to:

$$I_{\parallel}(\theta) \propto \cos^2 \theta \quad (3.9)$$

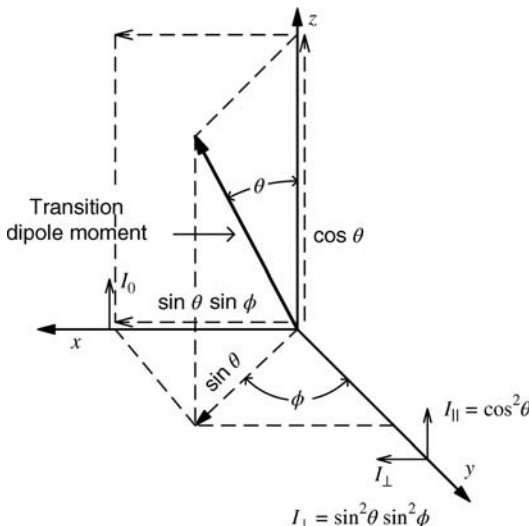


**Figure 3.13** Calculation of the anisotropy of a single molecule tilted from the  $z$ -axis by the angles  $\theta$  and  $\phi$ .

Similarly, the projection of the transition dipole moment onto the  $x$ -axis is  $\sin \theta$  if the transition dipole moment vector would be within the  $z$ - $x$  plane. The magnitude of this projection is reduced by  $\sin \phi$  when the transition dipole moment is additionally rotated out of the  $x$ - $z$  plane around the  $z$ -axis by the angle  $\phi$ . This angle is not to be confused with the rotational correlation time  $\phi$ . The remaining projection onto the  $x$ -axis is then proportional to  $\sin \theta \sin \phi$ . The fluorescence intensity detected in the detector parallel to the  $x$ -axis is then proportional to:

$$I_{\parallel}(\theta, \phi) \propto \sin^2 \theta \sin^2 \phi \quad (3.10)$$

The excitation probability is independent of the angle  $\phi$  of a molecule's transition dipole moment. Therefore, one can simplify (3.10) by using the average value  $\sin^2 \phi = \frac{1}{2}$ :

$$I_{\parallel}(\theta) \propto \frac{1}{2} \sin^2 \theta \quad (3.11)$$

This is the mean fluorescence intensity observed with perpendicular detection for all molecules tilted by  $\theta$  but averaged over all angles  $\phi$ .

Using (3.9) and (3.11) to calculate the anisotropy (3.2) results, after a few steps in:

$$r(\theta) = \frac{I_{\parallel} - I_{\perp}}{I_{\parallel} + 2I_{\perp}} = \frac{3 \cos^2 \theta - 1}{2} \quad (3.12)$$

This is the average anisotropy for all molecules whose transition dipole moment vector is tilted away from the  $z$ -axis by an angle  $\theta$ .

3. Let us now assume that all molecules are fixed, that means they do not diffuse or rotate before they emit a photon. The anisotropy averaged over all molecules corresponds to the integration over all angles  $\theta$  of the population weighted anisotropies  $f(\theta)r(\theta)$  normalized by the total population  $\int_0^{\pi} f(\theta)d\theta$ :

$$r_0 = \frac{\int_0^{\pi} f(\theta)r(\theta)d\theta}{\int_0^{\pi} f(\theta)d\theta} = \frac{\int_0^{\pi} \cos^2 \theta \sin \theta \frac{3 \cos^2 \theta - 1}{2} d\theta}{\int_0^{\pi} \cos^2 \theta \sin \theta d\theta} = 0.4 \quad (3.13)$$

This value is the maximum anisotropy that can be observed for a solution of randomly orientated molecules. However, there are several reasons why this maximum value can almost never be observed. First, the assumption of collinear transition dipole moments for excitation and fluorescence is only true in very few cases. From similar considerations to those necessary for the derivation of (3.12) one obtains for the maximum anisotropy for molecules having noncollinear transition dipole moments:

$$r_0 = 0.4 \left( \frac{3 \cos^2 \alpha - 1}{2} \right) \quad (3.14)$$

Here,  $\alpha$  is the angle between the transition dipole moment for absorption and emission (see Figure 3.9). An example for a molecule that has very similar absorption and fluorescence transition dipole moment vectors is diphenylhexatriene (DPH). It has an angle of only  $\alpha=7.4^\circ$  between the two dipole moments. However, most molecules have larger values of  $\alpha$ .

From (3.14) also the so-called “magic angle” can be easily deduced. This angle is called the “magic angle” because it can be used whenever it is necessary to avoid any dependence on the excitation polarization in fluorescence or other optical experiments. The anisotropy becomes 0 when  $3\cos^2\alpha=1$ . This corresponds to an angle of  $\alpha=54.7^\circ$ . To avoid any polarization effects in a fluorescence experiment, for example, the fluorescence must simply be measured with a polarizer that filters light having a polarization with an angle of  $54.7^\circ$  with respect to the excitation light.

4. Finally, we derive the averaged fluorescence anisotropy that is observed when the labelled particles undergo rotational diffusion. Remember that  $r(t)=r_0e^{-t/\phi}$  (3.6) describes the time-resolved decay of anisotropy of a molecule after it has been excited with linear-polarized light. The rotational correlation time,  $\phi$ , of a spherical particle, for example, depends on the viscosity ( $\eta$ ) and the temperature ( $T$ ) of the solution and on the particles volume ( $V$ ):

$$\phi = \frac{\eta V}{kT} \quad (3.15)$$

Simultaneously, the fluorescence also decays in most cases monoexponentially after excitation (compare with Eq. (1.19)):

$$I_{\text{Fl}}(t) = I_{\text{Fl}}^0 \cdot e^{-t/\tau_{\text{S}_1}} \quad (3.16)$$

The average anisotropy observed after an excitation of the fluorescence dye,  $\bar{r}$ , is equal to the integration of the time-dependent anisotropy  $r(t)$  decay (3.6) weighted by the simultaneous decay of fluorescence intensity  $I(t)$  (3.16). Conducting this integration results in:

$$\bar{r} = \frac{\int_0^\infty r(t)I_{\text{Fl}}(t)dt}{\int_0^\infty I_{\text{Fl}}(t)dt} = \boxed{\frac{r_0}{1 + (\tau_{\text{S}_1}/\phi)}} \quad (3.17)$$

This result stresses the important relationship between the excited-state lifetime of the fluorescence marker,  $\tau_{\text{S}_1}$ , and the rotational correlation time,  $\phi$ , for anisotropy measurements. The observed anisotropy will be large if the rotational diffusion is slow in comparison to the excited-state lifetime of the label. Then, the fluorescence label emits photons before the particle has rotated significantly. In contrast, the observed anisotropy will be small if the rotational diffusion is fast in comparison to the excited-state lifetime of the label. In this case, the labelled particle has changed its orientation significantly before fluorescence photons are emitted.

From these consideration it follows that for a certain fluorescence lifetime only a certain dynamic range of particle sizes can be differentiated by anisotropy measurements. This dynamic range is usually ideal to sense particle size changes ranging from small ligand molecules up to normal-sized proteins. However, for the detection of changes above these particle sizes, for example binding of a large protein to another protein, other techniques are usually more advantageous. Let us discuss now a few typical application examples.

### 3.4.2

#### Application Example: Receptor–Ligand Interactions

The determination of ligand–protein interactions is a classical application example of fluorescence anisotropy measurements. According to (3.3) the anisotropy of a mixture of the unbound fluorescing component and its associated form is given by:

$$\bar{r} = f_F r_F + f_B r_B \quad (3.18)$$

Here,  $f_F$  and  $f_B$  are the fractions and  $r_F$  and  $r_B$  are the anisotropies of the free and bound ligand, respectively. The dissociation constant,  $K$ , of a ligand L with a particular receptor R is defined as:

$$L + R \rightleftharpoons LR$$

$$K = \frac{C_L C_R}{C_{LR}} \quad (3.19)$$

Here,  $C_L$ ,  $C_R$  and  $C_{LR}$  are the corresponding concentrations of the free ligand, the free receptor and the receptor–ligand complex, respectively. From (3.19) it follows that the fraction of the bound ligand relates to  $K$  by:

$$f_B = \frac{C_{LR}}{C_L + C_{LR}} = \frac{C_R}{C_R + K} \quad (3.20)$$

Considering (3.18) and that  $f_B + f_F = 1$ , the fraction of the bound ligand can be written as

$$f_B = \frac{\bar{r} - r_F}{r_B - r_F} \quad (3.21)$$

Therefore, the measurement of the fluorescence anisotropy allows us to determine very accurately the fraction of bound or free ligand as well as the dissociation constant  $K$  from the measured anisotropy value  $\bar{r}$  if the anisotropies for the pure free and bound form have been measured previously. It is also very convenient to determine  $K$  from titration curves of the anisotropy as a function of the ligand or receptor concentration (Figure 3.14). Because  $f_B$  becomes 1/2 when  $K = C_R$  (3.20) in such a titration curve,  $K$  corresponds to the concentration for which an anisotropy value of  $(f_F + f_B)/2$  is observed (3.18).

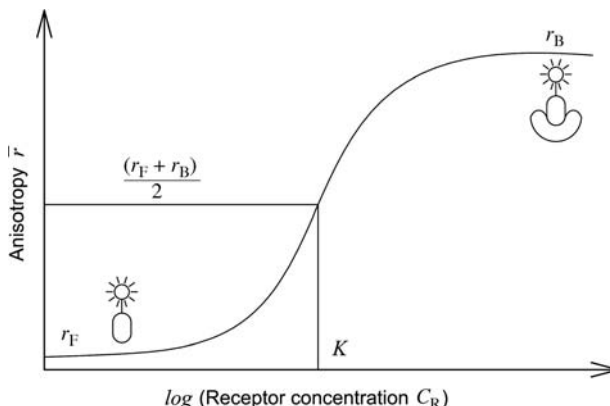


**Figure 3.14** Typical titration curve of anisotropy observed from a labelled ligand as a function of receptor concentration.

Unfortunately, sometimes the fluorescence quantum yield of the fluorescence label changes when the ligand binds to the receptor. A typical reason for such a change is a decreasing polarity of the fluorescence marker's environment in the presence of the receptor. In such cases the following modified equation can be used, if the changing fluorescence quantum yields of the fluorescence marker in the bound and free state,  $\phi_{\text{Fl}}^{\text{B}}$  and  $\phi_{\text{Fl}}^{\text{F}}$ , respectively, are known:

$$f_{\text{B}} = \frac{\bar{r} - r_{\text{F}}}{(r_{\text{B}} - \bar{r})R + \bar{r} - r_{\text{F}}}, R = \frac{\phi_{\text{Fl}}^{\text{B}}}{\phi_{\text{Fl}}^{\text{F}}} \quad (3.22)$$

### 3.4.3

#### Application Example: Estimation of Molecular Mass

Since the rotational correlation of a protein depends on its molecular mass,  $M$ , its mass can be estimated by measuring the anisotropy of its fluorescent conjugate and using (3.17) when the lifetime of the fluorescence marker is known. The corresponding relation between the rotational correlation time of a globular protein is approximately:

$$\phi \approx \frac{\eta V}{RT} = \frac{\eta M}{RT} (\bar{v} + h) \quad (3.23)$$

Here,  $\bar{v}$  is the specific volume of the protein; a rough approximation for this value is  $\sim 1 \text{ cm}^3 \text{ g}^{-1}$ .  $h$  is an additional term that takes into account that the proteins usually have a hydration shell in aqueous solution. Typically, a value of  $\sim 0.2 \text{ g H}_2\text{O}$  per gram protein can be assumed. Because (3.23) is based on the assumption that the biomolecules are spheres and because the fluorescence dye attached to the biomolecules often has some residual torsional degrees of freedom the determination of molecular masses from anisotropies can only be regarded as an estimate. However, (3.23) is certainly very useful in estimating

whether a particular biochemical transformation, for instance the binding of two proteins, can be expected to give detectable changes in anisotropy.

### 3.4.4

#### Application Example: Enzyme Function and Kinetics

Another important application example of fluorescence polarization measurements is monitoring enzyme kinetics. Enzymes are biocatalysts that can increase very effectively and specifically the reaction rate of certain biochemical reactions by lowering the corresponding reaction barrier (see example in Figure 3.15). In the lock-and-key model, specificity is achieved by a perfect match of the chemical surface of the substrate with the enzyme. In the induced-fit model, additional conformational transformations of the enzyme upon binding of the substrate help catalyse the reaction. The mechanism of many drugs is based on the inhibition of the active site of certain enzymes. An important example is penicillin, which inhibits enzymes responsible for the cell wall synthesis of bacteria but does not affect the corresponding mechanisms in humans.

For many biological relevant questions it is very important to know the kinetics of enzymatic product formation and the influences of the presence of regulators, activators or inhibitors. Figures 3.15 and 3.16 represent an example of monitoring an enzymatic cleavage reaction via fluorescence anisotropy. Cleaving the fluorescently labelled substrate reduces its molecular size, which results directly in a decrease in the observed anisotropy [see curve for  $C_S(t)$  in Figure 3.16]. The concentration of the substrate and product can be directly calculated from the

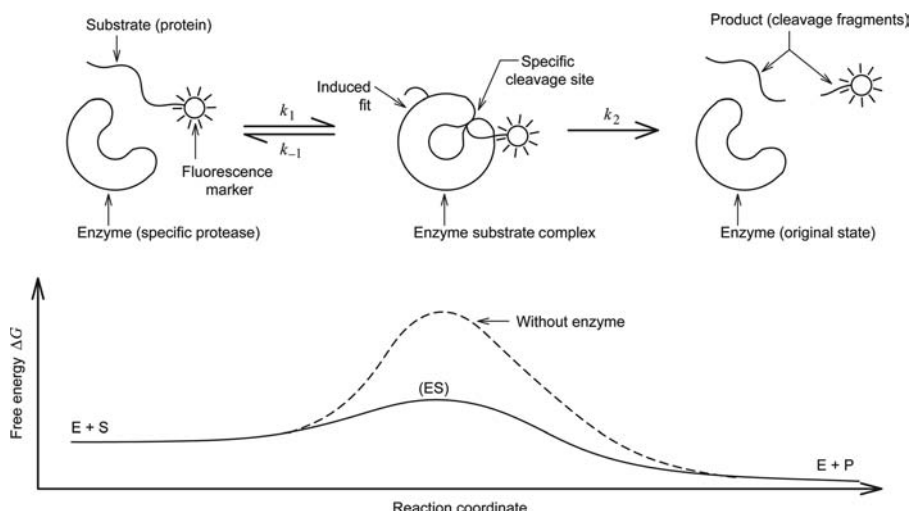


**Figure 3.15** Proteolytic cleavage of a fluorescently labelled biomolecule as a typical example of an enzymatically catalysed reaction that can be monitored by fluorescence anisotropy measurements. E denotes the enzyme, S

the substrate, P the products, and ES the enzyme–substrate complex. The example shown corresponds to an induced-fit mechanism.

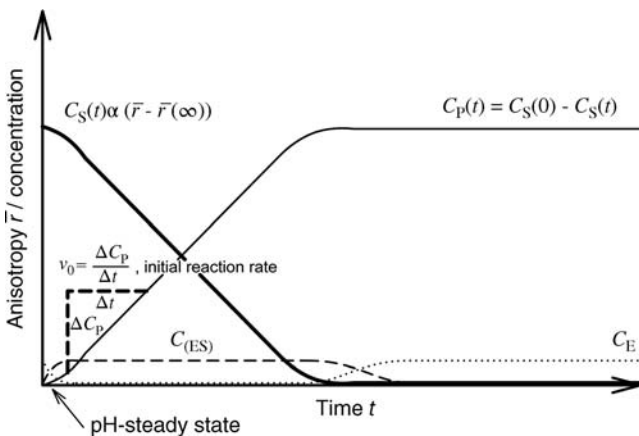


**Figure 3.16** Schematic time trace of the concentrations of substrate ( $C_S$ ), product ( $C_P$ ), the enzyme–substrate complex ( $C_{ES}$ ) and the free enzyme ( $C_E$ ). In the corresponding example the decrease of the fluorescence anisotropy

directly reflects the amount of uncleaved substrate [ $C_S(t)$ , thick line]. The concentration of the cleaving products can be calculated from Eqs. (3.24) and (3.25).

measured anisotropies:

$$C_S(t) = C_S(0) \frac{\bar{r}(t) - \bar{r}(\infty)}{\bar{r}(0) - \bar{r}(\infty)} \quad (3.24)$$

Here,  $C_S(t)$  is the substrate concentration at time  $t$ .  $\bar{r}(0)$ ,  $\bar{r}(t)$  and  $\bar{r}(\infty)$  are anisotropies measured at the beginning of the reaction, at time  $t$  and when the reaction has finished, respectively. The concentration of the product,  $C_P(t)$ , can be calculated from:

$$C_P(t) = C_S(0) - C_S(t) \quad (3.25)$$

for the simple reaction visualized in Figure 3.15.

The initial rate of the reaction,  $v_0$ , is a key parameter in enzyme kinetics. It can be directly determined from measurements such as shown in Figure 3.16. The initial reaction rate is usually discussed within the framework of the well-known Michaelis–Menten mechanism (see upper part of Figure 3.15). It assumes that there is an equilibrium between free substrate and substrate bound to the enzyme (rate constants  $k_1$  and  $k_{-1}$  in Figure 3.15), that the concentration of the enzyme–substrate complex,  $C_{ES}$ , remains more or less constant during the reaction (Figure 3.16), and that the products are formed from the enzyme–substrate complex in an irreversible reaction step (rate constant  $k_2$  in Figure 3.15). From these assumptions the following differential equations describing the time-dependent changes in the population of the enzyme–substrate complex and the products can be derived:

$$\frac{\Delta C_{ES}}{\Delta t} = +k_1 C_E C_S - k_{-1} C_{ES} - k_2 C_{ES} = 0, v_0 = \frac{\Delta C_P}{\Delta t} = +k_2 C_{ES} \quad (3.26)$$

Resolving the initial reaction rate,  $v_0$ , from these equations results in the Michaelis–Menten equation:

$$v_0 = \frac{\Delta C_p}{\Delta t} = \frac{k_2 C_{E0} C_S}{C_S + \frac{k_{-1} + k_2}{k_1}} = \frac{v_{\max} C_S}{C_S + K_M} \quad (3.27)$$

It describes the rate of enzymatic conversion as a function of the enzyme and the substrate concentration as well as of the Michaelis–Menten constant,  $K_M = \frac{k_{-1} + k_2}{k_1}$ , which is a specific parameter of the enzyme. Here,  $C_{E0}$  is the total concentration of the enzyme:  $C_{E0} = C_E + C_{ES}$ . Figure 3.17a is a graphical presentation of (3.27) and describes the reaction rate,  $v_0$ , as a function of initial substrate concentration,  $C_S$ . At high substrate concentrations the reaction rate is independent of the substrate concentration because all enzyme molecules are busy with substrate. Then the reaction rate only depends on the kinetics of the final reaction step and the enzyme concentration ( $v_0 \approx k_2 C_E = v_{\max}$ ). In contrast, at low substrate concentrations the reaction rate depends linearly on  $C_S$ , ( $v_0 \approx v_{\max} C_S / K_M$ ) because now the probability that an enzyme encounters a substrate molecule is rate limiting.  $K_M$  can be found at the coordinate for  $C_S$  at the half-value of  $v_{\max}$ . A better way to determine  $v_{\max}$  and  $K_M$  is a reciprocal plot of  $1/v_0$  against  $1/C_S$ , a so-called Lineweaver–Burk plot (Figure 3.17b). The intercept of the resulting line with the  $1/C_S$ -axis corresponds to  $-1/K_M$ , whereas the intercept with the  $1/v_0$ -axis corresponds to  $1/v_{\max}$ . It is possible to construct a Lineweaver–Burk plot by measuring the rate of the enzyme kinetics,  $v_0$ , via fluorescence anisotropy, as shown in Figure 3.16 for only two substrate concentrations,  $C_S$  (corresponding, for example, to the two dots in Figure 3.17b). This allows a quick determination of the important enzyme parameters  $v_{\max}$  and  $K_M$  from only two anisotropy–time traces.

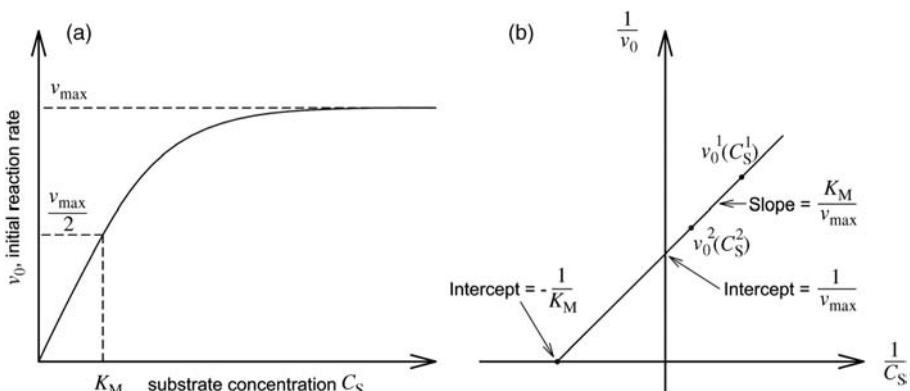


**Figure 3.17** (a) Linear plot of the enzymatic initial reaction rate as a function of the substrate concentrations. (b) Corresponding reciprocal Lineweaver–Burk plot. A complete

Lineweaver–Burk plot can be constructed from only two time-dependent anisotropy measurements for two different initial substrate concentrations [see two dots in (b)].

## 3.4.5

## Application Example: Enzyme Inhibition, Activation and Regulation

In nature the activity of many enzymes is activated or inhibited by the presence of regulating ligands, L. Also, many drugs are ligands that inhibit enzyme function. To describe these interactions the mechanistic scheme of enzyme function introduced in Figure 3.15 has to be extended by equilibria with the regulating ligands (Figure 3.18).

Here,  $K_L$  and  $K'_L$  are the equilibrium constants for binding of the ligand to the free enzyme or the enzyme–substrate complex, respectively. The rate constants  $k'_1$ ,  $k'_{-1}$  and  $k'_2$  are corresponding constants of the enzyme kinetics if the ligand has bound to the substrate or the enzyme–substrate complex. The ligand L is an inhibitor if the reaction  $E + S \rightleftharpoons (ES) \rightarrow P$  is faster than  $(LE) + S \rightleftharpoons (LES) \rightarrow P$ , whereas it is an activator if  $(LE) + S \rightleftharpoons (LES) \rightarrow P$  is faster than  $E + S \rightleftharpoons (ES) \rightarrow P$ . When an inhibiting ligand binds only to E but not to (ES), this is called competitive inhibition, because here L competes with S to bind to E. In contrast, an uncompetitive inhibition corresponds to the situation when the inhibiting ligand only binds to the enzyme–substrate complex (ES). Often mixed inhibition is present, in which case the ligand binds to both E and (ES). The special case in which the binding affinities are the same in both cases ( $K_L = K'_L$ ) is called noncompetitive inhibition. Each of these cases affects the measured, apparent  $K_M$  and  $v_{max}$  values in different ways. Thus, the four cases of inhibition can be immediately differentiated by two Lineweaver–Burk plots measured in the presence and the absence of the inhibitor. So, a total of four time-dependent anisotropy measurements are necessary for the determination of the type of extent of inhibition or activation.

Figure 3.19 shows Lineweaver–Burk plots for examples of competitive and uncompetitive inhibition. If solely competitive inhibition can occur, the Michaelis–Menten equation and the measured apparent Michaelis–Menten constants become:

$$v_0 = \frac{v_{max} C_S}{C_S + K_M \left( 1 + \frac{C_L}{K_L} \right)} \Rightarrow K_M^{\text{competitive}} = K_M \left( 1 + \frac{C_L}{K_L} \right) \quad (3.28)$$

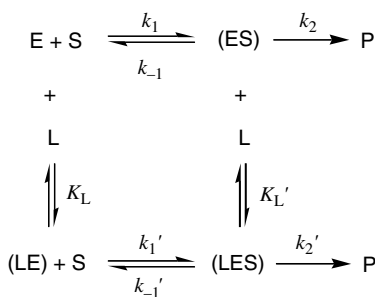


Figure 3.18 Kinetic scheme of enzymatic activity in the presence of regulating ligands, L.

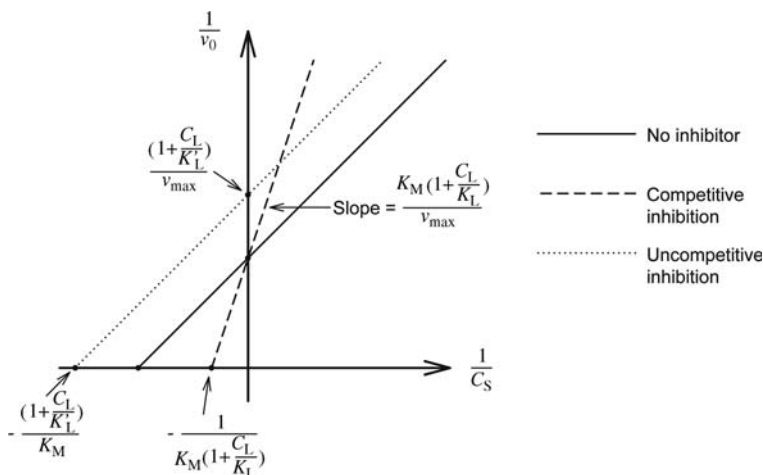


Figure 3.19 Lineweaver–Burk plots for competitive and uncompetitive inhibition.

Here,  $C_L$  is the concentration of the inhibitor L. In competitive inhibition the equilibrium concentration of the enzyme–substrate complex (ES) is reduced in favour of (LE) which has the same effect as if the constant  $k_{-1}$  would be larger and thus  $K_M = \frac{k_{-1}+k_2}{k_1}$  seems larger. Still, at very high concentrations  $C_s$ , the maximum reaction rate  $v_{max} = k_2 C_{ES}$  can be reached because of saturation of the enzyme E with substrate S. In contrast, if the enzyme is completely uncompetitive inhibited, (LES) does not form any P, and both the measured apparent Michaelis–Menten constant and the measured apparent maximum reaction velocity are affected:

$$v_0 = \frac{v_{max} C_s}{C_s \left(1 + \frac{C_L}{K'_L}\right) + K_M} \Rightarrow K_M^{\text{uncompetitive}} = \frac{K_M}{\left(1 + \frac{C_L}{K'_L}\right)}, v_{max}^{\text{uncompetitive}} = \frac{v_{max}}{\left(1 + \frac{C_L}{K'_L}\right)} \quad (3.29)$$

Here, the maximum velocity can't be achieved even at saturation substrate concentrations since a fraction of the enzymes is always blocked in the unproductive complex (LES). The case of mixed and uncompetitive inhibition corresponds to combinations of (3.28) and (3.29).

### 3.5

#### Förster Resonance Energy Transfer

##### 3.5.1

##### Principles and Theoretical Background

Förster resonance energy transfer (FRET) is another important fluorescence technique used to investigate receptor–ligand binding interactions, conformational

transitions of biomolecules, lipid membrane transformations, and last but not least to measure distances on the nm-scale as a molecular ruler. FRET is named after Theodor Förster, a German physical chemist (1910–1974). FRET is the transfer of excitation energy from an electronically excited molecule, called a donor (D), to an acceptor (A) molecule in the electronic ground state (3.30):



Here, the symbol  $*$  is usually employed to assign molecules in electronically excited states.  $k_{ET}$  is the rate constant for the energy transfer between a single donor and a single acceptor molecule.

FRET assays are usually based on the requirement that donor and acceptor molecules must be in close vicinity so that the transfer (3.30) can occur. The occurrence of acceptor fluorescence after selective excitation of the donor is a clear indication of the presence of energy transfer. If donor and acceptor have a large separation, little energy transfer occurs after selective donor excitation and the fluorescence of the donor molecule will dominate (Figure 3.20a). In contrast, for small donor–acceptor distances the acceptor fluorescence will dominate because of effective energy transfer (Figure 3.20b). Ratiometric comparison of both fluorescence intensities provides a very robust tool for the investigation of

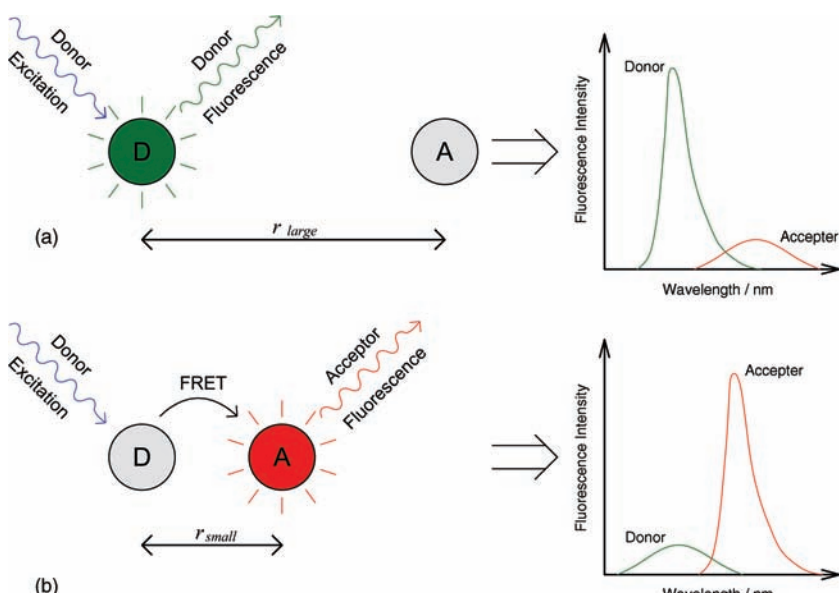


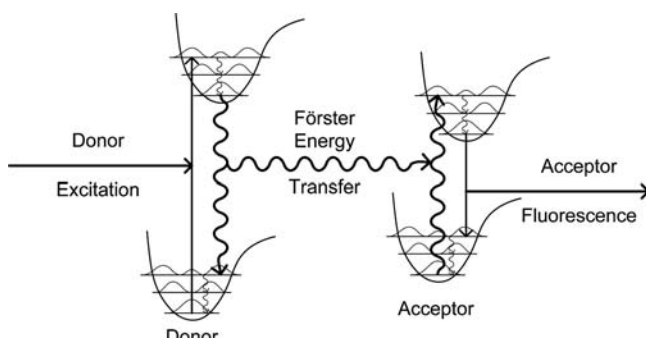
**Figure 3.20** The extent of Förster energy transfer is directly monitored by the relative fluorescence intensities from the donor and acceptor molecules. This provides a very sensitive tool to measure the proximity of fluorescently labelled biomolecules on the nm-scale.

many biological processes in which two fluorescently labelled partners vary their distance on the nm-scale.

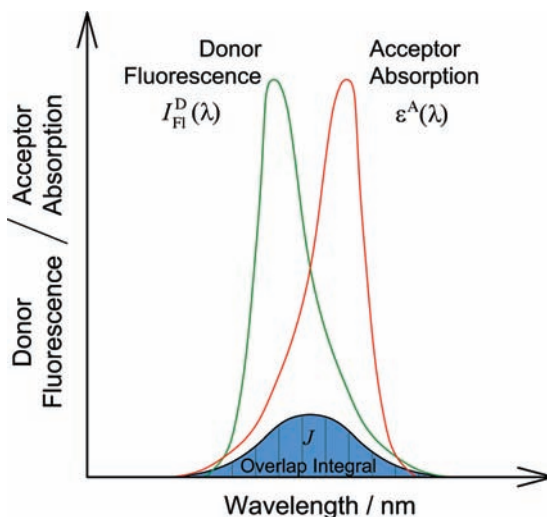
Before we discuss several biological application examples we have to examine what determines the magnitude of the rate of energy transfer,  $k_{ET}$ , and thus the fluorescence intensities observed from donor and acceptor molecules. This will enable us to calculate or estimate the efficiency of FRET and the donor-acceptor distance under certain biological conditions based on easily accessible experimental data such as absorption and emission spectra or fluorescence lifetimes of the donor and acceptor molecules.

Figure 3.21 visualizes the individual photophysical steps occurring during a FRET experiment. After selective excitation of the donor, as the first vibrational relaxation occurs in the donor. As a consequence, the energy transfer starts usually from the lowest vibrational state,  $v' = 0$ , of the excited donor molecule. Obviously, an energy transfer requires that the energy donated by the donor molecule matches exactly the energy accepted by the acceptor. After the energy transfer the acceptor molecule is in the electronic excited state, whereas the donor molecule has been de-excited into its electronic ground state. Usually, both molecules are vibrationally excited directly after energy transfer. As usual, this excess vibrational energy is quickly dissipated by vibrational relaxation. Now, fluorescence emission from the acceptor can occur even though it has not been excited originally.

From the previous considerations we have learned that the energy transfer is only possible if isoenergetic transitions are possible in the donor and acceptor. Thus, one important factor governing the magnitude of  $k_{ET}$  is the number or density of isoenergetic donor-acceptor transitions of a particular pair of fluorescence markers. When recalling the mechanisms that govern fluorescence and absorption, it is not surprising that this density of isoenergetic donor-acceptor transitions can be estimated from the spectral overlap,  $J$ , of the donor fluorescence with the acceptor absorption. However, it is important to note here that



**Figure 3.21** Förster energy transfer and energy diagram of donor and acceptor molecules along with the corresponding potential curves.



**Figure 3.22** The rate of energy transfer is proportional to the spectral overlap integral of donor fluorescence and acceptor fluorescence.

FRET is not associated with the generation and absorption of a photon (which is called the “trivial” mechanism). It is a pure nonradiative process occurring between donor and acceptor molecules based on a mechanism described further below.  $J$  is a mathematical entity described by (3.31) and visualized in Figure 3.22:

$$k_{\text{ET}} \propto J = \int I_{\text{Fl, Norm}}^D(\lambda) \epsilon^A(\lambda) \lambda^4 d\lambda \quad (3.31)$$

Here,  $I_{\text{Fl, Norm}}^D(\lambda)$  is the normalized donor fluorescence spectrum calculated from the experimental fluorescence spectrum,  $I_{\text{Fl}}^D(\lambda)$ , by  $I_{\text{Fl, Norm}}^D(\lambda) = I_{\text{Fl}}^D(\lambda) / \int I_{\text{Fl}}^D(\lambda) d\lambda$ , and  $\epsilon^A(\lambda)$  is the absorption spectrum of the acceptor as defined by (2.2)–(2.5). For sufficient spectral overlap the acceptor absorption and fluorescence has to be red-shifted with respect to the donor absorption and fluorescence. A direct consequence of this and the previous considerations is that FRET usually occurs only from a donor of higher  $S_1$  state energy to an acceptor of lower  $S_1$  state energy.

The mechanism of FRET can be described classically by a dipole–dipole interaction between the transition dipole moments of the donor and the acceptor molecules. If the transition dipole moment of the donor is exactly parallel with the transition dipole moment of the acceptor they can enter into resonance and the probability that energy transfer occurs is the highest.

Two consequences follow from this mechanistic base: (i) The energy transfer depends on the relative orientations of donor and acceptor molecules (Figure 3.23). (ii) The probability of energy transfer is proportional to the magnitude of the

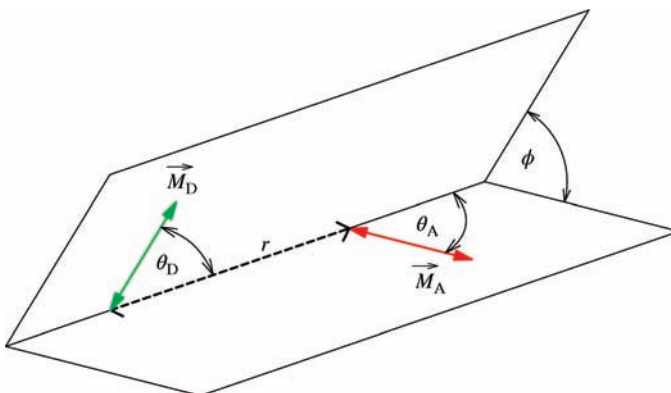


**Figure 3.23** FRET is based on the interaction of the transition dipole moments of donor and acceptor.

dipole–dipole interaction, which decays by  $1/r^6$  with distance between the two dipole moments.

Therefore, in addition to the requirement of isoenergetic donor–acceptor transitions (3.31) the rate for energy transfer is also proportional to:

$$k_{\text{ET}} \propto \frac{1}{r^6} \kappa^2 \quad (3.32)$$

Here,  $\kappa^2$  is the so-called orientation factor describing the relative orientations of the donor and acceptor transition dipole moments. It can be calculated from the angles described in Figure 3.23 by:

$$\kappa^2 = (\sin \theta_D \cdot \sin \theta_A \cdot \cos \phi - 2 \cos \theta_D \cdot \cos \theta_A)^2 \quad (3.33)$$

In liquid solution the orientation factor is often approximated by a mean value,  $\kappa^2 = \frac{2}{3}$ , which results from averaging over a random distribution of donor–acceptor orientations.

Theodor Förster developed a formula by which the rate of energy transfer can be calculated entirely from experimental data:

$$k_{\text{ET}} = 0.529 \cdot \frac{\Phi_{\text{Fl}}^{\text{D}}}{\tau_{S_1}^{\text{D}}} \cdot \frac{1}{r^6} \kappa^2 \cdot \frac{1}{n^4 \cdot N_{\text{A}}} \cdot \int I_{\text{Fl, Norm}}^{\text{D}}(\lambda) \epsilon^{\text{A}}(\lambda) \lambda^4 d\lambda \quad (3.34)$$

Here, it is assumed that  $J = \int I_{\text{Fl, Norm}}^{\text{D}}(\lambda) \epsilon^{\text{A}}(\lambda) \lambda^4 d\lambda$  (3.31) is calculated from  $\epsilon(\lambda)$  in units of  $\frac{1}{\text{mol} / \text{m}^3 \cdot \text{cm}}$ . Sometimes in the literature  $J$  is also derived from  $\epsilon(\lambda)$  in units  $\frac{1}{\text{M} \cdot \text{cm}}$ , then the factor 0.529 has to be replaced by  $0.529 \cdot 10^{-3}$ . Unfortunately, in the literature the units of  $J$  are often already given in  $\frac{\text{nm}^6}{\text{mol}}$ , which contains no information about the original units of  $\epsilon(\lambda)$  and causes a lot of confusion.

$\Phi_{\text{Fl}}^{\text{D}}/\tau_{S_1}^{\text{D}} = k_{\text{Fl}}^{\text{D}} \propto |\vec{M}_{S_1 \rightarrow S_0}^{\text{D}}|^2$  is directly related to the magnitude of the donor transition dipole moment determined by the experimentally accessible parameters  $\Phi_{\text{Fl}}^{\text{D}}$  and  $\tau_{S_1}^{\text{D}}$  [compare with (1.10), (1.15) and (1.16)].  $\Phi_{\text{Fl}}^{\text{D}}$  and  $\tau_{S_1}^{\text{D}}$  are the fluorescence quantum yield and first excited-state lifetime of the donor in the absence of any energy transfer. The magnitude of the acceptor transition dipole moment is already implemented in the extinction coefficient values  $\epsilon(\lambda) \propto |\vec{M}_{S_0 \rightarrow S_1}^{\text{A}}|^2$  [compare with (2.3) and (1.5)].  $n$  is the refractive index of the medium including solvent and solutes and  $N_A$  is Avogadro's number. Since water has a refractive index of 1.33 and biomolecules have somewhat higher indices the value for the refractive index is often approximated by  $n \sim 1.4$ .

The quantum efficiency for energy transfer can be calculated analogously to the quantum efficiencies for fluorescence or intersystem crossing [compare with (1.10) and (1.11)]:

$$\Phi_{\text{ET}} = \frac{k_{\text{ET}}}{k_{\text{Fl}}^{\text{D}} + k_{\text{IC}}^{\text{D}} + k_{\text{ISC}}^{\text{D}} + k_{\text{ET}}} = \frac{k_{\text{ET}}}{1/\tau_{S_1}^{\text{D}} + k_{\text{ET}}} \quad (3.35)$$

The fluorescence intensity observed from the acceptor,  $I_{\text{Fl}}^{\text{A}}$ , and the corresponding decrease in the donor fluorescence,  $I_{\text{Fl}}^{\text{D}}$ , are directly related to the efficiency of energy transfer (compare also with Figure 3.20):

$I_{\text{Fl}}^{\text{A}} \propto \Phi_{\text{ET}}$   
 $I_{\text{Fl}}^{\text{D}}/I_{\text{Fl}}^{\text{D},0} = 1 - \Phi_{\text{ET}}$

(3.36)

Here,  $I_{\text{Fl}}^{\text{D},0}$  is the fluorescence intensity observed from the donor in the absence of any energy transfer. For a distinct pair of donor and fluorescence dyes most parameters in (3.34) are constant when they are under the same environmental conditions. Then, only the distance,  $r$ , between the two dyes determines the efficiency of energy transfer when assuming also a constant orientation factor. From a comparison of (3.35) with (3.32) it follows for the transfer efficiency under these conditions that:

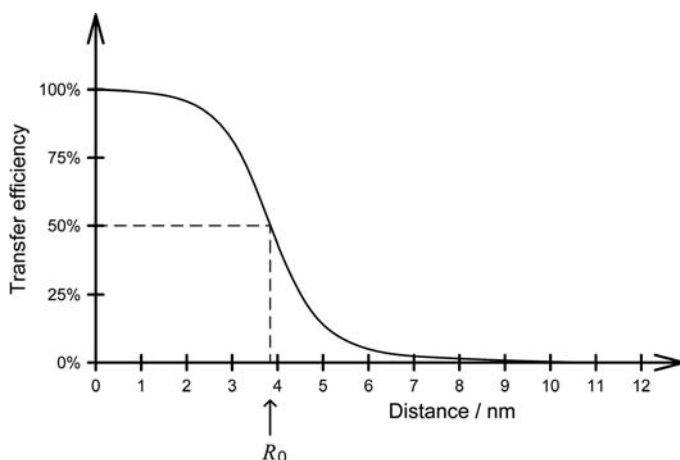
$$\Phi_{\text{ET}} = \frac{R_0^6}{R_0^6 + r^6}$$

(3.37)

Here,  $R_0$ , is the so-called Förster distance, which is a distinct property of each pair of donor–acceptor fluorescence dyes. The Förster distance defines the donor–acceptor distance,  $r$ , for which a transfer efficiency of 50% is observed. It is dependent on the individual parameters in (3.34) for the two dyes. Table 3.1 gives examples of Förster radii for various donor–acceptor pairs. Figure 3.24 shows a typical distance dependency of the energy-transfer efficiency according to (3.37). The transfer efficiency measured in a FRET experiment allows us to estimate the distance between donor and acceptor fluorescence dyes under differing biological conditions if the Förster radius is known or if it can be

**Table 3.1** Examples of donor–acceptor Förster radii.

Donor	Acceptor	$R_0$ (nm)
Tryptophan	Dansyl	~2
Pyrene	Coumarin	~4
$\beta$ -Carotene	Chlorophyll $\alpha$	~5
Fluorescein	Tetramethylrhodamine	~5
Rhodamine 6G	Malachite green	~6
Chlorophyll $b$	Chlorophyll $\alpha$	$\alpha$ ~10

**Figure 3.24** Typical distance dependence of FRET.

estimated using (3.34). Depending on the chosen pairs of dyes the typical dynamic range by which the measured FRET efficiency allows the donor–acceptor separation to be estimated is from ~1 to 10 nm.

### 3.5.2

#### Application Examples

FRET can be used for a multitude of biomolecular applications. Figures 3.25–3.28 show examples of the application of FRET to monitor biomolecular processes or to determine the properties of biomolecules. Details of these applications are described in the corresponding figure legends. Most applications are related to the determination of any kind of receptor–ligand interaction or measurement of conformational distance changes. The advantage of FRET is the high sensitivity of the acceptor fluorescence as an indicator for an interaction

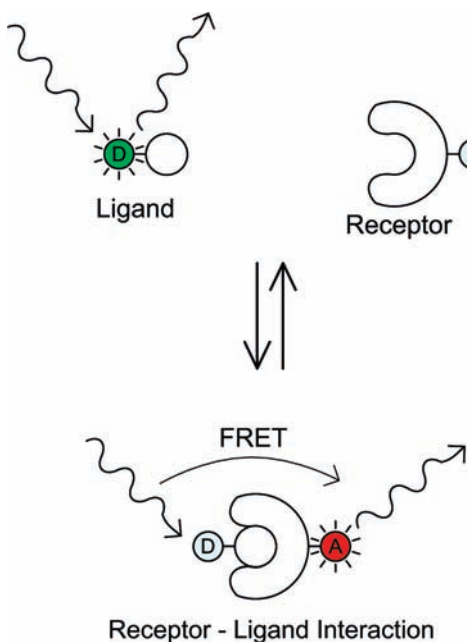


**Figure 3.25** In this example FRET is used to detect a receptor–ligand binding. The application of FRET for the measurement of receptor–ligand equilibria is useful, for example, when polarization assays, that need only one label, fail. This can be the case when the labelled ligand is already so large that binding to the receptor does not lead to a detectable change

in the rotational diffusion constant,  $\phi$ , and thus also not to a significant change in the anisotropy value. FRET, in contrast will always indicate binding independently of the molecular masses of the receptor and ligand, as long as the distance between donor and acceptor is small enough in the receptor–ligand complex.

and the possibility of estimating distances on a scale of a few nanometres, which is the scale of proteins and protein interactions. Since FRET is based on fluorescence detection, strong signals can be observed *in vitro* and *in vivo*. Simultaneous detection of donor and acceptor fluorescence is a kind of ratiometric detection, which explains why the observed results are usually very robust. A disadvantage, however, is the requirement of labelling two sites. In addition, the interaction is usually limited to small distances of only a few nm, which sometimes makes it hard to monitor the interactions of objects over larger distances in an appropriate way. For distance estimates, demanding site-selective labelling is necessary and often an exact determination of the distances is hindered by uncertainties in the relative orientations of the two dyes or other important parameters in (3.34).

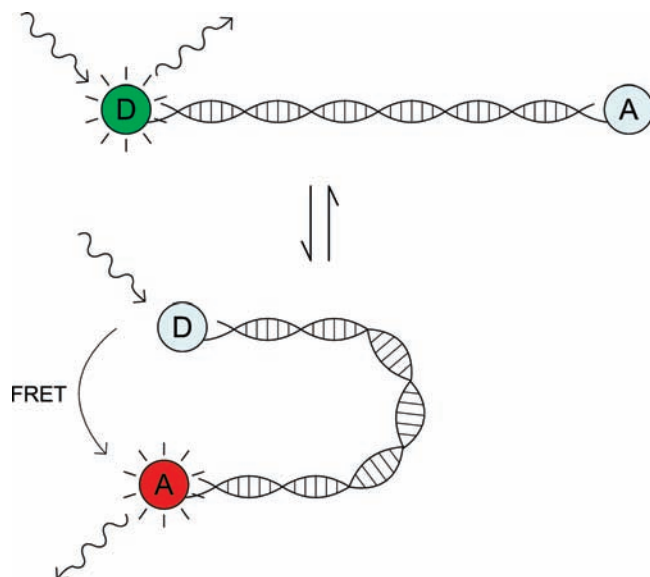


**Figure 3.26** Example of the application of a FRET assay for the determination of conformational changes in DNA. By observing single DNA molecules (Chapter 9) even a real-time observation of these conformational changes is possible.

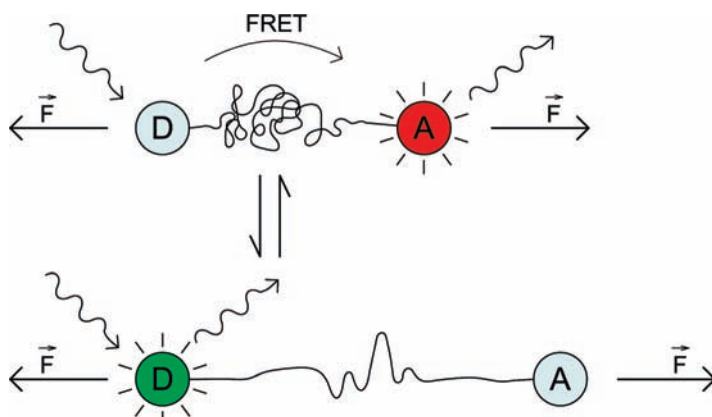


**Figure 3.27** Determination of the donor-acceptor distance by FRET of labels attached to a single protein. In this example the protein is unfolded using an atomic force microscope (Chapter 9). Simultaneous detection of the

applied force with the atomic force microscope and the distance from FRET signals allows one to determine what forces are necessary to unfold the protein to a certain degree.

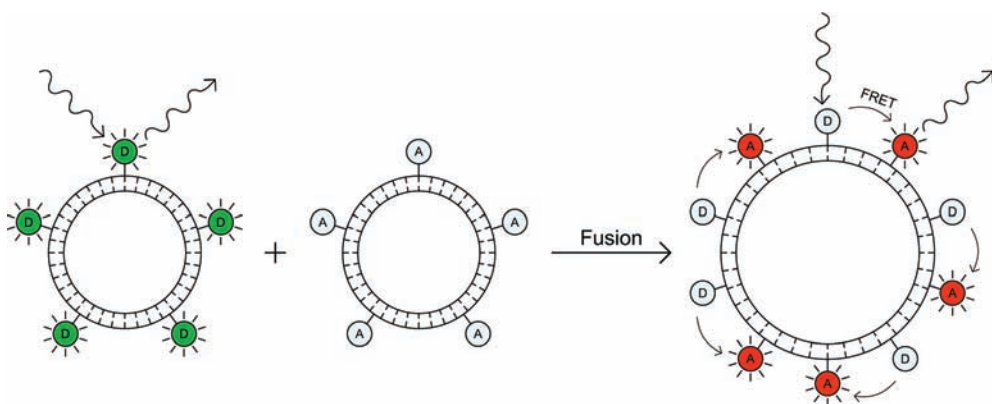


**Figure 3.28** Membrane fusion can be monitored if the lipids of two different vesicles, liposomes or other lipid bilayers are labelled with donor and acceptor fluorescence dyes,

respectively. A fusion of the membranes will be immediately indicated by FRET because then the donor and acceptor fluorescence markers are in close proximity.

### 3.6 Fluorescence Kinetics

In recent years, the measurement of fluorescence kinetic changes during biomolecular processes has become an increasingly popular tool. The fluorescence kinetics can be measured, for example, by the excitation of the sample using a short light pulse from a laser source and subsequent monitoring of the fluorescence kinetics described by Eqs. (1.17)–(1.19). In practice, usually many such light pulses are repetitively applied to collect sum kinetic data of sufficient quality. As described in Chapter 1, the measured fluorescence kinetics actually reflects the population dynamics of the first excited state  $S_1$  (1.19). Often, the fluorescence kinetics of a fluorescence dye depend on environmental conditions such as solvent polarity. Then, measuring the fluorescence kinetics can monitor changes in the biomolecular environment of the labelled species, for example because it binds to a large nonpolar protein or it is transported from the polar aqueous environment into the nonpolar environment of a lipid bilayer. Figure 3.29 is illustrating fluorescence decay curves observable in such an experiment. Measurement of the fluorescence kinetics is a very robust read-out because the fluorescence decay itself is in principle independent of variations in the absolute fluorescence intensity. It is thus insensitive to artefacts such as uncertainties in instrumental alignment or dilution errors. Often, the fluorescence kinetics corresponds to a monoexponential decay (1.19). Then, in a logarithmic plot the fluorescence decay is represented by a straight line with the slope  $-\tau_{S_1}$  (see inset in Figure 3.29). Since even two data points suffice to determine this slope, fluorescence kinetics measurements can be regarded as another type of “ratiometric” method.

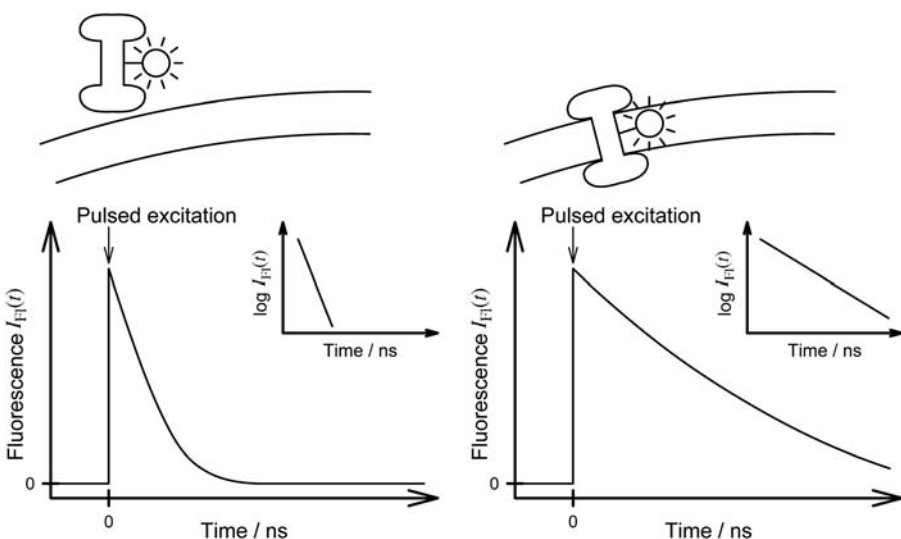


**Figure 3.29** The change of fluorescence lifetime of a fluorescence marker can be used to detect, for example, whether a protein is in a more polar or nonpolar environment.

The advantage of fluorescence kinetics measurement is clearly the robustness once a fluorescence dye has been found that monitors a biochemical transformation via fluorescence lifetime changes. However, the disadvantage is that often such a dependency of the fluorescence kinetics on biomolecular changes cannot easily be predicted. Some fluorescence dyes are known to be quite sensitive to such changes and, often, fluorescence dyes that show a fluorescence intensity dependence as a function of certain factors such as pH or  $\text{Ca}^{2+}$  concentration also show fluorescence kinetics dependencies. Another important example of a molecule whose fluorescence depends sensitively on biochemical transformation is NAD(P)H. The fluorescence of bound NAD(P)H in, for example, mitochondria decays with a time constant of 2–10 ns ( $\Phi_{Fl} = 8\text{--}25\%$ ), whereas free NAD(P)H decays with a time constant of 0.45 ns ( $\Phi_{Fl} = 2\%$ ). This can be used to visualize the location of bound and unbound NAD(P)H and thus the metabolic activity in different regions of a cell in fluorescence lifetime imaging (FLIM). FLIM is the measurement of the fluorescence kinetics with microscopic resolution yielding fluorescence decay curves for each pixel in a microscope fluorescence image (see Figure 3.8 and Chapter 7 for more details). Nevertheless, often it is a process of trial and error to develop an assay based on fluorescence kinetics.

Let us therefore discuss the mechanisms that can influence the fluorescence kinetics in order to develop some kind of intuition for this trial and error process. Why, for example, do the fluorescence kinetics often differ in environments of different polarity? In a more polar aqueous environment, the energies of the  $S_0$  and  $S_1$  states are usually lowered due to dipole–dipole interactions with the solvent molecules. Often, the energy of  $S_1$  is lowered to

a larger extent than for  $S_0$ . This is because the weaker bonding character of the excited state often results also in a larger polarizability of the larger electron orbitals [for a definition of the polarizability see (4.11)]. As a net result the energy gap between  $S_0$  and  $S_1$  states is somewhat smaller in polar environments than in nonpolar environments such as in the lipid bilayers. In Chapter 1 we learnt that internal conversion often increases for smaller energy gaps. Thus, the total lifetime of  $S_1$ ,  $\tau_{S_1}$ , observed via fluorescence decreases. Since such changes depend sensitively on factors such as changing the relative positions of potential energy curves (see Figure 1.13) and overlaps of vibrational wave functions (1.7) they are very hard to predict exactly.

Much more easy to predict are lifetime decreases due to energy transfer to, or quenching by, adjacent groups. Guanine, for example, can effectively quench the excitation from some fluorescence markers. A quencher is basically an acceptor of excitation energy that does not necessarily re-emit the excitation as fluorescence. Nonradiative processes such as internal conversion or even photochemistry are possible alternative de-excitation pathways for quenchers. FRET can always be monitored robustly by the fluorescence kinetics (Figure 3.30). Thus, all FRET applications, such as shown in Figures 3.25–3.28, can also easily be analysed using fluorescence kinetics detection.

The lifetime of the first excited state of the donor is reduced according to (3.38) [compare also with (1.15)]:

$$\tau_{S_1}^{D,ET} = (k_{ET} + k_{IC} + k_{FI} + k_{ISC})^{-1} \quad (3.38)$$

Here,  $\tau_{S_1}^{D,ET}$  corresponds to the first excited-state lifetime of the donor in the presence of any energy transfer. As a consequence, the energy transfer efficiency can also be determined directly from the measured lifetime:

$$\tau_{S_1}^{D,ET} / \tau_{S_1}^{D,0} = 1 - \Phi_{ET} \quad (3.39)$$

with,  $\tau_{S_1}^{D,0}$  being the excited-state lifetime of the donor in the absence of any energy transfer. The population kinetics of donor and acceptor are described by the differential equations:

$$\begin{aligned} \frac{dP_{S_1}^D}{dt} &= -(k_{ET} + k_{IC} + k_{FI} + k_{ISC}) \cdot P_{S_1}^D \\ \frac{dP_{S_1}^A}{dt} &= +k_{ET} \cdot P_{S_1}^D - (\tau_{S_1}^A)^{-1} \cdot P_{S_1}^A \end{aligned} \quad (3.40)$$

Here,  $\tau_{S_1}^A$  is the excited-state lifetime of the acceptor. Similar to Eqs. (1.20) and (1.21) the solution of this system of coupled differential equations for the excited state population of the donor is a biexponential rise and decay kinetic, which can be measured from the acceptor fluorescence:

$$I_{FI}(t) \propto \left( -e^{-t/\tau_{S_1}^{D,ET}} + e^{-t/\tau_{S_1}^A} \right) \quad \text{for } \tau_{S_1}^{D,ET} < \tau_{S_1}^A \quad (3.41)$$

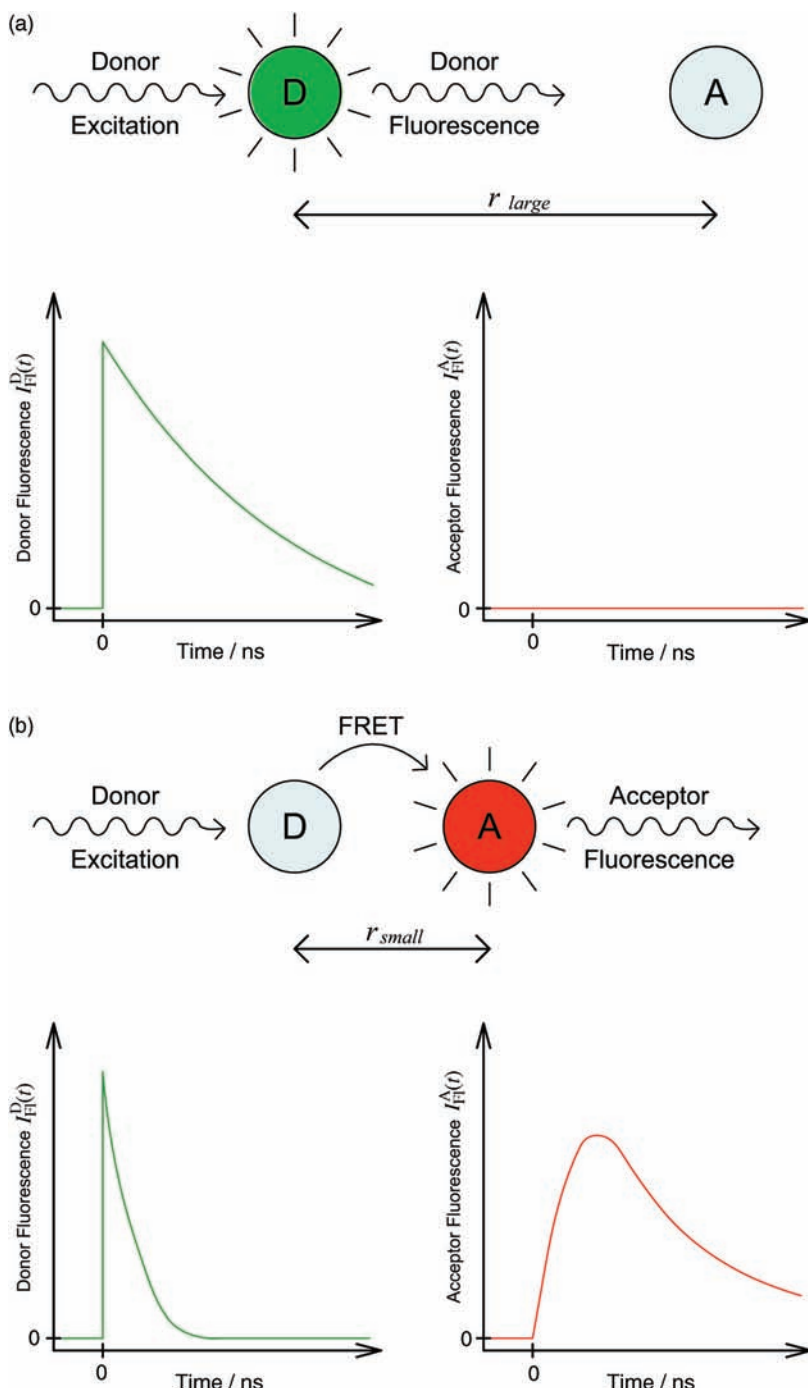


**Figure 3.30** Monitoring FRET by measuring the fluorescence kinetics of donor and acceptor. (a) In the absence of FRET the donor fluorescence decay is determined by  $\tau_{S_1}^{D,0}$  and no fluorescence is observed from the acceptor.

(b) In the presence of FRET, the excited state lifetime of the donor is reduced to  $\tau_{S_1}^{D,\text{ET}}$  and the kinetics of the acceptor fluorescence,  $I_{\text{Fl}}^A(t)$ , correspond to a biexponential population kinetics (3.41).

Notably, the time constant for the rise term always corresponds to the shorter time constant. Therefore, if the donor excited-state lifetime in the presence of energy transfer is still larger than the acceptor excited-state lifetime,  $\tau_{S_1}^{D,ET} > \tau_{S_1}^A$ , then the actual detected acceptor fluorescence is described by  $I_{Fl}^A(t) \propto (-e^{-t/\tau_{S_1}^A} + e^{-t/\tau_{S_1}^{D,ET}})$ .

Using polarized excitation and polarization filters, such as shown in Figure 3.9, also allows us to determine directly the time-dependent rotational diffusion and anisotropy decay (3.6). Figure 3.31 shows schematically the corresponding fluorescence kinetics for both a slow and a fast tumbling and rotating labelled particle. For the larger particle no significant rotational movement during the excited-state lifetime occurs. Thus, the fluorescence kinetics observed with the detector for parallel polarization basically follows the kinetics of the excited state population,  $S_1$  (Figure 3.31a). For a smaller labelled biomolecule, in contrast, the transition dipole moments, which were originally parallel with the excitation, rotate significantly during the excited-state lifetime,  $\tau_{S_1}$ . As a consequence, an additional initial decrease is observed using the detector for parallel fluorescence polarization (black curve in Figure 3.31b). This decrease is determined by the rotational correlation time,  $\phi$  (3.15), for the fluorescently labelled particle. Simultaneously, a corresponding increase can be detected using the detector for perpendicular

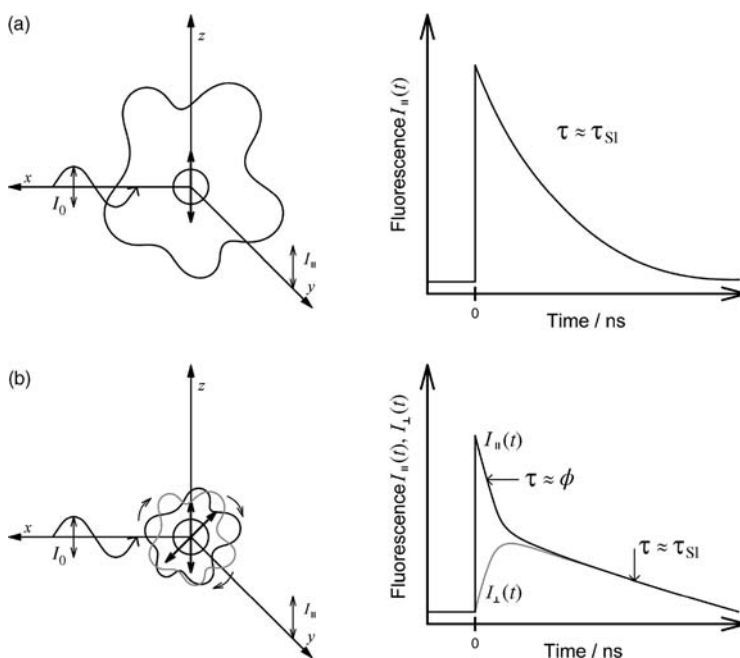


**Figure 3.31** Schematic presentation of fluorescence kinetics observed with polarized excitation and detection for a particle exhibiting (a) slow and (b) fast rotational diffusion.

fluorescence polarization. From the time-dependent signals from both detectors,  $I_{\parallel}(t)$  and  $I_{\perp}(t)$  (compare with Figure 3.9), the time-dependent anisotropy,  $r(t) = r_0 e^{-t/\phi}$  (3.6), can be calculated. It is thus possible to determine the rotational correlation time,  $\phi$ , from time-resolved fluorescence polarization measurements.

### 3.7

#### Fluorescence Recovery after Photobleaching

A fluorescence technique that is based on the photochemical bleaching of fluorescence dyes at distinct locations in the sample is fluorescence recovery after photobleaching (FRAP). In FRAP the fluorescence recovery kinetics are observed after a bleaching pulse has been applied (black area in Figure 3.32). These fluorescence recovery kinetics directly reflect the molecular diffusion of labelled species from regions where no bleaching excitation has been applied (Figure 3.32). The rate of recovery of fluorescence is thus an indicator of the mobility of the fluorescing molecules adjacent to the photobleached volume and relates to their diffusion coefficient. FRAP is frequently applied in studies of artificial and biological membranes. It can be used, for example, to measure the lateral diffusion of various membrane or cytoplasmic components. This in turn helps to characterize the mobility of membrane receptors and lipids under varying conditions. FRAP is also often used for analyses of cytoskeletal dynamics.

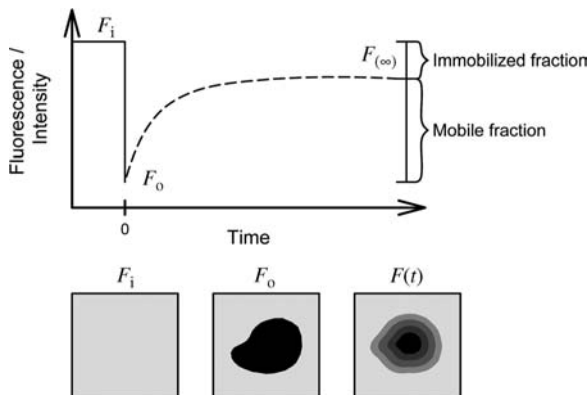


**Figure 3.32** FRAP is used to determine the molecular diffusion dynamics of labelled species in biological samples. In this example, the diffusion of labelled proteins in membranes is monitored.

3.8

## Biochemiluminescence

There are also assays that use the so-called chemiluminescence resulting from an enzymatic conversion of a molecule rather than fluorescence from an extrinsic tag. Some species in nature have evolved the ability to produce light by an enzymatic transformation of a chemical compound. An important example is the firefly *Photinus pyralis*, in which the enzyme luciferase transforms luciferin into oxyluciferin. A product of this reaction is photons of  $\sim 560$  nm wavelength (Figure 3.33). This mechanism is used by the fireflies to glow in the dark.

This is based on the formation of a luciferase-bound luciferyladenylate complex when luciferin,  $O_2$  and ATP are present. Successive oxidative decarboxylation produces  $CO_2$ , oxyluciferin, AMP and light of  $\sim 560$  nm with a quantum efficiency of  $\sim 90\%$ . As a consequence, this reaction is particularly well suited to monitor ATP concentrations. Figure 3.34 shows the mechanism of another luciferase, from the firefly *Renilla reniformis*. In contrast to luciferase from the firefly *Photinus pyralis* it does not require the presence of ATP or  $Mg^{2+}$  and results in photons at  $\sim 480$  nm. The corresponding firefly luciferase gene can be incorporated into the DNA of an organism, for example, in a way that fusion proteins of luciferase with native biomolecules are expressed by the organism. This then allows observation of the amount of transcription and location of the expressed protein with very high sensitivity.

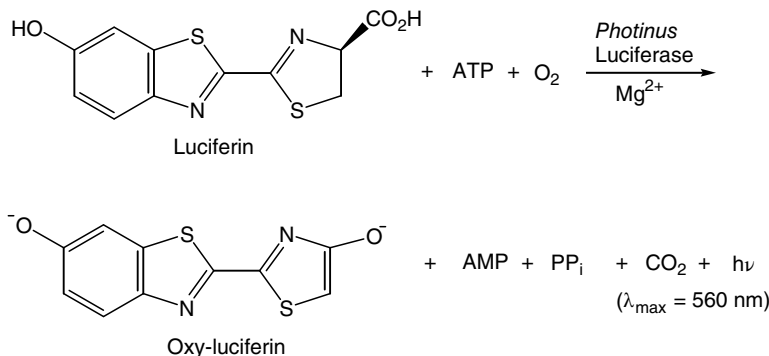


**Figure 3.33** Luciferase from the firefly *Photinus pyralis* catalyses the oxidation of luciferin to oxyluciferin in the presence of ATP, O<sub>2</sub> and Mg<sup>2+</sup>. The subsequent photoluminescent

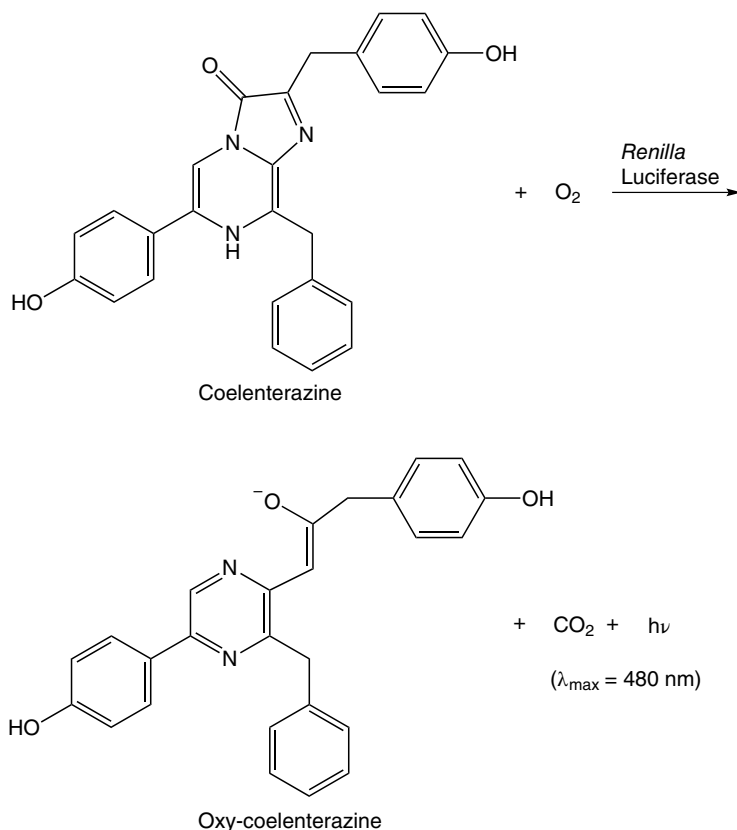


**Figure 3.34** Luciferase from the firefly *Renilla reniformis* catalyses the oxidation of coelenterazine to oxy-coelenterazine in the presence of O<sub>2</sub>. In contrast to luciferase from the firefly *Photinus pyralis* it does not require the presence of ATP or Mg<sup>2+</sup>, and results in photons at  $\sim$ 480 nm.

### Problems

- 3.1** Fluorescent labels are designed in such a way that the fluorescent quantum yield is as high as possible and that the fraction of triplet state remains as small as possible upon excitation. Some time constants of two different fluorescent labels are given below:

	Label A	Label B
Radiative S <sub>1</sub> $\rightarrow$ S <sub>0</sub> transition (fluorescence):	$\tau_{\text{FI}} = 5 \text{ ns}$	$\tau_{\text{FI}} = 5 \text{ ns}$
Nonradiative S <sub>1</sub> $\rightsquigarrow$ S <sub>0</sub> transition (internal conversion):	$\tau_{\text{IC}} = 25 \text{ ns}$	$\tau_{\text{IC}} = 25 \text{ ns}$
S <sub>1</sub> $\rightsquigarrow$ T <sub>1</sub> intersystem crossing:	$\tau_{\text{ISC}} = 100 \text{ ns}$	$\tau_{\text{ISC}} = 20 \text{ ns}$

Radiative  $T_1 \rightarrow S_0$  transition  
(phosphorescence):

$$\tau_{\text{Ph}} = 2 \text{ s}$$

Nonradiative  $T_1 \rightsquigarrow S_0$  transition  
(internal conversion):

$$\tau_{\text{ISC}}^{\text{T} \rightarrow \text{S}} = 20 \mu\text{s}$$

$$\tau_{\text{ISC}}^{\text{T} \rightarrow \text{S}} = 50 \mu\text{s}$$

Which dye is the better fluorescent label? Why? What other properties that can not be deduced from the given time constants are also important for a fluorescent dye to be a good label for biomolecules?

- 3.2 You have identified potential binding regions at the surface of two proteins that form a stable receptor–ligand complex. To check if they indeed bind together at these regions you plan to use a Förster energy-transfer experiment. Where would be the ideal labelling sites at the proteins? Would you rather use amino group reactive labels or thiol group reactive labels? How would you achieve a specific labelling?
- 3.3 You want to observe by fluorescence detection where in a cell a certain protein is the most abundant. The protein is expressed by the cell itself. It turns out that it is impossible to specifically attach fluorescence labels to these proteins within the cell. What alternative approach is possible to observe fluorescence that indicates the presence of these proteins in the cell?
- 3.4 Explain how you can purify proteins that contain sequences of histidines from a mixture of different proteins.
- 3.5 Assume you have a solution of 1 nM streptavidin. What concentration of biotin is necessary that the probability that a single biotin binds to one streptavidin subunit is at least 50%?
- 3.6 The fluorescence anisotropy of a free labelled ligand is 0.07, whereas it exhibits an anisotropy of 0.2 when the ligand has bound to an receptor. When equal parts of a solution containing 1 nM labelled ligand and a solution containing 1 nM receptor are mixed then a fluorescence anisotropy of 0.1 can be observed. What is the dissociation constant,  $K$ , for the corresponding receptor–ligand pair?
- 3.7 The dipole moment vectors for emission and excitation of a fluorescent label span an angle of  $20^\circ$ . The fluorescent label has an excited-state lifetime of  $\tau_{S_1} = 9 \text{ ns}$ . This label is attached to a small ligand.
- The rotational correlation time of this labelled ligand in water is  $\phi = 1 \text{ ns}$  when it is freely diffusing. What is the fluorescence anisotropy that can be observed with the free labelled ligand in water?
  - A large excess of a corresponding receptor is now added to the labelled ligand with the result that all labelled ligands bind to the receptor. The total molecular mass  $M$  of the receptor–ligand complex is 20 kDa. Estimate the fluorescence anisotropy that can be observed from the receptor–ligand complex in water. Assume that the

fluorescence dye is linked very rigidly to the ligand and that the labelled receptor–ligand complex can be approximated by a sphere. The viscosity of water is:  $\eta_{\text{H}_2\text{O}} = 0.89 \times 10^{-3} \text{ kg m}^{-1} \text{ s}^{-1}$ , the specific volume of this protein is  $1 \text{ cm}^3 \text{ g}^{-1}$  and the hydration is  $h = 0.2 \text{ cm}^3 \text{ g}^{-1}$ .  $R = 8.31441 \text{ J K}^{-1} \text{ mol}^{-1}$  at  $273.15 \text{ K}$ .

- 3.8** A compound is regulating an enzymatic reaction. The initial reaction velocity,  $v_0$ , has been measured by fluorescence anisotropy for two different initial substrate concentrations  $C_s(0)$  in the presence and in the absence of the regulator. All four points have been plotted in a Lineweaver–Burk plot. The intercept of the line connecting the two points measured in the presence of the regulator with the  $1/v_0$ -axis was the same as in the absence of the regulator. However, the slope was twice as large in the presence of the regulator. What kind of regulation does this situation correspond to?
- 3.9** In a Förster energy-transfer experiment the distance between two dyes attached to the outer and inner hydrophilic domains of a transmembrane protein is to be measured. In this experiment the lifetime of the excited donor state  $S_1$  was  $\tau_{S_1}^{\text{D,ET}} = 4 \text{ ns}$ . The Förster distance for the used pair of dyes is  $2 \text{ nm}$ . The lifetime of the excited  $S_1$  state of the donor without energy transfer was  $\tau_{S_1}^{\text{D,0}} = 10 \text{ ns}$ .
- Calculate the rate of energy transfer,  $k_{\text{ET}}$ .
  - Calculate the efficiency of energy transfer,  $\phi_{\text{ET}}$ .
  - Estimate the distance between the two dyes,  $r$ .
- 3.10** You plan to characterize the binding affinity of a receptor–ligand pair by fluorescence techniques. Discuss the advantages, disadvantages and limitations of measuring fluorescence polarization, Förster energy-transfer efficiencies and fluorescence kinetics for this task.
- 3.11** The Förster formula as given in eq. 3.34 contains a term in which the fluorescence quantum yield of the donor is divided by its excited state lifetime. Show that this term is equal to the donors rate constant for fluorescence,  $k_{\text{Fl}}$ , by using eq. 1.10, 1.15 and 1.16.
- 3.12** Eq. 3.20 provides a relation between the fraction of bound ligand, the concentration of the receptor and the corresponding dissociation constant. Derive it using eq. 3.18 and eq. 3.19.
- 3.13** Eq. 3.17 is a very important equation that describes how the anisotropy is determined by the relative magnitudes of the excited state lifetime of a marker and the rotational correlation time of the marker attached to a certain object. Try to derive this expression by conducting the integration.
- 3.14** In eq. 3.12 an expression for the average anisotropy observed for all molecules that span a certain angle  $\theta$  with the excitation polarization vector is given. Derive it using eq. 3.9 and eq. 3.11.

- 3.15** In eq. 3.13 the maximum anisotropy that can be observed from randomly oriented molecules is given. Try to follow how the integration yields the numerical value of 0.4.

## Bibliography

### General

- Allan, V. (ed.) (2000) *Protein Localization by Fluorescence Microscopy: A Practical Approach*, Oxford University Press, Oxford.
- Brand, L., Simon, M.I. et al. (1997) *Fluorescence Spectroscopy (Methods in Enzymology, Volume 278)*, Academic Press, New York.
- Cantor, C.R. and Schimmel, P.R. (1980) *Biophysical Chemistry: Part II: Techniques for the Study of Biological Structure and Function*, W.H. Freeman & Co.
- Dewey, T.G. (2007) *Biophysical and Biochemical Aspects of Fluorescence Spectroscopy*, Springer.
- Gore, M.G. (2000) *Spectrophotometry and Spectrofluorimetry: A Practical Approach*, Oxford University Press, Oxford.
- Lakowicz, J.R. (2006) *Principles of Fluorescence Spectroscopy*, Springer, Berlin.
- Royer, C.A. (1995) Approaches to teaching fluorescence spectroscopy. *Biophys. J.*, **68** (3), 1191–1195.
- Sharma, A. and Schulman, S.G. (1999) *Introduction to Fluorescence Spectroscopy*, John Wiley & Sons, Inc.
- Valeur, B. (2001) *Molecular Fluorescence: Principles and Applications*, Wiley-VCH Verlag GmbH, Weinheim.

### Specific

#### Fluorescence Labelling and Conjugation Techniques

- Haugland, R.P. (1996) *Handbook of Fluorescent Probes & Research Chemicals*, Eugene, Molecular Probes.
- Haugland, R.P. (2000) Antibody conjugates for cell biology, in *Current Protocols in*

- Cell Biology*, (eds M. Dasso, J. Lippincott-Schwartz, J.B. Harford, K.M. Yamada and J.S. Bonifacino), John Wiley & Sons, Inc., pp. 16.5.1–16.5.22.
- Hemmilä, I.A. (1991) *Applications of Fluorescence in Immunoassays*, John Wiley & Sons, Inc.
- Hermanson, G.T. (2008) *Bioconjugate Techniques*, Academic Press.
- Johnson, I. (1998) Review: Fluorescent probes for living cells. *Histochem. J.*, **30**, 123–140.
- Niemeyer, C.M. (ed.) (2004) *Bioconjugation Protocols: Strategies and Methods (Methods in Molecular Biology)*, Humana Press.

### Fluorescent Dyes

- Berlman, I.B. (1971) *Handbook of Fluorescence Spectra of Aromatic Molecules*, Academic Press, San Diego.
- Drexhage, K.G. (1990) Structure and properties of laser dyes, in *Dye Lasers*, (ed. F.P. Schäfer), Springer, Berlin, Heidelberg, pp. 155–200.
- Johnson, I.D., Ryan, D. et al. (1993) Comparing fluorescent organic dyes for biomolecular labeling, in *Methods in Nonradioactive Detection* (ed. G.C. Howard), Appleton & Lange, pp. 47–68.

### Linking Biomolecules to Gold Surfaces

- Hermanson, G.T., Smith, P.K. et al. (1992) *Immobilized Affinity Ligand Techniques*, Academic Press Inc.
- Katz, E.Y. (1990) A chemically modified electrode capable of a spontaneous immobilization of amino compounds due to its functionalization with succinimidyl groups. *J. Electroanal. Chem.*, **291** (1–2), 257–260.

### Fluorescent Proteins

- Chudakov, D.M., Lukyanov, S. *et al.* (2005) Fluorescent proteins as a toolkit for in vivo imaging. *Trends Biotechnol.*, **23** (12), 605–613.
- Heim, R., Cubitt, A.B. *et al.* (1995) Improved green fluorescence. *Nature*, **373** (6516), 663–664.
- Shaner, N.C., Steinbach, P.A. *et al.* (2005) A guide to choosing fluorescent proteins. *Nature Methods*, **2** (12), 905.
- Tsien, R.Y. (1998) The green fluorescent protein. *Annu. Rev. Biochem.*, **67** (1), 509–544.

### Structure of GFP (Figure 3.7)

- Ormö, M., Cubitt, A.B. *et al.* (1996) Crystal structure of the *Aequorea victoria* green fluorescent protein. *Science*, **273**, 1392–1395.

### His-Tags

- Casey, J.L., Keep, P.A. *et al.* (1995) Purification of bacterially expressed single

chain Fv antibodies for clinical applications using metal chelate chromatography. *J. Immunol. Methods*, **179** (1), 105–116.

Hochuli, E., Bannwarth, W. *et al.* (1988) Genetic approach to facilitate purification of recombinant proteins with a novel metal chelate adsorbent. *Biotechnology*, **6**, 1321–1325.

Hochuli, E., Döbeli, H. *et al.* (1987) New metal chelate adsorbent selective for proteins and peptides containing neighbouring histidine residues. *J. Chromatogr.*, **411**, 177–184.

### Fluorescence Kinetics

- Turconi, S., Bingham, R.P. *et al.* (2001) Developments in fluorescence lifetime-based analysis for ultra-HTS. *Drug Discov. Today*, **6**, 27–39.

## 4

## Chiroptical and Scattering Methods

## 4.1

### Chiroptical Methods

Chiroptical methods are based on the use of circular-polarized light and the differences obtained in experiments using left circular polarized or right circular-polarized light. Figure 4.1 shows schematically the behaviour of the electric-field component of circular-polarized light. In contrast to linear-polarized light (Figure 1.1), in which the electric field vector only oscillates within the polarization plane, the electric-field vector of circular-polarized light rotates around the propagation axis of the light.

In Chapter 1 we learnt that the probability of light absorption depends on the electric-field component of light and the transition density,  $\psi_F^* \psi_I$ , between the final and initial electronic state (see Figures 1.7, 1.8 and 1.9). To explain many optical phenomena it is usually sufficient to consider only the corresponding transition dipole moment vector, which is derived from the three-dimensional transition density by integration (1.4). This is because the dimensions of the light waves are a lot larger than the dimensions of the electronic wave functions and therefore it can usually be assumed that the entire electron orbitals sense just a linear oscillating electronic field. However, the three-dimensional transition density is often asymmetric and chiral for more complicated molecules such as biomolecules. It is thus not surprising that the chirally propagating electric field of either left or right circular-polarized light (Figure 4.1) interacts with these asymmetric three-dimensional transition densities slightly differently. The measurement of these small differences is the basis of chiroptical methods. These effects become especially evident if larger molecules such as proteins contain larger chiral structural elements such as  $\alpha$ -helices.

## 4.1.1

#### Circular Dichroism (CD)

Circular dichroism spectroscopy (CD spectroscopy) is one of the most important chiroptical methods for the investigation of biomolecules. It is based on

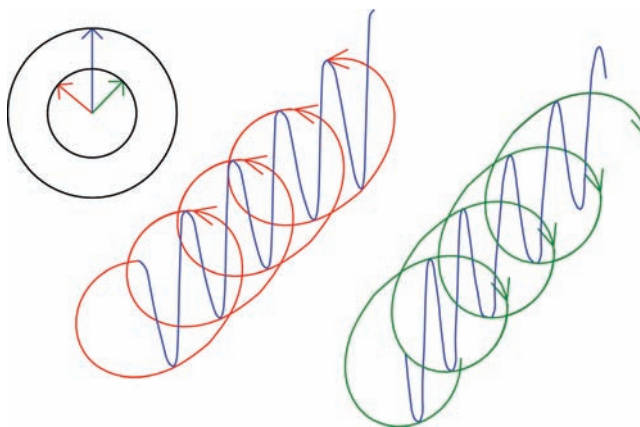


**Figure 4.1** The electric-field vector of circular-polarized light rotates either left- or right-handed around the propagation axis of the light. Linear polarized light, in which the

electric field vector only oscillates within the polarization plane (Figure 1.1), can be constructed by vector addition of left and right circular-polarized light.

differences in the absorption or extinction coefficient of biomolecules for left and right circular-polarized light:

$$\Delta\epsilon(\lambda) = \epsilon_l(\lambda) - \epsilon_r(\lambda) \quad (4.1)$$

Here,  $\epsilon_l(\lambda)$  and  $\epsilon_r(\lambda)$  are the molar extinction coefficients [see (2.5) and Figure 2.1] observed using left or right circular-polarized light, respectively. The observed difference is usually quantified by the so-called ellipticity:

$$\Theta(\lambda) = \frac{2.303[\text{OD}_l(\lambda) - \text{OD}_r(\lambda)] \cdot 180}{4\pi} \quad (4.2)$$

Here,  $\text{OD}_l(\lambda)$  and  $\text{OD}_r(\lambda)$  are the optical densities observed using left or right circular-polarized light, respectively. Typically, molar ellipticities are given, which are intrinsic parameters of the biomolecules. The molar ellipticity is defined by:

$$[\Theta](\lambda) = \frac{100 \cdot \Theta(\lambda)}{C \cdot l} = 3298 \cdot \Delta\epsilon(\lambda) \quad (4.3)$$

Again,  $C$  is the concentration of the molecules in  $\text{mol L}^{-1}$  and  $l$  is the optical path length of the sample cell in  $\text{cm}$  (compare with Figure 2.1). Please note the similarity of Eq. (4.3) with the Beer–Lambert law (2.5):

$$\Theta(\lambda) = 33\Delta\epsilon(\lambda) \cdot C \cdot l \quad \text{OD}(\lambda) = \epsilon(\lambda) \cdot C \cdot l \quad (4.4)$$

An important application of CD spectroscopy is the determination of secondary structure elements. Depending on secondary structure elements such as  $\alpha$ -helix,  $\beta$ -sheet or random coil, different conformations of the peptide bonds are present. The chirality of these conformations is to a major extent responsible for nonzero

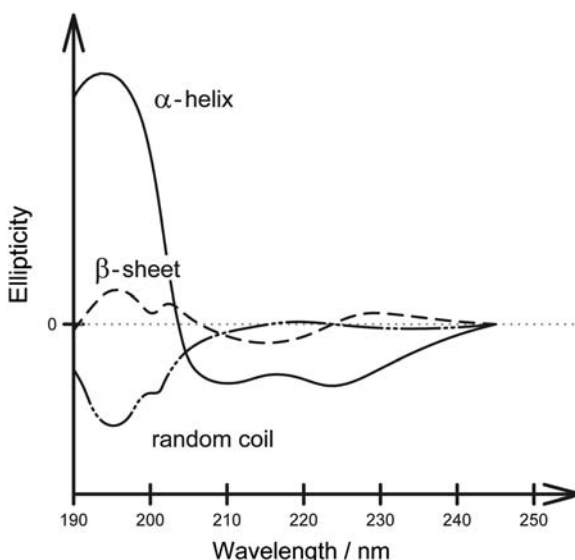


**Figure 4.2** CD spectra for hypothetical proteins with a pure  $\alpha$ -helix,  $\beta$ -sheet or random coil conformation.

molar ellipticities of proteins. The sign and magnitude of CD spectra depend on the amount of secondary structure elements in the proteins (Figure 4.2).

For proteins having differing contributions from secondary structure elements the CD spectra can be approximated by the sum of the pure secondary structure CD spectra of Figure 4.2 multiplied by the fraction of the secondary structure element contributing to the protein structure for each wavelength:

$$\Theta(\lambda) = f_\alpha \cdot \Theta_\alpha(\lambda) + f_\beta \cdot \Theta_\beta(\lambda) + f_r \cdot \Theta_r(\lambda) \quad (4.5)$$

Here  $f_\alpha$ ,  $f_\beta$  and  $f_r$  are the fractions of  $\alpha$ -helix,  $\beta$ -sheet and random coil conformation in the protein, respectively, and  $\Theta_\alpha(\lambda)$ ,  $\Theta_\beta(\lambda)$  and  $\Theta_r(\lambda)$  the corresponding CD spectra. From experimental values of  $\Theta(\lambda)$  measured at a least three wavelengths,  $\lambda_1$ ,  $\lambda_2$  and  $\lambda_3$ , one can estimate the fraction of  $\alpha$ -helix,  $\beta$ -sheet and random conformation of a protein using (4.5). For this estimate  $f_\alpha$ ,  $f_\beta$  and  $f_r$  have to be determined by solving the following system of coupled equations:

$$\begin{aligned} \Theta(\lambda_1) &= f_\alpha \cdot \Theta_\alpha(\lambda_1) + f_\beta \cdot \Theta_\beta(\lambda_1) + f_r \cdot \Theta_r(\lambda_1) \\ \Theta(\lambda_2) &= f_\alpha \cdot \Theta_\alpha(\lambda_2) + f_\beta \cdot \Theta_\beta(\lambda_2) + f_r \cdot \Theta_r(\lambda_2) \\ \Theta(\lambda_3) &= f_\alpha \cdot \Theta_\alpha(\lambda_3) + f_\beta \cdot \Theta_\beta(\lambda_3) + f_r \cdot \Theta_r(\lambda_3) \end{aligned} \quad (4.6)$$

#### 4.1.2

##### Optical Rotatory Dispersion

Optical rotatory dispersion (ORD) is based on differences in the refractive index,  $n$ , of a sample for left and right circular-polarized light. This difference is usually

given by the wavelength-dependent optical rotation:

$$\Phi(\lambda) = \frac{180 \cdot l \cdot [n_l(\lambda) - n_r(\lambda)]}{\lambda} \quad (4.7)$$

Here,  $n_l(\lambda)$  and  $n_r(\lambda)$  are the refractive indices observed using left and right circular-polarized light, respectively, and  $l$  is again the optical path length of the sample cell in cm. Similar to the molar ellipticity (4.3) the molar rotation is defined by:

$$[\Phi](\lambda) = \frac{100\Phi(\lambda)}{C \cdot l} \quad (4.8)$$

with  $C$  being the concentration of the sample. Note again the similarity of this equation with the Beer–Lambert law (2.5):

$$\Phi(\lambda) = [\Phi](\lambda) \cdot C \cdot l / 100 \quad \text{OD}(\lambda) = \epsilon(\lambda) \cdot C \cdot l \quad (4.9)$$

Usually, instead of measuring the differences in  $n_l(\lambda)$  and  $n_r(\lambda)$  (these differences are called circular birefringence) directly the rotation of the polarization of linear-polarized light is determined (Figure 4.3). This is possible because linear-polarized light can be thought to be constructed of the sum of equal parts of left and right circular-polarized light (Figure 4.1). The refractive index is directly related to the speed of light by  $c = c_0/n$ , where  $c_0$  is the speed of light in a vacuum. As a consequence, a larger refractive index for, for example, left circular-polarized light in the sample results in a lagging of this component behind the right circular polarized component of the linear-polarized light. A vector addition of the electric-field vector of both the right and the lagging left circular polarized components shows that this results in an increasing rotation of the polarization of the linear-polarized light with increasing sample cell length and sample concentration (Figure 4.3). Thus, actually,  $\Phi(\lambda)$ , as defined by (4.7), is the measured optical rotation of the polarization in units of degrees. Materials that rotate or change the polarization of light are said to be optically active.

Circular dichroism and optical rotatory dispersion spectra are very closely related because there is in general a close relationship between the absorption and the refractive index of a sample. The refractive index spectrum is usually

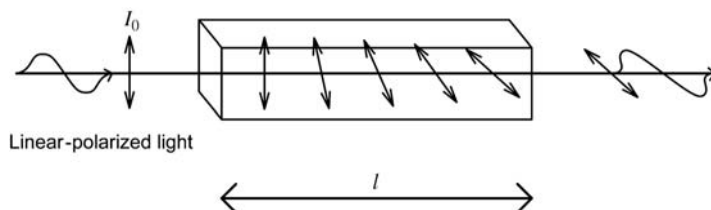


**Figure 4.3** The rotation of the polarization of linear-polarized light can be used to determine the optical rotatory dispersion of a sample.

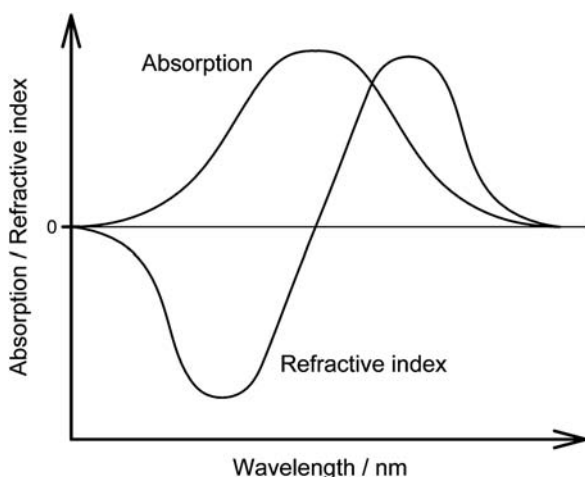


**Figure 4.4** The refractive-index spectrum is related to the first derivative of the absorption spectrum of a sample.

closely related to the first derivative of the absorption spectrum of a sample (Figure 4.4). In the same manner, circular dichroism, which is based on differences in absorptions measured with right- or left-handed circular-polarized light, and optical rotatory dispersion, which is based on corresponding differences in the refractive index, relate to each other. Quantitatively, CD and ORD spectra can be calculated from each other by so-called Kramers–Kronig transformations. The physical background of this relation goes beyond the scope of this book but the most important implication for the investigation of biomolecules is that both types of spectra basically contain very similar information.

## 4.2 Light Scattering

The measurement of light scattered at biomolecules or other particles is an important technique for the determination of particle sizes, shapes, aggregations and diffusional processes. In this section, we give some insight into the physical background of light scattering and its application for the characterization of biomolecules.

In Chapter 1 we discussed how the electric field of light interacts with electron clouds to induce transitions (see, for example, Figure 1.7). What happens, however, when the sample is exposed to electromagnetic radiation with a frequency or photon energy that does not match any energy difference between two electronic states of the molecule or, in other words, with light of wavelengths for which the sample or biomolecules show no significant absorption? In such a situation the electron clouds only oscillate with the same frequency as the electromagnetic component of the light. This oscillation is similar to the oscillation at

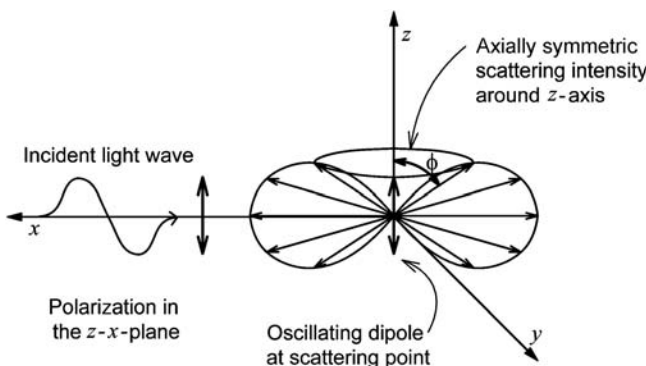


**Figure 4.5** Physical principle of light scattering. The electromagnetic radiation of the incident light induces an oscillation of the electron clouds with same frequency as the

incident light. The oscillating electron cloud is then itself an oscillating dipole that centrosymmetrically generates electromagnetic radiation. This radiation is the scattered light.

the beginning of a transition (Figure 1.7) but with the important difference that no transition can be finalized. In a classical description the oscillating electron clouds then represent an oscillating dipole that itself generates electromagnetic radiation with exactly the same frequency as the radiation that has induced the oscillation (Figure 4.5). Since light always behaves like waves and particles simultaneously this scattered radiation corresponds in the particle picture to photons having exactly the same frequency and energy as the incident photons but different propagation vectors. This phenomenon is the physical basis of elastic light scattering.

We can generally differentiate between scattering of light at particles that are significantly smaller than the optical wavelength and scattering at particles that are on the order of or larger than the optical wavelength. Many biomolecules are significantly smaller than the optical wavelength. We therefore begin the next section with a discussion of light scattering at particles that are smaller than the optical wavelength.

#### 4.2.1

#### Scattering of Light at Molecules Smaller than the Optical Wavelength

The oscillating electric field vector of the incident light wave travelling along the  $x$ -axis in Figure 4.5,  $\vec{E}(x, t)$ , can be described by a cosinoidal function:

$$\vec{E}(x, t) = \vec{E}_0 \cos[2\pi\nu(t - x/c)] \quad (4.10)$$

Here,  $\vec{E}_0$  is the maximum value of electric-field component of the light with an orientation corresponding to the polarization of the light wave,  $\nu$  is the frequency of the electromagnetic radiation,  $t$  is the time,  $x$  is the position on the  $x$ -axis and  $c$  is the speed of light.

This oscillating field induces an oscillating dipole in the electron clouds of the molecules. The magnitude of this oscillating dipole,  $\vec{\mu}_{\text{induced}}$ , is proportional to the polarizability  $\alpha$  of the molecule. The polarizability describes the ease of distortion of the electron clouds by an external electric field, such as the electric-field component of light. It is defined by:

$$\alpha = \vec{\mu} \text{ induced } \vec{E} \quad (4.11)$$

From (4.10) and (4.11) it follows that the induced oscillating dipole of molecules at the position  $x=0$  in Figure 4.5 is described by:

$$\vec{\mu}_{\text{induced}}(t) = \alpha \vec{E}_0 \cos(2\pi\nu t) \quad (4.12)$$

This oscillating dipole induced in the electron clouds generates electromagnetic radiation with a maximum intensity in all directions perpendicular to the polarization vector of the incoming light ( $\phi = 90^\circ$  in Figure 4.5). For angles other than  $\phi = 90^\circ$  the electric-field component of the scattered light decreases according to the relation:

$$E_{\text{Scat}} \propto \sin(\phi) \quad (4.13)$$

This gives rise to a doughnut-shaped distribution of the electric-field component,  $E_{\text{Scat}}$  around the induced dipole oscillating parallel to the  $z$ -axis in Figure 4.5.

If unpolarized light is used, then the resulting electric-field component distribution corresponds to a superposition of many such doughnuts rotated around the  $x$ -axis. The light intensity measurable at a certain point is always proportional to the square of the electric-field component at this point. As a result, the scattered light intensity,  $I_{\text{Scat}}$ , observed using unpolarized light decreases with the square of the distance,  $r$ , from the scattering point at  $x=0$ ,  $y=0$ ,  $z=0$ , and depends on the observation angle,  $\Theta$ , with respect to the  $x$ -axis (Figure 4.6) according to:

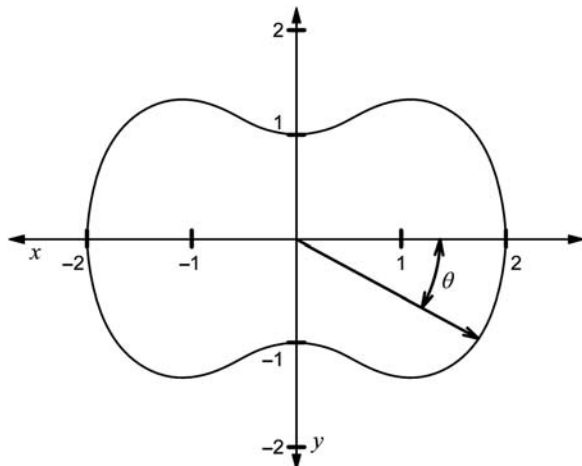


**Figure 4.6** Angle dependence of the light intensity scattered at small particles using unpolarized light.

$$\frac{I_{\text{Scat}}}{I_0} \propto \frac{8\alpha^2\pi^4}{\lambda^4 r^2} (1 + \cos^2\Theta) \quad (4.14)$$

Here,  $I_0$ , is the maximum scattered light intensity that would be observed directly at the scattering centre,  $x=0, y=0, z=0$ .

Usually, the intensity scattered by a solution containing many particles is given by the so-called Rayleigh ratio that is normalized by the distance dependence  $r^2$  and the angle dependence  $1 + \cos^2\Theta$ :

$$R_\Theta = \frac{I_{\text{Scat}}}{I_0} \frac{r^2}{V(1 + \cos^2\Theta)} = K \cdot c \cdot M \quad (4.15)$$

Here,  $c$  is the weight concentration of the particles,  $M$  the corresponding molecular weight and  $V$  the volume from which the scattered light is observed. The constant  $K$  contains information about the polarizability of the scatterers and the solvent (cf. (4.14)). It can be experimentally determined by measuring the refractive index of the solvent,  $n_0$ , and the specific refractive-index increment,  $dn/dc$ , that is the measured change in the refractive index with changing concentrations,  $c$ :  $K = 2\pi^2 n_0^2 (dn/dc)^2 / (N_A \lambda^4)$  ( $N_A$  = Avogadro's constant). Equation (4.15) is only entirely valid at infinite dilution. At higher concentrations deviations from linear behaviour are usually considered by expanding in a power series about  $c$ .

$$\frac{K \cdot c}{R_\Theta} T = \frac{1}{M} + 2A_2 c + 3A_3 c^2 + \dots \quad (4.16)$$

where  $A_2$  and  $A_3$  are the second and third virial coefficients. The exact Rayleigh ratio can be determined by measuring at several concentrations and extrapolating  $K_c/R_\Theta$  to  $c=0$ .

When a solution contains  $n$  different scattering components, the Rayleigh ratio can be calculated from the sum of the Rayleigh ratios of all components  $i$ :

$$R_\Theta = \sum_{i=1}^n R_\Theta^i = \sum_{i=1}^n K \cdot c_i \cdot M_i \quad (4.17)$$

The measured Raleigh ratio provides direct access to the molecular mass of the solute particles if their mass concentration and  $K$  are known. The molecular mass, in turn, is often a very important parameter for the characterization of biomolecules. The measurements of scattered light intensity can also be used to determine aggregations of biomolecules. The technique is uncomplicated and requires no artificial labelling of the biomolecules. However, it is limited to very pure samples for accurate determinations of the molecular mass or size of a protein.

#### 4.2.2

#### Scattering of Light at Particles Equal to or Larger than the Optical Wavelength

If a scatterer is of equal size or larger than the wavelength of the optical radiation, such as for example large DNA strands or viruses, then a more complicated

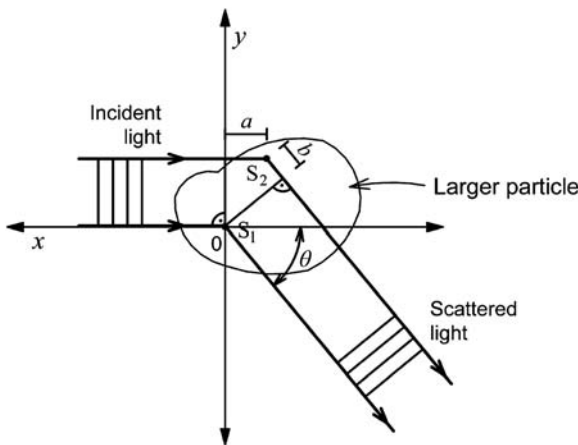


**Figure 4.7** A particle larger than the wavelength of light can be regarded as consisting of many scattering centres. The angle distribution of the observed scattered light depends on destructive interference of the light scattered at all these scattering centres. Light scattered at the scattering centres  $S_1$  and  $S_2$ , for

example, can interfere destructively depending on the optical path length  $a + b$ . Please note that the figure represents the view on the  $x$ - $y$  plane. The induced dipoles oscillate parallel to the  $z$ -axis, which is perpendicular to the  $x$ - $y$  plane.

angle distribution of the scattered light is observed. Particles of this size can be interpreted as being composed of many scattering centres. The radiation scattered from these centres gives rise to multiple interference effects (Figure 4.7).

For example, the light scattered with an angle  $\Theta$  at the point  $S_2$  in Figure 4.7 has an optical path length that is  $a + b$  longer than light scattered at  $S_1$  with the same angle. Only if  $a + b$  corresponds exactly to a multiple of the wavelength,  $\lambda$ , will no destructive interference be present. Therefore, for most  $\Theta$  destructive interferences reduce the detected intensity of the scattered light. The only direction for which no interference is observable independent of the particles size is in the same direction as the incident beam itself,  $\Theta = 0$ . Unfortunately, measurements at this angle are not feasible since the weak scattered light cannot be detected within the vastly more intense incident beam. Figure 4.8 visualizes how for larger scattering angles,  $\Theta$ , the scattered intensity decreases in comparison to Figure 4.6 due to the destructive interference.

The observed angle dependence of the intensity of light scattered at large particles is determined by the size and shape of the scatterer. The size and shape of the scatterer is usually described by a quantity called the radius of gyration:

$$R_G = \sqrt{\frac{\sum m_i r_i^2}{\sum m_i}} \quad (4.18)$$

Here,  $m_i$  is the mass of a point mass  $i$  and  $r_i$  is its distance from the particle's centre of mass. The summation described by (4.18) runs over all point masses  $i$  of the particle. The angle dependence of light scattering from larger particles with a known radius of gyration can be calculated by (4.19):

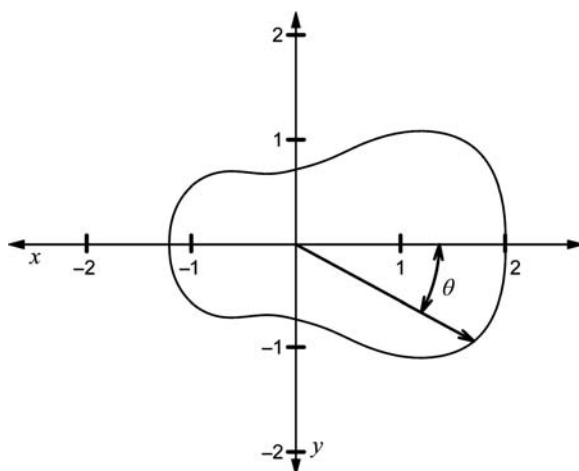


**Figure 4.8** Example of the angle dependence of the light intensity scattered at larger particles using unpolarized light.

$$\lim_{\Theta \rightarrow 0} \frac{K \cdot c}{R_\Theta} = \left( \frac{1}{M} + 2A_2 c \dots \right) \left( 1 + \frac{q^2 R_G^2}{3} \right) \quad (4.19)$$

Here, all variables, besides  $q$ , have the same definition as for (4.16). The parameter  $q$  is dependent on the angle  $\Theta$ , and the wavelength of the incident radiation,  $\lambda$ :

$$q = \frac{4\pi}{\lambda} \sin\left(\frac{\Theta}{2}\right) \quad (4.20)$$

By measuring the angular dependence of the scattering light intensity of solutions of several different concentrations, the average molecular weight can be determined with the help of so-called Zimm plots (Figure 4.9). This is done by measuring  $R_\Theta$  for different concentrations of the scatterer and different observation angles,  $\Theta$ . Each measured  $R_\Theta$  represents a point at  $q^2 + Kc$  versus  $Kc/R_\Theta$  in the Zimm plot. The concentration-dependent data points for each angle  $\Theta$  and thus  $q$  values [(4.20)] are then extrapolated to infinite dilution ( $c=0$ ) and connected by a line corresponding to  $c=0$ . Similarly, the angle-dependent data points are extrapolated for each concentration to a zero observation angle ( $q=0$ ) and connected by a line corresponding to  $\Theta=0$  and, that means  $q=0$ . Both lines are then connected and yield an intercept point with the  $Kc/R_\Theta$ -axis that is the reciprocal value of the average molecular weight [(4.19) for  $c=0$  and  $q=0$ ]. Additional information can be derived from the slopes of the extrapolated dependences for  $c=0$  and  $q=0$ . The slope observed for  $c=0$  is proportional to the radius of gyration. If higher virial coefficients can be neglected then the slope observed for  $q=0$  is proportional to the virial coefficient,  $A_2$ .

In summary, the measurement of light scattering of biomolecules that are larger than or on the order of the size of the radiation wavelength not only

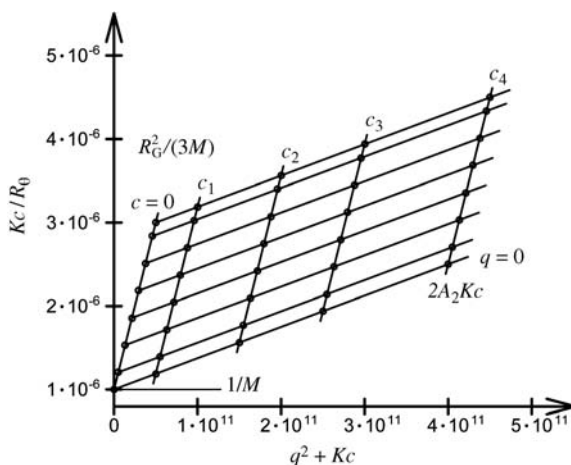


**Figure 4.9** Zimm plots help to determine the molecular weight and shape of larger particles from scattered-light intensities by extrapolation of the observed scattering parameters to zero concentrations and zero observation angles.

allows us to determine the corresponding molecular mass but also provides information about the shape of the biomolecules. For spheres, for example, the radius of gyration is  $R_G = r_{\text{Sphere}} \sqrt{\frac{3}{5}}$ , with  $r_{\text{Sphere}}$  being the radius of the spheres. For long rods,  $R_G = l_{\text{Rod}} \sqrt{12}$  with  $l_{\text{Rod}}$  being the length of the rod.

#### 4.2.3

##### Dynamic Light Scattering

With very small excitation volumes it is possible to monitor fluctuations in the observed light scattering intensity caused by the diffusion of particles into and out of the observation volume. This technique is called dynamic light scattering. From such measurements, diffusion coefficients, molecular masses, aggregations and also the shape of biomolecules can be derived. The theoretical framework for the analysis of such measurements is in principle identical to that for the analysis of fluorescence fluctuations observed from fluorescently labelled biomolecules diffusing into and out of a focal detection volume. Since the latter provides many additional parameters useful for biomolecular analysis we will discuss the details of this theoretical framework in the corresponding Section 9.3 on fluorescence correlation spectroscopy (Chapter 9).

#### 4.3

##### Vibrational Spectra of Biomolecules

The energies corresponding to vibrational eigenmodes of molecules are characteristic of their molecular structure. However, due to the large number of vibrational modes in biomolecules it is sometimes hard to elucidate very detailed information about them based on the measurement of vibrational spectra.

Nevertheless, valuable information, for example, on secondary structure elements, may often be derived.

The two most important techniques for measuring vibrational modes are absorption spectroscopy using photons in the infrared (IR) spectral range and Raman scattering (Figure 4.10). IR absorption is based on the same principles as absorption spectroscopy using light in the UV and visible spectral ranges but usually needs more sophisticated measurement equipment because the corresponding extinction coefficients are typically quite small. A major disadvantage of IR absorption spectroscopy for the investigation of biomolecules is the high absorption of IR radiation by water in the spectral region of interest. Unfortunately, water is in most cases needed for a physiological environment of the biomolecules. Using  $D_2O$  instead of  $H_2O$  is one way to solve this problem. However, this disadvantage can often be circumvented by using Raman spectroscopy instead of IR absorption spectrometry for the determination of vibrational modes in biomolecules. Raman spectroscopy is based on inelastic scattering of photons at the biomolecules and shares some characteristics with the elastic scattering of photons discussed in previous sections. In contrast to elastic scattering, however, with inelastic Raman scattering the photons additionally change their frequency  $\nu$ . In Raman scattering this frequency change is caused by a loss or gain in the photon energy corresponding to transitions between vibrational levels of the molecules at which the scattering occurred (Figure 4.10b).

Raman scattering is an important example of nonlinear optical processes. In Chapter 10 we will present more nonlinear optical effects that are important for the investigation of biomolecules and will also examine the physical basis for such processes in more detail. Here, we only briefly discuss what determines the effective probability for inelastic scattering of photons. The transition moment for Raman scattering is defined by:

$$\vec{M}_{I \rightarrow F}^{\text{Raman}} = \int \Psi_F^*(\vec{r}) \alpha \Psi_I(\vec{r}) dV \quad (4.21)$$

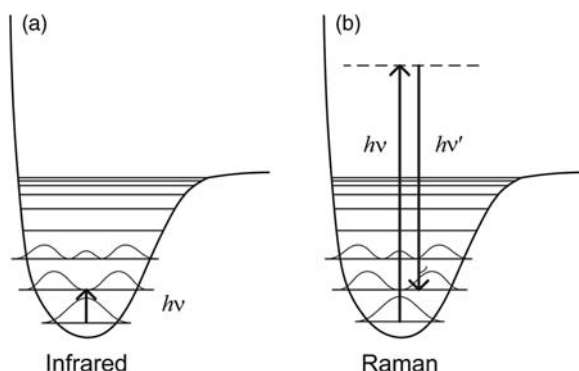


**Figure 4.10** (a) Infrared absorption spectroscopy and the measurement of (b) Raman scattering are the two most important methods used to measure vibrational spectra of molecules or biomolecules.

**Table 4.1** Typical energies of vibrational transitions of the protein amide backbone.

Band name	Wave number (cm <sup>-1</sup> )	Vibrations in the Amide Backbone
Amide A	3250–3300	N–H stretch vibrations in resonance with amide II overtones
Amide I	1630–1700	C=O stretch vibrations
Amide II	1480–1575	N–H bend/C–N stretch vibrations
Amide III	1230–1330	N–H bend/C–N stretch vibrations
Amide IV	625–770	Dominated by O=C–N deformation vibrations

with  $\psi_I$  and  $\psi_F$  being the initial and final states of the molecule, respectively;  $\alpha$  again represents the polarizability of the molecule [compare with (4.11)]. The transition moment for Raman scattering looks similar to the transition moment for absorption and fluorescence (1.4) with the important difference that now the transition probability is related to the polarizability of the molecule. The polarizability determines the ability of light to distort the electron clouds. The polarizability itself changes when the distances in the nuclear geometry of the molecule change. An important consequence of this is that the probability for inelastic Raman scattering is larger the more the polarizability differs between the initial and final vibrational states.

Table 4.1 shows the most important spectral regions of protein vibrations. In vibrational spectroscopy it is more common to display the spectra as a function of the wave number,  $\bar{\nu}$  [see (1.1)]. Very important regions are, for example, the amide band I ( $\bar{\nu} = 1630 – 1700\text{ cm}^{-1}$ ) and amide band II ( $\bar{\nu} = 1480 – 1575\text{ cm}^{-1}$ ). They are sensitive indicators of the amount of secondary structural elements and can be used to estimate the amount of  $\alpha$ -helix conformation and in  $\beta$ -sheet conformation. Figure 4.11 shows vibrational spectra of two model molecules, which consist almost exclusively of  $\alpha$ -helix and  $\beta$ -sheet conformations, respectively. C=O stretch vibrations with wave numbers in the region  $\bar{\nu} = 1640 – 1660\text{ cm}^{-1}$  usually indicate an  $\alpha$ -helix conformation, whereas the corresponding wave numbers in the region  $\bar{\nu} = 1630 – 1640\text{ cm}^{-1}$  usually indicate a  $\beta$ -sheet conformation. The presence of both result in a superposition in the vibrational spectra that can be used to some degree to determine the relative contributions from different secondary structure elements. Table 4.2 gives further wave number regions, indicating typical secondary structure elements.

**Table 4.2** Typical amide I band absorption wave numbers indicating different secondary structure elements of peptides or proteins.

Secondary Structure Element	Typical Absorption Wave number in Amide I Band (cm <sup>-1</sup> )
$\beta$ -Sheet	1630–1640, weaker band at $\sim 1680$
$\alpha$ -Helix	1640–1660
Random coil	1640–1650
$\beta$ -Turn	1670–1690

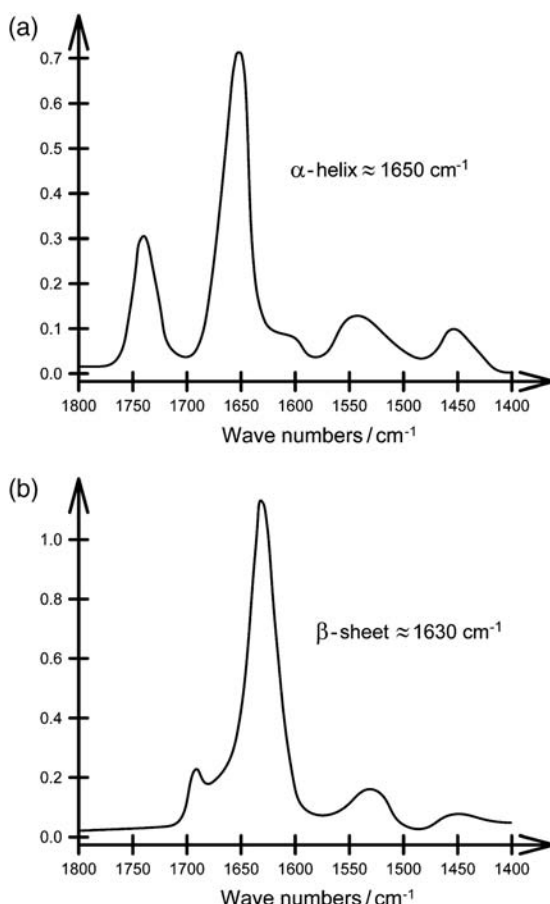


**Figure 4.11** Vibrational spectra of a polyglutamic acid model molecule (a) and a polyleucine/lysine model molecule (b). The poly-glutamic acid model molecule consists

almost exclusively of  $\alpha$ -helices, whereas the polyleucine/lysine model molecule consists almost exclusively of  $\beta$ -sheets.

### Problems

- 4.1** You measure the CD spectra of four proteins of unknown structure. For protein A you observe very large positive ellipticities at  $\sim 195 \text{ nm}$ , and negative ellipticities at  $\sim 225$  and  $\sim 230 \text{ nm}$ . For protein B you observe positive ellipticities at  $\sim 195 \text{ nm}$ , negative ellipticities at  $\sim 225 \text{ nm}$  and almost zero ellipticities at  $\sim 230 \text{ nm}$ . For protein C you observe positive ellipticities at  $\sim 195 \text{ nm}$ , almost zero ellipticities at  $\sim 225 \text{ nm}$  and positive ellipticities at  $\sim 230 \text{ nm}$ . For protein D you observe negative ellipticities at  $\sim 195 \text{ nm}$  and

almost zero ellipticities at  $\sim 225$  and  $\sim 230$  nm. Discuss qualitatively to what extent different secondary structural elements contribute to the overall structures of these proteins.

- 4.2 The optical rotation of a  $10^{-4}$  M solution of a protein in a  $l = 1$  cm cell was determined to be  $0.01^\circ$  at 300 nm. What is the difference in the speed of light for left- and right-handed circular-polarized light in that sample?
- 4.3 In a light-scattering experiment you observed a scattered-light intensity from the biomolecules (intensity corrected by solvent light scattering) perpendicular to the incident light ( $\theta = 90^\circ$ ) that is about half as large as the light intensity backscattered ( $\theta \sim 180^\circ$ ). What are the dimensions of the biomolecule in comparison to the wavelength of the incident light?
- 4.4 Water solutions of two biomolecules having masses of 100 and 50 kDa are measured in two separate light-scattering experiments. The concentration (not mass concentration) is equal in all experiments. Which type of elastic scattering does this situation correspond to? Calculate the quotient of the Rayleigh ratio  $R_\theta^{100 \text{ kDa}}$  to  $R_\theta^{50 \text{ kDa}}$  (corrected by solvent light scattering) for both samples for a scattering angle  $\theta = 0^\circ$ .
- 4.5 Explain why for objects larger than the dimensions of the scattering-light wavelength the only direction in which no destructive interference of the scattered light occurs is in the same direction as the incident light ( $\theta = 0^\circ$ ).
- 4.6 For a biological object having maximum dimensions on the order of 100 nm a Zimm plot is generated. From the slope of the line corresponding to  $c = 0$  a radius of gyration of  $\sim 350$  nm was determined. Is the object spherical or rod-like?
- 4.7 Discuss qualitatively what Raman spectra you expect in the amide I spectral region for proteins A–D of question 4.1.

## Bibliography

### General

- Berne, B.J. and Pecora, R. (2000) *Dynamic Light Scattering: With Applications to Chemistry, Biology, and Physics*, Dover Publications Inc.
- Cantor, C.R. and Schimmel, P.R. (1980) *Biophysical Chemistry: Part II: Techniques for the Study of Biological Structure and Function*, W.H. Freeman & Co.
- Colthup, N., Daly, L. et al. (1990) *Introduction to Infrared and Raman Spectroscopy*, Academic Press Inc., San Diego.

- Fasman, G.D. (ed.) (1996) *Circular Dichroism and the Conformational Analysis of Biomolecules*, Plenum Press, New York.
- Greenfield, N.J. (2006) Using circular dichroism spectra to estimate protein secondary structure. *Nature Protocols*, **1** (6), 2876–2890.
- Hecht, E. and Zajac, A. (2003) *Optics*, Addison-Wesley Longman, Amsterdam.
- Hollas, J.M. (1996) *Modern Spectroscopy*, John Wiley & Sons, Inc., New York.
- Long, D.A. (2002) *The Raman Effect: A Unified Treatment of the Theory of Raman*

- Scattering by Molecules*, John Wiley & Sons, Inc.
- Marshall, A.G. (1979) *Biophysical Chemistry: Principles, Techniques and Applications*, John Wiley & Sons, Inc.
- McHale, J.L. (1998) *Molecular Spectroscopy*, Prentice Hall, New Jersey.
- Pecora, R. (ed.) (2003) *Dynamic Light Scattering, Applications of Photon Correlation Spectroscopy*, Kluwer Academic Publisher.
- Rodger, A. and Nordén, B. (1997) *Circular Dichroism and Linear Dichroism*, Oxford University Press.
- Tanford, C. (1961) *Physical Chemistry of Macromolecules*, John Wiley & Sons, Inc.
- van Holde, K.E., Johnson, C. et al. (2005) *Principles of Physical Biochemistry*, Prentice-Hall.
- Winter, R. and Noll, F. (1998) *Methoden der Biophysikalischen Chemie*, Teubner Verlag.

### Specific

#### Infrared and Raman Spectroscopy of Proteins

- Ganim, Z., Chung, H.S. et al. (2008) Amide I two-dimensional infrared spectroscopy of proteins. *Accounts of Chemical Research*, **41** (3), 432–441.
- Humecki, H.J. (1995) *Practical Guide to Infrared Microspectroscopy*, Dekker, New York.
- Turrell, G. and Corset, J. (eds.) (1996) *Raman Microscopy: Developments and Applications*, Academic Press, San Diego.

## 5

# Magnetic Resonance Techniques

### 5.1

#### Nuclear Magnetic Resonance of Biomolecules

The increasing sensitivity of nuclear magnetic resonance (NMR) spectrometers together with the development of new and sophisticated detection schemes in recent years have made NMR spectroscopy a very powerful tool for the investigation of structural, mechanistic and dynamical properties of biomolecules under physiological conditions. Since an understanding of the physical principles of these techniques is demanding and often nonintuitive we will focus first, in the next section, on a thorough discussion of the basic principles of the elaborated techniques that are necessary for the investigation of biomolecules. Again, the intention is to provide a comprehensible but still concise and brief insight also for readers without a background in physics or chemistry. The latter sections of this chapter discuss biomolecular structural analysis as well as the advantages and limitations of NMR spectroscopy for the investigation of biomolecules.

##### 5.1.1

#### Principles

In Chapter 1 we learnt that each electron has an intrinsic angular momentum, called spin. Charged particles with a spin have a magnetic dipole moment and therefore tend to assume an energetically favourable orientation within an external magnetic field. As the spin is a quantum mechanical property of elementary particles, such as electrons or atomic nuclei, only distinct (quantized) orientations of the spin are observable in an external magnetic field. This is visualized in Figure 5.1. In the case of protons, the nuclei of hydrogen atoms, for example, only two orientations correspond to such steady states. In one orientation the magnetic moment is orientated with the external magnetic field and is called  $\alpha$ -spin. In the other orientation the magnetic moment is orientated against the external magnetic field and is called  $\beta$ -spin. The energy difference between these

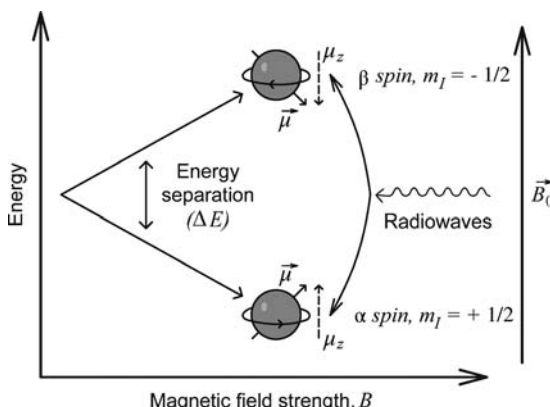


**Figure 5.1** The spin of a proton can be observed in two orientations with respect to an external magnetic field. An  $\alpha$ -spin corresponds to an orientation of the magnetic moment with the external field whereas a  $\beta$ -spin corresponds to an orientation of the magnetic moment against the external field. The energy difference between both spin states increases linearly with an increasing

magnetic field strength,  $B$ . The magnetic moments in both states are not orientated exactly parallel with the external field but are slightly tilted. Owing to this tilt, the magnetic moment rotates around the  $B$ -field axis with the Larmor frequency. Transitions between the two spins can be induced by electromagnetic radiation in the spectral region of radio-waves (compare with Figure 1.2).

two states scales linearly with the magnetic field strength,  $B$ . NMR spectroscopy is based on the measurement of the energy difference between these two states by absorption or emission of electromagnetic radiation on the radiowave scale (compare also with Figure 1.2). This energy difference is very sharply defined but depends very sensitively on the electronic environment around the nucleus. This is because the electron orbitals have a shielding effect on the external magnetic field (see, for example, the different electron orbitals visualized in Figures 1.3–1.6). The nuclei sense a reduced or even increased magnetic field that depends specifically on the electronic bond structure and bond angles between the nuclei. In addition, the magnetic moment of neighbouring nuclei influences the actual magnetic field at the nucleus of interest. As a consequence, NMR spectroscopy is one of the most sensitive techniques for the determination of molecular structures at room temperature and in liquid environments. For small unknown chemical compounds NMR spectroscopy allows a quick and full determination of the molecular structure. Because of the large number of nuclei in proteins, peptides or DNA, NMR spectroscopy of biomolecules requires a very good resolution of individual transitions energies, which can be achieved by using very high magnetic field strengths. In addition, advanced detection techniques are necessary when measuring biomolecules, which allow us to distinguish overlapping signals. With the help of computers and elaborate algorithms detailed structural, mechanistic and dynamical properties of biomolecules can then be derived from the large set of NMR data obtained with these techniques.

## 5.1.2

## Theoretical Framework

For nuclei consisting of more than one elementary particle, it depends on the number of protons and neutrons as to whether their individual angular momenta either cancel each other out or a net angular momentum, and thus a net spin, remains. Quantum mechanically the spin of a nucleus is described by the spin quantum number  $I$ . If  $I=0$ , then a nucleus has no net magnetic dipole moment and cannot be detected by NMR. The most abundant isotopes of carbon,  $^{12}\text{C}$ , or oxygen,  $^{16}\text{O}$ , are important examples that have a spin quantum number  $I=0$ . Other nuclei have spin quantum numbers like  $I=\frac{1}{2}, 1, 1.5, 2$  and so on. Only multiples of  $\frac{1}{2}$  are possible, corresponding to the magnetic moment of a single elementary particle such as protons or electrons. The magnitude of the magnetic moment,  $\vec{\mu}$ , of a nucleus is linked to the spin quantum number by the following equations:

$$\vec{\mu} = \gamma \cdot \vec{J} \quad (5.1)$$

$$|\vec{J}| = \sqrt{I(I+1)}\hbar \quad (5.2)$$

Here,  $\vec{J}$  is the spin angular momentum and  $\gamma$  is the magnetogyric ratio, which is characteristic of different nuclei, and  $\hbar$  is Planck's constant divided by  $2\pi$ ,  $\hbar = h/2\pi$ . From (5.2) it is apparent that from the spin quantum number,  $I$ , only the absolute value of the spin angular momentum,  $|\vec{J}|$ , and thus the absolute value for the magnetic moment,  $|\vec{\mu}|$ , can be calculated. However, the magnetic moment can have different orientations relative to the external magnetic field  $B_0$ . This is described by the vector character of  $\vec{\mu}$ . As mentioned earlier, in an external magnetic field  $\vec{\mu}$  can be observed only in a few quantized orientations. The possible, observable orientations are assigned by the secondary spin quantum number,  $m_I$ . For a given spin quantum number,  $I$ , possible secondary spin quantum numbers  $m_I$  run from  $m_I=-I$  to  $m_I=+I$  in steps of one:  $m_I=-I, -I+1, \dots, I-1, I$ . Consequently, in the simple case of protons with  $I=\frac{1}{2}$ , only orientations corresponding to  $m_I=-\frac{1}{2}$  and  $m_I=+\frac{1}{2}$  are possible. These two are the two orientations corresponding to  $\alpha$ -spin and  $\beta$ -spin, respectively (Figure 5.1).

The energy difference between the different orientations depends on the strength of the magnetic field,  $B_0$  and the vector component of the magnetic dipole,  $\vec{\mu}$ , in the direction of the magnetic field,  $\mu_z$  (see also Figure 5.1):

$$E = -\mu_z B_0, \quad \mu_z = m_I \gamma \cdot \hbar \quad (5.3)$$

Because of this energy difference there is a population difference between the different orientations. It is very small even for large magnetic field strengths. The  $\beta$ - to  $\alpha$ -spin population ratio using a 14 T magnetic field is only about 9995:10 000. The corresponding energy difference between  $\alpha$ - and  $\beta$ -spin of protons corresponds to frequencies of electromagnetic radiowave radiation of  $\sim 600$  MHz [(1.1), Figure 1.2].

The magnetic dipole moment,  $\vec{\mu}$ , of an individual nucleus rotates, or to be more exact precesses, around the vector of  $B_0$  with the Larmor frequency:

$$\omega = \frac{\Delta E}{\hbar} = \gamma \cdot B_0 = 2\pi\nu \quad (5.4)$$

Here,  $\Delta E$  is the energy difference between the spin states. The Larmor frequency corresponds exactly to the frequency of photons of that energy difference:  $\Delta E = \hbar\nu = \hbar\omega$  [compare with (1.1)]. The relative phase shifts between the nuclei, or in other words, the relative positions of the magnetic moments  $\vec{\mu}$  with respect to each other, are arbitrary under normal conditions (black vectors in Figure 5.2). However, since there are slightly more magnetic moments orientated with the external field, they sum up to a total magnetization,  $\vec{M}$  (red vector in Figure 5.2), that is orientated exactly parallel with the external field. The macroscopic magnetization is defined by:

$$\vec{M} = \sum_i \vec{\mu}_i \quad (5.5)$$

with  $\vec{\mu}_i$  being the magnetic moments of the individual nuclei  $i$ . As we will see in the next paragraphs it is the most important macroscopic measurable parameter in NMR spectroscopy for the investigation of the structure of biomolecules.

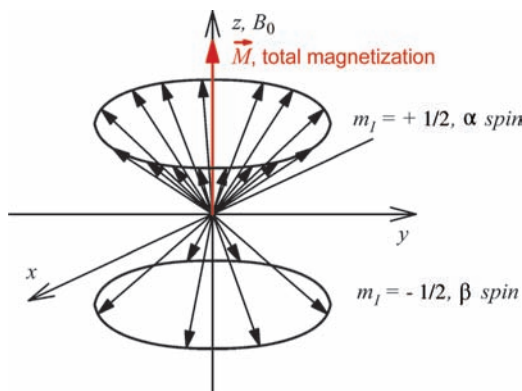


**Figure 5.2** Each black arrow corresponds to the magnetic moment of a single nucleus. For protons, only two orientations are observable, corresponding to  $\alpha$ - or  $\beta$ -spin. The magnetic moments rotate around the external magnetic field with the Larmor frequency. The relative phases of the individual magnetic moments are arbitrary under normal conditions. Since the energy of the  $\alpha$ -spin state is slightly lower a few more nuclei are observed in this state. However, even using very strong magnetic fields the population differences between the

states are very small. The large population difference presented here is only for better visibility. Nevertheless, the magnetic moments of all individual nuclei sum up to a small macroscopic magnetic moment, which is called the total magnetization,  $\vec{M}$  (red vector). It is exactly orientated with the external magnetic field in an unperturbed sample. The direction and behaviour of the total magnetization,  $\vec{M}$ , is the most important measurable parameter for the analysis of biomolecules by NMR.

## 5.1.3

## Primary Information Deduced from NMR Spectra

As mentioned earlier, different nuclei 'feel' slightly different effective strengths of the external magnetic field due to shielding or induced fields in the individual electronic environments. Therefore, they have slightly different absorption frequencies. Because these differences are very small this is usually measured in comparison to a reference compound with known frequency,  $\omega_{\text{reference}}$ , in parts per million:

$$\delta = \frac{\omega_{\text{signal}} - \omega_{\text{reference}}}{\omega_{\text{reference}}} \cdot 10^6 \text{ ppm} \quad (5.6)$$

The chemical shift,  $\delta$ , is a very sensitive parameter for the chemical or biochemical environment of a nucleus. It is, for instance, possible to determine whether a proton belongs to a hydroxy bond, an amide bond or to a certain amino acid. This is illustrated by the simple example of ethanol (Figure 5.3). Protons in the same electronic environment show similar chemical shifts ( $\delta$ ). The absolute value of  $\delta$  is a very good indicator of the presence of single or double bonds or the character of neighbouring atom groups and bonding angles. In addition, so-called scalar coupling between neighbouring nuclei with a spin allows us to determine how many other protons are in the vicinity of a certain proton. Owing to this scalar coupling between neighbouring spins, one nucleus exhibits more than one line in the NMR spectrum. In ethanol, for example, the energies of the protons in the  $\text{CH}_3$  group (c in Figure 5.3) are shifted due to the spin orientations of the protons in the  $\text{CH}_2$  group (b in Figure 5.3). The possible spin orientations of the two protons in the neighbouring  $\text{CH}_2$  group are  $\downarrow\downarrow$ ,  $\downarrow\uparrow$ ,  $\uparrow\downarrow$  and  $\uparrow\uparrow$ . Here, the arrows represent protons in either the  $\alpha$ - or  $\beta$ -spin state:

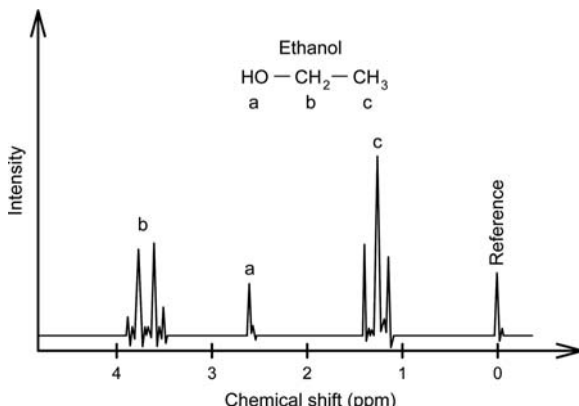


**Figure 5.3** Schematic representation of the NMR spectrum of ethanol. Protons in identical chemical environments have the same chemical shift. The line splitting for the protons in identical chemical environments is due to scalar coupling with neighbouring protons.

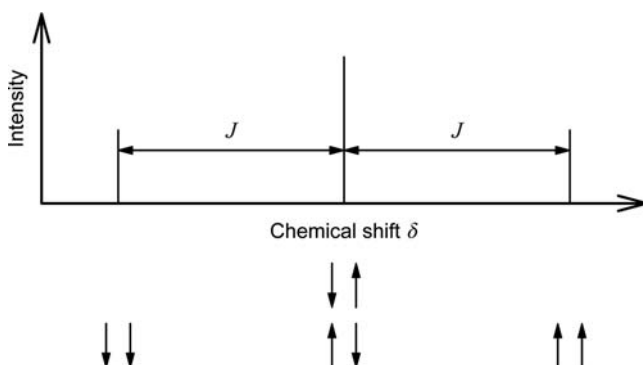


**Figure 5.4** Due to scalar coupling, the transition line for  $\text{CH}_3$  protons in ethanol is split into three lines depending on the spin states of neighbouring  $\text{CH}_2$  protons.

$\downarrow\downarrow$  and  $\uparrow\uparrow$  increase and decrease the effective field of the  $\text{CH}_3$  group protons, respectively;  $\downarrow\uparrow$  and  $\uparrow\downarrow$  are equivalent and have no effect on the effective field of the  $\text{CH}_3$  group protons. This explains the three lines observable in the NMR spectrum, with the middle line being twice as intense as the other two (Figure 5.4). The spectral splitting,  $J$ , is greater the larger the scalar coupling is between the two nuclei. The splitting of the methylene group signals (b in Figure 5.3) can be rationalized in the same way. Hydrogens bound to oxygen or nitrogen usually do not contribute to such line splittings because they are rapidly exchanged between molecules and solvents such as water with the consequence that the effect of their nuclear spin is averaged out.

For peptide bonds of proteins or peptides, the magnitude of the scalar coupling between the proton of the hydrogen at the  $\text{C}^\alpha$ -atom and the proton of the hydrogen bound to nitrogen,  $\text{H}^N$ , depends very strongly on the torsion angle at the  $\text{C}^\alpha$ -nitrogen axis of the peptide backbone (Figure 5.5). The dependence of the coupling constant,  $J$ , on the torsion angle  $\Phi$  can be described by the semi-empirical Karplus relation:

$$J(\Phi) = A \cos^2(\Phi - 60) - B \cos(\Phi - 60) + C \quad (5.7)$$

with  $A$ ,  $B$  and  $C$  being empirical constants. Determination of the peptide bond torsions angles,  $\Phi$ , from  $J$  provides very valuable information about dominant secondary structure elements in that region of a protein.

#### 5.1.4

##### Pulsed NMR Spectroscopy

The standard measurement technique to determine  $\delta$  and  $J$  is nowadays not the measurement of a direct absorption of the radiofrequencies. Since the populations difference between the spin states is so small and because the absorption for each transition energy would have to be measured separately this approach would take far too long.

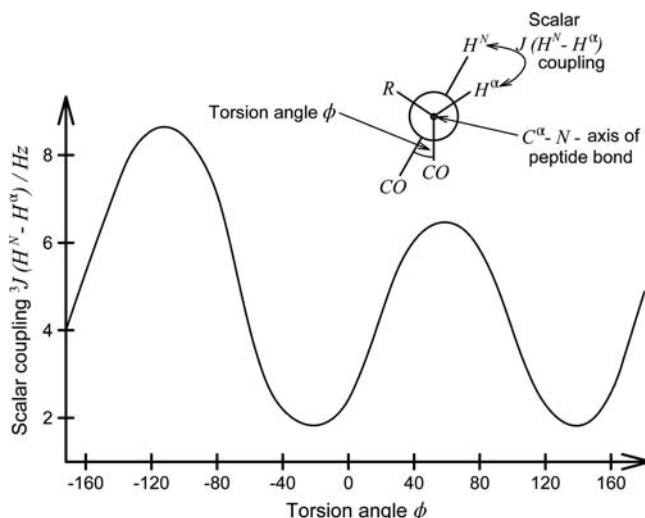


**Figure 5.5** The scalar coupling between the  $C^\alpha$ -hydrogen and hydrogen bound to the nitrogen of the peptide bond,  $H^N$ , depends strongly on the torsion angle of the  $C^\alpha$ -nitrogen axis of the peptide backbone. The scalar

couplings between these protons thus provide initial information about possible secondary structure elements and the conformation of the corresponding peptide bond.

Modern NMR spectrometers are based on an excitation of the sample with radiowave pulses. As mentioned in Chapter 1, electromagnetic radiation such as radiowaves consists of an oscillating magnetic and an orthogonal electric field (Figure 1.1). For NMR spectroscopy, we only have to consider the interaction of the oscillating magnetic field with the magnetic moments.

The oscillating magnetic field of the radiowaves can interact with the macroscopic magnetization in a similar way as static magnetic fields can interact with a static magnetic moment. Usually, to better visualize this interaction a transformed coordinate system is used for the presentation of the magnetic dipole moment and macroscopic magnetization vectors. This transformed coordinate system corresponds to a system rotating around the  $z(B_0)$ -axis with the radio-wave frequency and is called the 'rotating frame'. In this context, the 'normal' coordinate system, which is not rotating around the  $z$ -axis, is called the 'laboratory frame'. In the rotating frame a magnetic dipole moment of an individual nucleus that has a Larmor frequency identical to the radiowave frequency is represented by a static vector. If the Larmor frequency of an individual nucleus is higher or lower than the radiowave frequency it is represented by vectors that rotate around the  $z$ -axis, depending on the difference in the frequencies.

In this rotating frame a radiowave pulse leads to a rotation of the macroscopic magnetization. This is visualized in Figure 5.6a. A consequence of the identical rotating frame and radiowave frequencies is that one magnetic component of the radiowave corresponds to a static magnetic field in this coordinate system. When this static magnetization component of the incident radiowave is

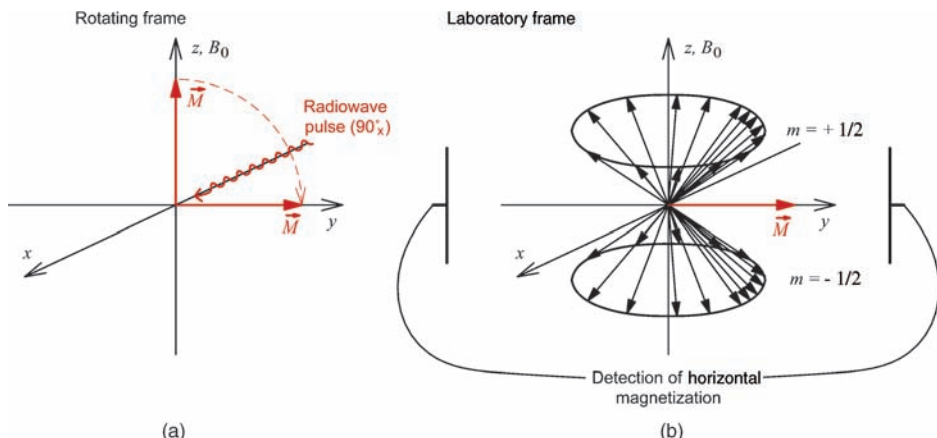


**Figure 5.6** (a) A radiowave pulse of correct energy, duration and orientation rotates the macroscopic magnetizations of a sample by  $90^\circ$  in the rotating frame; (b) by looking at the magnetic moments of individual nuclei this corresponds to spin flips that result in an equal population between both spin states but to a preferred orientation within the  $y$ -axis direction. In other words, the magnetic moments of several nuclei now rotate in phase with the Larmor frequency. This results

in a macroscopic magnetization of the sample in the  $x$ - $y$  plane. In the laboratory frame, the magnetization rotates around the  $z$ -axis with the Larmor frequency. The oscillation behaviour of this horizontal magnetization can be detected electronically. Since the Larmor frequency depends directly on the energy difference between the spin states (Eq. (5.4)), analysis of the oscillation allows direct determination of the corresponding transition energies (see Figure 5.7).

appropriately orientated with respect to the  $x$ -axis of the rotating frame, it rotates the macroscopic magnetization around the  $x$ -axis. When the duration of the radiowave is exactly adjusted it can rotate the macroscopic magnetization exactly by  $90^\circ$ . This is called a  $90_x^\circ$  pulse.

As a consequence, the population difference between the spin states is then zero but the macroscopic magnetization rotates with the Larmor frequency around  $z(B_0)$  in the laboratory frame as long as all nuclei are identical and feel the same  $B_0$  (Figure 5.6b). This oscillation of the macroscopic magnetization can be detected electronically (on the left in Figure 5.7). Obviously, the measured oscillation of the magnetization perpendicular to the external field corresponds directly to the Larmor frequency. The Larmor frequency, in turn, is directly proportional to the energy difference between the spin states (5.4). Consequently, the frequency found in this horizontal magnetization can be directly related to the transition energies. The normal mathematical procedure to determine frequencies of oscillating data is a Fourier transformation. If several oscillations with different frequencies are superimposed in the experimental data the Fourier transformation results in several peaks, corresponding to the frequencies for each oscillation superimposed in the experimental data. The great advantage of determining transition energies of spin states after application of a  $90_x^\circ$  pulse is

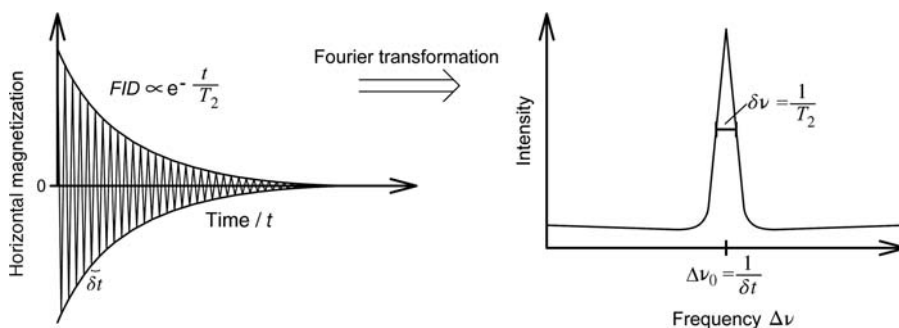


**Figure 5.7** The perpendicular (or horizontal) magnetization observed after pulsed radio-wave excitation oscillates with the Larmor frequency corresponding to the energies of the spin states. A Fourier transformation allows determination of the corresponding

radiowave transition frequency. If several different nuclei with different spin-state energies contribute to the observed horizontal magnetization the Fourier transformation yields several different frequency peaks, corresponding to each type of nucleus.

that the entire spectrum of transitions corresponding to a broad range of radio-wave energies can be determined simultaneously by the Fourier analysis. This saves an enormous amount of measuring time – a prerequisite to the analysis of the large number of nuclear spin transition energies simultaneously present in biomolecules.

If there were no relaxation back to the equilibrium (in which  $\vec{M}$  is orientated parallel with  $B_0$ , Figure 5.2) one would observe a superposition of oscillations with different Larmor frequencies, which would never stop. However, there are several mechanisms by which the nuclei relax back to the original equilibrium situation after a certain time. Two relaxation processes can be distinguished, which have two different relaxation time constants,  $T_1$  and  $T_2$ .  $T_1$  corresponds to the time the system needs to ‘relax’ to the equilibrium population between the different spin states (time scale about 1–10 s). This relaxation process is called longitudinal relaxation and is due to interactions of energy loss and uptake with the environment of the nuclei.  $T_2$  corresponds to the time in which the system loses the phase coherence between individual magnetic dipole moments rotating around  $z$ . As long as they rotate with the same frequency and phase they cause a macroscopic magnetization in the  $x,y$  direction. However, due to interactions between the individual spins, the phases are shifted and the spins are ‘dephasing’. This is called spin–spin relaxation (time scale 10  $\mu$ s up to seconds). Particularly, the  $T_2$  relaxation leads to a time-dependent decrease of the amplitude of the superposition of the different Larmor oscillations (Figure 5.7). This is called free induction decay (FID). Nevertheless, individual frequencies can still be deduced by a Fourier transformation of these decaying oscillations. The main effect of the decay in the oscillations is that the peaks, as determined by the Fourier transformation, become broader. The faster the decay  $T_2$  becomes the more uncertain is the determination of the corresponding frequencies, which results in increasing line broadening with decreasing times  $T_2$ .

## 5.1.5

**Two-Dimensional NMR Spectroscopy**

An NMR spectrum of a biomolecule contains an enormous number of signals. This makes it impossible to assign all signals observed in a linear NMR spectrum of typical biomolecules, such as shown in Figure 5.8.

This is why biomolecules are usually investigated using different two-dimensional (2D) or higher multi-dimensional NMR techniques, where many different kinds of correlations between single peaks are detected. These correlations help to unravel which of the multitude of peaks in the spectra, such as represented in Figure 5.8, are connected by distinct properties such as, for example, simply close proximity of the corresponding protons. In a 2D plot such correlations are represented by well-resolved, individual cross peaks. 2D NMR spectra are based on time-dependent sequences of radiowave pulses such as  $90^\circ_x$  pulses. The type and the sequence of the pulses determine which kind of relation between different nuclei is monitored. In the following sections we discuss the physical principles of two 2D NMR techniques that are especially important for the structural analysis of biomolecules.

## 5.1.6

**Correlated Spectroscopy (COSY)**

Let us begin step by step with the simplest 2D technique, the so-called COSY (correlated spectroscopy) pulse sequence. COSY spectra monitor directly neighbouring protons, and are based on the scalar coupling interaction between their spins.

In a COSY experiment two  $90^\circ_x$  pulses are applied to the sample. The first  $90^\circ_x$  pulse creates, as usual, a horizontal magnetization. After a variable time  $t_1$  the second  $90^\circ_x$  pulse is then applied and the FID is analysed using a Fourier transformation (Figure 5.9).

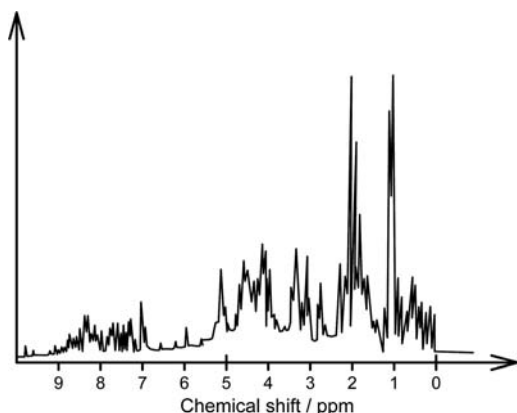


**Figure 5.8** Schematic of a NMR spectrum of a protein.

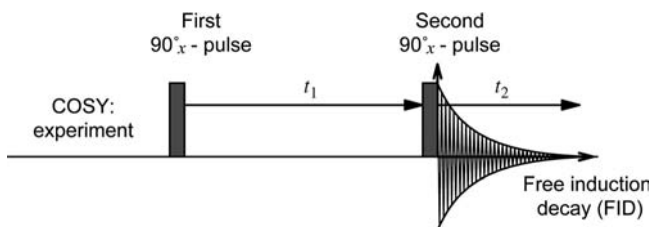


**Figure 5.9** In a COSY experiment, two  $90^\circ$  pulses are applied one after the other with a varying time delay,  $t_1$ . Analysis of the FID as a function of  $t_1$  allows identification of directly neighbouring protons that interact with each other by scalar coupling.

Let us first assume that we observe only one type of nuclei, all with the same spin energy difference and, therefore, the same Larmor frequency (Figure 5.10). How much of the horizontal magnetization remains after a COSY pulse sequence depends on the exact timing  $t_1$  of the second pulse. In the moment of the second  $90^\circ_x$  pulse the vector for the macroscopic magnetization is rotated out of the  $x$ - $y$  plane into the  $x$ - $z$  plane, maintaining the angle with the  $x$ -axis. When the vector was exactly parallel to the  $y$ -axis before the second  $90^\circ_x$  pulse arrived all of the horizontal magnetization is rotated back on the  $z$ -axis (Figure 5.10a). As a result, no horizontal magnetization remains and consequently no FID signal can be detected. When the vector was exactly parallel to the  $x$ -axis before the second  $90^\circ_x$  pulse arrived, none of the horizontal magnetization is rotated back on the  $z$ -axis (Figure 5.10c) – the entire horizontal magnetization remains and consequently a maximum FID signal can be detected. If the macroscopic magnetization was in between these two extreme positions when the second  $90^\circ_x$  pulse is applied then only a part is rotated back on the  $z$ -axis and, therefore, a fraction of the horizontal magnetization remains (Figure 5.10b). The remaining horizontal magnetization corresponds to the projection of the resulting vector for the macroscopic magnetization onto the  $x$ -axis.

From these considerations we see that it indeed depends on the exact timing between the two pulses as to how much horizontal magnetization remains and how large the amplitude and sign of the  $\text{FID}(t_2)$  measured after the second  $90^\circ_x$ -pulse is (Figure 5.11a). Performing a Fourier transformation of the  $\text{FID}(t_2)$  for each  $t_1$  results in a series of one-dimensional (1D) NMR spectra ( $\omega_2$ ). They look the same as if we have measured the FID directly after the first  $90^\circ_x$  pulse, but the overall intensities and the signs are now a function of  $t_1$  (Figure 5.11b). The frequency of the ‘downs and ups’ of these spectra on the  $t_1$ -time scale corresponds exactly to the Larmor frequency of the nucleus since the origin of this oscillation was the momentary position of the magnetization in the moment of the second  $90^\circ_x$  pulse. It is thus possible to also perform a Fourier transformation for this  $t_1$ -dependent oscillation for fixed  $\omega_2$  values (red line in Figure 5.11b). The result is again a 1D NMR spectrum ( $\omega_1$ ) that looks the same as if we had measured the FID directly after the first  $90^\circ_x$  pulse. By doing this for all frequencies  $\omega_2$  we can construct a 2D contour plot (Figure 5.11c), which has a single peak at a position corresponding to the same chemical shift for both axes.

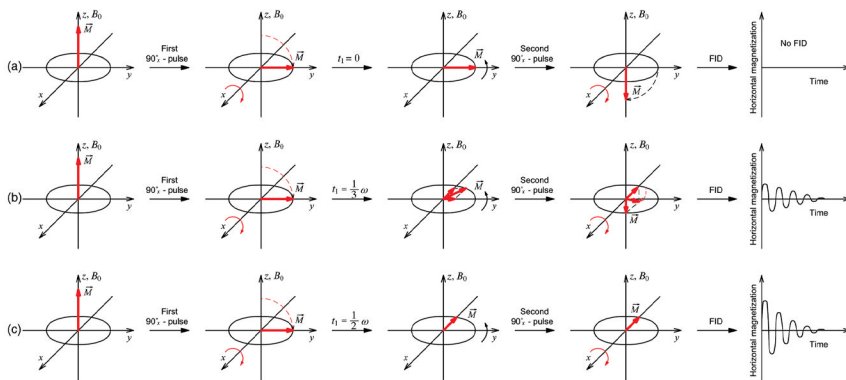


**Figure 5.10** Behaviour of the macroscopic magnetization of a proton A in a COSY experiment. Depending on the position of the macroscopic magnetization at the time  $t_1$  of the second  $90^\circ$  pulse either none, all or just a fraction of the macroscopic magnetization is rotated out of the  $x$ - $y$  plane. As a

consequence, it depends on the time  $t_1$  as to whether no horizontal magnetization can still be detected after the second  $90^\circ$  pulse (a) or only a fraction (b) or even the complete original horizontal magnetization (c).

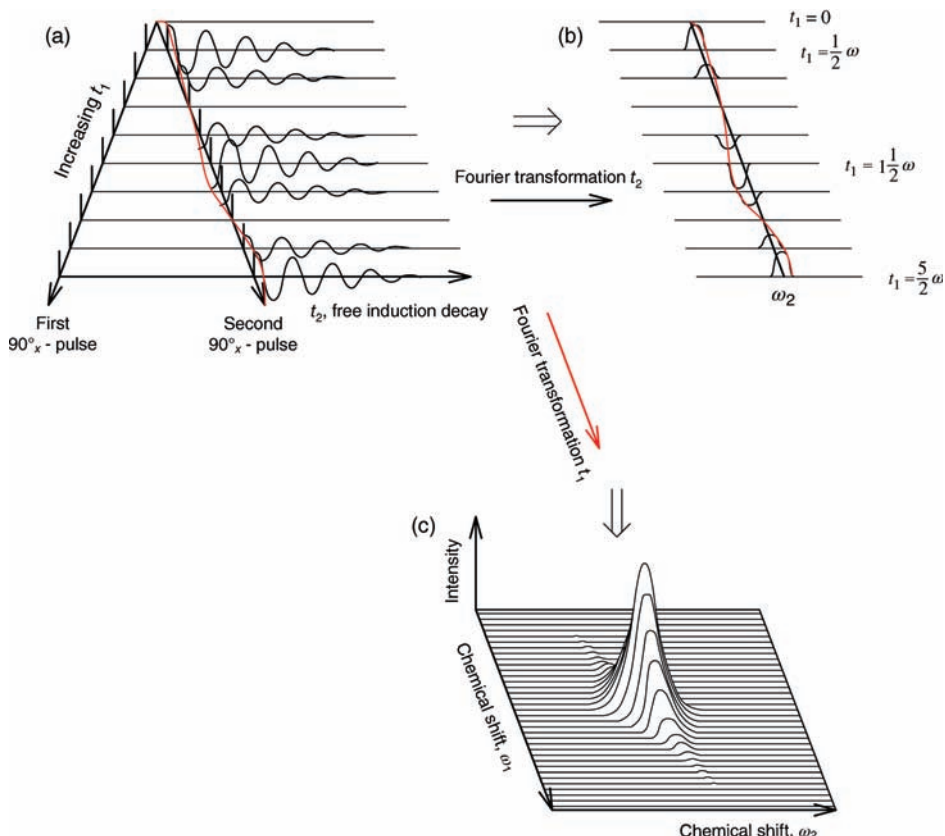


**Figure 5.11** (a) Since the position of the macroscopic magnetization before the second pulse depends on the Larmor frequency (Figure 5.10) the absolute amplitude of the FID observed after the  $90^\circ_x$ -pulse as function of  $t_1$  is itself oscillating with the Larmor frequency; (b) Fourier transformations of all FID result in spectra in

the same way as the amplitude of the FID signals; (c) a second series of Fourier transformations of these  $t_1$ -dependent peaks for each frequency  $\omega_2$  again results in peaks corresponding to the Larmor frequency. Plotting these  $\omega_2$ -dependent Fourier transformations in a 2D plot results in a 2D peak with identical frequencies  $\omega_1$  and  $\omega_2$ . See text for details.

When we have two different types of nuclei (A and B) in a sample with no interaction at all and repeat the same procedure we simply obtain the superposition of the two corresponding 2D spectra having two peaks at positions  $(\omega_1 = \omega_A, \omega_2 = \omega_A)$  and  $(\omega_1 = \omega_B, \omega_2 = \omega_B)$  (see peaks A and B at the diagonals in Figure 5.12).

But what happens when the two nuclei are close enough that a spin–spin interaction can occur between them during the time  $t_1$ ? Then, the precessing of the macroscopic magnetization vector for nucleus A is modulated by that of nucleus B during this so-called evolution period (the time between the two  $90^\circ_x$  pulses). In COSY this magnetization transfer is caused by spin–spin scalar coupling between the nuclei of type A and B. As a result the oscillating amplitudes

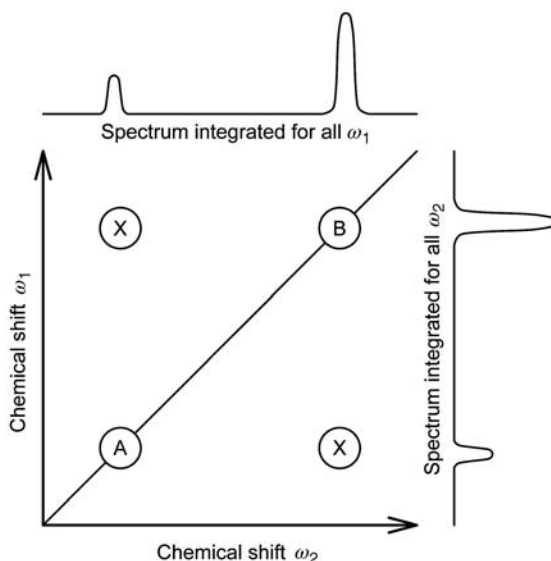


**Figure 5.12** Principle of 2D NMR spectroscopy. The linear 1D NMR spectrum can be found on the diagonal corresponding to  $\omega_1 = \omega_2$  of the 2D contour plot. If two peaks correspond to protons connected by a distinct property this results in cross peaks (X).

of the FIDs and peaks (Figures 5.11a and b) corresponding to the macroscopic magnetization of the A nuclei are additionally slightly modulated by the Larmor frequency of B. The bigger the spin–spin interaction the bigger this additional modulation will be. Fourier transformation of the oscillating A peak ( $\omega_2 = \omega_A$ ) modulated by the frequency of nucleus B will unravel this as additional peak corresponding to the frequency of B at the position ( $\omega_1 = \omega_B$ ,  $\omega_2 = \omega_A$ ) (see off-diagonal peaks X in Figure 5.12). Similarly, the oscillating amplitudes of the FIDs and peaks (Figures 5.11a and b) corresponding to the macroscopic magnetization of the B nuclei are also slightly modulated by the Larmor frequency of A, resulting in another cross peak at ( $\omega_1 = \omega_A$ ,  $\omega_2 = \omega_B$ ). As a consequence, COSY 2D NMR shows cross peaks for all protons for which a stronger spin–spin interaction is present. These cross peaks are clear evidence that the corresponding two protons must be in very close proximity, such as, for example, the  $C^\alpha$ -hydrogen and the hydrogen bound to the nitrogen in a peptide backbone.

Besides this correlation information, the chemical shift of protons,  $\delta$ , and the scalar coupling constants  $J$  can, of course, still be derived from the line splittings in 2D NMR. From these three parameters a multitude of information about the structure of proteins can already be derived: (i) The chemical shift  $\delta$  helps in identifying protons such as  $C^\alpha$ -hydrogens and hydrogens bound to the nitrogen of a peptide backbone. (ii) The cross peaks observed in COSY spectra help in identifying which of these protons are neighboured in the protein backbone. (iii) From the coupling constants  $J$  the corresponding torsion angles in the peptide bond backbone can be derived, which provides important first information for

the three-dimensional (3D) structure. Similar information from amino acid protons helps to estimate the position and orientation of the corresponding residues. In addition, usually, analogous information from the rare but not absent NMR-active carbon isotope  $^{13}\text{C}$  ( $\sim 1.1\%$  natural abundance, spin quantum number  $\frac{1}{2}$ ) can be collected.

### 5.1.7

#### Nuclear Overhauser Effect and NOESY Spectra

Scalar coupling can often only be observed for nuclei that are separated by up to three bonds. The information on scalar coupled protons alone is usually not sufficient to determine the overall 3D structure of proteins. For a complete structural analysis not only distances between nuclei that are chemically bound to each other have to be known (this is basically giving information on the scale of primary and secondary structure) but also, especially, the distances between nuclei interacting through space (giving information on the scale of secondary and tertiary structure). Fortunately, via cross-relaxation between nuclei mediated by dipolar couplings, the so-called nuclear Overhauser effect (NOE), distances between spins of up to  $\sim 5\text{ \AA}$  can be determined. The magnitude of NOE scales with  $1/r^6$ , with  $r$  being the distance between the interacting nuclei. NOE in NMR has certain similarities with the interactions governing FRET in optical spectroscopy. Both are based on the exchange of populations between energetically different states. In FRET, energy between populations of electronic excited state and ground states are exchanged, whereas the NOE is based on the exchange of energy between  $\alpha$ - and  $\beta$ -spin populations. Both transfer types are caused by dipole–dipole interactions, which explains that a  $1/r^6$  distance dependence can also be found for the NOE [compare with (3.32) and Figure 3.23]. The relative difference between the  $\alpha$ - and  $\beta$ -spin populations determines the  $z$ -component of the macroscopic magnetization (see Figure 5.2 and Figure 5.6). The important difference between NOE and spin–spin interactions is that, in the former, populations of  $\alpha/\beta$ -spins and thus  $z$ -components of the macroscopic magnetization are exchanged between nuclei, whereas in the latter phase relations between the spins are influenced and thus the two nuclei influence each other's horizontal  $x$ ,  $y$ -components of the macroscopic magnetization. The spin population transfer caused by the NOE affects the intensities of the corresponding proton peaks in a similar way as the fluorescence intensities of donor and acceptor are changed when FRET is present. To identify NOE couplings between protons, 2D NMR spectroscopy based on a three-pulse sequence is necessary (Figure 5.13).

The beginning of a NOESY-pulse sequence (nuclear Overhauser enhancement spectroscopy) is very similar to the COSY experiments, starting with a first  $90_x^\circ$ -pulse (Figure 5.14a). However, after the second pulse has been applied, a certain time, called the mixing period,  $t_m$ , elapses. During  $t_m$  the horizontal magnetization disappears and only a population difference of the spins remains (Figure 5.14b), when the spin–spin relaxation (decay of horizontal magnetization,  $T_2$ ) occurs on a faster time scale than the spin population relaxation ( $T_1 \sim 1\text{--}5\text{ s}$ ).

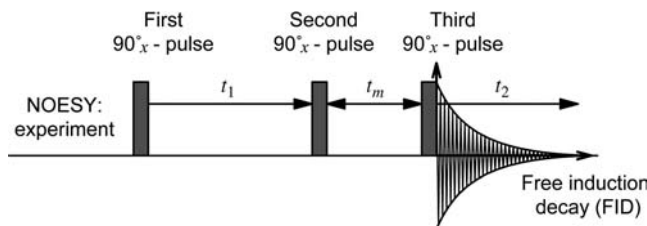
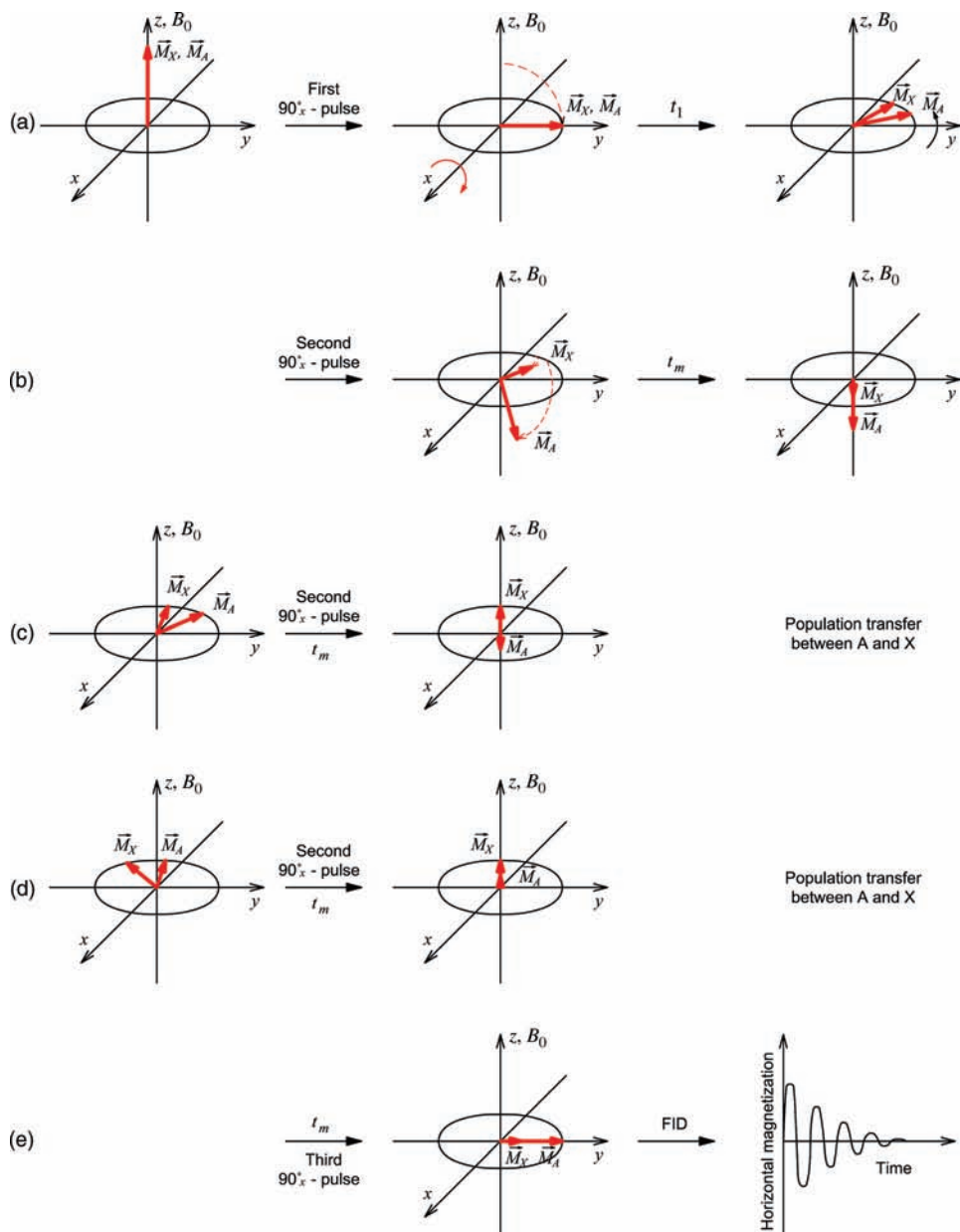


Figure 5.13 Pulse sequence for the identification of NOE couplings between protons.

10 s). During this time also energy transfer between the two populations of nuclei, typically called A and X in a NOESY experiment, can occur due to the NOE effect. The amount of energy transfer depends on the distance-dependent magnitude of the NOE effect and the different signs and magnitudes of the populations, which in turn depend on  $t_1$  (Figures 5.14c and d). The amount of energy transfer is greater the larger the difference is in the  $\alpha$ - and  $\beta$ -spin populations between the two nuclei (represented by the  $z$ -components of the macroscopic magnetizations  $\vec{M}_X$  and  $\vec{M}_A$  in Figures 5.14c and d). When the third  $90^\circ_x$ -pulse is now applied (Figure 5.14 e) the amplitude of the horizontal magnetization for a distinct nucleus is also dependent on the effectiveness of this energy transfer during  $t_m$ . The effectiveness of this energy transfer during  $t_m$  depends on the relative phases of the macroscopic magnetization vectors of the two nuclei in the moment of the second  $90^\circ_x$ -pulse. The relative phases in the moment of the second  $90^\circ_x$ -pulse depend on the Larmor frequencies of both nuclei and the corresponding time  $t_1$ . As an overall result, the  $t_1$ -dependent horizontal magnetization observed after the third  $90^\circ_x$ -pulse is modulated by the frequency of the other nucleus, but only if an NOE was possible between the two nuclei during the mixing period  $t_m$ . Again, the first Fourier transformation of the  $t_1$ -dependent FIDs( $t_2$ ) now yields signals that are amplitude modulated, depending on the Larmor frequency of the other nucleus, but only if a NOE transfer occurred during the mixing period.

In contrast to COSY peaks, NOESY cross peaks also occur between protons that are somewhat further apart. This can be the case, for example, when one proton at the end of one amino acid residue is close to another proton at the end of another amino acid residue. In the tertiary structure these residues can be close even if they are very remote from each other in the primary amino acid sequence. Consequently, NOESY cross peaks are very valuable for determining a protein's tertiary structure.

Of course, even more complex pulse sequences and 3D and 4D NMR sequences are available to further help the analysis of biomolecules. However, an explanation of these methods is beyond the scope of this book. Having insight into the fundamental aspects of COSY and NOESY 2D NMR spectroscopy suffices for an initial comprehension of the analysis of structural, dynamic and mechanistic aspects of biomolecules via NMR. In the next section we discuss



**Figure 5.14** Behaviour of the macroscopic magnetizations of two types of nuclei A and X in a NOESY experiment.

how the overall 3D protein structure or protein dynamics can be derived from the plethora of information contained in the various NMR spectra.

### 5.1.8

#### NMR-Based Structural Analysis of Biomolecules

Usually, for a structural analysis of proteins using NMR the primary sequence has to be known in advance. For a first assignment of proton signals to certain amino acid residues in this primary sequence, one can take advantage of the fact that distinct amino acids show characteristic patterns in the 2D  $^1\text{H}$  NMR spectra. NMR peaks corresponding to certain amino acids in this primary sequence can also be unravelled, for example, by synthesis of proteins in which these amino acids are specifically labelled with  $^{13}\text{C}$  or  $^{15}\text{N}$  isotopes or all other amino acids are deuterated. Such uniformly or selectively isotope-labelled proteins can be obtained from expression systems, such as *Escherichia Coli*, grown in media containing isotope-labelled amino acids and nutrients. The corresponding peaks in the  $^{13}\text{C}$  NMR spectrum, for example, will then appear with drastically increased intensity because the natural occurrence of the  $^{13}\text{C}$  isotope is much lower.

For the full three-dimensional structural analysis, multidimensional NMR techniques, as presented in this chapter, are of vital importance. For clarity, we will as an example focus only on six hydrogen atoms connected to the peptide bond backbone of the hypothetical protein structure shown in Figures 5.15 and 5.16. For each hydrogen atom the chemical shift,  $\delta$ , and scalar couplings,  $J$ , can be determined. In addition, COSY signals between hydrogen atoms can be identified. The chemical shift helps to assign which peaks, for example, correspond to hydrogens bound to the  $\text{C}^\alpha$ -atom or the nitrogen-atom at the protein backbone of a certain amino acid. From the scalar couplings important information on the secondary structure like  $\alpha$ -helix or  $\beta$ -sheet conformations can be derived using the Karplus relation, (Figure 5.5). For example, for hydrogens 1–4 scalar

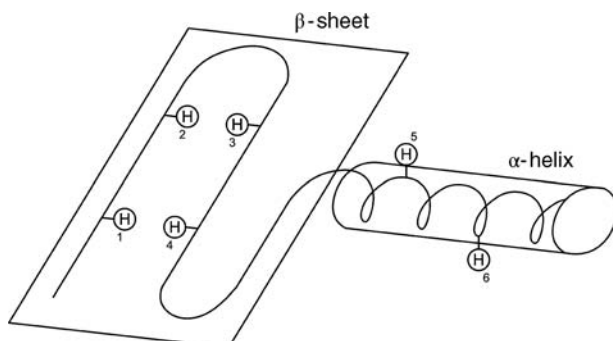


**Figure 5.15** With information about the primary sequence of the protein and the chemical shifts as well as spin–spin and NOE couplings the tertiary structure of a protein under ambient physiological conditions can be modelled.

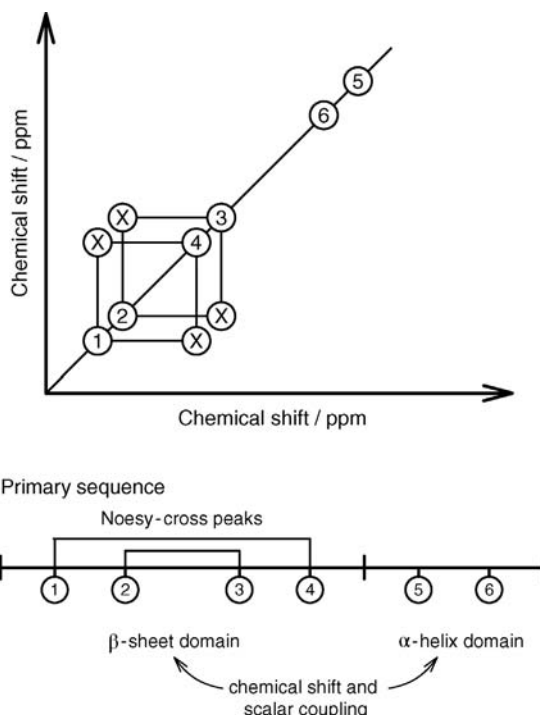


**Figure 5.16** Known chemical shift and spin-spin coupling patterns typical of certain amino acids and spin-spin as well as NOE couplings between neighbouring amino acids help to assign peaks in the 2D NMR spectra to protons in certain amino acids in the primary sequence. In the structure analysis of proteins, NOESY cross peaks help, for example, to find

amino acid residues that are remote in the primary sequence but are in close proximity in the tertiary structure of the protein. In addition, the chemical shift and scalar coupling constants of hydrogens bound, for example, to the peptide backbone help to determine the secondary structure.

couplings corresponding to a  $\beta$ -sheet conformation should be found, whereas hydrogens 5 and 6 should have corresponding values that indicate an  $\alpha$ -helix. Detailed local structural information along the protein backbone can be derived from the multitude of COSY signals and scalar coupling signals. In addition, through-space distances between the protons can be determined using, for example, the NOE effect. Strong NOESY correlation signals between hydrogens 1 and 4 as well as between 2 and 3 will help in determining the relative orientations of the  $\beta$ -strands in the  $\beta$ -sheet. In general, the NOESY signals from all nuclei help enormously in ascertaining the overall tertiary structure of the protein. Scalar and nuclear Overhauser signals also help to identify which signals correspond to neighbouring amino acids in the tertiary structure. Finally, all signals can also be used to elucidate the relative orientations and torsion angles of the amino acid residues.

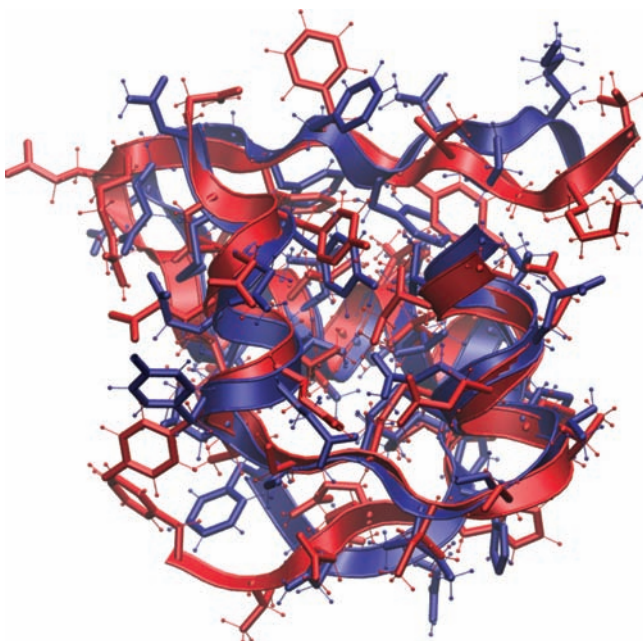


**Figure 5.17** Comparison of the structure of insulin derived from NMR spectroscopy (blue) and X-ray crystallography (red). Figure created using VMD (see Bibliography for details).

By taking all this information together, a complete 3D structural analysis of proteins is possible. Obviously, resolving the total structure of a protein via NMR requires an elaborate interplay between the help of powerful computer algorithms and human common sense. Usually, the structures found for biomolecules under physiological conditions at room temperature by using NMR are quite similar to X-ray structures (Figure 5.17). Nevertheless, important differences can be observed. They are often caused by flexible and nonrigid domains of the proteins (Figure 5.18).

The main advantage of multidimensional NMR in contrast to techniques such as X-ray crystallography is that a structural analysis can be performed on biomolecules in their natural aqueous environment at room temperature, without the need for high-quality crystals of the biomolecules. In addition, the conformational flexibility under these conditions can be determined. This can be used to elucidate decisive intermediate reaction steps of biomolecular processes or to investigate the influence of regulators on the protein conformation and dynamics. An advantage in contrast to, for example, fluorescence techniques is clearly that label-free mechanistic studies are possible. This requires, however, the presence of reliable NMR signals that monitor the biomolecular transformations of interest. Unfortunately, even using state-of-the-art NMR spectrometers, standard NMR analysis is limited to rather small proteins having masses of only about  $\sim 30\text{--}40\text{ kDa}$ . For larger proteins so many signals interfere that very sophisticated isotope labeling and multi-dimensional NMR techniques have to be applied.

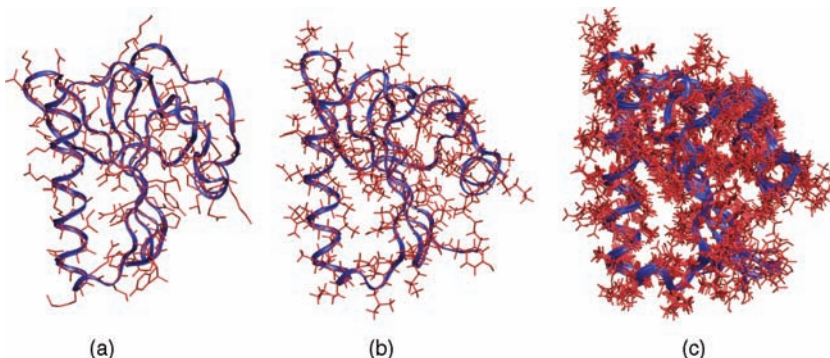


**Figure 5.18** Comparison of the structure of severin derived from X-ray crystallography at low temperatures (a) and NMR spectroscopy in aqueous solution at room temperature (b) and (c). The protein backbone is illustrated in blue and the amino acid residues are indicated in red. In (b) actually only one possible conformation derived from NMR data is

shown. Part (c) shows that NMR data provides in addition valuable information about the structural flexibility of proteins. This is visualized in (c) by a superposition of various different possible conformations derived by the NMR data for severin in aqueous solution at room temperature. Figure created using VMD (see Bibliography for details).

## 5.2 Electron Paramagnetic Resonance

Electron paramagnetic resonance (EPR) is closely related to NMR. In EPR, however, transitions between the  $\alpha$ - and  $\beta$ -spin of electrons are detected. As described in Chapter 1, electrons paired in one electronic orbital must have opposite spins. The magnetic moments of these electrons cancel each other out so that no net spin transitions can be detected. Only unpaired electrons can be detected by absorption and emission of electromagnetic radiation in the microwave range (Figure 1.2). Few biomolecules contain electrons that are not paired in an electronic orbital. However, in the cases where unpaired electrons are present in biomolecules, EPR can be a very powerful tool. This is because the unpaired electrons are often contained in paramagnetic metal ions like  $\text{Fe}^{3+}$ ,  $\text{Mn}^{2+}$  and  $\text{Cu}^{2+}$ , which are in many cases at a central position of cofactors essential for the function of these biomolecules. Important examples are cofactors involved in the primary processes of photosynthesis or the iron ion in haemoglobin. If biomolecules do not contain any unpaired electrons they can be labelled with a spin label. Spin labels are in most cases organic molecules that contain unpaired electrons. Such molecules that contain unpaired electrons are also called radicals. We will present an example of a spin label and applications further below.

EPR is based on a similar theoretical background as NMR. The spin quantum number of an electron is  $\frac{1}{2}$ . However, in contrast to NMR the total angular momentum of electrons,  $\vec{J}$ , is composed of the spin angular momentum,  $\vec{S}$ , and orbital angular momentum,  $\vec{L}$ . In a classical picture the latter describes the

motion of the electrons around the nucleus. Thus, the orbital angular momentum also gives rise to a magnetic moment that has to be considered. For electrons at nuclei that have only a small positive charge, interactions between the spin momentum and the angular momentum (called spin-orbit coupling) can be neglected. Then, the total angular momentum ( $\vec{J}$ ) can be calculated from the spin angular momentum ( $\vec{S}$ ) and orbital angular momentum ( $\vec{L}$ ) according to so-called the Russell–Saunders coupling:

$$\vec{J} = \vec{L} + \vec{S} \quad (5.8)$$

with  $|\vec{S}| = \sqrt{S(S+1)}\hbar$ ,  $|\vec{L}| = \sqrt{L(L+1)}\hbar$  and  $|\vec{J}| = \sqrt{J(J+1)}\hbar$ . Here,  $S$ ,  $L$  and  $J$  are the quantum numbers for the spin, orbit and total angular momentum, respectively [compare also with (5.2)]. In radicals, the contribution from the orbit angular momentum can often be neglected. Then, the resulting dipole moment can be approximated by:

$$\vec{\mu}_J \approx \vec{\mu}_S = g\mu_B\sqrt{S(S+1)} \quad (5.9)$$

Here,  $\mu_B$  is the Bohr magneton [ $\mu_B = (|e|\cdot\hbar)/2m_e$ ] and  $g$  is the  $g$ -factor, which typically has a value very close to two. As in NMR, the strength of the magnetic field ( $B_0$ ) and the component of the magnetic dipole moment in the field direction ( $\mu_z$ ) determine the energy difference between the spin orientations [compare with (5.1) and (5.3)]:

$$E = -\mu_z B_0 \quad (5.10)$$

However, in contrast to NMR  $\mu_z$  is significantly larger, which explains why EPR absorption and emission wavelengths are typically in the microwave range. Because the generation of different wavelengths in the microwave range is technically difficult, normally an EPR spectrum is recorded by absorption or emission of a fixed microwave wavelength and simultaneous sweeping of the magnetic field intensity. The resulting EPR spectrum is usually represented as a first derivative of the absorption (Figure 5.19). Often, a hyperfine structure is observed that is due to spin–spin coupling with the spin states of the nucleus coupled to the unpaired electron. An unpaired electron in a p-orbital of a nitrogen atom, for example, has a hyperfine splitting consisting of three lines. The lines correspond to the three possible nuclear spin states of the most abundant nitrogen isotope  $^{14}\text{N}$  ( $I=1$ ):  $m_N = -1, 0$  or  $1$ . The actual field sensed by the electron is the external field increased or reduced by the field caused by the nitrogen in its different spin states. The hyperfine coupling is characterized by the hyperfine coupling constant,  $\alpha$ , which corresponds to the distance between the hyperfine splitting lines in ESR spectra (Figure 5.19).

As mentioned earlier, most biomolecules have to be labelled with a spin label to be investigated by EPR. The stable organic radical 2,2,6,6-tetramethylpiperidin-1-oxyl (TEMPO) is an important example of such a spin label (Figure 5.20). The hyperfine coupling constant  $\alpha$  depends on the environmental polarity as

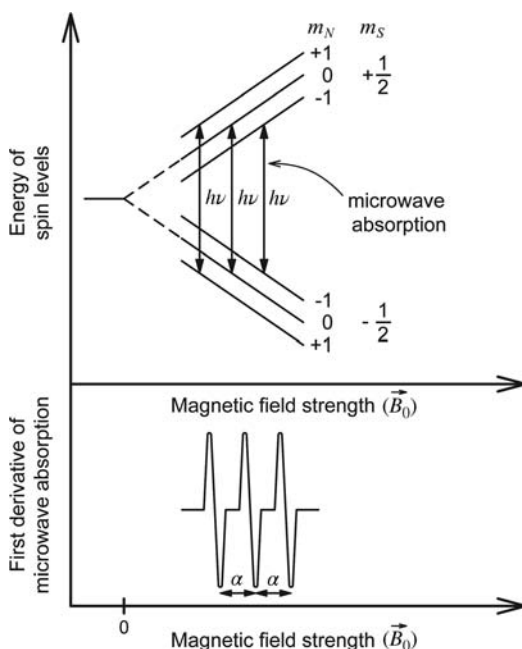


**Figure 5.19** Typical EPR spectrum with hyperfine splitting of an unpaired electron at a nitrogen atom. The hyperfine splitting is caused by the three different possible spin states of the nucleus:  $-1, 0$  and  $+1$ .

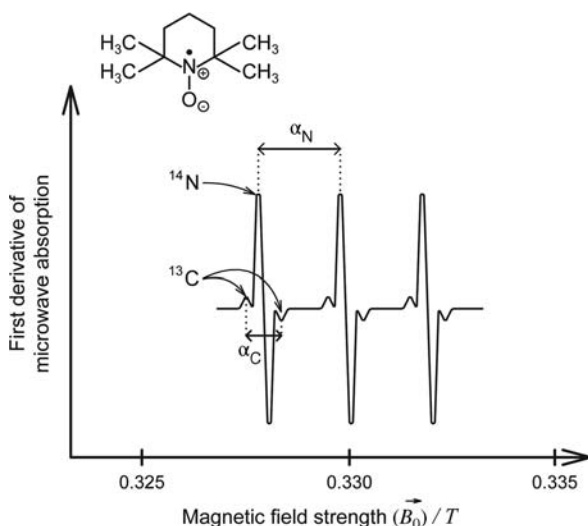


**Figure 5.20** Chemical structure and EPR spectrum of the spin label 2,2,6,6-tetramethylpiperidin-1-oxyl (TEMPO). The hyperfine splitting due to different spin states of the nitrogen atom,

$\alpha_N$ , dominates the spectrum. However, hyperfine splitting due to different spin states of the isotope  $^{13}C$ ,  $\alpha_C$ , is also visible.

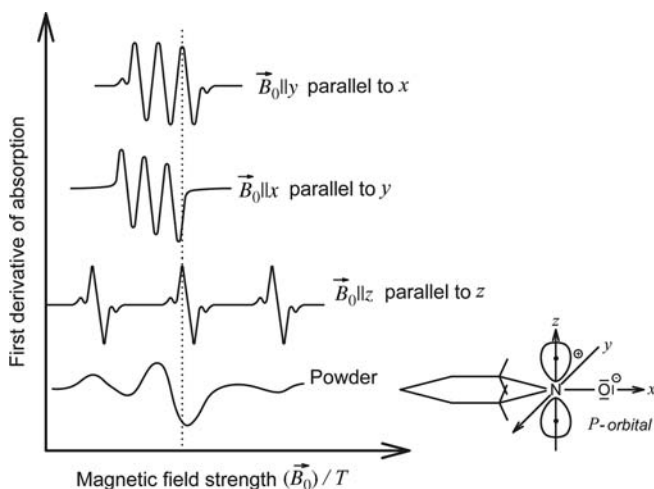


**Figure 5.21** The hyperfine coupling of TEMPO depends on the relative orientations of the radical electrons p-orbital and the external field.

well as on the orientation of the nitrogen p-orbital of the unpaired electron with respect to the external magnetic field. The dependence on the environmental polarity is a consequence of the strong permanent dipole present in the molecule. The dependence on the orientation between the p-orbital and the external magnetic field can be understood by considering the total field gradient sensed by the p-orbital in different orientations relative to the magnetic field (Figure 5.21). The orientation dependence of the hyperfine coupling constant,  $\alpha$ , also gives rise to characteristic spectra observed from TEMPO for different rotational correlation times,  $\phi$  [Figure 5.22, compare also with (3.23)]. Thus, in principle similar information about the spin-labelled species can be observed as in fluorescence anisotropy measurements (Chapter 3). However, an advantage of the determination of the rotational correlation time via EPR in comparison to fluorescence anisotropy measurements is the larger dynamic range of detectable rotational correlation times  $\phi$ . This is because the EPR signals are also sensitive for rotational correlation times that are significantly longer than the excited-state lifetime of fluorescence markers, which are typically on the order of only a few ns (Figure 5.22). Major drawbacks are, however, the uncertainties in a quantitative determination of the rotational correlation time from the observed EPR spectra and longer acquisition times. A typical application example of EPR is the determination of the molecular flexibility of spin-labelled lipids in natural or artificial lipid membrane bilayers. EPR data from corresponding samples provide valuable information about the structure of and dynamics within biological membranes (Figure 5.23). In addition, membrane proteins can be spin labelled. The diffusion properties of proteins within the membranes can then be examined using EPR.

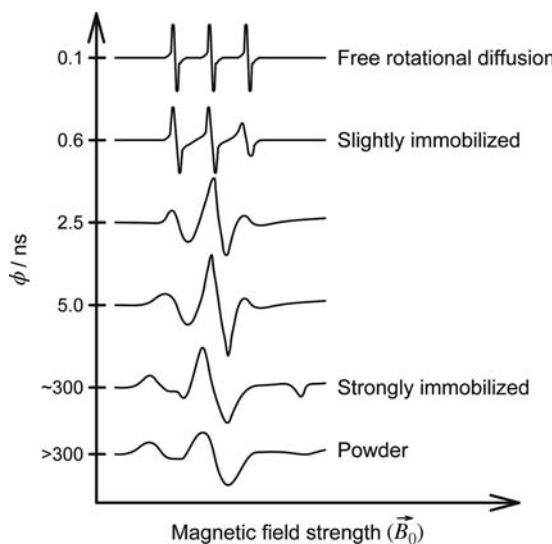


Figure 5.22 EPR spectra of TEMPO observed for different rotational correlation times,  $\phi$ .

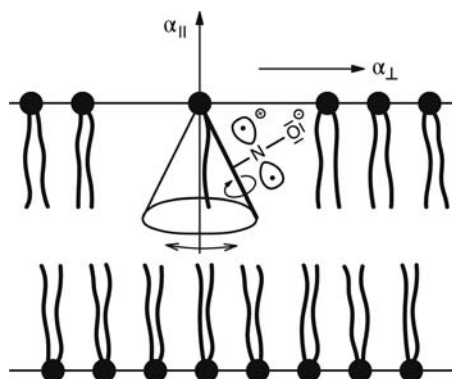


Figure 5.23 Spin labelling of lipids or membrane proteins can be used to determine the membrane structure and dynamics and diffusional properties of membrane proteins via EPR measurements.

### Problems

- 5.1 Explain why higher magnetic field strengths result in a better resolution of magnetic resonance spectrometers.
- 5.2 Discuss the advantages of pulsed NMR methods over NMR methods in which the absorption of continuous radiowaves is measured.
- 5.3 Figure 5.4 illustrates the reasons for the splitting and the intensities of the signals for the methyl group protons of ethanol (shown in Figure 5.3,

- marked as c). Explain in the same way the line splitting and intensities for the methylene protons marked by b in Figure 5.3.
- 5.4 Figures 5.2 and 5.6 illustrate schematically how the magnetic moments of individual nuclei sum to the total magnetization. Sketch graphically how the magnetic moments of individual nuclei can sum to a total magnetization that points in the direction of the half-diagonal between the  $z$ - and the  $y$ -axis.
- 5.5 In the rotating frame coordinate system a  $90_x^\circ$  pulse corresponds to the rotation of the total magnetization around the  $x$ -axis by  $90^\circ$ . Sketch graphically the trajectory of the total magnetization vector during a  $90_x^\circ$  pulse in the laboratory frame.
- 5.6 In a multidimensional NMR experiment a protein sample is first irradiated with a radiowave pulse that results in a zero population difference of  $\alpha$  and  $\beta$  proton spins. An identical second radiowave pulse is applied after a time that corresponds to  $1/8$  of a full Larmor rotation of the  $\alpha$ -carbon hydrogen spin of a distinct amino acid. After about  $1\text{ s}$  a third identical radiowave pulse is applied. Now the FID is measured.
- What kind of NMR experiment does this situation correspond to?
  - How much signal does the  $\alpha$ -carbon hydrogen contribute to the observed FID? Discuss various scenarios.
- 5.7 A protein with an unknown structure is investigated in a NOESY experiment. Extremely strong NOESY correlations are found between  $\alpha$ -carbon hydrogens,  $\text{H}^\alpha$ , and hydrogens bound to nitrogens,  $\text{H}^N$ , three amino acids further in the primary sequence [ $\text{H}^\alpha(i)\text{-H}^N(i+3)$ ,  $i$  = number of amino acids in the primary sequence]. Which secondary structure element is dominant here?
- 5.8 Ramachandran has developed a theory that explains the occurrence of certain secondary protein structure elements based on steric factors that allow, for example, only distinct torsional angles in the peptide backbone,  $\phi$  (for a definition of  $\phi$  refer to Figure 5.5). Depending on the size of the amino acid residues in the corresponding region of the protein different values for  $\phi$  are preferred. For example, a  $\phi$  of around  $-100^\circ$  dominates when  $\beta$ -strands are present, whereas an angle of around  $-70^\circ$  accounts for the common right-handed  $\alpha$ -helix. The rare case of a left-handed  $\alpha$ -helix is indicated by torsion angles,  $\phi$ , of around  $60^\circ$ . In a COSY experiment of a protein with unknown structure many scalar couplings between  $\alpha$ -carbon hydrogens,  $\text{H}^\alpha$ , and hydrogens bound to the nitrogen of the protein backbone,  $\text{H}^N$ , that are on the order of or even larger than  $J(\text{H}^N\text{-H}^\alpha) \sim 8\text{ Hz}$  are observed. Which secondary structure element is dominant in this protein?
- 5.9 Explain why in EPR spectroscopy the magnetic field is scanned rather than the microwave frequency?

- 5.10** Explain how rotational correlation times can be derived from EPR spectra. Discuss the advantages and disadvantages of determining rotational correlation times with EPR and fluorescence polarization measurements.

## Bibliography

### General

- Atta-Ur-Rahman, T.I. (1986) *Nuclear Magnetic Resonance: Basic Principles*, Springer, New York.
- Berliner, L.J. and Reuben, J. (eds) (1992) *Biological Magnetic Resonance*, Plenum Press, New York.
- Bovey, F.A., Mirau, P.A. et al. (1988) *Nuclear Magnetic Resonance Spectroscopy*, Academic Press, Inc.
- Cantor, C.R. and Schimmel, P.R. (1980) *Biophysical Chemistry: Part II: Techniques for the Study of Biological Structure and Function*, W.H. Freeman & Co.
- Cavanagh, J. et al. (2007) *Protein NMR Spectroscopy. Principles and Practice*, Academic Press.
- Croasmun, W.R. and Carlson, R.M. (eds) (1994) *Two-Dimensional NMR Spectroscopy: Applications for Chemists and Biochemists*, 2nd edn, Fully updated and expanded to include multidimensional work, Wiley-VCH Verlag GmbH, Weinheim.
- Derome, A.E. (1987) *Modern NMR Techniques for Chemistry Research*, Pergamon Press, New York.
- Ernst, R.R., Bodenhausen, G. et al. (1987) *Principles of Nuclear Magnetic Resonance in One and Two Dimensions*, Oxford University Press, Oxford.
- Evans, J.N.S. (1995) *Biomolecular NMR Spectroscopy*, Oxford University Press.
- Farrar, T.C. (1987) *Introduction to Pulse NMR Spectroscopy*, Farragut Press.
- Freeman, R. (1997) *A Handbook of Nuclear Magnetic Resonance*, Longman, Harlow.
- Friebolin, H. (2006) *Ein- und Zweidimensionale NMR-Spektroskopie*, Wiley-VCH Verlag GmbH, Weinheim.
- Fukushima, E. and Roeder, S.B.W. (1993) *Experimental Pulse NMR: A Nuts and Bolts Approach*, Perseus Books.
- Harris, R.K. (1986) *Nuclear Magnetic Resonance Spectroscopy: A Physicochemical View*, Longman.
- Humphrey, W., Dalke, A. and Schulten K. (1996) *VMD - Visual Molecular Dynamics*, *Journal of Molecular Graphics* 14, 33–38.
- Karplus, M. and Petsko, G.A. (1990) Molecular dynamics simulations in biology. *Nature*, **347** (6294), 631–639.
- Keeler, J. (2005) *Understanding NMR Spectroscopy*, John Wiley & Sons, Inc.
- Lebedev, Y.S. (1994) *High-Field ESR. Electron Spin Resonance*, vol. 14 (eds N.M. Atherton, M.J. Davies and B.C. Gilbert), Royal Society of Chemistry, Cambridge, p. 63.
- Lottspeich, F. and Zorbas, H. (eds) (2006) *Bioanalytik*, Spektrum Akademischer Verlag, Heidelberg, Berlin.
- Rhodes, C.J. (2000) *Toxicology of the Human Environment: The Critical Role of Free Radicals*, CRC Press, Inc.
- van de Ven, F.J.M. (1995) *Multidimensional NMR in Liquids: Basic Principles and Experimental Methods*, Wiley-VCH Verlag GmbH, Weinheim.
- van Holde, K.E., Johnson, C. et al. (2005) *Principles of Physical Biochemistry*, Prentice-Hall.
- Weil, J.A., Bolton, J.R. et al. (2007) *Electron Paramagnetic Resonance: Elementary Theory and Practical Applications*, John Wiley & Sons, Inc., New York.
- Winter, R. and Noll, F. (1998) *Methoden der Biophysikalischen Chemie*, Teubner Verlag.
- Wüthrich, K. (1986) *NMR of Proteins and Nucleic Acids*, John Wiley & Sons, Inc., New York.

### Specific

#### Structure of Insulin (Figure 5.17)

Smith, G.D., Pangborn, W.A. et al. (2003) The structure of T6 human insulin at 1.0 Å resolution. *Acta Crystallogr.*, **D59**, 474–482.

#### Structure of Severine (Figure 5.18)

Schnuchel, A., Wiltscheck, R. et al. (1995) Structure of severin domain 2 in solution. *J. Mol. Biol.*, **247** (1), 21–27.



**6****Mass Spectrometry****6.1****Introduction**

The molecular weight of biomolecules is one of the most important parameters for their characterization and identification. Since mass spectrometers have been developed that allow us to quickly determine the molecular weight of biomolecules, with an accuracy that even enables distinguishing isotopomers that differ by only a single isotope, they have become an indispensable tool in the biosciences. An important prerequisite for this development was the invention of gentle methods for the ionization and transfer of the biomolecules into the gas phase (Figure 6.1). During this first step it is essential to avoid destruction of the biomolecules by, for example, unintentional fragmentation, structural rearrangement, oxidation and so on.

The next step in mass spectrometry is the separation of the charged biomolecules by their mass( $m$ )-to-charge( $z$ ) ratio ( $m/z$ ) in a mass analyser;  $m/z$  is actually the decisive parameter that is determined in mass spectrometry. In a final step, the separated ions have to be detected by appropriate ion detectors.

In this chapter we discuss the two most common methods for the ionization of biomolecules in combination with their most common analysers. The methods are matrix-assisted laser desorption ionization (MALDI) combined with time-of-flight (TOF) analysers (i.e. MALDI-TOF) and electrospray ionization (ESI) mass spectrometers in combination with quadrupole mass analysers. Notably, however, the latest generation of instruments basically allows any combination of ionization method, mass analyser and detector.

**6.2****MALDI-TOF****6.2.1****Ionization**

In MALDI a non-destructive ionization and vaporization of the biomolecules is achieved by the following process. First, the biomolecules and matrix molecules

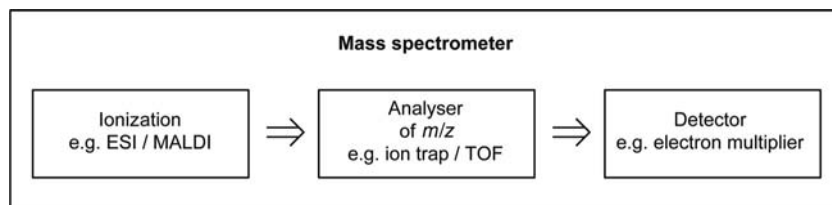


**Figure 6.1** Schematic representation of a mass spectrometer for analysing biomolecules.

are dissolved in two separate solutions. For the solutions typically volatile solvents such as methanol and acetonitrile are used in addition to water. The concentration of the matrix molecule solution is chosen to be about 1000 to 10 000 times higher than that of the biomolecule solution. The solutions are then mixed and about 1  $\mu$ L of the mixed solution is dried on a metallic support (sample holder) (Figure 6.2). As a result, the biomolecules are embedded in a solid matrix of the matrix molecules as a monodispersion.

The sample holder with the remaining small spot of solid matrix can now be transferred into an evacuated chamber. The matrix molecules are chosen such that they have a significant optical extinction coefficient in a certain spectral region, usually in the UV. Often, smaller aromatic organic molecules are chosen as matrix molecules. In the next step a nanosecond-laser pulse with a wavelength corresponding to the absorption wavelength of the matrix molecules is focused on the matrix (Figure 6.3). Typically, a pulsed nitrogen laser providing pulses of  $\sim 3\text{--}4$  ns duration at a wavelength of 337 nm is used. Since the matrix molecules make up nearly 100% of the matrix the amount of absorbed light

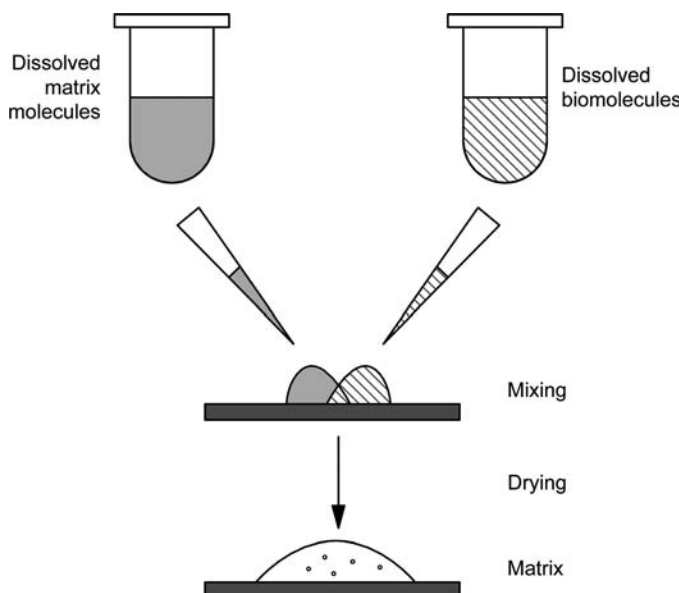


**Figure 6.2** The first step in MALDI mass spectrometry is always the preparation of a solid matrix in which the biomolecules are embedded.

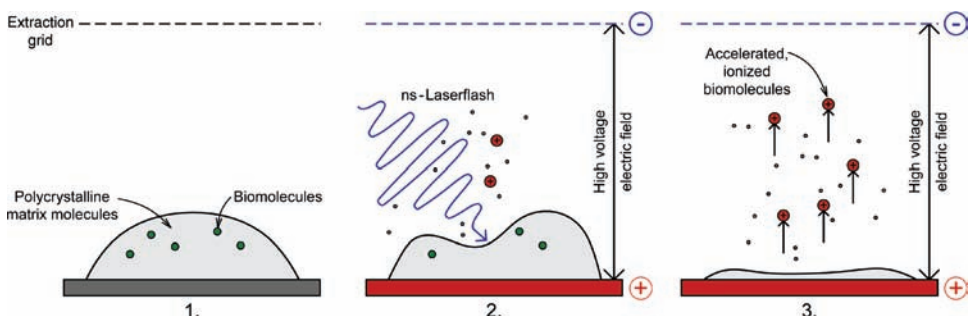


**Figure 6.3** Ionization and acceleration of the biomolecules is achieved in MALDI by irradiation of the matrix in the presence of a high-voltage electric field with a laser pulse having a wavelength corresponding to the absorption wavelength of the matrix molecules.

energy in a small volume and in a short time is enormous. The large excess in excitation energy leads in addition to processes such as transformation into heat via internal conversion (Chapter 1) to a sputtering and partial ionization of the entire matrix, including the biomolecules. Ionization occurs by proton transfer between matrix and biomolecules, for example from acidic matrix molecules (see examples below) to the protein, not by electron transfer, as is the case for more traditional ionization methods. As a consequence, the mass of the molecules to be analysed is increased or decreased by the mass corresponding to one proton compared to the neutral state. During the laser excitation the metallic matrix support also serves as one electrode for a high-voltage field of several kilovolts (kV). The other electrode spanning the field is a metallic grid (extraction grid). As a result, ionized biomolecules are accelerated in this electric field in the direction of the extraction grid.

The biggest advantage of MALDI is that it usually creates ions of isolated, unharmed biomolecules with only one or a few charges. However, the processes governing the ionization are still not entirely understood. Thus, the conditions of optimal matrix preparation and the matrix molecule choice for the ionization of certain biomolecules have to be established empirically. Depending on the class of biomolecules under investigation different matrix molecules and preparation procedures have been found to work well. Often, for example, traces of acids such as trifluoroacetic acid are added to the matrix molecule solution prior to drying. This seems to facilitate the formation of positive biomolecule ions during the laser flash exposure. In addition, the sign of the electric field, which determines whether either positive or negative ions are detected, is an important factor for optimization of the ionization conditions. A negatively charged grid electrode results in the detection of positively charged biomolecules, often in their protonated form ( $M_{\text{Biomolecule}} + H$ )<sup>+</sup> with  $M_{\text{Biomolecule}}$  being the neutral biomolecule. This mode is called the positive ionization mode and is usually better suited for the ionization of proteins or peptides. Conversely, a positively charged grid electrode results in negative ions, often deprotonated in the form ( $M_{\text{Biomolecule}} - H$ )<sup>-</sup>. This negative ionization mode is often preferred for oligonucleotides or oligosaccharides. Table 6.1 summarizes examples of preferred matrix compounds for different classes of biomolecules.

**Table 6.1** Typical matrix compounds used in MALDI mass spectrometry.

Matrix compound	Chemical formula	Typically used for			Excitable by $\lambda$ (nm)		
		Proteins	Peptides	Oligo-nucleotides	266	337	355
Sinapinic acid		•			•	•	•
$\alpha$ -Cyano-4-hydroxycinnamic acid			•		•	•	
4-Hydroxypicolinic acid				•	•	•	
Nicotinic acid		•	•		•		
2,5-Dihydroxybenzoic acid			•	•	•	•	•

### 6.2.2 Analyser

After the biomolecules have been accelerated in the electric field their mass-to-charge ratio  $m/z$  is analysed using, for example, a time-of-flight (TOF) analyser (Figure 6.4).

After being accelerated by the voltage  $U$  all ions have virtually the same kinetic energy:

$$E_{\text{kin}} = z \cdot e \cdot U \quad (6.1)$$

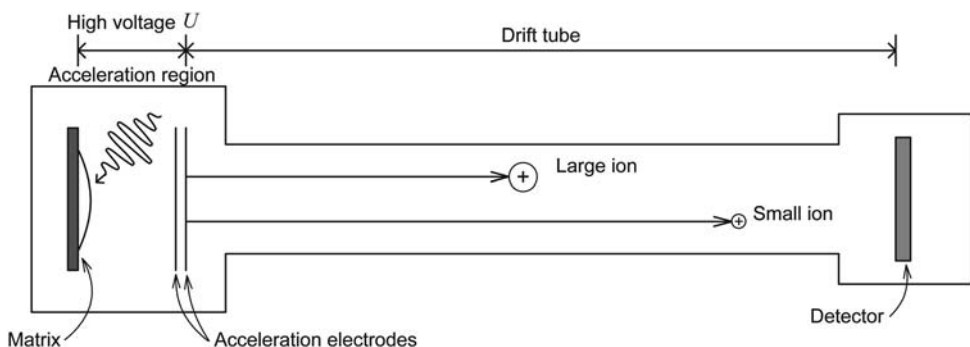


**Figure 6.4** After leaving the acceleration region all ions have virtually the same kinetic energy regardless of whether they have a large or a small mass. However, the same kinetic

energy of a larger ion corresponds to a smaller velocity than that of ions of smaller masses. The time-of-flight analyser is based on the measurement of these differences in velocities.

Here,  $z$  is the number of charges on the biomolecule and  $e$  is the elementary charge. The relation between the kinetic energy of a particle and its mass ( $m$ ) and velocity ( $v$ ) is:

$$E_{\text{kin}} = \frac{1}{2}m \cdot v^2 \quad (6.2)$$

The velocity ( $v$ ) can be determined from the time ( $t$ ) the particle needs to reach the ion detector after the pulsed matrix desorption:

$$v = \frac{L}{t} \quad (6.3)$$

Here,  $L$  is the length of the drift tube. Combining (6.1)–(6.3) yields:

$$z \cdot e \cdot U = \frac{1}{2}m \cdot \left(\frac{L}{t}\right)^2 \quad (6.4)$$

or, finally, for the mass-to-charge ratio:

$$\frac{m}{z} = \frac{2 \cdot e \cdot U}{L^2} t^2 \quad (6.5)$$

Even though all parameters in (6.5) are easily accessible, mass spectrometers are usually calibrated with molecules of known masses either before the actual measurement of the biomolecule or by adding them during the matrix preparation of the biomolecule (internal calibration).

### 6.2.3

#### Detector

Detection is usually performed by electron multipliers (Figure 6.5). The accelerated ions create electrons at a first electrode, the so-called conversion dynode. These electrons are then accelerated in an electric field towards another electrode. At this electrode (also called a dynode) an even larger number of electrons are created from the electron collisions; these electrons are again

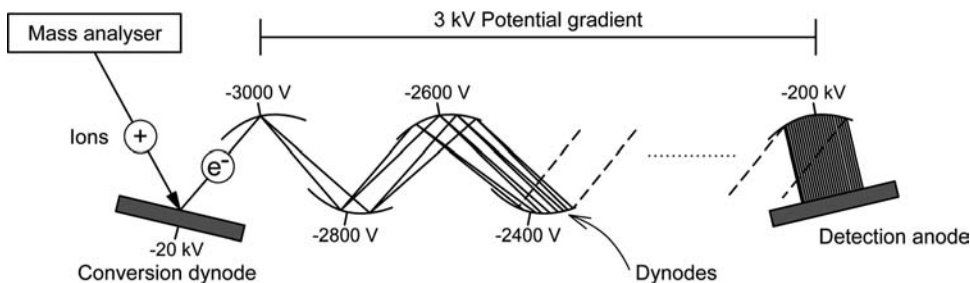


**Figure 6.5** The ions can be detected using electron multipliers. If an accelerated ion hits an electrode called a conversion dynode, which has a very negative electric potential then electrons are extracted from the conversion dynode and accelerated towards the opposing electrode, which is simultaneously the first electrode of a series of so-called

dynodes with increasing electric potential. Each time electrons hit a dynode more electrons are extracted from the dynode and accelerated towards the next dynode. As an overall result a very large number of electrons reach the detection anode and can be measured as an electronic current after electric amplification.

accelerated in an electric field towards the next dynode. In a cascade of dynodes the number of electrons increase until a detectable current can be measured at the last dynode, which is called detection anode.

#### 6.2.4

##### Signals and Signal Improvements

The simple set-up shown in Figure 6.4 achieves only a relatively low mass resolution. One important reason for this is that not all ions are formed at the same time and location in the matrix. Consequently, not all ions have exactly the same kinetic energy ( $E_{\text{kin}}$ ) after a pulsed irradiation and the starting times for their flight path also differ slightly. A first approach to improve the resolution is to apply the primary accelerating field not permanently but to switch it on shortly after the laser pulse has been applied. This helps to synchronize the starting time of the ion acceleration and is called delayed extraction. In addition, during this short delay, molecules cool down and lose some of their kinetic energy, caused by the laser pulse further reducing the spread in energy distribution of the ions before the extraction pulse is turned on. A convenient way to compensate for remaining differences in  $E_{\text{kin}}$  is the use of a TOF reflectron. Figure 6.6 shows the principle of a TOF reflectron. In a TOF reflectron the ions are reflected in an electric field that has an opposite orientation to the initial accelerating field. Ions of higher kinetic energy (2) but the same mass as ions with lower kinetic energy (1) penetrate deeper into the reflector field and therefore fly for a longer time than the slower ions. However, these ions then experience a larger acceleration in the opposite direction. As a consequence, all ions with the same mass-to-charge ratio focus at a certain location in the TOF reflectron. The detector only has to be positioned at this focus.

With these improvements it is no problem to resolve even different masses of the same protein caused by different isotopic composition of nuclei like H, N, C or O. Figure 6.7 shows schematic representations of typical MALDI-TOF mass

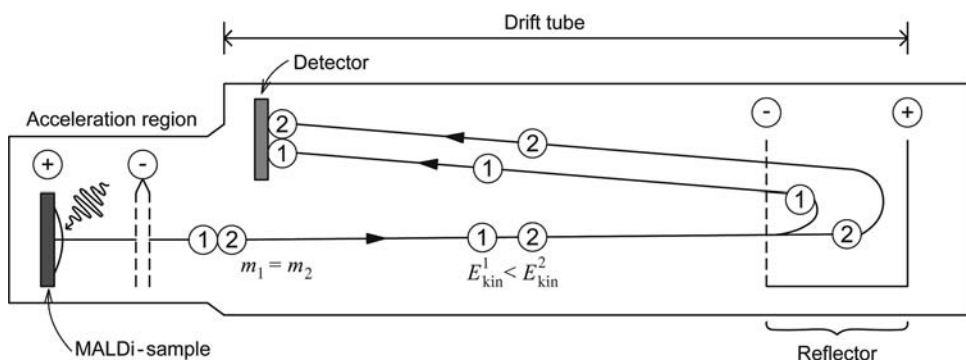


**Figure 6.6** In a TOF reflectron, differences in the kinetic energy caused by inhomogeneous ion acceleration are compensated by reflecting the ions in an opposing electric field. As a result extremely high resolutions in the determination of the mass-to-charge ratio can be achieved.

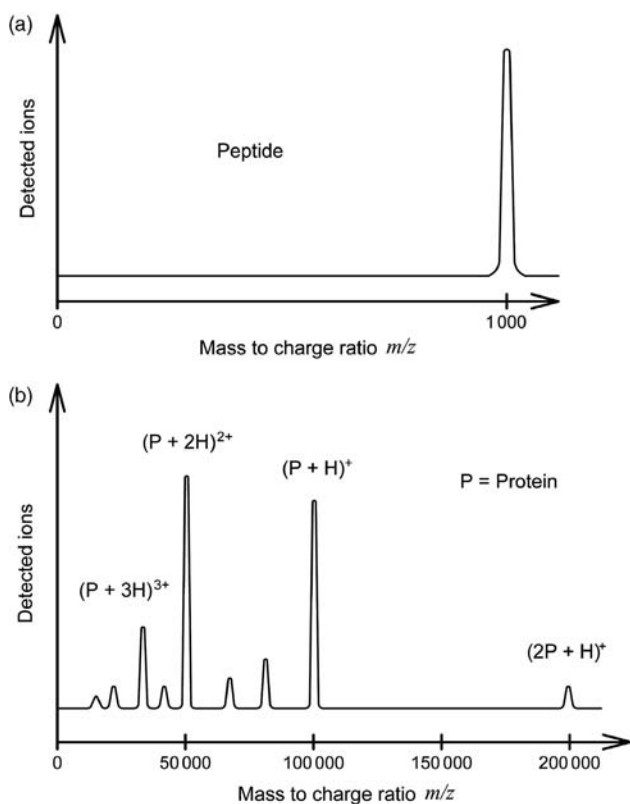


**Figure 6.7** Schematic presentation of a MALDI-TOF mass spectrum of (a) a peptide and (b) a protein.

spectra of a peptide and a protein. In MALDI spectra peptides are usually represented as one peak corresponding to a single charged biomolecule. Depending on the size of the protein, MALDI spectra can also contain peaks corresponding to higher charged species (e.g.  $(M_{\text{Protein}} + H)^+$ ,  $(M_{\text{Protein}} + 2H)^{2+}$ ,  $(M_{\text{Protein}} + 3H)^{3+}$  etc.) or other small peaks, for example, from matrix adducts. Also, non-covalent adducts with ions such as  $Na^+$  are often found. However, usually they can be distinguished easily from the main peak corresponding to one charge. Occasionally, aggregates such as  $(2 M_{\text{Protein}} + H)^+$  are also detected.

As mentioned earlier, modern mass spectrometers are even able to resolve the distribution of isotopes such as  $^{12}C/^{13}C$  in the biomolecules. The natural occurrence of  $^{13}C$  is  $\sim 1.11\%$ . Obviously, the probability of finding two or more  $^{13}C$  in a peptide is smaller than finding more than two  $^{13}C$  in a large protein. As a result, the distribution of different isotope peaks is broader for proteins than for peptides (Figure 6.8). Since the probability of finding a certain number of isotopes in a peptide or protein is normally governed by random statistics the isotope distribution usually corresponds to binomial distributions. If the mean value in the number of  $^{13}C$  isotopes is significantly larger than one then the distribution resembles a Gaussian distribution, such as is usually found for proteins (Figure 6.8b). For mean values in the number of  $^{13}C$  isotopes of around 1 the distribution rather resembles an exponential decay. This is the situation usually found for peptides (Figure 6.8a).

### 6.3 ESI-MS

#### 6.3.1 Ionization

In electrospray ionization (ESI) the biomolecules are directly ionized from their liquid solution (Figure 6.9). The solution of the biomolecules under standard pressure is evaporated from the tip of a small steel capillary, about  $100\text{ }\mu\text{m}$  in diameter, into a vacuum. In modern devices miniaturized metal-coated glass capillaries with a tip diameter of only a few micrometres are also used. The metal at the glass or of the steel capillary serves as one electrode for the generation of a high-voltage electric field of  $\sim 3\text{--}4\text{ kV}$ . The other electrode is again placed in the direction of the mass analyser. As a consequence, charged droplets are generated and accelerated towards the mass analyser. During the acceleration between the electrodes the solvent evaporates, resulting in smaller droplets with an increasing density of surface charges. A nebulizing gas flow, usually consisting of nitrogen, helps in the evaporation by flowing parallel around the liquid jet. Once the droplets are so small that repulsing Coulombic forces of the surface charges are larger than the surface tension of the droplets they completely evaporate and, due to proton transfers, a large number of the charges remain on the biomolecules. The biomolecules are now ionized in the gas phase and further accelerated towards the mass analyser.

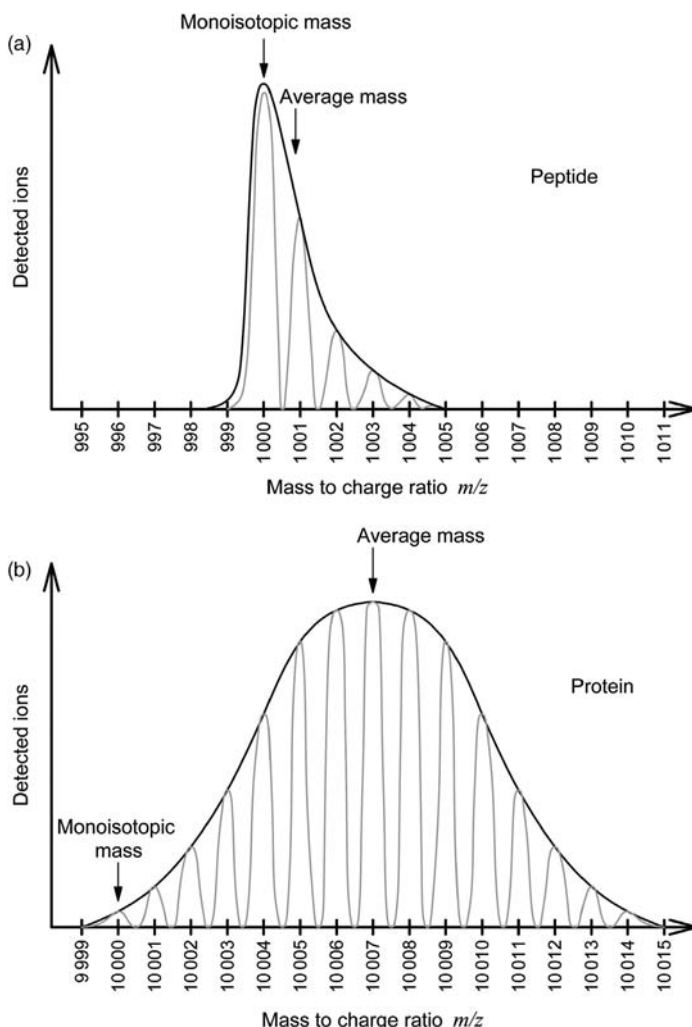


**Figure 6.8** Modern mass spectrometry even allows one to distinguish differences in protein masses caused by differing distributions of isotopes. Because the probability of finding one or more isotopes in a peptide (a) is much smaller than in a larger protein (b) the corresponding isotope distribution of proteins is much broader than that of peptides.

As in MALDI, either a positive or negative ionization mode can be applied. Again, proteins and peptides are preferentially ionized under positive ionization conditions. Often, traces of formic acid are added to the solutions to facilitate ionization. The negative ionization mode is again used mainly for the ionization of oligonucleotides and saccharides. Here, traces of ammonia or volatile amines can be added to facilitate ionization.

It has been found empirically that smaller flow rates result in improved ionization efficiencies. This, in turn helps increase the sensitivity of ESI mass

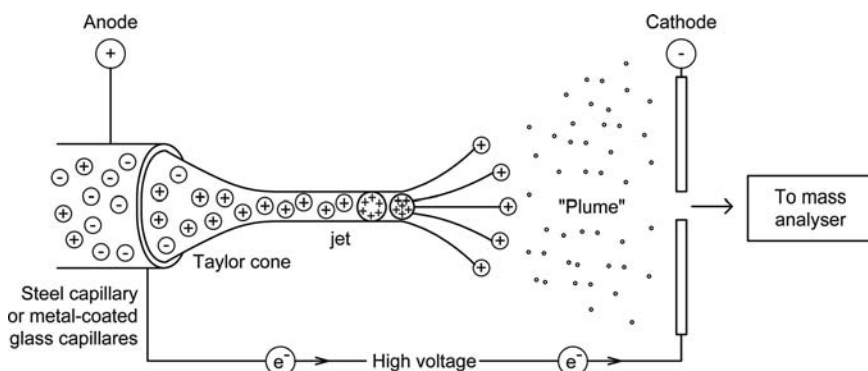


Figure 6.9 Principle of electrospray ionization of biomolecules.

spectrometry. This is why capillaries of inner diameters in the range 10–25  $\mu\text{m}$  and 3–5  $\mu\text{m}$  have been developed for modern ESI instruments. These techniques are called micro-ESI or even nano-ESI, respectively.

### 6.3.2

#### Analyser and Detection

Because of the continuous sample flow and ion generation, TOF analysis obviously can not be directly used for the determination of  $m/z$  after ESI. Therefore, quadrupole mass spectrometers and ion traps are typically used as mass separators that can also analyse masses from a continuous ion flow though even recent developments allow even to perform TOF analysis in combination with ESI when devices are used that extract, in a pulsed manner, ions perpendicularly from the continuous ion flow.

Figure 6.10 sketches the principle of a quadrupole mass spectrometer. It consists of four rod-like electrodes. All electrodes are connected to a constant voltage  $U$  and an oscillating voltage  $V \cos(2\pi ft)$ , where  $f$  is the frequency of the oscillation and  $t$  the time. Ions with a certain kinetic energy are directed from the ionization source into the central part of the mass analyser. It depends now on the  $m/z$  ratio of the ionized biomolecules as to how their trajectory through the mass analyser is affected by the accelerating and varying electric fields between the electrodes. For a certain  $m/z$  ratio only distinct combinations of  $U$ ,  $V$  and  $f$  lead to a stable trajectory guiding the ion finally towards the detector ( $m_1/z$  in Figure 6.10). Ions of other  $m/z$  ratios collide with the electrodes or leave the analyser in the  $x$  ( $m_2/z$ ) or  $y$  direction ( $m_3/z$ ). The detection of the ions after the quadrupole mass analyser can be performed using similar techniques as described for MALDI mass spectrometry.

Let us briefly discuss how the acceleration of the ions by the electric field created between the electrodes can be described quantitatively and what combinations of  $U$ ,  $V$  and  $f$  lead to stable trajectories through the analyser. The

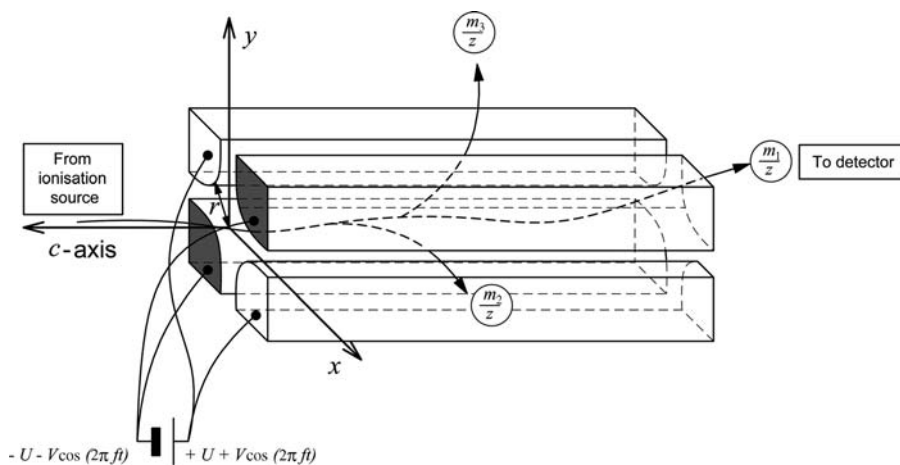


**Figure 6.10** Principle of a quadrupole mass analyser. For distinct combinations of constant and oscillating electric fields,  $U$  and  $V$ , applied at the four rod-like electrodes only ions with specific mass-to-charge ratios,  $m/z$ , have stable trajectories through the central part of the analyser.

time-dependent electric field between the electrodes is described by:

$$\phi(x, y, t) = (U + V \cos 2\pi ft) \cdot \frac{x^2 - y^2}{r^2} \quad (6.6)$$

Here,  $x$  and  $y$  are the coordinates of the electric field with respect to the axis  $c$  in the centre of the analyser and  $r$  is the inner distance of the electrodes from the axis  $c$  (cf. Figure 6.10).

Usually, a small acceleration voltage of about 10 to 20 V directs the ions along the  $c$ -axis. Their motion in the  $x$  and  $y$  directions can be described by:

$$\begin{aligned} m \frac{d^2x}{dt^2} &= z \cdot e \frac{d\phi(x, y, t)}{dx} = \frac{z \cdot e}{r^2} (U + V \cos 2\pi ft) \cdot x \\ m \frac{d^2y}{dt^2} &= z \cdot e \frac{d\phi(x, y, t)}{dy} = -\frac{z \cdot e}{r^2} (U + V \cos 2\pi ft) \cdot y \end{aligned} \quad (6.7)$$

Here,  $m(d^2x/dt^2)$  and  $m(d^2y/dt^2)$  generally correspond to the forces exerted on particles of mass  $m$  in the  $x$  and  $y$  directions, respectively, by an acceleration  $a_x = d^2x/dt^2$  or  $a_y = d^2y/dt^2$  (compare also with (6.2)). For the charged ions in the quadrupole mass spectrometer this force is caused by the electric-field gradients  $d\phi(x, y, t)/dx$  and  $d\phi(x, y, t)/dy$  in the  $x$  and  $y$  directions and is equal to:

$$z \cdot e \frac{d\phi(x, y, t)}{dx} \quad \text{and} \quad z \cdot e \frac{d\phi(x, y, t)}{dy}$$

respectively [cf. (6.1)]. Using (6.6) as the description of the electric field results in (6.7). It is advantageous to present this system of differential equations in the

form of so-called Mathieu equations:

$$\begin{aligned} \frac{d^2x}{f\pi \cdot dt^2} + (a + 2q \cos 2\pi f) \cdot x &= 0 \\ \frac{d^2y}{f\pi \cdot dt^2} - (a + 2q \cos 2\pi f) \cdot y &= 0 \end{aligned} \quad (6.8)$$

using the substitutions:

$$\begin{aligned} a &= \frac{2zeU}{m(\pi fr)^2} \\ q &= \frac{zeV}{m(\pi fr)^2} \end{aligned} \quad (6.9)$$

The presentation in the form of Mathieu equations is advantageous because analytical solutions for these equations have been known since the nineteenth century. These solutions describe the possible trajectories of the charged ions in the quadrupole mass spectrometer. We will not present detailed solutions here but it is advantageous to discuss possible trajectories of the ions as a function of the parameters  $a$  and  $q$ . The parameters  $a$  and  $q$  are proportional to the experimentally applied voltages  $U$  and  $V$  divided by the mass of the ions, respectively, (6.9). Generally, there are two kinds of solutions: one type corresponds to stable oscillations of the ions through the mass analyser with constant amplitudes, while the other type corresponds to amplitudes that increase exponentially in the  $x$  and  $y$  directions. The regions of these solutions are plotted in Figure 6.11 in a  $y=a$ ,  $x=q$  diagram.

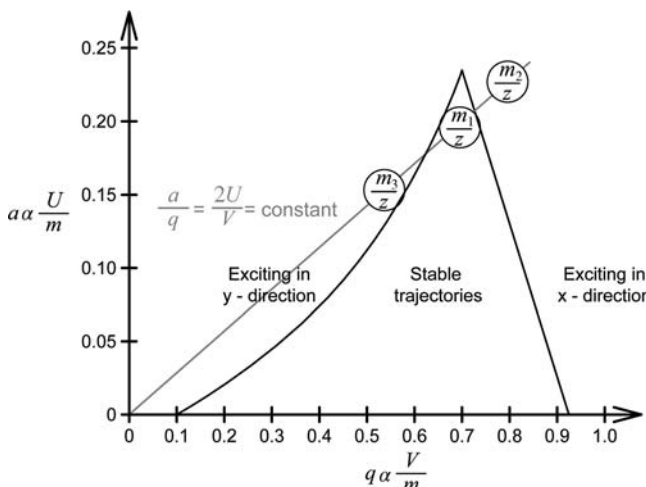


**Figure 6.11** The parameters  $a$  and  $q$  (Eq. (6.9)) in the Mathieu equation (Eq. (6.8)) determine whether an ion of a certain  $m/z$  either exits the mass spectrometer in the  $x$  or

$y$  direction or travels on a stable trajectory through the quadrupole mass spectrometer and towards the detector.

If the parameters  $U$  and  $V$  are chosen correctly then only a very narrow subset of  $m/z$  ratios can pass through the quadrupole mass spectrometer. For the ratio  $m_1/z$  in Figure 6.11 the values  $a \sim 0.23$  and  $q \sim 0.7$  are optimal so that only these ions can pass through to the analyser. Slightly smaller or higher ratios such as  $m_2/z$  or  $m_3/z$  exit the spectrometer in the  $x$  or  $y$  direction, respectively. To scan mass-to-charge ratios, usually the absolute values of  $U$  and  $V$  are increased linearly while keeping the ratio between  $U$  and  $V$  and thus between  $a$  and  $q$  constant. The result of this is that different  $m/z$  ratios successively reach the narrow region of stable trajectories through the quadrupole field corresponding to a line  $a/q = \text{constant}$  in the diagram that just touches the narrow tip at the top of the stable oscillation region. Consequently, the resolution of the spectrometer depends critically on the chosen ratio  $U/V$ , which determines the broadness of the mass-to-charge range that passes through the spectrometer.

### 6.3.3

#### Signals and Signal Improvements

An extension of the quadrupole field is the ion trap. It is a three-dimensional quadrupole field created between a ring-shaped electrode and two caps having small holes to allow the ions in and out of the ion trap (Figure 6.12).

Depending on the applied amplitude, signs and frequencies, ions of a certain range of mass-to-charge ratios oscillate in stable orbits within the trap. Which ions

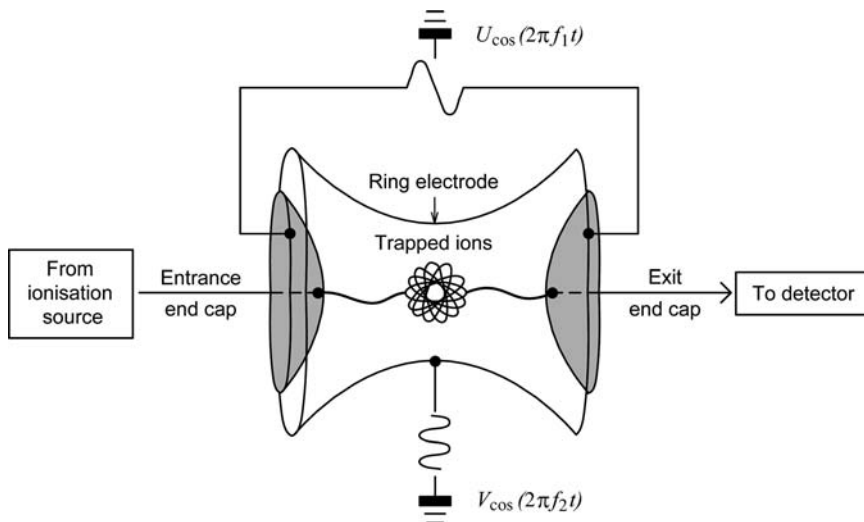


**Figure 6.12** An ion trap. By choosing the right amplitudes, signs and frequencies of the electric potentials at the entrance cap, the ring electrode and the exit cap, ions of different mass-to-charge ratios can be manipulated in many different ways. It is possible, for

example, to store ions with a certain range of  $m/z$  in stable orbits in the ion trap and eject subsequently ions with increasing  $m/z$  values through the exit end-cap hole towards the detector.

have stable orbits in an ion trap can again be described by similar considerations as in the previous section. A small amount of helium ( $3 \times 10^{-6}$  bar) helps ions that have been sent into the trap to dissipate their excess kinetic energy by collisions with the gas atoms. In contrast to quadrupole mass spectrometers, conditions are often chosen to keep ions corresponding to a rather large range of different  $m/z$  ratios within the trap. Ions corresponding to only a very narrow subpopulation of distinct  $m/z$  values can then be ejected by applying another oscillating electric field solely to the end caps. By varying the electric-field properties ions with increasing or decreasing  $m/z$  values can be ejected and analysed one after another.

As mentioned earlier, ESI spectra result in ions with more than one charge per molecule (Figure 6.13). While peptides appear in the spectra usually as only a

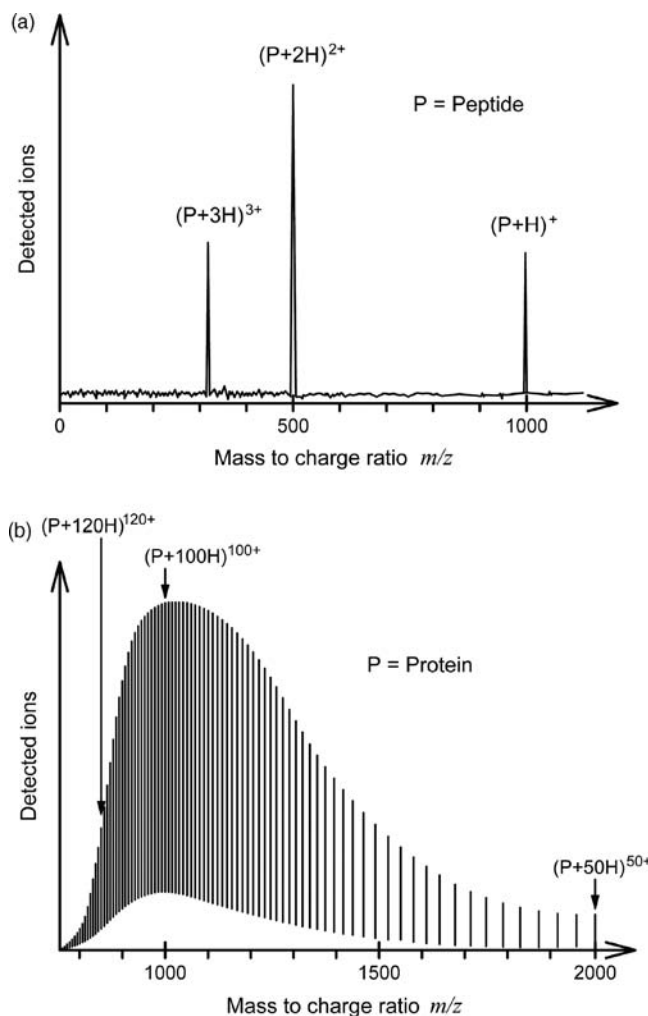


Figure 6.13 Schematic representation of ESI mass spectra of (a) peptides and (b) proteins.

few peaks, proteins often exhibit hundreds of peaks. As a consequence, the evaluation of the original mass of proteins, which is often called hypermass in this context, has to be done with the help of computer algorithms. The result of such a reconstruction is a virtual mass spectrum with a mass rather than a mass-to-charge scale. The reconstructed mass spectrum contains only one mass peak or isotope distribution for each biomolecule that was present in the originally analysed sample.

A very important advantage of ESI is that no special preparation of the sample solutions or very time-consuming optimizations of the ionization conditions are necessary for the mass analysis. The biomolecules can be analysed directly from their liquid solutions at room temperature and under physiological conditions. This allows us to combine ESI mass spectrometry directly with liquid chromatography techniques and to analyse, for example, in real-time biomolecules that are eluted one after another from a column.

## 6.4

### Structural and Sequence Analysis Using Mass Spectrometry

Using modern mass spectrometry, very valuable tools for analysing the structure of biomolecules or the primary sequence of peptides or proteins have been established.

In this context, so-called MS-MS or  $MS^n$  techniques are very important. These are techniques in which, for example, three or more quadrupole mass analysers are arranged in a row. The corresponding set-ups are often called triple-quadrupole mass spectrometers or tandem mass spectrometers. In one of these analysers the ions are purposely fragmented. From the observed fragments important aspects about the structure of the original biomolecules can often be reconstructed. For example, the analysis of peptides using MS-MS or  $MS^n$  techniques takes advantage of the fact that peptide fragmentation occurs preferentially at the nitrogen and carbon atoms between two amino acids in the peptide backbone.

Fragmentation and analysis of fragments using MS-MS or  $MS^n$  techniques can be performed in many different ways. As previously mentioned, one way is to arrange three quadrupole mass analysers in a row. The first quadrupole analyser is used to select ions of a certain mass-to-charge ratio and send them into the second quadrupole analyser. In the second quadrupole analyser an inert gas such as nitrogen, argon or helium is present at a certain pressure. Owing to collisions with the atoms of the inert gas the ions tend to fragment. Finally, the fragments are sent into the third quadrupole mass spectrometer, where their  $m/z$  ratio is analysed. It is also possible to purposely generate fragments in an ion trap. Here, the fragments are generated by accelerating the ions to larger orbits by applying appropriate electric fields. Owing to this acceleration the ions experience significantly more frequent collisions with the helium gas atoms, which are always present in ion traps, and fragment. After this fragmentation period, distinct subgroups of the generated ion fragments can then be kept in or

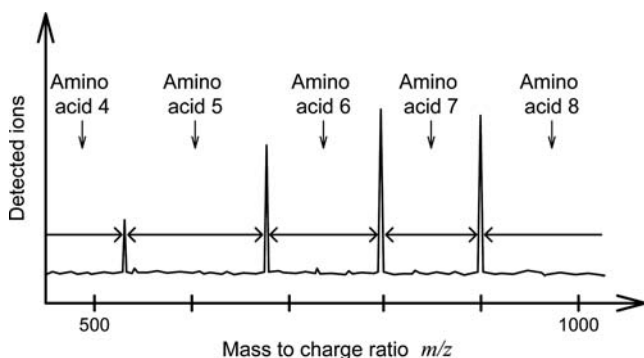


**Figure 6.14** Peptide ladder sequencing. The differences between the mass peaks correspond to the masses of amino acid subunits. The amino acid sequence of the original peptide corresponds to the sequence of mass differences in the spectrum.

ejected from the ion trap. A repetition of several different fragmenting and selecting steps yields a multitude of valuable information about the original structure of the fragmented biomolecules.

A technique for analysing the primary sequence using mass spectrometers is a method called peptide ladder sequencing. It is based on the combination of a modified Edman sequencing with mass spectrometry. For this analysis Edman sequencing is conducted with about 5% of the normal Edman reagent phenyl isothiocyanate (PITC) being replaced by phenyl isocyanate (PIC). Normally, in Edman sequencing PITC is used to remove step-wise one amino acid after another from the N-terminus of the peptide and analyse it in a certain reaction cycle. However, if the reagent PIC reacts in the modified Edman sequencing procedure with the N-terminus of a certain peptide fragment it remains at this position and no further step-wise removal of single amino acids occurs with that specific peptide fragment. As an overall result, a statistical mixture of peptide fragments is present after several reaction cycles that differ by masses corresponding exactly to single amino acids. Since in MALDI these masses are usually represented by single peaks of very high resolution the mass spectrum of this mixture corresponds to a 'ladder' of mass peaks in which the differences between the mass peaks correspond to the masses of the respective amino acids. The sequence of the amino acids is then identical to the corresponding sequence of mass differences in the mass spectrum (Figure 6.14).

### Problems

- 6.1 Modern mass spectrometers allow us to combine electrospray ionization with a time-of-flight analyser. Discuss the potential advantages of such an arrangement.
- 6.2 a. In a MALDI-TOF experiment ions are detected 250  $\mu$ s after laser irradiation. What is the mass of one mole of the investigated molecules

- when no ions can be detected at other times? The tube is 2 m long and the acceleration voltage is 5 kV. Is the sample a peptide or a protein?
- b. At what time after the laser irradiation would you expect the ions of a fluorescent label of molecular weight  $100 \text{ g mol}^{-1}$ ?
- 6.3 You want to analyse a mixture of different biomolecules by MALDI mass spectroscopy. You are not sure if the mixture contains exclusively proteins or also oligonucleotides. What compound would you select for the matrix preparation?
- 6.4 The natural abundance of  $^{13}\text{C}$  is  $\sim 1.11\%$ . Calculate the intensity distribution of the isotope peaks in the MALDI mass spectra of a singly charged 1 kDa peptide and a singly charged 10 kDa protein. Assume that no other elements than carbon occur in different isotopes in the biomolecules and that carbon accounts for  $\sim 80\%$  of the total mass of the biomolecules.
- 6.5 A quadrupole mass analyser is adjusted in such a way that only proteins corresponding to a very narrow distribution of mass-to-charge ratio values can pass the analyser. What instrumental parameters do you have to change, and in what way, if you want to use the analyser to select proteins corresponding to a larger range of mass-to-charge ratio values?
- 6.6 Ion traps can be used to store biomolecule ions of a distinct sample and eject and analyse biomolecule ions of distinct mass-to-charge ratio one after another. In what situation is such a procedure especially useful?
- 6.7 Sketch the mass spectrum you would expect in a peptide ladder sequencing of the peptide Pro-Lys-Gly-Cys-Trp-His-Gly. Consider the convention that the primary sequence of peptides or proteins starts at the N-terminus.
- 6.8 You are not sure whether a distinct protein occurs as a trimer or a tetramer. How could you distinguish between these two possibilities?

## Bibliography

### General

- Chapman, J.R. (ed.) (1996) *Protein and Peptide Analysis by Mass Spectrometry*, Humana Press, Totowa, New Jersey.
- Cole, R.B. (ed.) (1997) *Electrospray Ionization Mass Spectrometry: Fundamentals, Instrumentation, and Applications*, John Wiley & Sons, Inc., New York.
- Dass, C., Desiderio, D.M. et al. (2001) *Principles and Practice of Biological Mass Spectrometry*, John Wiley & Sons, Inc., New York.

- Hillenkamp, F. and Peter-Katalinic, J. (eds) (2007) *A Practical Guide to MALDI-MS: Instrumentation, Methods and Applications*, Wiley-VCH Verlag GmbH, Weinheim.
- de Hoffmann, E. and Stroobant, V. (2001) *Mass Spectrometry: Principles and Applications*, John Wiley & Sons, Ltd, Chichester.
- Lehmann, W.D. (1996) *Massenspektrometrie in der Biochemie*, Spektrum Akademischer Verlag, Heidelberg.

- Lottspeich, F. and Zorbas, H. (eds) (2006) *Bioanalytik*, Spektrum Akademischer Verlag, Heidelberg, Berlin.
- McLafferty, F.W. and Choi, J. (1993) *Interpretation of Mass Spectra*, University Science Books, Sausalito.
- Pasch, H. and Schrepp, W. (2003) *MALDI-TOF Mass Spectrometry of Synthetic Polymers*, Springer, Berlin.
- Pramanik, B.N. Ganguly, A.K. *et al.* (eds) (2002) *Applied Electrospray Mass Spectrometry: Practical Spectroscopy Series*, vol. 32, Marcel Dekker, Inc., New York.
- Siuzdak, G. (1996) *Mass Spectrometry for Biotechnology*, Academic Press, Boston.
- Snyder, A.P. (ed.) (1996) *Biochemical and Biotechnological Applications of Electrospray Ionization Mass Spectrometry*, Oxford University Press, Oxford.

## Part Two

### Advanced Methods in Biophysical Chemistry

The techniques discussed in Part 1 of this book are essential and broadly applicable tools for the characterization and investigation of biomolecules. However, many important biomolecular questions have been answered in recent years by more specialized techniques. Some of them are already very widespread in many laboratories. The intention of this part is to give an insight into the possibilities and advantages of such techniques along with selected application examples. The application examples are often primarily chosen to illustrate the technical capabilities of the modern techniques and which parameters can be observed using them. Of course there are many more very important application examples that can not be shown within the scope of this book.

The first chapter, Chapter 7, describes important aspects of modern fluorescence microscopy techniques. Chapter 8 provides a thorough overview into subdiffraction limited fluorescence microscopy and general aspects such as imaging in living cells and multicolour images. In addition to giving an insight into modern methods of fluorescence microscopy in general Chapters 7 and 8 also provide the basis for some of the techniques described in subsequent chapters. Chapter 9 describes several techniques that each observe the behaviour of single biomolecules. The elucidation of many important biomolecular mechanisms is only possible by these methods, which allow us to observe the movements of, forces exerted by, or ion currents flowing through single biomolecules. Chapter 10 discusses methods based on the use of ultrafast lasers. This chapter covers the advantages of important nonlinear optical methods in the biosciences, such as two-photon excitation, including a brief insight into the physical basis of methods such as second-harmonic generation or coherent anti-Stokes Raman microscopy. Also, the observation of the fastest processes in nature, such as the ultrafast energy conversion in photosynthesis, using ultrafast lasers is discussed. Chapter 11 gives an overview of traditional as well as modern next-generation DNA sequencing methods that have had a significant impact in many fields of recent research. Chapter 12 presents some special techniques that are optimized for very distinct biological questions. Important examples are flow cytometry, DNA chips and DNA origami. This

chapter also discusses some general special techniques like the use of fluorescing nanoparticles or microspheres or surface plasmon resonance detection. Finally, in the last chapter, Chapter 13, important general aspects of the development of assays to monitor certain biomolecular processes are discussed. This chapter also presents typical plate formats and plate reader technologies for the measurement of larger series of samples. The chapter ends with an application example illustrating how assays for high-throughput screening help in the initial phase of industrial drug development.

## 7

# Fluorescence Microscopy

### 7.1

#### Introduction

The detection of the intrinsic or extrinsic fluorescence in fluorescence microscope set-ups is a very sensitive technique that enables even the investigation of single fluorescently labelled biomolecules under physiological conditions. In this chapter we discuss a few aspects that are important in achieving a high resolution and sensitivity in fluorescence microscopy. We also present several modern fluorescence microscopy techniques, including the latest developments such as light-sheet and TIRF-microscopy. This will provide the basis for several of the very sensitive and high-resolution techniques presented in part two of this book such as super-resolution microscopy techniques (Chapter 8), optical single-molecule detection (Chapter 9, Section 9.2), fluorescence auto- and cross-correlation spectroscopy (Chapter 9, Section 9.3), optical tweezers (Chapter 9, Section 9.4), nonlinear microscopy techniques such as multiphoton or CARS microscopy (Chapter 10, Section 10.2) and also next-generation DNA sequencing methods (Chapter 11), or confocal readers (Chapter 13, Section 13.3).

### 7.2

#### Conventional Fluorescence Microscopy

##### 7.2.1

#### Confocal Fluorescence Microscopy

We begin this section by discussing step by step the details of a typical confocal microscope set-up because it is best suited to explaining some of the most important optical principles in fluorescence microscopy. In Figure 7.1 a schematic presentation of such a confocal microscope set-up is shown.

For excitation, typically first a collimated laser beam is expanded by a set of two lenses (blue beam in Figure 7.1). The focal lengths of the lens pair is chosen such that a light beam with a diameter corresponding to the back aperture of the microscope objective is generated. The reason for this is that the best resolution

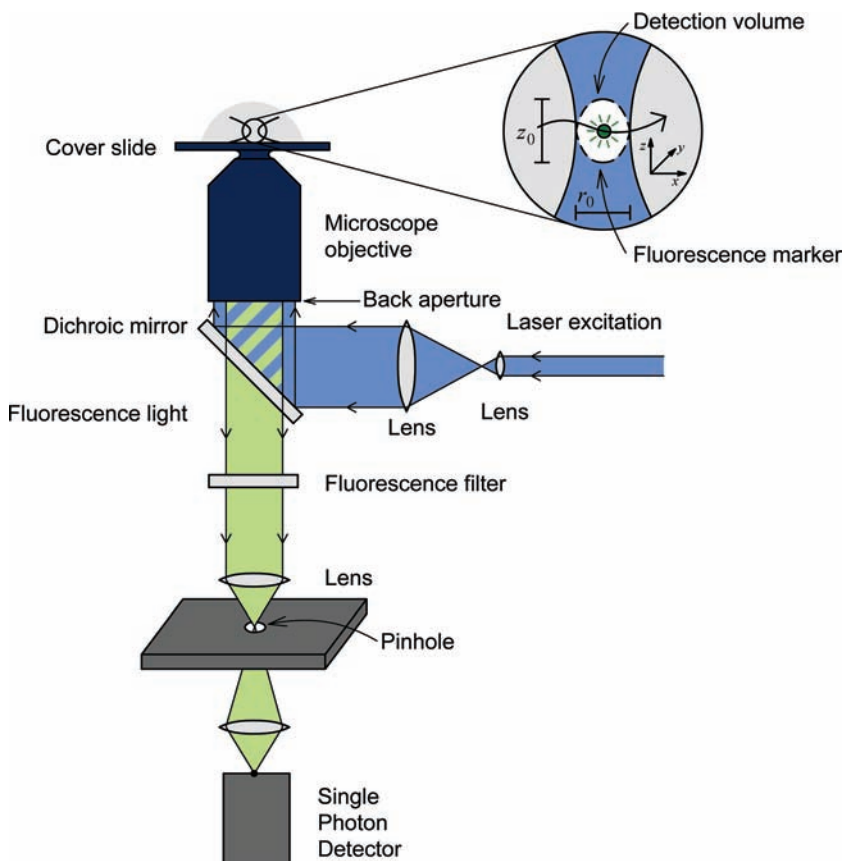
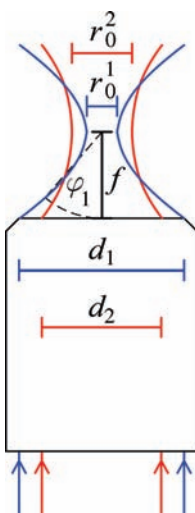


Figure 7.1 Schematic representation of a microscope set-up for confocal fluorescence detection.

of a microscope objective can only be achieved when its back aperture is completely illuminated. This fact is a consequence of a general and very important optical principle governing the resolution of any optical set-up. If only a smaller part of the objective's back aperture is illuminated the half-angle of the light cone focused by the objective is smaller. However, as a result of the wave properties of light, incident light waves coming from a smaller range of angles cannot result in an intensity distribution in the focal region as confined as if the light waves come from a broader angle range. The consequences for microscope resolution are illustrated in Figure 7.2. In classical microscopy the diffraction limited value  $r_0$  (see also Figure 7.1), which characterizes the smallest possible dimensions of the beam diameter in the focal region, is given by Abbe's law:

$$r_0 \approx \frac{\lambda}{2n \cdot \sin \varphi} \quad (7.1)$$



**Figure 7.2** Abbe's law (Eq. (7.1)) determines the diameter of the focal area. If the back aperture of the microscope objective is not fully illuminated ( $d_2$ ) then the ratio  $d/f$  becomes smaller and, consequently, the resolution ( $r_0^2$ ) is worse (7.1).

Here,  $\lambda$ , is the wavelength of the light and:

$$n \cdot \sin \varphi = n \cdot \sin \left( \arctan \frac{d}{2f} \right) \approx n \cdot \frac{d}{2f}, \text{ for small angles, } \varphi \quad (7.2)$$

is the so-called numerical aperture, with  $\varphi$  being the half-angle of the light cone irradiating the sample with the microscope objective and  $n$  the refractive index of the medium between the microscope objective and sample.  $d$  is the maximum diameter of the light cone at the objective and  $f$  the focal length of microscope objective. According to (7.1) focal diameters on the order of 200–300 nm can be achieved when using light in the visible range and typical objectives with a numerical aperture of around 1.2–1.4. Of course it is necessary to use microscope optics of very high quality that have as few optical imperfections as possible. Imperfections such as spherical, chromatic aberration, astigmatism and coma cause parallel light beams hitting the back aperture at different positions or having different wavelengths to not ideally focus at the same point. Only with high-quality optics and very well collimated laser beams is it possible to really achieve the resolution given by (7.1).

If a sample such as a natural fluorescing or a fluorescently labelled biomolecule, is within the focal region of a confocal microscope set-up and if its absorption spectrum corresponds to the laser excitation wavelength, it will be excited and will emit fluorescence. Because of the high numerical aperture of microscope objectives a large fraction of this fluorescence light is then collected by the same objective and leaves the back aperture as collimated beam (green beam in Figure 7.1). Basically, the light emitted from a small spot that is located exactly in the middle of the focus travels exactly the same optical path way as the

focused excitation light but in the opposite direction. It is also subject to all consequences that arise from its wave properties in the same way as the excitation light is. Therefore, even if the emission comes from a spot much smaller than the wavelength of the light (e.g. a single molecule) it cannot be resolved better than as a spot of the dimensions of  $r_0$ , as calculated with Eq. (7.1) using the wavelength,  $\lambda$ , of the emitted light. A typical microscope objective optimized for water as the immersion liquid between the objective and cover slip has a numerical aperture of  $\sim 1.2$  corresponding to a maximum half-angle of the light cone of approximately  $\sim 60^\circ$ . This corresponds to a collection efficiency of about  $\frac{1}{2}(1 - \cos \varphi) \sim 25\%$  of the light originally emitted by the fluorescing samples.

Usually, the excitation light is directed upon the back aperture of the microscope objective by means of a so-called dichroic mirror (Figure 7.1). The function of the dichroic mirror is to reflect light of wavelengths corresponding to the excitation source but to let pass light corresponding to the fluorescence wavelength of excited fluorescence markers (Figure 7.3). As a consequence, light almost exclusively originating from the samples fluorescence passes through the dichroic mirror. Usually another optical filter is placed in the optical path of the fluorescence light that only transmits wavelengths corresponding to the fluorescence spectrum of the sample and blocks very effectively wavelengths corresponding to residual scattered excitation light.

After the optical filter the collimated fluorescence beam is focused again by another lens. The highest probability of exciting fluorescence molecules is in the focal region of the microscope objective because here the intensity, which is the radiated power per area, is the highest (see also inset in Figure 7.1). However,

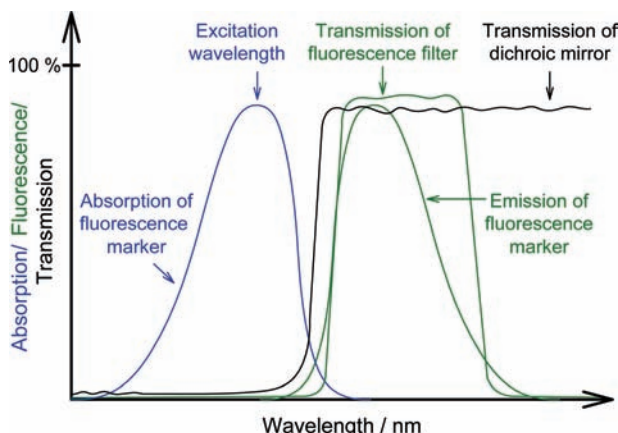


**Figure 7.3** Spectral characteristics of the dichroic mirror and optical filter used for the separation of fluorescence light from the excitation light. The dichroic mirror is designed such that it reflects the excitation light and transmits the fluorescence of the fluorescence marker. The optical filter also transmits a major part of the fluorescence light and

additionally blocks very effectively light of wavelengths corresponding to the excitation light. A set of dichroic mirror and optical filter is usually optimized only for a distinct fluorescence marker. As a consequence, the use of other fluorescence markers usually requires a different dichroic mirror and filter.

depending on the distance from the focal region there is of course still a significant excitation probability also at other positions than the focal region. To block light not emerging from the actual focal detection volume a small optical aperture, a so-called 'pinhole', is placed exactly in the image of the focus (cf. Figure 7.1). The function of the pinhole is sketched in Figure 7.4. Only light originating from the focal excitation region can fully pass the pinhole (see red spot a in Figure 7.4). Light from other excitation regions is suppressed because the aperture entirely or at least partially blocks the corresponding light path (green and blue spots b and c, respectively, in Figure 7.4). This special optical arrangement is why the detection scheme is called confocal: the detection is restricted to the area in the image that is confocal with the excitation focus. The final resulting observation volume is only  $\sim 200\text{--}300\text{ nm}$  in diameter ( $r_0$  in Figure 7.1) and  $\sim 500\text{--}1000\text{ nm}$  long ( $z_0$  in Figure 7.1) when using ideal optics and visible laser

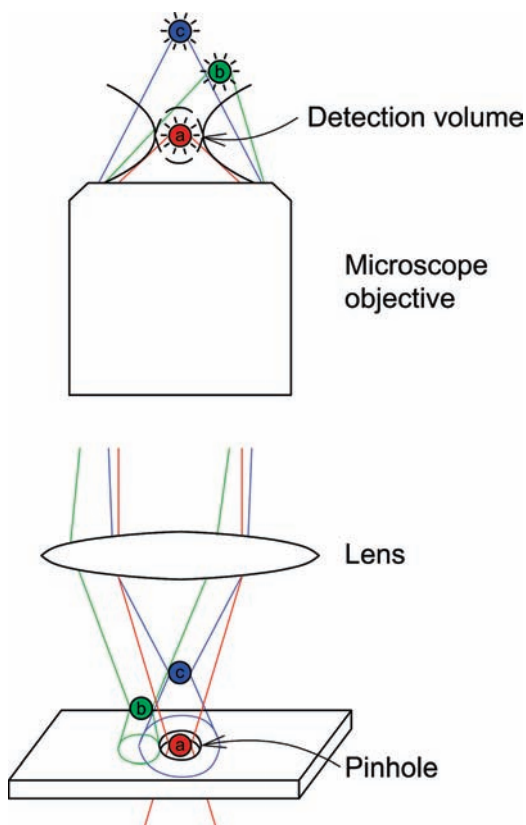


**Figure 7.4** Function of a pinhole. Only fluorescence light originating from the focal excitation volume of the microscope objective can fully pass the pinhole (fluorescence marker a). Fluorescence light originating from regions

other than the focal volume are either fully (fluorescence marker b) or partially (fluorescence marker c) suppressed because the aperture blocks their corresponding light path.

light. The actual size of  $r_0$  and  $z_0$  is predominantly determined by Abbes law, the quality of the optics and by the pinhole size and alignment. These dimensions correspond to a very small detection volume of less than a femtolitre ( $10^{-15}$  L). This small detection volume is the reason for the high optical sectioning capability of all methods based on confocal microscope set-ups.

After the pinhole, another lens focuses the fluorescence light on very sensitive light detectors. Usually, photomultiplier tubes (PMTs) or avalanche photodiodes (APDs) are used, which detect single photons with a time resolution of less than nanoseconds. APDs can detect up to  $\sim 90\%$  of all photons that are focused onto their sensitive area as single events. Because of the high detection efficiency and the large reduction in background signals confocal setups even allow us to monitor the passage of single fluorescently labelled biomolecules diffusing through the focal volume. In Section 9.2 we will discuss further requirements and applications for such optical single-molecule detection methods.

### 7.2.2

#### Laser Scanning Microscopy

The focal detection volume of a confocal set-up can be placed on any spot of a biological sample when the sample support (cover slide) is connected to a three-dimensional (3D) translation stage. Then, in principle, all fluorescence methods described in Chapter 3 can be applied at individual spots of the biological sample. If the 3D translation stage is used to systematically scan the sample, 3D pictures of the chosen fluorescence parameter can be constructed. Such methods are called confocal laser scanning microscopy. It is also possible to scan the focus through the sample by systematically tilting the angle of the collimated excitation beam by movable mirrors mounts (Figure 7.5) instead of moving the sample. When following the optical path of excitation and fluorescence light for the mirror positions 1., 2. and 3. in Figure 7.5 it becomes obvious that the path way of the fluorescence light after the dichroic mirror always stays the same even though the excitation and detection focus are both moving together through the sample. Thus, if a lens and a pinhole are placed in the fluorescence light path after the dichroic mirror, the pinhole also always remains confocal with the excitation and detection focus even though both foci are moving together through the sample and thus any detector can remain at the same position. By additionally scanning the distance of the sample from the microscope objective it is again possible to construct three-dimensional fluorescence pictures. The advantage of changing the focal position by movable mirrors is that the sample can be scanned much faster than by moving the entire sample itself.

### 7.2.3

#### Wide-Field Fluorescence Microscopy

For fluorescence microscopy, excitation of a larger sample volume is also possible. The excitation of a larger area in the focal region can be achieved, for

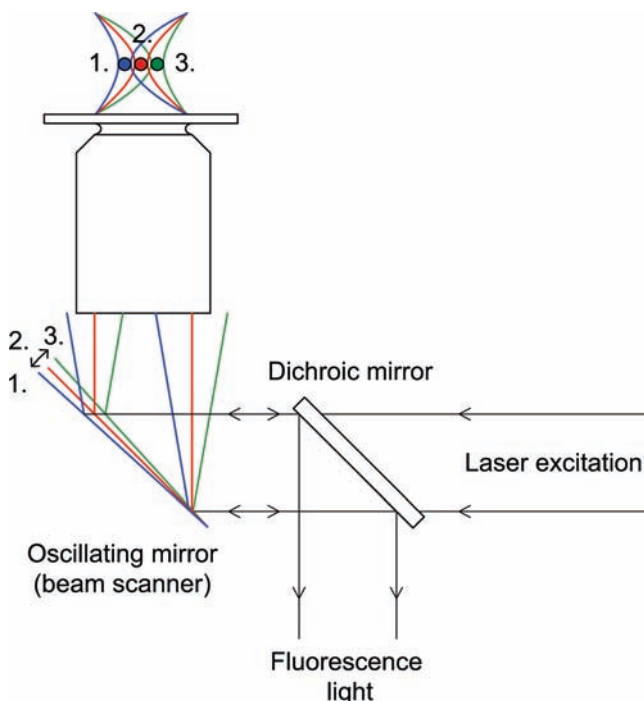


**Figure 7.5** A beam-scanner is based on a mirror that can be very quickly tilted. This allows rapid scanning of the focus through the sample. If the mirror is moved in an appropriate way the optical path way of the

fluorescence light after the beam-scanner does not change and the pinhole of a confocal set-up can remain at the same position during scanning.

example, by slightly focusing the excitation beam on the back aperture of the microscope objective (Figure 7.6). Instead of a pinhole in the focal image plane, usually, two-dimensional (2D) detectors such as charged coupled devices (CCDs) are used. CCDs can also register up to  $\sim 90\%$  of the irradiated photons but only with significantly lower time resolutions than APDs.

In general, such an optical arrangement is referred to as wide-field fluorescence microscope. An important advantage of wide-field fluorescence microscopy is that it allows us to record the entire 2D fluorescence pictures in one shot. Since no collimated excitation beam is necessary when no diffraction limited focusing is required, excitation sources other than lasers can also be used. Important examples are mercury lamps and light-emitting diodes. An important drawback of wide-field microscopy is that the resolution and depth of field is significantly worse than for confocal detection technologies because fluorescence light from above and below the focal plane also reaches the detector.

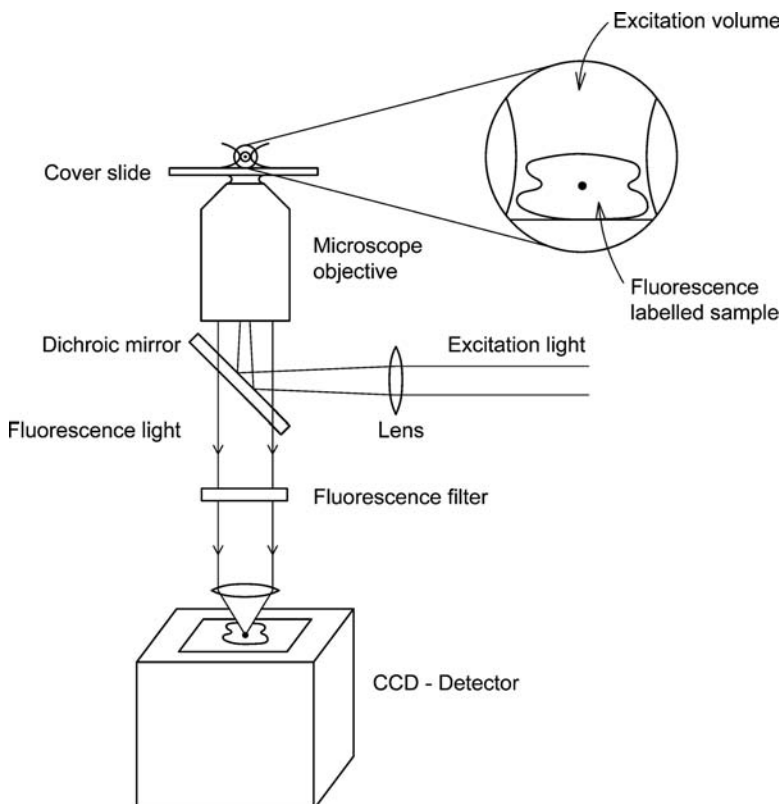


Figure 7.6 Wide-field fluorescence microscope.

### 7.3

#### Total Internal Reflection Fluorescence Microscopy

For some applications the use of total internal reflection fluorescence (TIRF) microscopy is an advantageous alternative approach. In TIRF only fluorescence from molecules that are in the direct vicinity of the interface between the glass support and the aqueous sample itself is sensitized (Figure 7.7). Let us briefly discuss the physical mechanisms of this surface excitation. When light reaches a surface between two optically transparent but different materials, such as glass and water, under a very narrow angle, total reflection of the light can occur. The critical angle under which such total reflection occurs depends on the refractive indices of the two materials,  $n_1$  and  $n_2$ :

$$\cos \alpha_C = \frac{n_2}{n_1} \quad (7.3)$$

$n_1$  must be larger than  $n_2$ . (7.3) is equivalent to Snell's law (9.26) which we will discuss in more detail in the section on optical tweezers in Chapter 9 (Section 9.4).

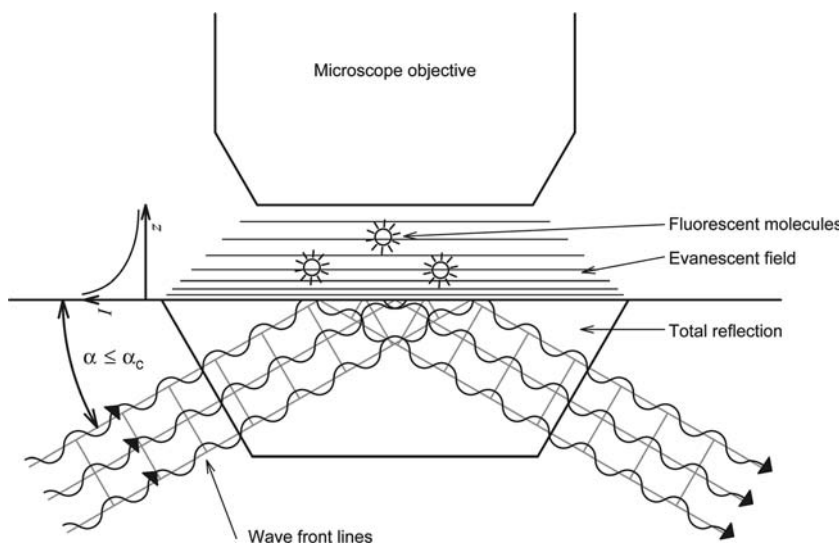


**Figure 7.7** Principle of total internal reflection fluorescence (TIRF) microscopy. Only fluorescence of labelled biomolecules in the direct vicinity of the glass/sample interface contributes to the observed TIRF images.

For a surface between glass ( $n_1 \sim 1.52$ ) and water ( $n_2 = 1.33$ ) the angle under which total reflection occurs must be smaller than a critical angle of  $\alpha_C \sim 29^\circ$ . TIRF is based on the fact that even though the light waves are totally reflected at the surfaces, its oscillating electric-field component still reaches to some extent into the other material. This residual electric field is also called the evanescent field. For visible light it reaches about 100–200 nm into the other material and decays exponentially:

$$I(z) = I(0) \cdot e^{-\frac{z}{d}} \quad \text{with} \quad d = \frac{\lambda}{4\pi \sqrt{\left(\cos \alpha / \cos \alpha_C\right)^2 - 1}} \quad (7.4)$$

Here,  $z$  is the distance from the reflecting surface (see Figure 7.7),  $\lambda$  is the excitation wavelength and  $\alpha$  is the actual angle of the totally reflected excitation light with the reflecting surface. The electric-field component of the evanescent field oscillates with same frequency as the reflected light. Fluorescently labelled biomolecules with the correct orientation of their transition dipole moment can now be excited by this evanescent light field based on the same principles as normal excitation. In TIRF the fluorescence is then collected with a microscope objective and typically detected with a CCD. In some TIRF set-ups the microscope objective itself is used to direct the excitation light under a very narrow angle onto the surface (Figure 7.8). In these set-ups this is achieved by illumination of only the outermost regions of the objectives back aperture with collimated excitation light. Since light focused from the outermost regions of the

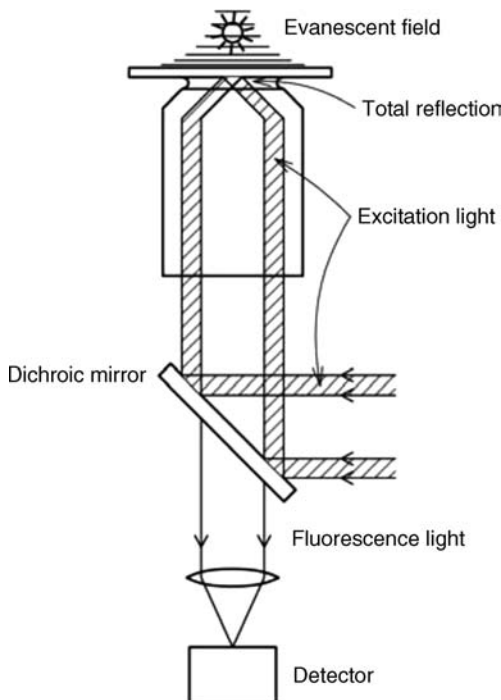


**Figure 7.8** In many TIRF microscopes the microscope objective itself is used for the generation of the evanescent field. This is achieved by directing the excitation beam only to the far edges of the back aperture.

This results in very small incident angles at the glass/sample interface leading to total reflection and an evanescent field, similarly as depicted in Figure 7.7.

microscope objective has a very narrow angle with the cover slide/sample surface the necessary total reflection can be achieved.

The advantage of TIRF is that 2D fluorescence images can be obtained that originate only from labelled biomolecules in the direct vicinity of the glass/sample interface. Intrinsically, no background fluorescence from other regions contributes to the observed signals.

#### 7.4

#### Light-Sheet Microscopy

TIRF microscopy is a special technique that allows reduction of the background significantly by exciting only molecules in a very well defined, thin sheet in the sample. An obvious drawback of this approach is the fact that this sheet is restricted to the direct interface between coverslip and the sample. This disadvantage can be overcome by light-sheet microscopy techniques. Figure 7.9 illustrates this approach. The fluorescence of a labelled sample (placed, for

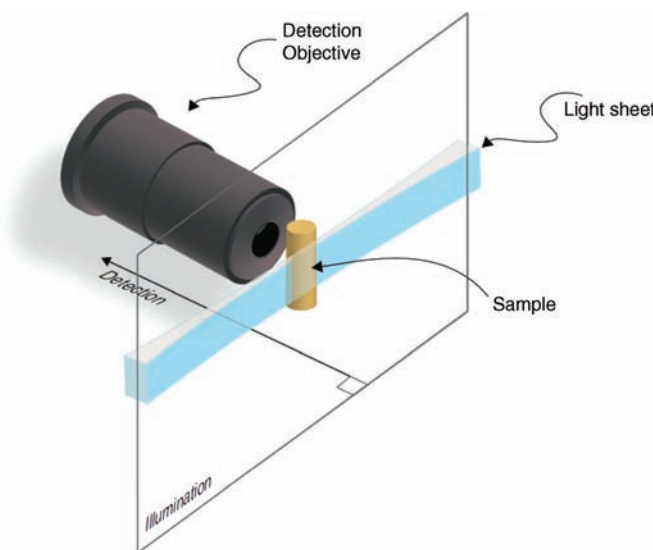


**Figure 7.9** Principle of light-sheet microscopy. A very thin excitation light sheet is generated in the sample perpendicular to the optical observation axis by either scanning a very thin beam up and down or by focusing

with a cylindrical lens. By this way only sections of the sample are observed which improves resolution, sectioning capabilities and decreases photobleaching. Source: Tomer 2011. Reproduced with permission of Elsevier.

example, within the cylindrical sample holder) is detected with a microscope objective similarly as in a wide-field set-up (Figure 7.6). The main difference is that the sample is illuminated by a thin light sheet perpendicular to the detection axis. One way to generate the illumination sheet is by scanning a diffraction-limited thin pencil beam perpendicular to the observation axis through the sample. Another way is to focus a Gaussian beam only in one dimension by using, for example, a cylindrical lens. As a consequence, of the light sheet illumination sectional views of the sample can be dissected (Figure 7.10). These views can be taken at different depths of the sample, which allows reconstructing a very accurate 3D-representation of the object.

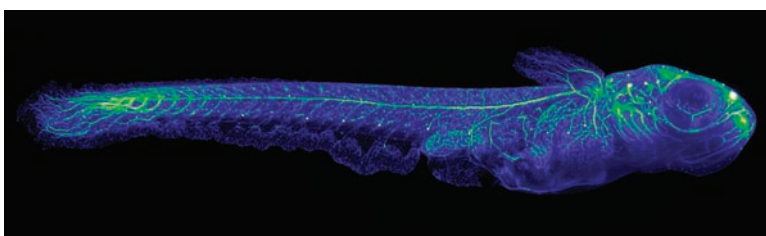


**Figure 7.10** Example of an image taken with a light-sheet microscope. Shown is a juvenile Medaka fish, which occurs in southeast Asia. Copyright EMBL/P.Keller & E.Stelzer.

The diffraction-limited thickness of the light sheet can be derived using the same principles that led to Abbe's law. As a consequence, an intrinsic trade-off exists between the size of the field-of-view in which the sheet's thickness remains sufficiently uniform (compare with Figure 7.9) and the minimal central thickness of the sheet. The larger the half-angle,  $\varphi$ , of the focused light sheet the smaller the central thickness of the sheet. From  $\varphi$  the thickness can be estimated using Eq. (7.1). However, obviously a larger angle,  $\varphi$ , will also result in a smaller area in the light sheet of sufficiently uniform thickness. Typically, lenses with numerical apertures of  $\sim 0.1$  are used, corresponding to a full illumination light cone angle of  $\sim 10^\circ$  or an half-angle of  $\varphi \sim 5^\circ$  for wavelengths of  $\lambda \sim 488$  nm and refractive indices of  $n \sim 1.33$ . This can be achieved with lenses having a focal length of  $f \sim 25$  mm and results in central thicknesses of the light sheet of  $> \sim 2$   $\mu\text{m}$ . Under these conditions the field-of-view of the sheet's area having a sufficiently uniform thickness has a dimension of  $\sim 60$   $\mu\text{m}$  in size. Clearly, the thickness of the sheet is much greater than that of the evanescent field in TIRF microscopy. However, the big advantage of light-sheet microscopy is the possibility to record real-time 3D images of living organisms with acquisition times of better than 1.5 billion voxels (volumetric pixel) per minute. This very high 3D-data acquisition capability allows, for example, for observing and recording globally the cell division in an entire, living zebra fish.

### Problems

- 7.1 In the inset of Figure 7.1 the characteristic dimensions of a confocal detection volume are defined by the axial and lateral resolution,  $z_0$  and  $r_0$ , respectively. What are the most important factors that determine the magnitude of these two parameters?
- 7.2 What is the diffraction-limited resolution of a microscope objective with a numerical aperture of 1.2 when using light of 400, 600 and 800 nm? How does the resolution change when using a microscope objective with a numerical aperture of 1.0 or 1.33? What are the collection efficiencies of microscope objectives with a numerical aperture of 1.0, 1.2 or 1.33? Assume that a water immersion objective is used and the refractive index of water is 1.33.
- 7.3 Explain why different angles of collimated beams entering or exiting the back aperture of a microscope objective (Figure 7.5) correspond to a lateral shift of the excitation or emission focus, respectively. Describe the microscope objective as a single lens and use ray optics for your explanation. Discuss the beam path for both excitation and emission. In what direction does the focus shift if the excitation beam is not collimated but is slightly divergent or focused?

- 7.4 Explain why slightly focusing the excitation beam for wide-field fluorescence microscopy allows illumination of a larger area in the focal region but still enables us to detect the fluorescing object with diffraction-limited resolution.
- 7.5 In a distinct TIRF microscope an excitation wavelength of  $\lambda \sim 488$  nm is used and the angle of the reflected excitation light with the reflecting surface is  $\alpha = 20^\circ$ . Calculate the distance from the surface by which the intensity of the evanescent field drops to 50% when assuming for the refractive indices of glass and water  $n_1 \sim 1.52$  and  $n_2 = 1.33$ , respectively.
- 7.6 In light-sheet microscopy there exists a trade-off between the size of the field-of-view in which the sheet's thickness remains sufficiently uniform and the minimal central thickness of the sheet. Calculate the central thickness of the light sheet when a lens with a numerical aperture of 0.1 and a focal length of  $f \sim 30$  mm, an excitation wavelength of  $\lambda \sim 532$  nm and a medium with a refractive index of  $n \sim 1.33$  is used. Try to estimate the approximate thickness of the light sheet in a distance of about 30  $\mu\text{m}$  from the focus by using ray optics.

## Bibliography

### General

- Allan, V. (ed.) (2000) *Protein Localization by Fluorescence Microscopy: A Practical Approach*, Oxford University Press, Oxford.
- Bradbury, S. and Evenett, P. (1996) *Contrast Techniques in Light Microscopy*, BIOS Scientific Publishers, Oxford.
- Kohen, E. and Hirschberg, J.G. (1989) *Cell Structure and Function by Microspectrofluorometry*, Academic Press, San Diego.
- Pawley, J.B. (ed.) (2006) *Handbook of Biological Confocal Microscopy*, Springer, Berlin.
- Periasamy, A. (ed.) (2001) *Methods in Cellular Imaging*, Oxford University Press, Oxford.
- Rost, F. and Oldfield, R. (2000) *Photography with a Microscope*, Cambridge University Press, Cambridge.
- Rizzuto, R. and Fasolato, C. (eds) (1999) *Imaging Living Cells*, Springer, Berlin.
- Sheppard, C.J.R. and Shotton, D.M. (1997) *Confocal Laser Scanning Microscopy*, BIOS Scientific Publishers.

Slavík, J. (ed.) (1998) *Fluorescence Microscopy and Fluorescent Probes*, vol. 2, Springer.

Stevens, J.K., Mills, L.R. *et al.* (eds) (1994) *Three-Dimensional Confocal Microscopy: Volume Investigation of Biological Systems*, Academic Press, San Diego.

Wang, X.F. and Herman, B. (eds) (1996) *Fluorescence Imaging Spectroscopy and Microscopy*, John Wiley & Sons, Inc.

Wilson, T. and Sheppard, C. (1984) *Theory and Practice of Scanning Optical Microscopy*, Academic Press, Orlando.

### Specific

#### TIRF

- Axelrod, D. (1999) Surface fluorescence microscopy with evanescent illumination, in *Light Microscopy in Biology*, (ed. A. Lacey), Oxford University Press, New York, pp. 399–423.
- Tokunaga, M., Kitamura, K. *et al.* (1997) Single molecule imaging of fluorophores and enzymatic reactions achieved by objective-type total internal reflection

- fluorescence microscopy. *Biochem. Biophys. Res. Commun.*, **235**, 47–53.
- Tamm, L. (1993) Total internal reflectance microscopy, in *Optical Microscopy: Emerging Methods and Applications*, (eds B. Herman and J. Lemasters), Academic Press, New York, pp. 295–337.
- Light-sheet microscopy**
- Keller, P.J., Schmidt, A. D. *et al.* (2008) Reconstruction of Zebrafish early embryonic development by scanned light-sheet microscopy. *Science*, **322**, 1065–1069.
- Keller, P.J. and Stelzer, E.H.K. (2008) Quantitative *in vivo* imaging of entire embryos with digital scanned laser light sheet fluorescence microscopy. *Curr. Opin. Neurobiol.*, **18**, 624–632.
- Pampaloni, F., Ansari, N. *et al.* (2013) High-resolution deep imaging of live cellular spheroids with light-sheet-based fluorescence microscopy. *Cell Tissue Res.*, **352**, 161–177.
- Reynaud, E.G., Kržič, U. *et al.* (2008) Light sheet-based fluorescence microscopy: more dimensions, more photons, and less photodamage. *HFSP J.*, **2** (5), 266–275.
- Tomer, R., Khairy, K. *et al.* (2011) Shedding light on the system: studying embryonic development with light-sheet microscopy. *Curr. Opin. Genet. Dev.*, **21** (5), 558–565.

**8**

## Super-Resolution Fluorescence Microscopy

Super-resolution fluorescence microscopy has become an essential part of many modern biophysical studies. Super-resolution fluorescence microscopy is the observation of fluorescently labelled structures at resolutions higher than the diffraction-limited resolution as defined in the previous chapter by the law of Abbe (Eq. (7.1)). From this law it follows that the best resolution one can achieve in traditional fluorescence microscopy is not better than  $\sim 200$  nm. Unfortunately, this is by far larger than the dimensions of most biomolecules. Typical proteins, for example, are not larger than 10 nanometres in size. The low resolution in comparison to typical biomolecular dimensions prevented the investigation of many important processes on the biomolecular level by fluorescence microscopy. In recent years, however, far-field fluorescence microscopy techniques have been developed that are able to achieve resolutions even beyond the diffraction limit as calculated by Abbe's law.

This enables us to bridge the gap between electron- and X-ray microscopic techniques and conventional fluorescence microscopy. Whereas the former allows resolution of individual proteins, but only under nonphysiological conditions, the latter allows observation of living organisms and dynamical biological processes, but at the cost of resolutions not better than corresponding to the dimensions of typical cell organelles. In contrast, super-resolution fluorescence microscopy allows observation of living organisms or other samples under much more physiological conditions, while still providing resolutions that allow the observation of structures much smaller than the diffraction limited value of  $\sim 200$  nm. In this chapter we will first discuss two major basic principles that enable us to break the diffraction-limited resolution barrier in fluorescence microscopy and their physical background. The first principle was introduced as stimulated emission depletion microscopy (STED) and is based on narrowing the focal volume that is exciting molecules in laser scanning microscopy (Chapter 7.2.2) significantly. The second principle is called photoactivated localization microscopy (PALM) or stochastic optical reconstruction microscopy (STORM) and is based on the subsequent observation and localization of single fluorescence markers with nm accuracy in a wide-field microscope. Based on and besides these two major approaches many further developments exist that will be discussed in the subsequent sections of this chapter. Finally, advantages and

limitations of these techniques will be discussed and a scheme will be provided that helps to decide which technique is best suited for which imaging aim.

### 8.1

#### Stimulated Emission Depletion (STED) Microscopy

STED was first developed based on a physical process called stimulated emission. Stimulated emission, together with absorption and spontaneous emission, (see chapter 1), are the three fundamental interaction possibilities of photons with electronic states of molecules. If a photon is illuminating a molecule in the excited state and the photon has an energy exactly corresponding to a certain transition,  $S_1^{v'=0} \rightarrow S_0^{v'' \geq 0}$ , of the molecule (Figure 8.1) it can actually induce this transition to occur. As a result of this stimulated emission a second photon having absolutely identical properties (e.g. with respect to propagation direction, wavelength and polarization) as the inducing photon is generated. The probability of this process is not low. Between the exact same two vibronic states the probability that a photon stimulates such an induced emission is exactly the same as the probability of a corresponding absorption.

Stimulated emission can be used to almost completely de-excite excited fluorescence markers. Such a de-excitation of an excited molecule is illustrated in Figure 8.1. First, the molecule is excited by photons having a wavelength,  $\lambda_{\text{Excitation}}$ , typically corresponding to the maximum of the absorption spectrum. Then as usual, quick vibrational relaxation into the vibrational ground state of the electronically first excited state,  $S_1^{v'=0}$ , occurs on the femto- to picosecond

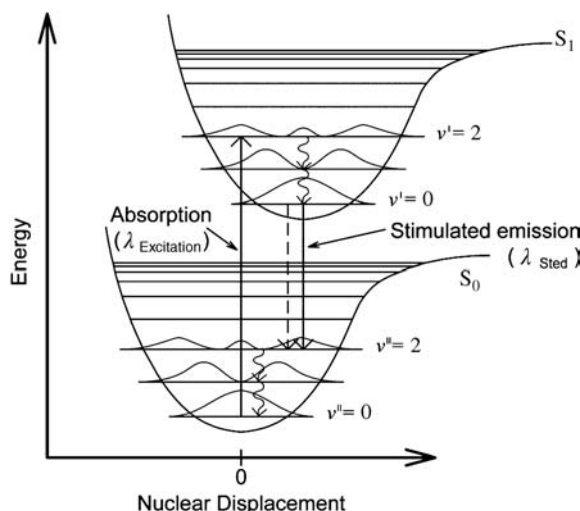


**Figure 8.1** Stimulated emission is one of three fundamental possibilities of the interaction of photons with electronic states of molecules. (The other two are absorption and radiative emission, e.g. fluorescence). In

STED-microscopy stimulated emission is used to almost de-excite excited fluorescence markers in regions outside the high-resolution fluorescence spot.

time scale (see also Chapter 1). Now the molecule is irradiated with redshifted photons with a wavelength,  $\lambda_{\text{STED}}$ , corresponding to the energy difference between this state and a vibrational state of the electronic ground state,  $S_0^{\nu''>0}$ . These photons can now induce the de-excitation of the molecule into the latter state,  $S_1^{\nu=0} \rightarrow S_0^{\nu''>0}$ , by stimulated emission. We will call these photons in the following STED photons. Since the state  $S_0^{\nu''>0}$  of the molecule corresponds to a vibrational excited state again it is very quickly depopulated by vibrational relaxation into the vibrational ground state of the electronic ground state of the molecule,  $S_0^{\nu''>0} \rightsquigarrow S_0^{\nu=0}$ . Because of this fast vibrational relaxation illumination of the molecules with STED photons results in an almost complete depletion of the first excited state when the intensity of the irradiation with STED photons is significantly higher than the irradiation intensity of the excitation.

In STED microscopy the possibility of a de-excitation of excited molecules at distinct locations is used to achieve a drastic resolution enhancement in fluorescence microscopy. In Figure 8.2 a typical STED set-up and the principle of this resolution enhancement is illustrated. A STED microscope is also based on a confocal microscope set-up. A collimated excitation beam is directed onto the back aperture of the microscope objective using a dichroic mirror that only reflects light of the wavelength,  $\lambda_{\text{Excitation}}$ . All other wavelengths are transmitted by this dichroic mirror. The result is first a normal excitation of the fluorescing molecules of the sample in the focal region of the set-up (blue in Figure 8.2). According to Abbe's law (Eq. (7.1)) the minimum diameter of the corresponding focus is not smaller than  $\sim 200$  nm for visible light. In addition, however, a collimated STED beam is also directed onto the back aperture of the microscope objective using a second dichroic mirror that only reflects light of the

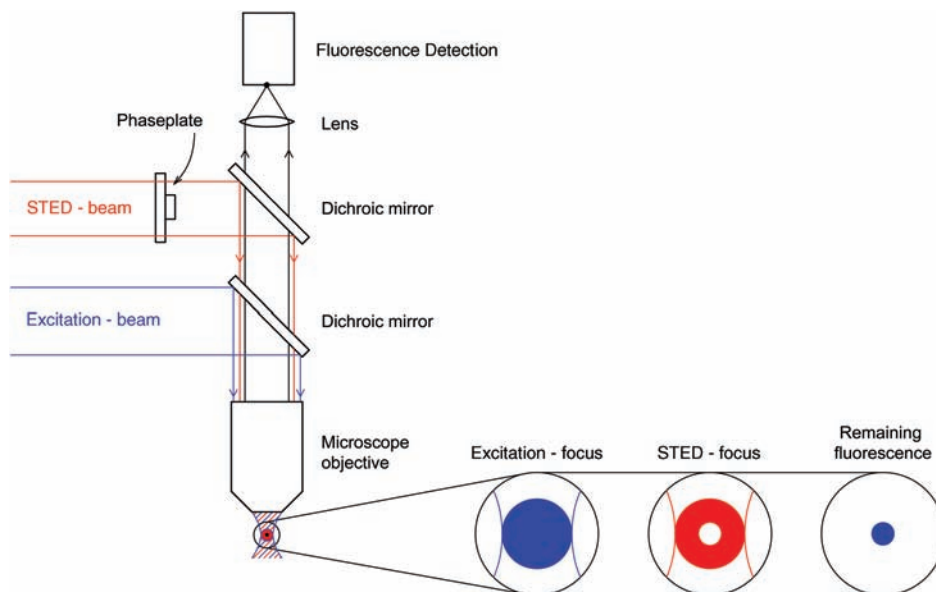
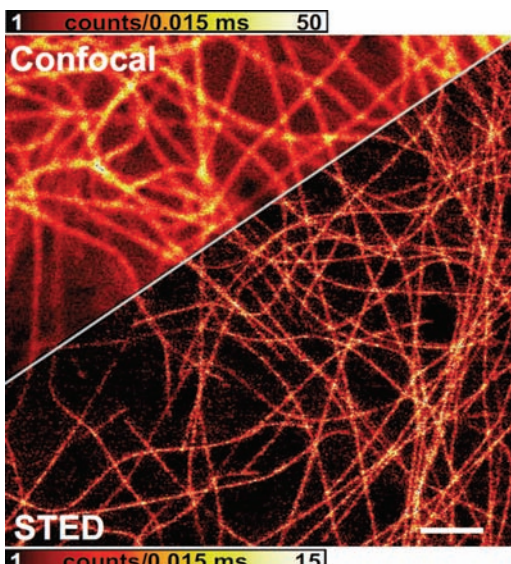


Figure 8.2 Basic principle of STED microscopy.

wavelength,  $\lambda_{\text{STED}}$ . The intensity of this beam is a lot higher than that of the excitation beam. Also, an optical element called a phase plate is inserted into the STED beam optical path way. This phase plate affects the wave front of the STED beam in such a way, that the corresponding STED focus has a central intensity 'hole' in the focal region of the microscopy set-up (doughnut-shape, red in Figure 8.2). This is because the phase plate is chosen such that one part of the light of the STED beam reaching the central spot of the focus is exactly destructively interfering with the other parts of the STED beam. As a consequence, the STED beam will deplete all excitation of fluorescence markers in the focal region but the central spot. The overall result is that only fluorescence can be observed from molecules that are in this central spot of the sample. The diameter of this remaining spot depends on the photophysical properties of the fluorescence dyes and most importantly on the intensity of the STED light. The larger the STED intensity the better the spatial resolution of the STED microscope. In principle, a STED microscope can realize unlimited resolution. However, due to the current limitations in the photostability of the fluorescent labels, the best resolutions which were achieved so far are on the order of  $\sim 10\text{--}20$  nanometres. This is a huge step in fluorescence microscopy because now objects can be resolved that have dimensions that are on the order of typical biomolecules or biomolecular structures such as proteins or membranes. Again, the biological objects can be scanned by this focus in order two construct highly resolved fluorescence images (Figure 8.3).



**Figure 8.3** Comparison of a conventional confocal with a STED image. Visualized are labelled microtubules inside a living kidney cell from kangaroo rats. The resolution improvement is purely physical in nature, which means without mathematical

processing of recorded data. Reprinted from Birk Hein, Katrin I. Willig, and Stefan W. Hell, PNAS, 105, 14271–14276 (2008), with permission of the National Academy of Sciences of the United States of America. Copyright (2008) National Academy of Sciences, U.S.A.

## 8.2

### Photoactivated Localization Microscopy (PALM) and Stochastic Optical Reconstruction Microscopy (STORM)

In contrast to STED, that is based on laser scanning microscopy (Section 7.2.2), Photoactivated localization microscopy (PALM) and stochastic optical reconstruction microscopy (STORM) are both based on wide-field or TIRF microscopy (Sections 7.2.3 and 7.3) and on the optical single-molecule detection of photoactivatable, photoconvertible or photoswitchable fluorescence markers (Figure 8.4). In Section 3.2.6 we have already discussed the possibility of the generation of fusion-proteins that are connected to fluorescence proteins such as the green-fluorescent protein. The location and behaviour of these fusion-proteins within the cells can then be imaged in fluorescence microscopy. The special photoactivatable, photoconvertible or photoswitchable fluorescence proteins used for PALM/STORM can be switched photochemically between two states in which they have different fluorescence properties. For example photoactivatable green fluorescent proteins (PA-GFP) can be switched on by a light-induced activation of the chromophore with light of  $\lambda_{\text{Switch}} \sim 405 \text{ nm}$  (Figure 8.4a). To then observe fluorescence from the switched-on FPs another excitation wavelength,  $\lambda_{\text{Excitation}}$ , is used. Other photoconvertible fluorescent proteins can be converted from green to red fluorescence by irradiating them with light of

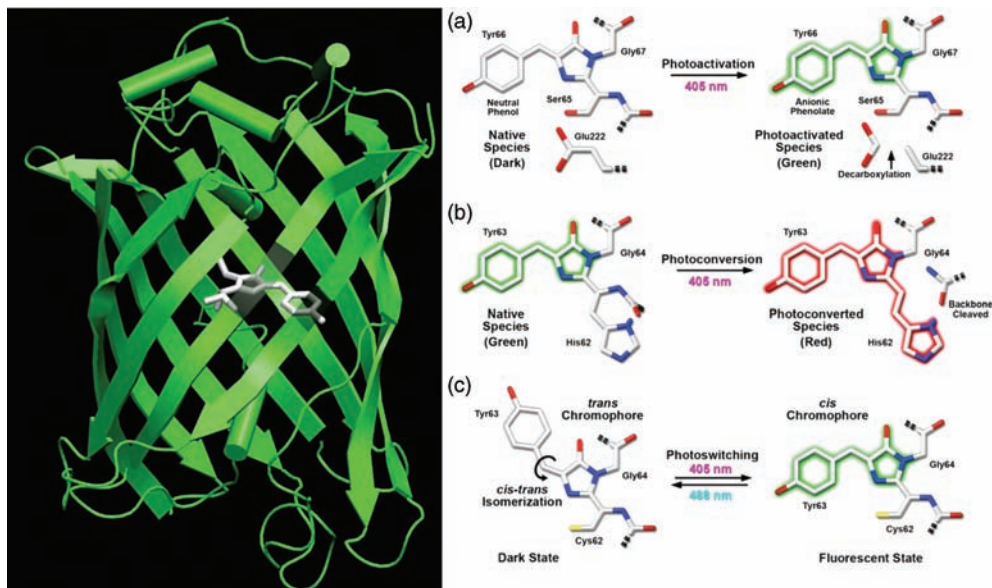


**Figure 8.4** The chromophore in special fluorescent proteins can be switched between two states by various different mechanisms. Adapted from Nathan C. Shaner, George H.

Patterso and Michael W. Davidson, the Journal of Cell Science, 120, 4247–4260 (2007), with permission of Company of Biologists Ltd.

certain wavelengths (Figure 8.4b). Examples are the fluorescent proteins EosFP and Kaede that show a shift in the emission spectrum from 516 to 581 nm and 518 to 580 nm, respectively. The underlying molecular mechanisms of photoactivation differ for different FPs. PA-GFPs, for example, undergo chromophore conversions from neutral to anionic states as a response to a photoinduced decarboxylation of Glu222, whereas in Kaede FPs light-induced cleavage between the amide nitrogen and  $\alpha$ -carbon atoms in a histidine residue and subsequent formation of a conjugated dual imidazole ring system occurs. Even reversible switching between on and off is possible with certain FPs (Figure 8.4c). A typical mechanism in such proteins is a *cis-trans* photoisomerization induced by two different switching wavelengths.

In PALM/STORM a sample labelled with these FPs is irradiated with only very little switching light of the wavelength,  $\lambda_{\text{Switch}}$  (Figure 8.5). The result is that at most one FPs within a diffraction-limited area of  $\sim 200$  nm in diameter switches from one state to the other. If using appropriate spectral filters only fluorescence originating from these few switched FPs can be observed, for example at the glass-sample surface of a TIRF imaging microscope and by using the excitation wavelength,  $\lambda_{\text{Excitation}}$  (compare with Figure 7.7 and 7.8, important requirements for the fluorescence detection of single molecules will be discussed in more detail in the section on optical single-molecule detection, Section 9.2). Again, the resolution of the observed fluorescence spots is limited by Abbe's law. As a consequence, the spots can only be detected as intensity distributions similar to a two-dimensional Gaussian distribution that have a diameter of  $\sim 200$  nm (indicated by the Gaussian peaks in Figure 8.5). However, even though these Gaussian-like intensity distributions have a diameter of  $\sim 200$  nm the *centre* of these spots can be determined with nanometre- accuracy. If they originate only from single fluorescing molecules this centre corresponds to the position of the fluorescing molecules (indicated by the lines and dots in the Gaussian peaks in Figure 8.5). So, in a first step, it is possible to determine the exact positions of the

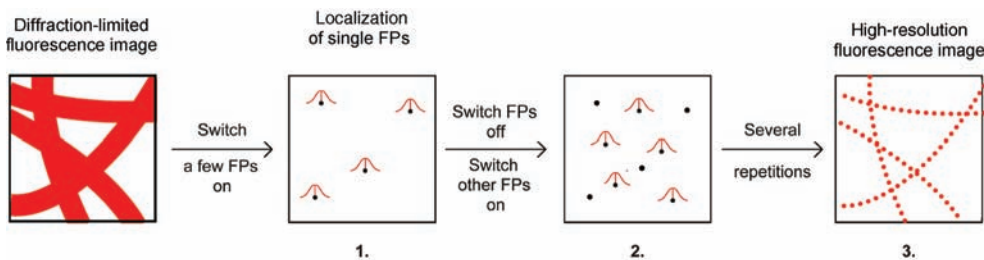


**Figure 8.5** Principle of photoactivated localization microscopy (PALM). 1. Red Gaussian peaks with black dots indicate photoactivatable fluorescent proteins that are currently observed. 2. Sole black dots indicate photoactivatable fluorescent proteins that are 'switched off' but for which the exact central

position has already been determined in a previous step. 3. By recording the centre position of all individual fluorescence proteins after each other (red dots) structural details become visible that cannot be discerned in a conventional diffraction-limited fluorescence image.

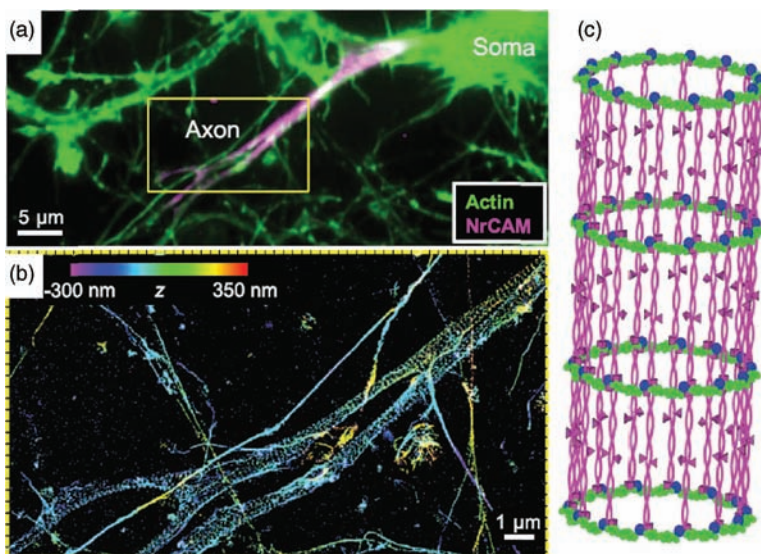


**Figure 8.6** (a) Conventional fluorescence image of labelled actin filaments in a neuron. (b) Super-resolution fluorescence image observed by STORM of the inset indicated by the yellow box. (c) The super-resolution fluorescence data revealed that the actin filaments

form a ring like structure that wraps around the circumference of neuron axons. From Ke Xu, Guisheng Zhong, Xiaowei Zhuang, *Science* 339, 6118, 452–456 (2013). Reprinted with permission from AAAS.

few switched FPs with a resolution on the order of only a few nanometres (1. in Figure 8.5). The localization accuracy is proportional to the square-root of the number of photons detected per FP. For example, 1000 photons detected from a single FP corresponds to a localization accuracy of  $\sim 10$  nm. Once the position of these FPs is determined they can be switched off, for example, by irreversible photobleaching or *cis-trans* photoisomerization. The entire procedure can then be repeated by switching on again a few isolated FPs. Because it is arbitrary which FPs are switched on by only little light of the wavelength,  $\lambda_{\text{Switch}}$ , now different FPs will fluorescence. Again, their positions can be determined with a resolution of a few nanometres (2. in Figure 8.5). After that, they can be switched off again using  $\lambda_{\text{Excitation}}$ . When this procedure is repeated several times, finally a total image, with sub-diffraction spatial resolution, can be constructed from the positions of all localized FPs (3. in Figure 8.5).

In Figure 8.6a a conventional fluorescence image of labelled actin filaments in a neuron (Figure 8.6a) is exemplarily compared with an inset of its super-resolution fluorescence image obtained by STORM (Figure 8.6b). These super-resolution fluorescence images revealed that the actin filaments form a ring-like structure that wraps around the circumference of neuron axons and are evenly spaced with a periodicity of  $\sim 180$  to 190 nm (Figure 8.6c). This observation would not have been possible either with an electron microscopic or with conventional fluorescence microscopy methods.

### 8.3

#### 3D Super-Resolution Fluorescence Microscopy

When STED and PALM/STORM were first applied both allowed the enhancement of the resolution in the  $x$  and  $y$  (lateral) direction (as defined in Figure 7.1) significantly below 100 nm. Today, the best reported lateral resolutions of biological samples are in the range of  $\sim$ 20–30 nm using STED-microscopy and of  $\sim$ 20 nm using the PALM/STORM approach. However, in the first STED as well as PALM/STORM set-ups the resolution in the  $z$  direction remained more or less diffraction limited, that is on the order of  $\sim$ 500 nm to 1  $\mu$ m when using visible light. Of course, it is highly desirable to observe the structures with high resolution in all three dimensions. In this section we will discuss extensions of STED as well as STORM/PALM that allow additionally enhancing the resolution also in the  $z$ -dimension.

##### 8.3.1

###### 3D-STED

In the first STED-set-ups the doughnut-like depletion patterns shown schematically in Figure 8.2 (red STED - focus) were actually only present in the  $x$ - $y$  plane as visualized in Figure 8.7 ( $\text{STED}_{x,y}$ ). In the  $z$ - $x$  plane (or  $z$ - $y$  plane) there was no depletion intensity along the central optical axis and therefore the excitation of molecules along this axis could not be restricted to a smaller volume in the  $z$

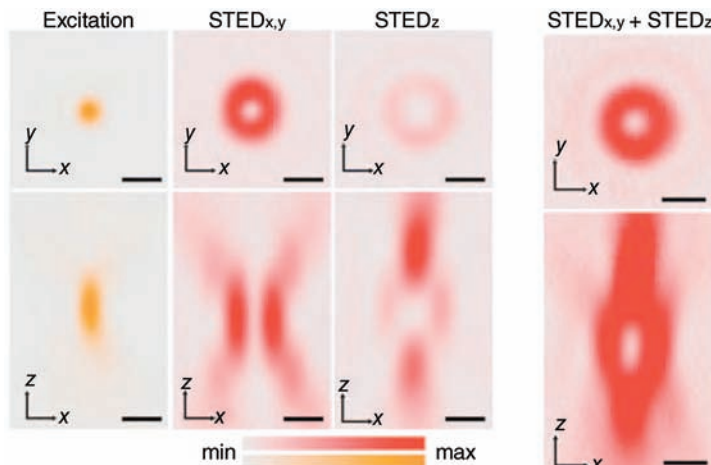


**Figure 8.7** Comparison of the focal intensity distribution of the excitation beam in STED-microscopy, (orange) a classical doughnut-like STED-pattern that results in a de-excitation confinement of excited molecules in the  $x$  and  $y$  directions ( $\text{STED}_{x,y}$ , axes as defined in Figure 7.1), a STED pattern that results in a de-

excitation confinement of excited molecules in the  $z$  direction ( $\text{STED}_z$ ), and a combination of both that results in an confinement in all three dimensions ( $\text{STED}_{x,y} + \text{STED}_z$ ). Source: Harke 2008. Reproduced with permission of American Chemical Society.

direction. However, using different phase-plate configurations it is possible to achieve an interferometric pattern in the focal area that has a predominant depletion light intensity along the optical axis but only above and below the focal plane ( $\text{STED}_z$  in Figure 8.7). Since this pattern has less intensity in the focal  $x$ - $y$  plane this axial depletion pattern is superimposed with the lateral STED  $x$ , $y$  depletion pattern to achieve real 3D-STED ( $\text{STED}_{x,y} + \text{STED}_z$  in Figure 8.7). With such a 3D-STED pattern a resolution of  $\sim 40$  nm in the  $x$ - $y$  plane and of  $\sim 125$  nm in the  $z$ - $x$  (or  $z$ - $y$ ) plane can be achieved.

When using two opposing objectives the effective numerical aperture can be further increased. With this approach – called isoSTED – a resolution of  $\sim 30$  nm can be achieved in all three dimensions.

### 8.3.2

#### 3D-PALM/STORM

To achieve high axial resolutions in PALM/STORM different approaches are used. All these approaches are based on different,  $z$ -dependent image intensity distributions detected from single molecules on the CCD camera that are observed when certain optical modifications are applied to the fluorescence microscope. For example, when adding a cylindrical lens in the detection light path, the intensity distribution of a single-molecule detected on the CCD is only a rotationally symmetric Gaussian-like spot when the molecule is exactly within the focal plane. As soon as it is positioned slightly above or below the focal plane, it has a more rod-like shape that depends in orientation and aspect ratio on the distance of the molecule from the focal plane (Figure 8.8).

When analysing this shape observed from the single molecules the  $z$ -position can be derived in addition to localization in the  $x$ - $y$  plane and a three-dimensional image can be reconstructed. Axial resolutions of better than  $\sim 50$  nm in the  $z$  direction while simultaneously having lateral resolutions of  $\sim 20$  nm in the  $x$ , $y$  direction can be achieved by this so-called astigmatism approach. In fact, the images presented in Figures 8.6 and 8.9 were observed with an extension of this approach by using two opposing objectives and the insets in Figure 8.9 show impressively how the ring-like actin structure of axons can be resolved in all three dimensions. As in isoSTED the use of two opposing objectives further increases the resolution observable with STORM/PALM to  $\sim 10$  nm in the  $z$  direction and  $\sim 20$  nm in the  $x$ - $y$  plane. This approach is sometimes also referred to as iPALM.

## 8.4

### Imaging of Live Cells

The super-resolution images shown in Figures 8.6 and 8.9 were observed using fixed cells, which implies they were dead. However, one big advantage of fluorescence microscopy over methods like electron microscopy is that the biology can be observed in living systems. The question arises as to what extent this is also

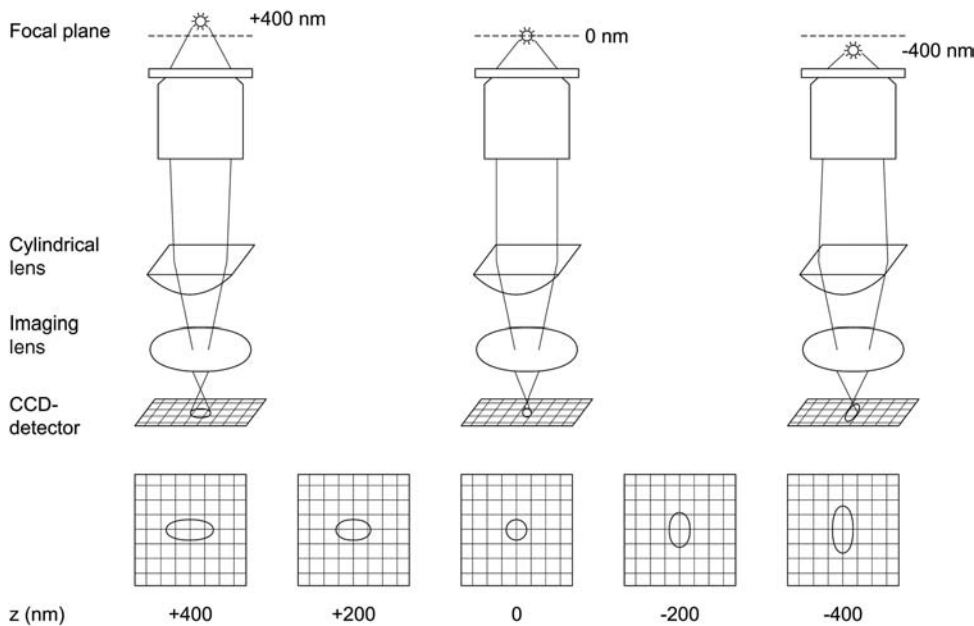


**Figure 8.8** When a cylindrical lens is used in the detection path of a TIRF microscope used for PALM/STORM (compare with Figure 7.8) then the image of a fluorescing single molecule is only circular, when it is located exactly within the focal plane. Displacements of this molecule in the z direction (axes as defined in

Figure 7.1) can be directly and quantitatively determined from the rod-like pattern. When localizing individual molecules in PALM/STORM (compare with Figure 8.5) this additional information can then be used for an accurate three-dimensional high-resolution reconstruction of the image.

possible when using super-resolution fluorescence microscopy. Four key aspects have to be considered here: 1. Observation duration, 2. Irradiation Intensity, 3. Imaging depths, 4. Labelling conditions.

#### 8.4.1

##### Observation Duration

Both principle approaches, STED and PALM/STORM can easily take several tens of seconds and even up to minutes when a larger field of view is to be observed with 3D resolution. In STED, scanning of the entire observation volume takes longer the smaller the effective focal detection volume becomes and the larger the entire two or three-dimensional field-of-view is. Thus, while the fastest scanning of a quite small two-dimensional field of view of  $\sim 2 \times 2 \mu\text{m}$  has been reported to take  $\sim 30$  ms, more typical fields of view of  $\sim 20 \times 20 \mu\text{m}$  usually takes several seconds and if a three-dimensional scan is required the times increases quickly more than ten-fold. PALM/STORM approaches, on the other hand, depend more critically on the number of switching cycles that are required

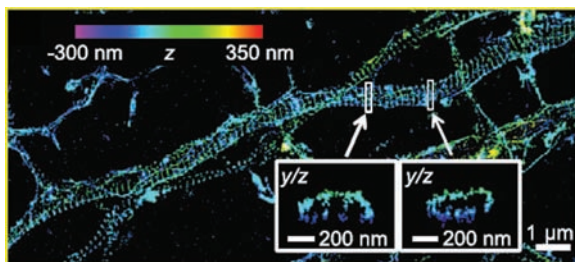


**Figure 8.9** Super-resolution fluorescence image observed by STORM of labelled actin filaments in a neuron using the 3D-astigmatism approach (Figure 8.8). The insets demonstrate that this approach allows high resolution also in sectional views including the z-axis and

visualize nicely the ring-like structure of the actin filaments that wrap around the circumference of neuron axons. From Ke Xu, Guisheng Zhong, Xiaowei Zhuang, *Science* 339, 6118, 452–456 (2013). Reprinted with permission from AAAS.

to observe enough molecules to resolve the structure under investigation. The so-called Nyquist criterion requires that the number of localized molecules must correspond to a point-to-point distance between them that is at most half as large as the structural features that shall be resolved. Since usually several thousands of camera frames are required to achieve this density PALM/STORM images typically take several tens of seconds. This is, however, independent of the two-dimensional field of view as long as the camera captures the entire field of view per camera frame. It is to some extent also independent of the z localization for a range of  $\sim 1 \mu\text{m}$  that is covered by astigmatism methods or similar, as illustrated in Figures 8.8 and 8.9. Obviously, long observation durations that are required to obtain a full image are an important obstacle when observing living cells that are quite dynamic. Often, at observation times exceeding 10 s the structure of living cells itself might have already changed on length scales that are significantly larger than the potential improvement in the resolution. So it depends on a combination of dynamical behaviour of the sample, the desired field of view as well as to what extent 3D information is required in a particular study to decide which of the methods is better suited.

#### 8.4.2

##### Irradiation Intensity

Higher irradiation intensities affect fluorescently labelled biological samples basically in two ways: 1. The fluorescence label is more quickly destroyed by photo-bleaching, thus preventing longer observation times or higher numbers of observation snap-shots and 2. The biological sample itself might be denatured thus severely affecting the actual biologically relevant question under investigation. Both effects also represent a major problem in conventional fluorescence microscopy but they become more severe when using super-resolution fluorescence microscopy and therefore represent an important limitation for live-cell imaging. A main difference in the two methods is that while STED imposes

extremely high intensities only at a very limited period of time at various spots of the sample PALM/STORM imposes much less peak intensity but requires significantly longer irradiation of the entire sample also in the  $z$  direction.

#### 8.4.3

##### **Imaging Depths**

Many fluorescence imaging studies that are done with living biological samples are done with cells that are directly attached to the surface of an optical transparent material such as cover-slips. However, often decisive processes in biological samples actually occur at significant depths within the entire organism, for example in nerve cells within deeper areas of the brain. Super-resolution methods are currently limited in this respect. An essential requirement for PALM/STORM approaches is the ability to detect single molecules. As outlined in more detail in Section 9.2 this requires an excellent signal-to-noise ratio that is usually significantly worsened when penetrating deeper into biological samples due to increasing background intensity. Therefore, most STORM/PALM studies are still done with TIRF illumination. This, of course, restricts the penetration depth to only a few hundred nanometres. In contrast, the focus generated in STED can penetrate significantly deeper into the sample and is theoretically limited by the working distance of the objective that is typically in the range of several hundreds of  $\mu\text{m}$  up to  $\text{mm}$  in special cases. However, the sensitive generation of the interference patterns as shown in Figures 8.2 and 8.7 becomes increasingly affected at deeper penetration depths due to the inhomogeneous nature of the sample itself. Thus, the deepest penetration depth reported for STED was so far also only  $\sim 100\text{ }\mu\text{m}$  and the resolution enhancement at this depth was not as significant as at small penetration depths.

#### 8.4.4

##### **Labelling Conditions**

Fluorescence investigations of living cells require special labelling conditions. For example, it is rather difficult to apply the chemical labelling strategies introduced in Section 3.2 to living cells because of the lack in specificity and the question of how chemical treatments are affecting the vitality of the cells and how the chemicals should be brought into the cells. Also, classical immunolabelling can cause artifacts in living cells such as protein extraction or relocalization. One of the most common ways in super-resolution fluorescence microscopy is the use of fluorescent fusion-proteins as described in Section 3.2.6. STED requires an FP that can be reasonably well switched off by stimulated emission and that is sufficiently photostable in order to persist comparatively high STED peak intensities. For example, yellow fluorescent protein (YFP, which is a genetic mutant of GFP, Figure 3.7) has been used to image neurons in the brain of a living mouse. PALM/STORM approaches rely on photoconvertible, photoswitchable or

photoactivatable proteins such as shown in Figure 8.4. While FPs currently are considered the fluorescent labels of choice for live-cell imaging, it should be noted that the use of fluorescent proteins also has limitations for live-cell imaging. On the one hand, the proteins of interest that are fused with the FPs might have lost their natural biological function and on the other hand, they might be expressed in an abnormal location within the organism.

## 8.5

### Multicolour Super-Resolution Fluorescence Microscopy

The example images shown in Figures 8.6 and 8.9 also represent an example in which different parts or proteins are labelled by different colours. Multicolour labelling strategies are often desired in fluorescence microscopy because frequently it is the interaction between two or more different biological key players that explains the functioning of a particular process under investigation. In STED, two or more different labels require at least two light beams for each label, one excitation and one depletion beam. In addition, each of the depletion beams must be modified in a way that a nanometric focal depletion structure is present. Even though the focal regions for different labels don't have to be overlapped perfectly because the detection pathways are separated anyway (similar as shown in Figure 9.16) the overall optical arrangement can quickly become quite demanding. Therefore, so far only two-colour STED imaging was reported.

Since the optical requirements for the PALM/STED approach are far less restrictive here also three labels can be separated. Of course very special dichroic mirrors that are able to transmit three different emission wavelengths while reflecting all excitation as well as activation wavelengths become necessary. Further dichroic mirrors that combine all irradiating and separate all emission wavelengths are also required.

## 8.6

### Structured Illumination Microscopy

As outlined above, both super-resolution fluorescence microscopy approaches so far discussed can yield superior optical resolution but are sometimes limited in comparison to conventional fluorescence microscopy, for example because they require special photoswitchable fluorescence markers or high illumination intensities. A compromise between high resolution and these limitations is represented by approaches that are generally named structured illumination microscopy (SIM). SIM can be applied basically to all samples and problems accessible by conventional fluorescence microscopy. A significant resolution enhancement is still provided albeit not as high as in STED or PALM/STORM approaches. In Figure 8.10 the basic principle of the approach is illustrated.

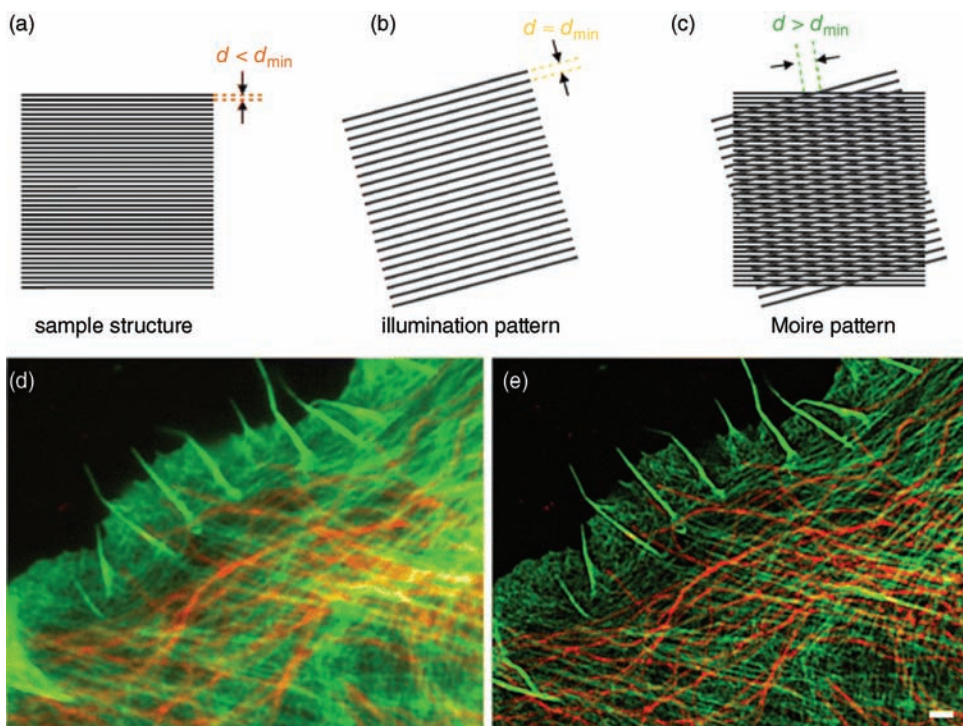


**Figure 8.10** Principle of structured illumination microscopy (SIM). When illuminating a sample structure of subdiffraction limited dimensions (a) with a periodic, diffraction limited illumination pattern (b) the resulting Moiré pattern (c) contains information about the subdiffraction-limited sample structure.

This approach can be used to improve the resolution of conventional fluorescence images (d) twofold (e) in all three dimensions without the use of special fluorescence markers or higher illumination intensities. Source: Hedde 2010. Reproduced with permission of Springer Science and Business Media.

Figure 8.10a illustrates exemplarily a hypothetical sample with a line pattern (for example of fixed fluorescence dyes) with distances between the lines that are smaller than the diffraction limit, on the order of  $r_o$  as defined by Abbe's law (7.1). By using interference effects it is possible to generate an illumination structure that also consists of a periodic pattern in which the intensity maxima run along parallel lines that are separated by a distance corresponding to the diffraction limit (Figure 8.10b). In Figure 8.10b only the maximum intensity lines of this illumination pattern are shown for better visibility but in reality the pattern consists of periodically increasing and decreasing intensities perpendicular to the maximum intensity lines. When the structure shown in Figure 8.10a is now illuminated with this tilted illumination pattern shown in Figure 8.10b the resulting image contains periodic intensity variations not only in the direction of the illumination pattern but also in other directions (Figure 8.10c). Such a resulting

pattern is called a Moiré pattern. The period length and direction of this additional intensity variation depends directly on the angle of the illumination pattern with the sample structure and the period length within the sample structure. The Moiré pattern shown in Figure 8.10c gives an idea of how the period length and direction of this additional intensity variation depends on the angle and period length of the sample structure. This very basic example illustrates that additional information can be obtained about the original sample structure that goes beyond the diffraction limit when the sample is illuminated with structured patterns. When illuminating biological samples with illumination patterns as shown in Figure 8.10d the additional information is no longer obvious to the human eye. However, the resolution-enhanced SIM image is constructed with computational help from a set of images of a certain sample that has been illuminated with the illumination pattern at various angles. Even though the maximum resolution enhancement that can be achieved in this way is only a factor of two in all three dimensions the example shown in Figures 8.10d and e demonstrates that this enhancement already yields significant more structural insights than a conventional fluorescence image.

## 8.7 SOFI

Another approach for the improvement of the resolution of fluorescence images that does not require switchable fluorescence markers or demanding optical set-ups is based on the information that is contained in intensity fluctuations observed from fluorescing nanoparticles (see Section 12.2) or also normal fluorescence dyes. Individual nanoparticles, also called quantum dots, as well as conventional fluorescence markers typically ‘blink’ stochastically on different timescales. SOFI (super-resolution optical fluctuation imaging) takes advantage of the fact that these fluctuations occur statistically independent for each quantum dot or fluorescence marker (Figure 8.11).

Rather than localizing individual fluorescence markers by turning them on and off like in PALM/STORM approaches, SOFI spatially disentangles the different fluorescence contributions from different statistically independently ‘blinking’ fluorescence sources.

Figure 8.11 shows schematically the principle of SOFI. Figure 8.11b illustrates the intensity distribution recorded by individual CCD pixels for two quantum dots marked in the inset of Figure 8.11a. The dots are closer than the diffraction limit resulting in a significant spatial overlap of their fluorescence signals. Figure 8.11c shows that due to this overlap the average intensity in the pixel in the middle between the two quantum dots (assigned by  $i$ ) is higher than in image positions closer to the two quantum dots (e.g. at  $i-1$  and  $i+1$ ). However, the magnitude of the blinking fluctuations relative to this average intensity is smaller at this position (illustrated in Figure 8.11d by

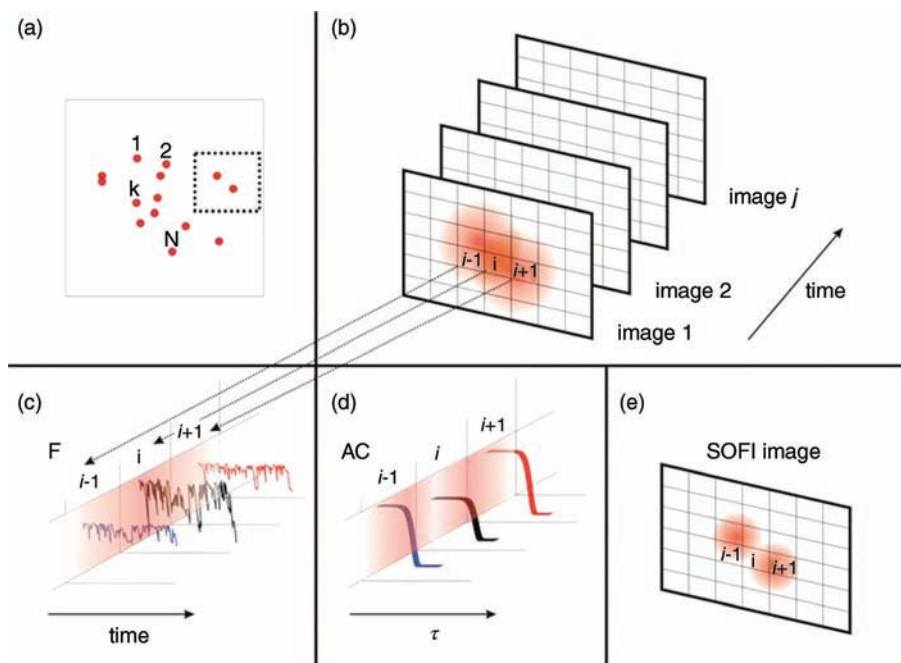


**Figure 8.11** Principle of super-resolution optical fluctuation imaging (SOFI). Individual quantum dots as well as conventional fluorescence markers typically 'blink' stochastically on different timescales. SOFI spatially

disentangles the different fluorescence contributions from different statistically independently 'blinking' fluorescence sources. Source: Dertinger 2009. Reproduced with permission of PNAS.

the amplitude of an autocorrelation function, AC, such as described in Section 9.3.1) because more quantum dots contribute and therefore the fluctuating signal from one quantum dot is partially averaged out by fluctuations from the other quantum dot. Thus, the higher the number of statistically blinking emitters that contribute to a signal the smaller the relative fluctuations become, similar as described in detail in Section 9.3.1 (Figure 9.10). These fluctuations are now analysed by SOFI and an image of the magnitudes of the fluctuations provides an image of the underlying structure with improved resolution (Figure 8.11e). It is also possible to correlate fluctuations of neighbouring pixels by methods similar as described in Section 9.3.5, (XC-SOFI). Such cross-correlation information helps to further assign the intensities to different signal sources at different positions. The general advantage of the method is that it requires only a conventional fluorescence microscope with a fast camera that is able to resolve the intensity fluctuations from the fluorescence markers in the image. Figure 8.12 demonstrates the resolution improvement that is possible by using a conventional wide-field microscope and SOFI analysis.

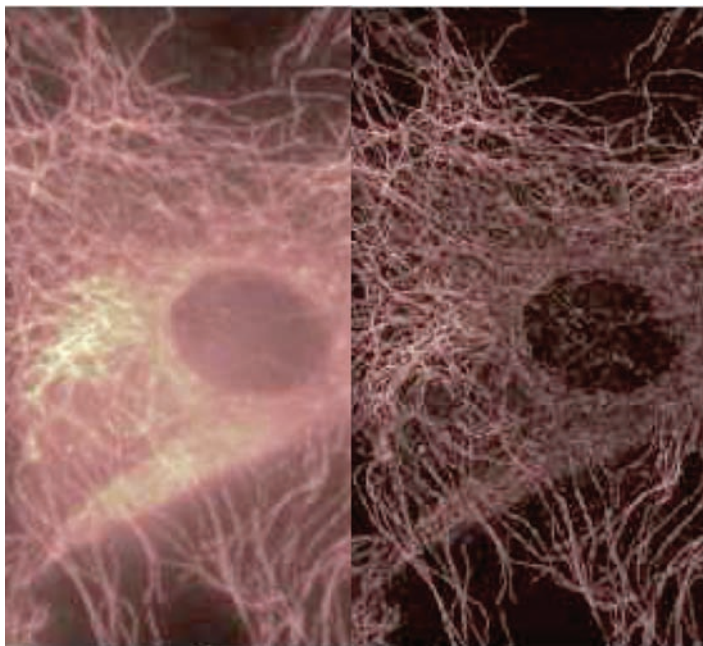


**Figure 8.12** Comparison of a conventional with a SOFI image of a tubulin network of a 3T3 fibroblast immuno-labelled with QD800 quantum dots. Source: Dertinger 2010. Reproduced with permission of The Optical Society.

## 8.8

### Final Comparison

All the techniques are still quite young and have different advantages and disadvantages and even newer techniques still emerge. For example, recently a technique has been proposed that distinguishes different fluorescent markers by their orientation, which might enable PALM/STORM approaches that do not require switchable markers. Groups of randomly orientated molecules at different image positions fluoresce at different times when excited by rotating linear-polarized light. The periodicity and modulation of these signals allow super-resolution by polarization demodulation (SPoD) image analysis. To better distinguish molecules of different orientations, excitation polarization-angle narrowing (ExPAN, cf. also to Figure 3.11) can be achieved by additionally using linear polarized STED beams. This illustrates that one future direction might be combining the advantages of different super-resolution methods allowing, for example, the use of more standard fluorescent markers (like in STED) in more simple optical set-ups (like in PALM/STORM). In any case, it depends critically on the sample or biological question under investigation which of the established super-resolution methods is best suited for a particular question. To make a decision, the following table might help as it summarizes the technical capabilities that have been described in the previous sections and that have so far been reached with the different approaches. The given resolutions all refer to resolutions observed experimentally with biological samples.

	STED	PALM/STORM	SIM	SOFI
Lateral resolution ( $x,y$ ), one objective	30 nm	20 nm	110 nm	50 nm
Axial resolution ( $z$ ), one objective	100 nm	50 nm	250 nm	100 nm
Lateral resolution ( $x,y$ ), opposing objectives	30 nm	20 nm	110 nm	—
Axial resolution ( $z$ ), opposing objectives	30 nm	10 nm	110 nm	—
Time resolution 2-dimensional	~6 s for $20 \times 20 \mu\text{m}^2$ , scales linear with field of view area	~3 s for 60 nm lateral resolution, independent of field of view	~0.1 s for 110 nm lateral resolution, independent of field of view	1 s to several minutes
Time resolution 3-dimensional	~60 s for $20 \times 20 \times 0.6 \mu\text{m}^3$ , scales linear with total observation volume	3 s for 60 nm lateral resolution and ~600 nm $z$ depth	~1.0 s for 110 nm lateral resolution, and ~600 nm $z$ depth, independent of field of view and scales linear with $z$ depth	
Sample penetration depth	100 $\mu\text{m}$ , decreased lateral resolution	A few hundred nm	As conventional fluorescence microscopy (several hundreds of $\mu\text{m}$ )	As conventional fluorescence microscopy (several hundred $\mu\text{m}$ ) ( $\geq 4$ , theoretically) Quantum dots, some conventional fluorescence markers
Multicolour imaging	2	3	$\geq 4$	
Label requirements	Highly photostable labels, depletable by inducing emission light in the red	Photoconvertible, - switchable or activatable or switchable by chemicals.	As conventional fluorescence microscopy	
Optical set-up requirements	Highly-demanding interferometric confocal set-up	As conventional fluorescence microscopy with fast camera	As conventional fluorescence microscopy but with less demanding interference-pattern generation	As conventional fluorescence microscopy with fast camera
Mode of operation	scanning	wide field	wide field	wide field
Live-cell capabilities	++	+	+++	+

## Problems

- 8.1** Discuss which super-resolution method you would use for (a) a living cell labelled by a standard GFP, (b) a fixed cell for which you have to image 3 different structural elements with labels of your choice, (c) a living cell labelled with a dye of low photostability, (d) a fixed cell when having only one excitation wavelength.
- 8.2** Explain why it is easier to image more than two differently coloured labels in SIM or SOFI than in STED or PALM.
- 8.3** Discuss important technical prerequisites in STED microscopy and in PALM microscopy.
- 8.4** For a distinct vibronic transition the probability that a photon stimulates a induced emission from the excited state is exactly the same as the probability that the photon is absorbed with the result of an excitation from the ground into the excited state. Discuss why it is impossible in STED microscopy to deplete the excited state by using a STED beam that has the same wavelength,  $\lambda_{\text{STED}}$ , as the excitation beam,  $\lambda_{\text{Excitation}}$  (Figure 8.1). Discuss also why it is necessary that the process  $S_0^{v'=2} \rightsquigarrow S_0^{v'=0}$  shown in Figure 8.1 is fast compared to  $S_1^{v'=0} \rightarrow S_0^{v' \geq 0}$  to achieve a nearly complete depletion of  $S_1$  by irradiation with high STED light intensities.
- 8.5** Discuss what factors might limit the resolution in PALM.
- 8.6** The localization precision in PALM microscopy can be calculated using  $\sigma_{x,y} = \sqrt{\frac{s^2 + q^2/12}{N} + \frac{8\pi s^4 b^2}{q^2 N^2}}$ . Here,  $s$  is the diffraction-limited resolution of the microscope system,  $q$  is the pixel size in the image space,  $N$ , is the total number of photons collected from a localized label and  $b$  is the number of photons that are additionally detected per pixel as background during the time of fluorescence photon collection. What number of fluorescence photons need to be detected from a single molecule to achieve a resolution two times higher than the diffraction-limited resolution when  $s = 250$  nm,  $q = 50$  nm and  $b = 100$  photons? What numbers are needed to achieve resolutions that are 10 times or 25 times higher?
- 8.7** In a system with a ground state  $S_0$  and an excited state  $S_1$  and taking stimulated emission into account the population of the excited state,  $S_1$  can be described by  $N_1 = k_{\text{exc}} / (k_{\text{exc}} + k_{\text{fl}} + k_{\text{SE}})$  when neglecting internal conversion and intersystem crossing. Here,  $k_{\text{exc}}$  is the rate constant for excitation,  $k_{\text{fl}}$  the fluorescence rate and  $k_{\text{SE}}$  the rate constant for stimulated emission. How much more STED irradiation intensity than excitation intensity is necessary to decrease the fluorescence by 99% when the fluorescence rate is  $k_{\text{fl}} = 0.1 \text{ ns}^{-1}$  and the excitation rate is  $k_{\text{exc}} = 0.02 \text{ ns}^{-1}$ ? Assume that the excitation wavelength is 600 nm and the stimulated emission wavelength 700 nm.

## Bibliography

### General

- Hadde, P.N. and Nienhaus, G.U. (2010) Optical imaging of nanoscale cellular structures. *Biophys. Rev.*, **2**, 147–158.
- Hell, S.W. (2009) Microscopy and its focal switch. *Nature Meth.*, **6**, 24.

### Specific

#### STED

- Eggeling, C., Willig, K.I. *et al.* (2013) STED microscopy of living cells – new frontiers in membrane and neurobiology. *J. Neurochem.*, **126** (2), 203–212.
- Harke, B., Ullal, C.K. *et al.* (2008) Three-dimensional nanoscopy of colloidal crystals. *Nano Lett.*, **8** (5), 1309–1313.
- Hell, S.W. (2007) Far-Field Optical Nanoscopy. *Science*, **316**, 1153–1158.
- Hell, S.W. (2003) Toward fluorescence nanoscopy. *Nature Biotechnol.*, **21**, 1347–1355.
- Hein, B., Willig, K.I. and Hell, S.W. (2008) Stimulated emission depletion (STED) nanoscopy of a fluorescent protein-labeled organelle inside a living cell. *Proc. Natl. Acad. Sci. USA*, **105**, 14271–14276.

#### Stimulated Emission

- Einstein, A. (1917) Zur quantentheorie der strahlung. *Phys. Zeit.*, **18**, 121–128.
- Einstein, A. (1966) *Quantum Theory of Radiation and Atomic Processes*, Basic Books, New York.

#### PALM/STORM

- Betzig, E., Patterson, G.H. *et al.* (2006) Imaging intracellular fluorescent proteins at nanometer resolution. *Science*, **313** (5793), 1642–1645.
- Hess, S.T., Girirajan, T.P.K. and Mason, M.D. (2006) Ultra-high resolution imaging by fluorescence photoactivation localization microscopy. *Biophys. J.*, **91**, 4258–4272.
- Huang, B., Wang, W. *et al.* (2008) Three-dimensional super-resolution imaging by stochastic optical reconstruction microscopy. *Science*, **319** (5864), 810–813.

- Lukyanov, Konstantin A., Chudakov, Dmitry M., Lukyanov, Sergey, and Verkhusha, Vladislav V. (November 2005) Innovation: Photoactivatable fluorescent proteins. *Nature Reviews Molecular Cell Biology*, **6**, 885–890.

- Rust, M.J., Bates, M. and Zhuang, X. (2006) Sub-diffraction-limit imaging by stochastic optical reconstruction microscopy (STORM). *Nature Methods*, **3**, 793–796.

- Shaner, N.C., Patterson, G.H. *et al.* (2007) Advances in fluorescent protein technology. *J. Cell Sci.*, **120**, 4247–4260.
- Xu, K., Zhong, G. *et al.* (2013) Actin, spectrin and associated proteins form a periodic cytoskeletal structure in axons. *Science*, **339** (6118), 452–456.

#### SIM

- Gustafsson, M.G.L. (2000) Surpassing the lateral resolution limit by a factor of two using structured illumination microscopy. *J. Microsc.*, **198**, 82.

- Gustafsson, M.G.L. (2005) Nonlinear structured-illumination microscopy: Wide-field fluorescence imaging with theoretically unlimited resolution. *Proc. Natl. Acad. Sci.*, **102**, 13081.

- Heintzmann, R. and Jovin, T.M. (2002) Saturated patterned excitation microscopy—a concept for optical resolution improvement. *J. Opt. Soc. Am. A*, **19**, 1599.

#### SOFI

- Dertinger, T., Colyer, R. *et al.* (2009) Fast, background-free, 3D super-resolution optical fluctuation imaging (SOFI). *Proc. Natl. Acad. Sci.*, **106** (52), 22287–22292.

- Dertinger, T., Colyer, R. *et al.* (2010) Achieving increased resolution and more pixels with Superresolution Optical Fluctuation Imaging (SOFI). *Opt. Exp.*, **18** (18), 18875–18885.

#### ExPAN/SPoD

- Hafi, N., Grunwald, M. *et al.* (2014) Fluorescence nanoscopy by polarization modulation and polarization angle narrowing, *Nat. Meth.*, **11**, 579–584.

## 9

# Single-Biomolecule Techniques

### 9.1

#### Introduction

The ability to measure the behaviour of single biomolecules is very valuable for the biosciences because many important mechanistic questions can only be answered on the single-molecule level. The averaging of parameters in ensemble measurements often prevents the detection of decisive mechanistic details, for example, because it is impossible to trigger the start of important intermediate reactions steps for all biomolecules simultaneously. In addition, not all biomolecules typically behave in the same way and important details of this heterogeneous behaviour of single biomolecules is lost in ensemble measurements. By looking at a certain single biomolecule, however, one can simply wait until a certain intermediate step naturally occurs and, consequently, very detailed information on biomolecular mechanisms can be derived from such investigations.

This chapter summarizes methods that allow such an observation of the behaviour of single biomolecules. The first two sections discuss the requirements for and application examples of optical single-molecule detection of fluorescently labelled biomolecules in fluorescence microscope set-ups. These techniques allow us to follow the trajectories of labelled single biomolecules or to statistically evaluate, for example, the binding behaviour of biomolecules diffusing in and out of a small confocal detection volume. The next two sections then present the two most important techniques to measure forces exerted by or at single biomolecules. These two techniques are optical tweezers and atomic force microscopy. Again, typical application examples will be given. Finally, at the end of this chapter, patch clamping is explained, which allows us to measure the ion current flowing through single ion channels of cell membranes.

### 9.2

#### Optical Single-Molecule Detection

As mentioned in Chapter 7, confocal set-ups even enable the detection of single fluorescing molecules that are in or passing through the focal detection volume.

Also, with TIRF microscopy, and to some extent with wide-field fluorescence microscopy, single-molecule detection based on fluorescence techniques can be accomplished.

Depending on the signal intensities, in principle the entire range of fluorescence parameters described in Chapter 3 can also be observed on a single-molecule level. Important examples are observations of single-molecule fluorescence signals based on Förster energy transfer as well as on the detection of fluorescence kinetics and fluorescence polarization anisotropy. The detection of all these parameters can be combined with single-molecule imaging as well as with single-molecule detection in a single, fixed confocal detection volume. In addition, all labelling techniques described in Chapter 3, including methods using fluorescing proteins such as GFP, are feasible for single-molecule experiments.

In general, to achieve optical single-molecule detection the following issues have to be considered:

- 1) A small observation volume is an important prerequisite for optical single-molecule detection. A small observation volume avoids background signals from the surrounding solvent or the environment of the fluorescing particle. Very small observation volumes can be achieved using confocal set-ups, for example. As mentioned in Chapter 7, a detection volume of less than a femtolitre ( $10^{-15}$  L) is observed. The thin excitation layer in TIRF microscopy also fulfils to a large extent the requirement of small observation volumes and is therefore also very suitable for optical single-molecule spectroscopy. Wide-field fluorescence microscopy is only suited to observe single fluorescence molecules to a certain degree, because the fluorescence background from regions other than the focal image plane contribute to a major extent to the observed signals. However, if as many of the following issues as possible are considered, usually robust single-molecule signals using wide-field fluorescence microscopes can also be observed.
- 2) A small concentration of the fluorescing particles is a prerequisite so that at most one molecule is present in the smallest volume that can be resolved by fluorescence microscopy. Typically, concentrations on the order of a few nanomolar or less are necessary so that on average only about one molecule is within each diffraction-limited detection volume.
- 3) A high fluorescence quantum yield, if possible larger than 80–90%, of the fluorescence marker guarantees high contrast over background luminescence and scattering. Usually, excitation intensities are chosen that are close to the saturation intensity of the fluorescence marker. If a fluorescence marker is irradiated with saturating excitation intensities it will be almost directly re-excited each time it has emitted a fluorescence photon. Since the excited-state lifetime of fluorescence markers is typically on the order of a few nanoseconds the highest theoretical number of photons that can be emitted from a fluorescence marker is not larger than a few million photons per second. However, this number is usually significantly reduced

because the fluorescence marker remains intermittently at longer periods in the triplet state. Details about this behaviour of single-fluorescence markers are discussed in Section 9.3 on fluorescence correlation methods. In addition, the photochemical stabilities of the chosen fluorescence markers also determine how many photons are emitted before they are irreversibly photodestroyed. In general, excitation intensities have to be chosen that almost saturate the fluorescence marker but that are low enough to keep photobleaching, as well as background originating from scattered light, as low as possible.

- 4) A large numerical aperture of the microscope objective is another important prerequisite for the collection of a sufficient number of fluorescence photons from the molecules. As mentioned in Chapter 7, a numerical aperture of 1.2 of typical high-quality water immersion microscope objectives corresponds to a collection efficiency of  $\sim 25\%$ . Transmission of the light through the microscope objectives is typically  $\sim 80\text{--}90\%$ . As a consequence, in total about 20% of the originally emitted photons exit the back aperture of the microscope objectives.
- 5) The signal-to-noise ratio also depends critically on the right choice of high-quality dichroic mirrors and optical filters. These optical elements should be chosen such that as much as possible of the light scattered from the intense excitation beam is suppressed without suppressing too much of the fluorescence light (compare also with Figure 7.3). By choosing the right filter optics and excitation intensities, fluorescence photons are detected almost exclusively. Typically, losses in fluorescence intensity of around  $\sim 20\%$  occur at the dichroic mirrors, optical filters and lenses in the optical detection pathway.
- 6) Finally, also, the high photon detection efficiency and low background noise of modern detectors such as APDs, PMTs or CCDs are necessary to obtain a large signal-to-noise ratio. State-of-the-art APDs, for example, have a background noise of less than 100 erratically detected photons per second and a maximum detection efficiency of  $\sim 90\%$ . CCDs can achieve an even lower background noise of significantly less than one erratically detected photon per second and also detection efficiencies of  $\sim 90\%$ . With these detection efficiencies an overall detection efficiency,  $\Phi_{\text{Det}}$ , of around  $\sim 10\%$  of the photons originally emitted by the fluorescence markers can be achieved in confocal set-ups. As a result, about 100 000 to 200 000 fluorescence photons per second are typically observed from a single fluorescence marker.

Naturally, during the short diffusional transit of a single fluorescence marker through the detection volume of a confocal set-up only a limited number of photons can be detected. A single diffusional transit of a free fluorescence label through a confocal detection volume of  $\sim 200\text{--}300\text{ nm}$  in diameter takes about  $50\text{ }\mu\text{s}$ . This corresponds to about 5–10 detected photons per transit. Fortunately, labelled biomolecules exhibit typically average diffusional transit times that can be up to a few ms. This corresponds to several thousand detected photons per

single biomolecule transit, if the biomolecule is labelled with only one fluorescence marker. Higher numbers of fluorescence markers per single biomolecule naturally increase the amount of detectable photons, accordingly. Statistical analysis of such signal fluctuations provides important information about diffusion times, local concentrations or, also, binding reactions and is described in detail in Section 9.3.

To extend the time available for the observation of single biomolecule fluorescence, the biomolecules can also be immobilized on a solid support such as a cover slide. The entire range of linking techniques described in Chapter 3 can be used to immobilize the biomolecules. Of course, the immobilizing procedures and the search for the immobilized biomolecules on the support are usually significantly more time consuming than the observation of biomolecules freely diffusing.

It is also possible to image the movements of single fluorescing molecules using TIRF or wide-field microscope set-ups (Chapter 7). Obviously, this approach has the advantage that information on spatial movements of singly observed biomolecules in the context of whole cells, for example, can be derived. With this approach it is, for example, possible to track single viruses while infecting a cell. The two application examples presented in the following section are both based on imaging single biomolecules. They give a first insight into the possibilities provided by optical single-molecule detection. Both examples represent cases of biomolecular mechanisms that can be only be directly observed on a single biomolecule level.

### 9.2.1

#### Application Example 1: Observation of the Rotation of Single ATPase Complexes

In biology, the molecule adenosine triphosphate (ATP) is one of the most important chemical stores of energy. ATP is generated in the chloroplasts in photosynthesis or in mitochondria in human or animal cells. The energy is stored in the phosphate bonds (Figure 9.1). The large amount of energy released during the hydrolysis of the phosphate bonds is used to drive many biochemical reactions.

Healthy cells usually maintain a very high ATP to ADP ratio of:

$$\frac{C_{\text{ATP}}}{C_{\text{ADP}} C_{\text{P}}} \approx 500 \quad (9.1)$$

Here,  $C_{\text{ATP}}$ ,  $C_{\text{ADP}}$  and  $C_{\text{P}}$  are the concentrations of ATP, ADP and free phosphate, respectively. The large driving force created by this high ratio is used in biology to set thermodynamically unfavourable reactions in motion. In the simplest case such a biomolecular reaction is the transformation of a metabolite A into a metabolite B:



Because the reaction is thermodynamically unfavourable the normal equilibrium lies towards the formation of the educt A. However, if this reaction is coupled to

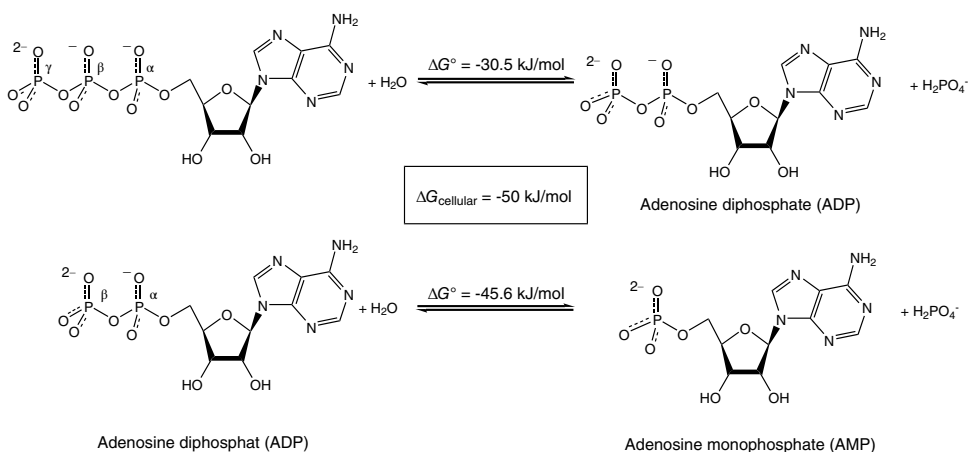
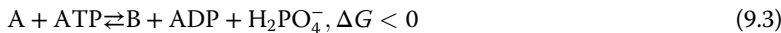


**Figure 9.1** The energy contained in ATP can be released in two steps by hydrolysis to ADP and AMP. The corresponding free energies under standard conditions are  $\sim 30$  and  $\sim 46 \text{ kJ mol}^{-1}$ . Under cellular conditions, however, both steps have free energies of about  $\sim 50 \text{ kJ mol}^{-1}$ .

a simultaneous ATP hydrolysis:



the equilibrium shifts to a preferred formation of product B. Under natural conditions the involvement of ATP hydrolysis can shift the equilibrium ratio of biochemical reactions by a factor of about  $10^8$  in favour of the products.

The question arises as to how cells can maintain the incredibly powerful ATP/ADP ratio of  $C_{\text{ATP}}/C_{\text{ADP}}C_{\text{P}} \approx 500$ ? In nature this job is done by a transmembrane protein called ATP synthase (ATPase) (Figure 9.2). This protein complex consists of the static units  $\alpha$ ,  $\beta$ ,  $b$  and  $a$  and the units  $\gamma$  and  $c$  that start to rotate when a transmembrane proton gradient is present. In photosynthesis this proton gradient is built up directly by primary light-harvesting and charge-transfer processes whereas mitochondria build the proton gradient by oxidation of nutrients. During rotation of the  $c$  and  $\gamma$  units, the protons flow through the enzyme by a mechanism that is not yet completely understood.

The formation of ATP occurs in the  $\alpha/\beta$  units and is driven by the rotation of the  $\gamma$  unit. The corresponding mechanism is visualized in Figure 9.3, which represents the top view of ATPase. Depending on the rotational position of the  $\gamma$  unit the  $\alpha/\beta$  units can adopt three different conformations: a loose conformation, a tight conformation and an open conformation. In the loose conformation ADP + P can bind to the active site between the  $\alpha$  and  $\beta$  subunits. After a  $120^\circ$  rotation of the  $\gamma$  unit this conformation is converted into the tight conformation in which ATP is formed from ADP and P. A further  $120^\circ$  rotation results in the open conformation, from which the generated ATP is finally released.

This process can be impressively confirmed and observed in real time by single-molecule studies (Figure 9.4).

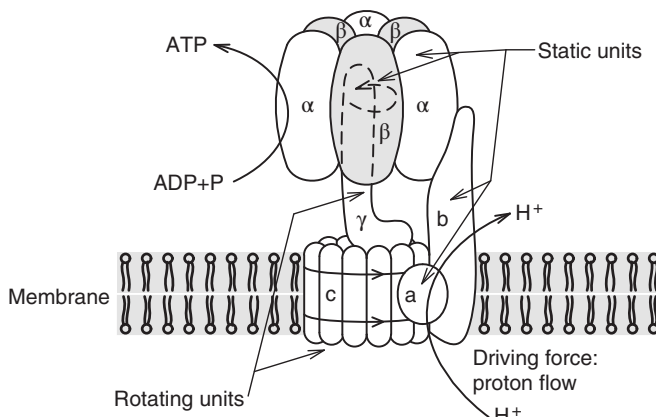


**Figure 9.2** The protein ATP synthase literally works like a little mill driven by a proton flow. The driving force is caused by a proton gradient across the membrane, which is generated by photosynthesis in chloroplasts

or by oxidation of nutrients in mitochondria. The proton driven rotation of the  $\gamma$  and  $c$  units catalyses the formation of ATP from ADP in the  $\alpha$  and  $\beta$  units.

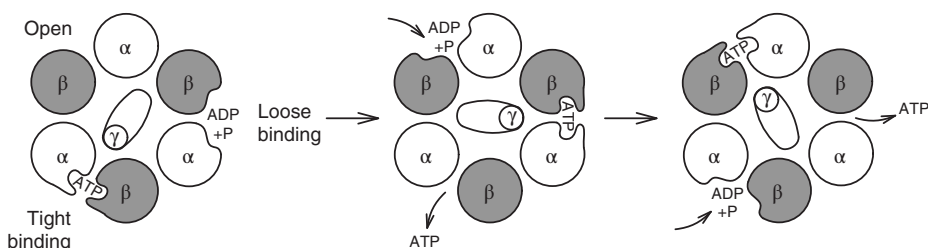


**Figure 9.3** The rotational force of the  $\gamma$  unit is used for the formation of ATP from ADP by conformational changes in the  $\alpha$  and  $\beta$  subunits.

For this experiment, researchers took advantage of the fact that the enzymatic mechanism can be reversed when ATP is present but no driving proton gradient is available. Then the opposite process, ATP hydrolysis and rotation of the  $\gamma$  unit in the contrary direction, occurs. In the experiment, first histidine-modified  $\alpha/\beta$  subunits were immobilized on a  $\text{Ni}^{2+}$  surface via His-Tags (such linking techniques are described in Chapter 3). The  $\gamma$  subunit in the centre of the  $\alpha$  and  $\beta$  subunits was biotinylated at the opposite end of the complex. A fluorescently labelled, biotinylated actin filament was then attached to the  $\gamma$  subunit via an avidin tetramer. When ATP was then added to the aqueous solution surrounding the ATPase subunits, the filament indeed started to rotate. This could be observed in real time in a wide-field fluorescence microscope (see schematic, diffraction-limited top view in the lower part of Figure 9.4). The rotation invariably occurred contraclockwise. If the concentration of ATP was reduced the rotation speed also decreased. At lower ATP concentrations it could even be

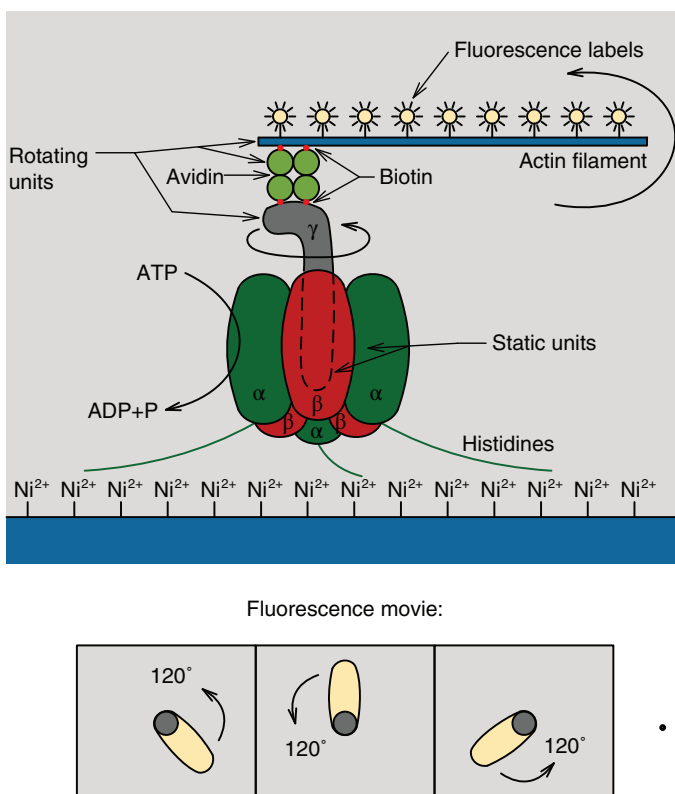


**Figure 9.4** The rotation of important ATP synthase subunits can be observed in real time by single-protein experiments.

observed that the rotor stalls every 120° until the next rotation's step occurred. From the consumption of ATP it could be concluded that, indeed, three ATP molecules were hydrolysed per full rotation.

## 9.2.2

### Application Example 2: Single-Molecule Observation of the Elementary Steps of Biomolecular Motors

For macroscopic or microscopic motion or transportation nature has developed molecular motor proteins. In most cases binding of ATP to a so-called P-loop domain in these proteins results in a large conformational transition of a swing-type domain of the proteins. Either sequences of single conformational movements are used on a microscopic level to transport cell compounds or metabolites within a cell, or the force of many such movements is used to achieve macroscopic movement such as muscle contractions. There are three major classes of molecular motor proteins. Myosins are predominantly responsible for muscle motion by using the conformational force to move along actin filaments.

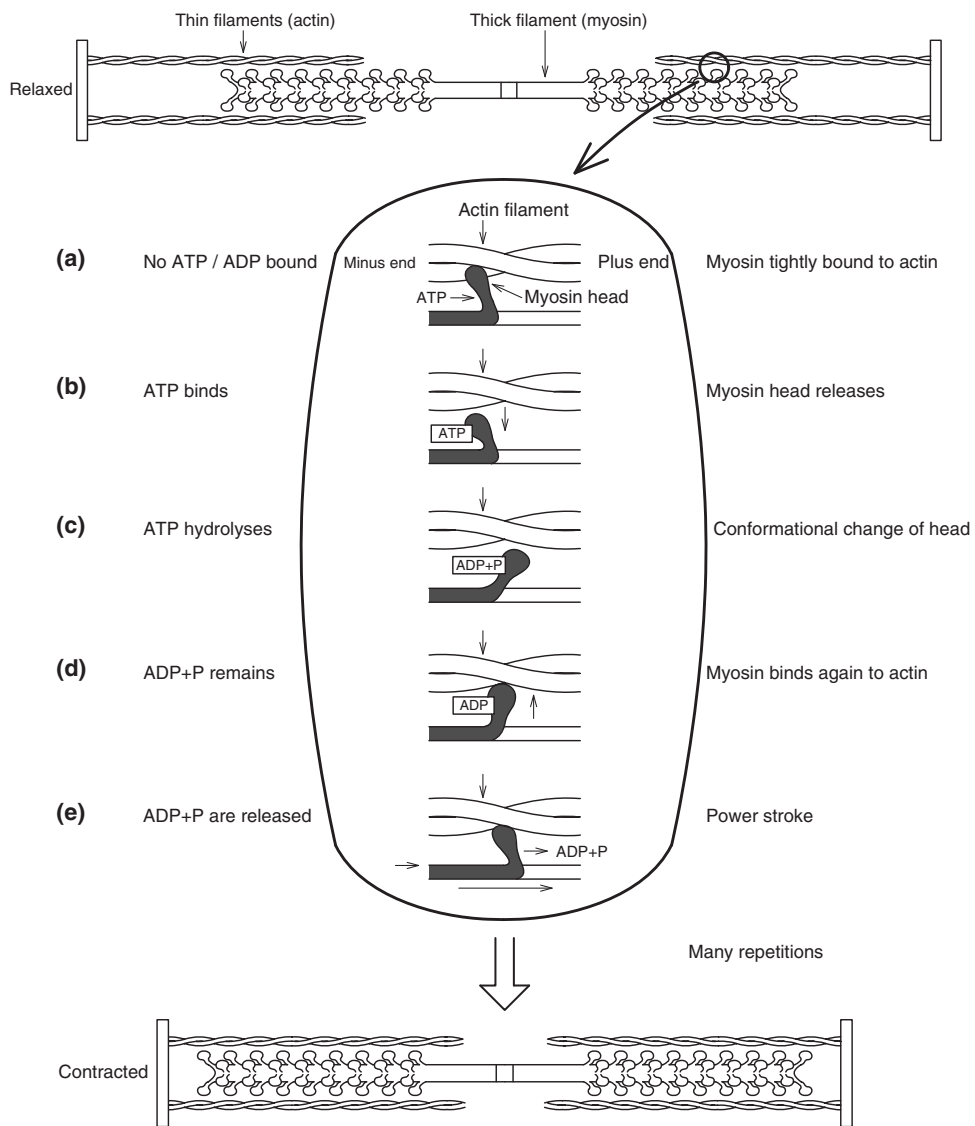


**Figure 9.5** Muscle function is based on the interplay of many individual movements of myosin proteins moving along actin filaments.

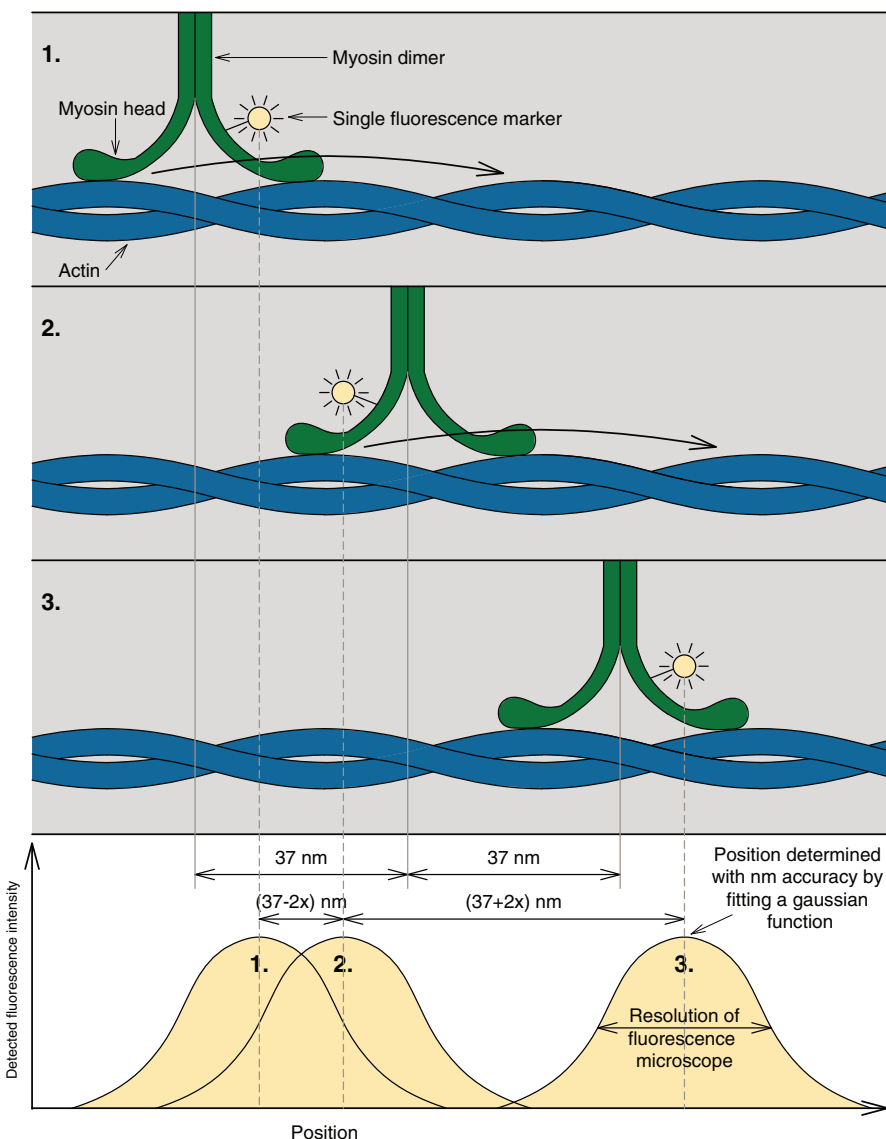
Kinesins are used for the transportation of proteins, organelles and vesicles within cells along the microtubuli of the cell cytoskeleton. Finally, dyneins power cilia and flagella of cells, for example, to move them around as a whole.

Figure 9.5 shows a general overview of muscle function and the role of myosin, actin and ATP. The macroscopic motion is based on the summation of many ATP-driven myosin power strokes. Myosin has a head group, which contains the P-loop, and an extended long-chain domain consisting of  $\alpha$ -helices. The

$\alpha$ -helix domains of many myosins are bundled into the so-called thick filaments of muscles with the head groups sticking out of these bundles. The head groups are in the direct vicinity of the muscles thin filaments, which consists of long extended polymers of actin protein subunits.

If no ATP is present, the myosin heads are tightly bound to the actin filaments (Figure 9.5a). However, upon binding of ATP to the myosin's P-loop this tight bond is first released (Figure 9.5b). In a next step, ATP hydrolysis induces a 'flipping' of the myosin's head group (Figure 9.5c). In the presence of the hydrolysis product ADP the head group has again a larger binding affinity for the actin subunits (Figure 9.5d). Consequently, the head group binds at a position at the actin filament that is slightly more to the right than previously. Finally, release of the hydrolysed ADP leads to a backflipping of the myosin's head group into its original confirmation. This step corresponds to the actual power stroke the myosin molecule exerts on the actin filaments. The head group is again tightly bound during this conformational change (Figure 9.5e). The parallel and sequential summation over many such power strokes finally leads to contraction of the entire muscle, which consists of many thick and thin filaments.

In recent years, many important mechanistic details of such molecular motion events have been investigated by real-time observations of single fluorescently labelled myosin or kinesin proteins. Figure 9.6 illustrates an example of such an experiment. Observing single fluorescently labelled myosin dimers shows that they literally 'walk' along actin filaments in the presence of ATP. The motional mechanism of kinesins transporting proteins, organelles and vesicles along the cytoskeleton microtubuli is similarly based on 'walking' dimers of kinesins. The question arises as to how this walking occurs mechanistically. Does it occur like an 'inchworm', whereby one head group always steps behind the other, or is the motion hand over hand, whereby the two head groups step alternately in front of each other? To answer that question, researchers first attached a single fluorescence dye close to one head group of a myosin dimer. This first step requires site-selective, or at least region-selective, labelling by techniques such as described in Chapter 3. In a next step, they attached actin filaments onto a cover slip. Then they added the labelled myosin dimers to the actin filaments with the result that they started walking along the filaments in the presence of ATP. The movement of the single fluorescence dyes was observed with a TIRF microscope set-up. Even though the step sizes of myosins were, at  $\sim 37$  nm, significantly smaller than the resolution of conventional fluorescence microscopy (about 200–300 nm), the exact position of the fluorescence marker could be observed with an accuracy of only a few nm. Similarly as in the PALM-technique (see Section 8.2) this is possible because the fluorescence of only a single fluorescence dye is observed: Even though it gives rise to an observed fluorescence spot of about 200–300 nm in diameter in the TIRF images the *centre* of the corresponding Gaussian-like distribution can be determined with a very high accuracy as long as enough photons are available for good quality data (see Gaussian intensity distributions in the lower part of Figure 9.6). The top view of the fluorescence dye positions for two myosin movements, as determined from the



**Figure 9.6** Observation of a single fluorescence marker allows the determination of its position with a resolution of a few nm even though this is significantly below the resolution of fluorescence microscopes, which is usually limited by Abbe's law (Eq. (7.1)) to  $\sim 200\text{--}300$  nm. Exact determination of the fluorescence marker positions takes advantage of the fact that even though only a larger fluorescence spot with a 2D Gaussian-

like intensity distribution of  $\sim 200\text{--}300$  nm can be observed in the fluorescence microscope, the *centre* position of this Gauss distribution can be determined with a few nm accuracy from single fluorescence markers. In the case of fluorescently labelled single myosin head groups this allowed the determination of important mechanistic details about the ATP-driven movement of myosin dimers walking along actin filaments (see Figure 9.7).

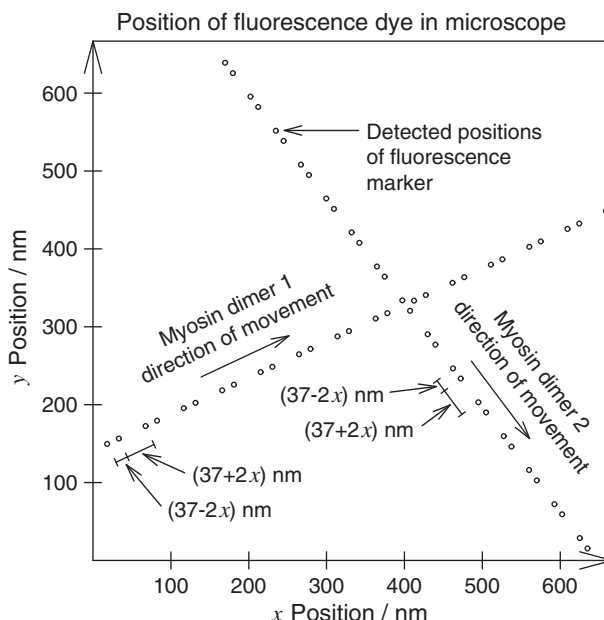


**Figure 9.7** The movement of single fluorescently labelled myosin dimers ‘walking’ along actin filaments can be observed in a TIRF microscope. The centre of the fluorescence spot, originating from a single fluorescence marker, can be determined with a resolution

that is far better than the spot size itself. The asymmetric pattern of the exact positions of the fluorescence dyes observed during the walking steps of myosin along the actin filaments provides clear evidence for a ‘hand-over-hand’ walking mechanism.

Gaussian fluorescence distribution centres, is shown schematically in Figure 9.7. The head groups of the myosins stay still for a certain time between the individual steps. This time is long enough to accurately determine the fluorescence dye positions. It could be unambiguously observed that the fluorescence dyes are at asymmetric positions during the walking steps of the myosins. Since the step-dependent positions of the head groups would have been symmetrical if an inchworm mechanism were present the findings shown schematically in Figures 9.6 and 9.7 clearly provide evidence for a hand-over-hand mechanism. Similar results have been observed for kinesin dimers walking along microtubuli.

### 9.3

#### Fluorescence Correlation Spectroscopy

The previous examples have shown that biomolecular mechanisms can be investigated in great detail by applying optical single-molecule techniques. However, very often the statistical significance observed from the fluorescence detection of single events is not sufficient to unambiguously answer biochemical questions. Therefore, often, many single events are observed and a statistical evaluation of these events is conducted. The most important statistical evaluation of signals

observed from single fluorescently labelled biomolecules is fluorescence correlation spectroscopy (FCS). In FCS one typically analyses the fluctuations arising from a few labelled biomolecules diffusing in and out of the detection volume of a confocal set-up. From this analysis it is possible to determine parameters like the average number of individual fluorescently labelled biomolecules in the confocal volume and the average size- and viscosity-dependent diffusional time the labelled biomolecules need to diffuse through the confocal detection volume. It is also possible to determine the brightness of the fluorescing particles, which provides information about aggregations of the biomolecules, and binding interactions via cross-correlational analysis of differently labelled biomolecules. A multitude of such parameters can be analysed not only *in vitro* but also in various cell compartments or entire cells when the detection volume is placed in or scanned through biomolecular objects. In the next sections we discuss the mathematical background and important application examples of FCS.

### 9.3.1

#### Autocorrelation Analysis and Observable Key Parameters

In fluorescence autocorrelation analysis, typically, fluctuations of the fluorescence signals caused by the diffusion of labelled biomolecules in and out of the confocal detection focus are evaluated. This is illustrated by a first application example in Figures 9.8 and 9.9. In this example the binding of a small, fluorescently labelled ligand 'L' to a large receptor 'R' is monitored using FCS. If no binding occurs (Figure 9.8b) then the relatively small labelled ligand diffuses quickly in and out of the confocal detection volume. As a consequence, the observed fluorescence fluctuations occur on a fast timescale. If the ligand binds successfully to a larger receptor (Figure 9.8a), it diffuses significantly slower through the confocal detection volume. As a consequence, the observed fluorescence fluctuations occur on a much slower timescale. Of course, not all diffusional transits take exactly the same time and result in the same peak height (Figure 9.8 suggests otherwise only for better visibility). Therefore, from a single transit it would not be possible to accurately determine whether the actual situation corresponds to a free or a bound ligand. Nevertheless, statistically the single transits of the receptor–ligand complexes take longer than the single transits of the free ligand. Mathematical evaluation of these statistics is carried out by autocorrelational analysis. For ease of understanding let us start with a simple autocorrelation function and some basic conclusions from this function:

$$G(\tau) = \langle I_{\text{Fl}}(t) \cdot I_{\text{Fl}}(t + \tau) \rangle \quad (9.4)$$

Here,  $I_{\text{Fl}}(t)$  is the fluorescence intensity observed at a certain time  $t$  in the fluorescence traces (Figure 9.8). The brackets  $\langle \cdot \rangle$  in (9.4) symbolize that the product  $I_{\text{Fl}}(t) \cdot I_{\text{Fl}}(t + \tau)$  is calculated for all measured times  $t$  and that the average of these products constitutes the correlation amplitude  $G(\tau)$  for the correlation time  $\tau$  (Figure 9.9). For single-particle transits the magnitude of the correlation amplitude  $G(\tau)$  is dependent on the probability that fluorescence is still observed

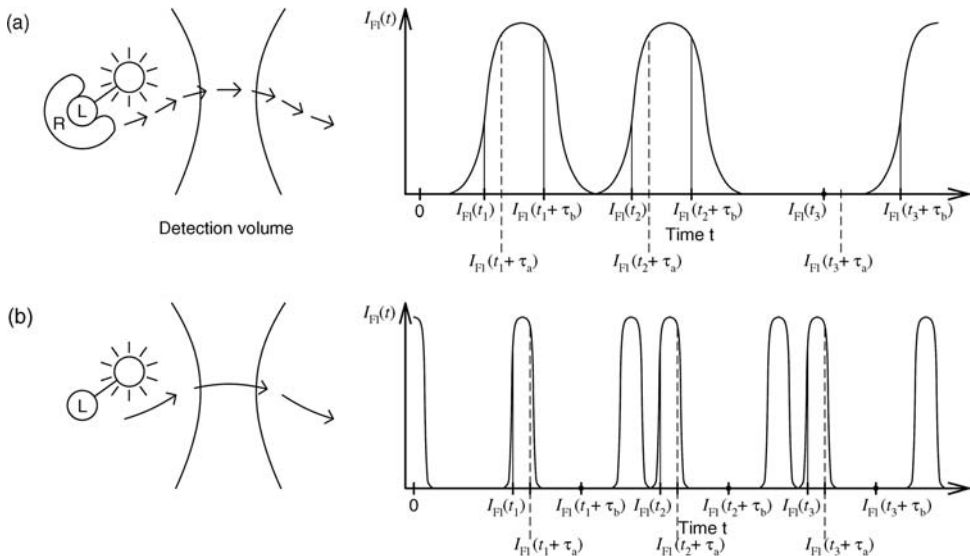


**Figure 9.8** Schematic presentation of the fluorescence fluctuations caused by a bound (a) and a free (b) fluorescently labelled ligand diffusing in and out of the confocal detection volume. If a small, fluorescently labelled ligand is bound to a large receptor protein it diffuses slowly through the confocal detection volume. In contrast, if the ligand is not bound it

diffuses quickly through the confocal volume. As a result, the fluorescence fluctuations observed from the receptor–ligand complex (a) occur on a slow timescale, whereas the fluorescence fluctuations observed from the free ligand occur on a faster timescale (b). For more details see text.

at the time  $t + \tau$  when there was already fluorescence at the time  $t$  (Figure 9.8). If single particle transits usually take longer times, such as in the case of the receptor–ligand complex in Figure 9.8a, the product  $I_{\text{FI}}(t) \cdot I_{\text{FI}}(t + \tau)$  is a lot more often non-zero for longer correlation times such as  $\tau_b$  in Figure 9.8a (see, for example,  $t_1$  and  $t_2$ , solid vertical lines) than if the particles diffuse on average quickly through the detection volume (Figure 9.8b, here the product  $I_{\text{FI}}(t) \cdot I_{\text{FI}}(t + \tau_b)$  is zero for  $t_1$ ,  $t_2$  and  $t_3$ ). For shorter correlation times (e.g.  $\tau_a$  in Figure 9.8, dashed vertical lines) the product  $I_{\text{FI}}(t) \cdot I_{\text{FI}}(t + \tau_a)$  is more often nonzero even in the case of fast fluctuations (Figure 9.8b). As an overall result the autocorrelation amplitude,  $G(\tau)$ , drops at earlier correlation times when the fluorescence fluctuations occur on a faster timescale (Figure 9.9). More precisely, autocorrelation analysis provides information on the self-similarity of fluctuating signals on different time-scales,  $\tau$ . For FCS it provides a measure for the average diffusion time,  $\tau_D$ , the particles need to diffuse through the confocal detection volume. The diffusion time  $\tau_D$  is the correlation time,  $\tau$ , for which the correlation amplitude,  $G(\tau)$ , has dropped to approximately 50% of its initial value. The determination of  $\tau_D$  can be used, as in the present example, to obtain the degree of binding. We will discuss a more detailed mathematical description of  $\tau_D$  below. Here it is noted that  $\tau_D$  is on the order of  $\sim 50\text{ }\mu\text{s}$  for a free fluorescence marker

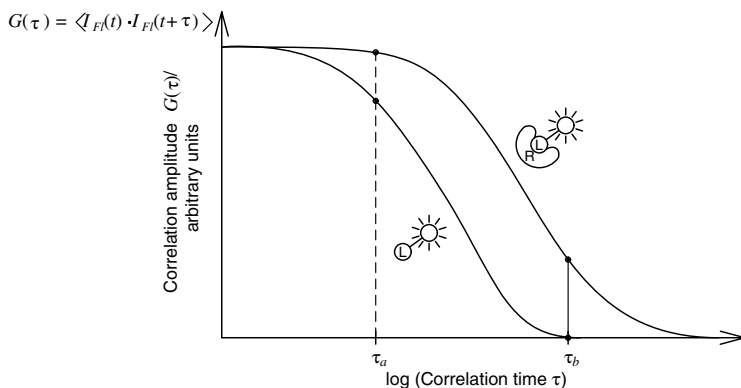


**Figure 9.9** Schematic presentation of the autocorrelational analysis of the fluorescence fluctuations shown in Figure 9.8. As a consequence, of the faster fluorescence fluctuations observed from the free ligand (b) the autocorrelational amplitude  $G(\tau)$  decays at shorter correlation times,  $\tau$ , than in the corresponding

curve for the larger receptor-ligand complex. The  $\tau$  scale (correlation time) in plots of the autocorrelation curve is not to be confused with the  $t$  scale (timescale of experiment) in plots of the primary fluctuation data shown in Figure 9.8. For more details see text.

at room temperature and in aqueous solution. Typical  $\tau_D$  values for monomeric proteins can be up to a few ms, depending on the actual protein sizes.

The question arises how FCS curves look like if, on average, more than one molecule is in the focal detection volume. The corresponding fluorescence traces are schematically visualized in Figures 9.10. To discuss this question we introduce here a normalized autocorrelation function that is the actual one that is usually used to calculate FCS curves:

$$G(\tau) = \frac{\langle I_{\text{Fl}}(t) \cdot I_{\text{Fl}}(t + \tau) \rangle}{\langle I_{\text{Fl}}(t) \rangle^2} - 1 \quad (9.5)$$

Here,  $\langle I_{\text{Fl}}(t) \rangle$  is the mean or average fluorescence intensity. It is the integrated sum of the fluorescence intensity observed during the entire experiment divided by the total measurement time,  $T$ :

$$T : \langle I_{\text{Fl}}(t) \rangle = \frac{\int_0^T I_{\text{Fl}}(t) dt}{T}$$

(see, for example, the solid horizontal lines in Figure 9.10). The quotient in (9.5) becomes 1 if no correlation is present in the observed fluctuations (e.g. for purely, noncorrelated noise or correlation times,  $\tau$ , that are significantly longer than the time scale that is necessary for the particles to diffuse in and out of the detection volume). Therefore, the numerical number 1 is subtracted from this quotient in (9.5) resulting in a function that typically drops to zero values for large correlation times. The overall shape of the curves as calculated by (9.5) is similar as for (9.4).

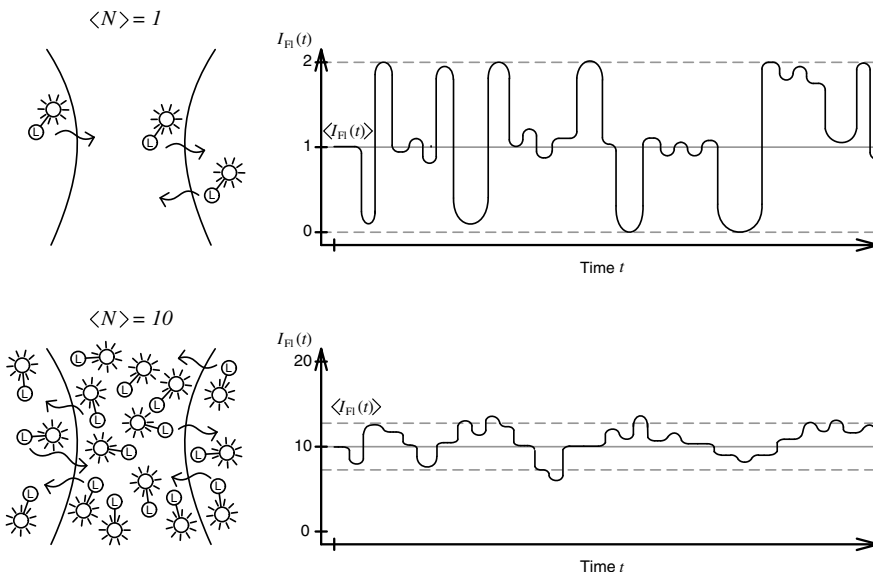


**Figure 9.10** If more than one molecule is on average in the detection volume, still fluorescence fluctuations in  $I_{\text{FI}}(t)$  occur on a timescale corresponding to the time a single particle needs to diffuse in and out of the confocal detection volume. However, the relative fluorescence fluctuations become

smaller the higher the average number of particles  $\langle N \rangle$  in the detection focus. As a consequence, the magnitude of the normalized autocorrelation amplitude (Eq. (9.5)) is inversely proportional to  $\langle N \rangle$  (Figure 9.11).

How do different particle concentrations now influence correlation curves calculated using (9.5)? The average number of molecules in the focal detection volume is defined as the particle number,  $\langle N \rangle$ . If  $\langle N \rangle > 1$ , then fluorescence fluctuations are still observed on timescales that correspond to diffusional transits of the particles. Consequently, the correlation amplitude,  $G(\tau)$ , decays at the same correlation times  $\tau$  as if only single particles would transit the focus (Figure 9.11). However, (9.5) describes the magnitude of the observed fluorescence intensity fluctuations  $\langle I_{\text{FI}}(t) \cdot I_{\text{FI}}(t + \tau) \rangle$  divided by the square of mean fluorescence intensity,  $\langle I_{\text{FI}}(t) \rangle$ . As can be seen in Figure 9.10, the magnitude of the relative fluorescence intensity fluctuations in comparison to the average fluorescence,  $\langle I_{\text{FI}}(t) \rangle$ , is significantly smaller for larger particle numbers than for smaller particle numbers (compare the dashed, horizontal lines in Figure 9.10 with the solid horizontal lines). Consequently, the calculated correlation  $\langle I_{\text{FI}}(t) \cdot I_{\text{FI}}(t + \tau) \rangle / \langle I_{\text{FI}}(t) \rangle^2$  also becomes smaller for larger  $\langle N \rangle$ . If we use the normalized autocorrelation function (9.5) then the correlation amplitude observed at very short correlation times is directly proportional to the inverse of the particle number (Figure 9.11):

$$G(\tau \approx 50 \mu\text{s}) = \frac{1}{\langle N \rangle} \quad (9.6)$$

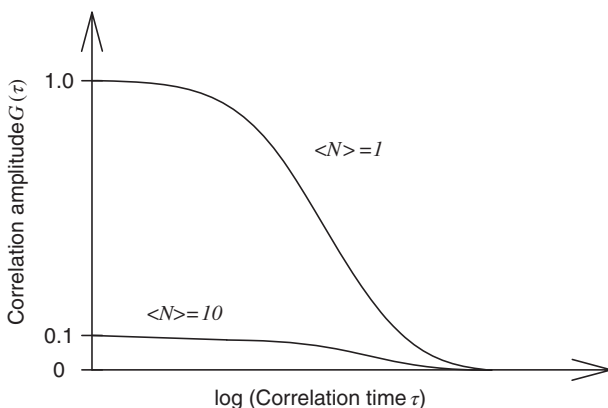


**Figure 9.11** The correlation amplitude at shorter correlation times is the direct inverse of the average number of particles in the detection volume,  $\langle N \rangle$ .

This relation is a very valuable tool to determine concentrations of labelled species via FCS. For a typical confocal detection volume of about 1 fL a particle number of 1 corresponds to a concentration of a few nanomoles. Determination of the particle number via FCS has its limitations of course. For very large particle numbers the relative fluctuation derivations from the mean value  $\langle I_{\text{Fl}}(t) \rangle$  are so small that a reliable determination of  $\langle N \rangle$  is no longer possible. In contrast, very small particle numbers correspond to very rare diffusional transits of fluorescing particles through the detection volume. In such a situation the statistical evaluation of the fluctuation signals takes a very long time and background noise will severely affect the calculated correlation amplitudes. As a consequence, optimum particle numbers are in the range of about 1 to 100, corresponding to concentrations on the order of about 1 to 100 nanomolar of fluorescently labelled biomolecules. Notably, the correlation amplitude for correlation times significantly smaller than 50  $\mu\text{s}$  is usually affected by other effects like triplet-state dynamics, rotational diffusion and the fluorescence re-excitation dynamics. We will discuss these effects below (Section 9.3.4; further correlation effects).

When the particle number of a distinct sample is known then another parameter, the so-called particle brightness, can be directly calculated. The particle brightness is the average fluorescence intensity observed from the sample divided by the particle number:

$$I_{\text{Fl}}^{\text{Particle}} = \frac{\langle I_{\text{Fl}}(t) \rangle}{\langle N \rangle} \quad (9.7)$$

It is a measure of the fluorescence intensity observed from a single fluorescing particle. For single fluorescence molecules it is predominantly determined by the fluorescence quantum yield and the detection efficiency of the confocal apparatus. As described in the introduction to Section 9.2, for a good fluorescence dye

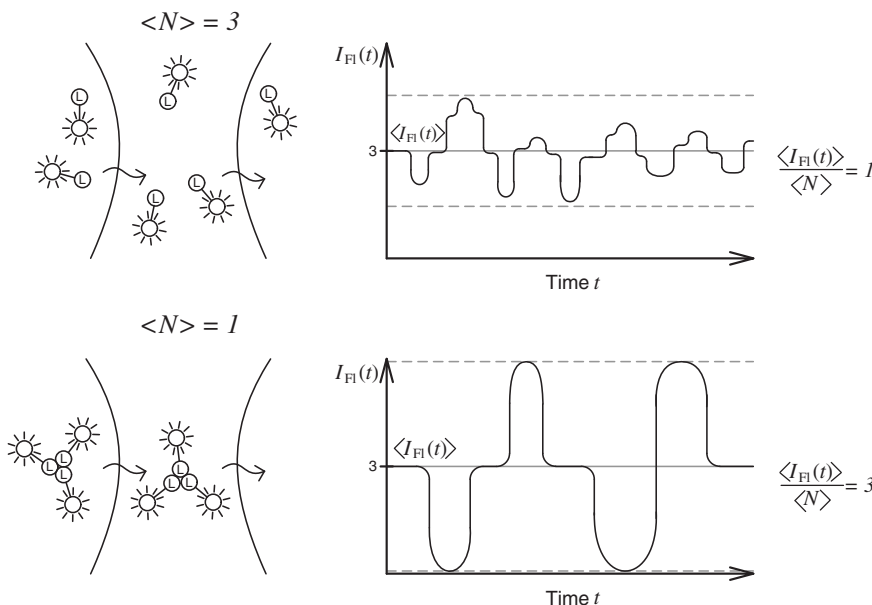


**Figure 9.12** If fluorescently labelled biomolecules aggregate, the detected average fluorescence intensity,  $\langle I_{\text{Fl}}(t) \rangle$ , remains approximately the same as long as the fluorescence quantum yield of the fluorescence dye does not change significantly. However, the particle number,

$\langle N \rangle$ , decreases because of the aggregation. Consequently, the particle brightness,  $I_{\text{Fl}}^{\text{Particle}} = \langle I_{\text{Fl}}(t) \rangle / \langle N \rangle$ , is approximately linearly proportional to the number of labelled monomers contributing to a single aggregate.

a typical value of  $I_{\text{Fl}}^{\text{Particle}}$  of around 100 000–200 000 photons per second can be observed under optimal excitation and detection conditions. The particle brightness can be used, for example, to monitor the aggregation behaviour of labelled biomolecules. This is illustrated in Figure 9.12. An aggregation results in a decrease of the particle number as observed by FCS analysis. However, the average fluorescence intensity observed from the confocal volume remains approximately the same, as long as the aggregation does not affect the fluorescence quantum yield of the fluorescence dyes too much. Consequently, the particle brightness increases accordingly. The particle brightness can therefore serve as a measure for the number of fluorescing units contributing to a multimer or an aggregate independently from the actual measured concentration or fluorescence intensity. Of course, larger background fluorescence would severely affect the determination of  $I_{\text{Fl}}^{\text{Particle}}$  and must be subtracted from  $\langle I_{\text{Fl}}(t) \rangle$  prior to the calculation of  $I_{\text{Fl}}^{\text{Particle}}$  via (9.7). Notably, sometimes the aggregation influences the fluorescence quantum yield. However, in most such cases the particle brightness can still serve at least as a clear indicator for the presence of aggregation processes. Of course, other phenomena affecting the fluorescence quantum yield, such as FRET, can also be monitored by the molecular brightness.

## 9.3.2

**Autocorrelation Analysis, Mathematical Background**

To calculate the diffusion time of the particle from correlation curves such as shown in Figures 9.9 and 9.11 we have to derive a theoretical function describing the observed FCS data. In a confocal set-up the fluorescence intensity,  $I_{\text{Fl}}(t)$ , observed at the time  $t$  depends on the following factors:

- 1) The excitation intensity function,  $I_{\text{ex}}(\vec{r})$ , which describes the three-dimensional (3D) distribution of the excitation intensity in the focal region [compare with inset in Figure 7.1,  $\vec{r} = (x, y, z)$ ].
- 2) The local, microscopic concentration of fluorescing particles,  $C(\vec{r}, t)$ , which depends on the diffusion of the particles in and out of the focal region.
- 3) The absorption coefficient of the fluorescence markers for the corresponding excitation wavelength,  $\epsilon(\lambda)$ .
- 4) The fluorescence quantum yield,  $\Phi_{\text{Fl}}$ , of the fluorescence markers.
- 5) The optical transfer function,  $S(\vec{r})$ , which describes the probability that photons are detected that have been emitted from a certain position,  $\vec{r}$ , in the focal region. This function depends, amongst other factors, critically on the relative positions and properties of the microscope objective, the pin-hole and the detector.
- 6) Finally, it depends on the overall detection efficiency,  $\Phi_{\text{Det}}$ , of the confocal apparatus.

The fluorescence intensity,  $I_{\text{Fl}}(t)$ , observed at time  $t$  is proportional to a spatial integration of all these factors:

$$I_{\text{Fl}}(t) \propto \int I_{\text{ex}}(\vec{r}) \cdot C(\vec{r}, t) \cdot \epsilon(\lambda) \cdot \Phi_{\text{Fl}} \cdot S(\vec{r}) \cdot \Phi_{\text{Det}} \, dV \quad (9.8)$$

Here, the polarization dependence of excitation or emission as well as possible fluctuations in extinction coefficients or quantum yields and excitation saturation effects are neglected. The excitation intensity function,  $I_{\text{ex}}(\vec{r})$ , together with the optical transfer function,  $S(\vec{r})$ , determines the 3D probability function for detecting fluorescence from a molecule at position  $\vec{r}$ . The product of these two functions determines the shape of the detection volume. The corresponding probability distribution,  $W(\vec{r})$ , is usually approximated by a 3D Gaussian function:

$$I_{\text{ex}}(\vec{r}) \cdot S(\vec{r}) \propto W(\vec{r}) \approx e^{-\frac{2x^2+y^2}{r_0^2}} \cdot e^{-\frac{2z^2}{z_0^2}} \quad (9.9)$$

Here,  $z_0$ , describes the dimension or 'length' of the focal detection volume in the axial direction and  $r_0$  is the dimension or 'diameter' in the lateral direction ( $x, y$ ) perpendicular to the optical axis (see again inset in Figure 7.1).

Substituting (9.8) in (9.5) using the approximation (9.9) results in:

$$G_{\text{Dif}}(\tau) = \frac{\iint W(\vec{r})W(\vec{r}')\langle C(\vec{r}, t)C(\vec{r}', t + \tau) \rangle dV dV'}{\left(\int W(\vec{r})\langle C(\vec{r}, t) \rangle dV\right)^2} - 1$$

$$= \frac{\iint W(\vec{r})W(\vec{r}')\langle \delta C(\vec{r}, t)\delta C(\vec{r}', t + \tau) \rangle dV dV'}{\left(\int W(\vec{r})\langle \delta C(\vec{r}, t) \rangle dV\right)^2} \quad (9.10)$$

Here, all constants,  $I_{\text{ex}}(\vec{r})$ ,  $\epsilon(\lambda)$ ,  $\Phi_{\text{Fl}}$ ,  $S(\vec{r})$ ,  $\Phi_{\text{Det}}$ , in (9.8) vanish due to the normalization by  $\langle I_{\text{Fl}}(t) \rangle^2$ ;  $\vec{r}$  and  $\vec{r}'$  are the coordinates for the integration in space,  $dV$  and  $dV'$ , at the two different times  $t$  and  $t + \tau$ , respectively.  $\delta C(\vec{r}, t) = C(\vec{r}, t) - \langle C \rangle$  describes the deviation of the local concentration at the place  $\vec{r}$  and the time  $t$ ,  $C(\vec{r}, t)$ , from the average concentration of the fluorescing particles,  $\langle C \rangle$ , which is macroscopically measurable.  $\langle \delta C(\vec{r}, t)\delta C(\vec{r}', t + \tau) \rangle$  in (9.10) is a correlation term that describes the probability of finding a particle that was at place  $\vec{r}$  at time  $t$  at a certain other place  $\vec{r}'$  after the correlation time  $\tau$  has passed. For the case of a free 3D diffusion this term can be described by:

$$\langle \delta C(\vec{r}, 0)\delta C(\vec{r}', \tau) \rangle = \langle C \rangle \frac{1}{(4\pi D\tau)^{3/2}} \cdot e^{-\frac{(\vec{r}-\vec{r}')^2}{4D\tau}} \quad (9.11)$$

Here,  $D$  is the diffusion coefficient of the fluorescing particles;  $D$  is related to the diffusion time,  $\tau_{\text{D}}$ , by:

$$\tau_{\text{D}} = \frac{r_0^2}{4D} \quad (9.12)$$

Equation (9.11) together with (9.12) can be used to solve the integration in (9.10) after inserting (9.9). The result is:

$$G_{\text{Dif}}(\tau) = \frac{1}{\langle C \rangle \pi^{3/2} r_0^2 z_0} \cdot \frac{1}{1 + \frac{\tau}{\tau_{\text{D}}}} \cdot \frac{1}{\sqrt{1 + \left(\frac{r_0}{z_0}\right)^2 \frac{\tau}{\tau_{\text{D}}}}} \quad (9.13)$$

### 9.3.3

#### Quantitative Determination of Important Parameters from Autocorrelation Curves

Equation (9.13) actually describes mathematically fluorescence correlation curves as observed in cases of free 3D diffusion of fluorescent particles through a confocal detection volume such as shown in Figures 9.9 and 9.11. The term  $\pi^{3/2} r_0^2 z_0$  in (9.13) corresponds to the effective focal detection volume  $V_{\text{eff}} = \pi^{3/2} r_0^2 z_0$  of the confocal microscope set-up (compare also inset in Figure 7.1). For zero correlation times,  $\tau = 0$ , (9.13) simplifies to:

$$G_{\text{Dif}}(0) = \frac{1}{\langle C \rangle V_{\text{eff}}} = \frac{1}{\langle N \rangle} \quad (9.14)$$

This is the previously qualitatively discussed (9.6) inverse relationship between the correlation amplitude observed at short correlation times and the particle number. The average number of fluorescing particles in the detection volume is the direct product of the macroscopic concentration of the fluorescing particles,  $\langle C \rangle$ , and the detection volume:  $\langle N \rangle = \langle C \rangle V_{\text{eff}}$ . If the ratio  $r_0/z_0$  is known for a particular experimental set-up then the diffusion time of the investigated fluorescing particles can be determined by fitting (9.13) to the experimental curves. To determine  $r_0/z_0$  usually fluorescence markers with known diffusion times are measured prior to the actual measurement of the samples and the values of  $r_0/z_0$  are then varied until (9.13) fits the experimental data. Equation (9.13) accounts only for fluorescence fluctuations caused by diffusion of the molecules in and out of a confocal detection volume. Therefore, attention has to be paid in the application of (9.14) when effects other than particle diffusion affect the observed fluorescence fluctuations. Fortunately, they usually affect the correlation curves only at correlation times shorter than  $\sim 50 \mu\text{s}$ . The influence of these effects on the observed correlation curves will be discussed in detail below (Section 9.3.4; further correlation effects).

### 9.3.3.1 Relationship Between Volume and Molecular Mass of a Protein and its Diffusion Time

By assuming that proteins can be approximated as spherical particles their mass,  $m$ , can be roughly estimated from  $\tau_D$ , or, in turn,  $\tau_D$  can be estimated from  $m$  in order to calculate what expected FCS curves might look like. The diffusion time is related to the diffusion coefficient by (9.12). The diffusion coefficient, in turn, for spherical particles is described by the Stokes–Einstein equation:

$$D = \frac{k_B T}{6\pi r_p \eta} \quad (9.15)$$

Here,  $r_p$  is the radius of the particle and  $\eta$  is the viscosity of the solvent. Usually, for  $\eta$  the value of water at room temperature is used;  $k_B$  is the Boltzmann constant. The approximate volume of the protein can be derived from its radius  $r_p$ , which can be estimated using (9.15) and (9.12), and the corresponding formula for a sphere:  $V = 4/3\pi r_p^3$ . Finally, from this volume an approximate value for its mass can be calculated using  $V = m\partial$ . Here,  $\partial$ , is the specific volume of the biomolecule, including the hydration shell. Typically, a value of  $\partial \sim 1.2 \text{ cm}^3 \text{ g}^{-1}$  can be assumed for proteins. Of course, such estimates provide only a very rough approximation of the volume, mass and diffusion times of the biomolecules as they are usually not spherical particles.

### 9.3.3.2 Two-Dimensional Diffusion and Active Transport

Equation (9.13) only accounts for situations in which the diffusion of the fluorescing particles corresponds to a free 3D diffusion. For other types of

**Table 9.1** Motility terms for different types of correlated motion.

Type of correlated motion	Motility term
Free 3D diffusion	$M(\tau) = \frac{1}{1 + \frac{\tau}{\tau_D}} \cdot \frac{1}{\sqrt{1 + \left(\frac{r_0}{z_0}\right)^2 \frac{\tau}{\tau_D}}}$
Free 2D membrane diffusion	$M(\tau) = \frac{1}{1 + \frac{\tau}{\tau_D}} \cdot \left(\frac{r_0}{z_0}\right)^2$
Active transport parallel to $r_0$ through the detection volume with velocity $v$	$M(\tau) = e^{-\left(\frac{v\tau}{r_0}\right)^2}$
Free 3D diffusion and active transport parallel to $r_0$	$M(\tau) = \frac{1}{1 + \frac{\tau}{\tau_D}} \cdot \frac{1}{\sqrt{1 + \left(\frac{r_0}{z_0}\right)^2}} \cdot e^{-\frac{\left(\frac{v\tau}{r_0}\right)^2}{1 + \frac{\tau}{\tau_D}}}$

motions of the fluorescing particles (9.13) can be replaced by a more general expression:

$$G(\tau) = \frac{1}{\langle N \rangle} \cdot M(\tau) \quad (9.16)$$

where  $M(\tau)$  is the so-called motility term, as defined by Table 9.1.

The shape of the correlation curves thus gives additional information about the type of diffusional motion. Notably, however, the two-dimensional (2D) membrane diffusion, for example, results in quite similar FCS curves in comparison to free 3D diffusion. Therefore, superior data quality is often necessary to distinguish unambiguously different cases, if it is not known a priori which type of diffusion is present in a particular sample.

### 9.3.3.3 Mixtures of Fluorescing Particles

If mixtures of different fluorescing particles are measured, for example of the free and the bound ligand shown in Figure 9.9, the correlation curves can be calculated by:

$$G(\tau) = \frac{1}{\left(I_{\text{Fl,F}}^{\text{Particle}} \langle N_F \rangle + I_{\text{Fl,B}}^{\text{Particle}} \langle N_B \rangle\right)^2} \cdot \left[ \left(I_{\text{Fl,F}}^{\text{Particle}}\right)^2 \langle N_F \rangle M_F(\tau) + \left(I_{\text{Fl,B}}^{\text{Particle}}\right)^2 \langle N_B \rangle M_B(\tau) \right] \quad (9.17)$$

with  $I_{\text{Fl,F}}^{\text{Particle}}$  and  $I_{\text{Fl,B}}^{\text{Particle}}$ ,  $\langle N_F \rangle$  and  $\langle N_B \rangle$  and  $M_F(\tau)$  and  $M_B(\tau)$  being the particle brightnesses, numbers and motility terms corresponding to the free and the bound ligand, respectively. However, notably, a very large difference of at least a factor of ten in the molecular mass is necessary to unambiguously differentiate both particle numbers and diffusional times for both types of fluorescing particles in a mixture from fitting (9.17) to a single FCS curve. Usually, different particle numbers for the two types of fluorescing particles can only be determined

robustly in a mixture when the corresponding individual diffusion times are already known from experiments conducted with the pure samples. An alternative and more convenient method to follow the receptor–ligand binding via FCS is, therefore, simply fitting (9.13) to several FCS curves of mixtures observed in a titration series and take the magnitude of experimentally determined average  $\tau_D$  values as a parameter for the binding degree. For details on determining the accuracy of such assay approaches see Chapter 13 (Section 13.2).

### 9.3.4

#### Further Correlation Effects

For correlation times shorter than  $\sim 50\text{ }\mu\text{s}$ , deviations in the FCS curves from (9.13) can usually be observed. The most important effect is additional correlation signals caused by ‘dark periods’ in which the fluorescence markers are, for example, in the long-lived triplet state. Figure 9.13 shows this ‘blinking’ behaviour schematically. The resulting fluorescence fluctuations have some similarities with the fluorescence fluctuations observed for diffusional transits (Figure 9.8) except that they occur on a much faster timescale. It is thus not surprising that they give rise to additional correlation signals superimposed on the curves that would be expected for a pure diffusional correlation (Figure 9.14). To consider these effects in calculated FCS curves, (9.13) has to be multiplied by a term  $X_{\text{triplet}}(\tau)$  that takes additionally the triplet-state dynamics into account:

$$G(\tau) = \frac{1}{\langle N \rangle} \cdot M(\tau) \cdot X_{\text{triplet}}(\tau) \quad (9.18)$$

$$X_{\text{triplet}}(\tau) = 1 + \frac{T}{1 - T} e^{-\tau/\tau_T}$$

Here,  $\tau_T$  is the triplet-state lifetime of the fluorescence marker, as defined by Eq. (1.14) [ $\tau_T = (k_{\text{Ph}} + k_{\text{ISC}}^{\text{T} \rightarrow \text{S}})^{-1}$ ], and  $T$  is the fraction of molecules that are in

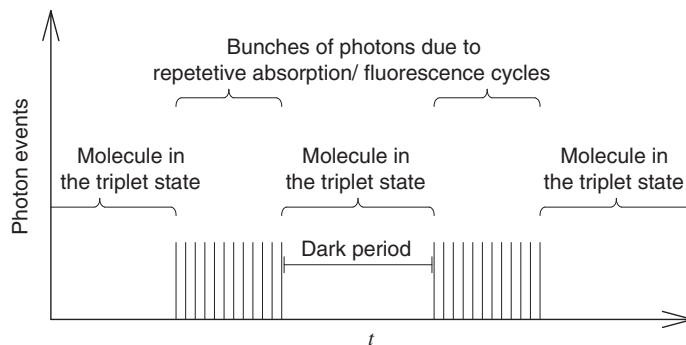


**Figure 9.13** Photons emitted from single fluorescence markers come in ‘bunches’ because during the periods the molecules are in the long-lived triplet states they cannot emit fluorescence photons. These ‘dark periods’ give rise to additional signals in the correlation analysis.

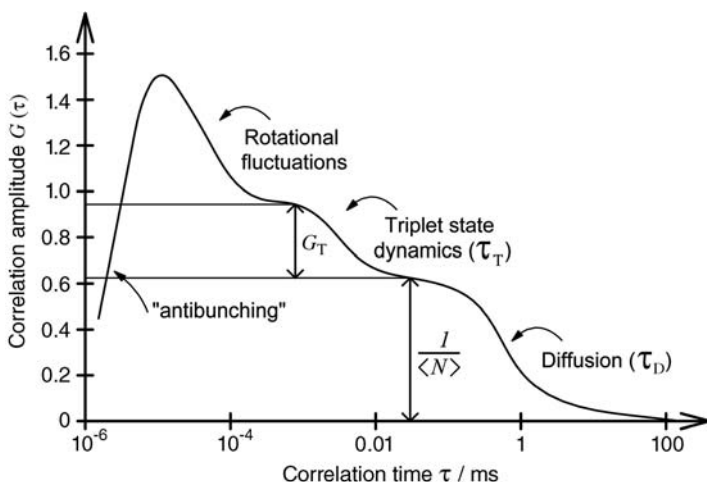


**Figure 9.14** Triplet-state dynamics (Figure 9.13) give rise to additional correlation signals superimposed on the correlation curve expected for pure diffusion. This additional term depends on the excitation intensity. This is because the fluorescence markers accumulate in the long-lived triplet state under saturating excitation conditions. When using experimental equipment that allows

measurement of FCS for even shorter correlation times then further correlated effects can be observed. These are, for example, another increase in the correlation amplitudes due to rotational diffusion and a drop in the correlation curve for very small correlation times caused by the minimum time needed for a re-excitation of the molecules (antibunching). Correlation times are given in milliseconds.

the triplet state;  $\tau_T$  for fluorescence markers is usually on the  $\mu\text{s}$  timescale. The term  $T$  can be calculated from the fraction of the correlation amplitude in FCS curves that is due to the triplet-state dynamics,  $G_T$  (as defined in Figure 9.14), and  $\langle N \rangle$  by:

$$T = \frac{G_T \cdot \langle N \rangle}{1 + G_T \cdot \langle N \rangle} \quad (9.19)$$

This fraction is dependent on the laser excitation intensity. For increasing excitation intensities more and more fluorescence markers accumulate in the long-lived triplet state. As a result, the relative population of molecules in the triplet state increases under saturating excitation conditions and the shoulder in the FCS curves increases correspondingly.

By using equipment that allows us to record FCS curves at even shorter correlation times, further correlation effects can be observed. When linear polarized excitation light is used at sub- $\mu\text{s}$  timescales intensity fluctuations can be observed that reflect the diffusional rotation of the fluorescence markers transition dipole moment (see again Figure 9.14). At even shorter times, on the nanosecond timescale, one observes a drop in the correlation curve. This is caused by intensity fluctuations that are due to the minimum time necessary for an emission and re-excitation cycle of a molecule. This minimum time is simply

determined by the excited-state lifetime of the singlet state,  $\tau_{S_1}$ . The resulting 'antibunching' behaviour of the emitted photons is the reason why for  $\tau=0$  a zero correlation amplitude  $G(0)=0$  is observed if the time resolution of the experimental equipment is sufficient.

In addition to the correlations based on the photophysical properties of the fluorescence molecules all other correlated fluorescence intensity fluctuations also contribute to the observed FCS signals. Such correlated fluorescence intensity fluctuations can be due to biomolecular dynamics. It has been shown, for example, that changing FRET efficiencies of a FRET pair of dyes attached to the termini of DNA (compare with Figure 3.26) can be used to determine the dynamics of conformational fluctuations of the DNA strand by FCS analysis.

### 9.3.5

#### Cross-Correlation Analysis

In addition to the previously discussed autocorrelation, correlations between different fluorescence signals can also be analysed by fluorescence cross-correlational spectroscopy (FCCS). It is possible to correlate fluorescence signals originating from many different sources. Here, we will focus on one type of fluorescence cross-correlation that is especially relevant for biomolecular applications. This type of FCCS is dual-colour cross-correlation analysis and it is especially valuable for the determination of binding processes of biomolecules or biological objects. Figure 9.15 shows the principle of FCCS. First, two potential

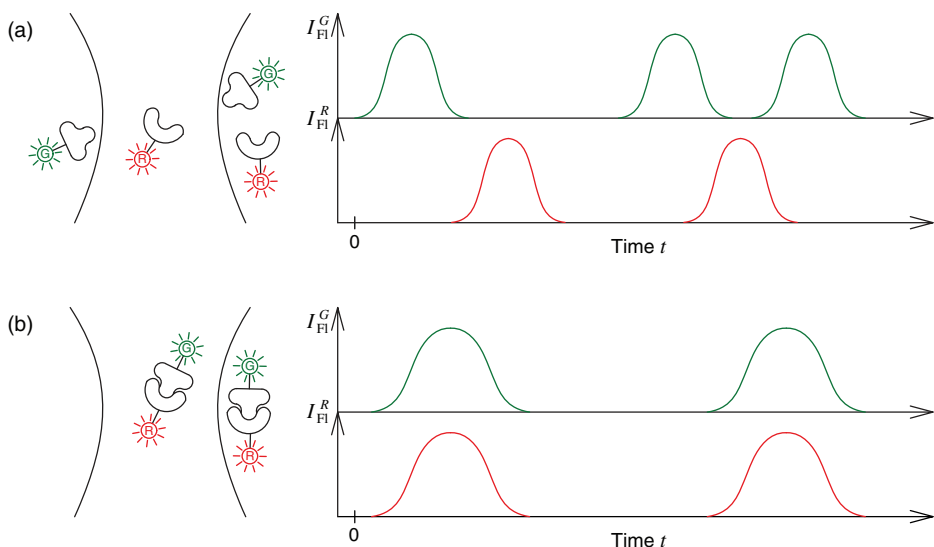


**Figure 9.15** In dual-colour fluorescence correlation, binding reactions of differently labelled biomolecules can be analysed. (a) If no binding occurs, uncorrelated signals are

observed from the two dyes. (b) For complete binding, only correlated fluorescence bursts can be observed.

binding partners are labelled with two different fluorescence dyes. The two fluorescence markers can be, for example, a green fluorescing and a red fluorescing marker. Now, the fluorescence of each fluorescence markers is detected separately using a confocal microscope set-up modified for dual-colour fluorescence detection (Figure 9.16). This set-up allows us to excite both types of fluorescence dyes simultaneously in the focal region of the microscope objective and to detect the resulting fluorescence signals from both types of fluorescence dyes separately. If no binding occurs, the fluorescence signals originating from the two different reaction partners occur arbitrarily and uncorrelated (Figure 9.15a). However, if binding occurs it results in correlated fluorescence signals in the green and red detection channels (Figure 9.15b). Statistical analysis of these correlations can be performed by FCCS.

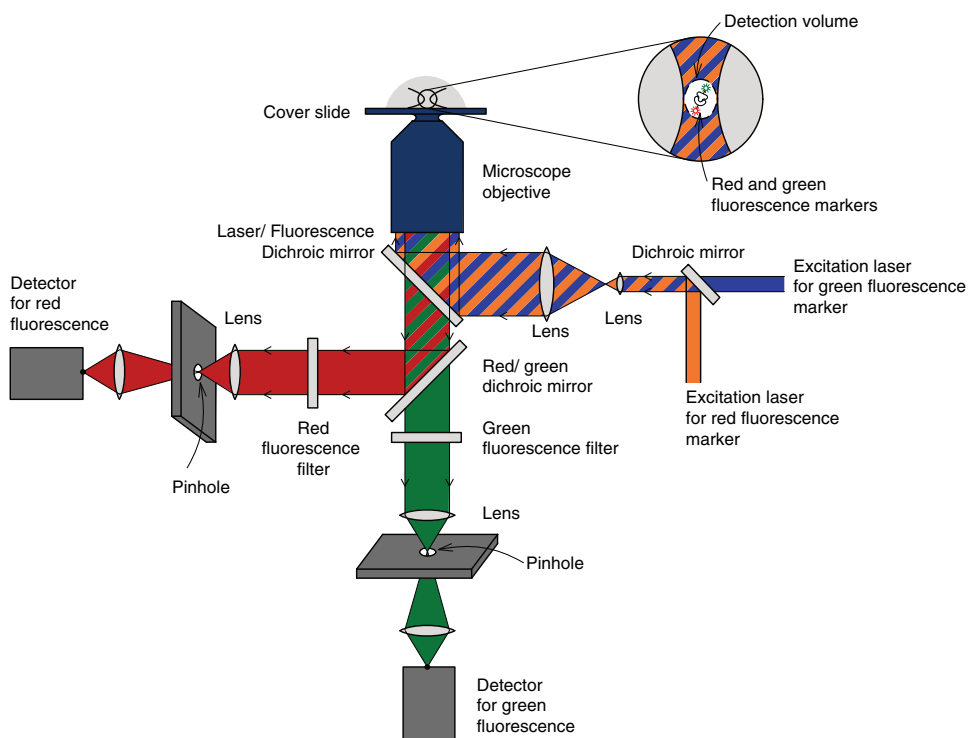


**Figure 9.16** Confocal microscope set-up for dual-colour cross-correlation analysis. In comparison to a normal confocal set-up (Figure 7.1) it is extended by a second excitation laser and a second detector. The second laser is needed to be able to excite a second type of fluorescence dye in the detection volume. It is combined with the other laser beam by a dichroic mirror. Another, more sophisticated, dichroic mirror is used to

direct both excitation laser beams towards the microscope objectives back aperture and transmits most of the fluorescence light of the two types of fluorescence dyes. Finally, another dichroic mirror along with two optical filters is used to separate the fluorescence from the two dyes spectrally and to direct the fluorescence of both types of fluorescence dyes towards a corresponding pinhole and detector.

The corresponding cross-correlation curves are calculated using:

$$G_X(\tau) = \frac{\langle I_{\text{Fl}}^G(t) \cdot I_{\text{Fl}}^R(t + \tau) \rangle}{\langle I_{\text{Fl}}^G(t) \rangle \cdot \langle I_{\text{Fl}}^R(t) \rangle} - 1 \quad (9.20)$$

Here,  $I_{\text{Fl}}^G(t)$  and  $I_{\text{Fl}}^R(t)$  are the intensities observed with the detector for green and red fluorescence and  $\langle I_{\text{Fl}}^G(t) \rangle$  and  $\langle I_{\text{Fl}}^R(t) \rangle$  are the corresponding average intensities, respectively. In contrast to the autocorrelation analysis (9.5), where one signal is investigated with respect to self-similarity, cross-correlation analysis compares the similarities of two different signals with each other.

The resulting cross-correlation and single-colour autocorrelation curves are shown in Figure 9.17 for various scenarios. Autocorrelation curves according to (9.5) and (9.13) can be calculated for each detector individually and separately. They look the same as if no other fluorescence dye were present. In Figure 9.17a, for example, no binding occurs. As a direct consequence, a cross-correlation curve calculated according to (9.20) results in a zero cross-correlation amplitude for all correlation times. The situation is different though in Figure 9.17b. When an equimolar binding is present a complete correlation is present between the signals in the red and the green detector:  $I_{\text{Fl}}^G(t)/\langle I_{\text{Fl}}^G(t) \rangle = I_{\text{Fl}}^R(t)/\langle I_{\text{Fl}}^R(t) \rangle$ . No difference can be observed for the normalized signals from the red and green detectors. As a consequence, the cross-correlation curves are identical to the autocorrelation curves of each detector. If only 50% of an equimolar mixture of binding partners bind, then the cross-correlation curve drops to 50% of the autocorrelation values (Figure 9.17c). A comparison of the amplitudes of the red and green autocorrelation curves with the cross-correlation amplitude therefore allows us to determine the concentration of red and green labelled particles (9.14) as well as the number of bound partners. This is also illustrated in Figure 9.17d. Here, the autocorrelation curves show that the concentration or number of green labelled binding partners is twice the concentration or number of red-labelled binding partners. All red binding partners bind to a green partner. The cross-correlation amplitude cannot exceed the autocorrelation amplitude of the green binding partner. As a result, the cross-correlation curve is 100% of the green autocorrelation curve in the case of 100% binding efficiency. In general, the concentration of the doubly labelled particles can be calculated by:

$$C_{\text{RG}} = \frac{G_X(0)}{G_R(\sim 50 \mu\text{s})G_G(\sim 50 \mu\text{s}) \cdot V_{\text{eff}}} \quad (9.21)$$

if the fluorescence markers quantum yields remain the same during binding. Here,  $G_X(0)$ ,  $G_R(\sim 50 \mu\text{s})$  and  $G_G(\sim 50 \mu\text{s})$  are the cross-correlation and autocorrelation amplitudes of the red and the green detector for small correlation times, respectively.

The examples shown in Figure 9.17 show how powerful cross-correlation analysis is for a detailed quantification of binding partner concentrations and binding

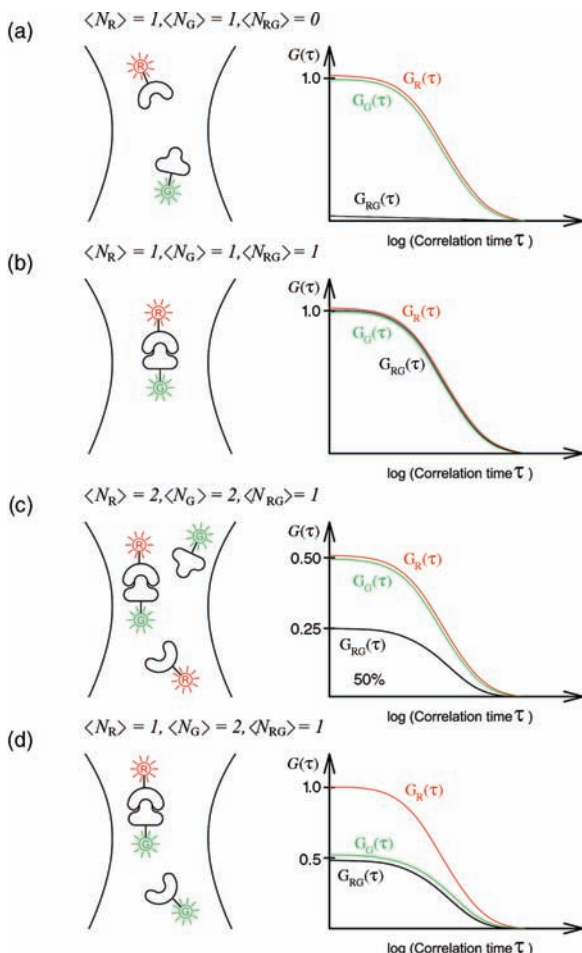


**Figure 9.17** Cross-correlation (black) and single-colour autocorrelation (red and green) curves for various scenarios. (a) No binding occurs between equal numbers of potential binding partners; (b) efficient binding

between equal numbers of binding partners; (c) only 50% of an equal number of potential binding partners bind; and (d) effective binding between binding partners but double excess of one binding partner.

affinities. It is especially useful in all cases where other fluorescence-based binding assays such as fluorescence polarization or FRET (see Chapter 3) do not work. This is, for example, very often the case when both the binding partners are larger biomolecules, such as, for example, an antibody and a large protein–antigen or complementary DNA strands. In these cases, often the dynamic range of fluorescence polarization does not suffice because the rotational diffusion of both binding partners is larger than the fluorescence lifetime of fluorescence markers. A FRET assay, in contrast, often either does not work or is demanding because it requires the fluorescence dyes to be close enough after binding.

Cross-correlation, in contrast, still provides very robust information about binding regardless of the size of the binding partners or the labelling sites. Of course, cross-correlation as performed by an apparatus such as shown in Figure 9.16 also has some major drawbacks. One is the demanding alignment required to overlap both excitation volumes and detection volumes by positioning the separate pin-holes. Obviously, a 100% cross-correlation can only be observed when all these volumes ideally overlap. A small misalignment results immediately in a smaller measured cross-correlation amplitude and thus estimated binding percentage. For estimating binding affinities using (9.21), another draw back is that correlations due to triplet-state formation or other fluctuations of the dyes can again impair the auto correlation values  $G_R$  and  $G_G$  for small correlation times. Fortunately, in the cross-correlation curves,  $G_X$ , these effects are not present because the triplet-state dynamics occur completely uncorrelated for both dyes. In any case, both drawbacks can be circumvented by using nonlinear two-photon processes for excitation of the fluorescence markers. The principles of such nonlinear optical processes and their application in the biosciences as well as for cross-correlational analysis will be discussed in detail in Chapter 10.

## 9.4

### Optical Tweezers

Optical tweezers have been increasingly applied in recent years to investigate forces exerted by or at single biomolecules. Optical tweezers are based on the trapping of spherical objects diffusing in an aqueous environment into the focal region of a laser illuminated microscope objective (Figure 9.18). The trapping forces are generated by the radiation pressure of photons being refracted and scattered at the sphere. To investigate biomolecules, usually, micrometre-sized polymeric spheres are trapped. If single biomolecules are attached between a trapped sphere and an immobile object, biomechanical forces on the pN scale can be measured by detecting the movements of the sphere within the trap. In this section we first discuss the theoretical background that describes the forces responsible for the trapping of spheres that are large compared to the wavelength of light and will then present application examples in which specific biomolecular questions are addressed.

#### 9.4.1

##### Theoretical Background

The basis of radiation pressure is the fact that even photons have a small nonzero momentum. For a particular wavelength the momentum  $p$  of a single photon is:

$$p = \frac{h}{\lambda} \quad (9.22)$$

Here,  $\lambda$  is the wavelength and  $h$  is Planck's constant. To consider the direction of the photons momentum we have to use its vector representation:

$$\vec{p} = \hbar \vec{k} \quad (9.23)$$

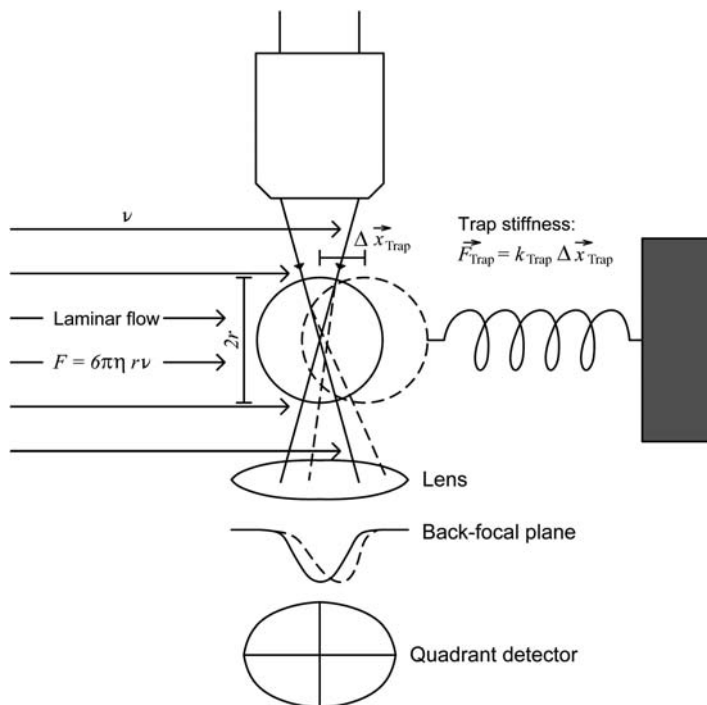


**Figure 9.18** Principle set-up of an optical trap. A polymer sphere of  $\sim 1 \mu\text{m}$  in diameter is trapped by the radiation pressure of photons in the focal region of a microscope objective irradiated by a collimated laser beam. A displacement of the sphere from its

trapped equilibrium position,  $\Delta \vec{x}_{\text{Trap}}$ , requires a certain force,  $\vec{F}_{\text{Trap}}$ , that is determined by the trap stiffness,  $k_{\text{Trap}}$ . The position of the sphere can be detected by, for example, a quadrant detector.

Here,  $\vec{k}$  is called the wave vector of the photon. It points in the propagation direction of the photon and has the absolute value  $|\vec{k}| = 2\pi/\lambda$ . Substituting  $\lambda = 2\pi/|\vec{k}|$  into (9.22) shows that (9.23) is nothing more than the vector representation of (9.22) (remember that  $\hbar = h/2\pi$ ).

The forces generated by refracting and scattering photons at objects that are large compared to the wavelength of light can be described by ray objects. If, for example, photons are refracted entering the sphere their propagation direction and thus their momentum change.<sup>1)</sup> The change in the momentum ( $\Delta \vec{p}$ )

1) Actually, the momentum of a photon in different condensed matter also changes because the velocity of light differs in these different media. The velocity of light is anti-proportional to the refractive index,  $n$ , of the medium in which the photon travels.

Intriguingly, it is still a matter of debate

whether the momentum of a photon in condensed matter such as water or polystyrene relates to its refractive index by  $p = (E/c_0)n$  or by  $p = E/c_0 n$ . Here,  $E$  is the energy of the photons [cf. (1.1)] and  $c_0$  is the speed of light in a vacuum.

corresponds to the vector difference between the momentums before and after the surface:

$$\Delta\vec{p} = \vec{p}_A - \vec{p}_B = \hbar\vec{k}_A - \hbar\vec{k}_B \quad (9.24)$$

Here,  $\vec{p}_B, \vec{p}_A$  and  $\vec{k}_B, \vec{k}_A$  are moment vectors and wave vectors of the photon before and after the refraction, respectively. According to the law of momentum conservation the change in the momentums of photons must be compensated by an opposite change in the momentum of the sphere that caused the refraction of the photons. If  $dN/dt$  is the number of photons,  $N$ , entering the sphere per time,  $t$ , the force compensating the change in the photon momentums is:

$$\vec{F} = -\frac{dN \cdot \Delta\vec{p}}{dt} \quad (9.25)$$

This force is orientated exactly opposite to the direction of the photons momentum change,  $\Delta\vec{p}$ , caused by the refraction. When the photons transit the sphere their momentum change twice (Figure 9.19). A first counterforce,  $\vec{F}^1$ , occurs when the photons cross the water to the sphere surface. The second compensating force,  $\vec{F}^2$ , occurs when the photons cross the sphere to the water surface. The summation of these forces over all photons in the trapping beam results in a force trapping the sphere in the focal region of the microscope objective. Notably, however, this is only the case if the refractive index of the sphere is

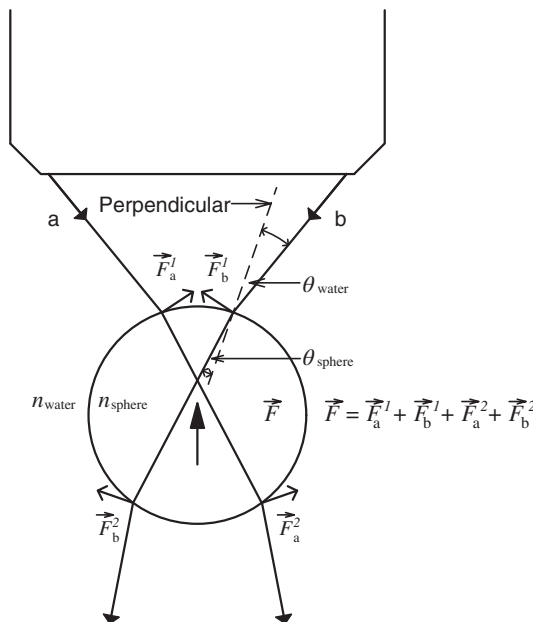


**Figure 9.19** If the sphere is displaced in the axial direction away from the microscope's objective then the forces compensating the changes in the photon momenta sum up to a total force pushing the sphere towards the focus.

higher than that of the surround medium. For polystyrene spheres and water this is the case since the corresponding refractive indices are  $n_{\text{sphere}} = 1.55$  and  $n_{\text{water}} = 1.33$ , respectively.

To better understand how the counterforces can sum up to a total trapping force we first discuss in detail the counterforces created by the outermost beams focused by the microscope objective (a and b in Figures 9.19 and 9.20).

In Figure 9.19 the sphere is displaced from the focus in an axial direction away from the microscope objective. Because the refractive index of the sphere is higher than that of water, photons entering the sphere are always refracted to a smaller angle with respect to the perpendicular of the water–sphere surface (see, for example, the first refraction of beam b). This is a direct consequence of the application of Snell's law for refraction:

$$\frac{\sin \theta_{\text{water}}}{\sin \theta_{\text{sphere}}} = \frac{n_{\text{sphere}}}{n_{\text{water}}} \quad (9.26)$$

Here,  $\theta_{\text{water}}$  and  $\theta_{\text{sphere}}$  are the angles of the photon's propagation directions with the perpendicular of the water–sphere surface (see again the first refraction of beam b in Figure 9.19), respectively. Conversely, when photons exit the sphere they are always refracted to a larger angle with respect to the perpendicular of the sphere–water surface. Let us first discuss the counterforces generated by the refraction of beam a. When this beam is refracted the first time at the sphere, the corresponding change in the momenta of the photons results in a compensating counterforce at the sphere,  $\vec{F}_a^1$ , which points in the opposite direction to the refraction of the beam. Also, the second refraction leads to a counterforce  $\vec{F}_a^2$ . Both forces point upwards and to the right in the example shown in Figure 9.19. The horizontal components of the forces  $\vec{F}_a^1$  and  $\vec{F}_a^2$  are exactly evened out by the horizontal components of the analogue forces  $\vec{F}_b^1$  and  $\vec{F}_b^2$  of beam b. However, the axial components of all forces  $\vec{F}_a^1, \vec{F}_a^2, \vec{F}_b^1$  and  $\vec{F}_b^2$  point upwards and therefore also the summation over all forces  $\vec{F}_a^1, \vec{F}_a^2, \vec{F}_b^1$  and  $\vec{F}_b^2$  results in a total force  $\vec{F}$  that points upwards. As an overall result, the sphere is pushed back in the direction of the microscope's focus. This force increases the larger the original angles

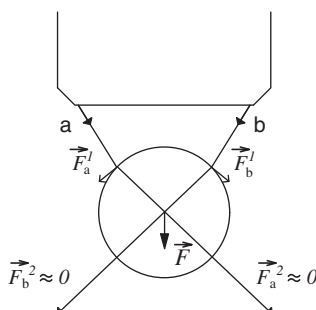


**Figure 9.20** If the sphere is displaced in the axial direction towards the microscope's objective then the forces compensating the changes in the photon momentums sum to a total force pushing the sphere away from the objective.

between the beams a and b were. In general, the total restoring force summarized over the forces  $\vec{F}^1$  and  $\vec{F}^2$  of all beams is larger the greater the numerical aperture of the microscope objective is (the numerical aperture of a microscopy objective is defined by (7.2) in Section 7.2.1 and the corresponding Figure 7.2). As a consequence, strong optical tweezers need microscope objectives with high numerical apertures.

Figure 9.20 illustrates an example in which the sphere is displaced from the focal region in the axial direction towards the microscope objective. Here, the beams are now refracted in the opposite direction to the case shown in Figure 9.19 because they hit the water–sphere surface under a different angle. As a result, the forces  $\vec{F}_a^1$  and  $\vec{F}_b^1$  point in the opposite direction than in the situation shown in Figure 9.19. In the particular example shown in Figure 9.20 the forces  $\vec{F}_a^2$  and  $\vec{F}_b^2$  are almost zero because the beams hit the sphere–water surface perpendicular on exiting the sphere. As an overall result, summation over all forces  $\vec{F}_a^1$ ,  $\vec{F}_a^2$ ,  $\vec{F}_b^1$  and  $\vec{F}_b^2$  results in a net force pushing the sphere downwards. Again, a restoring force is present that pushes the sphere back in the direction of the focus.

Finally, Figure 9.21 shows the situation of horizontally displaced spheres. In the more central parts of the focused light beam higher intensities are usually present ( $\vec{F}_c$ , thick beam in Figure 9.21). A higher intensity corresponds to a larger number of photons,  $N$ , per unit time and thus to a larger compensating counterforce for these central beams (9.25). If the sphere is displaced in the horizontal direction the horizontal component of this large force always points in the opposite direction of the displacement. Together with the forces of the other beams, again a total counterforce is generated that points towards the focus of the microscope objective.

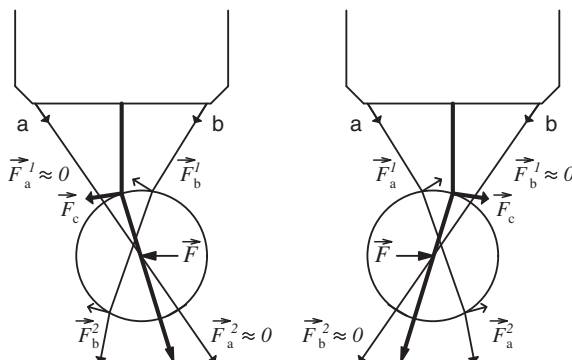


**Figure 9.21** If the sphere is displaced in the horizontal direction then the forces compensating the changes in the photon momenta again cause restoring forces that push the sphere back to the focal region. The horizontal restoring force is additionally supported by the higher intensity of the beams in the

central part of the photon flux (thick beam). Please note that here exemplary situations are chosen, in which either beam a or beam b hit the water–sphere’s surfaces exactly perpendicularly. As a result, no net compensating force results from these beams.

So far, we have neglected forces caused by reflection of the photons at the water–sphere surfaces (Figure 9.22). The counterforces generated by photons scattered at the spheres are based on the same equations as for refracted photons, (9.24) and (9.25). The sum of these forces,  $\vec{F}_{\text{reflection}}$ , always points away from the microscope objective. Therefore, the equilibrium position of the sphere in a normal optical trap such as shown in Figure 9.22a is always moved slightly away from the focus in the direction of the light beam. If very stable optical traps are necessary, this can be compensated by using a second set of microscope objective and trapping beam opposite the first one (Figure 9.22b). If the sphere is now displaced from the equilibrium position in the axial direction, for example, (Figure 9.22c) then both trapping beams restore the sphere back to the equilibrium position. The forces caused by the reflection, however, approximately compensate each other.

For small displacements  $\Delta\vec{x}_{\text{Trap}}$  from the sphere's equilibrium position the net restoring force acting on the sphere,  $\vec{F}_{\text{Trap}}$ , usually varies linearly with the displacement. Therefore, the restoring forces in the optical trap can normally be described by Hooke's law (see also Figure 9.18):

$$\vec{F}_{\text{Trap}} = -k_{\text{Trap}} \cdot \Delta\vec{x}_{\text{Trap}} \quad (9.27)$$

The constant  $k_{\text{Trap}}$  is called the trap stiffness. The key parameters derived from optical trap experiments are forces that attached biomolecules exert on the

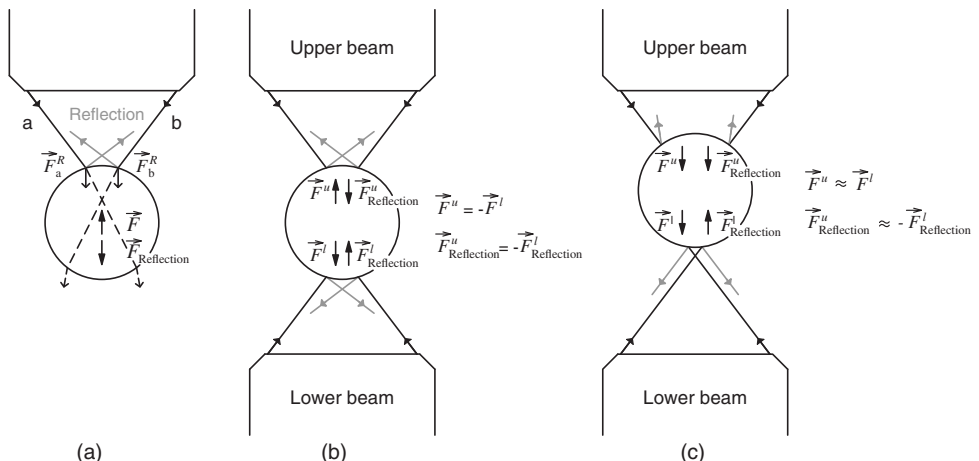


**Figure 9.22** (a) Forces generated by photons reflected at the water–sphere surface,  $\vec{F}_{\text{reflection}}$ , result in a decrease of the trapping force in axial direction. Therefore, usually, the equilibrium position of the sphere is shifted slightly away from the microscope objective focus. (b) If strong trapping forces are necessary the reflection forces can be compensated by using

two trapping beams from both sides. (c) If the sphere is then displaced upwards, for example, then both beams pull the sphere back to the equilibrium position. The reflection force of the upper beam,  $\vec{F}_{\text{reflection}}^u$ , however, is approximately compensated by the reflection forces of the lower beam:  
 $\vec{F}_{\text{reflection}}^u \sim -\vec{F}_{\text{reflection}}^l$ .

spheres and the resulting displacements from their equilibrium position. The displacement of the sphere can be monitored by detecting the influence of the sphere's position on the optical path of light travelling through the sphere. This can be done by various optical detection techniques, including the use of quadrant detectors, imaging devices and also interferometric detection of the detection beam properties. In Figure 9.18 the influence of the sphere's position on the light path and its detection is illustrated by a position-dependent intensity distribution sensed by a quadrant detector. A quadrant detector is an arrangement of four light detectors that can monitor very sensitively differences in the light intensity irradiated on one of the detector areas. Of interest is the magnitude of the detector signals as a function of the forces exerted on the sphere or the displacement of the sphere. An accurate calibration function of the detector signal dependence on the forces exerted on the sphere can be derived, for example, by recording the amplitudes and timescales of the detector-signal fluctuations as a function of the Brownian motions of the sphere within the trap. An important parameter in such calibration procedures is the drag force. The drag force corresponds to the force that a laminar liquid flow exerts on a spherical particle and can be calculated according to:

$$\vec{F}_{\text{laminar}} = 6\pi\eta r\nu \quad (9.28)$$

Here,  $r$  is the radius of the particle,  $\nu$  is the velocity of the laminar flow and  $\eta$  is the viscosity of the liquid, which is usually water at room or physiological temperatures. A laminar flow around the sphere can be generated, for example, by sweeping the trap through the fluid with different velocities. This can be used for a first estimate of trap stiffness (compare (9.28) with (9.27)).

The forces that can be sensed by optical tweezers usually range from far below one piconewton (pN) to an upper limit of a few hundred pN. Accuracies in the determination of absolute values of the sphere's position significantly below the nanometre scale are possible.

#### 9.4.2

#### Application Examples

Since typical biomolecular forces are often in the range of pN, optical tweezers are an ideal tool to determine such forces. It is possible, for example, to directly measure forces exerted by motor proteins such as myosin and kinesin, which we have already discussed extensively in Section 9.2 on optical single-molecule detection. In the following we present a few other typical application examples of force measurements using optical tweezers.

##### 9.4.2.1 Unfolding of RNA and DNA Hairpins

A very elementary question is how large are the forces keeping double strands of DNA or RNA together? Using optical tweezers these forces can be measured directly. Figure 9.23 shows a typical set-up for such an experiment. In this example, an RNA strand having a hairpin structure was used. A hairpin structure

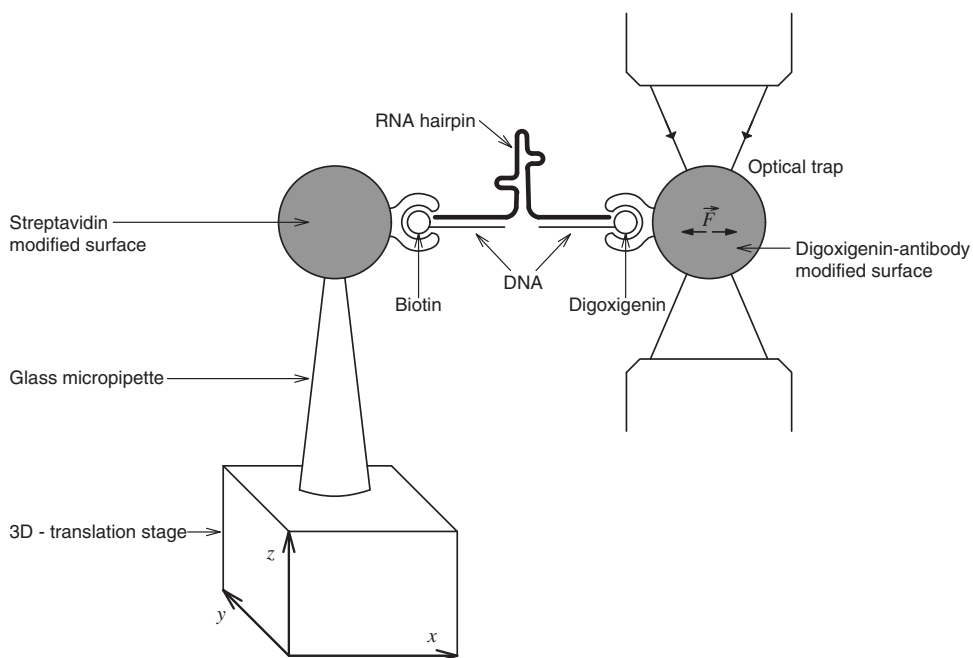


**Figure 9.23** The forces necessary to break RNA double strands can be measured by stretching hairpins of RNA clamped between a trapped sphere and a sphere mounted onto a 3D piezostage.

typically originates from sequences of complementary RNA or DNA bases within the same RNA or DNA strand, respectively. The RNA was clamped between an optically trapped sphere and another sphere fixed to a glass micropipette.

Biomolecules can be attached to the spheres in optical tweezers experiments in various ways. The preparation procedure of the clamped RNA described in the following therefore only illustrates an example of the typical steps that are necessary for biomolecule–sphere attachments in optical-tweezers experiments (cf. the linking and labelling procedures described in Section 3.2). First, the ends of the RNA are hybridized with two different complementary DNA strands. The corresponding DNA strands are linked to a biotin and an digoxigenin molecule, respectively. Digoxigenin is a small steroid molecule found in *Digitalis purpurea* plants. Then, the RNA–DNA hybrid can be added to a solution containing spheres with a digoxigenin-antibody-modified surface. Such surface modifications can often be performed by procedures similar to those described in Chapter 3 when the surfaces carry chemically groups that can be linked to biomolecules. A single sphere attached to the RNA–DNA hybrid is then trapped in the optical tweezers. This can be done simply by waiting until one of the freely diffusing spheres carrying the RNA enters the trap area. In a next step a weak laminar flow pointing in the direction of the sphere fixed to the micropipette is

applied. As a result, the RNA–DNA hybrid is orientated towards the fixed sphere. By carefully changing the relative positions of fixed and trapped spheres, eventually the biotin of the DNA binds to the streptavidin-modified surface of the fixed sphere. The change in the relative sphere positions can be induced by, for example, moving the glass micropipette using a 3D piezoactuated translation stage. Such 3D translation stages achieve a positioning accuracy in the subnanometre range. Another approach is to change optically the position of the trapping focus (see Figure 7.5 in Chapter 7). When the biotin has successfully attached to the streptavidin-modified sphere, the optical tweezers set-up detects forces that are correlated with the movement of the 3D translation stages.

To actually measure the forces necessary to break the hydrogen bonds responsible for RNA hybridization the translation stage is moved in the  $x$  direction (compare with Figure 9.23) away from the optical trap. The detected force exerted on the trapped sphere first increases until a certain point when the RNA hairpin starts to be pulled apart. This maximum force corresponds to the force keeping the RNA strands together. The corresponding values are around 15 pN. Using RNA or DNA homogenously containing either only the possible base pairings guanine–cytosine or adenine–uracil/adenine–thymine, respectively, allows one to determine the individual forces present between base pairs containing two or three hydrogen bonds. Section 9.5 (atomic force microscopy) presents further details of the force–distance dependence measured with such homogeneous base-pair samples.

#### 9.4.2.2 RNA Polymerase

When proteins are synthesized an elementary intermediate step is the transcription of the corresponding genetic code from DNA into RNA by RNA polymerase. During this process RNA polymerase moves along the DNA and adds step by step new RNA nucleotides to the newly synthesized RNA strand. Using optical tweezers it is actually possible to measure the polymerization velocity and the force RNA polymerase exerts on the DNA strand during its movement along it. Figure 9.24 shows the corresponding experimental arrangement. In this experiment the RNA polymerase is linked directly to the fixed sphere. The DNA is again linked to the trapped sphere. Then, nucleotides are offered to the RNA polymerase under the physiological conditions necessary for the transcription process. Again, the DNA strand can be directed to the RNA polymerase with the help of the 3D translation stage and weak laminar flows. At a certain time after the transcription has started, the polymerases have reached a position on the DNA that corresponds to the situation where the DNA starts to be stretched between the two spheres. Now, a force can be detected with the optical tweezers that corresponds to the force the RNA polymerase exerts on the DNA strand. If the 3D stage is not moved towards the trapped sphere along the  $x$  direction the transcription actually stalls when the maximum force is reached that the RNA polymerase can exert on the DNA-strand ( $\sim 25$  pN). Reducing the separation between fixed and trapped sphere causes the RNA polymerase to reversibly start working again. This allows us to follow the polymerization velocity of RNA

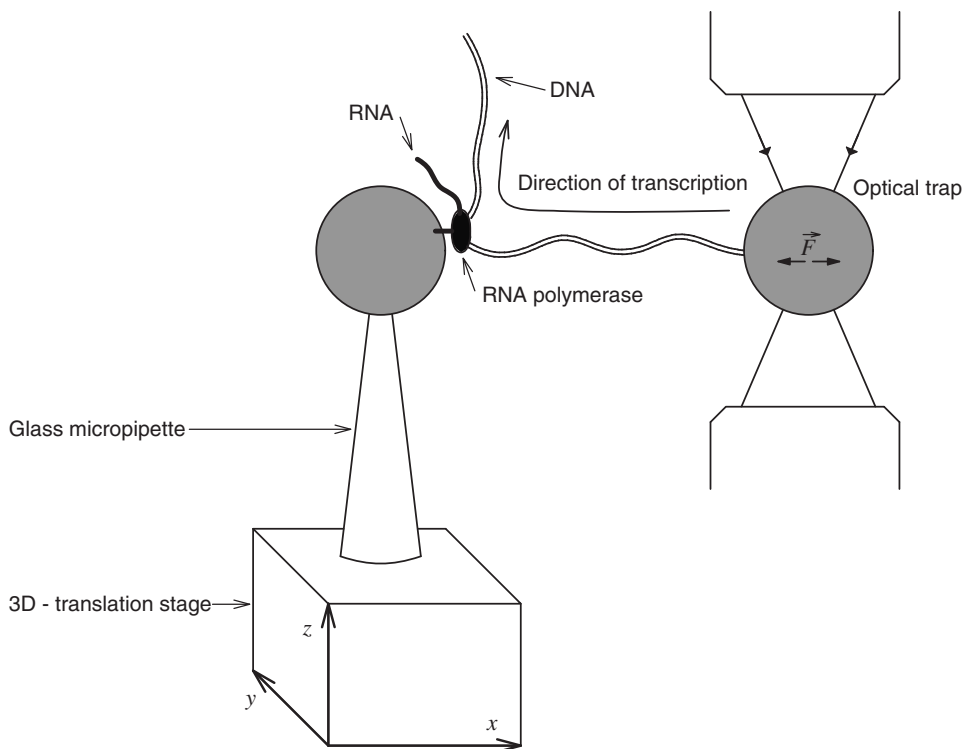


**Figure 9.24** Optical tweezers allow one to measure the forces exerted by RNA polymerase on the DNA strand during the transcription process.

polymerase. It turned out to be independent of the tension as long as no complete stalling occurs. Nevertheless, the exact DNA sequence has an influence on the actual polymerization velocity and force. Such experiments are very valuable for finding out what factors govern transcription and how its biomolecular mechanisms takes place.

#### 9.4.2.3 DNA-Polymerase

It is also possible to observe the synthesis of double-stranded DNA from single-stranded DNA by DNA-polymerase using optical tweezers. Such experiments take advantage of the fact that the per base length of double-stranded DNA is shorter than that of single-stranded DNA (Figure 9.25). For such experiments a single-stranded DNA is first clamped between a fixed and a trapped sphere. Then DNA-polymerase is added in the presence of nucleotides under conditions that allow it to start catalysing the generation of the complementary second strand. The polymerization stalls again when the shrinking of the double-stranded DNA leads to a high tension between the two spheres. The corresponding forces are on the order of  $\sim 35$  pN. As in the previous example, polymerization continues when the tension is released by movements of the 3D stage in the

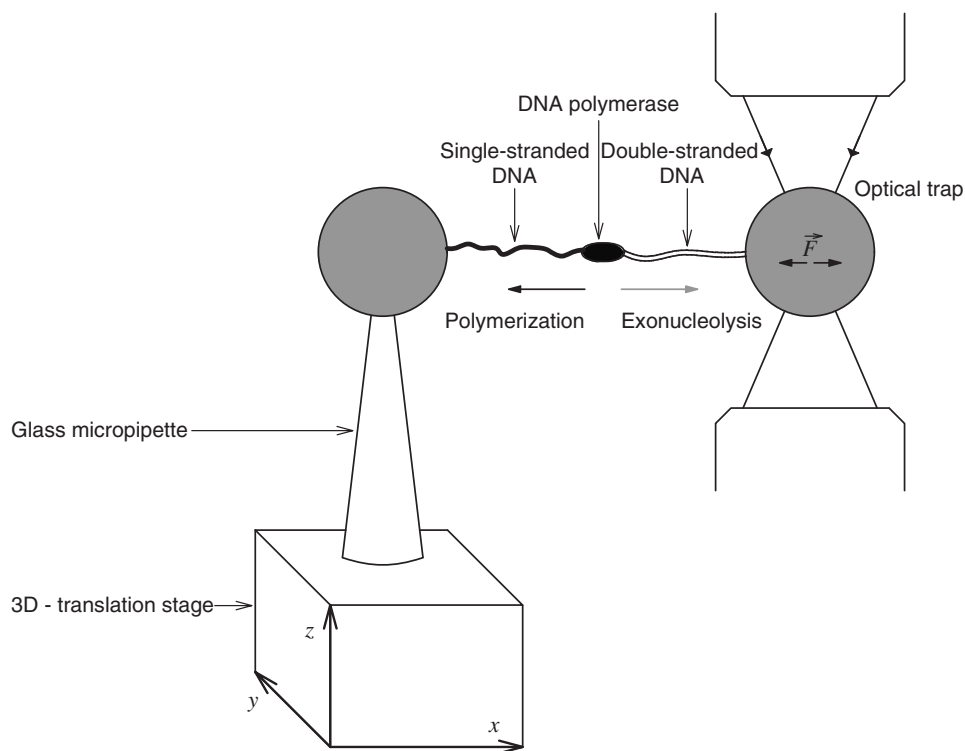


**Figure 9.25** The dependence of the tension on DNA-polymerase catalysed polymerization or exonucleolysis can be observed using optical tweezers.

$x$  direction. An intriguing additional effect can be observed when the tension is actually increased to forces higher than 35 pN by moving the piezostage in the opposite direction. In this case DNA-polymerase starts to catalyse the opposite processes, the formation of single-stranded DNA from double-stranded DNA by simultaneously releasing free nucleotides. This process is called exonucleolysis.

## 9.5

### Atomic Force Microscopy of Biomolecules

Another technique that enables the measurement of forces on a biomolecular level is atomic force microscopy (AFM). AFM was developed originally as a means of scanning the surfaces of solid samples with nm resolution. Since typical biomolecules such as proteins have dimensions of only a few nm AFM is also used to determine the topology of proteins immobilized on surfaces or even of native membranes containing trans-membrane proteins. With only minor modifications AFM devices can also be used to gain valuable information about other physical properties of biochemical molecules such as the forces necessary to

unfold them. In this section we first discuss the basic principles of AFM and then focus on a few application examples related to the measurement of forces occurring during biomolecular processes.

### 9.5.1

#### Principle of an AFM

Figure 9.26 illustrates the basic principle of an AFM. A key component is the cantilever tip, which ideally consists of a single or only a few atom(s). The cantilever itself is about  $\sim 100 \mu\text{m}$  long and can be translated with subnanometre resolution by a 3D piezotranslation stage. If the stage is used to slowly move the tip towards a surface the cantilever will be deflected when attractive or repulsive forces occur between cantilever tip and the surface. This deflection can be detected very sensitively when the reflection of a laser beam at the cantilever is monitored using a quadrant detector. As mentioned above, a quadrant detector is an arrangement of four light detectors that can monitor very sensitively differences in the light intensity irradiated on the four quadrants of the detector. After appropriate calibration, the signal observed from the quadrant detector directly provides a measure for the vertical deflection,  $\Delta z$ , of the cantilever tip in the  $z$  direction. The dependence of  $\Delta z$  on the actual forces between the surface and the cantilever tip can again be described by Hooke's law:

$$\vec{F}_{\text{AFM}} = -k \cdot \Delta z \quad (9.29)$$

If the constant  $k$  is known from calibration experiments then the force exerted on the cantilever tip can be calculated directly. AFM microscopy is also sensitive enough to measure forces on the order of a few pN. AFMs can generally

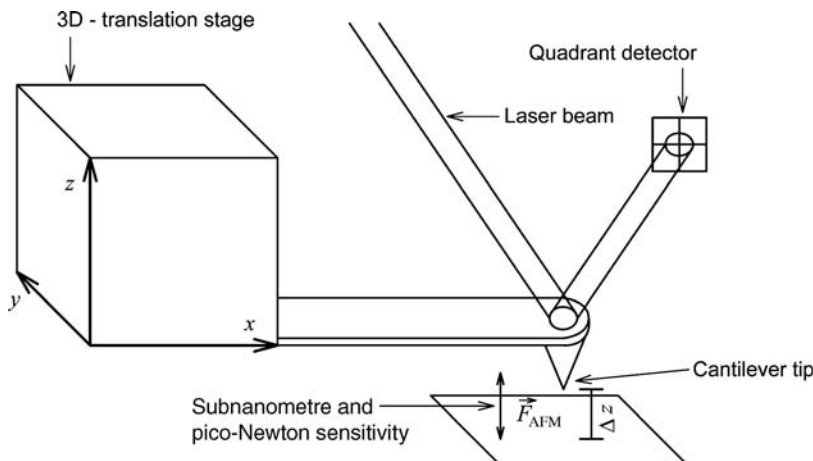


Figure 9.26 Principle scheme of an atomic force microscope (AFM) set-up.

measure larger forces than optical tweezers. Since the force constant  $k$  of AFMs is typically larger, AFMs are less sensitive to the Brownian motion noise in the measured deflections  $\Delta z$ . Optical tweezers, in contrast, are more advantageous when weaker forces have to be detected.

To determine the topology of a surface, AFMs can be operated in different modes. In the constant force or contact mode the cantilever tip is two-dimensionally scanned in the  $y$  and  $x$  dimensions over the surface. The detector signal is used to keep the force acting between the tip and the surface constant in a feedback cycle. As a result, the  $z$ -positions of the piezotranslation stage necessary to keep the tip–surface forces constant corresponds directly to the surface topology of the sample. In the dynamic mode the cantilever is oscillating at or close to its mechanical resonance frequency. This oscillation is usually induced by an extra piezoelement. In the presence of attractive or repulsive forces the amplitude, frequency and phase of this oscillation change significantly. Detection of these changes in the oscillation behaviour allows us again to control the tip–surface interactions while scanning the surface or to determine the attractive and repulsive forces between the tip and the surface as a function of  $x$  and  $y$ .

### 9.5.2

#### Application Examples

Scanning of surfaces carrying immobilized biomolecules has helped, for example, to determine heterogeneities in the quaternary structures of proteins. As mentioned earlier, it is also possible to image membrane proteins embedded in native membranes by scanning the surface of the membrane adsorbed on a solid support. This is especially valuable because membrane proteins and in particular their structure and structural arrangement in membranes are often hard to investigate by other methods, for example, because no crystals can be grown for X-ray crystallography. When biomolecules are attached to the cantilever tip and to the surface, additional information on biomolecular forces can be obtained. In the following we discuss how biomolecules can be spanned between cantilever tip and surface and we will provide a few application examples based on this approach.

##### 9.5.2.1 Unfolding of DNA Hairpins

Figure 9.27 illustrates schematically the measurement of forces between the DNA base pairs guanine–cytosine and adenine–thymine in double-stranded DNA, respectively. For such experiments again a DNA-hairpin structure is attached on one side to the cantilever tip and on the other side to a fixed surface. Often, biomolecules can be linked to surfaces by using gold-covered surfaces. It is then possible to attach linkers to the gold surface that carry thiol residues (see Section 3.2.5 on thiolinkers and gold surfaces). Biomolecules can be attached to the cantilever tip by various procedures. For example, one way is to coat the cantilever tip with biotinylated bovine serum albumin (BSA). The protein BSA sticks very well to clean metal surfaces. Further typical linking procedures via streptavidin and complementary strands of biotylated DNA can then be carried

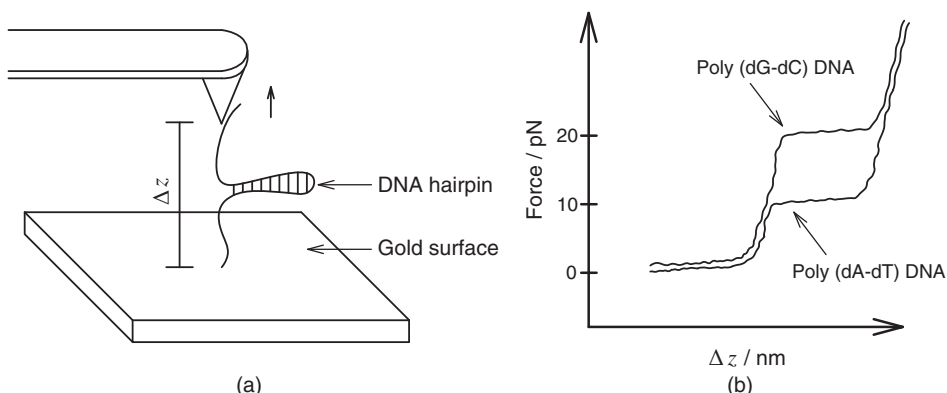


**Figure 9.27** AFMs can be used to measure the forces between base pairs in a DNA double strand.

out, for instance. Examples of other typical linking procedures are given in Section 9.4 (optical tweezers) and Chapter 3. Now, the cantilever is continuously moved away from the surface in the  $z$  direction. For smaller  $z$  displacements, at first only little restoring forces can be detected. The forces then start to increase approximately exponentially as a function of  $\Delta z$ . This behaviour corresponds to the entropic forces that are first necessary to unfold the random coiled DNA and then to stretch it to a point just before the first base pair is pulled apart. Figure 9.27a corresponds approximately to the situation in which the entire DNA but the hairpin has been unfolded. After this displacement  $\Delta z$  the force does not significantly increase for increasing  $\Delta z$ . Now, single base pairs are split one after the other by pulling with the cantilever arm. The force at which this plateau starts corresponds directly to the force of a single base-pair binding. Figure 9.27b illustrates the resulting force–displacement curves for two types of DNA-hairpins. If hairpins consisting exclusively of adenine–thymine pairs are used then the force to pull the base pairs apart is  $\sim 9$  pN. In contrast, hairpins consisting exclusively of guanine–cytosine base pairs require a force of  $\sim 20$  pN to be pulled apart. This observation is in good agreement with the fact that the binding of guanine–cytosine base pairs is actually based on three hydrogen bonds, whereas the binding of adenine–thymine pairs is based on only two hydrogen bonds. If the DNA strands are stretched beyond a point at which the last base pair is split then the force starts to further increase approximately as an exponential function of displacement  $\Delta z$ . These forces correspond to last bond rotations and stretchings that allow the DNA to be elongated without bond breakage. The relation of these forces with  $\Delta z$  is very similar for all types of DNA strands. At some point, finally, bond breakage will occur. If the cantilever tip is slowly moved back to the original position before breakage of the DNA occurs, often a reversible behaviour of the forces can be observed. However, for DNA as well as for proteins irreversible unfolding steps are also observed. In such cases the curves observed with increasing and decreasing  $\Delta z$  differ and describe a hysteresis.

### 9.5.2.2 Receptor–Ligand Binding Forces

AFM measurements can also be used to determine the actual binding force between receptors and ligands. Figure 9.28 shows an example of such a receptor–ligand binding force measurement. The ligand can be attached to the cantilever tip via an extended chemical linker molecule and the receptor to the fixed surface. In a first step, the cantilever tip is slowly moved in the direction of the surface until a repulsive force is detected. The probability is high that during this approach a receptor–ligand binding has occurred. Then the cantilever is slowly moved back. When the spacer starts to get stretched again an approximately exponentially increasing force is detected. Then, suddenly, the detected force drops back to zero. At this moment the ligand was pulled away from the receptor. This type of experiment can be repeated several times. The maximum force detected during such experiments corresponds to the binding force between receptor and ligand. The measured force also depends on the velocity by which the receptor and ligand are pulled apart. By measuring the forces at different velocities it is possible to deduce further important biomolecular parameters such as the distance dependence of the repulsive and attractive forces between the receptor and ligand and the dissociation rate in the absence of any external force.

### 9.5.2.3 Protein Unfolding

In the previous two examples we have seen that a longer period of a small increase in force followed by a subsequent approximately exponentially increasing force observed during the extension of the cantilever tip–surface distance often corresponds to an initial unfolding and then stretching of a (bio)polymer. In general, AFM is very useful for determining the distinct unfolding forces of a particular protein. An example of a protein whose unfolding properties is thought to play an essential role for the regulation of muscle movement is titin (Figure 9.29). It is responsible for the stability and elasticity of muscle and determines the muscle's contraction velocity. Titin contains several identical coiled

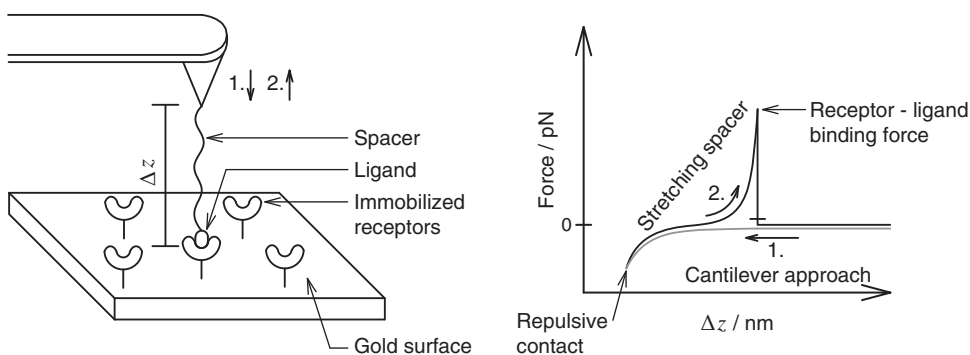


**Figure 9.28** AFM generally allows one to determine the forces that govern the binding between ligands and receptors.

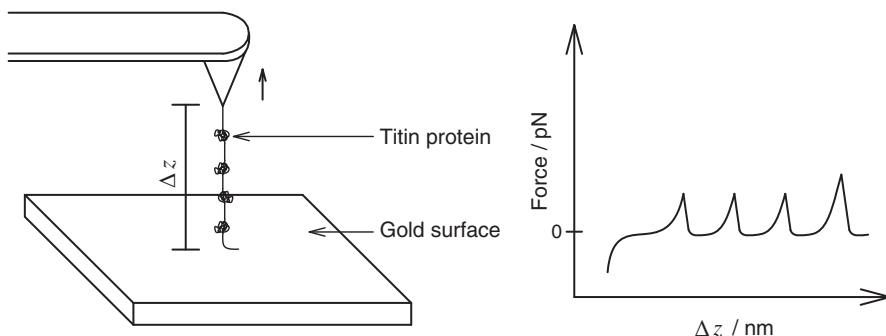


Figure 9.29 AFM measurement of the step-wise protein unfolding of titin.

domains that are separated by elongated protein sequences. When titin is clamped between the cantilever tip and a fixed surface and slowly pulled, several force spikes can be observed. Each of these spikes corresponds to the subsequent unfolding of a coiled subunit. The single-domain unfolding can be resolved up to single amino acid precision. Determination of the special biomechanical properties of titin via AFM has very important implications for the understanding of the role of titin in muscle function.

## 9.6

### Patch Clamping

#### 9.6.1

##### Ion Channels

Ion channels are membrane proteins that govern the exchange of specific ions such as  $\text{Na}^+$ ,  $\text{K}^+$ ,  $\text{Ca}^{2+}$  and  $\text{Cl}^-$  and many others across the membrane of cells. The controlled release or uptake of certain ions play a decisive role in many biological processes such as signal-transduction, muscle function, cell–cell communication and so on. Also, in drug design quite a number of targets are ion channels (see Figure 13.9), for which researchers try to find specific inhibitors, activators or regulators. But how can the activity of ion channels be measured to understand their biological function and to investigate the influence of certain regulators? A very valuable tool for answering such questions is the patch clamp technique. This technique allows us to observe the ion current even through single ion channels. In this section, after a brief introduction to different classes of ion channels, we will discuss important requirements that allow us to conduct patch clamp experiments and we will also present the most important patch clamp configurations.

Figure 9.30 shows a few classes of ion channels. In contrast to ion transporters, ion channels do not actively transport the ions across the membrane. The force driving the corresponding ions through the channels is usually an

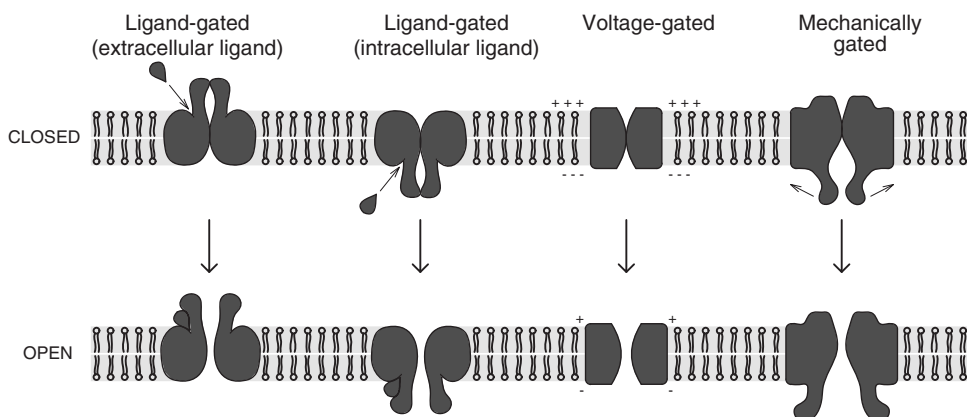


Figure 9.30 Classes of ion channels.

electrochemical gradient. The ion channels form a polar pore through the membrane that allows the passage of the charged and thus highly polar ions through the unpolar part of the lipid bilayer. Polar amino acid residues in the channels tunnel help the passage of the ions from one end to the other. The distinct electric fields of these residues and the shape of the channel usually make the ion channels very specific for a certain type of ion. It is an essential task of the ion channels to open the ion passage only 'on demand' of the cell or other regulating factors. Figure 9.30 shows four types of ion channels gated by different signals. Many ion channels are gated upon binding of a specific ligand. The ligand binding site can be either at the cytosolic side of the membrane or outside of the cell. Especially in neurotransmission, voltage-gated ion channels also play an important role. These channels are gated by changes in the electric potential across the membrane. In addition, mechanically gated ion channels exist. These channels are important, for example, in sensing mechanical forces such as hearing sound waves with hair cells in the ear.

### 9.6.2

#### Patch Clamp Configurations

Figure 9.31 illustrates schematically the measurement of the ion current through single ion channels with the patch clamp technique. A very small, clean glass pipette tip is first attached to the membrane of a cell. In a next step a slight under-pressure in the inner of this patch pipette is applied. The under-pressure and the use of fresh, clean patch pipettes are essential to generate a tight contact with the cell membrane. As a result, the electric resistance of this contact is very high, in the giga-ohm range. This 'giga-seal' is essential to avoid electric currents across the membrane–pipette contact. Electrical currents across the membrane–pipette contact would prevent the detection of single ion channel currents because the noise introduced by this larger current would easily be greater than

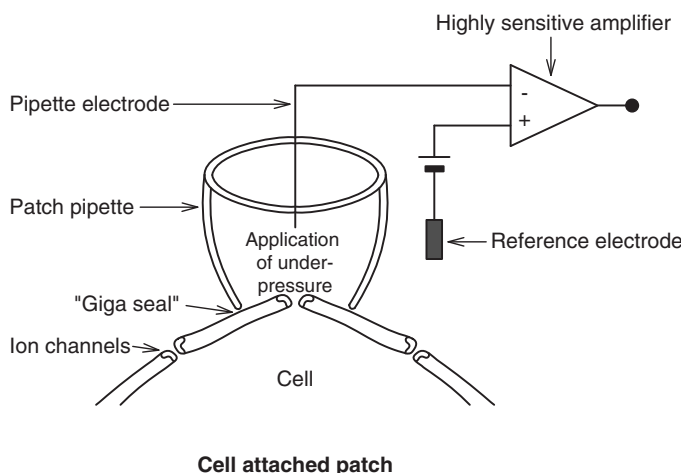


**Figure 9.31** With the patch clamp technique the ion current flowing through single ion channels can be measured. A very high electric resistance at the contact between the

patch pipette and the cell membrane ('Giga seal') as well as a very sensitive amplifier are essential prerequisites for such measurements.

the single-channel current signal itself. After the giga-seal has been formed, the under-pressure can be released. The giga-seal persists because a very tight and mechanically stable connection between pipette and plasma membrane has been established. Now the electric current between an electrode in the inner of the patch pipette and a reference electrode in the solution surrounding the cell is measured with a high-end electric amplifier. If the patch covered by the small opening of the pipette contains just one open ion channel in the cell membrane then a current through the open single channel can be detected by the highly sensitive amplifier when a small voltage is applied. In this patch clamp configuration the electrical circuit is closed by currents through the rest of the cell's membrane. This type of patch clamp configuration is also called a cell-attached patch (CAP).

The main advantage of the CAP configuration is that the cell is still intact, and therefore the normal physiological regulation of the channel is still present. However, if the environmental conditions of the intracellular side of the channel are to be controlled in a defined manner then the so-called inside-out patch (IOP) configuration is more advantageous (Figure 9.32). For the IOP configuration, again the pipette is first attached to the cell with a slight under-pressure. Then, however, the pipette is pulled away from the membrane. As a result, a small membrane patch still containing the ion channel sticks to the pipette. The giga-seal is not affected by this procedure. Now, for example, the concentration of regulators at the intracellular side can be controlled by the solution outside the pipette. Figure 9.33 illustrates, schematically, typical traces of patch clamp currents measured at single ion channels. The present example corresponds to

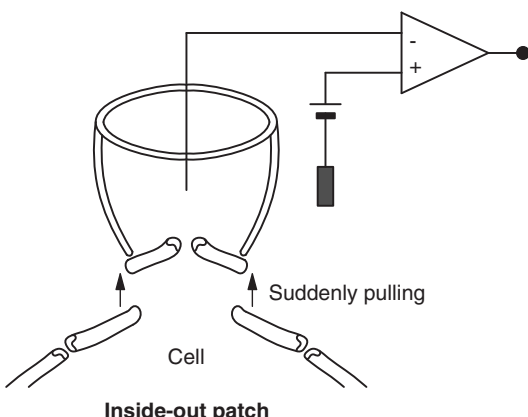
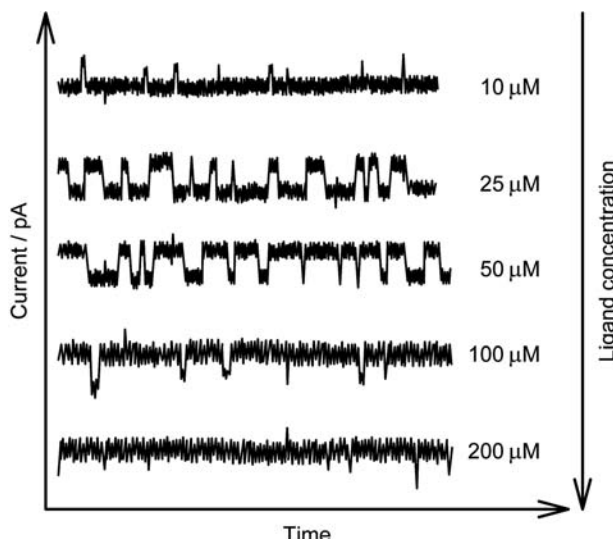


**Figure 9.32** In the inside-out patch configuration a small patch of the membrane is disrupted from the cell by pulling the patch pipette away from the cell. The inside out

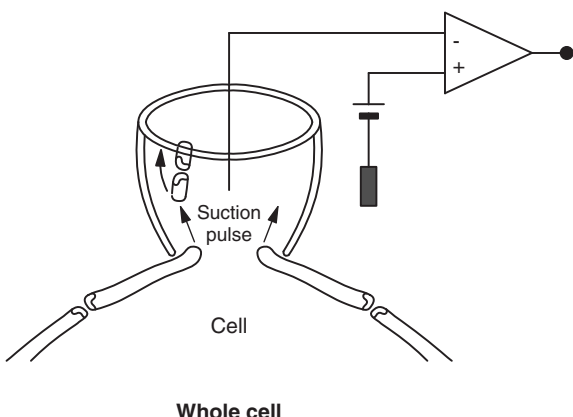
patch configuration allows exact control of the concentration of, for example, regulators also at the intracellular side of the ion channel.

an intracellular ligand-gated ion channel measured in the IOP configuration. If the ligand concentration is increased, the open periods of the channel also increase.

If the ion current through all or most of the cell's ion channels is to be measured simultaneously then the whole cell (WC) configuration can be applied (Figure 9.34). For the WC a short pulse of under-pressure ('suction pulse') is



**Figure 9.33** Typical patch clamp currents measured at a single ligand-gated ion channel as a function of ligand concentration.

**Whole cell**

**Figure 9.34** In the whole-cell configuration a 'suction pulse' of under-pressure in the patch pipette is applied. This ruptures the membrane patch sealed by the pipette. The current

that can then be measured corresponds to the current through almost all ion channels of the cell simultaneously.

applied to the inner surface of the patch pipette. As a consequence, a larger membrane piece originally covered by the pipette opening is removed. Now the measured current depends on the opening and closing and ion currents of all remaining ion channels of the whole cell.

By applying a somewhat more complicated patch preparation procedure it is even possible to generate an outside-out patch (OOP) configuration in which the extracellular side of the channel is in contact with the surrounding solution (Figure 9.35). This can be used, for example, to measure the ion currents through an extracellular gated ion channel as a function of the ligand concentration. The generation of a OOP configuration starts from the WC configuration. Then, the pipette is again pulled away from the cell. In contrast to the generation of an IOP, however, the pipette is pulled only very slowly. As a consequence, the membrane does not rupture. Rather, it slowly narrows between cell and pipette until the membranes eventually merge at the narrowest region. The final result of this procedure is that indeed the outer membrane parts are outside the patch.

As can be seen from these various patch clamp configurations there are a multitude of possibilities that can be used to investigate individual or several ion channels of a cell. This depends on the particular biological questions as to what ion channels are to be investigated by what technique. Certainly, patch clamping is still an advanced technique that requires some experimental skills not only in the operation of a patch clamp apparatus but also in the generation and preparation of the cell samples. Since the technique is based on the sensitive measurement of very small currents, detailed knowledge of electrical circuits and currents in biological samples is also necessary to be able to interpret the measured signal currents correctly (Figure 9.36). Nevertheless, in recent times patch clamping has even been automated successfully for industrial high-throughput screening (for a definition of high-throughput screening see Chapter 13).

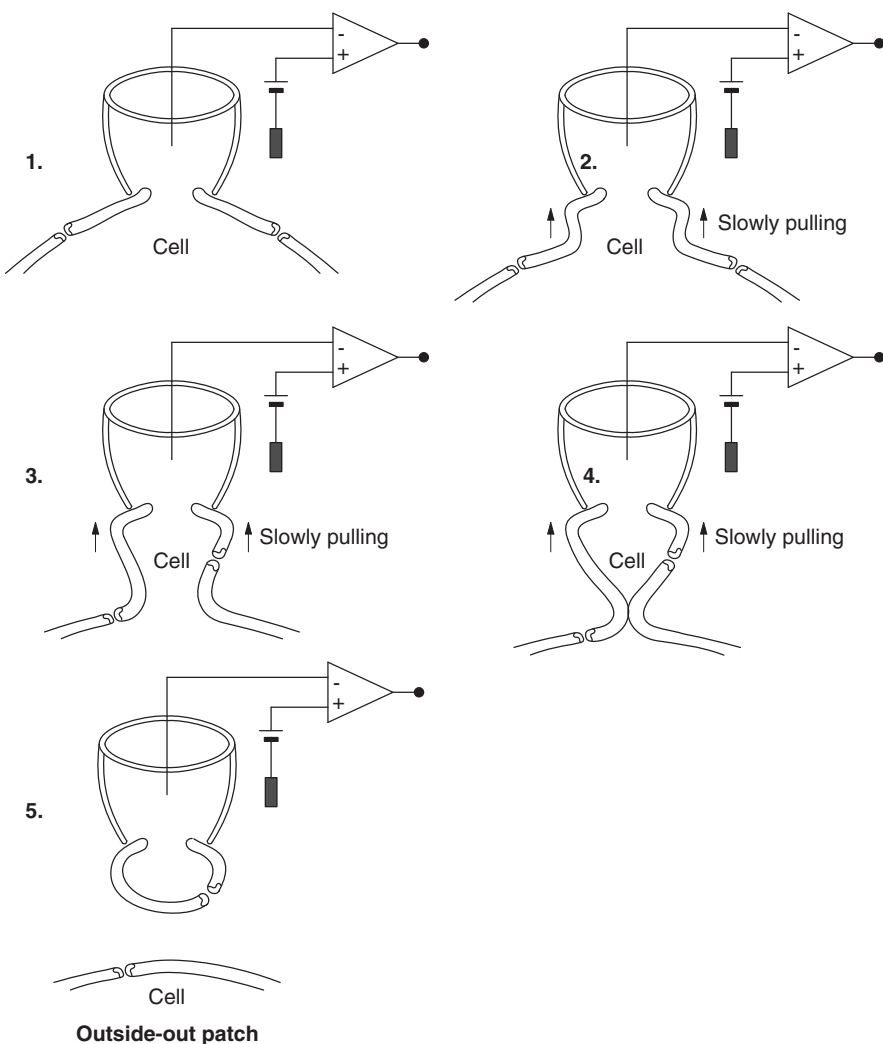


**Figure 9.35** An outside-out patch can be generated by slowly pulling the pipette away from the cell.

### Problems

- 9.1** What are the most important prerequisites for the optical detection of single biomolecules? Discuss also in what situations an observation of single biomolecules is especially advantageous in elucidating biomolecular mechanisms.
- 9.2** Figure 9.4 illustrates the observation of intermediate steps of the rotation of single ATP synthase subunits by fluorescence detection. It is also possible to observe this rotation on a single-biomolecule level using Förster resonance energy transfer. Discuss how you would perform such an

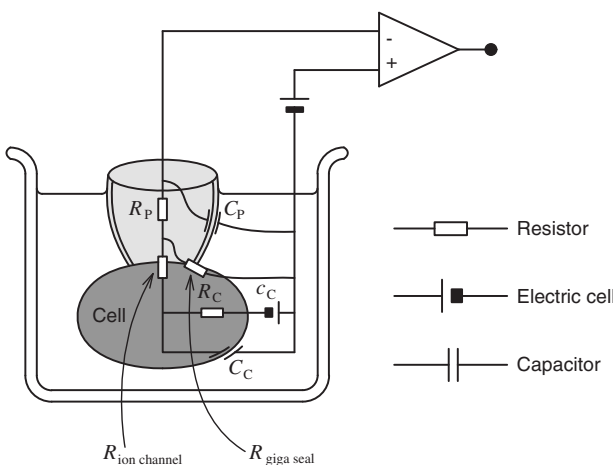


**Figure 9.36** Currents measured in patch clamp experiments can often only be understood by describing the amplifier, the pipette and the cell in terms of electrical equivalent circuits. This figure shows such an electrical equivalent circuit for the cell-attached configuration. The electrical resistance, capacity and sources of electric potentials are abbreviated by the symbols,  $R$ ,  $C$  and  $c$ , respectively. The decisive parameter measured in the CAP configuration is the gating dependent resistance of the ion channel,  $R_{\text{ion channel}}$ . It can only be measured if the resistance of the giga-seal,

$R_{\text{giga seal}}$ , is large enough. The measured current also depends on the resistance of the whole cell ( $R_C$ ), and of the electrode and liquid in the pipette,  $R_p$ . Additionally, the cell membrane behaves like a capacitor ( $C_C$ ) and even a potential ( $c_C$ ) is present between the inner of the cell and the extracellular space. The latter is caused, for example, by ion concentration gradients across the cell membrane, partly generated by ion transporters of the cell itself. In addition, the pipette wall constitutes a small capacitor,  $C_p$ .

experiment. Explain also your choice of fluorescence labels and linking techniques.

- 9.3** Figure 9.7 shows the positions of a single fluorescence label attached to a myosin dimer observed during the motion of the myosin along actin filaments. Sketch the positions of the fluorescence label if the biomolecular motion of myosin were based on an inchworm mechanism instead of a hand-over-hand mechanism.
- 9.4** A sample containing a fluorescently labelled protein of 60 kDa mass is digested using the proteases subtilisin and thrombin. The digestion resulted in  $\sim 20$  kDa fragments using thrombin and  $\sim 6$  kDa fragments using subtilisin. These two samples, a sample of the untreated fluorescently labelled protein and a sample of the free fluorescent label (0.4 kDa) were measured in an FCS experiment. The excitation intensity was low so that triplet-state formation can be neglected. The following parameters were observed:

	Correlation amplitude for small correlation times $G(\sim 0)$	Average number of detected photons $\langle I_{Fl}(t) \rangle$ ( $s^{-1}$ )
Fluorescently labelled protein	6	100 000
Protein digested using thrombin	2	100 000
Protein digested using subtilisin	1	100 000
Free fluorescent label	1	100 000

- What is the average number of fluorescing proteins, fragments or dyes in the focus of each sample? What is the corresponding macroscopic concentration of fluorescing proteins, fragments or dyes? The detection volume can be approximated by a 3D Gaussian function with the lateral constant  $r_0 = 0.2 \mu\text{m}$  and an axial constant  $z_0 = 1 \mu\text{m}$ .
- Assuming that the fluorescence quantum yield of the fluorescence label does not change when bound to the protein or its fragments, how many labels are bound per protein or fragment? On average, what percentage of protein fragments in the sample digested by subtilisin still carries a fluorescence label? Relate your answer to the observed number of fluorescing fragments for the corresponding sample.
- What is the average number of photons detected per biomolecule or fragment of each sample (particle brightness)?
- Estimate the diffusional time constant of the undigested, fluoresently labelled protein and the free fluorescent label. Assume for the estimate that both species can be treated as spheres. The viscosity of water is  $\eta_{H_2O} = 0.89 \times 10^{-3} \text{ kg m}^{-1} \text{ s}^{-1}$ , the specific volume of this protein and the free fluorescent label is  $1.2 \text{ cm}^3 \text{ g}^{-1}$  including the hydration of  $h = 0.2 \text{ cm}^3 \text{ g}^{-1}$ ;  $RT = 8.314 \text{ J K}^{-1} \text{ mol}^{-1}$  (300 K).
- What are the autocorrelation amplitudes measured with the undigested, fluoresently labelled protein and the free fluorescent label at a correlation time of  $\tau = 100 \mu\text{s}$ ?
- Estimate the average number of photons detected per transit of a single fluoresently labelled protein and a single free fluorescent label through the focal volume.
- Assume that you were to detect the fluorescence light from the same confocal set-up using a polarizing beam splitter and two detectors instead of just one detector. Estimate the values of the anisotropy  $r$  obtained with the undigested, fluoresently labelled protein and the free fluorescent labels. Assume for this estimate again that both species can be treated as spheres. The dipole

moment vectors for emission and excitation of the fluorescent label span an angle of  $0^\circ$ . The fluorescent label has an excited-state lifetime of  $\tau = 4\text{ ns}$ . How many photons would you detect on average per single-molecule transit in the parallel and the perpendicular detector of solutions containing the fluorescently labelled protein and the free fluorescent label?

- 9.5** In an FCS experiment you obtain values for  $G_T$  and  $1/\langle N \rangle$  of 0.3 and 0.6, respectively. What is the fraction of molecules in the triplet state under these conditions?
- 9.6** Discuss in what situations it is more advantageous to determine the degree of a receptor–ligand binding by the measurement of fluorescence polarization anisotropy or by dual-colour fluorescence cross-correlation spectroscopy.
- 9.7** Figure 7.3 shows the spectral characteristics of the dichroic mirror and optical filter for detecting a certain fluorescence dye in a confocal set-up. Sketch the spectral characteristics of the dichroic mirrors and optical filters that are necessary for a dual-colour confocal set-up (Figure 9.16).
- 9.8** You use a red fluorescing ligand and a green fluorescing receptor to determine the dissociation constant in a dual-colour fluorescence cross-correlation spectroscopy experiment. You observe the following values:  $G_R(\tau) = 0.5$ ,  $G_G(\tau) = 1$  and  $G_{RG}(\tau) = 0.3$ . What is the dissociation constant as defined by (3.19) for this receptor–ligand binding pair? Assume that the confocal detection volume can be approximated by a 3D Gaussian function with the lateral constant  $r_0 = 0.2\text{ }\mu\text{m}$  and an axial constant  $z_0 = 1\text{ }\mu\text{m}$  and that a perfect overlap of the confocal volume for red and green detection is present.
- 9.9** Calculate the counterforce that is generated by perpendicularly reflecting 100 W light of wavelength 550 nm at a perfect mirror.
- 9.10** In an optical tweezers a sphere of  $1\text{ }\mu\text{m}$  diameter is trapped. The trap stiffness of the optical tweezers set-up is  $50\text{ pN }\mu\text{m}^{-1}$ . When you move the focus in the solution with a velocity of  $1\text{ mm s}^{-1}$  what displacement of the sphere from the focus do you expect?
- 9.11** In early experiments using optical tweezers, power strokes of myosins and kinesins were detected. Discuss how you would set up such an experiment. Explain how you would assemble and link the key components to actually detect the power strokes.
- 9.12** Figure 9.28 illustrates the determination of receptor–ligand binding forces using an AFM. Discuss how you can make sure that you actually have linked only one ligand to the cantilever and how the signals would look like if two or more ligands are attached to the cantilever. Discuss various possible scenarios.

- 9.13** If you pull the ligand away from the receptor with different velocities in an experiment, as illustrated in Figure 9.28, different velocity-dependent forces are observed before the binding breaks. This is because the binding between the ligand and the receptor is actually governed by distinct potentials that describe the attractive and repulsive forces present when ligand and receptor are separated by certain distances. Discuss qualitatively how the breaking force can depend on the “pulling” velocity.
- 9.14** Discuss what patch clamp configurations are more advantageous for determining the influence of the ligand concentration on both an extracellular ligand-gated and an intracellular ligand-gated ion channel.
- 9.15** Figure 9.36 shows the electrical equivalent circuit for a CAP configuration. The electrical resistance ( $R$ ) can be defined by  $R = U/I$ , where  $I$  is the electrical current that flows through that resistor when a voltage  $U$  is applied. If an electrical current flows sequentially through several resistors  $R_1, R_2 \dots$  the overall resistance is  $R_{\text{Total}} = R_1 + R_2 \dots$ . If an electrical current flows parallel through several resistors  $R_1, R_2 \dots$  the overall resistance is  $R_{\text{Total}} = (R_1^{-1} + R_2^{-1} \dots)^{-1}$ . Derive an expression for the total resistance measured between the pipette and reference electrode in the CAP configuration assuming that we can neglect  $C_C$ ? Through a typical open ion channel an electrical current on the order of  $\sim 10 \text{ pA}$  flows when a voltage of  $\sim 10 \text{ mV}$  is applied. How high must the resistance of the giga-seal be in order to be at least ten times higher than the resistance of the open ion channel?

## Bibliography

### Specific

#### Optical Single-Molecule Detection

- Basché, T., Moerner, W.E. *et al.* (1997) *Single Molecule Optical Detection, Imaging and Spectroscopy*, Wiley-VCH Verlag GmbH, Weinheim.
- Ishijima, A. and Yanagida, T. (2001) Single molecule nanobioscience. *Trends Biochem. Sci.*, **26**, 438.
- Moerner, W.E. and Kador, L. (1989) Optical detection and spectroscopy of single molecules in a solid. *Phys. Rev. Lett.*, **62** (21), 2535.
- Orrit, M. and Bernard, J. (1990) Single pentacene molecules detected by fluorescence excitation in a p-terphenyl crystal. *Phys. Rev. Lett.*, **65** (21), 2716.
- Zander, C., Keller, R.R. *et al.* (2002) *Single-Molecule Detection in Solution: Methods and Applications*, Wiley-VCH Verlag GmbH, Weinheim.

*and Applications*, Wiley-VCH Verlag GmbH, Weinheim.

#### Observation of Single ATPase Rotation (Figure 9.4)

- Noji, H., Yasuda, R. *et al.* (1997) Direct observation of the rotation of F1-ATPase. *Nature*, **386**, 299–302.

#### Observation of the Motion of Single Myosins (Figures 9.6 and 9.7) or Kinesins

- Vale, R.D., Funatsu, T. *et al.* (1996) Direct observation of single kinesin molecules moving along microtubules. *Nature*, **380** (6573), 451.
- Yildiz, A., Forkey, J.N. *et al.* (2003) Myosin V walks hand-over-hand: single fluorophore

imaging with 1.5-nm localization. *Science*, **300**, 2061–2065.

## FCS

- Bacia, K. and Schwille, P. (2007) Practical guidelines for dual-color fluorescence cross-correlation spectroscopy. *Nature Protocols*, **2** (11), 2842–2856.
- Blom, H., Kastrup, L. *et al.* (2006) Fluorescence fluctuation spectroscopy in reduced detection volumes. *Curr. Pharm. Biotechnol.*, **7**, 51.
- Cypionka, A., Stein, A. *et al.* (2009) Discrimination between docking and fusion of liposomes reconstituted with neuronal SNARE-proteins using FCS, *PNAS*, **106**, 18575–18580.
- Kim, S.A., Heinze, K.G. *et al.* (2007) Fluorescence correlation spectroscopy in living cells. *Nature Methods*, **4** (11), 963–973.
- Magde, D., Elson, E. *et al.* (1972) Thermodynamic fluctuations in a reacting system – measurement by fluorescence correlation spectroscopy. *Phys. Rev. Lett.*, **29** (11), 705.
- Magde, D. and Elson, E.S.E. (1974) Fluorescence correlation spectroscopy. I. Conceptual basis and theory. *Biopolymers*, **13** (1), 1–27.
- Magde, D. and Elson, E.S.E. (1974) Fluorescence correlation spectroscopy. II. An experimental realization. *Biopolymers*, **13** (1), 29–61.
- Palmer, A.G. 3rd and Thompson, N.L. (1987) Molecular aggregation characterized by high order autocorrelation in fluorescence correlation spectroscopy. *Biophys. J.*, **52** (2), 257–270.
- Qian, H. and Elson, E.L. (1990) On the analysis of high order moments of fluorescence fluctuations. *Biophys. J.*, **57** (2), 375–380.
- Rigler, R. and Elson, E.S. (eds) (2001) *Fluorescence Correlation Spectroscopy*, Springer.
- Schwille, P. and Haustein, E. (2001) Fluorescence correlation spectroscopy In Vitro and In Vivo, in *Single-Molecule Techniques: A Laboratory Manual* (eds P. R. Selvin and T. Ha), Springer, Berlin, Chapter 12.

W. Vennekate, W., Schröder, S. *et al.* (2012) Cis- and trans-membrane interactions of synaptotagmin-1, *PNAS*, **109**, 11037–11042.

## Optical Tweezers

- Ashkin, A. (1997) Forces of a single-beam gradient laser trap on a dielectric sphere in the ray optics regime. *Methods Cell Biol.*, **55**, 1–27.
- Block, S.M. (1992) Making light work with optical tweezers. *Nature*, **360** (6403), 493.
- Denk, W. and Webb, W.W. (1990) Optical measurement of picometer displacements of transparent microscopic objects. *Appl. Optics*, **29** (16), 2382–2391.
- Gittes, F. and Schmidt, C.F. (1998) Signals and noise in micromechanical measurements, in *Laser Tweezers in Cell Biology (Methods in Cell Biology)*, vol. 55 (ed. M.P. Sheetz), Academic Press, San Diego, pp. 129–156.
- Gittes, F. and Schmidt, C.F. (1998) Interference model for back-focal-plane displacement detection in optical tweezers. *Opt. Lett.*, **23** (1), 7–9.
- Kuo, S.C. (2001) Using optics to measure biological forces and mechanics. *Traffic*, **2** (11), 757–763.
- Rohrbach, A. and Stelzer, E.H.K. (2002) Trapping forces, force constants, and potential depths for dielectric spheres in the presence of spherical aberrations. *Appl. Opt.*, **41** (13), 2494–2507.
- Svoboda, K. and Block, S.M. (1994) Biological applications of optical forces. *Annu. Rev. Biophys. Biomol. Struct.*, **23**, 247–285.
- Williams, M.C. (2002) Optical tweezers: Measuring piconewton forces, in *Single Molecule Techniques*, Petra Schwille, ed., A volume of the Biophysics Textbook Online L. DeFelice, editor-in-chief, Biophysical Society, Bethesda, MD, pp. 650.
- Williams, M.C. and Rouzina, I. (2002) Force spectroscopy of single DNA and RNA molecules. *Curr. Opin. Struct. Biol.*, **12** (3), 330–336.
- Zlatanova, J., Lindsay, S.M. *et al.* (2000) Single molecule force spectroscopy in biology using the atomic force microscope. *Prog. Biophys. Mol. Biol.*, **74**, 37–61.

### Momentum of Light in Transparent Materials

Leonhardt, U. (2006) Optics: Momentum in an uncertain light. *Nature*, **444** (7121), 823–824.

### Unfolding RNA Hairpin (Figure 9.23)

Liphardt, J., Onoa, B. *et al.* (2001) Reversible unfolding of single RNA molecules by mechanical force. *Science*, **292** (5517), 733–737.

### Forces Generated by RNA Polymerase (Figure 9.24)

Davenport, R.J., Wuite, G.J. *et al.* (2000) Single-molecule study of transcriptional pausing and arrest by *E. coli* RNA polymerase. *Science*, **287** (5462), 2497–2500.

### Forces Generated by DNA-polymerase (Figure 9.25)

Wuite, G.J., Smith, S.B. *et al.* (2000) Single-molecule studies of the effect of template tension on T7 DNA-polymerase activity. *Nature*, **404**, 103–106.

### Atomic Force Microscopy of Biomolecules

Binnig, G. and Rohrer, H. (1986) Scanning tunneling microscopy. *IBM J. Res. Dev.*, **30** (4), 355.

Butt, H.J., Cappella, B. *et al.* (2005) Force measurements with the atomic force microscope: Technique, interpretation and applications. *Surf. Sci. Rep.*, **59**, 1–152.

Florin, E.L., Moy, V.T. *et al.* (1994) Adhesion forces between individual ligand-receptor pairs. *Science*, **264** (5157), 415–417.

Florin, E.L., Rief, M. *et al.* (1995) Sensing specific molecular interactions with the atomic force microscope. *Biosens. Bioelectron.*, **10**, 895.

Janshoff, A., Neitzert, M. *et al.* (2000) Force spectroscopy of molecular systems – single molecule spectroscopy of polymers and biomolecules. *Angew. Chem.*, **39** (18), 3212–3237.

Kühner, F., Erdmann, M. *et al.* (2006) Scaling exponent and Kuhn length of pinned polymers by single molecule force spectroscopy. *Phys. Rev. Lett.*, **97** (21), 218301–218304.

Lee, G.U., Chrisey, L.A. *et al.* (1994) Direct measurement of the forces between complementary strands of DNA. *Science*, **266** (5186), 771–773.

Lee, G.U., Kidwell, D.A. *et al.* (1994) Sensing discrete streptavidin-biotin interactions with atomic force microscopy. *Langmuir*, **10**, 354–357.

Rief, M., Gautel, M. *et al.* (1997) Reversible unfolding of individual titin immunoglobulin domains by AFM. *Science*, **276** (5315), 1109–1112.

Scheuring, S., Seguin, J. *et al.* (2003) Nanodissection and high-resolution imaging of the Rhodopseudomonas viridis photosynthetic core complex in native membranes by AFM. *Proc. Natl. Acad. Sci.*, **100** (4), 1690–1693.

### Patch Clamping

Hille, B. (2001) *Ion Channels of Excitable Membranes*, Sinauer Associates, Inc., Sunderland.

Kandel, E.R., Schwartz, J.H. *et al.* (2000) *Principles of Neural Science*, McGraw-Hill, New York.

Molleman, A. (2002) *Patch Clamping: An Introductory Guide to Patch Clamp Electrophysiology*, John Wiley and Sons, org.

Numberger, M. and Draguhn, A. (1996) *Patch-Clamp-Technik*, Spektrum Akademischer Verlag, Heidelberg.

Sakmann, B. and Neher, E. (eds) (2007) *Single-Channel Recording*, Plenum Press, New York.

Walz, W., Boulton, A.A. *et al.* (eds) (2007) *Patch-Clamp Analysis: Advanced Techniques*, Humana Press, New Jersey.

## 10

### Ultrafast- and Nonlinear Spectroscopy

#### 10.1

##### Introduction

In this chapter we discuss techniques that are based on the application of ultrafast laser systems for the investigation of biological samples. An ultrafast laser provides very short laser flashes of up to a few hundred femtoseconds duration. A femtosecond (fs) corresponds to  $10^{-15}$  s, which is an extremely short time period. Even light itself travels only  $\sim 0.3\text{ }\mu\text{m}$  during 1 fs.

In the biosciences basically two major application fields have been established in recent years. One is the investigation of processes that are amongst the fastest in nature, for example the primary steps in photosynthesis or vision. Both processes occur on the femto- to picosecond timescale ( $10^{-15}$ – $10^{-12}$  s). Since no other techniques allow resolution of the corresponding short times (the fastest electronic devices such as oscilloscopes reach at best picosecond resolution) first robust ultrafast laser systems had to be developed before these important biological processes could be investigated. The other application field of ultrafast lasers in biology is the observation of nonlinear optical signals from biological samples.<sup>1)</sup> For the investigation of biological samples by nonlinear optical techniques ultrafast lasers are mandatory to avoid destruction of the samples by the necessary extremely high light intensities that are employed (a detailed explanation for this is provided in section 10.2.3).

In the Section 10.2 we introduce applications of nonlinear optical techniques in the biosciences. The most important optical nonlinear technique in biology is certainly two-photon excitation. We will discuss the advantages of two-photon excitation for important fluorescence techniques such as confocal fluorescence microscopy and fluorescence cross-correlation spectroscopy. We will also briefly discuss other important nonlinear optical methods such as second- and third-harmonic generation as well as CARS microscopy. In Section 10.3 we introduce the basic principles of ultrafast spectroscopy and discuss the measurement of

1) As we will see in the corresponding section, actually all techniques for the investigation of ultrafast processes are also in principle nonlinear optical techniques.

ultrafast Förster energy transfer and the processes occurring in photosynthesis as application examples.

## 10.2

### Nonlinear Microscopy and Spectroscopy

Nonlinear optical effects occur when a sample is irradiated by light so intense that the response of the electron clouds to the light's strong electric-field component is no longer linear. An important consequence of this is that in nonlinear spectroscopy more than one photon can interact simultaneously with the molecule. Important examples of processes in which more than one photon interacts simultaneously with molecules are two-photon excitation (TPE), second-harmonic generation (SHG) and coherent anti-Stokes Raman scattering (CARS).

In the next subsection we start with a detailed discussion of the basics and applications of two- or multiphoton excitation. Then, a somewhat more detailed discussion of the physical background of nonlinear optical phenomena is provided as this is necessary to understand the techniques explained subsequently. Finally, techniques such as SHG and CARS and their application in the biosciences will be discussed.

#### 10.2.1

##### Multiphoton Excitation

Two-photon excitation (TPE) is based on the simultaneous absorption of two photons by a molecule. As with normal one-photon excitation (OPE), TPE also promotes the molecules into a higher electronic state (Figure 10.1). Obviously, the sum of the energy of both photons must correspond to the energy that is necessary to complete the transition.

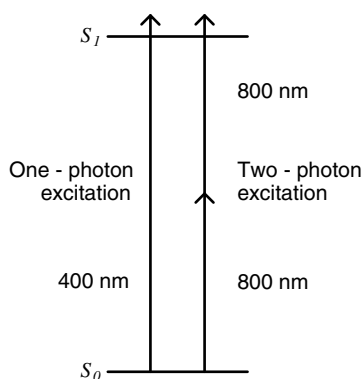


**Figure 10.1** In two-photon excitation, transitions are excited by two photons simultaneously.

In conventional one-photon spectroscopy the probability of absorbing a photon is linearly proportional to the incoming light intensity or the number of photons irradiating the molecules:

$$P_{\text{Absorption}}^{\text{One-Photon}} \propto I_{\text{Excitation}} \quad (10.1)$$

In two-photon spectroscopy, however, the probability of exciting a transition is proportional to the square of the incoming light intensity because two photons have to be taken out of the light field simultaneously:

$$P_{\text{Absorption}}^{\text{Two-Photon}} \propto I_{\text{Excitation}}^2 \quad (10.2)$$

It is not necessary that both photons possess the same energy. Generally, it is possible that a single transition can be excited by one or more photons simultaneously when the sum of their photon energies (or frequencies) corresponds to the energy (or frequency) of the transition:

$$\nu_{\text{Transition}} = \nu_1 + \nu_2 + \nu_3 \dots \quad (10.3)$$

Here,  $\nu_1$ ,  $\nu_2$ ,  $\nu_3 \dots$  are the frequencies of the incoming light fields and  $\nu_{\text{Transition}}$  is the frequency corresponding to the transition energy (Eq. (1.1)). The corresponding probability that such multiphoton transitions occur is:

$$P_{\text{Absorption}}^{\text{Multiphoton}} \propto I_1 \cdot I_2 \cdot I_3 \dots \quad (10.4)$$

with  $I_1, I_2, I_3 \dots$  being the intensities of the corresponding light fields.

## 10.2.2

### Advantages and Disadvantages of Two-Photon Excitation in Fluorescence Microscopy

The important advantage of all microscopy techniques that are based on nonlinear optical effects is the intrinsically restriction of the observation volume to a small spot in the focus of the microscope objective, where the highest light intensities are present. This is a direct consequence of the nonlinear excitation intensity dependence of these effects [cf. (10.2) and (10.4)] and is illustrated in Figure 10.2 by a comparison of the spatial excitation volumes observed with one- or two-photon excitation, respectively. Of course, in one-photon microscopy the fluorescence intensity in the focal region is also the highest but, nonetheless, considerable one-photon excitation also occurs in regions remote from the focus. In contrast, in two-photon microscopy excitation in regions other than the focal region is almost completely negligible because of the quadratic dependence of the excitation probability on the light intensity (10.2).

A consequence of the restriction of two-photon excitation exclusively to the focal area of the microscope objective is that the resolution of the fluorescence spot is significantly enhanced, especially on the  $z$  direction (as defined in the inset of Figure 7.1) of the effective focal excitation and thus also detection volume. This gives rise to an improved resolution of the 3D picture observed in

## One - photon microscopy Two - photon microscopy

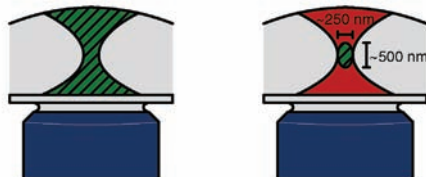


**Figure 10.2** All nonlinear optical microscopy techniques, such as two-photon excitation, depend nonlinearly on the light intensities. As a result, the corresponding effects are observed exclusively from the focal region of the microscope objective where the highest light intensities are present. In two-photon

fluorescence microscopy, for example, this greatly reduces background fluorescence from out-of-focus regions. This makes the use of a pinhole in confocal microscopy superfluous while the three-dimensional resolution is even increased in two-photon scanning microscopy.

two-photon fluorescence scanning microscopy. Another important advantage of the intrinsically restricted excitation volume is that the pinhole necessary in conventional confocal one-photon microscopy becomes superfluous in confocal two-photon fluorescence microscopy. This is a great advantage because, usually, pinhole alignment is one of the most critical and time-consuming steps in the everyday alignment of confocal set-ups. In principle, confocal two-photon set-ups are very similar to conventional confocal one-photon set-ups (Figure 7.1) with the important difference that the detector can be placed directly at the position where a pinhole is necessary in the conventional one-photon set-up. Using two-photon excitation a biological object like a cell can be investigated exclusively at certain points without the interference of fluorescence from optical markers or autofluorescence in areas other than in the focal excitation volume. In principle, all fluorescence methods described in Chapters 2 and 3, and Chapters 7, 9 and 12, can then specifically be applied at only this spot. Another consequence is that photobleaching in areas other than the detection volume is also reduced. Notably, however, the photobleaching of fluorescence markers within the focal area is usually larger using TPE than with OPE.

TPE also has intrinsic advantages for fluorescence correlation spectroscopy. In OPE-FCS, the exact pinhole alignment is critical for the observation of correct results because it determines directly the shape,  $W(\vec{r})$ , of the effective focal detection volume,  $V_{\text{eff}}$  (see Section 9.3.3). The shape of the detection volume,  $W(\vec{r})$ , in turn, critically affects the values observed for the diffusion times,  $\tau_D$ , and the particle numbers,  $\langle N \rangle$ . By using TPE for FCS analysis, however, the shape of  $W(\vec{r})$  is determined exclusively by the excitation volume. The excitation volume in TPE depends primarily on the quality of the microscope objective and the beam profile of the collimated laser beam that illuminates the objectives back aperture. Both parameters are usually very stable during day-to-day operation.

In fluorescence cross-correlation spectroscopy the pinhole-free observation of confocal TPE fluorescence is especially advantageous (Figure 10.3). The

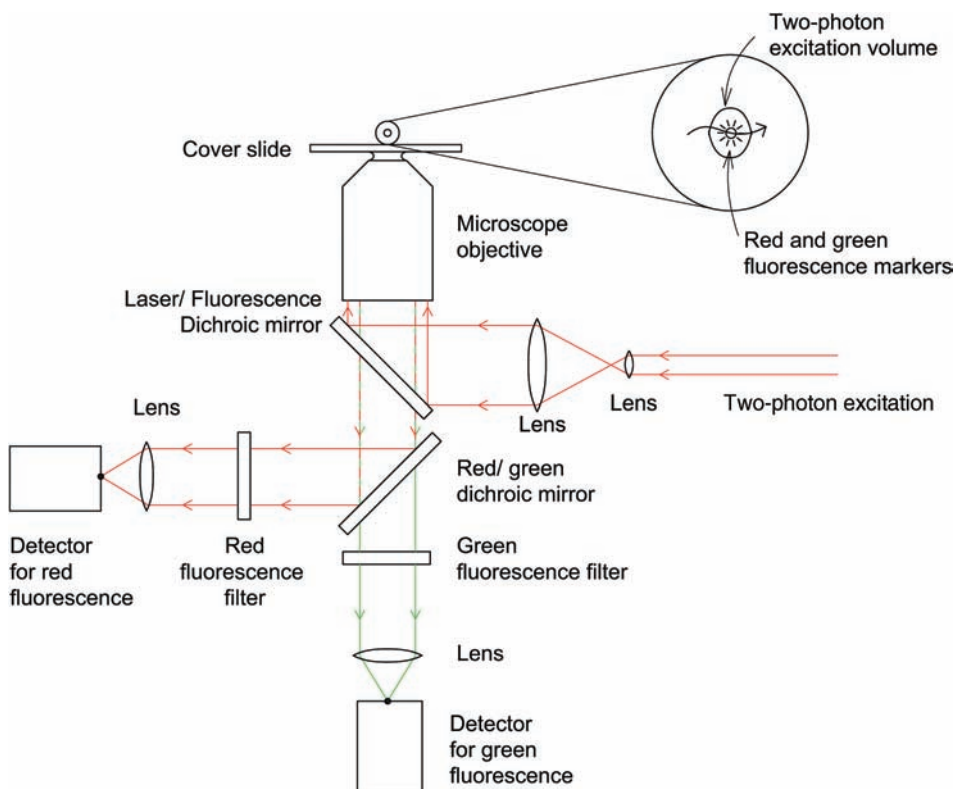


**Figure 10.3** Set-up for confocal two-photon excitation and fluorescence cross-correlation analysis. In comparison to a conventional one-photon microscopy set-up (Figures 7.1 and 9.16) alignment demanding pinholes can be

omitted and the same dichroic mirror separating excitation light in the infrared spectral region from fluorescence light in the visible spectral region can be used for many different fluorescence dyes.

observation of a 100% cross-correlation requires a 100% perfect overlap of the detection volumes for both detection channels. In confocal OPE this is almost impossible to achieve because of the critical relative alignment necessary to overlap the foci of both excitation beams and the pinholes (see Figure 9.16). In addition, complicated sets of dichroic mirrors and fluorescence filters are necessary to separate both excitation wavelengths as well as detection wavelengths. Both difficulties can be easily circumvented by TPE fluorescence cross-correlation spectroscopy. This is because it is possible to find, for many fluorescence dye pairs, an effective common two-photon excitation wavelength. As a result, a single two-photon excitation laser source focused into the sample solution defines exactly identical excitation volumes for both fluorescence dyes. Because intrinsically no pinhole is necessary using TPE the detection volumes are also identical. As a result, the comparison of observed cross-correlation and autocorrelation amplitudes using TPE reflects a lot more reliably the absolute concentration of

double-labelled species because excitation and detection volumes are intrinsically perfectly overlapping using a single two-photon excitation beam.

Another advantage of using TPE in everyday operation is the large spectral separation of the excitation light from the fluorescence light. In OPE fluorescence microscopy, usually different sets of the dichroic mirrors and fluorescence filters must be employed for each type of fluorescence dye because the maxima of the absorption and fluorescence are typically separated spectrally by no more than  $\sim 50$  nm (see Figure 7.3). By using TPE, however, the excitation wavelength is always in the near-infrared spectral region at  $\sim 700$ – $1200$  nm, whereas the fluorescence of most optical markers is in the visible spectral region. This is a direct consequence of the fact that TPE requires photons having only half the energy of the transition energy. Since the two-photon excitation light is always in the infrared spectral region and the observed fluorescence is always in the visible spectral region, regardless of which fluorescence marker is used, the same visible/infrared separating dichroic mirror can be used for many different markers and no time-consuming optical realignment is necessary when switching fluorescence markers. In addition, in many cases a single fluorescence filter that simply blocks any residual infrared excitation light and transmits the entire range of visible light is sufficient for most dyes.

The biggest disadvantage of TPE fluorescence microscopy as well as all other nonlinear optical techniques is the requirement of using fs-lasers as excitation sources. The cost of purchasing and maintaining these laser system is still significantly higher than for conventional excitation sources. In the next subsection we discuss why a fs-laser system is necessary for the investigation of biological samples with TPE or other nonlinear optical techniques.

### 10.2.3

#### How are Nonlinear Optical Signals Observed From Biological Samples?

From the previous considerations it is obvious that, usually, extremely high light intensities are needed to observe any nonlinear optical effect. The question arises as to how these high light intensities can be applied without a simultaneous destruction of the biological samples. Usually, this is achieved by using pulsed irradiation (Figure 10.4) from an ultrafast laser system. Ultrafast lasers provide very high peak intensities during the pulses without applying very high average light intensities. For example, typical fs-lasers used for two-photon excitation provide pulses of about 100 fs duration with a repetition rate corresponding to about 10 ns time delay between the pulses. Depending on the fluorescence dyes used, typical average excitation intensities at the back aperture of the microscope objective in a confocal set-up of  $\sim 30$  mW of light with wavelengths ranging from  $\sim 700$  to 1100 nm are used for efficient two-photon excitation. Using this average light intensity usually results only in little or no photodamage of the fluorescence dyes and the biological samples. If this excitation intensity were equally applied to the sample without pulsing, the excitation intensity would not suffice for an effective two-photon excitation. This is visualized by the comparison of an

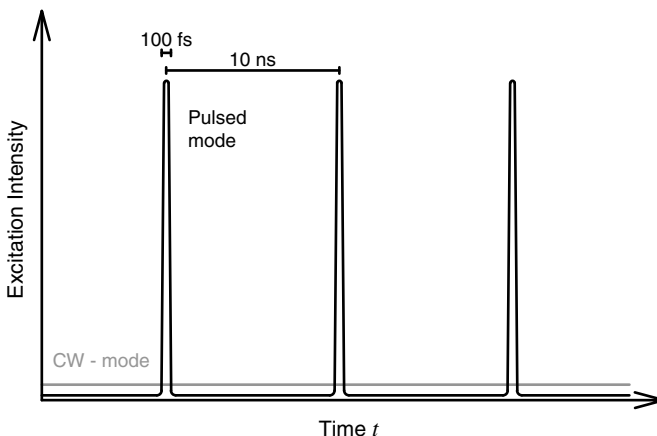


**Figure 10.4** The use of pulsed fs-excitation allows the achievement of high peak intensities necessary for nonlinear optics without applying large average intensities. CW mode = continuous-wave mode.

intensity–time trace of a laser in continuous-wave (CW) mode (grey line in Figure 10.4) with the corresponding trace for the pulsed mode (black line in Figure 10.4). If the laser is run in the pulsed mode most of the excitation energy that exits the laser during a period of 10 ns in the CW mode is compressed into the short pulses of only 100 fs duration (black line in Figure 10.4). As a consequence, during the pulses a  $10\text{ ns}/100\text{ fs} = 10^5$  times higher peak intensity is observed than in the CW mode. Since the probability for two-photon excitation depends on the square of the excitation intensity (10.2) it is  $10^{10}$  times higher during the pulses than during the same time period of the CW mode. Of course, it has to be considered that in the CW mode the sample is irradiated for  $10^5$  times longer by the lower excitation intensity than in the pulsed mode. Consequently, the actual difference in excitation efficiency between the two modes in this particular example is actually only  $10^5$ . Nevertheless, this is still very well suited for an effective two-photon excitation at comparatively moderate average excitation intensities.

#### 10.2.4

##### Further Distinct Properties and Advantages of Two-Photon Excitation

Here, we briefly discuss further distinct properties that differentiate two-photon excitation from conventional one-photon excitation and that can be used to elucidate certain biological questions.

In Chapter 1 we learnt that absorption of a photon is only possible if the corresponding transition dipole moment is nonzero (1.5). The dependence of the two-photon excitation probability on the wave functions of the initial and final state, however, can not be described by the transition dipole moment as defined by (1.4). We will not discuss the mathematical background of the transition

probability for TPE here but we will discuss the most important qualitative results. A first striking difference is that the optical selection rules are different for this nonlinear process since the electric-field components of two photons or light fields have to act simultaneously on the electron orbitals in order to promote a transition. In a very qualitative picture one can imagine that the electric field of the first light field is necessary to 'prepolarize' the electron orbitals in such a way that the electric field of the second light field can finally promote the entire transition. The 'prepolarized' state can be regarded as a virtual intermediate state similar to the virtual state in Raman scattering (cf. dashed line in Figure 4.10b). Nevertheless, both light fields must be present simultaneously to ensure the progress of the nonlinear transition. Having this simplified picture in mind helps in understanding a few of the following facts about two-photon excitation. For example, the parity selection rule, or Laporte's rule (Chapter 1), is no longer valid for TPE. In TPE the corresponding selection rules are exactly opposite to those in one-photon spectroscopy. For OPE only  $u \rightarrow g$  and  $g \rightarrow u$  transitions are allowed, whereas in TPE only  $g \rightarrow g$  and  $u \rightarrow u$  transitions are allowed.

A direct application example of the TPE selection rules is the selective observation of carotenoids in photosynthetic pigment–protein complexes (Figures 10.5 and 10.6). In Chapter 2 we discussed the fact that the natural orange colour of carotenoids is actually due to absorption into the second electronic state,  $S_2$ . A normal one-photon absorption or fluorescence involving the first excited state is optically forbidden due to Laporte's rule ( $g \rightarrow g$ ). However, because the internal conversion  $S_2 \rightsquigarrow S_1$  occurs within 200 fs the dark carotenoid state  $S_1$  plays in general, and also within the photosynthetic apparatus, a significant role. By applying two-photon excitation the optically dark  $S_1$  state of carotenoids can directly be excited because the transition  $S_0 \rightarrow S_1$  is a  $g \rightarrow g$  transition. Figure 10.6 shows the one-photon absorption spectrum of  $\beta$ -carotene together with its two-photon absorption spectrum. Two-photon excitation at the maximum of the two-photon excitation band allows us to

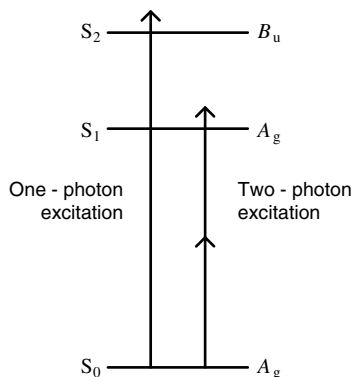


**Figure 10.5** The different optical selection rules for two-photon excitation enables direct excitation of the optical forbidden first excited state of carotenoids.

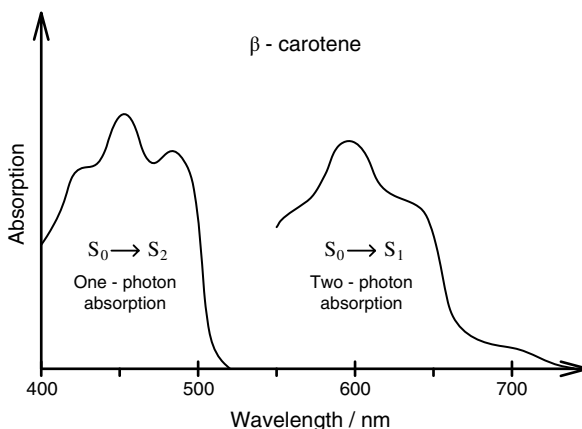


**Figure 10.6** One- and two-photon absorption spectra of carotenoids. Note that the two-photon spectrum is plotted versus  $\lambda = 1/(2\bar{v}_{\text{TPE}})$  to reflect the actually excited energies.

selectively excite and investigate the carotenoids in isolated photosynthetic pigment–protein complexes and even in intact plants. Other molecules such as chlorophylls have low two-photon absorption probabilities in the corresponding spectral region. Therefore, the selective two-photon excitation of the carotenoids significantly helps in understanding their role in photosynthesis.

Not only are the selection rules different for two-photon excitation, another distinct feature of TPE is the fact that the excitation probability can be very different when using linear or circular-polarized light. This is expressed by the so-called polarization ratio:

$$\Omega = \frac{P_{\text{TPE}}^{\text{circ}}}{P_{\text{TPE}}^{\text{lin}}} \quad (10.5)$$

Here,  $P_{\text{TPE}}^{\text{circ}}$  and  $P_{\text{TPE}}^{\text{lin}}$  are the two-photon excitation probabilities using circular or linear-polarized light, respectively. Depending on the symmetries of the initial and final electron state of a certain molecule,  $\Omega$  can have values ranging from 0 to 1.5 using TPE. This range is far larger than the differences in the absorption coefficients responsible for the circular dichroism effect (see Chapter 4). Since the polarization ratio is a distinct property of the investigated molecules it can be used to identify the molecules in complex samples.

Finally, the maximum observable fluorescence anisotropy from a sample of randomly orientated molecules,  $r_0$  [see (3.13) in Chapter 3], is also different when using TPE. This is because the photoselection is more restrictive for multiphoton excitation. The corresponding values are  $r_0^{\text{two-photon}} = \frac{4}{7}$  and  $r_0^{\text{three-photon}} = \frac{2}{3}$  for two- or three-photon excitation, respectively. In some cases this can help to extend the dynamic range of fluorescence polarization assays.

## 10.2.5

**Wavemixing and Other Nonlinear Optical Techniques**

Here, we first describe the theoretical background of nonlinear optics in more detail. This provides the basis for further understanding optically nonlinear methods that are important in the biosciences and that will be discussed later in this section.

In Chapter 4 (Section 4.2 on light scattering) we discussed that for normal light intensities the electric-field component ( $\vec{E}$ ) of incoming light induces an oscillating dipole moment ( $\vec{\mu}_{\text{induced}}$ ) at a molecule (4.11). As a consequence, for example, scattering of electromagnetic radiation (photons) with the same frequency can occur. If, however, the light intensity is very large, then the electron clouds can be distorted nonlinearly as a function of  $\vec{E}$ . This is illustrated schematically in Figure 10.7. Depending on the properties of the material the nonlinear response can result, for example, in the generation of electromagnetic radiation of twice the fundamental frequency. This is called second-harmonic generation (SHG) and can be used to create, for example, photons with a

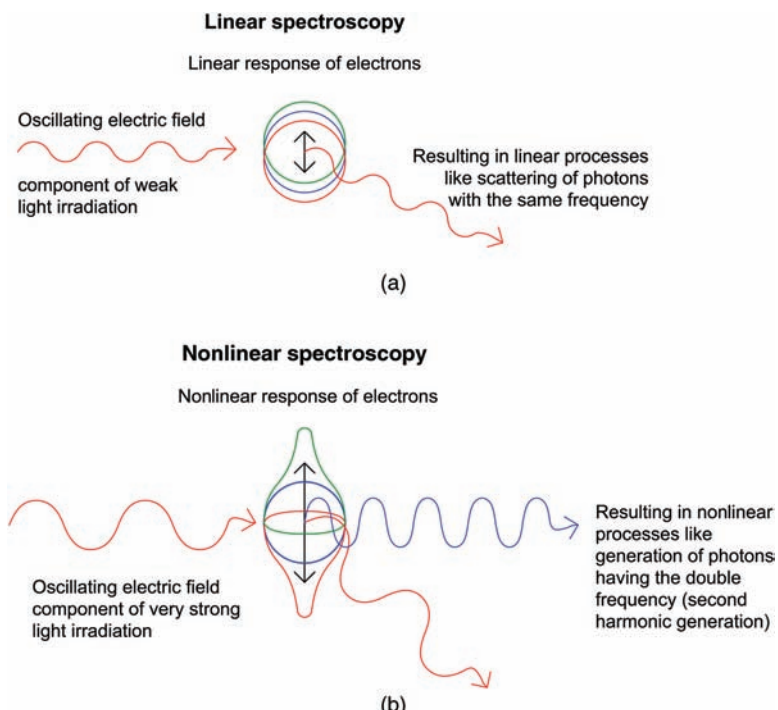


**Figure 10.7** Schematic presentation of the different response of a molecule's electron cloud to (a) normal light irradiation intensities and (b) very high intensities. Blue electron clouds symbolize the situation in the absence

of any electromagnetic radiation whereas green and red electron clouds symbolize the most extreme, time-dependent responses to electromagnetic radiation of different intensities.

wavelength of 400 nm from two photons with a wavelength of 800 nm. In the following, we provide a quantitative description of these qualitative statements.

If a material with a certain density of molecules is irradiated with normal light intensities then the sum of the induced dipole moments of many molecules in this material is described by the induced dielectric polarization,  $\vec{P}$ :

$$\vec{P} = \epsilon_0 \chi \vec{E} \quad (10.6)$$

Here,  $\chi$  is the electric susceptibility,  $\epsilon_0$  is the dielectric constant and  $\vec{E}$  is the inducing electric-field vector of the light. Equation (10.6) is closely related to (4.11), which defines the polarizability,  $\alpha = \vec{\mu}_{\text{induced}} / \vec{E}$ . The term  $\vec{P}$  describes the sum of the induced dipole moments of many molecules in a material, whereas  $\vec{\mu}_{\text{induced}}$  describes the magnitude of the dipole moment induced at a single molecule. The susceptibility,  $\chi$  describes the ease with which the electric field induces a dielectric polarization  $\vec{P}$  of a material, whereas the polarizability,  $\alpha$ , describes the ease with which the electric field induces a dipole moment at a single molecule.

In the presence of very high light intensities the collective nonlinear response of the electron clouds of many molecules in a material is described by:

$$\vec{P} = \epsilon_0 (\chi \vec{E} + \chi_2 \vec{E}^2 + \chi_3 \vec{E}^3 + \dots) \quad (10.7)$$

Here,  $\chi, \chi_2, \chi_3$  and so on, are the first-, second-, third- and so on order susceptibilities. The higher-order susceptibilities,  $\chi_2, \chi_3 \dots$ , of a material determine how large nonlinear effects become when the material is irradiated by strong light intensities.

Second-harmonic generation, for example, depends on the magnitude of the second-order susceptibility,  $\chi_2$ . To be able to actually observe SHG, however, the presence of a certain structure in the molecule or atom orientations and positions within in the material is also necessary. Similar to the scattering centres in linear light scattering (Figure 4.7 in Chapter 4) the irradiated material can be regarded as being composed of many SHG radiating sources. In an ordered crystal, for example, the maxima and minima of the electric field waves of the incoming as well as the resulting nonlinear optical fields must match with the positions of the atoms and their electron clouds in the crystal lattice to avoid multiple destructive interferences of the resulting SHG radiating sources. If the structure does not match with the incoming and resulting light waves no SHG can be observed. The prerequisite that the structures of the crystal match the incoming and generated light waves is called the phase-matching condition.

The requirement that certain molecular structures with certain orientations must be present in a sample to observe SHG is used in SHG microscopy of biological samples. In general, only noncentrosymmetrical spatial distributions of molecules can give rise to a SHG signal. If the molecular distribution is centrosymmetric the resulting SHG signals from these molecules interfere destructively. This can be the case, for example, when an equal number of the same molecules are orientated in opposing directions in a membrane. Based on these requirements, strong SHG signals can often be observed from certain structures such as collagen,

muscle fibres and also certain cell membranes. An advantage of SHG is that for the observation of these structures no fluorescence labelling is necessary.

For SHG microscopy a confocal set-up similar to the one shown in Figure 7.1 is used. The main difference is the use of a dichroic mirror that reflects wavelengths corresponding to the fundamental frequency of the laser irradiation and transmits the resulting SHG-light wavelength. Correspondingly, the optical filter in the detection pathway is chosen to block all wavelengths but the SHG wavelengths.

SHG is only one example of a multitude of further possible nonlinear optical processes. In general, in nonlinear optics many different resulting frequencies can be created from different incoming light fields:

$$\nu_{\text{wavemixing}} = \pm \nu_1 \pm \nu_2 \pm \nu_3 \dots \quad (10.8)$$

Here,  $\nu_1, \nu_2, \nu_3 \dots$ , are the corresponding frequencies of the incoming light fields and  $\nu_{\text{wavemixing}}$  is the resulting frequency. When the light fields differ in their wave vectors (for the definition of wave vectors see section 9.4.1) then the wave vector of the resulting light field can be correspondingly calculated by a vector addition:

$$\vec{\nu}_{\text{wavemixing}} = \pm \vec{\nu}_1 \pm \vec{\nu}_2 \pm \vec{\nu}_3 \dots \quad (10.9)$$

One possibility is, for example, third-harmonic generation (THG) microscopy. In THG, photons of energy corresponding to the sum of three photons of the incoming fundamental light field are generated:  $\nu_{\text{wavemixing}} = 3 \times \nu_{\text{fundamental}}$ . The observed THG intensity depends on the third-order susceptibility,  $\chi_3$ , of the material. In THG microscopy of biological samples, for example, often a high contrast of lipid bodies is observed.

From (10.8) it is obvious that it is even possible to generate resulting frequencies that are difference frequencies of the incoming light field frequencies. What kind of signals can be observed depends on the higher-order susceptibilities and structures of the investigated sample, the used frequencies of the incoming light fields and their propagation or wave vectors relative to the sample.

An important example of a method in which difference frequencies are generated is coherent anti-Stokes Raman scattering (CARS) microscopy. CARS microscopy allows label-free imaging of the three-dimensional structure of biological samples based on the vibrational eigenfrequencies of the chemical bonds in the biomolecules. In CARS microscopy two beams of short pulses with slightly different frequencies,  $\nu_{\text{Pump}}$  and  $\nu_{\text{Stokes}}$ , are sent simultaneously into the back aperture of the microscope objective of a microscope set-up (Figure 10.8). If the energy difference between photons of frequencies  $\nu_{\text{Pump}}$  and  $\nu_{\text{Stokes}}$  ( $\nu_{\text{Pump}} > \nu_{\text{Stokes}}$ ) correspond exactly to vibrational transitions of a larger number of chemical bonds of biomolecules in the focal region then a nonlinear optical signal, called an anti-Stokes signal, can be generated. The frequency of the generated anti-Stokes is:

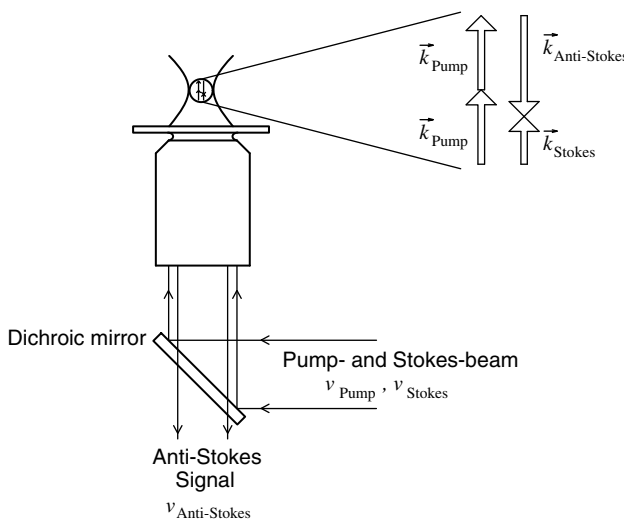


**Figure 10.8** Schematic illustration of the wave-vector diagram along the optical axis in CARS microscopy.

$$\nu_{\text{Anti-Stokes}} = \nu_{\text{Pump}} + \nu_{\text{Pump}} - \nu_{\text{Stokes}} = 2\nu_{\text{Pump}} - \nu_{\text{Stokes}}$$

The signal intensity is proportional to the square of the number of corresponding chemical bonds and depends also on the third-order susceptibility,  $\chi_3$ . Typically, these signals are a lot stronger than signals observed in Raman scattering experiments (see Figure 4.10 and Section 4.3 on the vibrational spectra of biomolecules). In CARS, anti-Stokes signals in both directions:

$$\vec{k}_{\text{Anti-Stokes}} = 2\vec{k}_{\text{Pump}} - \vec{k}_{\text{Stokes}} \text{ and } \vec{k}_{\text{Anti-Stokes}} = -(2\vec{k}_{\text{Pump}} - \vec{k}_{\text{Stokes}})$$

are generated. Closer inspection of the vector addition  $\vec{k}_{\text{Anti-Stokes}} = -(2\vec{k}_{\text{Pump}} - \vec{k}_{\text{Stokes}})$  reveals that the latter signal points in the opposite direction to the incoming beams,  $\vec{k}_{\text{Pump}}$  and  $\vec{k}_{\text{Stokes}}$  (see inset in Figure 10.8). Consequently, the anti-Stokes signal can also be collected by the same microscope objective and is then registered by a PMT, APD or CCD detector (Figure 10.8). This detection scheme is called Epi-CARS.

As with all multiphoton processes such as TPE, SHG and THG, CARS also has a high sectioning capability. In addition, similar to SHG and THG, CARS is a label-free technique and it generates very little photobleaching. The main advantage of CARS is, however, that the imaging of the vibrational transitions is sensitive to the distinct type of chemical bonds present in the biological sample. When using broad-band light for the Stokes beam fast imaging of the samples is possible in which each pixel contains the information of an entire vibrational spectrum. This allows us, for example, to detect label-free parts of living cells

that are enriched in lipids, DNA or other components that can be easily identified via their characteristic vibrational structure.

### 10.3

#### Ultrafast Spectroscopy

As described in the Introduction the fastest processes occurring in biology can only be resolved using ultrafast lasers providing pulses on the fs-timescale. No other technique provides the time resolution necessary for the observation of these fast processes. In this section we give an insight into how ultrashort light pulses can be used to investigate ultrafast processes in biology. As an example, we will explain pump–probe techniques, which are actually also a type of nonlinear spectroscopy because they are based on the interaction of two photons with a molecule or biomolecule. In Section 10.3.2 we discuss why it is essential for photosynthetic light-harvesting and energy-conversion apparatus to work on an ultrafast timescale and how the underlying mechanisms can be elucidated using ultrafast laser systems.

##### 10.3.1

#### Pump–Probe Spectroscopy

To gain a basic understanding of the functioning of ultrafast laser techniques we will discuss the application of the most basic ultrafast technique, the so-called pump–probe technique, for the investigation of ultrafast Förster resonance energy transfer. In Chapter 3 we learnt that the rate of energy transfer between a donor and an acceptor fluorescence marker depends critically on the distance between the two molecules (3.33). If there is a good spectral overlap and if the molecules are almost in van der Waals contact, then the rate for energy transfer,  $k_{ET}$ , can easily be on the fs-timescale.

To investigate such a fast energy transfer a suitable ultrafast laser system is aligned in such a way that it provides two different light beams that both consist of ultrashort laser pulses. One beam, called the pump beam, is tuned to a wavelength corresponding to the absorption of the donor fluorescence marker (Figure 10.9). The second beam, called the probe beam, is tuned to a wavelength corresponding to the absorption of the acceptor fluorescence marker.

The principle of the pump–probe experiment is now as follows. First, a pump pulse excites the donor at a time that we define as  $t=0$ . Subsequently, the donor transfers energy into the acceptor molecule. Depending on the rate constant for the energy transfer,  $k_{ET}$ , more and more acceptor molecules are then in the first excited state,  $S_1^A$ , with increasing time  $t$ . A measurable consequence of this is that the absorption of the acceptor is slightly reduced simply because fewer molecules are available for a  $S_0^A \rightarrow S_1^A$  transition. This phenomenon is called bleaching of the ground-state absorption. If a probe pulse now arrives at the sample at a certain time  $t>0$  then the amount of

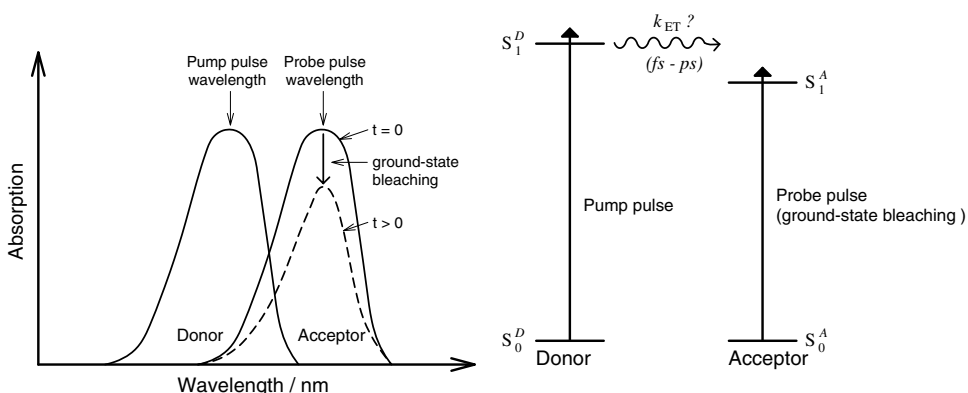


**Figure 10.9** To investigate ultrafast resonance energy transfer the pump- and probe-pulse wavelengths of an ultrafast laser system are tuned to the absorption wavelengths of the donor and acceptor fluorescence markers, respectively. If energy transfer results in acceptor molecules excited into  $S_1^A$  then the measurable  $S_0^A \rightarrow S_1^A$  absorption is reduced because fewer acceptor molecules are in the

electronic ground state,  $S_0^A$ . The dependency of this acceptor-absorption reduction, called ground-state bleaching, thus provides direct information about the population of acceptor molecules excited by energy transfer at a certain time  $t$  after the pump pulses have excited the donor molecules. For more details see the text.

energy transferred at this time can be directly determined from the magnitude of the reduced probe-beam absorption.

Figure 10.10 shows a typical set-up for a pump–probe experiment. In ultrafast laser set-ups repetitive pump- and probe-pulse sequences are usually generated simultaneously from a single sequence of very intense laser pulses by nonlinear optical techniques such as described in the previous section. As a consequence, the relative time delay between individual pump and probe pulses is usually extremely constant. Both beams are focused together on the same spot in a sample cell containing the donor–acceptor sample. The exact time delay between pump and probe pulses,  $t$ , is aligned by changing the optical pathway length of one of the two beams. This can be achieved by translating two perpendicular mirrors on a translation stage. Given that the speed of light is  $c \sim 3 \times 10^8 \text{ m s}^{-1}$  a translation of  $15 \mu\text{m}$  corresponds to a change in the delay between the pump and probe pulses of  $\sim 10 \text{ fs}$ . (Note that the translation of the stage by a certain distance  $\Delta x$  changes the optical path length of the probe beam by  $2 \times \Delta x$ .) Using highly sensitive detection equipment the small absorption changes caused by the acceptor ground state bleaching can be sensed as a  $t$ -dependent increase in the probe beam light intensity  $I(t)$  observed after the sample cell (Figure 10.11). The corresponding increase in the intensity reflects directly the increasing excited state population of the acceptor,  $P_{S_1}^A$ . It is proportional to:<sup>2)</sup>

2) Actually, this equation is only an approximation that is true for small changes in the excited-state populations. For larger population changes the excited-state populations must rather be derived from the measured intensities using the Beer–Lambert law (2.5).

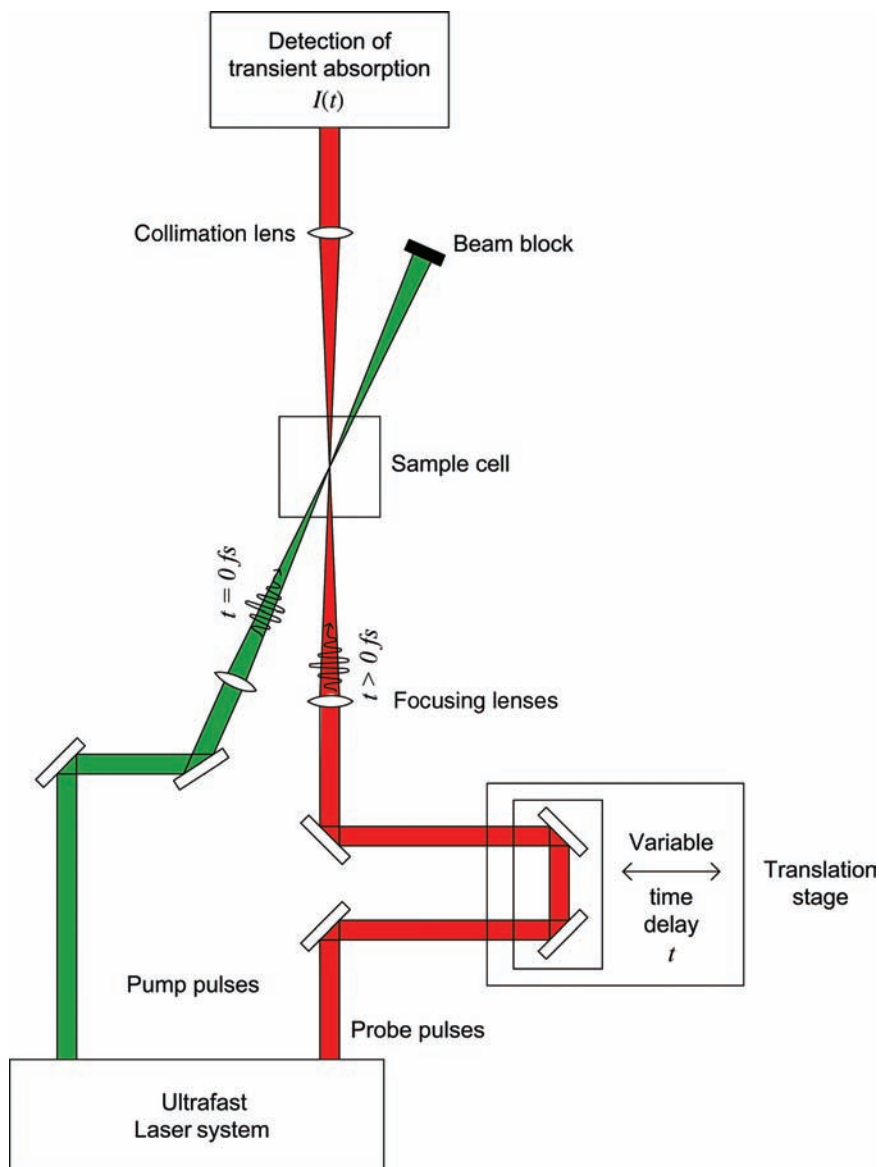


**Figure 10.10** Typical set-up for pump-probe experiments. In the present example, the pump pulses (green) first excite the donor at time  $t = 0$ . The arrival time  $t > 0$  of the probe pulses (red) relative to the pump pulses can be adjusted exactly by changing the optical path length of the probe beam. This is achieved by translating the mirror pair on the translation stage. A translation of  $\sim 15 \mu\text{m}$  corresponds to a pump-probe pulses delay of

$\sim 10\text{ fs}$ . If the acceptor molecules ground-state absorption at  $t > 0$  is decreased due to energy transfer this results in a slightly lower absorption of the pump beam and thus in a slightly larger intensity detected after the sample cell. Repeating the experiment for many different pump-probe time delays  $t$  results in curves such as shown in Figure 10.11. Figure 10.11 directly reflects the excited-state dynamics of the acceptor during the energy transfer.

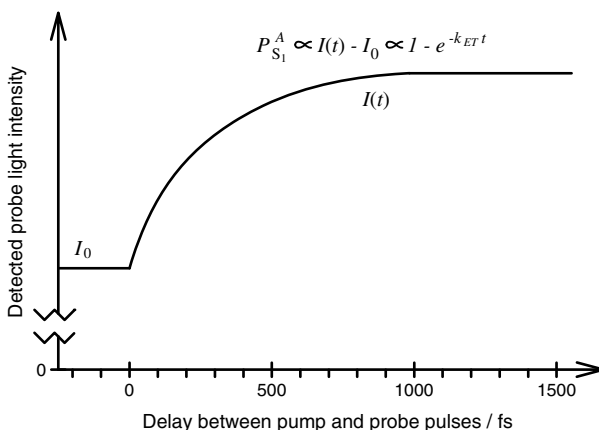


**Figure 10.11** The increasing light intensity detected from the probe beam pulses after the sample cell reflects directly the acceptor ground-state bleaching caused by the energy

transfer. Fitting an exponential function to the observed kinetics unravels directly the corresponding rate constant for energy transfer.

$$P_{S_1}^A \propto I(t) - I_0 \propto 1 - e^{-k_{ET}t} \quad (10.10)$$

Here,  $I_0$  is the detected probe beam intensity observed in the absence of the pump pulses or if the probe pulses arrive prior to the pump pulses ( $t < 0$ ).  $k_{ET}$  corresponds to the rate of energy transfer between donor and acceptor dye [compare with (3.34) and Figure 3.30].<sup>3)</sup> Please note that the decay of the acceptor-state population ( $P_{S_1}^A$ ) corresponding to its excited-state lifetime ( $\tau_{S_1}^A$ ) in the ns range is not visible on the timescale of a fs experiment and can thus be neglected ( $e^{-t/\tau_{S_1}^A} \approx 1$ ).

In the present example we focused only on the ground-state bleaching of the acceptor caused by a depopulation of its ground state,  $S_0^A$ . However, often the disappearance of the ground-state absorption gives rise to the appearance of a new excited-state absorption,  $S_1^A \rightarrow S_n^A$ , corresponding to an excitation of the first excited state into higher excited states  $S_n^A$ . If the probe wavelength were tuned to the corresponding absorption wavelengths, then new additional transient absorptions and thus a decrease in  $I(t)$  could be observed. Often, both bleaching of the ground-state absorption and excited-state absorption are

3) Also, the assumption that the acceptor population increase is only determined by  $k_{ET}$  is only an approximation. For a single donor–acceptor pair this increase is actually determined by the excited-state lifetime of the donor in the presence of energy transfer,  $\tau_{S_1}^{DET}$ . However, since a  $k_{ET}$  on the fs-timescale is much larger than the corresponding rate constants for all other processes depopulating the excited state of the donor it is a good approximation to assume that  $\tau_{S_1}^{DET} \approx k_{ET}^{-1}$ .

convoluted in such experiments.<sup>4)</sup> In more complex systems, often the entire kinetic behaviour of all excited-state intermediates from all involved molecules can be elucidated from time-dependent absorption measurements at various probe wavelengths or wavelength ranges. In the next section we will, as an example, describe how this can be applied to investigate the mechanisms in light harvesting and energy conversion occurring in photosynthesis.

### 10.3.2

#### Application Example: Ultrafast Light-Harvesting and Energy Conversion in Photosynthesis

Figure 10.12 shows schematically the extremely efficient light-harvesting apparatus of photosynthesis as it would be observed when viewed on the thylakoid membranes in chloroplasts. It consists of various different photosynthetic pigment–protein complexes. The pigments responsible for light harvesting in photosynthesis are chlorophylls and carotenoids. In Figure 10.12 they are visualized by green and orange, respectively. The entire system works like an ‘energy funnel’. Regardless of the position of a pigment that has absorbed a photon of sunlight the excitation energy will be transferred via energy-transfer steps until it has reached the so-called special pair of chlorophylls in the reaction centre pigment–protein complex. Hundreds of chlorophyll and carotenoid molecules ‘feed’ one reaction centre in this way. The special pair of chlorophylls are arranged in such a way that the electronic excitation energy is used for a primary electron charge separation. After several electron-transfer steps the energy of this charge separation is then used to drive all subsequent biochemical reactions. An important consequence of the charge separation is, for example, the build up of a proton gradient across the thylakoid membranes that is used to drive ATPase (see Figure 9.2).

The overall quantum efficiency of the excitation energy transfer steps in the ‘energy funnel’ can be very high. To be so efficient the individual energy transfer steps must occur very rapidly, namely on the fs-timescale. Otherwise, concurring reactions such as the conversion of the excitation energy into heat via internal conversion would dissipate a large amount of excitation energy during the multitude of energy transfer steps before it could reach the reaction centre. Also, the primary charge separation occurs quite rapidly, on a ps-timescale. Consequently, it was not before the development of ultrafast laser systems that the elementary steps of these vital processes could be investigated in detail.

4) A further effect that can contribute to the observed signals is stimulated emission of the donor (for an explanation of stimulated emission see Section 8.1 on STED microscopy). Since the fluorescence spectrum of the donor will also have wavelengths corresponding to the probe wavelength the probe beam will also stimulate emission from the excited donor molecule. As a consequence, photons are generated that have the same wavelength and propagation direction as the pump beam photons. This process will actually also increase the intensity measured in the optical pump-beam pathway after the sample. The total probe-beam intensity detected at a various wavelengths depends on the sum of all three processes - ground state bleaching, transient absorption and stimulated emission.

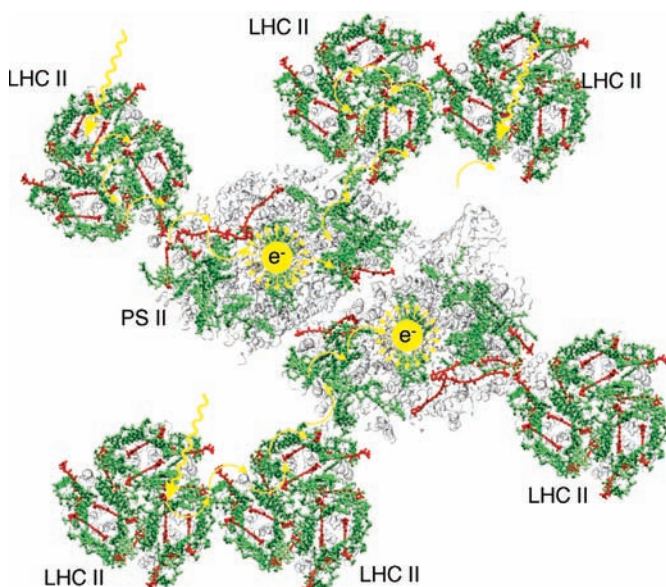


**Figure 10.12** Schematic view of the photosynthetic light-harvesting apparatus in the thylakoid membrane of chloroplasts. The light-harvesting pigments are chlorophyll and carotenoid molecules (indicated by green and red, respectively). The photosynthetic reaction centres are part of pigment-protein complexes called photosystem I (PS I) and photosystem II (PS II). The photosystems are surrounded by light-harvesting pigment-protein complexes (LHCs). Here, only PS II with a few trimers of light-harvesting pigment-protein complexes II (LHC II) is shown. If a sunlight photon is absorbed by any of the light-harvesting pigments (indicated by the wavy arrows) the excitation energy is transferred on a fs-timescale between neighbouring pigments (indicated by the curved arrows) until it reaches a special pair of chlorophylls in the reaction centre. The special pair has a lower excitation energy than most of the surrounding chlorophylls. This lowered energy is due to excitonic interactions that occur when the electron orbitals of two molecules with a similar excited-state energy can resonate because they are very close and have transition dipole

moments that are similarly orientated. As a consequence, the special pair act as an 'energy trap' for the excitation energy of the entire light-harvesting pigment pool. In addition, it initiates the conversion of the excitation energy into an electron charge separation (indicated by  $e^-$  in the figure). This primary charge separation also occurs on a ps-timescale. Depending on the environmental conditions of plants the overall quantum efficiency of this process can be very high. Then, almost every photon absorbed by a light-harvesting pigment is finally used for a primary charge separation in the reaction centre. Both the ultrafast light-harvesting and primary electron-transfer processes can only be investigated using ultrafast laser spectroscopy. After primary charge separation has occurred the electrons are further transferred through other protein complexes (not shown here). The interplay of the light-harvesting and charge-separation processes of both PS I and PS II finally drives all subsequent biochemical reactions, resulting also in the build up of chemically stored energy.

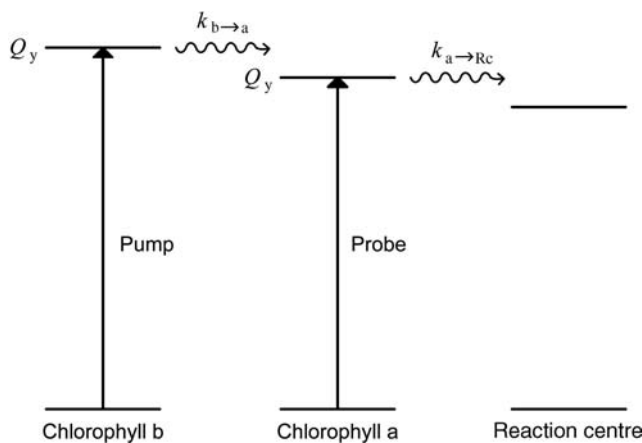


**Figure 10.13** Relative energy levels of the lowest excited states of chlorophyll *a* and *b* and the special pair chlorophylls.

In the previous section we discussed how pump–probe spectroscopy can be used to investigate an ultrafast energy transfer between a pair of donor–acceptor fluorescence dyes. We will now discuss, as an example, how a few of the elementary primary steps in photosynthesis can be investigated by the same technique. In the next two sections we will focus on two examples: The flow of absorbed light energy from chlorophyll *b* to chlorophyll *a* molecules and of absorbed light energy from the carotenoids to the chlorophylls.

#### 10.3.2.1 Chlorophyll *b* $\rightarrow$ Chlorophyll *a* $\rightarrow$ Reaction Centre Energy Flow

In the direct vicinity of PS II are the so-called minor light-harvesting complexes CP24, CP26 and CP29 (not shown in Figure 10.12) whereas more remote regions

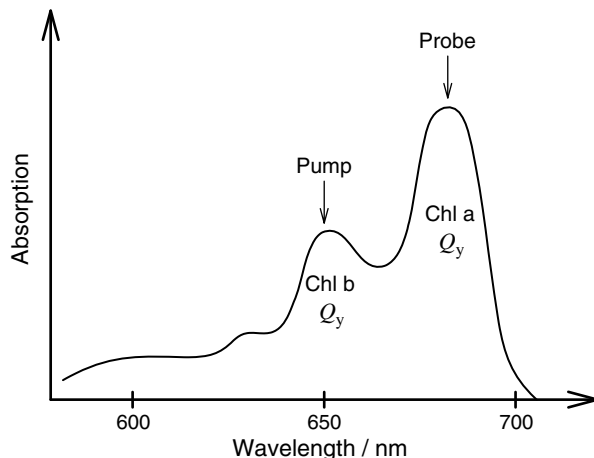


**Figure 10.14** The energy flow between chlorophyll *b* and *a* molecules in photosynthetic pigment–protein complexes can be investigated by tuning the pump beam to the chlorophyll *b* absorption and the probe beam to the chlorophyll *a* absorption.

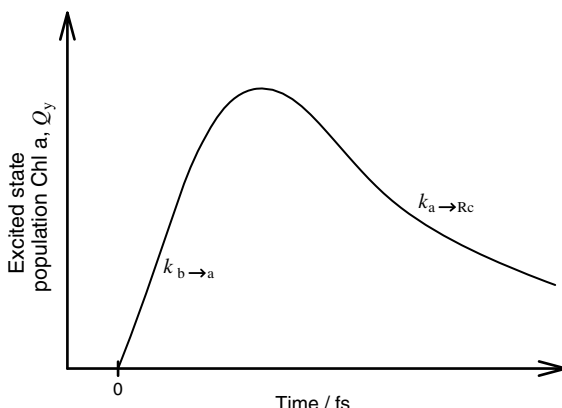


**Figure 10.15** From pump–probe data observed with excitation of chlorophyll *b* and detection of chlorophyll *a* the kinetics of the chlorophyll *b*  $\rightarrow$  chlorophyll *a* energy flow,  $k_{b \rightarrow a}$ , as well of the chlorophyll *a*  $\rightarrow$  reaction centre energy flow,  $k_{a \rightarrow R_c}$ , can be elucidated. This can be performed for isolated pigment–

protein complexes as well as for entire thylakoid membrane fractions. The information on the kinetics of individual energy-flow pathways deduced from such experiments gives valuable insights into the overall functioning of the photosynthetic apparatus.

are dominated by the major light-harvesting complex LHC II. Interestingly, the ratio of chlorophyll *b* to chlorophyll *a* molecules decreases in the order LHC II > minor LHCs > PS II ( $\sim 0.8 \gtrsim 0.5 > 0$ ). Since the lowest excited state,  $Q_y$ , of chlorophyll *b* is slightly higher in energy than that of chlorophyll *a* the energy usually flows from chlorophyll *b* to chlorophyll *a* (Figure 10.13, see also Figure 2.15). Therefore, the decrease in chlorophyll *b* content might facilitate directing the excitation energy towards the reaction centre. Using pump–probe spectroscopy the kinetics of the chlorophyll *b*  $\rightarrow$  chlorophyll *a* energy flow can be investigated within isolated pigment–protein complexes as well as within entire thylakoid fragments. Similar to the example discussed in the previous section the pump wavelength can be tuned to the absorption of the chlorophyll *b*  $Q_y$  band at  $\sim 650$  nm (Figure 10.14). The pump light will then initiate the same light harvesting, energy transfer and – depending on the sample – initial charge-transfer processes as if chlorophyll *b* would have normally absorbed sunlight. To follow the subsequent energy-transfer steps, the probe beam can then be tuned to the chlorophyll *a* absorption band at  $\sim 680$  nm. The energy-flow-dependent excited-state population dynamics of the chlorophyll *a* molecules can now be monitored by detecting the ground-state bleaching of the chlorophyll *a*  $Q_y$  band as a function of the pump–probe pulses delay,  $t$  (Figure 10.15). The rise component of the observed population kinetics corresponds to the chlorophyll *b*  $\rightarrow$  chlorophyll *a* energy flow kinetics,  $k_{b \rightarrow a}$ <sup>3)</sup>. Depending on the observed samples, the decay component of the observed population kinetics can correspond to the chlorophyll *a*  $\rightarrow$  reaction centre energy flow kinetics,  $k_{a \rightarrow R_c}$ , or also other subsequent energy flow dynamics<sup>3)</sup>.

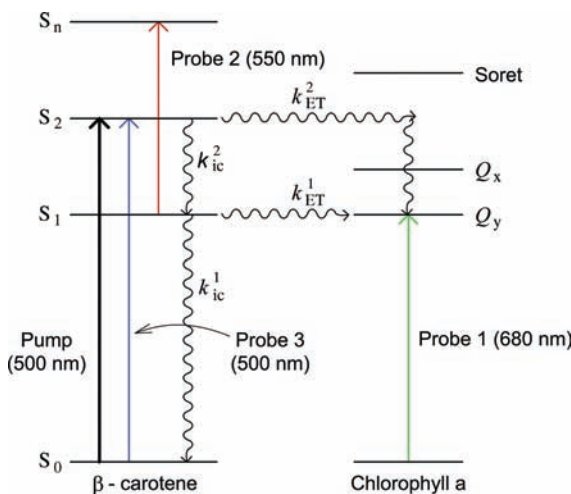


**Figure 10.16** Possible energy pathways between  $\beta$ -carotene and chlorophyll *a* after absorption of light exciting the carotenoid into the  $S_2$  state along with various probe wavelengths monitoring different possible excited-state dynamics.

### 10.3.2.2 Carotenoid $\rightarrow$ Chlorophyll Energy Flow

Carotenoids contribute significantly to light-harvesting by absorption in the blue spectral region of sunlight and might also play further decisive roles, for example, in the regulation of photosynthesis. However, as discussed in the previous section and in Chapter 2 the blue absorption is entirely due to  $S_0 \rightarrow S_2$  transitions because the first excited state of carotenoids,  $S_1$ , is optically forbidden. Since the internal conversion,  $S_2 \rightsquigarrow S_1$ , of isolated carotenoids occurs typically within 100–300 fs it is of interest how the energy flow between the two carotenoid states and the chlorophylls takes place in photosynthesis and how the optically forbidden  $S_1$  state participates in these energy flows. From Figure 10.16 it is obvious that even for a single pair of a  $\beta$ -carotene molecule with a chlorophyll *a* molecule multiple energy pathways are possible. Here, we only discuss, as an example, detection of the excited state population dynamics of the two carotenoid states  $S_1$  and  $S_2$  as well of the chlorophyll state  $Q_y$ . When carotenoids absorb sunlight in nature, first the second excited state,  $S_2$ , is populated. Therefore, to investigate the energy flow dynamics observed after carotenoid absorption the pump wavelength can be tuned to  $\sim 500$  nm to excite almost exclusively this carotenoid  $S_2$  state (Figures 10.16 and 10.17).

To follow the subsequent overall energy transfer to the chlorophylls the probe beam can be tuned to the chlorophyll absorption band at  $\sim 680$  nm (green Probe 1 in Figures 10.16 and 10.17 and  $Q_y$  population in Figure 10.18). The energy transfer depends on the rate of direct energy transfer from the allowed carotenoid state  $S_2 \rightsquigarrow$  chlorophyll,  $k_{ET}^2$ , as well as on the rate of carotenoid internal conversion  $S_2 \rightsquigarrow S_1$ ,  $k_{IC}^2$ , and the rate of energy transfer from the forbidden carotenoid state  $S_1 \rightsquigarrow$  chlorophyll,  $k_{ET}^1$ . If further energy transfer occurs, for example to the reaction

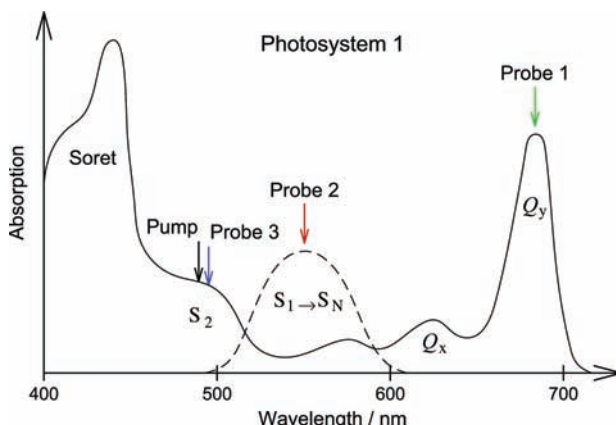


**Figure 10.17** Ground-state absorption spectrum of the pigment–protein complex PS I, which contains only the pigments  $\beta$ -carotene and chlorophyll *a*. The dashed line corresponds to the excited-state absorption of the optically forbidden carotenoid  $S_1$  state.

centre, this could be monitored also from the chlorophyll  $Q_y$  population or directly by probing the absorptions corresponding to the charge transfer state of the reaction centre. To monitor the population dynamics of the optically forbidden  $S_1$  state, fortunately its very strong excited-state absorption  $S_1 \rightarrow S_n$  at around  $\sim 550$  nm can be used (dashed line in Figure 10.17 and red Probe 2 in Figures 10.16 and 10.17). This is an additional, optically allowed absorption that is only present when the carotenoid  $S_1$  state is populated. The corresponding population kinetics are governed by internal conversion  $S_2 \rightsquigarrow S_1$ , energy transfer to the chlorophylls,  $S_1 \rightsquigarrow$  chlorophyll  $Q_y$ , and by internal conversion,  $S_1 \rightsquigarrow S_0$ , back to the ground state (red  $S_1$  population in Figure 10.18). Finally, to monitor relaxation back into the electronic ground state of the carotenoids the probe wavelength can simply be tuned also to the wavelength of the carotenoid ground-state absorption,  $S_0 \rightarrow S_2$  (blue Probe 3 in Figures 10.16–10.18).

From these examples it becomes obvious that the pump and probe wavelengths can be basically tuned to monitor any desired electronic state and also charge-transfer population, respectively. It is also possible to pump the optically forbidden carotenoid  $S_1$  state directly by two-photon excitation pulses and monitor the subsequent excited-state dynamics as usual by one-photon probe pulses. In addition, most components of the photosynthetic apparatus can be either investigated in isolation or in groups. There is a plethora of further ultrafast detection technologies that can be very useful for the investigation of ultrafast processes in nature. One of these techniques is fluorescence upconversion. This technique allows us, for example, to monitor the fluorescence kinetics of a sample on the ultrafast timescale. Along with the increasing detailed structural data available for individual protein complexes, such experiments provide very

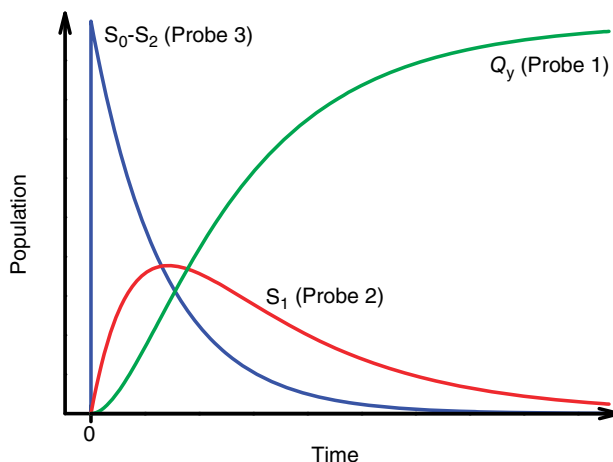


**Figure 10.18** Probing at various wavelengths (see Figures 10.16 and 10.17) allows us to follow the excited-state populations of the two carotenoid states  $S_1$  and  $S_2$  as well as that of the chlorophyll state  $Q_y$ .

**Table 10.1** Typical timescales of important elementary steps in photosynthetic light-harvesting and energy conversion.

Energy transfer from chlorophyll $b$ to chlorophyll $a$	~50 to ~500 fs
Energy transfer from the carotenoids to chlorophylls	~50 to ~5 ps
Energy transfer from the chlorophylls to the special pair	~1 to ~5 ps
First charge separation	~1 to ~10 ps

detailed insights into the overall functioning of the energy conversion in photosynthesis. Table 10.1 summarizes typical timescales for important intermediate steps in photosynthetic sunlight harvesting and energy conversion as revealed by ultrafast laser spectroscopy.

In recent years increasing efforts have been undertaken to develop artificial photosynthesis by combining artificial molecular light-harvesting structures with artificial reaction centres. As in natural photosynthesis, many of these approaches are based on ultrafast energy-transfer and electron-transfer steps. It can thus be expected that the characterization of these artificial systems using ultrafast detection technologies will become increasingly significant on the road to the ultimate goal of developing a robust, economical artificial system that converts sunlight into chemically storable energy.

### Problems

- 10.1** In an experiment molecules with a one-photon absorption maximum at  $\lambda \sim 400$  nm are excited by two-photon excitation with a  $\lambda = 800$  nm laser beam. The laser can be run in continuous wave and in a pulsed mode. In

the pulsed mode the laser provides pulses of about 200 fs FWHM with a repetition rate of 80 MHz. In both modes the laser provides the same average power. How much higher is the efficiency of two-photon excitation when the laser is run in the pulsed in comparison to the continuous-wave mode?

- 10.2** Figure 7.3 shows the spectral characteristics of a dichroic mirror and optical filter for detecting fluorescence from a certain fluorescence dye in a confocal set-up. Sketch in a similar way the spectral characteristics of the dichroic mirrors and optical filters that are necessary for a two-photon excitation, dual-colour confocal set-up (Figure 10.3). Assume that for the two-photon excitation only wavelengths of a typical titanium-sapphire laser are used ( $\lambda_{\text{Exc}} \sim 700\text{--}1200\text{ nm}$ ).
- 10.3** Two-photon absorption spectra often look different from the corresponding one-photon absorption spectra of the same molecules. One example is  $\beta$ -carotene, for which the corresponding spectra are shown in Figure 10.6. It might be a surprise that Laporte's rule still applies for carotenoids even if they are unsymmetrically substituted or distorted by their biological protein environment. What simple experiment can be done to unambiguously provide evidence that the transition  $S_0 \rightarrow S_1$  is indeed almost completely forbidden for a particular carotenoid?
- 10.4** Figure 3.11 shows the dependence of the excitation probability on the relative orientation between a molecule and the polarization vector of light (3.7). How do you expect the corresponding dependence to look for two- or three-photon excitation? Discuss the influence of this dependence on the maximum fluorescence anisotropy,  $r_0$ , observable from a mixture of randomly orientated fluorescence labels after two- or three-photon excitation. Remember that the corresponding values are  $r_0^{\text{two-photon}} = \frac{4}{7}$  or  $r_0^{\text{three-photon}} = \frac{2}{3}$  for two- or three-photon excitation, respectively.
- 10.5** Two different beams are used for two-photon excitation of the same molecules as in question 10.1. The corresponding wavelengths of the two beams are 600 nm and 1200 nm, respectively.
- What transition wavelength corresponds to a two-photon excitation with one 600-nm and one 1200-nm photon?
  - The probability of two-photon excitation in question 10.1 depends on the intensity of the 800-nm beam by  $P_{\text{Absorption}}^{\text{Two-Photon}} \propto I_{\text{Excitation}}^2$ . What is the corresponding relation between the probability for two-photon excitation in the case of a two-photon excitation with one 600-nm and one 1200-nm photon?
  - Assume that the molecule also has a significant absorption at around 300 nm. How can we ensure that only two-photon excitation with

600-nm and 1200-nm photons occurs, with almost no two-photon excitation with two 600-nm photons?

- 10.6** A crystal with a high second-order susceptibility,  $\chi_2$ , is illuminated with two beams of 600- and 1200-nm photons. It is irradiated under phase-matching conditions such that the sum frequency is generated. What is the dominant sum-frequency that can be generated? In what direction, relative to the wave vectors of the incoming beams, does the generated light beam point when the 600- and 1200-nm beams are at an angle of  $20^\circ$  to each other?
- 10.7** In a CARS experiment, for the pump beam a wavelength of 800 nm is used, whereas for the Stokes beam a wavelength of 870 nm is used. The angle between the beams is  $30^\circ$ . What is the wavelength of the generated anti-Stokes beam? In what direction, relative to the wave vectors of the incoming beams, does the generated anti-Stokes beam point?
- 10.8** Table 3.1 gives the Förster radius of the donor–acceptor pair chlorophyll *b*–chlorophyll *a*. What is the rate constant for the energy transfer between these pigments when the distance  $r$  is 1.43 nm? Assume for the excited-state lifetime of chlorophyll *a* in the absence of energy transfer a value of about  $\tau_{S_1}^{D,0} \sim 6$  ns. Table 3.1 also gives the Förster radius of the donor–acceptor pair  $\beta$ -carotene–chlorophyll *a*. What special aspects of the  $\beta$ -carotene to chlorophyll *a* energy transfer have to be considered?
- 10.9** Assume that in photosynthesis the excitation energy has to be transferred on average over ten pigments in single steps with a time constant for energy transfer of  $\tau_{ET} \sim 100$  fs before it reaches the special pair. What is the total quantum efficiency of this process if the excited-state lifetime of the pigments in the absence of energy transfer would be about  $\tau_{S_1} \sim 5$  ns?
- 10.10** Even though the quantum efficiency of the light-harvesting processes is high a large amount of the photon energy is usually already lost in the first pigment due to vibrational relaxation in the excited state. What percentage of the photon energy is lost when a photon of 480 nm wavelength is absorbed by a chlorophyll *a* molecule with a fluorescence maximum at  $\sim 690$  nm (Figure 2.15).

## Bibliography

### Specific

#### Nonlinear Spectroscopy

Levenson, M.D. and Kano, S.S. (1989)  
*Introduction to Nonlinear Laser Spectroscopy*, Academic Press, San Diego.

Maeda, S., Kamisuki, T. *et al.* (1988)  
Condensed phase CARS, in *Advances in Non-Linear Spectroscopy* (eds R.J.H. Clark and R.E. Hester), John Wiley & Sons, Ltd., Chichester, pp. 253–297.  
Mukamel, S. (1999) *Principles of Nonlinear Optical Spectroscopy*, Oxford University Press, New York.

- Pubanz, J.A. and Nibler, J. (1988) Coherent Raman spectroscopy of gases, in *Advances in Non-Linear Spectroscopy* (eds R.J.H. Clark and R.E. Hester), John Wiley & Sons, Ltd., Chichester, pp. 1.
- Shen, Y.R. (2002) *The Principles of Nonlinear Optics*, John Wiley & Sons, Inc., New York.
- Two-Photon Spectroscopy, Microscopy and FCS**
- Denk, W., Strickler, J.H. *et al.* (1990) Two-photon laser scanning fluorescence microscopy. *Science*, **248** (4951), 73–76.
- Diaspro, A. (ed.) (2001) *Confocal and Two-Photon Microscopy: Foundations, Applications and Advances*, John Wiley & Sons, Inc., New York.
- Friedrich, D.M. and McClain, W.M. (1980) Two-photon molecular electronic spectroscopy. *Annu. Rev. Phys. Chem.*, **31** (1), 559–577.
- Haustein, E.P. and Schwille, P. (2008) Ultrashort laser pulses in single molecule spectroscopy, in *Ultrashort Laser Pulses in Biology and Medicine* (eds M. Braun, P. Gilch and W. Zinth), Springer, pp. 279–306.
- Schwille, P. and Haustein, E. (2001) Fluorescence correlation spectroscopy in vitro and in vivo, in *Single-Molecule Techniques: A Laboratory Manual* (eds P.R. Selvin and T. Ha), Springer, Berlin, Chapter 12.
- Walla, P.J., Yom, J. *et al.* (2000) Two-photon excitation spectrum of light-harvesting complex II and fluorescence upconversion after one- and two-photon excitation of the carotenoids. *J. Phys. Chem. B*, **104** (19), 4799–4806.
- Wehling, A. and Walla, P.J. (2005) Time-resolved two-photon spectroscopy of photosystem I determines hidden carotenoid dark-state dynamics. *J. Phys. Chem. B*, **109** (51), 24510–24516.
- SHG/THG Spectroscopy**
- Barad, Y., Eisenberg, H. *et al.* (1997) Nonlinear scanning laser microscopy by third harmonic generation. *Appl. Phys. Lett.*, **70** (8), 922–924.
- Campagnola, P.J., Wei, M.-D. *et al.* (1999) High resolution non-linear optical microscopy of living cells by second harmonic generation. *Biophys. J.*, **77**, 3341–3349.
- Débarre, D., Supatto, W. *et al.* (2006) Imaging lipid bodies in cells and tissues using third-harmonic generation microscopy. *Nature Methods*, **3**, 47–53.
- Gannaway, J.N. and Sheppard, C.J.R. (1978) Second-harmonic imaging in the scanning optical microscope. *Opt. Quantum Electron.*, **10**, 435–439.
- Wilk, L., Grunwald, M. *et al.* (2013) Direct interaction of the major light-harvesting complex II and PsbS in nonphotochemical quenching. *PNAS*, **110**, 5452–5456.
- Moreaux, L., Sandre, O. *et al.* (2001) Coherent scattering in multi-harmonic light microscopy. *Biophys. J.*, **80** (3), 1568–1574.
- Scheuring, S., Seguin, J. *et al.* (2003) Nanodissection and high-resolution imaging of the Rhodopseudomonas viridis photosynthetic core complex in native membranes by AFM. *Proc. Natl. Acad. Sci.*, **100** (4), 1690–1693.
- Bode, S., Quentmeier, C.C. *et al.* (2009) On the regulation of photosynthesis by excitonic interactions between carotenoids and chlorophylls. *PNAS*, **106**, 12311–12316.
- Yelin, D. and Silberberg, Y. (1999) Laser scanning third-harmonic-generation microscopy in biology. *Opt. Express*, **5** (8), 169–175.
- CARS Microscopy**
- Maker, P.D. and Terhune, R.W. (1965) Study of optical effects due to an induced polarization third order in the electric field strength. *Phys. Rev. Lett.*, **137**, A801–A818.
- Volkmer, A., Cheng, J.-X. *et al.* (2001) Vibrational imaging with high sensitivity via epideTECTED coherent anti-Stokes Raman scattering microscopy. *Phys. Rev. Lett.*, **87** (2), 023901–023904.
- Volkmer, A. (2005) Vibrational imaging and microspectroscopies based on coherent anti-Stokes Raman scattering microscopy. *J. Phys. D Appl. Phys.*, **38** (5), R59–R81.

- Zumbusch, A., Holtom, G.R. *et al.* (1999) Three-dimensional vibrational imaging by coherent anti-Stokes Raman scattering. *Phys. Rev. Lett.*, **82** (20), 4142–4145.
- Ultrafast Spectroscopy and Lasers**
- van Amerongen, H., Valkunas, L. *et al.* (2000) *Photosynthetic Excitons*, World Scientific Publishing Company.
- Demtröder, W. (2007) *Laserspektroskopie: Grundlagen und Techniken*, Springer, Berlin.
- Diels, J.C. and Rudolph, W. (1996) *Ultrashort Laser Pulse Phenomena: Fundamentals, Techniques, and Applications on a Femtosecond Time Scale*, Academic Press, San Diego.
- Herek, J.L., Sundstrom, V. *et al.* (2009) *Femtosecond Photobiology*, Taylor & Francis.
- Sundström, V. (ed.) (1996) *Femtochemistry and Femtobiology: Ultrafast Reaction Dynamics at Atomic-Scale Resolution*, Imperial College Press, London.
- Zewail, A.H. (1994) *Femtochemistry*, World Scientific, Singapore.
- Photosynthesis**
- Blankenship, R.E. (2002) *Molecular Mechanisms of Photosynthesis*, Blackwell Publishers.
- Structures of LHCII and PSII (Contained in Figure 10.12)**
- Ferreira, K.N., Iverson, T.M. *et al.* (2004) Architecture of the photosynthetic oxygen-evolving center. *Science*, **303** (5665), 1831–1838.
- Standfuss, J., Terwisscha van Scheltinga, A.C. *et al.* (2005) Mechanisms of photoprotection and nonphotochemical quenching in pea light-harvesting complex at 2, 5 Å resolution. *EMBO J.*, **24**, 919–928.

## 11

# DNA Sequencing and Next-Generation Sequencing Methods

Many important and major advances in the biosciences are based on modern methodologies for DNA sequencing. It was not long ago when the traditional fluorescence-based Sanger method was one of the dominating methods. However, the high demand in fast and affordable sequencing of large DNA sequences and entire genomes has resulted in the development of new sequencing methods with significantly increasing pace. It has been just a decade since an entire human genome was sequenced for the first time in a joint effort of many research groups around the world (and later also of a private company) taking several years. However, nowadays the development of so-called next-generation sequencing methods allows the same task to be performed in one laboratory even within only a few days. This development enables, for example, also a thorough analysis of the genome of ancient DNA such as from the 5300 year old mummy of Ötzi in a comparatively short time. Fascinating details became available such that he likely had brown eyes, is genetically related to modern day Sardinians and Corsican (which doesn't exclude that this genetic relation was very common when Ötzi lived) had a lactose intolerance (like most of the people in these days) and some DNA sequences indicated that he had a Lyme disease.

In this chapter, we give first a brief insight into how the traditional fluorescence-based Sanger method works. Then, the most important principles of modern next-generation sequencing methods will be described that all enable much faster sequencing by highly parallelized sequencing. These methods are quite diverse and technically sophisticated while still being interconnected by several important steps. To facilitate keeping track of the different methods a flow diagram (Figure 11.2) is provided that visualizes common and different procedures and contains references to all figures and sections that explain the corresponding steps in detail.

### 11.1

#### Sanger Method

Figure 11.1 shows the principle of the traditional fluorescence-based Sanger DNA-sequencing method. In a first step, the DNA sequence of interest is

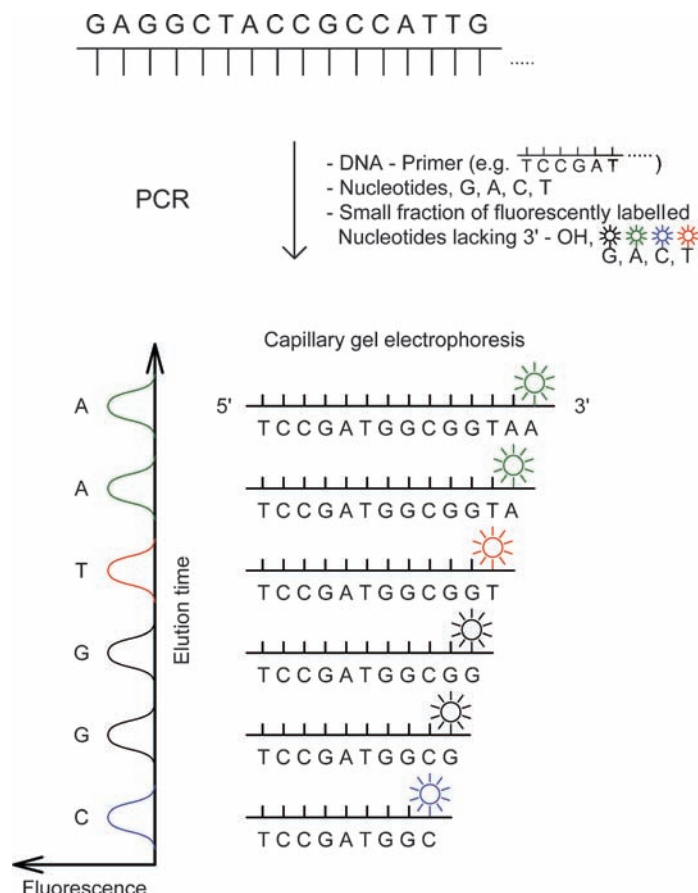


**Figure 11.1** DNA sequencing can be carried out by polymerase chain-reaction amplification of the DNA of interest in the presence of a small fraction of nucleotides carrying differently fluorescence-labelled nucleotides and lacking the hydroxyl group at the 3' end. As a result, PCR generates differently sized DNA

fragments with a fluorescence dye at the 3'-end encoding the corresponding DNA base. In capillary gel electrophoresis the differently sized fragments exit the capillary one after the other. The sequence of the DNA can then be determined from the observed sequence of fluorescence colours.

replicated by the enzyme DNA-polymerase in a process called the polymerase chain reaction (PCR). For the Sanger method the standard PCR process is slightly modified. As in normal PCR, the exact starting point for the replication is determined by a DNA primer, which is a short sequence of DNA complementary to the DNA sequence at the desired starting point. Once DNA-polymerase has started the replication it continues adding complementary DNA in the direction 5'-end to 3'-end of a single-stranded DNA until a certain stop signal is present. (The ends of DNA are named after the 5'- and 3'-hydroxyl groups of the deoxyribose sugars of the DNA backbone.) In normal PCR this replication

process is reiterated many times by repeatedly separating the freshly synthesized double DNA strands into single strands. This separation can be achieved simply by heating the double-stranded DNA over 80 °C (cf. the DNA hypochromism curve in Figure 2.8). Obviously, for DNA replication the presence of the individual nucleotides, guanine, adenine, cytosine and thymine (G, A, C and T) is necessary. In contrast to normal PCR, for the DNA sequencing a small fraction of the natural nucleotides is substituted by nucleotides labelled with different fluorescence markers. In addition, these nucleotides are modified in such a way that the deoxyribose is lacking the hydroxyl group at the 3'- end. As a consequence, DNA replication of an individual strand stops as soon as such a fluorescently marked nucleotide has been built into the newly synthesized DNA. Overall, PCR generates under these circumstances various sized DNA fragments that all start with the same primer sequence but end at different lengths with a fluorescence dye at the 3'-end, which encodes the corresponding base by its specific fluorescence colour. This mixture of fluorescently labelled DNA fragments is now separated using capillary gel electrophoresis (CGE). CGE can separate each fragment size one after the other. At the end of the capillary the smallest fragments will rise first, followed by fragments with increasing numbers of nucleotides. Since only the nucleotides at the 3'-end of the fragments are labelled the sequence of detectable fluorescence corresponds exactly to the complementary sequence of the original DNA. Modern DNA sequencers based on this technology can sequence DNA strands of up to 1000 bases in a few hours.

## 11.2

### Next-Generation Sequencing Methods

As of today it seems not to be clear yet which of the currently available next-generation sequencing methods will be the golden standard in the future and even newer approaches emerge at the horizon. Nevertheless, because of the very high relevance of these methods for modern biophysical chemistry we will discuss here exemplarily five methods. As discussed already in the introduction to this book also this selection shall not indicate that these methods are the most important ones but they cover a large part of the different concepts that have allowed the development of these high-throughput sequencing methods. One conceptual principle is common in all of these methods – namely the vast parallelization of sequencing. However, important details such as preparation steps and read-out technologies differ significantly.

All methods can be divided into three steps: 1. Random *fragmentation* of the DNA into a fragment library. 2. *Immobilization* of the fragments at different surfaces and 3. *Sequencing*. Because of the high diversity of different sequencing approaches albeit still being interconnected by some elementary steps we will discuss them based on the flow diagram shown in Figure 11.2. As mentioned above, Figure 11.2 also contains references to the corresponding figures and sections in which the individual steps are explained in detail. The fragmentation

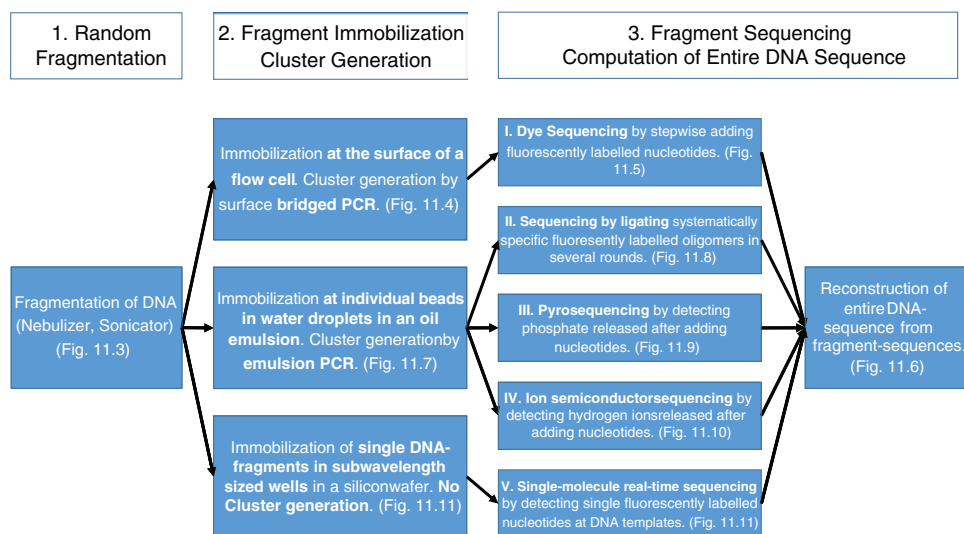


**Figure 11.2** Flow diagram illustrating the most important steps in five different next-generation sequencing approaches.

step 1 is crucial for sequencing many fragments in parallel, which is a key principle for fast sequencing. In all approaches the fragments are then immobilized at different surfaces (step 2), which is also crucial for sequencing each fragment at a different location in parallel. In most approaches the fragments are additionally locally amplified by different PCR approaches to generate clusters of identical DNA before sequencing. The sum signal from many identical DNA fragments provide high signal-to-noise ratios in the sequencing steps of the various technologies. Three of the five methods share the same cluster-generation technology (PCR at bead surfaces in an oil/water emulsion), while one method is based on PCR at different localized points on a flow-cell surface. One method uses a sequencing technology that is sensitive enough to directly sequence single fragments without any cluster generation. Since all five approaches differ substantially in step 3, their sequencing method, we will use this step to assign and distinguish them: The sequencing of the five methods is based on I. fluorescent *dye sequencing* (sharing similarities with the Sanger method), II. *sequencing by ligating* systematically different short complementary and fluorescently labelled oligomers (for details see below), III. *pyrosequencing* that senses the pyrophosphate release upon nucleotide incorporation, IV. *ion semiconductor sequencing* that senses hydrogen ion release upon nucleotide incorporation and V. *single-molecule real-time sequencing*.

At the end, in all approaches the sequence information of all fragments is used to reconstruct the sequence of the entire original DNA by matching overlapping sequence information of different fragments. In the following we will first describe approach I. in which DNA clusters are generated on a flow-cell surface and then sequenced using nucleotides labelled by fluorescence dyes.

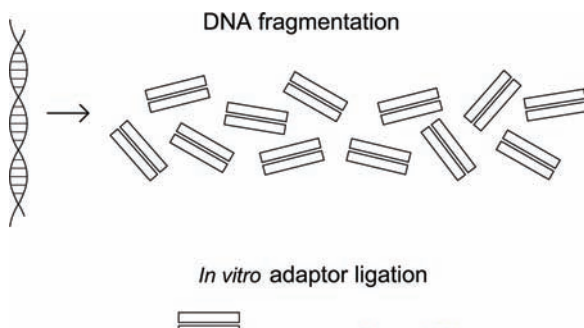


**Figure 11.3** All next-generation sequencing methods first start with the fragmentation of the original DNA and ligation of adaptor sequences.

#### 11.2.1

##### Dye Sequencing (Approach I)

Like in all other next-generation sequencing approaches the DNA is first fragmented (Figure 11.3). This can be done, for example, by a so-called nebulizer in which the DNA is forced through a small hole but also other mechanical shearing approaches are possible. An alternative fragmentation approach is, for example, using a sonicator in which sound energy of ultrasonic frequencies is applied. The resulting mixture of fragments is called a fragment library or sequencing library. Then, synthetic DNAs – called adaptors (red and green in Figure 11.3) – are added covalently to each fragment using DNA ligase. These adaptors have specific sequences that are complementary to adaptors covalently linked to a surface. In the case of the dye sequencing (I) procedure this is the surface of a flow cell (Figure 11.4). In the initial replication cycle the DNA-template fragment is replicated starting at such surface-linked adaptors (green) that are also the primers for PCR amplification (initial extension). Due to the following temperature increase the original, not covalently linked mobile DNA fragment is then removed (denaturation) and washed away. A covalently linked complementary strand remains. A speciality in the dye sequencing (I) approach is that the DNA is then bridged to other adaptors at the surface that are complementary to the adaptors at the other end (red, Figure 11.4). This is necessary to keep further replications at local positions. Then, PCR can be applied to generate the next complementary strands that are again covalently linked to the surface. This complementary copy is now identical to the sequence of the original mobile DNA fragment. Now the two anti-parallel strands can be denatured again yielding two strands that are both covalently attached to the surface. These can now serve for the next extension round. Obviously, with each PCR cycle new DNA either complementary or identical in sequence to the original mobile DNA template is generated, all covalently linked to the flow-cell surface in a very localized region. As a result, after several back and forth PCR cycles, each cluster consists

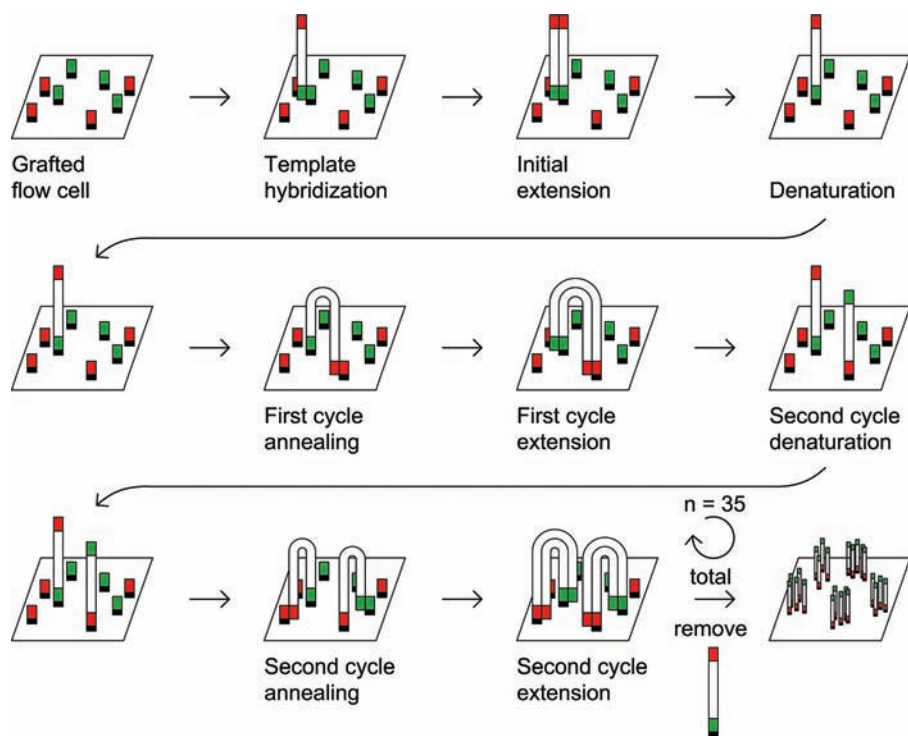


**Figure 11.4** In the dye sequencing (I) approach clusters of identical DNA fragments are generated at different locations on a flow-cell surface. In most next-generation sequencing methods the generation of such clusters is necessary to get a sufficient signal-to-noise

ratio in the different parallel sequencing procedures. Since in a flow cell the original DNA template needs to be washed away after the initial replication round, bridged PCR is necessary to keep further replications at local positions. For details see the text.

of about 1000 copies of sequences identical or complementary to a single original mobile library fragment. The bridging and alternating DNA generating cycle might seem inconvenient at first glance but is necessary because the original, mobile DNA fragment from the library can be used only once for initiating cluster generation at a distinct spot. Since in PCR the double strands are always separated in each cycle by the temperature increase the released mobile library fragment needs to be washed away. Otherwise more and more clusters would be initiated by this fragment at various different spots of the cell surface in an uncontrolled manner and the generated clusters could no longer be locally distinguished because they would become overcrowded. Therefore only the remaining covalently linked DNA-copy can be used for further PCR. If the next copy shall also be covalently linked to the same local region a bridging to another covalently linked primer for PCR is unavoidable as well as alternating replication directions.

After cluster generation, all DNA bound to the cell surface with one of the two adaptor types (for example the green ones) are cleaved so that only one sequence

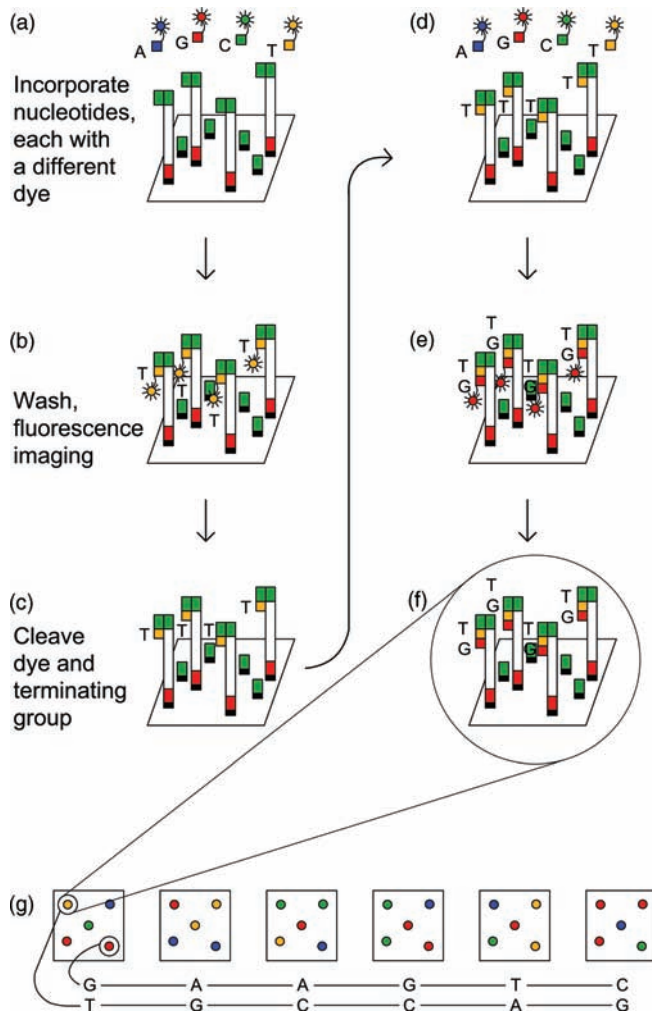


**Figure 11.5** In the dye sequencing (I) approach labelled nucleotides that are blocked at the 3'-OH are added together with DNA-polymerase. As a result only a single nucleotide is added to each strand. The residual nucleotides are then washed away

and the current base added to each cluster is indicated by the fluorescence marker colour specific for the base. In the next step, the fluorescence dyes are cleaved and the 3'-OH are regenerated so that the next base can be sequenced.

direction remains at this local cluster. The next step in the dye sequencing (I) approach is analysing this sequence for all clusters simultaneously using an image-based fluorescence approach. First, specifically labelled nucleotides are added together with DNA-polymerase and an appropriate primer (Figure 11.5a). The nucleotides are blocked at the 3'-OH group and therefore only one nucleotide can be added to each DNA fragment. The residual labelled nucleotides are then washed away (Figure 11.5b). The nucleotides in each cluster can now be identified

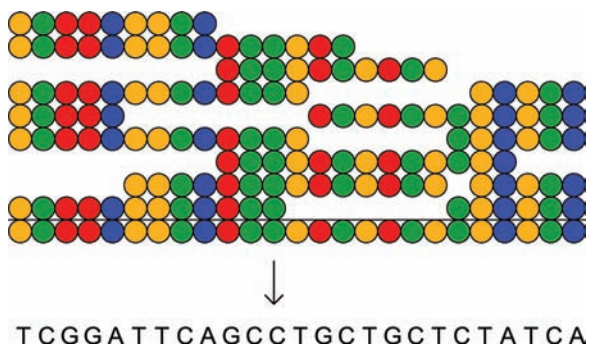


**Figure 11.6** In the final step, the sequence of all fragments are aligned in order to reconstruct the entire original genome.

by a standard wide-field microscope (Figure 7.6), capable of differentiating the different clusters spatially and the colours of the actually added nucleotides in the different clusters by spectral filters. Here, the advantage of the cluster generation becomes obvious: the thousands of identical fluorescence dyes in a cluster give a very robust, intensive fluorescence signal that can be used to identify the nucleotide that has currently been added in this specific cluster. After read-out, a cleavage step removes the fluorescence dye and regenerates the 3'-OH group of the added nucleotide (Figure 11.5c). Then, the cycle can be repeated and the next added nucleotides in each cluster can be identified (Figure 11.5d-f). In Figure 11.5g exemplarily two clusters (in the top left and bottom right) are highlighted by a circle. In each cycle the fluorescence spot originating from the cluster at this position has an emission wavelength that corresponds to the newly added complementary nucleotide. In this particular case the sequence deduced for the top left spot is TGCCAG, whereas the sequence deduced for the bottom right spot is GAAGTC.

After analysis the sequence for a multitude of fragments is available. In the final step, the sequences obtained from all individual fragments have to be aligned in such a way that the entire original genome is reconstructed (Figure 11.6). It is obvious that it is advantageous to have several different fragments of the same DNA in order to reconstruct the entire genome robustly and that advanced bioinformatical analysis is mandatory for this task.

### 11.2.2

#### Sequencing by Ligation, Pyrosequencing and Ion Semiconductor Sequencing (Approaches II to IV)

##### 11.2.2.1 Emulsion PCR

These three approaches differ from the previous one first in the immobilization of the fragments and in the environment in which fragment clusters are generated (Figure 11.7). In these approaches a water–oil emulsion and beads carrying primers are used. In the emulsion aqueous droplets represent many minireactors within the oil phase. The beads as well as the DNA fragments are present in

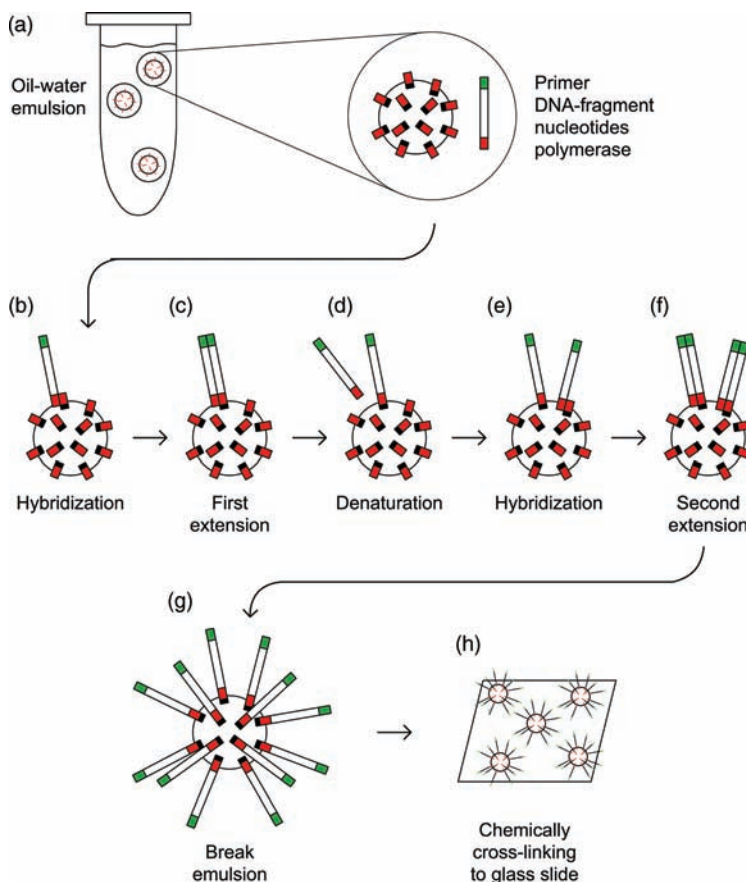


**Figure 11.7** In emulsion PCR, clusters of identical DNA fragments are generated at individual beads that are contained in aqueous droplets within an oil phase. These droplets represent minireactors in which at most one bead carrying covalently linked primers and at most one mobile DNA fragment is present. Each droplet also contains DNA-polymerase. Thus, after several PCR cycles many

DNA strands complementary to the mobile fragment are connected to the covalently linked primers at the beads and in a next step the identical DNA at each bead can be analysed bead by bead using various different sequencing methods. In the sequencing by ligation approach (II), for example, they are immobilized on a glass slide and analysed with a sophisticated fluorescence approach.

these water minireactors. The concentrations are adjusted in a way that one minireactor contains at the beginning either one or no DNA fragment. Also, the bead concentration is adjusted in such a way that only either one or none is present in a single minireactor (Figure 11.7a). Then, emulsion PCR is conducted. In the initial cycle the mobile fragments attach to primers at the beads thereby allowing the generation of complementary DNA at the primers covalently linked to the beads (Figure 11.7b and c). During the next PCR cycles both are generated, DNA complementary to the original mobile fragment as well as DNA fragments

identical to the original mobile fragment (Figure 11.7d-f). New mobile fragments are generated at the DNA covalently linked to the beads and released during each temperature rise of a PCR cycle (Figure 11.7d). Since, in contrast to the bridged PCR described in the previous section, the mobile fragments stay here very localized in one minireactor they can be used multiple times at the same bead to generate more and more complementary, covalently linked DNA copies. After several cycles a bead in a single minireactor carries exclusively a large number of identical DNA strands complementary to the initial fragment sequence (Figure 11.7g).

After the generation of DNA clusters at the bead surfaces the methods of sequencing by ligation (II), pyrosequencing (III), and ion semiconductor sequencing (IV) differ significantly in the actual way the sequence is determined. We will start by describing the sequencing by ligation (II) approach.

#### 11.2.2.2 Sequencing by Ligation (Approach II)

The principle of the sequencing by ligation approach is not easy to follow but is actually applied quite successfully as demonstrated, for example, in the case of the analysis of the Ötzi genome.

In the sequencing by ligation approach the beads are first chemically cross-linked to a glass slide (Figure 11.7h). Sequencing is then done as follows: First, a universal primer is added (red in Figure 11.8), that fits the adaptor sequence (red) of the template DNA fragment linked to the beads (in the following, we will call the DNA covalently linked to the beads template DNA.). In a next step, short special oligomers are added. The properties of the synthetic oligomers are unique. Each oligonucleotide has only 8 bases. Three bases of them are degenerate (depicted in the Figure 11.8 by n) meaning they fit any DNA base. Also the three universal bases (depicted in Figure 11.8 by z) have no influence on the binding specificity of the oligomer. Only the two remaining bases are specific (depicted in Figure 11.8 by x and y), that is if they find two complementary bases at the template DNA the oligomer can bind to it and can be connected to the primer sequence by ligation through a DNA-ligase enzyme. Thus, if a mixture of oligomers, each containing different pairs of selective bases x,y, is added only the type of oligomer that contains a pair of bases that match the template DNA will be ligated to the primer. Figure 11.8a and b illustrates exemplarily the complementary attachment of an oligomer containing an AT sequence (marked by red colour) to the template DNAs TA sequence in the first ligation round. The different oligomers carrying different pairs of selective bases x,y can be differentiated in a wide-field microscope by different fluorescence markers (indicated by the blue, green yellow and red stars). In a next step the last three bases (marked previously by z) and the fluorescence dye at the 5'-end of the oligomer are cleaved (Figure 11.8c). Then, the ligation cycle is repeated that allows identification of two further bases (in the present example TT, indicated by blue colour, Figure 11.8d) but they are located in the sequence three unknown bases further than the previously identified bases AT. Thus, when further repeating the

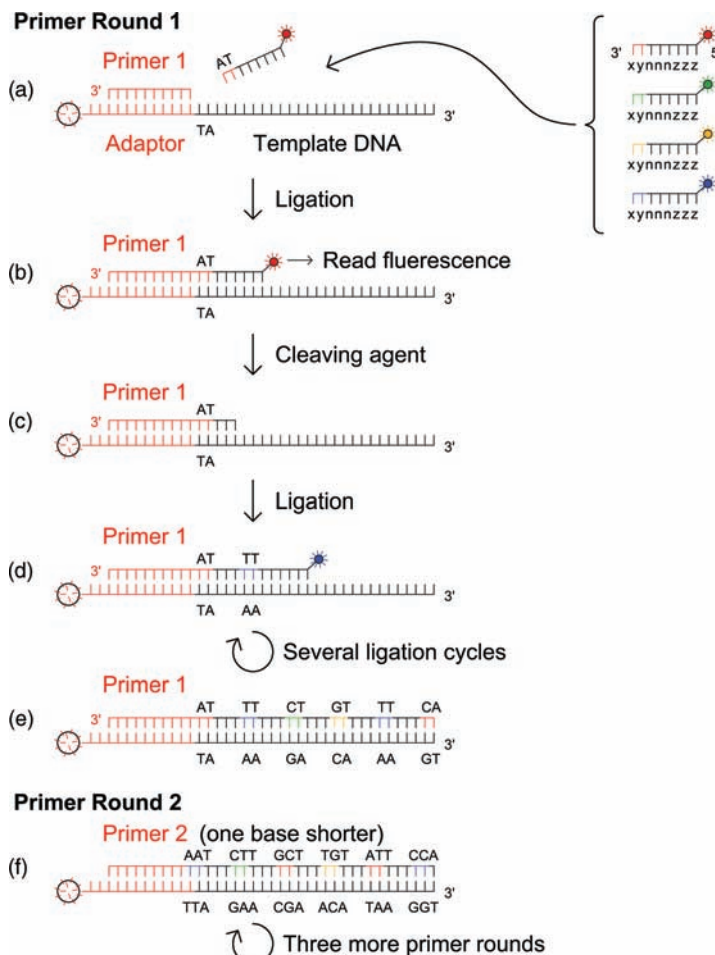


**Figure 11.8** Principle of sequencing by ligation (II). In this approach, in each ligation cycle only two of five added nucleotides can be identified by fluorescence markers (visualized by colour in the ligation cycles). However, when using primers of different length in different primer rounds after

stripping away DNA ligated in a previous round, the position of the periodically identified two per five bases can be shifted. Thus, from several rounds with different primers of different length the entire sequence information can be obtained. For details see the text.

ligation and cleavage cycles this always gives periodic information about the sequence of the first two out of five consecutive bases (Figure 11.8e; Cycle 3: CT, indicated by green colour; Cycle 4: GT, indicated by yellow colour and so on). To obtain the missing sequence information, the newly generated DNA is then entirely stripped from the template DNA and the procedure is repeated but now with a primer that is one base shorter (Figure 11.8f). So, in the second primer round, again periodic information about the sequence of the first two of five consecutive bases is obtained but now the periodic information pattern is

shifted by one base to the left. After several rounds with different primers the entire sequence information of the fragments is available by using computer algorithms. Again, the entire genome sequence can be reconstructed by aligning the sequences obtained from all individual fragments (see Figure 11.6 above). It should be noted that actually only four different fluorescence markers can be robustly differentiated spectrally and not 16, which is the possible number of different oligonucleotides containing two different bases, x and y. However, because of the redundancy in the sequencing information obtained in the different primer rounds the entire sequence can still be deduced also from a four colour coded set of the 16 oligonucleotides using advanced computer algorithms.

#### 11.2.2.3 Pyrosequencing (Approach III)

In contrast to the sequencing by ligation (II) approach in pyrosequencing (III) the beads observed from the emulsion PCR procedure are first randomly deposited into an array of picoliter wells of a size so small that they can only bear one bead (Figure 11.9). Then, a single type of nucleotide (e.g. only guanosine phosphate, as illustrated in Figure 11.9) is flown across the wells. If this nucleotide is complementary to the base at the template DNA in a certain well then DNA-polymerase can incorporate this nucleotide to a primer (green in Figure 11.9) and pyrophosphate ( $PP_i$ ) is released. Smaller beads carrying the enzymes sulphurylase and luciferase are also added. Sulphurylase converts the pyrophosphate into ATP in the presence of adenosine 5' phosphosulfate (APS). ATP, in turn, is necessary for the biochemiluminescence reaction of luciferin to oxyluciferin by luciferase as described in Section 3.8 and Figure 3.33. To detect the biochemiluminescence signals from the picoliterwells they are bonded to a fibre-optic bundle that directs the light collected from different wells to different pixels of a CCD. In the next cycle, a different nucleotide is flown across the wells. Again, biochemiluminescence is only detected in a specific picoliter well if this nucleotide is complementary to the bases at the DNA template. After flowing all four nucleotides across the wells, the bases of the template strands at the first position are known for each fragment and the procedure can be repeated to analyse the next position. This procedure is repeated until the sequences of all fragments are known. Again, the entire genome information can be reconstructed by aligning the sequences of the individual fragments. The method is named pyrosequencing (III) since the biochemiluminescence is caused by a sequence of reactions that are initially started by the pyrophosphate release upon a successful incorporation of a correct, unlabelled nucleotide. It should be noted that in each cycle of flowing a specific nucleotide across the wells it is possible that more than one nucleotide is incorporated when more than one consecutive position in the template DNA carries the same, complementary nucleotide. However, this can be identified by the brightness of the biochemiluminescence signal. Two or three identical bases in a row lead to the incorporation of two or three times more nucleotides and consequently to the release of two or three times more pyrophosphate. As a consequence, the brightness of the biochemiluminescence detected from such wells is also two or three times higher.

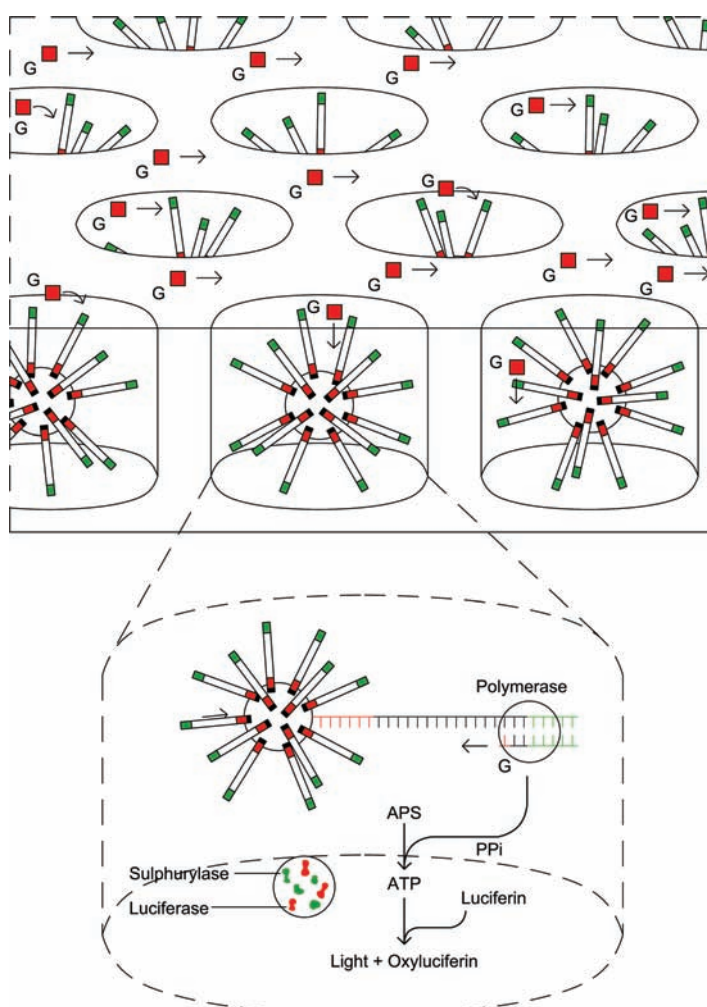


**Figure 11.9** Principle of pyrosequencing (III). In this approach, only one out of four possible types of the unlabelled, native nucleotides is flown over the beads that are themselves contained in picoliter wells. If this type of nucleotide is complementary to the next base in the DNA-template, DNA-polymerase will

incorporate it and pyrophosphate is released. In an enzymatic cascade the pyrophosphate is detected by bioluminescence. Then, the next type of nucleotide is added. Repeating this procedure periodically with all four types of nucleotides yields the DNA sequence of each individual bead. For details see the text.

#### 11.2.2.4 Ion Semiconductor Sequencing (Approach IV)

Conceptually, the ion semiconductor sequencing (IV) shares similarities with the pyrosequencing (III) approach. As in pyrosequencing (III) also in ion semiconductor sequencing (IV) the beads covered with clusters of identical DNA

fragments are loaded into various wells and single types of unlabelled nucleotides are added step by step. The main difference is the way the addition of an unlabelled nucleotide complementary to the template DNA is detected. In ion semiconductor sequencing (IV) the detection of bioluminescence in pyrosequencing (III) is replaced by the detection of a pH change caused in each reaction step by the release of hydrogen ions that occurs when nucleotides are incorporated. This pH change is actually sensed by a specialized silicon chip (Figure 11.10). As with the pyrosequencing (III) no labelled nucleotides are needed but in addition no special enzymes such as sulphurylase or luciferase are required. The analysis of the obtained fragment sequences is the same as with the previous approaches.

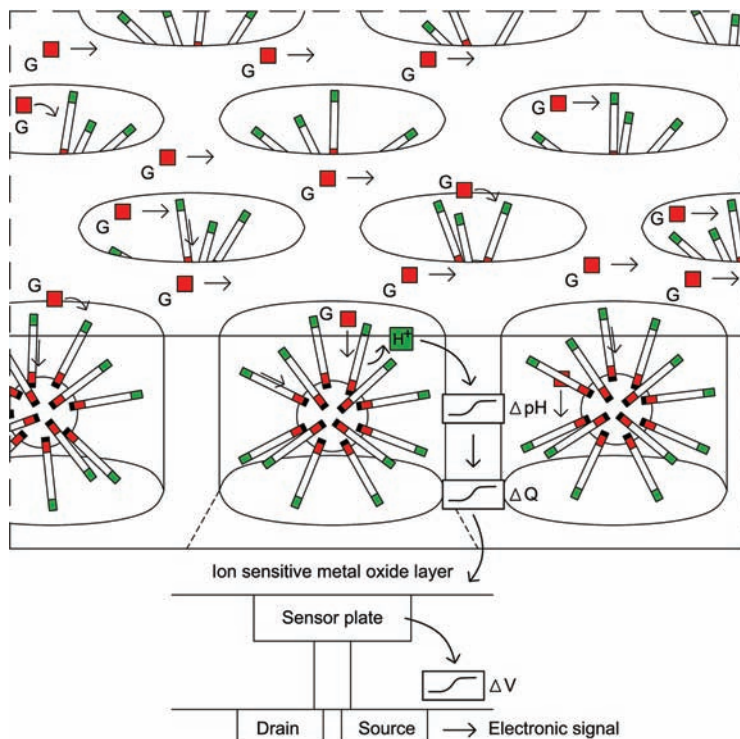


**Figure 11.10** Principle of ion semiconductor sequencing (IV). Again, only a single type out of four possible unlabelled nucleotides is flown over the beads that are themselves contained in picoliter wells. If this type of nucleotide is complementary to the next base in the DNA template, DNA-polymerase will

incorporate it and hydrogen ions are released. The following pH-change is then sensed by a specialized silicon chip. Afterwards, the next type of nucleotide is added. Repeating this procedure periodically with all four types of nucleotides yields the DNA sequence of each individual bead. For details see the text.

### 11.2.3 Single-Molecule Real-Time Sequencing (Approach V)

As indicated by its name single-molecule real-time sequencing does not require the generation of clusters of identical fragments as it is based on highly sensitive single-molecule detection techniques such as described in Sections 9.2 and 9.3. This approach has very high read lengths of consecutive bases but limitations exist of course in the sensitivity of single-molecule detection techniques. In Figure 11.11 the principle of single-molecule real-time sequencing (V) is visualized. A nanostructure is generated in which a silicon wafer surface contains a regular array of thousands of wells that are smaller than the wavelength of light (Figure 11.11). At the bottom of these wells DNA-polymerase with the DNA fragments are deposited. The DNA-polymerases are specially engineered. They have a decreased rate of polymerization and the ability to incorporate fluorescently modified nucleotides. Then, four types of fluorescently phospholinked hexaphosphate nucleotides are added and the DNA-polymerases in each well start introducing the differently labelled nucleotides after each other. Simultaneously, the wells are illuminated from below. Since the dimensions of the wells

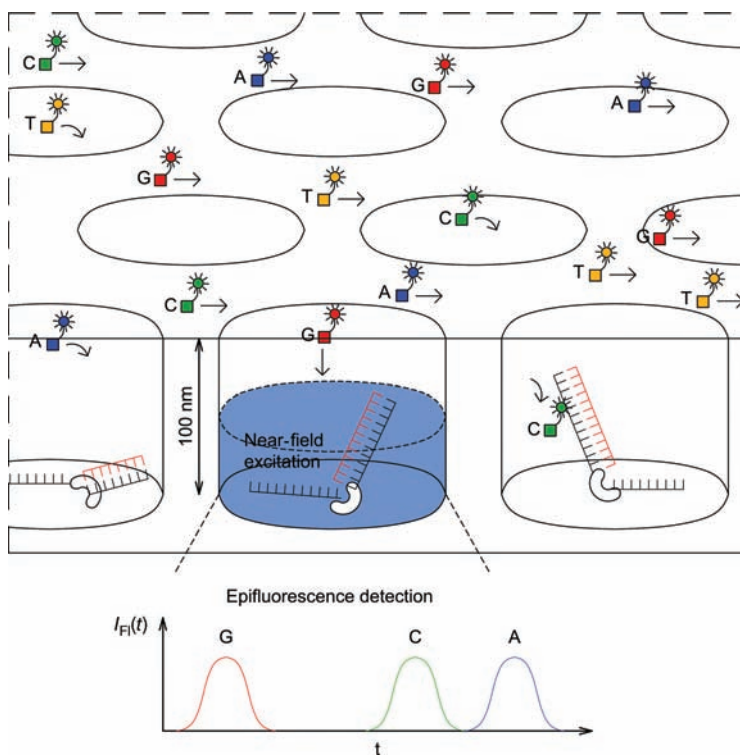


Figure 11.11 Principle of single-molecule real-time sequencing (V). For details see the text.

are smaller than the diffraction-limited resolution of light only an evanescent excitation light field of significantly less than 200 nm protrudes into the well with the polymerase (schematically indicated in Figure 11.11 by blue cylinder). When light is guided into a volume that is smaller than the wavelength of the used light this is called a zero-mode waveguide. The limited excitation volume in the zero-mode waveguide is based on very similar principles to the evanescent field in TIRF-microscopy (see Chapter 7) and thus has similar advantages that allow for robust single-molecule detection. In particular, as in TIRF-microscopy, the background signal is significantly reduced because much less solvent is excited per fluorescence single molecule, enabling superior single molecule signal-to-noise ratios. Thus, the polymerase can actually be observed “at work” since each nucleotide introduced gives rise to a fluorescence burst detectable with a microscope set-up similar as in TIRF microscopy (Figure 7.8). The wavelengths of these bursts are specific for one of the four bases in the nucleotides and the chronological colour order of these bursts correspond directly to the DNA sequence. The limited excitation volume in the zero-mode waveguide is also very important to ensure that really only one nucleotide is observed at a time. For the polymerase micromolar nucleotide concentrations are necessary that are far too high for single-molecule observations in diffraction-limited detection volumes of standard fluorescence set-ups. As outlined in Section 9.3, optical single-molecule detection, the concentration of labelled particles would have to be on the order of nanomoles to be detected individually in such a set-up which is by far too low for the polymerase to work properly. However, by using the very limited volume excited in the zero-mode waveguides single-molecule detection of nucleotide at micromolar concentrations is not a problem.

### Problems

- 11.1** Assume that the probability of a false read-out in DNA sequencing is 1/10 000 for a single base. What is the probability that none, exactly one or more than one base is incorrectly assigned when sequencing a DNA strand of 1000 bases?
- 11.2** What would be the major problems if those components in bridged PCR are removed that allow for PCR amplification not only in the forward but also the backward direction?
- 11.3** Discuss what next-generation sequencing approach might have a comparatively low and what a comparatively high error rate.
- 11.4** Assume you have 30 fragments of 300 base pairs in size from statistically different positions of an original circular DNA-plasmid of 3000 base pairs in size. How large is the probability that you cannot reconstruct the original DNA because one specific base pair is not represented in the fragments?

- 11.5** How high is the probability that a droplet contains no DNA fragment in emulsion PCR if the probability for having two different fragments is 1% or 0.1%? What percentage of productive droplets would exist if the probability to have exactly one bead in the droplet is the same as initially having exactly one DNA fragment?
- 11.6** How many detected photons are necessary per inserted nucleotide in the pyrosequencing approach to ensure the ability to differentiate one, two and three nucleotides of the same type in a row with an error rate of better than only 1 false read-outs per 1.000.000?
- 11.7** What is the drop in pH when 10000 protons are released in ion semiconductor sequencing into a neutral solution contained in a volume of 1 pL?
- 11.8** In Section 9.3.3 we defined the effective focal detection volume of a normal diffraction-limited confocal microscope set-up to be  $V_{\text{eff}} = \pi^{3/2} r_0^2 z_0$ . Calculate the average number of nucleotides that are present in such a detection volume when assuming a concentration of one micromole and values for  $r_0$  and  $z_0$  of 250 nm and 1000 nm, respectively. How much smaller does the size of the detection volume in single-molecule real-time sequencing need to be to ensure that it contains on average only 1 nucleotide when assuming the same concentration?

## Bibliography

### Sanger Method

- Sanger, F. (1988) Sequences, sequences, and sequences. *Annu. Rev. Biochem.*, **57**, 1–28.
- Sanger, F. *et al.* (1977) Nucleotide sequence of bacteriophage phi X174 DNA. *Nature*, **265**, 687–695.

### General Next-Generation Sequencing Methods

- Mardis, E.R. (2013) Next-Generation Sequencing Platforms. *Annu. Rev. Anal. Chem.*, **6**, 287–303.
- Mardis, E.R. (2008) The impact of next-generation sequencing technology on genetics. *Trends Genet.*, **24** (3), 133–141.
- Metzker, M.L. (2010) Sequencing technologies – the next generation. *Nature Rev. Genet.*, **11**, 31–46.
- Pop, M. and Salzberg, S.L. (2008) Bioinformatics challenges of new

sequencing technology. *Trends Genet.*, **24** (3), 142–149.

Shendure, J. and Ji, H. (2008) Next-generation DNA sequencing. *Nature Biotechnol.*, **26**, 1135–1145.

### Specific Next-Generation Sequencing Methods

- Bentley, D.R. (2006) Whole-genome re-sequencing. *Curr. Opin. Genet. Dev.*, **16**, 545–552.
- Dressman, D., Yan, H., Traverso, G., Kinzler, K.W. and Vogelstein, B. (2003) Transforming single DNA molecules into fluorescent magnetic particles for detection and enumeration of genetic variations. *Proc. Natl. Acad. Sci. USA*, **100**, 8817–8822.
- Eid, J., Fehr, A., Gray, J., Luong, K., Lyle, J. *et al.* (2009) Real-time DNA sequencing from single polymerase molecules. *Science*, **323**, 133–138.

- Fedurco, M., Romieu, A., Williams, S., Lawrence, I. and Turcatti, G. (2006) BTA, a novel reagent for DNA attachment on glass and efficient generation of solid-phase amplified DNA colonies. *Nucleic Acids Res.*, **34**, e22.
- Margulies, M. *et al.* (2005) Genome sequencing in microfabricated high-density picolitre reactors. *Nature*, **437**, 376–380.
- Ronaghi, M., Karamohamed, S., Pettersson, B., Uhlen, M. and Nyren, P. (1996) Real-time DNA sequencing using detection of pyrophosphate release. *Anal. Biochem.*, **242**, 84–89.
- Rothberg, J.M., Hinz, W., Rearick, T.M., Schultz, J., Mileski, W. *et al.* (2011) An integrated semiconductor device enabling non-optical genome sequencing. *Nature*, **475**, 348–352.
- Shendure, J. *et al.* (2005) Accurate multiplex polony sequencing of an evolved bacterial genome. *Science*, **309**, 1728–1732.

## 12

# Special Techniques

### 12.1

#### Introduction

Many biomolecular processes or biological questions can only be investigated or answered by distinct techniques that are optimized for these problems. In this chapter we will discuss a few important examples of such special techniques that are already in very widespread use in many industrial and basic research laboratories worldwide. Examples are DNA microarrays, fluorescence-assisted cell sorters, fluorescence *in situ* hybridization or DNA Origami. This chapter also covers some special technologies that can be used when techniques described in the previous chapters do not work well in solving a particular problem. Examples of these technologies are the use of fluorescing nanoparticles, microspheres or the technique of surface plasmon resonance detection. Many of the techniques presented, such as fluorescing nanoparticles and fluorescence-assisted cell sorters, are partly based also on the detection of fluorescence. Other techniques, such as surface plasmon resonance detection, are based on completely different detection technologies. The methods presented in this chapter can only comprise a selection of important special technologies. Certainly, there are many more relevant and interesting methods that can not be covered by a single book. Nevertheless, together with the techniques and application examples provided in the chapter, the selected methods will give the reader a broad overview of what methods are possible to investigate certain biochemical or biological questions.

### 12.2

#### Fluorescing Nanoparticles

In recent years the use of fluorescing nanoparticles or quantum dots has become a very useful substitute for organic fluorescence markers, especially for applications where increased photostability is necessary. In this section we discuss the special properties of such fluorescence markers, the physical principles on which the absorption and fluorescence properties of these nanoparticles are based and how they can be attached to biomolecules.

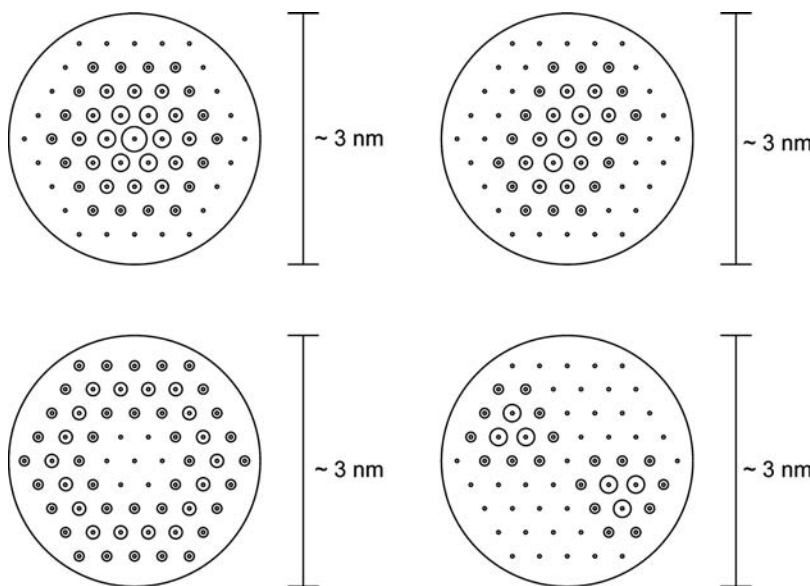


**Figure 12.1** Two-dimensional representation of possible probability distributions of electron states in nanoparticles. The dots represent the atomic nuclei of the particles, whereas the electron probabilities are presented by circles around the nuclei.

Quantum dots are typically spherical or elliptical particles a few nm in diameter. The cores of these nanoparticles often consist of semiconductor materials such as cadmium sulfide (CdS), cadmium selenide (CdSe) or cadmium telluride (CdTe). In larger semiconductor structures the electrons can be excited by light into higher states within the the conduction band and can then move around through the entire semiconductor structure. However, if the dimensions of the semiconductor structure are restricted to a few nm, such as in quantum dots, then this movement is restricted due to limited available space. In such dimensions the wave properties of the electrons again become important. As a consequence, only distinct resonances or eigenstates of the electrons' probability distributions within the nanoparticle are possible (Figure 12.1). This phenomenon is called quantum confinement. It is based on similar physical principles to those that cause the distinct probability distribution, or in other words orbitals, of electrons around the nucleus of atoms (see Figures 1.3–1.6). Also here, the number of nodal planes separating larger regions of increased electron density often provides a good indication of the energetic order of various states.

Similar to the excitation of electrons from a molecular ground state to molecular excited state (see Figure 1.7) light can also promote electrons from certain states in the nanoparticles to another state. As an example, Figure 12.2 visualizes the excitation of an electron from the valence-band maximum (VBM), which corresponds to the HOMO of the nanoparticle, to a state in the conduction band, which corresponds to one state above the LUMO of the nanoparticle. In

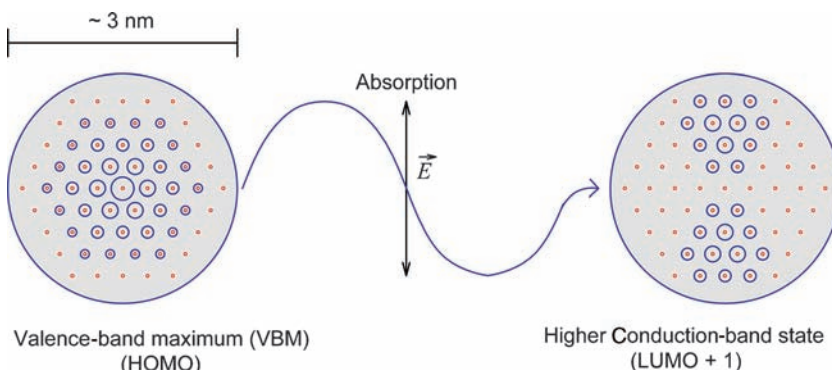


**Figure 12.2** Electromagnetic radiation can promote electrons from one quantum state to another quantum state of the nanoparticle.

nanoparticles a very broad range of states in the conduction band is available. Therefore, the absorption is typically very broad and uncharacteristic (Figure 12.3). However, usually, the electron relaxes very quickly into the conduction band minimum (CBM) or LUMO of the nanoparticle. As a consequence, fluorescence from the nanoparticles corresponds to a spectrally rather sharp transition between the CBM and the VBM. This energy gap between the CBM and VBM, in turn, depends critically on the size of the nanoparticles (see Figures 12.3 and 12.4).

These optical properties constitute several advantages in comparison to conventional fluorescence dyes. The fluorescence spectrum is significantly narrower than that of traditional fluorescence dyes (Figure 12.5). As a consequence, a larger number of different quantum dots can be separately distinguished in

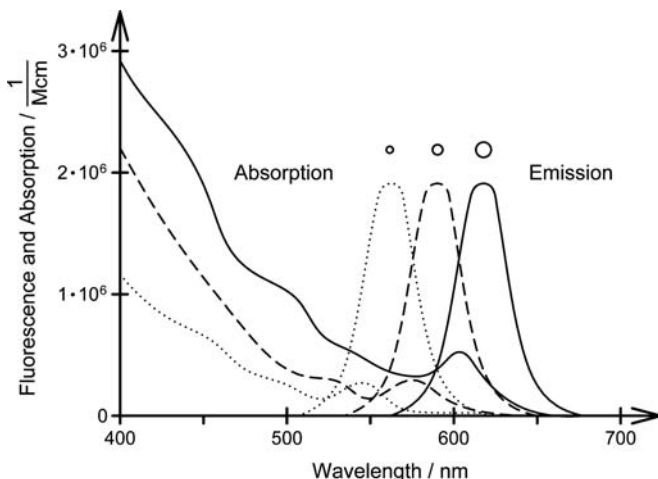


**Figure 12.3** Absorption and emission spectra of differently sized quantum dots.

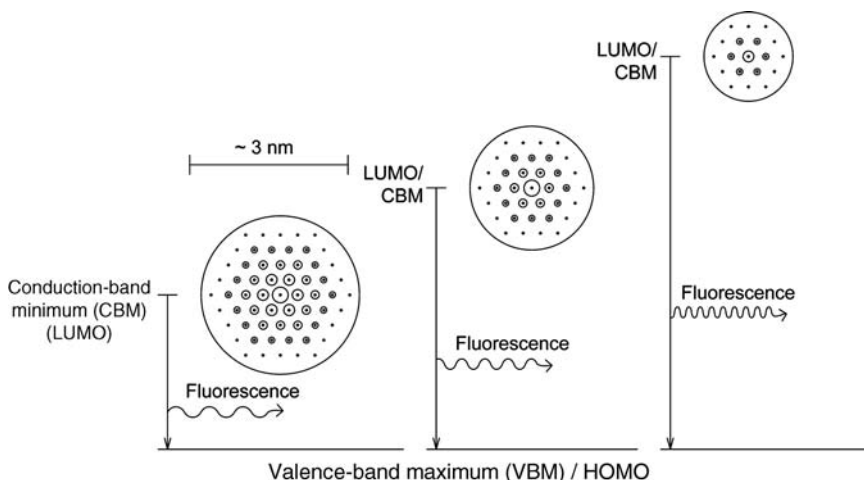


**Figure 12.4** The fluorescence wavelength is determined by the difference between the CBM and the VBM, which depends critically on the size of the nanoparticle.

fluorescence experiments in comparison to fluorescence dyes. In addition, the broad absorption spectra of quantum dots allow us to excite them all simultaneously with a single excitation wavelength in the blue spectral region. The biggest advantage of quantum dots over fluorescence dyes is, however, the significantly higher photostability and achievable particle brightness,  $I_{\text{Fl}}^{\text{Particle}}$  [see also (9.7)]. In single-molecule experiments this allows us to observe the labelled species significantly longer before the label bleaches. In conventional fluorescence microscopy the signal-to-noise ratio is typically one order of magnitude better when using quantum dots instead of organic fluorescence dyes.

The improved optical properties, however, come with the price that the labelling of biomolecules is somewhat more demanding. First, quantum dots are significantly bigger than conventional fluorescence dyes. A potential drawback therefore is a greater potential influence on the biochemical properties of the labelled biomolecules. In addition, a semiconductor nanoparticle itself is not stable in physiological aqueous environments. To protect the semiconductor core a nanoparticle/biomolecule interface must be established. As a consequence, the nanoparticle core is covered by further layers such as a polymer coating with a chemical derivatization (Figure 12.6). This can be, for example, a carboxylic derivatization in order to attach biomolecules by procedures similarly to those described in Chapter 3. The biomolecule itself can be, for example, an avidin or streptavidin. This allows us to attach effectively the nanoparticles to other biotinylated biomolecules (see Figure 3.5). Once biomolecules have been labelled in such a way (or by similar means) with nanoparticles, in principle most of the fluorescence methods described in Chapters 3, 7 and 8 can be applied. Some restrictions may apply, however, for certain techniques such as, for example, fluorescence depolarization methods.

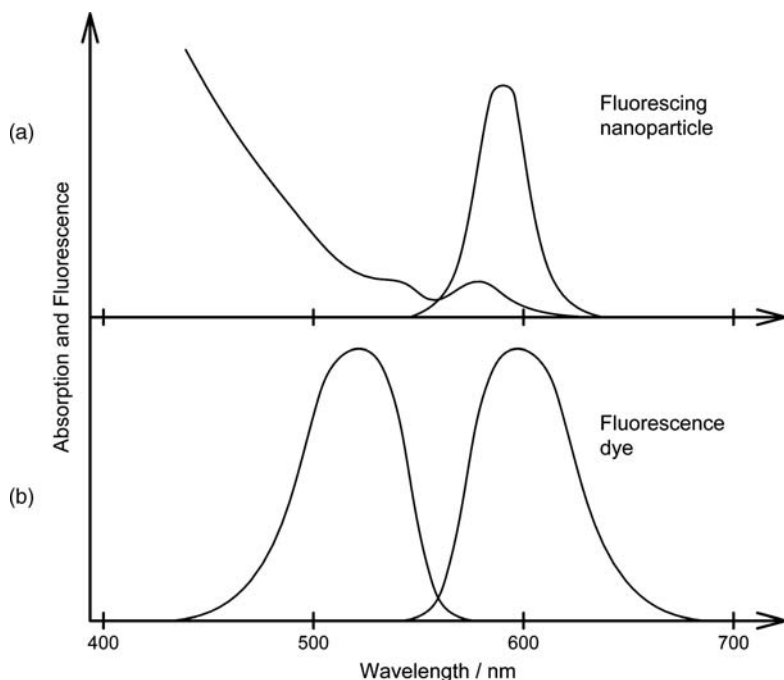


**Figure 12.5** Comparison of the fluorescence and absorption spectra of (a) a fluorescing nanoparticle with (b) a conventional fluorescence dye.

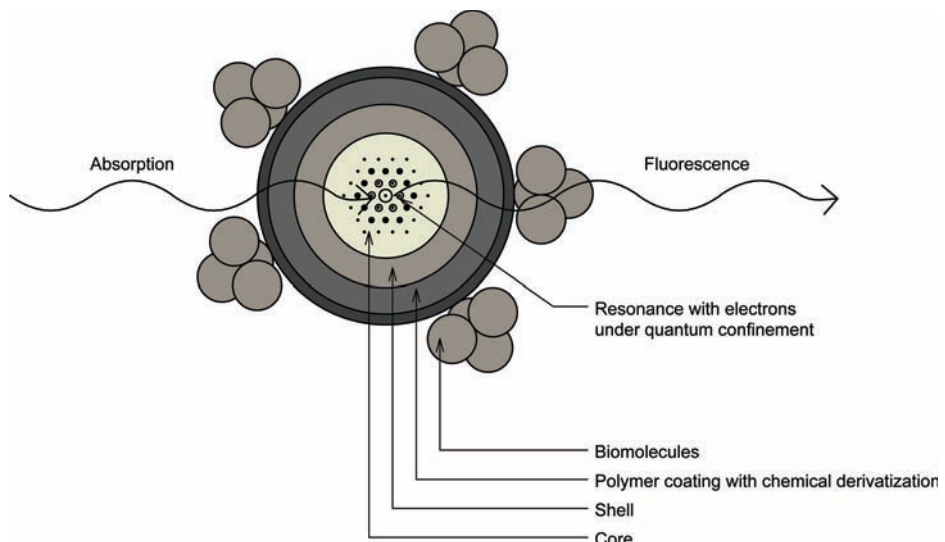


**Figure 12.6** Structure of nanoparticles used for biomolecular labelling.

### 12.3

#### Surface Plasmon Resonance Detection

Surface plasmon resonance (SPR) detection is a technique that allows us to quantify very sensitively the binding and dissociation, for example, of protein ligands to receptors typically immobilized on a derivatized gold surface. Advantages of this technique are, amongst others, that the ligand does not have to be labelled for the detection and that the receptors attached to the gold surface can be reused several times after appropriate washing steps. The technique is not easy to understand. Therefore, we focus first on some basic aspects of the underlying physical mechanisms and then present what the measurement of typical binding and dissociation kinetics looks like.

In general, plasmons are collective, quantized oscillations of an electron gas within a metal. They have both wave- and particle-like properties: they are constituted of wave-like oscillations of the electrons in the metal but occur only as single quanta. In that sense they do not differ from quantum particles such as photons or electrons. A special class of such plasmons is surface plasmons (Figure 12.7). Surface plasmons occur only at the surface between a medium with a negative dielectric constant such as electric conductors (e.g. metals like gold) and a medium with a positive dielectric constant, which are electric isolators (like glass, water, proteins, etc.). Surface plasmons are collective longitudinal oscillations of the electrons parallel to the surface. As a consequence, periodically some regions at the surface have momentarily an increased or decreased density of negatively charged electrons (symbolized by the wave at metal surface in Figure 12.7). In the regions of decreased electron density the remaining nuclei cause a positive charge density that is only partly compensated by the remaining electron density. As a result, a periodic electric field is present at the surface, also reaching somewhat into the electric isolating material. The periodic electric-field component of electromagnetic radiation can excite these surface plasmons when the periodicity of the electric-field components match in space and time. If a thin metal layer is irradiated with light of a certain wavelength under the correct angle this excitation gives rise to a detectable absorption of the light. However, the 'wavelength' of the surface plasmons depends very sensitively on the average refractive index of the nonmetallic side at the surface. As a consequence, small refractive index changes, which can be caused by a binding of larger ligands to receptors immobilized at a gold surface, can be detected sensitively by changes in the surface plasmon absorption. This is the basis of the quantitative determination of biomolecular binding and dissociation reactions using SPR. Usually, the absorption for a range of detection angles is simultaneously detected. Measurement of the detection angle with the largest absorption allows us to determine the refractive-index changes in the aqueous phase and thus to estimate the total amount or mass concentration of bound ligand.

Figure 12.8 shows the progress of a typical SPR measurement. First, only a pure buffer solution flows over the receptor-modified gold surface. From the

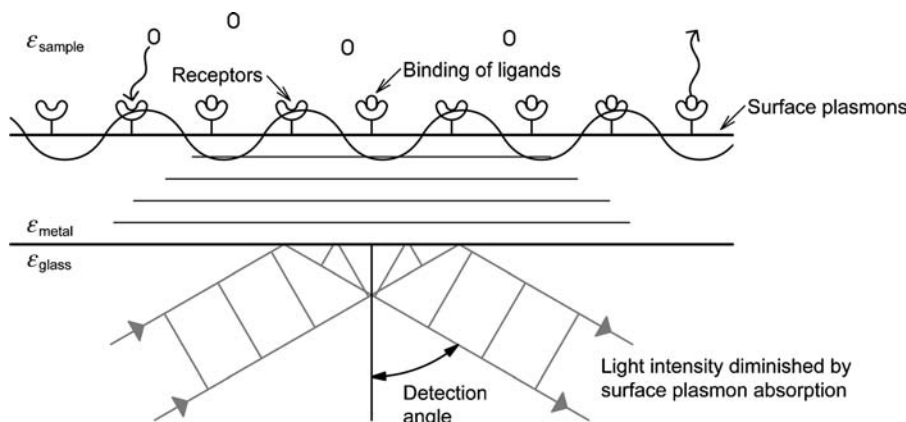


**Figure 12.7** Surface plasmons are collective oscillations of electrons at the surface between a metal and an electrically isolating material such as an aqueous solution. Under certain conditions, light can excite these oscillations. These conditions are very sensitive to the refractive index and thus the dielectric constant of the nonmetallic material. The

binding of proteins (the refractive index of pure proteins is  $\sim 1.5$ ) changes the average refractive index of the aqueous environment at the surface (the refractive index of pure water is  $\sim 1.3$ ). As a consequence, binding can be very sensitively detected by a change in the resonance of the detection light with the surface plasmons.

moment a binding ligand is presented to the surface, the SPR response changes considerably. The binding continues until a steady state is reached. From these kinetics it is possible to determine the association kinetics and the overall binding affinity. An advantage of SPR technology is that unpurified samples such as cell extracts can be applied directly and that ligand concentrations in the

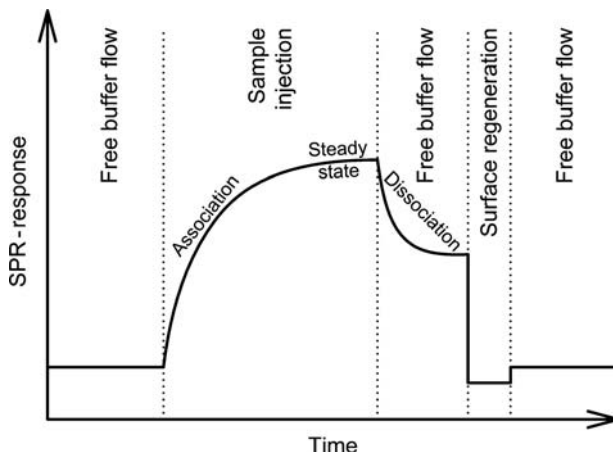


**Figure 12.8** Typical SPR sensorgram observed during the measurement of receptor–ligand binding.

nanomolar range suffice. After the steady state is reached, the dissociation kinetics can be observed by a flow of pure buffer again. When the measurement is terminated the receptors at the surface can often be cleaned of any noncovalently bound ligands with appropriate regeneration solutions and the device is ready for the next measurement.

## 12.4

### DNA Origami

A major breakthrough in the generation of nanostructures was achieved when a simple method was invented for folding long, single-stranded DNA molecules into arbitrary two-dimensional shapes. This fascinating method is called DNA Origami and is based on the self-assembly of a long single-stranded DNA scaffold ( $\sim 7$  kb) with many short oligonucleotide strands into a predesigned desired nanostructural shape. The DNA scaffold lays the fundament of the desired shape and is held together by a large number of short oligonucleotide 'staple strands' that have an according complementary sequence and form branches. The resulting DNA-Origami structures are quite rigid, often very complex and typically about 100 nm large. A key feature of this method is the fact that this self-assembly of the scaffold strand with the staple strands occurs in only one step. Working with one long DNA scaffold and an excess of staple strands avoids the necessity of keeping the stoichiometry extremely accurate and allows the formation of Origami structures to proceed highly parallel and without many misfoldings.

In Figure 12.9a the dimensions and structure of a normal DNA double helix is shown. Figure 12.9b envisages how two single-stranded DNA strands (white-grey) can be tightly connected together by three (yellow, red and blue) specifically designed staple-strand oligonucleotides, thereby generating double-helical domains connected by interhelix cross-overs. The same principle can be used to connect a specifically designed scaffold strand (Figure 12.9c) by several different oligonucleotides (red, green, blue and yellow in Figure 12.9d) robustly into any desired two-dimensional nanometric structure (Figure 12.9e). As can be seen from the colour code the number of different types of oligonucleotides necessary to generate complex structures remains limited. The AFM-images (compare to Section 9.5, Figure 9.26 for a brief introduction into the AFM technique) in Figure 12.10 demonstrate that this concept can be used to generate a large variety of different structures of high complexity. In addition, functionalized staple strands, such as biotin or fluorescently labelled strands, can be used to direct these functions to very distinct positions in the nanostructure.

A practical application of these nanostructures is the generation of highly precise nanorulers for the calibration and validation of super-resolution fluorescence microscopy methods discussed in Chapter 8. For this purpose, a rectangular Origami structure carries two fluorescently labelled strands at very well defined positions at diagonally opposing corners of the Origami structure

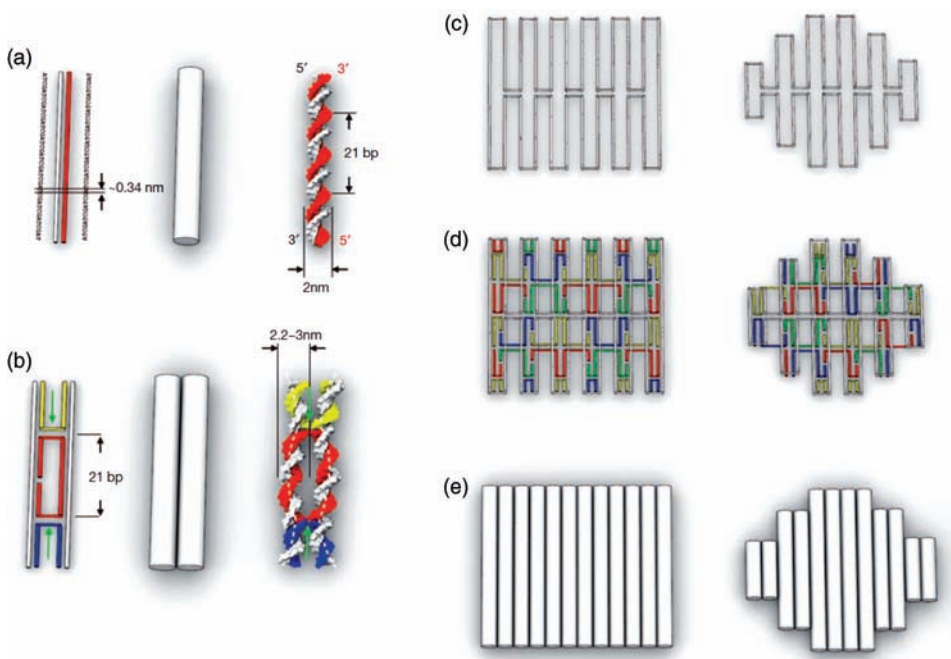


**Figure 12.9** General principle of DNA Origami. Nanostructures of any desired shape can be generated by connecting a long single-strand DNA scaffolds (grey) by a larger number of short oligonucleotide 'staple strands',

that have an appropriate complementary sequence (coloured). For details see the text. Source: Castro 2011. Reproduced with permission of Nature Publishing Group.

(Figure 12.11). For example, the distance of the fluorescence tags could be 90 nm, which is much less than what can be resolved with diffraction-limited fluorescence microscopy (see Chapter 7). Therefore, in a TIRF image of these structures they appear only as a single fluorescence spot of  $\sim 250$  nm diameter (Figure 12.11a). When using a super-resolution method, however, two spots appear for each structure that are separated exactly by the distance defined in the ruler (Figure 12.11b). Because of the rigidity of the DNA-Origami structure this distance is very accurate. Therefore, the optical magnification of a super-resolution microscope can be very accurately verified and optical aberrations in the system can easily be corrected.

When having a two-dimensionally DNA-Origami structure at hand the conceptually next step is of course to extend this approach to three-dimensional objects. The AFM as well as transmission electron microscopy (TEM) images shown in Figure 12.12 demonstrate the successful generation of a hollow nano-flask of 70 nm in length and 40 nm in width. In this approach the out-of-plane surface curvature of the DNA-Origami structure was generated by selecting appropriate positions and patterns of cross-overs between adjacent DNA double helices. Also, inplane curvature exists and was generated by complementary,

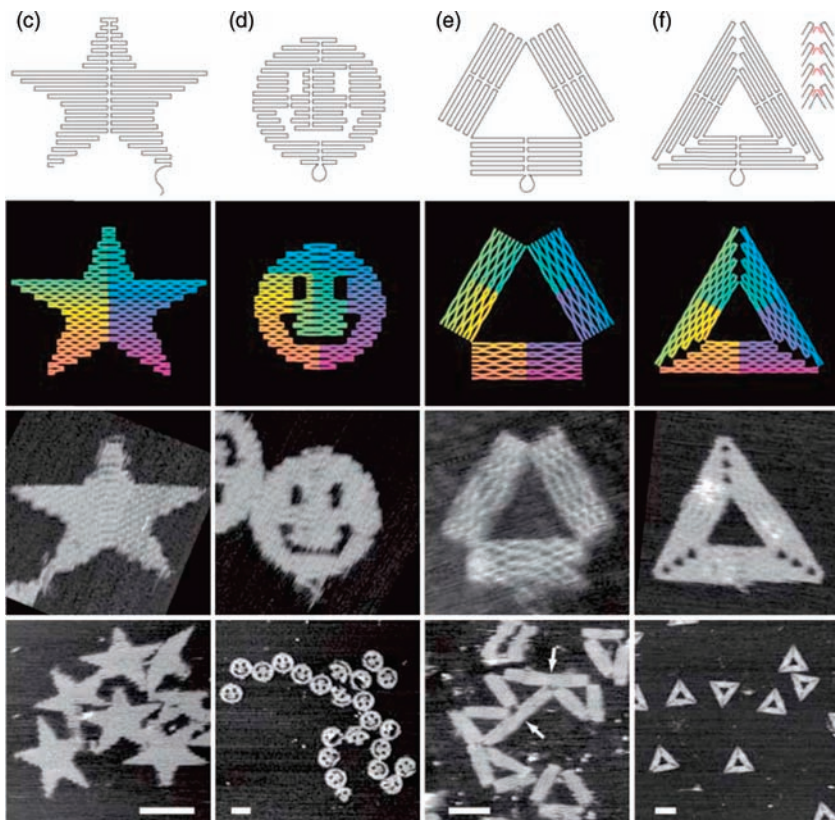


**Figure 12.10** Different DNA Origami shapes. The first two rows show the DNA-folding paths and the bend of helices at cross-overs (where helices touch). Colour indicates the base-pair index along the folding path from

red to purple. The bottom two rows show AFM images of the corresponding DNA-Origami structures. Source: Rothemund 2006. Reproduced with permission of Nature Publishing Group.

concentric DNA rings. This example demonstrates the fascinating versatility of the DNA-Origami approach.

In another 3D approach it has been demonstrated that it is even possible to design DNA-brick structures analogous to structures built from LEGO® bricks. The analogy with LEGO® bricks is actually introduced to facilitate understanding the concept of this approach. Figure 12.13a visualizes the structure of a '1×2 brick'. It consists of a single DNA strand that can be subdivided into four domains 1 to 4, each consisting of 8 nucleotides. When incorporated into the target structure the domains form two antiparallel helices of 16 nucleotides. Figure 12.13b shows that the domains depicted  $\alpha$  and  $\alpha^*$  of two bricks are designed complementary in such a way that they hybridize in a stereospecific fashion. This results in three parallel helices with a 90° dihedral angle. Extending this elementary step multiple times allows generation of a cuboid in which each brick carries a particular sequence that directs it to fit only to its predetermined position (Figure 12.13c).

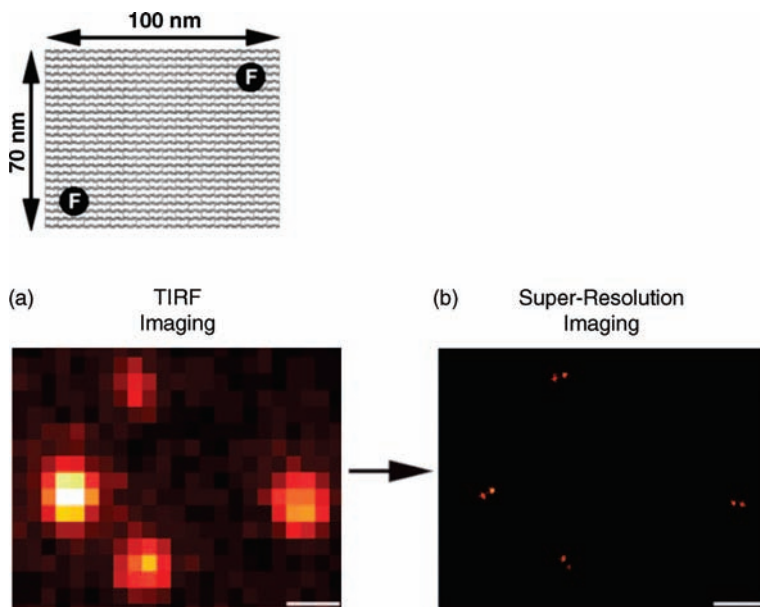


**Figure 12.11** Application of DNA Origami as a nanoruler. A rectangular DNA Origami carries fluorescently labelled strands at two very well defined positions. With this rigid structure the magnification and optical aberrations of

super-resolution microscopes can be evaluated. Source: Steinhauer 2009. Reproduced with permission of Wiley-VCH Verlag GmbH & Co. KGaA.

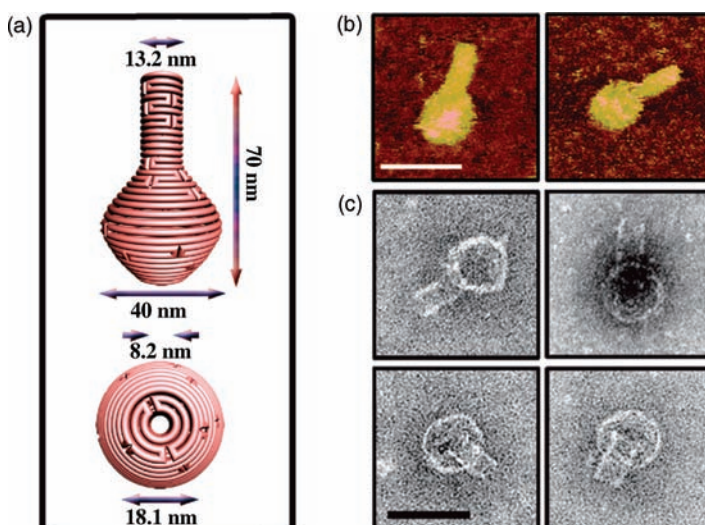


**Figure 12.12** Also, three-dimensional nanoobjects can be generated by DNA Origami as demonstrated by these hollow nanoflasks of 70 nm in length and 40 nm in width. (a) shows the DNA-folding paths, whereas (b) and

(c) are AFM as well as transmission electron microscopy (TEM) images of the flasks. Source: Adapted from Han 2011. Reproduced with permission of RSC.

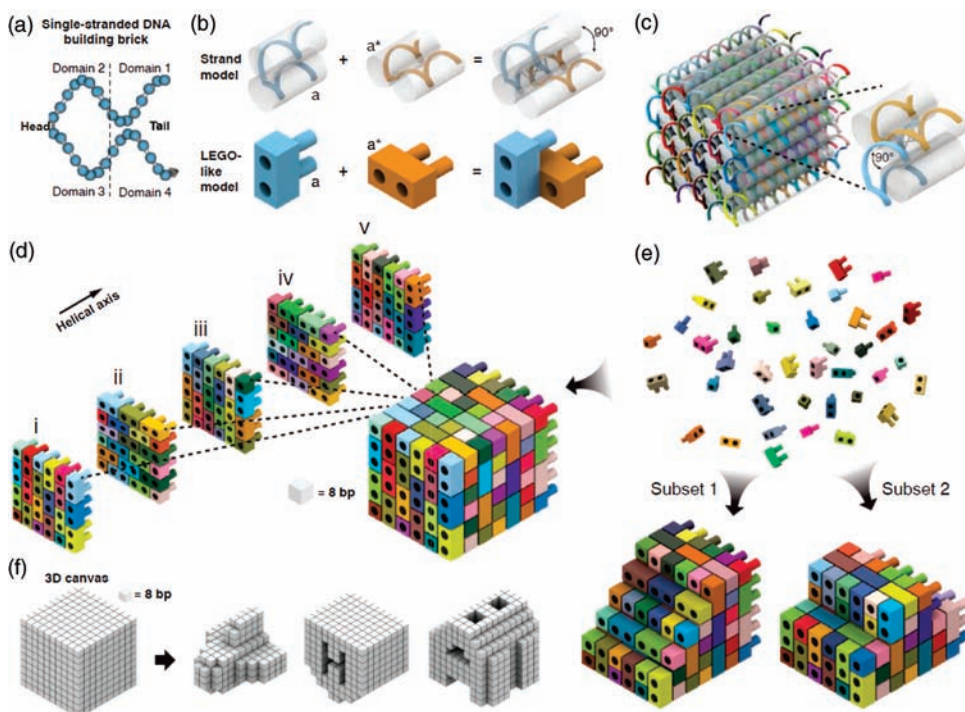


**Figure 12.13** Concept of generating three-dimensional nanostructures from a set of self-assembling DNA-Origami 'bricks' (a–c). The entire set forms a cuboid (d). If only subsets

are used, customized three-dimensional shapes can be generated (e and f). For details see the text.

Also '1 × 1 bricks' are needed at the boundary of the cuboids layers (see e.g. the green 1 × 1 brick in the top left of layer V in Figure 12.13d). These consist of a single helix with only two domains, as defined in Figure 12.13A. Once a set of bricks is generated for a cuboid, customized three-dimensional shapes can simply be generated by using only subsets of the bricks necessary for the entire cuboid (see e.g. Subset 1 and 2 in Figure 12.13e). The selection of the strand list necessary for a particular shape is done with the aid of a computer program that is used to direct an automated liquid-handling robot to mix the strands. Figure 12.13f visualizes the high complexity of structures that are available from this concept.

## 12.5

### DNA Microarrays

Even though cells carry a large set of DNA sequences encoding proteins (exons) not all proteins are generated in a cell simultaneously and to the same extent. Up- and downregulation of this gene expression is one of the most important

mechanisms governing specifically the functioning of a cell. Often, it is important to know how distinct compounds influence the regulation of gene expression. This helps, for example, in understanding how a certain biological regulator or a potential drug candidate might affect the cell metabolism. But how can the gene expression for a large number of proteins be monitored simultaneously in a reasonable time? For such and similar problems DNA microarrays represent a very useful tool.

Figure 12.14 shows the principle of monitoring effects on the gene expression of cells using DNA microarrays. A DNA microarray is a small substrate having a regular pattern of spots that carry immobilized sequences of DNA. The DNA sequences at the different spots correspond to the sequence of different messenger RNA (mRNA) encoding important cell proteins. To monitor the regulation of gene expression by certain compounds, usually a procedure similar to the one described here is applied. First, a cell population is divided into two parts. One part is treated with the compound or any procedure for which the influence on the gene expression shall be found. The other part is not treated. After a certain incubation time the mRNA of both cell lines is isolated from their cell extracts. The amount of DNA transcribed into mRNA is a very important parameter in regulation of gene expression. The more mRNA that is transcribed the more of the corresponding protein will be generated by translation in the cells ribosomes. In the case shown in Figure 12.14, for example, the treated cells contained three times more mRNA 2 but no mRNA 3. The treatment has upregulated the gene expression of mRNA 2 and completely downregulated mRNA 3. Only the gene expression of mRNA 1 is unaffected. In a next step, complementary DNA (cDNA) is generated from the isolated mRNA by the enzyme reverse transcriptase. One reason amongst others for this intermediate step is that DNA is far more stable than RNA. RNA is very quickly degraded by enzymes that are quite abundant in natural environments. Then, the cDNA of both cell-line parts is labelled with different fluorescence dyes (green and red in Figure 12.14). It is important that both cell populations are treated equally in order to properly compare them later on. In the next step, the DNA microarray is now exposed to both labelled cDNA preparations simultaneously. Finally, the fluorescence from each spot on the DNA microarray is imaged in one shot. From the fluorescence emission of individual spots it is immediately possible to determine the gene expression in the treated and untreated cells as well as the effect of treatment on the gene expression. The gene expression of mRNA 1, for example, was unaffected by the treatment. As a result, the corresponding spot on the DNA microarray carries about equal amounts of red and green fluorescence dye (spot 1 in the lower part of Figure 12.14). The additive mixture of these colours appears as a yellow spot. A yellow fluorescence spot indicates no effect on the gene expression of this particular gene. In contrast, gene 2 (mRNA 2) was upregulated by a factor of three in comparison to the untreated cells. As a consequence, the corresponding spot on the DNA microarray shows an almost exclusively red fluorescence (spot 2 in

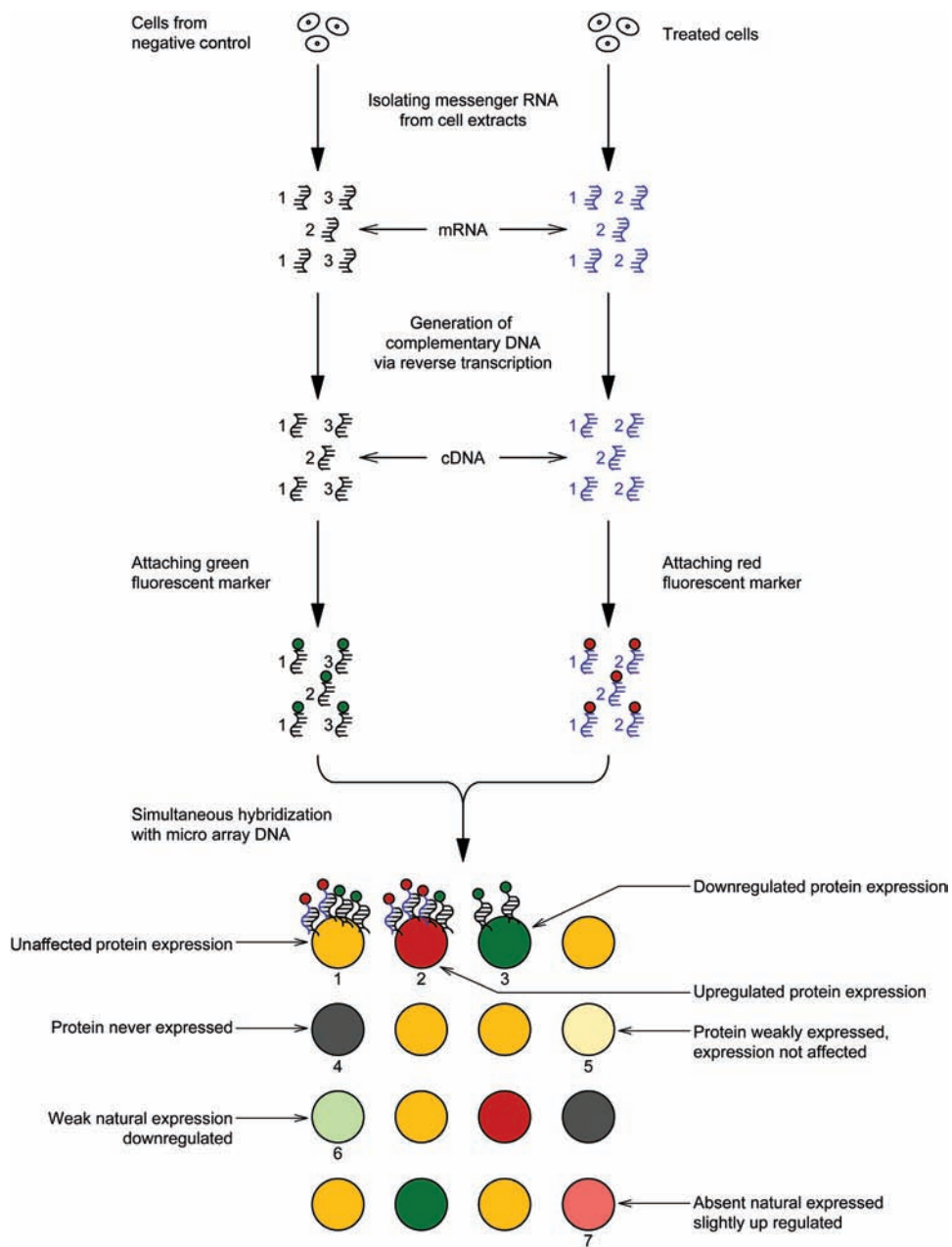


**Figure 12.14** DNA microarrays allow us to determine, compare and to quantify the gene expression of many genes simultaneously. Real DNA microarrays can carry tens of thousands of spots corresponding to the gene expression for different proteins.

Figure 12.14). A red fluorescence spot indicates upregulated genes. Finally, gene 3 was completely downregulated. Consequently, only green fluorescence can be detected at the corresponding spot (spot 3 in Figure 12.14). The detection using DNA microarrays provides further important information about the gene expression. The absence of any fluorescence on spot 4 in Figure 12.14 indicates, for example, that the protein corresponding to this gene is apparently never produced by the investigated cell line. The weaker yellow fluorescence at spot 5 indicates weak gene expression that is apparently unaffected by the treatment. The weak green fluorescence at spot 6 indicates a weak gene expression in the untreated cells that is downregulated by the treatment. Finally, the weak red fluorescence at spot 7 might indicate a gene expression that is absent in the untreated cells but is slightly upregulated by the treatment. Of course, it is also possible to measure the entire fluorescence spectrum of the spots to quantify the relative amounts of red and green fluorescence more precisely.

Often, the large amount of information deduced from such an analysis is compared with databases that contain typical regulation patterns. This helps to identify the functioning of certain genes, drug candidates or the toxicity of certain compounds. Also, very valuable information on the metabolic pathways in cells and the reasons for certain diseases can be identified using this information.

## 12.6 Flow Cytometry

Even in a population of cells from a single cell line not all cells are completely identical. Therefore, for some purposes it is important to sort out cells from a population that have certain distinct properties. For such applications, often a fluorescence-assisted cell sorter (FACS) can be used. A FACS can sort out of a population individual cells that are specifically labelled by fluorescence markers. In principle, almost the entire range of fluorescence methods discussed in this book can be used as fluorescent indicators. For example, fluorescent antibodies can report the presence and concentration of certain cell-surface components or  $\text{Ca}^{2+}$  or pH-sensitive fluorescence markers can be used. When incorporating DNA vectors into expression organisms, often only a fraction of the cells actually take up and express the DNA of interest. To sort out the cells where this transformation was not successful it is possible to incorporate the DNA of interest together with the DNA sequence for a fluorescent protein, such as green fluorescent protein (GFP) (Section 3.2.6). As a result, only those cells express GFP and consequently are fluorescent, indicating that the transformation procedure was successful. These cells can then be sorted using a FACS.

Figure 12.15 illustrates schematically the principle of a FACS. A solution containing the differently labelled cells is first released into a small tube. A lens focuses laser light into the liquid flow in the tube. If now a cell passes this excitation focus, fluorescence can be collected by another lens and

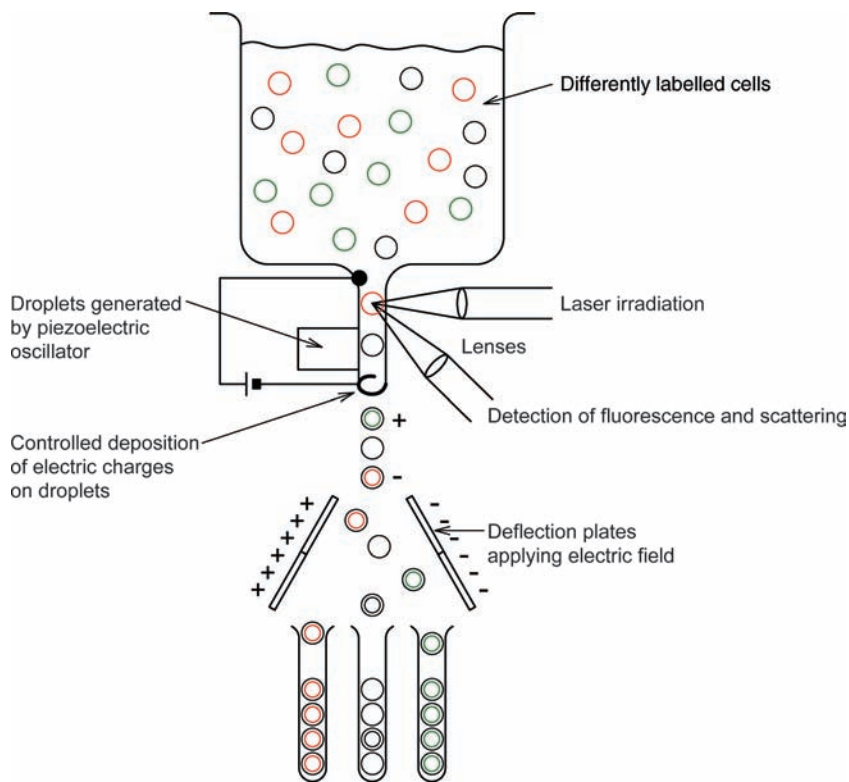


**Figure 12.15** In a fluorescence-assisted cell sorter (FACS) fluorescing and nonfluorescing cells can be sorted. FACS is based on the detection of scattering and fluorescence from

the cells. The FACS then generates charged droplets. Depending on the cells contained in these droplets, electric fields guide them into the correct collection vessel.

detected by methods similar to those illustrated in Figures 2.2 and 7.1. If a nonfluorescing cell passes the focus it can also be detected reliably by the considerable scattering of the laser light by the cell (see also Section 4.2 on light scattering). The tube is also tightly mounted to a piezoelectric oscillator. The high frequencies provided by this oscillator result in the generation of small droplets at the exit of the tube. Simultaneously, this end of the tube is connected to an electrode. This electrode is used to deposit either a positive, a negative or no electrical charge onto the droplets. The sign and magnitude of the deposited charges depend on the type of scattering and fluorescence signal that was previously detected from the cells. It is also possible, for example, to sort cells only by size, as the scattering signals will be significantly different for different cell sizes. Finally, the charged or noncharged droplets are deflected between electrically charged plates and fall into the correct collection vessel.

## 12.7

Fluorescence *In Situ* Hybridization

The DNA of humans contains about 3 billion base pairs. Even though the technology of DNA sequencing has made great progress in recent years (see Chapter 11), a total sequencing of the entire DNA information of an individual human being or other organism is still a time-consuming and elaborate process. For some questions, however, only knowledge about the presence and location of certain DNA sequences encoding specific proteins within chromosomes is required. This information might be important to identify or understand a genetic disease, for example. A quick and reliable method to find answers to such questions is fluorescence *in situ* hybridization (FISH) (Figure 12.16). In FISH, first a sequence of single-stranded DNA is synthesized that encodes the gene of interest. Then, a fluorescence label is attached to this fragment, for example, at the 3'-hydroxyl groups of the deoxyribose sugar at the 3'-end of the DNA. In a next step, this fluorescently labelled fragment of DNA is exposed to the native DNA of the organism for several hours. During this time hybridization of the fluorescently labelled DNA fragment with the native DNA occurs if the corresponding complementary code is present in the DNA. Then, after washing steps that remove the excess labelled DNA fragments, the presence or absence of the gene of interest within the genome of the organism is monitored by the presence or absence of detectable fluorescence. The fluorescence detected from the labelled DNA fragment can also be used to identify the exact location of this gene within a set of chromosomes of an organism.

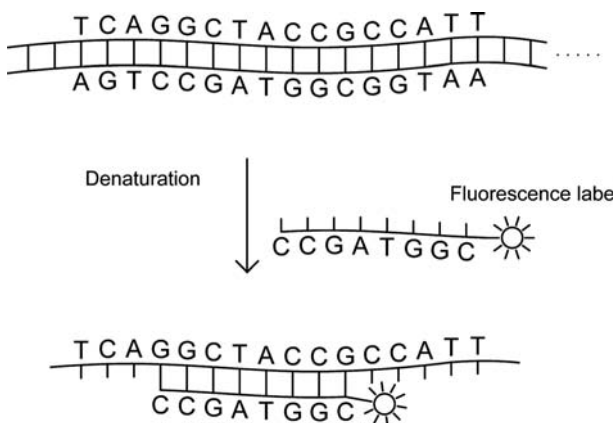


**Figure 12.16** In fluorescence *in situ* hybridization a single, fluorescently labelled DNA strand encoding the gene of interest is exposed to the entire chromosomal DNA of the organism under investigation. If the

complementary sequence is present in the organism the binding of the corresponding DNA fragment to the native DNA can be detected by its fluorescence signal.

## 12.8

## Microspheres and Nanospheres

Microspheres are small spheres of diameters ranging from  $\sim 2\text{ }\mu\text{m}$  down to a few tens of nanometres. The latter are often also referred to as nanospheres. Typically, they consist of organic polymers such as polystyrene. For applications in the biosciences their surface is usually modified by chemically reactive groups such as carboxylic acids, which can be used to attach all sorts of bioactive material to the spheres. We have already discussed one application of such microspheres in Section 9.4 on optical tweezers. Such microspheres can also be purchased containing different fluorescence dyes. The presence of these microspheres can then be detected easily by fluorescence imaging. They also give very strong signals in confocal single-particle detection (Section 9.2) as even the smallest spheres of  $\sim 20\text{ nm}$  diameter still contain fluorescence dyes corresponding to an equivalent in fluorescence intensity of  $\sim 200$  fluorescence dye molecules. The application possibilities of microspheres are vast and it depends only on the imagination of the researcher as to how they use microspheres to investigate particular scientific questions. A typical application would be, for example, the derivatization of the microsphere surface with certain antibodies. The presence of the corresponding antigen can then be monitored by the binding of a fluorescing microsphere to the antigen. Magnetic microspheres are also available. If these are derivatized with antibodies, the corresponding antigen can be 'fished' out of a heterogeneous mixture by the use of a magnet. A technical application of the distinct properties of fluorescing nanoparticles (Section 12.2) is their use in encoded microspheres (Figure 12.17). Encoded microspheres contain differing amounts of fluorescing nanoparticles. Because of the broad absorption

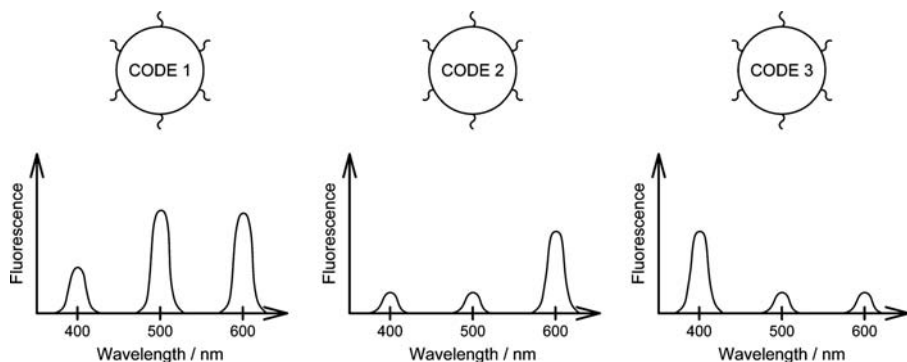


**Figure 12.17** Encoded microspheres can contain fluorescing nanoparticles of, for example, three distinct colours. The generation of microspheres containing differing amounts of these three nanoparticles allows the differentiation of an almost unlimited number of

differently 'bar-coded' microspheres. When each 'code' carries different specific surface receptors this can be used to test the presence of many different specific ligands in just one experiment.

of the fluorescing nanoparticles usually all of the different nanoparticles can be excited by a single excitation wavelength (cf. Figure 12.3). Since the fluorescence spectra of the fluorescing nanoparticles are spectrally very narrow, however, the different concentrations per microsphere can be very well detected. This provides a code that allows us to distinguish a large number of different microspheres. The surface of these encoded microspheres can be derivatized with different biomolecules, such as antibodies. The specific binding of these antibodies to the corresponding antigens then allows us to identify in a single experiment distinct antigens that are present in a sample, for example at cell surfaces, from a large number of possible antigens.

### Problems

- 12.1 What are the most important advantages and disadvantages of using quantum dots for fluorescence labelling of biomolecules?
- 12.2 Assume you want to analyse the binding between a small ligand and a large receptor. In what situations would you rather use SPR or FPA (fluorescence polarization anisotropy) for this task?
- 12.3 Explain why differing labelling efficiencies for different cDNAs have only a minor influence on the read-out information provided by DNA chips.
- 12.4 To obtain information about the genetic code, in what situations would you use fluorescence *in situ* hybridization and when would you prefer DNA sequencing?

### Bibliography

#### Specific

##### Surface Plasmon Resonance Detection

- Jonsson, U., Fagerstam, L. *et al.* (1991) Real time biospecific interaction analysis using surface plasmon resonance and a sensor chip technology. *BioTechniques*, **11**, 620–627.
- Jönsson, U. and Malmqvist, M. (1992) Real time biospecific interaction analysis. *Adv. Biosens.*, **2**, 291–336.

##### Nanoparticles

- Frenzel, J., Joswig, J.O. *et al.* (2007) Optical excitations in cadmium sulfide nanoparticles. *J. Phys. Chem.*, **111** (29), 10761–10770.

- Li, J. and Wang, L.-W. (2004) First principle study of core/shell structure quantum dots. *Appl. Phys. Lett.*, **84**, 3648.

#### Encoded Microspheres

- Adams, E.W., Ueberfeld, J. *et al.* (2003) Encoded fiber-optic microsphere arrays for probing protein-carbohydrate interactions. *Angew. Chem. Int. Edit.*, **42** (43), 5317–5320.

#### DNA-Origami

- Castro, C.E., Kilchherr, F. *et al.* (2011) A primer to scaffolded DNA origami. *Nature Methods*, **8** (3), 221–229.

- Han, D., Pal, S. *et al.* (2011) DNA origami with complex curvatures in three-dimensional space. *Science*, **332** (6027), 342–346.
- Ke, Y., Ong, L.L. *et al.* (2012) Three-dimensional structures self-assembled from DNA bricks. *Science*, **338**, 1177–1183.
- Rothemund, P.W.K. (2006) Folding DNA to create nanoscale shapes and patterns. *Nature*, **440**, 297–302.
- Steinhauer, C., Jungmann, R. *et al.* (2009) DNA origami as a nanoscopic ruler for super-resolution microscopy. *Angew. Chem. Int. Edit.*, **48**, 8870–8873.
- Tørring, T., Voigt, N.V. *et al.* (2011) DNA origami: a quantum leap for self-assembly of complex structures. *Chem. Soc. Rev.*, **40** (12), 5636–5646.

#### DNA Chips

- Schena, M. (ed.) (1999) *DNA Microarrays: A Practical Approach*, Oxford University Press, Oxford.

#### Fluorescence *in Situ* Hybridization

- Andreeff, M. and Pinkel, D. (eds) (1999) *Introduction to Fluorescence *In Situ* Hybridization: Principles and Clinical Applications*, Wiley VCH Verlag GmbH, Weinheim.

#### Flow Cytometry

- Givan, A.L. (2001) *Flow Cytometry: First Principles*, John Wiley & Sons, Inc., New York.
- Haugland, R.P. (1994) Spectra of fluorescent dyes used in flow cytometry. *Mol. Cell Biol.*, **42**, 641–663.
- Ormerod, M.G. (2000) *Flow Cytometry: A Practical Approach*, Oxford University Press, Oxford.

## 13

# Assay Development, Readers and High-Throughput Screening

### 13.1

#### Introduction

This chapter discusses important aspects in the process of developing an appropriate assay to monitor a certain biochemical transformation or to determine a certain biomolecular parameter. Parameters that determine whether a certain read-out is well suited to yielding robust and quantitative information about a biochemical process are presented. In addition, typical instrumentation for the optical detection of a larger number of samples, such as plate readers and plate formats, will be presented. Finally, an application example of optical high-throughput screening detection technologies in the context of drug development is given.

### 13.2

#### Assay Development and Assay Quality

When a specific biomolecular parameter or mechanism has to be determined or measured an experimental test has to be developed to reliably provide a read-out for this parameter or mechanism. Such an experimental test is called an assay. The procedure of finding an appropriate assay for a particular bimolecular question is called assay development. It can be distinguished between end-point assays, where a certain parameter is only measured once, or kinetic assays where the parameter is used to follow the progress of a certain biochemical reaction. To develop an appropriate assay, all of the methods described in this book can be used. The assay principle can be based on biophysical assay parameters, such as fluorescence polarization measurements, or also on rather biochemical principles, for example enzyme cascades that result finally in the generation of oxyluciferin luminescence (see Section 3.8). An assay can also be based on radioactive labelling of biomolecules or metabolic compounds with radioactive isotopes such as  $^{14}\text{C}$  or  $^3\text{H}$ ; the metabolic pathway can then be determined by detecting or isolating radioactive metabolic cell products and components. It depends on the imagination of

the assay developer to find out which of the multitude of possible assay principles is best suited. Often, assay development is time consuming and is the essential step in answering a specific scientific question in the biosciences.

In the development of suitable assays, determination of the assay quality is very important. The assay quality is governed by the accuracy with which a certain read-out parameter reflects the biochemical variable or mechanism of interest. As mentioned earlier, this parameter can be any parameter described in this book, such as fluorescence parameters, NMR signals, scattering intensities, and so on. Let us inspect, for example, how well the measured fluorescence anisotropy,  $r$ , reflects the affinity of a potential drug candidate for a certain receptor in the competition assay described in the Introduction to this book. For the quality of  $r$  as read-out parameter one important factor is how large the observed difference in  $r$  is when the fluorescently labelled ligand is free or bound to the receptor. Determination of this difference requires the preparation of both a negative control, which consists of a sample in which all fluorescently labelled ligands are still bound to the receptor, and a positive control, which consists of a sample containing only the pure, free labelled ligand. Remember that a high affinity of a potential drug candidate typically results in displacement of the labelled ligand from the binding pocket – this is why the free labelled ligand corresponds to the positive control. The respective anisotropies of these two samples are then measured. To determine the statistical accuracy of the measured values in  $r$  these measurements are repeated several times. Then, one calculates the arithmetic mean value of the positive control according to:

$$\bar{r}^+ = \frac{\sum_{i=1}^n r_i^+}{n} \quad (13.1)$$

and estimates the corresponding statistical error or standard deviation by:

$$\delta^+ = \sqrt{\frac{\sum_{i=1}^n (r_i^+ - \bar{r}^+)^2}{n-1}} \quad (13.2)$$

Here,  $r_i^+$  is the anisotropy observed from an individual measurement,  $i$ , of the positive control and  $n$  is the total number of repeated measurements. Similarly, the mean anisotropy and standard deviation of the negative control is calculated from:

$$\bar{r}^- = \frac{\sum_{i=1}^n r_i^-}{n} \quad \text{and} \quad \delta^- = \sqrt{\frac{\sum_{i=1}^n (r_i^- - \bar{r}^-)^2}{n-1}} \quad (13.3)$$

where  $r_i^-$  is the anisotropy observed in an individual measurement,  $i$ , of the negative control and  $n$  is the total number of repeated measurements. Obviously,  $r$  would be a poor read-out parameter for this particular assay if the mean values

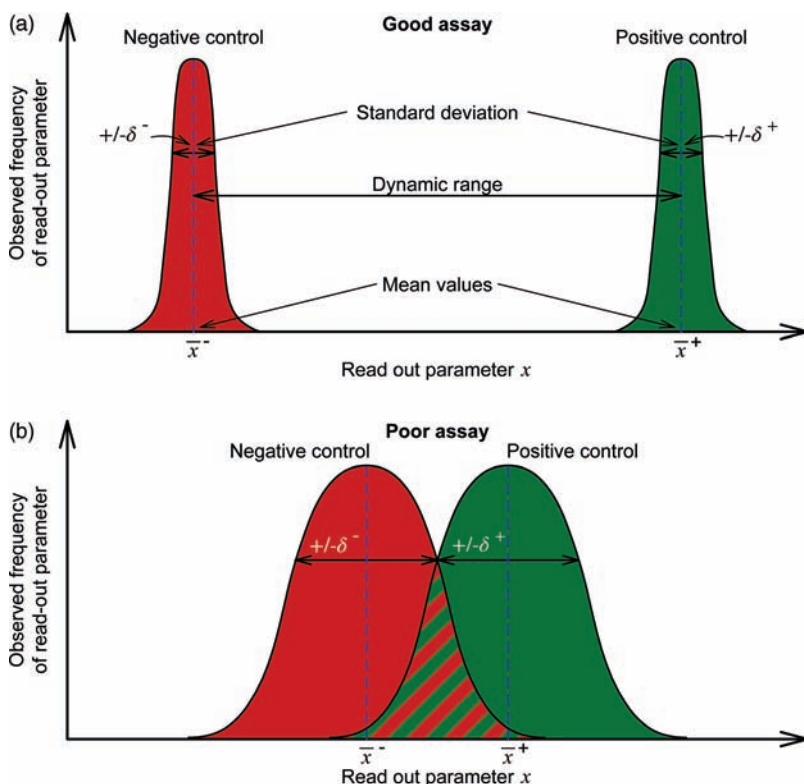


**Figure 13.1** An assay parameter is good when it has a large dynamic range,  $|\bar{x}^+ - \bar{x}^-|$ , and small read-out errors,  $\delta^+$  and  $\delta^-$ .

of the negative and positive controls,  $\bar{r}^-$  and  $\bar{r}^+$ , respectively, differ very little and if the corresponding measuring errors,  $\delta^+$  and  $\delta^-$ , are large compared to that difference. In contrast, the anisotropy would be a very good assay parameter if  $\bar{r}^-$  and  $\bar{r}^+$  were very different and could be determined with only small  $\delta^+$  and  $\delta^-$ . In general, any assay parameter  $x$  is a good assay parameter if the dynamic range,  $|\bar{x}^+ - \bar{x}^-|$ , is large and the corresponding errors,  $\delta^+$  and  $\delta^-$ , are small (Figure 13.1a). Then, experimental values  $x$  lying between or at the extreme values,  $\bar{x}^+, \bar{x}^-$ , for a distinct sample can be determined with high accuracy. For the polarization assay, for example, for samples containing different potential drug candidates the closer the observed anisotropy value,  $r$ , is to  $\bar{r}^+$  the higher the affinity of the candidate is for the receptor. The larger the dynamic range of the anisotropy assay,  $|\bar{r}^+ - \bar{r}^-|$ , and the smaller the errors,  $\delta^+$  and  $\delta^-$ , the better different drug candidate affinities can be differentiated. If the dynamic range,  $|\bar{x}^+ - \bar{x}^-|$ , of a certain assay parameter is small, however, and in addition the corresponding  $\delta^+$  and  $\delta^-$  are large, then this parameter will not even allow us to unambiguously differentiate a negative from a positive control (Figure 13.1b).

In general, the quality of an assay can be quantified by the so-called  $Z'$  factor:

$$Z' = 1 - 3 \frac{\delta^+ + \delta^-}{|\bar{x}^+ - \bar{x}^-|} \quad (13.4)$$

The  $Z'$  factor is a measure of the magnitude of the experimental errors,  $\delta^+$  and  $\delta^-$ , in comparison to the dynamic range,  $|\bar{x}^+ - \bar{x}^-|$ , of an assay. The larger  $Z'$ , the better the assay quality. An ideal assay would correspond to a  $Z'$  factor of 1. An assay is regarded as very good when the  $Z'$  factor is higher than 0.8. However,  $Z'$  factors higher than 0.5 still correspond to a reasonable assay quality even though the dynamic sensitivity is significantly reduced. Finally,  $Z'$  factors below 0 correspond to poor assays. For  $Z'$  factors below 0 it becomes difficult to differentiate positive from negative controls. A  $Z'$  factor of 0 corresponds to the situation in which the mean values of positive and negative controls,  $\bar{x}^+, \bar{x}^-$ , differ by no more than three standard deviations ( $\delta^+, \delta^-$ ). When the measured parameters can be described by Gaussian distributions a difference of three standard deviations,  $\delta^-$ , between two mean values,  $\bar{x}^+, \bar{x}^-$ , corresponds to a probability of only 0.3% that a value measured with a sample containing a negative control,  $x_i^-$ , is obtained that is actually larger than the mean value of the positive control,  $\bar{x}^+$ . The corresponding values for two and one standard deviation are 4.5% and 32%, respectively.

Depending on the experimental error sources dominating the errors,  $\delta^+$  and  $\delta^-$ , the  $Z'$  factor may be improved by longer measuring times per sample. If the dominant error source is purely instrumental, for example because too few photons are detected to accurately calculate the anisotropy values, then longer measurement times will improve the errors and thus the assay quality. There are of course limitations to this approach to improving the  $Z'$  factor. When measuring biological samples, sample degradation must always be considered. The measuring time must be short enough that sample degradation does not affect the measured results. In addition, in high-throughput screening (see the application example at the end of this chapter) the measuring time available per sample is usually limited to at most a few seconds. If the dominant error source is rather biological, for example because of inhomogeneities in the sample preparation or the biological sample itself, longer measurement times will not help to improve the assay quality. In these cases, biochemical procedures must be found to provide better samples of reproducible quality. A further important source of assay variability is the influence of the different compounds tested on the individual samples, that is when testing a large library of chemicals with respect to their potential to bind to a receptor. Often, these compounds degrade signal quality by their intrinsic fluorescence or scattering.

### 13.3

#### Microtitre Plates and Fluorescence Readers

Most fluorescence assays and also many other assay types are usually conducted in microtitre plates containing a multitude of wells for the analysis of different

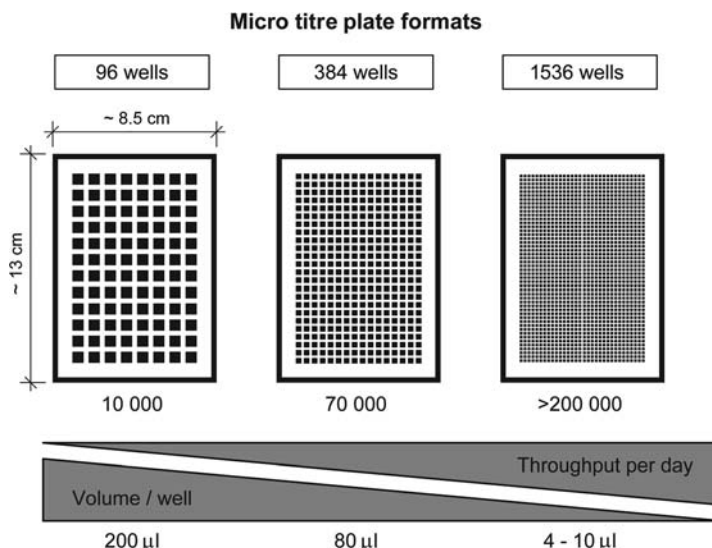


**Figure 13.2** Standard microtitre plate formats.

samples. A very common standard format is a 96-well plate with dimensions of  $\sim 8.5 \times 13$  cm. (Figure 13.2). With this format manual pipetting is still comfortable but the number of available wells is sufficient to conduct most everyday routine tasks in assay development. The 96 wells are sufficient to measure several dilution series and an appropriate number of positive and negative controls on one plate. However, if a high-throughput of measured samples is necessary, then microtitre plates containing more wells have to be used. Over the past several years plates with 1536 wells have become standard in some industrial, as well as university, laboratories. Occasionally, microtitre plates containing higher numbers of wells have also been used. These plates have the advantage that a lot less sample volume is necessary per well and the number of necessary plates is drastically reduced. This allows a large number of tests to be conducted per day. A throughput of up to 100 000 tests per day is usually called high-throughput screening (HTS). Higher numbers of tests per day corresponds to ultrahigh-throughput screening (uHTS). However, the pipetting and liquid handling is far more demanding and usually has to be done in automated environments. In addition, not all instruments are capable of detecting the corresponding parameters in these plates.

A device that detects the selected assay parameter in microtitre plates is usually called a plate reader, or simply a reader. In the following we discuss a few typical designs of readers for various optical detection technologies. Figure 13.3 shows a schematic illustration of a typical optical arrangement in a fluorescence reader. If a broadband excitation light source is used the wavelength of the excitation light can usually be chosen by the use of filters and gratings similar to the ones used in fluorescence spectrometers (see Figure 2.2). It is focused by a lens

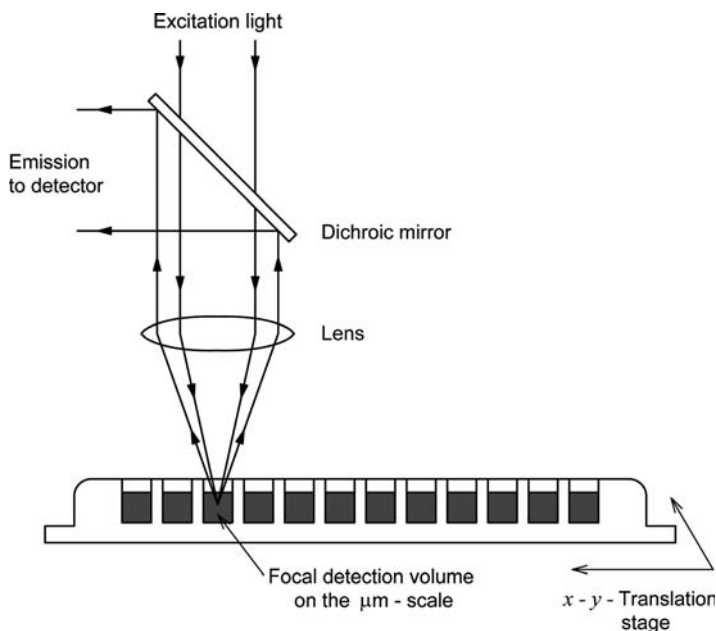


Figure 13.3 Typical optical arrangement of a fluorescence reader.

to a spot within a certain well of the microtitre plate. The distinct well can be selected by translating the entire plate perpendicular to the excitation and detection pathway on a two-dimensional translation table. Alternatively, the excitation and detection optics can also be translated. Obviously, the precision of the focal alignment must be higher for a higher number, and thereby smaller size, of wells. Usually, the measured wells, measurement times and measurement repetitions can be programmed exactly.

If the bottom of the plate does not have a high quality optical transparency then it is advantageous to detect fluorescence, which is emitted upwards in the opposite direction of the incoming excitation light. The same lens that focused the excitation light is then used to collect and collimate the fluorescence, thereby guaranteeing that excitation and detection volume overlap within the sample. The excitation and detection light can be separated by a dichroic mirror (see also Figure 7.1). After spectral filtering, the corresponding signals are detected. For the detection, a single detection wavelength, several different detection wavelengths or even the entire spectra can be recorded. The distance between the lens for excitation and collimation and the plate cannot be arbitrarily reduced and the lens can have only a limited diameter. Therefore, the size of the detection volume in the sample is usually on the micrometre scale, according to Abbe's law (7.1).

Figure 13.4 depicts a corresponding set-up for an optical absorption reader. Since the measurement of absorption requires a defined passage of the detection

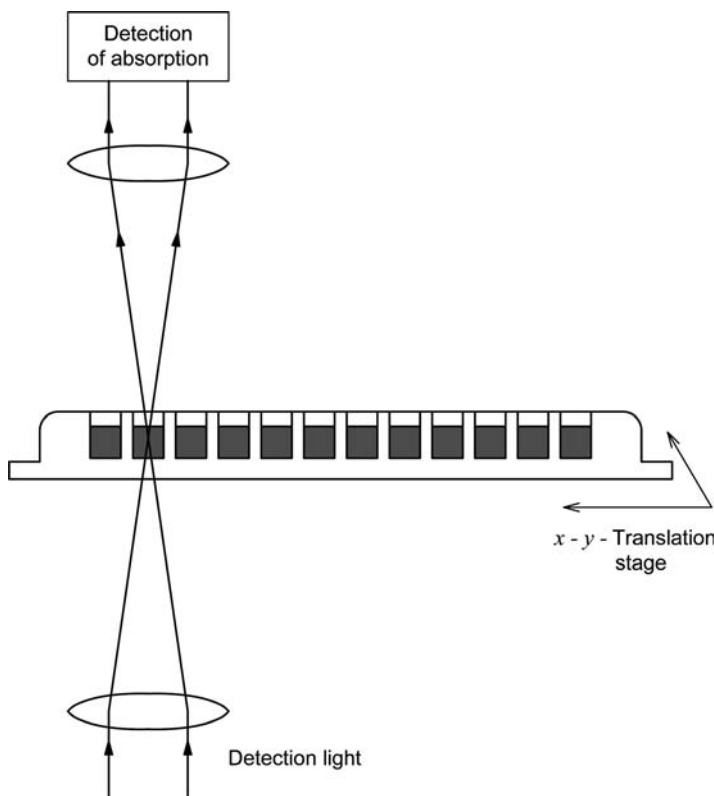


Figure 13.4 Typical optical arrangement of an absorption reader.

light through the sample, the bottom of the plates must be optically transparent, allowing the light to pass through without major deflections of the optical pathway. Such plates are usually significantly more expensive than plates that can only be used for fluorescence detection. A further difficulty in comparison to fluorescence detection is the fact that the absorption depends on the optical path length of the light through the sample volume. Therefore, either the sample volumes must be defined very well or calibration procedures are necessary for reliable results. The selection of the detection light is similar to the selection of the excitation and detection light in fluorescence readers. Also, the positioning of the microtitre plate is similar.

Of course, commercial plate readers are available that enable simultaneous measurements of both fluorescence and absorption. Some readers also allow analysis of entire fluorescence images from, for example, cells in the wells. Screening many wells by this type of analysis is called high-content screening.

Depending on the measurement time necessary per well to achieve good  $Z'$  factors, scanning of entire plates can be quite time consuming, especially with plates suitable for HTS. In cases where the overall measuring time per

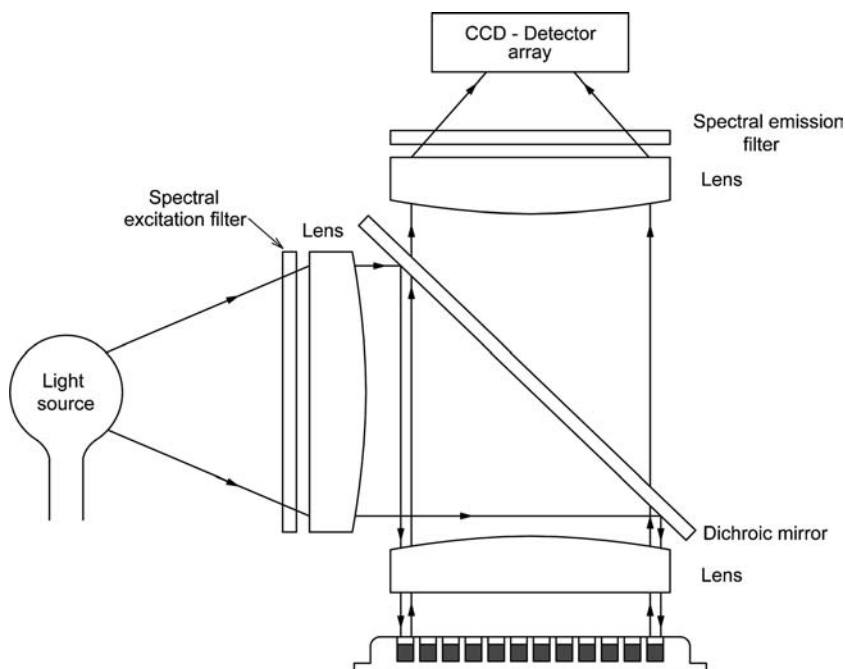


Figure 13.5 Schematic illustration of a fluorescence reader imaging the entire microtitre plate.

plate has to be reduced, readers can be used that image the fluorescence of an entire microtitre plate (Figure 13.5). Such readers excite all wells of a microtitre plate simultaneously and detect the fluorescence using a two-dimensional detector such as a CCD (charge coupled device). The detection of the fluorescence of all wells in one shot reduces, of course, the necessary measurement time enormously. However, especially for HTS plates, it is technically demanding to achieve a homogenous excitation and detection of all wells simultaneously. As a consequence, and because of the costs of scientific CCD detectors, such imaging readers are still quite expensive.

If highly sensitive confocal and single-molecule detection methods are desired, readers containing microscope objectives are necessary (Figure 13.6). In addition, microtitre plates with transparent bottoms are necessary that meet the high standards required for optical microscopy. Inhomogeneities or roughness at any surfaces between the microscope objective and the sample can severely affect the quality of the read-out parameters. Also, the scanning of the wells is more demanding since the distance between microscope objective and the bottom of the plate must be kept constant by active regulation. Finally, some mechanism is necessary that ensures continuously the presence of a film of immersion liquid between the microscope objective and microtitre plate. As a consequence, confocal readers are quite expensive. However,

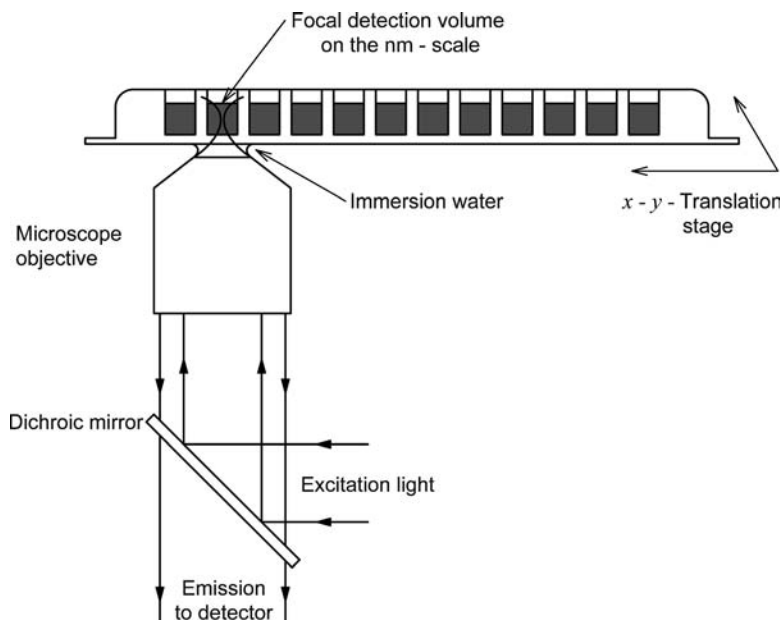


Figure 13.6 Arrangement of a confocal detection reader.

besides the fact that they enable the detection of highly sensitive parameters such as fluorescence auto- or cross-correlation data they usually also provide the best  $Z'$  factors for conventional fluorescence assays such as fluorescence anisotropy.

A major drawback in the use of single-molecule-based fluorescence detection technologies for screening or assay purposes is the longer measurement times that are usually necessary to collect a statistically sufficient number of single-molecule events. In a latest development of confocal fluorescence readers this problem has been circumvented by the creation and detection of multiple detection volumes in a single well (Figure 13.7). An arrangement with  $n$  detection volumes in one well allows us to reduce the necessary measurement time by a factor of  $n$ . Alternatively, it allows us to reduce the instrumental standard deviation,  $\delta$ , by a factor of  $\sqrt{n}$  in comparison to single foci confocal set-ups. This development has enabled the effective use of confocal single-molecule detection technologies in HTS or uHTS, where measurement times below one second per well are necessary.

Multifocal or microscopic fluorescence imaging is also used for whole-cell assays in which read-out parameters are deduced from the image of fluorescently labelled cells. Such assays have, for example, the advantage that only the effect of compounds can be measured that are actually able to penetrate the cell membrane and affect intracellular biomolecules or organelles of interest.

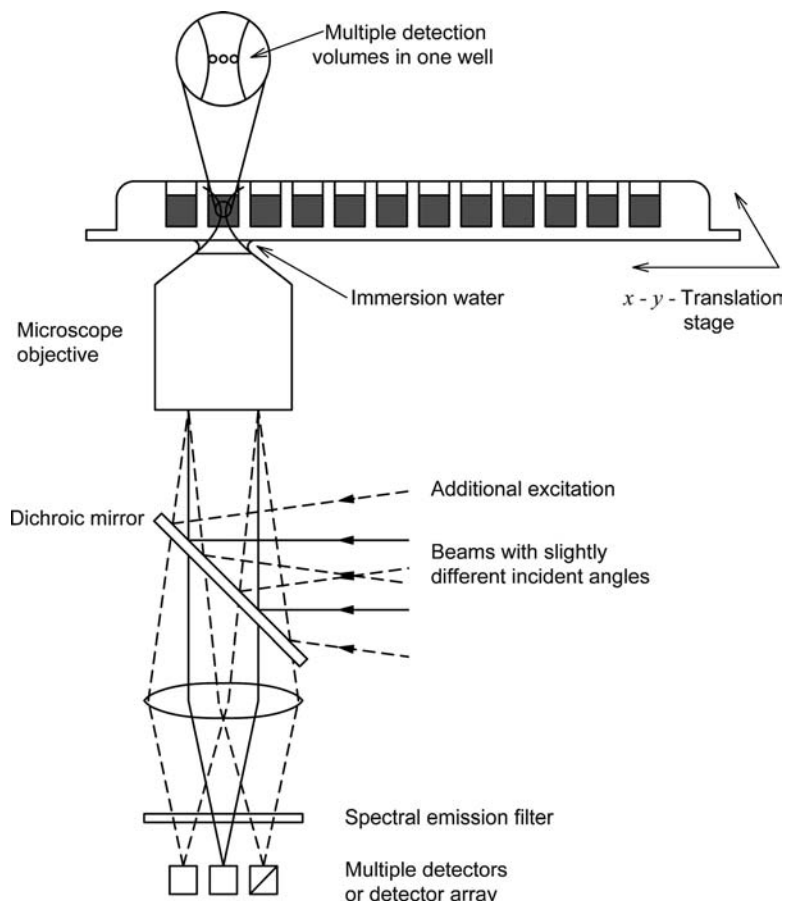


Figure 13.7 Arrangement of a multifocal detection reader.

#### 13.4

#### Application Example: Drug Discovery and High-Throughput Screening

The process of drug discovery and development is extremely time and cost consuming. Before a new drug is released onto the market pharmaceutical companies have typically spent close to one billion ( $10^9$ ) euros and a total time of about 12–15 years have elapsed from the start of the project to market entry. Figure 13.8 shows schematically the most important phases and milestones for the discovery and development of a new drug and the associated timelines. Obviously, such a long process is associated with a high risk of failure of a potential drug candidate at any stage. Typically, only about ten out of 10 000 potential drug candidates tested in animal models during the discovery phase are approved for clinical studies in humans. Out of these ten drug candidates approximately one will finally enter the market.

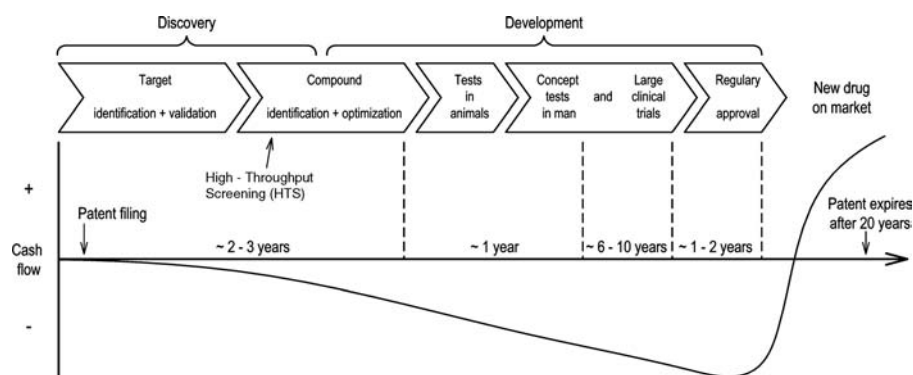


Figure 13.8 Typical timescales and costs of key steps in the development of a new drug.

The first step of modern drug discovery and development is in most cases the identification and the validation of a drug target, that is distinct biomolecules, mostly proteins, that are closely associated with the development or progression of a certain disease. For example, the biomolecular targets of many antibiotics are enzymes responsible for the cell wall synthesis of bacteria, the inhibition of which causes the death of these organisms without effecting the corresponding mechanism in human cells. Prominent target classes are enzymes, such as kinases and proteases, as well as receptors or ion channels (Figure 13.9).

Once a drug target has been identified and validated compounds have to be found that affect the target and can serve as a starting point ('lead structure') for further optimization. As a common strategy towards this goal pharmaceutical companies test large libraries of compounds to find lead structures that qualify as such starting points. Consequently, pharmaceutical companies have collected

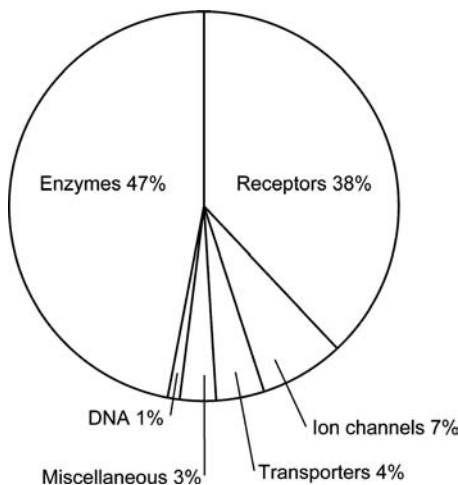
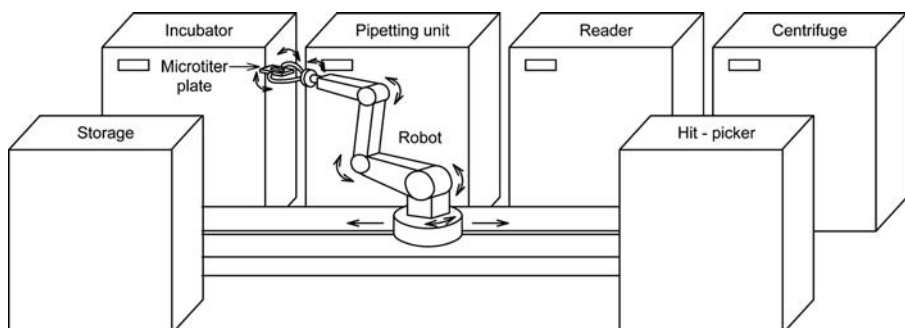


Figure 13.9 Important targets for drugs and drug development.



**Figure 13.10** High-throughput screening of millions of potential drug candidates is usually carried out in fully automated robotic environments. The plate reader, which identifies promising molecular structures by appropriate assays, is an essential part of this process.

large stocks of up to several million synthesized compounds. To increase the chances of successful drug discovery much emphasis has been put on the quality of these libraries with respect to multiple parameters such as structural diversity, proprietary structural space and physicochemical properties. In this lead-finding process high-throughput screening (HTS) and fast and reliable detection technologies play an important role. Figure 13.10 illustrates schematically a typical industrial HTS set-up. A robot transports HTS microtitre plates between different devices that are responsible for the preparation, handling, detection and picking of the drug candidates and assays. The exact sequence depends on the assay developed to identify drug candidates for the disease in question. A typical screen could be as follows. Often, a library of compounds is already dissolved in appropriate solvents in microtitre plates that are ready for use in the storage. The robot takes a plate out of the storage and transports it to the pipetting unit. Here, the assay solution is added to the compound solution. For example, this could be a receptor for which an effective inhibitor is to be found, already carrying a weakly bound, fluorescently labelled ligand as described in the Introduction to this book. Then the robot carries the plate to an incubator. Here, the assay can evolve for a selected time and under selected conditions such as temperature or humidity. Meanwhile, the robot might transport the next plate carrying drug candidates to the pipetting unit. After the incubation time the robot takes the first plate from the incubator to the reader. The reader determines now, for example, the fluorescence anisotropy for each well. Of course, many other read-out parameters are also possible, depending on the specific assay. If a well is found that exhibits very low anisotropy values, indicating that the fluorescently labelled ligand has been forced out of the binding pocket of the receptor by a test compound with apparently a significantly higher binding affinity, a 'hit' has been detected. Then, the robot might transport the plate to a hit-picking unit, which collects all hits from a screen and puts them into separate microtitre plates for further investigation.

The hit set from the initial HTS has to be further analysed to identify one or more leads from a distinct structural class that will be used for further

optimization towards potential drug candidates. In a multiparameter, iterative approach the physicochemical properties, pharmacokinetic, pharmacological and toxicological profiles of the compound series are optimized with respect to the targeted route of administration of the final drug. For example, solubility and permeability are two important parameters addressed by medicinal chemistry ring optimization in order to increase the chance that the pharmacokinetic profile of a potential drug candidate will be sufficient for oral intake. For the optimization of physicochemical properties and the overall pharmacokinetic profile of a lead series the so-called Lipinski's 'rule of 5' very often serves as a guidance tool. The rule states that the molecular weight of a good oral drug candidate should not exceed  $500\text{ g mol}^{-1}$ , that the number of hydrogen bond donors such as NH or OH should not be larger than five, that the number of hydrogen acceptors such as nitrogen and oxygen atoms should not exceed ten, and that their relative concentrations in a two-phase mixture of an organic solvent such as octanol and water should not have a corresponding partition coefficient of greater than 5:

$$\log P = \log \frac{C_{\text{octanol}}}{C_{\text{water}}} < 5$$

If none or only one of these rules is violated the probability is higher that the drug will demonstrate sufficient systemic bioavailability after oral application.

In parallel with the pharmacological characterization of a potential drug candidate a large number of established *in vitro* and *in vivo* test assays have to be performed to address the safety profile. Preclinical toxicology studies are performed in animals and are very important for an initial assessment of the therapeutic window of a drug, that is the difference between a minimum dose to achieve a therapeutic effect (MED, minimum effective dose) and the maximum tolerated dose (MTD). Only drug candidates with a sufficient therapeutic window will be taken on into the clinic for human studies (Figure 13.11). If all tests

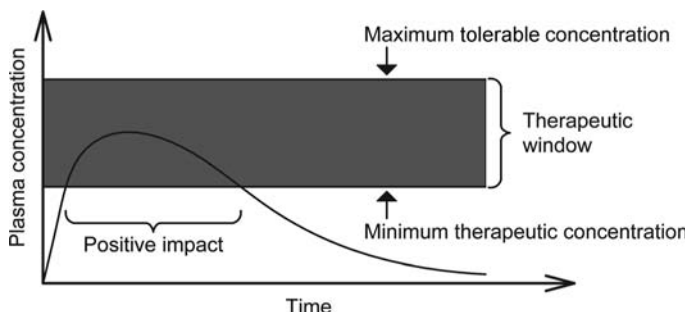


**Figure 13.11** A drug should have a therapeutic window that is as large as possible. The therapeutic window is limited by the concentration that is necessary to achieve a therapeutic effect and by the maximum tolerable

concentration. A good drug should remain at an appropriate concentration in the blood plasma as long as it is therapeutically indicated.

have been successful then approval of the new drug can be applied for at the regulatory institutions of different countries. It is only after the approval and successful market launch of a drug that the developing organization will receive a return on their large investment of time and money during the discovery and development phase.

### Problems

- 13.1** It is your task to develop a binding assay for an industrial high-throughput screening. You have to measure the binding affinity of potential drug candidates with a certain receptor. For the assay you first label a low molecular weight ligand that has a moderate binding affinity for the receptor with a fluorescent dye and let it bind to the receptor.
- How can you use this system to measure the binding affinity of potential drug candidates?
  - You measure the binding of the labelled ligand by three methods: fluorescence polarization, fluorescence correlation and fluorescence lifetime spectroscopy. Your positive control is the free labelled ligand and your negative control is the ligand bound to the receptor.

You observe the following values for the three measurement methods with a measurement time of 100 ms per sample:

Method/parameter	Positive control	Negative control
Fluorescence polarization, anisotropy, $r$	$0.01 \pm 0.001$	$0.1 \pm 0.001$
Fluorescence correlation, diffusion time, $\tau_D$	$80 \pm 100 \mu\text{s}$	$500 \pm 100 \mu\text{s}$
Fluorescence lifetime, $\tau_{S_1}$	$4.3 \pm 0.1 \text{ ns}$	$3.1 \pm 0.1 \text{ ns}$

Which parameter is best suited for the high-throughput screen?

- 13.2** How many samples can be tested in a single day when the per well measurement time is 100 ms? Does this correspond to HTS or uHTS? Estimate the amount of solvent necessary for such a screen when using microtitre plates with 1536, 384 or 96 wells.
- 13.3** You have developed an assay which is based on counting the number of fluorescence photons emitted during a certain measuring time from each sample. This number is basically equivalent to the fluorescence intensity. The fluorescence intensity of the negative control is two times smaller than that of the positive control. Like for all assays based on fluorescence detection the assay quality is also limited by the shot noise associated with

detecting a limited number of photons. Assume that for a measuring time of 1 s the assay quality is almost exclusively limited by the shot noise. For this measuring time it has a  $Z'$  factor of 0.4. Even though this value is probably sufficient for your tests you want to improve it by longer measuring times. If you increase the measurement time per well by a factor of three, the  $Z'$  factor improved to 0.6. A further increase in the measurement time by a factor of three improves the  $Z'$  factor only to 0.65. What  $Z'$  factor improvements would have been expected by the extension of the measuring time if the errors would only depend on the photon shot noise? Discuss reasons that are responsible for the fact that the  $Z'$  factor measured at longer measuring times than 1 s are actually worse than if only shot noise would be limiting? What would be your choice in the measuring time considering these reasons and what can you try to further improve the  $Z'$  factor if necessary?

## Bibliography

### Selected literature

#### $Z'$ Factor

Zhang, J.-H., Chung, T.D.Y. *et al.* (1999) A simple statistical parameter for use in evaluation and validation of high throughput screening assays. *J. Biomol. Screen.*, **4** (2), 67–73.

#### Assay Development

Minor, L.K. (ed.) (2006) *Handbook of Assay Development in Drug Discovery*, CRC Press.

#### High-Throughput Screening

Hüser, J. (ed.) (2006) *High-Throughput Screening in Drug Discovery (Methods and Principles in Medicinal Chemistry)*, Wiley-VCH Verlag GmbH, Weinheim.

Taylor, D.L., Haskins, J.R. *et al.* (eds) (2006) *High Content Screening (Methods in Molecular Biology)*, Humana Press, New Jersey.

#### Fluorescence Techniques in High-Throughput Screening

Jäger, S., Brand, L. *et al.* (2003) New fluorescence techniques for high-

throughput drug discovery. *Curr. Pharm. Biotechnol.*, **4** (6), 463–476.

#### Multifocal Reader

Walla, P.J., Kettling, U. *et al.* (2003) Multi-parameter fluorimetric analysis in a massively parallel multi-focal arrangement and the use thereof. United States Patent 7170598.

#### Lipinski Rules

Lipinski, C.A., Lombardo, F. *et al.* (1997) Experimental and computational approaches to estimate solubility and permeability in drug discovery and development settings. *Adv. Drug Deliv. Rev.*, **23**, 3.

Lipinski, C.A., Lombardo, F. *et al.* (2001) Experimental and computational approaches to estimate solubility and permeability in drug discovery and development settings. *Adv. Drug Deliv. Rev.*, **46**, 3–26.

#### Drug Design

Silverman, R.B. (2004) *The Organic Chemistry of Drug Design and Drug Action*, 2nd edn, Academic Press.



## Index

### **a**

Abbe's law 170, 185, 212, 328  
 absorbance 43  
 absorption 28, 306  
 absorption coefficient 42, 220f  
 absorption spectrometer 42  
 absorption spectroscopy 5, 41ff  
 absorption spectrum 24ff, 41  
 – experimental determination 41ff  
 absorption spectrum of haemoglobin 50  
 acceptor 86ff, 93ff, 95, 96, 270f  
 actin 210, 211  
 activator 83  
 active transport 222  
 adaptor 289  
 adenosine triphosphate (ATP) 206ff, 210f  
 amino acids 45  
 analyser 152, 156ff  
 anisotropy 75ff, 80, 253  
 anthracene 20  
 antioxidative reagents 56  
 applications fields 5ff  
 aromatic amino acids  
 – absorption spectra 46  
 – fluorescence spectra 47  
 assay development 323ff  
 assay quality 323ff  
 atomic force microscopy (AFM) 9, 240ff  
 – application examples 242ff  
 – principle 241  
 atomic orbital 18  
 ATPase 206ff  
 – rotation 206ff  
 – subunits 208  
 ATP hydrolysis 207  
 ATP synthase *See* ATPase 207  
 autocorrelation analysis 214ff  
 – important parameters 221

– mathematical background 220ff  
 autofluorescence 54, 62  
 avalanche photodiode (APD) 174, 175, 205  
 avidin-biotin techniques 65f

### **b**

basics in molecular photophysics 13ff  
 Beer-Lambert law 47, 108  
 binding affinity 309  
 bioluminescence 6, 99ff, 296  
 biomolecular motor 209  
 biomolecule  
 – optical properties 41ff  
 biophysical chemistry 1  
 – advanced methods 11, 167  
 – definition 1  
 biotin 66, 209, 237  
 blueshift 47  
 Bohr magneton 142  
 bridged PCR 289ff  
 butadiene 19

### **c**

cantilever tip 241, 242ff  
 β-carotene 56, 265, 278f  
 – absorption spectrum 57  
 carotenoids 56ff, 278ff  
 cell-attached patch (CAP) 247  
 charged coupled device (CCD) 175, 177, 205, 330  
 chemical shifts 125, 134, 138  
 chiroptical methods 105ff  
 chlorophyll 54f, 276ff  
 – absorption and fluorescence spectra 55  
 chromophore 62  
 circular dichroism (CD) 6, 105ff  
 circular dichroism spectroscopy 105  
 coelenterazine 100

- cofactors 49ff  
 – optical properties 49  
 coherent anti-stokes Raman scattering (CARS) 258, 268f  
 competitive binding assay 3  
 competitive inhibition 83  
 complementary DNA (cDNA) 315  
 conduction band minimum (CBM) 305f  
 confocal fluorescence 170  
 confocal fluorescence microscopy 169ff  
 continuous wave (CW) 263  
 conversion dynode 153  
 cooperativity 51  
 correlated spectroscopy (COSY) 130ff  
 correlation amplitude 214  
 correlation effects 224ff  
 cross-correlation 228f  
 cylindrical lens 179, 191
- d**  
 detection anode 154  
 delayed extraction 154  
 detector 153, 330  
 dielectric polarization 267  
 diffusion time 221  
 digoxigenin 237  
 dipole moment 142  
 dissociation constant 78  
 DNA 45ff  
 – hybridization 48  
 – optical properties 45  
 DNA cluster generation 288ff  
 DNA fragmentation 289  
 DNA fragment alignment 292  
 DNA-hairpins, unfolding 243  
 DNA hypochromism 48  
 DNA microarrays 314f  
 DNA origami 310ff  
 DNA-polymerase 296, 297  
 DNA primer 286  
 DNA replication 287  
 DNA sequencing 9, 287  
 donor 86ff, 95, 270f  
 donor-acceptor distance 92  
 drug development 333  
 drug discovery 332ff  
 drug screening 1, 332f  
 dye sequencing 289ff  
 dynamic light scattering 115  
 dynode 153
- e**  
 electromagnetic radiation 13, 14, 122  
 electronic structure 15ff, 20f, 29  
 electronic wave function 15  
 electron multiplier 154  
 electron paramagnetic resonance (EPR) 7, 141ff  
 electrospray ionization (ESI) 149, 156  
 electrospray ionization-mass spectrometry (ESI-MS) 156ff  
 ellipticity 106, 108  
 emulsion PCR 292ff  
 energy gap law 29, 95  
 energy level 19  
 enzyme 80ff  
 enzyme activation 83f  
 enzyme function 80  
 enzyme inhibition 81  
 enzyme kinetics 80  
 enzyme regulation 83f  
 enzyme-substrate complex 81  
 evanescent field 177  
 excitation 21, 96f  
 excitation energy 15  
 excitation intensity function 220  
 excited state 36  
 exon 314  
 external magnetic field 31
- f**  
 flavin 53  
 flavin mononucleotide (FMN) 53  
 – absorption and fluorescence spectra 54  
 flow cytometry 10, 317f  
 fluorescein 62f  
 fluorescence 27ff, 33, 35, 44, 220, 306  
 fluorescence anisotropy 71f, 324f, 331, 334  
 fluorescence assay 326  
 fluorescence-assisted cell sorter (FACS) 317f  
 fluorescence correlation spectroscopy (FCS) 8, 214ff  
 fluorescence cross-correlational spectroscopy (FCCS) 226f  
 fluorescence fluctuation 214ff  
 fluorescence *in situ* hybridization (FISH) 10  
 fluorescence kinetics 6, 93ff  
 fluorescence labelling 5, 61ff  
 fluorescence lifetime 37, 61, 94  
 fluorescence lifetime imaging (FLIM) 94  
 fluorescence linking 61f  
 fluorescence marker 61, 86, 94, 186, 204, 212, 220, 222, 303

fluorescence microscopy 7, 169ff, 259f  
 – conventional fluorescence microscopy 169ff  
 fluorescence polarization 71, 97  
 fluorescence polarization anisotropy (FPA) 5, 70ff, 253  
 – principles 70, 70ff  
 fluorescence polarization assay 265  
 fluorescence quantum yield 34, 62, 219f  
 fluorescence reader 326ff  
 fluorescence recovery after photobleaching (FRAP) 98  
 fluorescence spectrometer 43, 44ff  
 fluorescence spectrum 28, 43ff, 44  
 fluorescence techniques 61ff  
 fluorescence transition dipole moment 72  
 fluorescent protein (FP) 67, 188  
 fluorescing nanoparticle 9, 303, 320  
 fluorescing particle 222  
 Fourier transformation 128f, 133  
 fragment library 289  
 Frank-Condon integral 27f, 42  
 Frank-Condon principle 24ff  
 free induction decay (FID) 129  
 Förster distance 89  
 Förster resonance energy transfer (FRET) 6, 22, 65, 69, 85ff, 226, 229  
 – application examples 90ff  
 – energy diagram 85  
 – principles 84ff  
 – theoretical background 84ff

**g**

gene expression 316  
 Giga-seal 246ff  
 gold surface 67  
 green fluorescent protein (GFP) 204, 317  
 – structure 68  
 ground state bleaching 270f

**h**

haemoglobin 50ff  
 – oxygen binding 51  
 haeme 49ff  
 highest occupied molecular orbital (HOMO) 19, 30f, 304f  
 high-resolution fluorescence microscopy 13, 184  
 high-throughput screening (HTS) 2, 4, 249, 323, 327, 329, 332ff  
 His-Tag 66  
 Hooke's law 235, 241  
 hypermass 163

**i**

immunolabelling 64  
 infrared spectroscopy 116  
 inhibitor 83  
 inside out patch (IOP) 248f  
 internal conversion 30f  
 intersystem crossing 32, 89  
 intrinsic absorption 45ff  
 intrinsic fluorescence spectroscopy 5  
 ion channel 245f  
 – classes 245f  
 ion detection 158ff  
 ionization 156ff  
 ion semiconductor sequencing 297ff  
 ion trap 161  
 iPALM 191  
 isoSTED 191  
 isosurface 17

**j**

Jablonski diagram 33

**k**

Karplus relation 126  
 Kasha's rule 30  
 kinesin 210  
 Kramers-Kronig transformation 109

**l**

laboratory frame 127  
 Laporte's rule 24  
 Larmor frequency 124f  
 laser scanning microscopy 174  
 lead structure 333  
 light 14  
 – interaction with molecules 20  
 light-harvesting complex (LHC) 277  
 light intensity 111, 119, 170, 172, 271  
 light scattering 7, 109ff  
 light-sheet microscopy 178ff  
 Lineweaver-Burk plot 82ff  
 lowest unoccupied molecular orbital (LUMO) 19, 304  
 luciferase 99, 296  
 luciferin 99  
 luminescence 33

**m**

macroscopic magnetization 124, 127f  
 magnetic dipole moment 123  
 magnetic moment 31  
 magnetic resonance techniques 121ff  
 magnetogyric ratio 123

- MALDI spectra 156  
 MALDI-TOF mass spectrum 156  
 mass spectrometer 149, 153, 156, 160  
 mass spectrometry 7, 149ff  
 Mathieu equation 160  
 matrix-assisted laser desorption ionization (MALDI) 149, 157  
 matrix-assisted laser desorption ionization time-of-flight detection (MALDI-TOF) 149ff  
 matrix compound 151  
 maximum tolerated dose (MTD) 335  
 messenger RNA (mRNA) 315  
 Michaelis–Menten constant 82  
 micro-ESI 158  
 microscope 171  
 microscope objective 169, 232f  
 microspheres 303, 320f  
 microtitre plate 326ff  
 microtitre plate formats 327  
 minimum effective dose (MED) 335  
 molar circular birefringence 108  
 molar extinction coefficient 43  
 molecular orbital 17f  
 molecular weight 149  
 – estimation 79  
 momentum 230ff  
 MS-MS techniques 163  
 multifocal detection reader 332  
 multiphoton excitation 9, 258f  
 muscle function 210  
 myoglobin 51f  
 myosin 209f, 213, 251
- n**  
 nano-ESI 158  
 nanoparticle 306  
 near infrared (NIR) region 14  
 negative ionization mode 151, 157  
 next generation sequencing 287ff  
 nicotinamide adenine dinucleotide 52ff  
 – absorption spectrum 53  
 – fluorescence spectrum 53  
 NMR-based structural analysis 138ff  
 noncompetitive inhibition 83  
 nonlinear microscopy 258ff  
 nonlinear optical signal 262  
 nonlinear optical techniques 266ff  
 nonlinear spectroscopy 257ff  
 nonradiative relaxation 30  
 nonradiative transition 27ff  
 nuclear magnetic resonance (NMR) 7, 121ff  
 – primary information deduced from NMR spectra 125  
 – principles 121  
 nuclear Overhauser effect (NOE) 135f  
 nuclear Overhauser effect spectroscopy (NOESY) 135  
 nucleotides 47  
 – absorption spectra 47  
 numerical aperture 171
- o**  
 one-dimensional (1D) NMR spectra 131  
 one-photon excitation (OPE) 258, 260  
 one-photon microscopy 259  
 optical density (OD) 43  
 optical rotatory dispersion 108  
 optical single-molecule detection 203ff  
 optical trap 231, 235  
 optical tweezer 230ff  
 – application examples 236ff  
 – theoretical background 230ff  
 orbital 15ff, 24  
 oscillating dipole 110f  
 outside out patch (OOP) 249
- p**  
 patch clamp configurations 245  
 patch clamping 9, 245ff  
 patch pipette 247ff  
 Pauli's rule 31  
 peptide 45f  
 peptide ladder sequencing 164  
 phase-matching condition 267  
 phenylisocyanate (PIC) 164  
 phenylisothiocyanate (PITC) 164  
 phosphorescence 33, 35  
 photoactivated localization microscopy (PALM) 187ff  
 photoactivatable fluorescent proteins 187  
 photoactivation 187  
 photoconversion 187  
 photomultiplier tube (PMT) 174, 205  
 photon 13, 230ff, 252  
 photoselection 71  
 photoswitching 187  
 photosynthesis 54, 56, 274ff, 280  
 photosynthetic energy conversion 274ff  
 photosynthetic energy flow 276ff  
 photosynthetic energy funnel 274  
 photosystem 275  
 pigment-protein complex 279  
 pinhole 173, 220  
 polarizability 95, 111

polarization 2, 14, 21, 220  
 polarization filter 3, 70  
 polarization ratio 265  
 polarization vector 14, 21, 23, 281  
 polymerase chain reaction (PCR)  
     286  
 positive ionization mode 151, 157  
 primary amino group reactive label 63f  
 probability density 15  
 protein 41ff  
     – isotope distribution 157  
     – optical properties 45  
     – relationship between volume and molecular mass 222f  
 protein sequence analysis 163  
 protein unfolding 244  
 pulsed NMR spectroscopy 126  
 pump beam 270  
 pump-probe spectroscopy 270ff, 276f  
 pyrosequencing 296ff

**q**  
 quadrupole mass analyser 159  
 quadrupole mass spectrometer 159  
 quantum confinement 304  
 quantum dots 304, 305  
 quantum efficiency 34  
 quantum yield 34, 35, 204  
 quencher 95

**r**  
 radiative transitions 27f  
 radiowave pulse 127f  
 radius of gyration 113  
 Raman spectroscopy 116  
 rate constant 34  
 ratiometric methods 69  
 Rayleigh ratio 112  
 reaction centre 277  
 reactive label 61  
 receptor-ligand binding forces 244  
 receptor-ligand complex 216  
 receptor-ligand interactions 78f, 90  
 redshift 47  
 retinal 56  
 RNA 41  
 RNA hairpins, unfolding 238  
 RNA polymerase 238f  
 rotating frame 127  
 rotational correlation time 73, 76,  
     145  
 rotational fluctuation 70  
 Russell-Saunders coupling 142

**s**  
 sanger sequencing 285ff  
 scalar coupling 125, 126  
 scattering methods 105ff  
 second-harmonic generation (SHG) 258,  
     266, 267  
 sequencing library 289  
 sequencing by ligation 294ff  
 single-biomolecule techniques 203ff  
 single-molecule real-time sequencing 299ff  
 singlet oxygen 56  
 Snell's law 176, 233  
 spin angular momentum 123  
 spin labelling 145  
 spin orbit coupling 32  
 spin quantum number 123  
 spin state 124  
 stimulated emission depletion microscopy  
     (STED) 183, 184ff  
     – principle 185  
 Stochastic Optical Reconstruction Microscopy  
     (STORM) 187ff  
 Stokes-Einstein equation 222  
 Stokes shift 29  
 streptavidin 65, 238  
 structural analysis 138  
 structured illumination microscopy  
     (SIM) 195ff  
 suction pulse 249f  
 sulphurylase 296  
 super-resolution optical fluctuation imaging  
     (SOFl) 197ff  
 surface plasmon resonance (SPR) 308f  
 susceptibility 267

**t**  
 tandem mass spectrometer 163  
 2,2,6,6-tetramethylpiperidin-1-oxyl  
     (TEMPO) 142f  
 thiol group reactive labels 64f  
 thiolinker 67  
 third-harmonic generation (THG) 668f  
 three dimensional (3D) super-resolution  
     fluorescence microscopy 190f  
 time-of-flight (TOF) 149  
 titin 244f  
 TOF analyser 149  
 TOF reflectron 154  
 total internal reflection fluorescence (TIRF)  
     microscopy 176ff, 188, 204, 206, 211, 213  
 transient absorption 273  
 transition 15  
 transition density 20

- transition dipole moment 20ff, 23, 35, 73  
transmission 41  
trap stiffness 235  
triplet state 27f, 32  
triplet-state dynamics 224  
two-dimensional diffusion 222  
two-dimensional (2D) NMR spectroscopy 130  
– principle 134  
two-photon excitation (TPE) 258, 260,  
    264, 279  
– advantages 259ff, 263ff  
– disadvantages 259ff  
– properties 263ff  
two-photon microscopy 259
- u**  
ultrafast laser system 262  
ultrafast light-harvesting 274ff  
ultrafast spectroscopy 9, 257ff, 270ff  
ultra high-throughput screening (uHTS) 327  
ultraviolet (UV) 14  
uncompetitive inhibition 83
- v**  
valence band maximum (VBM) 304ff  
vector 1  
vibrational energy 27  
vibrational relaxation 27  
vibrational spectroscopy 7  
vibrational spectrum 115ff  
vibrational transition 117, 118  
vibronic transition 26, 42
- w**  
wave function 15  
wavelength 14  
wavemixing 266ff  
wave vector 231, 268  
whole cell (WC) 249f  
wide-field fluorescence microscopy 174
- z**  
zero mode waveguide 300  
Z'-factor 114  
Zimm plots 326f, 331

# **WILEY END USER LICENSE AGREEMENT**

Go to [www.wiley.com/go/eula](http://www.wiley.com/go/eula) to access Wiley's ebook EULA.